

EVALUATION OF THE NASA-KSC-MILA  
RF BORESIGHT TEST FACILITY  
AT X-BAND AND S-BAND

T.J. Lyon  
Senior Research Engineer  
S.F. Hutchins  
Chief Mechanical Engineer  
C.S. Young  
Research Engineer  
J.S. Hollis  
Principal Engineer

GPO PRICE \$ \_\_\_\_\_  
CFSTI PRICE(S) \$ \_\_\_\_\_  
Hard copy (HC) \$ 7.00  
Microfiche (MF) 1.75

# 653 July 65

Scientific-Atlanta, Inc.  
Atlanta, Georgia 30324

FINAL REPORT

Contract No. NAS10-2103

Prepared  
for

Ground Support Systems Branch  
National Aeronautics and Space Administration  
Merritt Island Launch Area  
John F. Kennedy Space Center

May 1966

N67 13025  
(ACCESSION NUMBER)  
381  
(PAGES)  
80430  
(NASA CR OR TMA OR AD NUMBER)  
G-3  
(THRU)  
11  
(CATEGORY)

207-41370

**EVALUATION OF THE NASA-KSC-MILA  
RF BORESIGHT TEST FACILITY  
AT X-BAND AND S-BAND**

**T.J. Lyon  
Senior Research Engineer  
S.F. Hutchins  
Chief Mechanical Engineer  
C.S. Young  
Research Engineer  
J.S. Hollis  
Principal Engineer**

**Scientific-Atlanta, Inc.  
Atlanta, Georgia 30324**

**FINAL REPORT**

*Contract No. NAS10-2103*

*Prepared  
for*

**Ground Support Systems Branch  
National Aeronautics and Space Administration  
Merritt Island Launch Area  
John F. Kennedy Space Center**

**May 1966**

## ABSTRACT

This report presents results of a program of theoretical and experimental investigation of the NASA-KSC-MILA RF Boresight Test Facility. The objectives of the program were to determine the performance of the range in the elevated and ground-reflection modes of operation at X- and S-bands, and to investigate the compatibility of the range capabilities with the Lunar Excursion Module rendezvous radar and landing radar pre-launch test requirements. Experimental results are presented to demonstrate the capability of the range for obtaining high-accuracy boresight and radiation pattern measurements at X- and S-bands. A study of the rendezvous radar and landing radar test problems is presented, and the range compatibility with specific test requirements is discussed. Theoretical developments pertinent to the program are included as appendices.

PRECEDING PAGE BLANK NOT FILMED.

# TABLE OF CONTENTS

<u>Chapter</u>		<u>Page No.</u>
1	INTRODUCTION	1
2	THE NASA-KSC-MILA RF BORESIGHT TEST FACILITY	2-1
	2.1 Physical Configuration	2-1
	2.2 Source Positioning Equipment	2-3
	2.3 Test Positioning Equipment	2-5
	2.4 Control Room Equipment	2-8
	2.5 The Gemini Spacecraft Mockup	2-8
	2.6 Integration of Delivered Equipment	2-11
3	RANGE EVALUATION TECHNIQUES AND DEVICES	3-1
	3.1 Aperture Field Amplitude Measurements	3-2
	3.2 Polarization Measurements	3-4
	3.3 Boresight Measurements	3-6
4	MEASURED AND CALCULATED DATA	4-1
	4.1 X-Band Measurements	4-1
	4.2 S-Band Measurements	4-40
	4.3 Mechanical Accuracy Measurements	4-53
5	SUMMARY OF THEORETICAL AND EXPERIMENTAL PROGRAM	5-1
	5.1 Theoretical Developments	5-1
	5.2 Experimental Investigations	5-8
6	CAPABILITY OF THE MILA RF TEST FACILITY IN RELATION TO THE LEM RENDEZVOUS RADAR AND LANDING RADAR BORESIGHT PROBLEMS	6-1
	6.1 Introduction	6-1
	6.2 Rendezvous Radar Boresight Test Problem	6-1
	6.3 The LEM Landing Radar Test Problem	6-18

PRECEDING PAGE BLANK NOT FILMED.



## TABLE OF CONTENTS - Continued

<u>Chapter</u>	<u>Page No.</u>
7 RECOMMENDATIONS	7-1
7.1 Facility Modifications	7-1
7.2 Validation Capabilities	7-4
7.3 LEM Landing Radar	7-8
 <u>Appendices</u>	
A THE RECEIVING-APERTURE FIELD OVER A REFLECTING SURFACE	A-1
A.1 Introduction	A-1
A.2 Surface Irregularities	A-1
A.3 Theoretical Development of a General Reflection Coefficient	A-4
A.4 Aperture-Field Components for the MILA Range Configuration	A-11
A.5 Ground-Reflection Operation of the MILA Range	A-13
A.6 Elevated Operation of the MILA Range	A-22
B HEIGHT OF THE APPARENT SOURCE OF RADIATION OVER A PLANAR REFLECTING SURFACE AS SENSED BY A PHASE-MONOPULSE RADAR	B-1
C HEIGHT OF THE APPARENT SOURCE OF RADIATION OVER A PLANAR REFLECTING SURFACE AS SENSED BY AN AMPLITUDE-MONOPULSE RADAR	C-1
C.1 Introduction	C-1
C.2 Apparent Versus Actual Source Height	C-1
D EFFECT OF EXTRANEEOUS SIGNALS ON BORESIGHT MEASUREMENT ACCURACIES	D-1
D.1 Introduction	D-1
D.2 Errors in Amplitude-Monopulse Systems	D-1
D.3 Errors in Phase-Monopulse Systems	D-12

## TABLE OF CONTENTS - Continued

<u>Appendices</u>	<u>Page No.</u>
E APPARENT SOURCE HEIGHT VERSUS ELEVATION SQUINT ANGLE FOR THE GROUND-REFLECTION MODE	E-1
F DIFFRACTION FENCE PLACEMENTS ON A PLANAR RANGE SURFACE	F-1
F. 1 Introduction	F-1
F. 2 Fresnel Zones on a Planar Range Surface	F-2
F. 3 Diffraction Effects of Fence Placements	F-21
G POLARIZATION MEASUREMENTS	G-1
H ANGULAR MEASUREMENT ACCURACY OF THE MILA RF BORESIGHT TEST FACILITY	H-1
H. 1 Introduction	H-1
H. 2 Angle Measurements on a Boresight Range With Specific Reference to the Gemini and LEM Rendezvous Radars	H-1
H. 3 Angle Measurement Error on a Boresight Range	H-9
I SPHERICAL COORDINATE TRANSFORMATION BY EULER ANGLES	I-1
J THE EFFECTS OF PARALLAX IN BORESIGHT MEASUREMENTS OF ASYMMETRICAL ANTENNAS	J-1
J. 1 Introduction	J-1
J. 2 Definition of Terms	J-2
J. 3 Radiation Pattern Calculations	J-10
J. 4 Presentation of Data	J-14
K A PRECISION GROUND-REFLECTION ANTENNA BORESIGHT TEST RANGE	
BIBLIOGRAPHY	

# LIST OF ILLUSTRATIONS

<u>Figure</u>		<u>Page No.</u>
2. 1	Plan View of Radar Boresight Range	2-2
2. 2	Source Positioning Equipment With Four-Foot Paraboloidal Antenna	2-4
2. 3	NASA-MILA RF Boresight Test Facility Positioner Mounted on Special Tilt Base.	2-6
2. 4	Earth-Fixed Spherical Coordinate System Utilized in Boresight Measurements	2-7
2. 5	Relation of the Earth-Fixed Coordinate System to the MILA Range Geometry	2-9
2. 6	Centralized Console of the NASA-KSC-MILA RF Boresight Test Facility	2-10
2. 7	Block Diagram of MILA Boresight Range Instrumentation -- X-Band	2-12
2. 8	Block Diagram of MILA Boresight Range Instrumentation -- S-Band	2-13
3. 1	Schematic Diagram of Field Probe Mechanism	3-3
3. 2	Schematic of X-Band Single-Plane Amplitude-Monopulse System	3-8
3. 3	X-Band Monopulse Device Mounted on Gemini Spacecraft Mockup	3-10
3. 4	Schematic of S-Band Single-Plane Phase-Monopulse System	3-11
4. 1	Aperture Field Patterns -- Ground Reflection Mode -- X-Band	4-4
4. 2	Aperture Field Patterns for Several Transmitter Squint Angles -- Ground Reflection Mode -- X-Band	4-5
4. 3	Circular Polarization Axial Ratio Versus Aperture Position -- Ground-Reflection Mode -- X-Band	4-7
4. 4	Circular Polarization Axial Ratio Versus Frequency -- Ground-Reflection Mode -- X-Band	4-8
4. 5	Apparent Source Height Versus Actual Source Height -- Ground-Reflection Mode -- X-Band	4-9
4. 6	Apparent Source Height Versus Elevation Squint Angle -- Ground-Reflection Mode -- X-Band	4-11
4. 7	Apparent Source Location Versus Azimuth Squint Angle -- Ground-Reflection Mode -- X-Band	4-12
4. 8	Vertical Field Patterns -- X-Band Elevated Range	4-14
4. 9	Vertical Aperture Field Amplitude Patterns -- X-Band Elevated Range	4-16
4. 10	MILA Elevated Range Geometry	4-17

# LIST OF ILLUSTRATIONS - Continued

<u>Figure</u>		<u>Page No.</u>
4. 11	Theoretical and Measured Pitch of Vertical Amplitude Pattern Ripple -- Elevated Mode -- X-Band	4-18
4. 12	Typical A and B Channel Radiation Patterns for the X-Band Amplitude-Monopulse Test Device	4-20
4. 13	Theoretical and Measured Variation of Apparent Source Height with Actual Source Height. Elevated Mode -- X-Band	4-21
4. 14	Multiple Scattering From Diffraction Fences	4-24
4. 15	Pattern Distortion Caused by Multiple Scattering by Diffraction Fences -- Configuration (b)	4-25
4. 16	Vertical Aperture Field Patterns -- Elevated Mode With Three Diffraction Fences -- X-Band -- Configuration (b)	4-26
4. 17	Vertical Aperture Field Patterns -- Elevated Mode With Two Diffraction Fences -- X-Band -- Configuration (e)	4-27
4. 18	Aperture Field Patterns -- Elevated Mode With One 8-Foot Diffraction Fence -- X-Band -- Configuration (h)	4-28
4. 19	Vertical Aperture Field Variation Caused by Diffraction Over A Conducting Fence -- X-Band	4-30
4. 20	Effects of Elevation Squint Angle on Aperture Field Patterns -- Elevated Mode with Three Diffraction Fences -- X-Band	4-31
4. 21	Axial Ratio as a Function of Aperture Position -- Elevated Mode with Single Diffraction Fence -- X-Band	4-32
4. 22	Axial Ratio Versus Frequency -- Elevated Mode with Single Diffraction Fence -- X-Band	4-33
4. 23	Apparent Source Height Versus Actual Source Height -- Elevated Mode with Diffraction Fences -- X-Band -- Vertical Polarization Configuration (h)	4-34
4. 24	Apparent Source Height Versus Actual Source Height -- Elevated Mode with Diffraction Fences -- X-Band -- Horizontal Polarization -- Configuration (b)	4-35
4. 25	Apparent Source Height Versus Actual Source Height -- Elevated Mode with Diffraction Fences -- X-Band -- 45-Degree Linear Polarization -- Configuration (b)	4-36
4. 26	Summary of X-Band Boresight Data for Elevated Mode -- Vertical Sensing (a) With Diffraction Fences (b) Without Diffraction Fences	4-37
4. 27	Measured Azimuth of Source Versus Azimuth Null Offset Angle -- Elevated Mode with Diffraction Fences -- X-Band	4-38
4. 28	Effect of Varying Elevation Squint Angle on Apparent Source Height -- Elevated Mode with Diffraction Fences -- X-Band	4-39

## LIST OF ILLUSTRATIONS - Continued

<u>Figure</u>		<u>Page No.</u>
4. 29	Measured Azimuth of Source Versus Azimuth Squint Angle -- Elevated Mode with Diffraction Fences -- X-Band	4-40
4. 30	Vertical Aperture Field Patterns -- Ground-Reflection Mode -- S-Band	4-42
4. 31	Horizontal Aperture Field Patterns -- Ground-Reflection Mode -- S-Band	4-43
4. 32	Axial Ratio Versus Aperture Position -- Ground-Reflection Mode -- S-Band	4-44
4. 33	Variation of Apparent Source Height with Actual Source Height -- Ground-Reflection Mode -- S-Band	4-46
4. 34	Variation of Apparent Source Height with Vertical Null Offset Angle -- Ground-Reflection Mode -- S-Band	4-47
4. 35	Variation of Apparent Source Height with Horizontal Null Offset Angle -- Ground-Reflection Mode -- S-Band	4-47
4. 36	Aperture Field Patterns -- Elevated Mode -- S-Band	4-49
4. 37	Aperture Field Patterns -- Elevated Mode with Diffraction Fence -- S-Band -- Horizontal Polarization	4-50
4. 38	Vertical Aperture Field Patterns -- Elevated Mode with Diffraction Fence -- S-Band -- Vertical Polarization	4-51
4. 39	Axial Ratio Versus Aperture Position -- Ground-Reflection Mode -- S-Band	4-52
4. 40	Measured Height of Apparent Source Versus Actual Source Height -- S-Band Elevated Range with a Single 8-Foot Fence -- Vertical Polarization	4-54
4. 41	Measured Height of Apparent Source Versus Actual Source Height -- S-Band Elevated Range with a Single 8-Foot Fence -- Horizontal Polarization	4-55
5. 1	Illustration of Parallax Error in Testing an Asymmetrical Antenna with an Asymmetrical Source Antenna	5-7
6. 1	Interpretation of Rendezvous Radar Boresight Specifications	6-3
6. 2	LEM Landing Radar Beam Geometry	6-20
6. 3	Single-Sideband Modulator for Two-Way Boresight Measurement System	6-25
6. 4	Symbolic Diagram of Two-Way Antenna Test System Using SSB Modulation for Making Boresight and Pattern Measurements of the Landing Radar	6-26
6. 5	Phasor Diagram of Signal Incident on Detector of Two-Way Pattern Measurement System Employing Single-Sideband Modulation	6-27

## LIST OF ILLUSTRATIONS - Continued

<u>Figure</u>		<u>Page No.</u>
7. 1	Air-Conditioned, Inflated Radome to Provide Environmental Control During Radar Testing	7-2
7. 2	Moving Target for Line-of-Sight Tracking Tests	7-6
7. 3	Test Positioner Geometry for LEM/LR Tests	7-10
	(a) Method of Measuring the Angle Between the Beam Group Normal and the Altimeter Beam	
	(b) Method of Measuring the Angles Between the Velocity Sensor Beams	
A. 1	Phase Difference Between Rays Reflected From Two Levels	A-3
A. 2	Sketch of the Geometry Relating to the Helmholtz Integral	A-5
A. 3	Coordinate System for Scattering From a Surface	A-7
A. 4	Beam Angles Related to Range Geometry	A-13
A. 5	Planar Wavefronts Related to Range Geometry	A-16
A. 6	Phase of the Aperture Field with $k$ as a Parameter in the Ground-Reflection Mode	A-19
A. 7	Plot of the Aperture Field $E(x)/E_D$ with $k$ as a Parameter in the Ground-Reflection Mode	A-20
A. 8	Decibel Taper of the Normalized Aperture Field $[E(x)/E(x)_{MAX}]$ with $k$ as a Parameter in the Ground-Reflection Mode	A-21
A. 9	Relation of Range Coordinates and Aperture Field Components for a Single Extraneous Signal in the Elevated Mode of Operation	A-23
	(a) Extraneous Signal from a Single Extraneous Reflecting Region of the Range Surface	
	(b) Spatial Period and Amplitude of Resulting Aperture Field Fluctuation in Plane of $E_D$ and $E_R$	
A. 10	Magnitude of Perturbed Field Variation Versus the Ratio of Reflected-Signal to Direct-Signal Strengths for a Plot in the Plane of $E_R$ and $E_D$	A-25
A. 11	Parameters of the Direct-Path and Specularly Reflected Waves Incident on the Test Aperture in the Elevated Mode	A-26
B. 1	Measurement Functions of a Single-Plane Interferometer Antenna Pair	B-1
B. 2	Parameters for the Study of the Receiving-Aperture Phasefront	B-3
B. 3	Apparent Versus Actual Source Height With $k$ as a Parameter as Sensed by a Phase-Monopulse Radar at 1.428 GHz on the MILA Range	B-7

# LIST OF ILLUSTRATIONS - Continued

<u>Figure</u>		<u>Page No.</u>
B. 4	Apparent Versus Actual Source Height With $k$ as a Parameter as Sensed by a Phase-Monopulse Radar at 2.3 GHz on the MILA Range	B-8
B. 5	Apparent Versus Actual Source Height With $k$ as a Parameter as Sensed by a Phase-Monopulse Radar at 10 GHz on the MILA Range	B-9
C. 1	Schematic Representations of Monopulse Devices for Single-Plane Direction Sensing (a) Phase-Monopulse Device (b) Amplitude-Monopulse Device	C-2
C. 2	Relation of Difference-Channel Phasors to Points of Incidence of $\bar{E}_D$ and $\bar{E}_R$ on the Monopulse Directivity Patterns (a) Pattern Angles Related to Incident Signals (b) Direct-Path and Reflected Signals in $\Delta$ Channel	C-2
C. 3	The Apparent Height ( $H$ ) of the Source of Radiation Related to the Test Range Geometry	C-5
D. 1	The Effects of Wide-Angle Extraneous Signals on the Sum- and Difference-Channel Phasors of an Amplitude-Monopulse Radar	D-2
D. 2	Amplitude-Monopulse Radiation Patterns About the Crossover (Boresight) Axis (a) Individual Patterns (b) Straight-Line Approximation-Expanded Scale	D-4
D. 3	Orthogonality of $\bar{\Sigma}$ and $\bar{\Delta}$ Phasors at Corrected Boresight	D-5
D. 4	Maximum Allowable Level of Extraneous Phasors in an Amplitude-Monopulse Circuit Versus Specified Maximum Boresight Errors	D-7
D. 5	Extraneous Signal Level Referenced to Direct-Path Signal	D-11
D. 6	The Effects of Wide-Angle Extraneous Signals on the Phasors of a Phase-Monopulse Radar Circuit (a) Single-Plane Phase-Monopulse Radar (b) Alteration of the Monopulse-Circuit Phasors due to an Extraneous Signal	D-13
D. 7	Required Suppression of Extraneous Energy Incident on a Phase-Monopulse Radar Versus Boresight Error for Worst-Case Phasing at the Summation Point.	D-17
E. 1	Parameters for Consideration of the Effect of Variations in Elevation Squint Angle on the Operation of a Ground-Reflection Antenna Test Range	E-1

# LIST OF ILLUSTRATIONS - Continued

<u>Figure</u>		<u>Page No.</u>
E. 2	Apparent Source Height and the Ratio of Reflected-to Direct-Wave Amplitude as a Function of Elevation Squint Angle in the Ground-Reflection Mode.	E-5
E. 3	Elevation Squint Settings Versus Frequency Ground-Reflection Operation of the MILA Range.	E-6
F. 1	Sketch of Fresnel Zone Boundary on a Planar Range Surface	F-2
F. 2	Relation of Diffraction Parameters to Range Geometry for a Single Diffraction Fence at the Center of the Range	F-21
F. 3	Illustration of the Application of the Cornu Spiral to the Straight-Edge Diffraction Problem (a) Section Through Wavefront (b) Sketch of Cornu Spiral (c) Resultant Field Amplitude	F-23
F. 4	<u>Normalized</u> Field Amplitude for Diffraction Over an Absorbing Straight Edge (Point-Source Illumination)	F-27
F. 5	Envelope and Free-Space Asymptote for the Straight-Edge Diffraction Field	F-28
F. 6	Diffraction Field Distances and Cornu Spiral Factors Versus Source Height at 1.428 GHz with Fence and Receiver Heights as Parameters	F-29
F. 7	Diffraction Field Distances and Cornu Spiral Factors Versus Source Height at 2.3 GHz with Fence and Receiver Heights as Parameters	F-30
F. 8	Diffraction Field Distances and Cornu Spiral Factors Versus Source Height at 10 GHz with Fence and Receiver Heights as Parameters	F-31
F. 9	Relative Fresnel Zone Screening on the MILA Range Provided by 8-Foot and 12-Foot Fences at 10 GHz	F-33
F. 10	Relative Fresnel Zone Screening on the MILA Range Provided by 8-Foot and 12-Foot Fences at 2.3 GHz	F-34
G. 1	Polarization Ellipse for Right-Hand Elliptical Polarization	G-2
G. 2	Geometry Showing Relationship of Polarization Pattern to Polarization Ellipse	G-4
G. 3	Field Components Used in Multiple Component Method of Polarization Analysis	G-5
H. 1	Standard Antenna Coordinate System	H-2
H. 2	IRIG Consolidated Vehicle and Antenna Coordinate System	H-3
H. 3	LEM/RR Coordinate System	H-5



# LIST OF ILLUSTRATIONS - Continued

<u>Figure</u>		<u>Page No.</u>
H. 4	View Along the LEM/RR OY Axis of a Partial LEM Mockup Mounted on a Three-Axis Boresight Positioner	H-6
H. 5	LEM Mockup Inclined Such That the LOS is at an Angle of $+\alpha$ From the LEM/RR $OZ_L$ Axis	H-6
H. 6	View Along the LEM/RR $OZ_L$ Axis of a Partial LEM Mockup Mounted on a Three-Axis Boresight Positioner	H-8
H. 7	View Along the LEM/RR $OZ_L$ Axis of a Configuration Utilizing the Positioner Upper-Azimuth Axis for LEM/RR Shaft Motion	H-8
H. 8	Spherical Coordinate System Employed with Two Orientations of MILA Test Positioner	H-10
H. 9	A Direction Described in Two Coordinate Systems	H-12
H. 10	Antenna Positioner With Orthogonality Error	H-13
H. 11	Spherical Triangles of Figure H. 10	H-14
H. 12	Antenna Positioner With Collimation Error	H-15
H. 13	Spherical Triangles of Figure H. 12	H-16
I. 1	Coordinate Axes Rotated Through the Euler Angles $\alpha, \beta, \gamma$	I-1
I. 2	A Direction Described in Two Coordinate Systems	I-2
I. 3	Spherical Triangles From Figure I. 2	I-3
J. 1	Coordinate Systems Employed for Antenna Measurements, Showing Parallax	J-2
J. 2	Geometry Defining Center of Parallax	J-6
J. 3	Geometry Defining Center of Phase	J-8
J. 4	Schematic Representation of Single-Plane Monopulse Sensor	J-9
J. 5	Aperture Geometry for Theoretical Development of Aperture Field Method	J-11
J. 6	Aperture Geometry Employed in Antenna Pattern Calculations	J-13
J. 7	Functions $F(o, y, z)$ Employed in Computer Calculations	J-15
J. 8	Results of Parallax and Center-of-Phase Calculations, $K_2=0, K_5=0$	J-16
J. 9	Results of Parallax and Center-of-Phase Calculations, $K_2=0.5, K_5=0$	J-17
J. 10	Results of Parallax and Center-of-Phase Calculations, $K_2=1.0, K_5=0$	J-18
J. 11	Results of Parallax and Center-of-Phase Calculations, $K_2=0, K_5=\pi/2$	J-19

# LIST OF ILLUSTRATIONS - Continued

<u>Figure</u>		<u>Page No.</u>
J. 12	Results of Parallax and Center-of-Phase Calculations, $K_2=0.5$ , $K_5=\pi/2$	J-20
J. 13	Results of Parallax and Center-of-Phase Calculations, $K_2=1.0$ , $K_5=\pi/2$	J-21
J. 14	Results of Parallax and Center-of-Phase Calculations, $K_2=0$ , $K_5=-\pi/2$	J-22
J. 15	Results of Parallax and Center-of-Phase Calculations, $K_2=0.5$ , $K_5=-\pi/2$	J-23
J. 16	Results of Parallax and Center-of-Phase Calculations, $K_2=1.0$ , $K_5=-\pi/2$	J-24
J. 17	Calculated Boresight Direction, $K_5=0$	J-26
J. 18	Calculated Boresight Direction, $K_5=\pi/2$	J-27
J. 19	Calculated Boresight Direction, $K_5=-\pi/2$	J-28

## ABBREVIATIONS

A partial listing of abbreviations and acronyms used in the text of this report is given below, in alphabetical order.

BW --- Beamwidth of main radiation lobe  
CSM --- Command and Service Module  
CW --- Continuous wave  
DC --- Direct current  
FM --- Frequency modulated  
GAEC --- Grumman Aircraft Engineering Corporation  
IEEE --- Institute of Electrical and Electronic Engineers  
IRIG --- Inter-range Instrumentation Group  
KSC --- Kennedy Space Center  
LEM --- Lunar Excursion Module  
LOS --- Line of Sight  
LR --- Landing Radar  
MILA --- Merritt Island Launch Area  
MIT --- Massachusetts Institute of Technology  
MSC --- Manned Spacecraft Center  
NAA --- North American Aviation  
NASA --- National Aeronautics and Space Administration  
RCA --- Radio Corporation of America  
RF --- Radio Frequency  
RMS --- Root-mean-square  
RR --- Rendezvous Radar  
RSS --- Root-sum-square  
RYAN --- Ryan Electronics  
SSB --- Single-sideband  
TR --- Transponder  
WSMR --- White Sands Missile Range

## CHAPTER 1

### INTRODUCTION

This report presents results of a program of theoretical and experimental evaluation to determine the extended frequency capability of the NASA-KSC-MILA Radio Frequency Boresight Test Facility. The work was accomplished by Scientific-Atlanta, Incorporated, for the Ground Support Systems Branch of the John F. Kennedy Space Center of the National Aeronautics and Space Administration, under Contract NAS 10-2103.

The objectives of the program were to:

- (1) determine the performance of the range in the elevated and ground-reflection modes of operation at X- and S-bands, and
- (2) investigate the compatibility of the range capabilities with the Lunar Excursion Module rendezvous radar and landing radar pre-launch test requirements, and recommend facility modifications for testing these radars.

The various systems of the Apollo program are being developed under the direction of NASA-Manned Spacecraft Center. Grumman Aircraft Engineering Corporation is the prime contractor for the Lunar Excursion Module. Radio Corporation of America, under sub-contract from GAEC, is responsible for the rendezvous radar and landing radar systems. The rendezvous radar is being developed by RCA, and the landing radar is being developed under sub-contract by Ryan Electronics.

The experimental program was accomplished with support and assistance of personnel of the Ground Support Systems Branch under the direction of Mr. J. H. Lane and the direct supervision of Messrs. L. W. Bell and W. R. Parry.

A brief description of the major features of the MILA facility is given in Chapter 2 of this document. The techniques and devices employed in the experimental evaluation program are described in Chapter 3, and resulting measured and calculated data are presented in Chapter 4. Theoretical developments pertinent to the evaluation program are included as Appendices; a summary of the results of the experimental and theoretical program is given in Chapter 5. Chapter 6 relates the capabilities and limitations of the existing facility to the requirements of the LEM/RR and LEM/LR boresight test problems. Chapter 7 presents recommendations for modifications of the facility indicated by the requirements of the LEM program, and describes basic test procedures.

## CHAPTER 2

### THE NASA-KSC-MILA RF BORESIGHT TEST FACILITY

The MILA antenna test range was originally fabricated specifically to meet KSC test requirements under the Gemini program<sup>2-1</sup>, and secondarily as a general purpose antenna test facility. The range was designed and validated as a ground-reflection facility for operation at L-band as a cooperative effort between Scientific-Atlanta, Inc., and McDonnell Aircraft Corporation, the prime contractor for the Gemini Spacecraft, and is instrumented with Scientific-Atlanta, Inc., equipment. Pertinent details of the range geometry and instrumentation are presented in the following paragraphs.

#### 2.1 Physical Configuration

The MILA range provides a nominal separation between source and test antennas of 1000 feet, and has the dual capability of operating as a ground-reflection range and as a conventional elevated range. As shown in the plan view of Figure 2.1, the primary range surface is compacted fill, graded to  $\pm 0.5$  inch and covered with Bermuda grass. Suppression of wide-angle and diffuse scattering of radiated energy is afforded by an ancillary cleared area which extends 500 feet to each side of the range axis and 500 feet beyond the test site. Restriction of vehicular traffic is accomplished with a traffic gate which is remotely operated from the control building.

A 50-foot timber tower at the transmitting end of the range supports a dual-rail track for positioning the source antenna in height from ground level to approximately 45 feet. Protective enclosures adjacent to the tower are provided for the source hoisting machinery, the microwave power supply, and other mechanisms and instrumentation described in paragraph 2.2 of this chapter.

The range control building is a two-story concrete block structure oriented such that its sides make angles of 45 degrees with the range axis. To further suppress

<sup>2-1</sup>

J.S. Hollis, R.E. Pidgeon, Jr., and R.M. Schutz, "A Precision Ground-Reflection Antenna Boresight Test Range," presented at the Fourteenth Annual Symposium on USAF Antenna Research and Development, University of Illinois, October 6-8, 1964. (This paper is included as Appendix K of this document.)

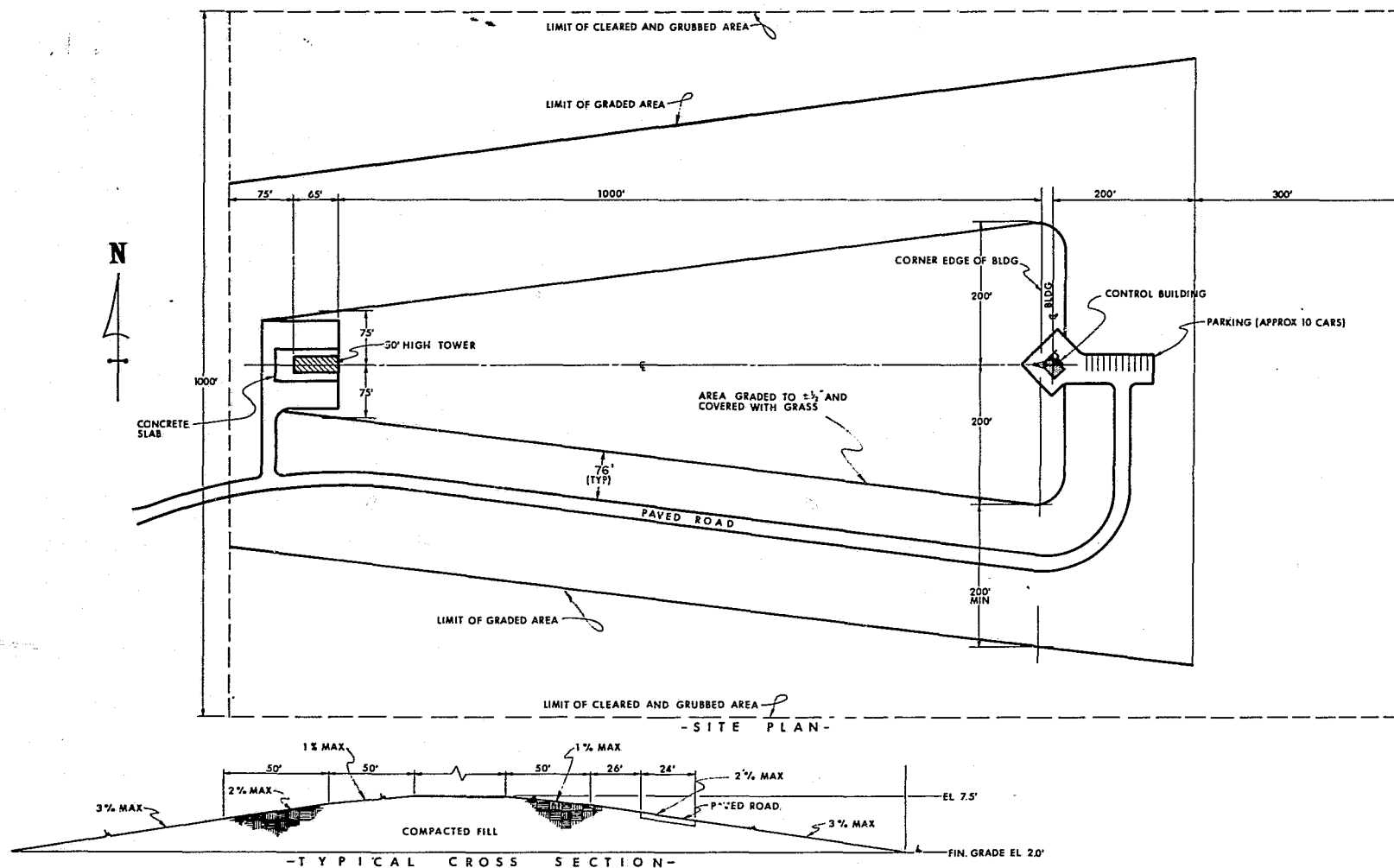


Figure 2.1. Plan View of Radar Boresight Range

reflections from the support structure, the two illuminated sides of the building are covered with weatherproof, high performance microwave absorbing material. Floor space in each level is approximately 350 square feet, and the roof deck is a 20x30 foot rectangle including a raised square positioner platform which is 9-2/3 feet on a side. The first level houses air conditioning equipment, an electronics work area and head facilities. Range instrumentation discussed in paragraph 2.4 below, and, at present, test sets for the Gemini rendezvous radar, are housed in the main control room on the second level. The positioner platform is mounted on a support column, which is independently mounted on high-strength footings and is totally enclosed within the air-conditioned control building structure.

Prime power for the range is provided by a 3-phase, 112.5 kva substation adjacent to the control building, which supplies 60 Hz, 480-120/208 volt power.

## 2.2 Source Positioning Equipment

The signal-source antenna is supported by a positioning system that provides polarization rotation, azimuth and elevation pointing-angle adjustment (squint), and height control. The source antenna is attached to the mounting flange of the polarization positioner (see Figure 2.2) so that the antenna axis is concentric with the axis of polarization rotation. Motorized, remotely controlled, linear actuators provide azimuth- and elevation-angle adjustment to the mounted antenna unit; in the illustrated configuration, the axis of the transmitted signal can be directed above or below the horizontal and right or left of the range center-line by any selected angle up to 4.5 degrees.

Supporting the complete assembly is a carriage that moves on vertical rails to position the source antenna at any selectable height from 0.5 foot above ground level to over 40 feet above ground level. The dc-drive hoist mechanism is provided with adjustable limit switches for each direction of travel to prevent over travel.

All motions of the source antenna positioning assembly are driven by dc motors that provide reversible, variable-speed control from the console in the control room. Each of the four motions, polarization, azimuth squint, elevation squint, and height, are provided with synchro readouts. Synchro indicators in the

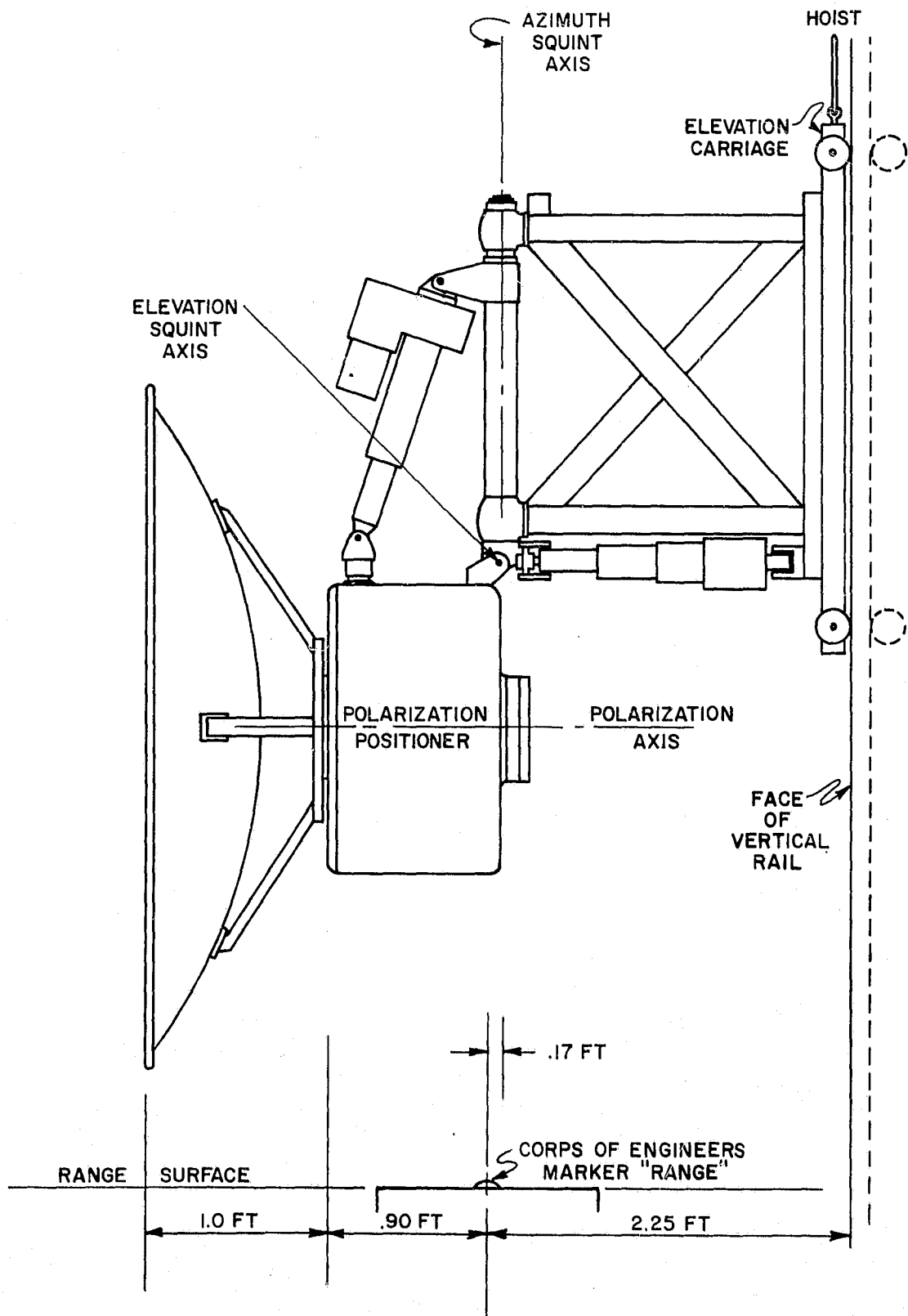


Figure 2.2. Source Positioning Equipment With Four-Foot Paraboloidal Antenna



console provide a means of continuously monitoring each function. In addition to the linear actuators and the polarization positioner, outboard weatherproof enclosures are mounted on the motorized carriage for housing such instrumentation as RF oscillators, phase-lock synchronizer units, and transmitter phase and amplitude circularity systems. These units are also equipped for remote control and indication at the control room console.

### 2.3 Test Positioning Equipment

The heavy duty three-axis antenna positioner which was utilized in the experimental measurements is a Scientific-Atlanta, Inc., azimuth-over-elevation-over-azimuth unit. It is mounted on a special tilt-base (Figure 2.3) that permits the inclination of the lower azimuth axis to be adjusted up to 5 degrees from the vertical. The axis of the tilt mechanism is normal to the range center-line. The summary below is a partial listing of the positioner specifications:

Maximum Vertical Load	40,000 pounds
Maximum Bending Moment	75,000 pound-feet
Torque, Lower Azimuth	18,000 pound-feet
Torque, Upper Azimuth	6,000 pound-feet
Synchro Ratio, All Axes	1:1 and 36:1
Upper and Lower Azimuth	
(1) Position Command Accuracy	0.01 degree
(2) Position Readout Accuracy	0.01 degree
Elevation	
(1) Position Command Accuracy	0.05 degree
(2) Position Readout Accuracy	0.05 degree

The accuracy specifications listed above for the azimuth and elevation axes are over the total travel of each axis, that is, for 360 degrees of azimuth rotation and 135 degrees of elevation rotation. Over small angles the readout and the position command accuracy of each axis is better than 0.005 degree. (See section 4.3.)

The calibration and measurements procedure for the Gemini Rendezvous Radar required the lower azimuth axis to be inclined toward the signal source transmitter antenna through an angle of  $1^{\circ}44'34''$  (Figure 2.3). The same angle of inclination was utilized for all measurements of this study.

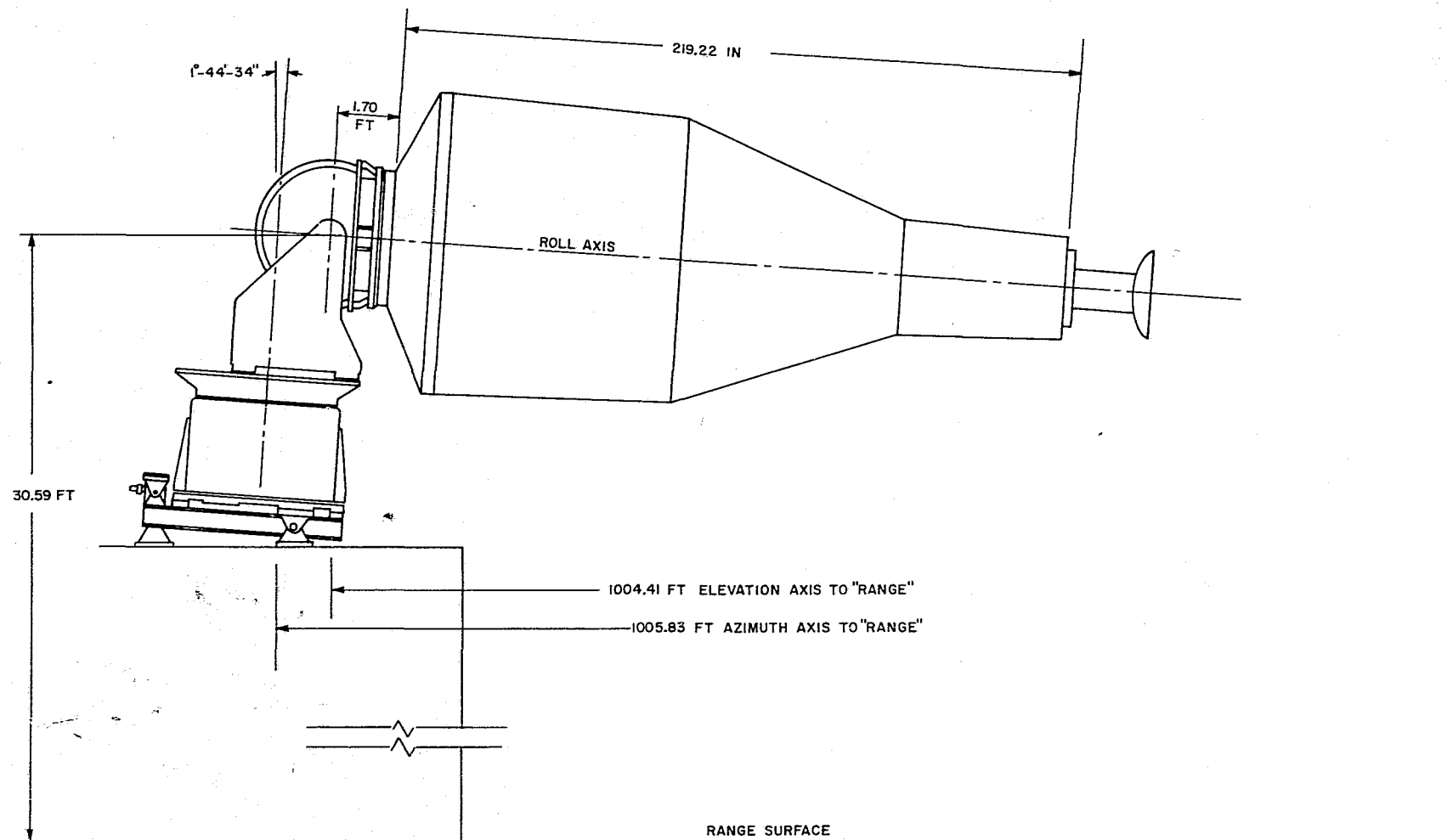


Figure 2.3. NASA-MILA RF Boresight Test Facility Positioner Mounted on Special Tilt Base. In the picture the Gemini Spacecraft Mockup is employed as a "bracket". The test device shown mounted on the mockup is an X-band amplitude monopulse sensor which was employed in the evaluation program.

In making antenna pattern measurements the positioner is used to rotate or position an antenna relative to a stationary signal source antenna. The direction of the signal source antenna relative to the antenna under test is described in terms of  $\phi$  and  $\theta$  of the antenna's spherical coordinate system, which is considered fixed to the antenna under test and moves with the antenna. In making boresight measurements two of the positioner's motion axes move a sighting or pointing axis to specific selected directions relative to an earth-fixed coordinate system. The directions are described in terms of  $\phi$  and  $\theta$  of the fixed spherical coordinate system, as indicated by digital indicators; these directions are compared with the directions indicated by the readout of the system under test after correction for parallax (see Appendix J). In the latter application the positioner is referred to as a direction instrument.

The monopulse measurements described in Chapter 3 of this document were made with the MILA positioner system being utilized as a direction instrument. The earth-fixed spherical coordinate system in which the azimuth and elevation angles were measured is shown in Figure 2.4. Figure 2.4 illustrates the conventional spherical coordinate system of an elevation ( $\theta$ ) over azimuth ( $\phi$ ) configuration. Rotation of the elevation axis OA permits movement of the direction

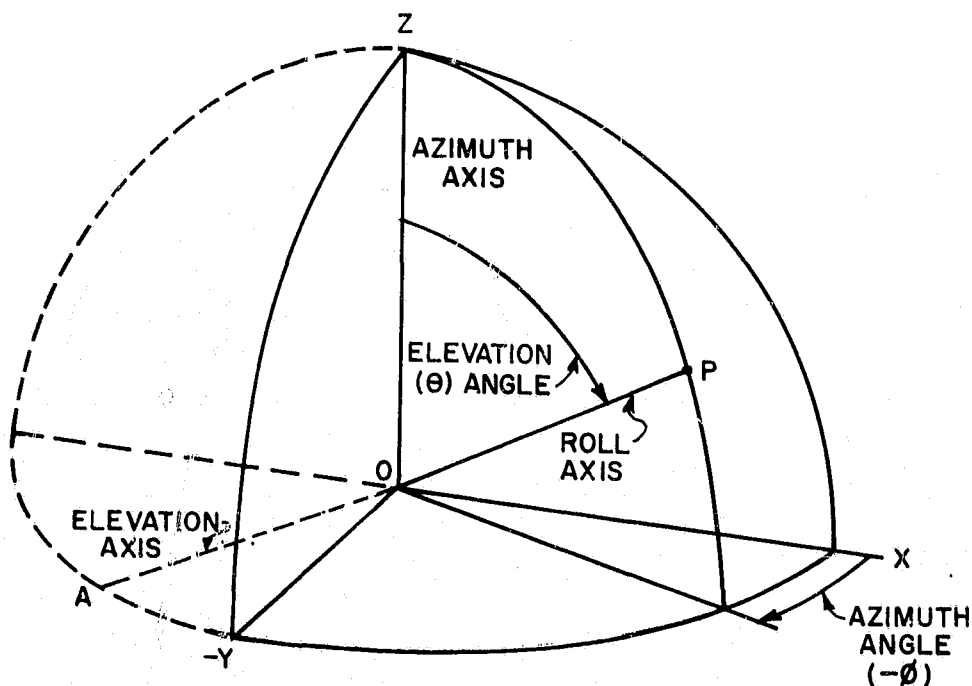


Figure 2.4. Earth-Fixed Spherical Coordinate System Utilized in Boresight Measurements

or pointing axis to selected elevation ( $\theta$ ) angles. For the MILA monopulse measurements the upper azimuth or roll axis was utilized as the direction axis. Rotation of the lower azimuth ( $\phi$ ) axis moves both the elevation axis and the pointing axis so that the pointing axis is positioned to the required azimuth ( $\phi$ ) angle.

In the three-space coordinate system XYZ the polar axis OZ is coincident with the stationary, earth-fixed, lower azimuth axis of the positioner. Coordinate axis OX is the direction from the positioner to the U.S. Army Corps of Engineers marker "RANGE". Marker "RANGE" (Figure 2.5) is approximately level with the antenna range surface and 0.17 foot in front of the source antenna azimuth squint axis. The MILA multi-axis positioner has elevation angle zero defined as the position of coincidence of the positioner's roll axis (OP) with the azimuth axis OZ.

Azimuth ( $\phi$ ) angle zero is defined as coincidence of the roll axis with the vertical plane through OX. The azimuth angle indicator in the control room console provides two readouts. One shows increasing angle with counterclockwise rotation and the other shows increasing angle with clockwise rotation of the azimuth axis<sup>2-1</sup>. All azimuth angles in the current study are from the indicator that gives increasing angle with clockwise rotation.

#### 2.4 Control Room Equipment

Operation of the range either as a general purpose antenna measurement facility or as a boresight facility is conducted from the centralized console depicted in Figure 2.6. The units shown are, with the exclusion of the optical boresight equipment, standard Scientific-Atlanta range instrumentation items, and are not discussed in detail here. With integration of the equipment delivered under Contract NAS10-2103, the range is instrumented for operation at frequencies in L-, S- and X-band.

#### 2.5 The Gemini Spacecraft Mockup

The bulk of the measurements reported in this document were made with the Scientific-Atlanta multi-axis test positioner used in the same manner that a

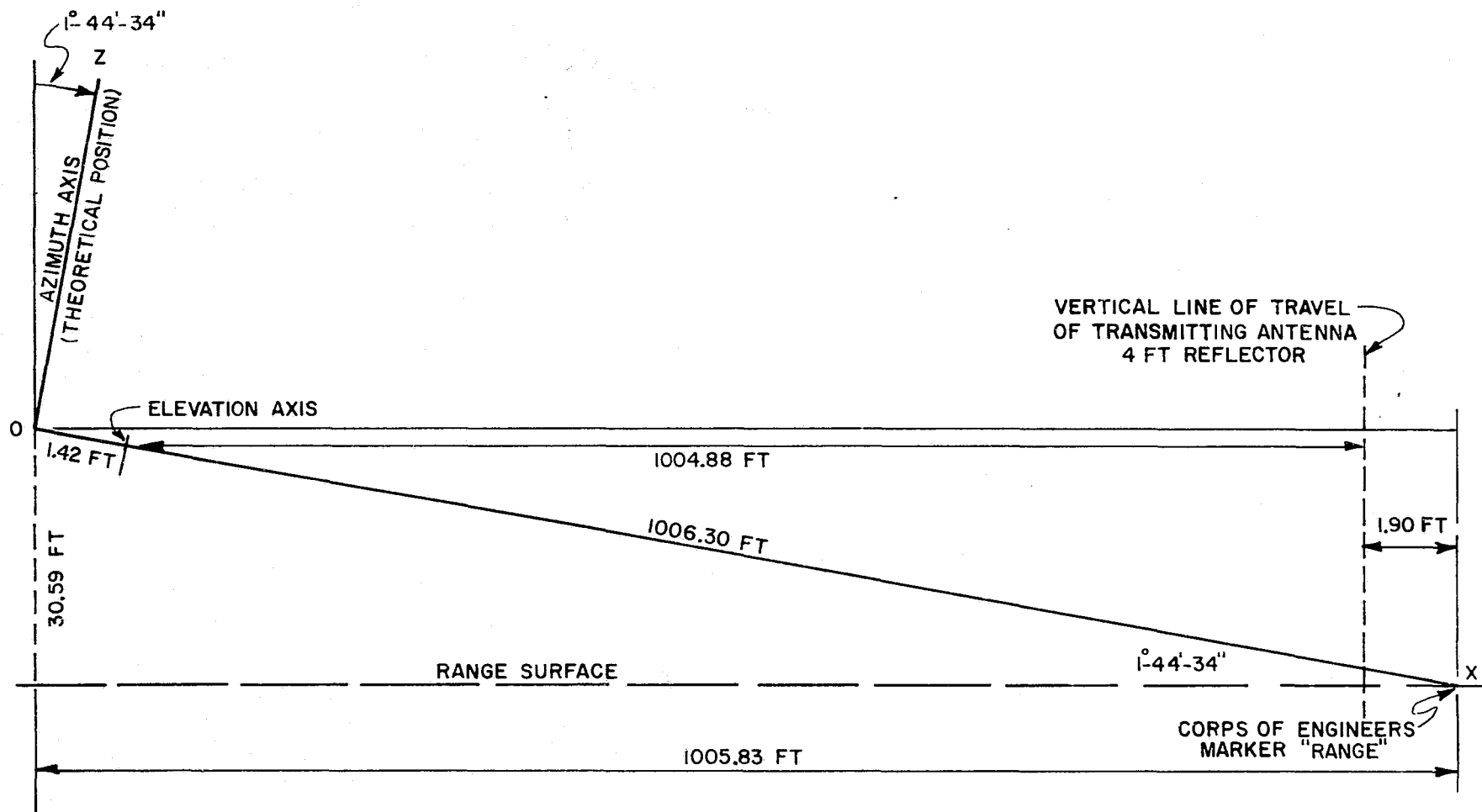


Figure 2.5. Relation of the Earth-Fixed Coordinate System to the MILA Range Geometry. The 1004.88-foot throw distance is calculated for a 4-foot diameter paraboloidal transmitting antenna.

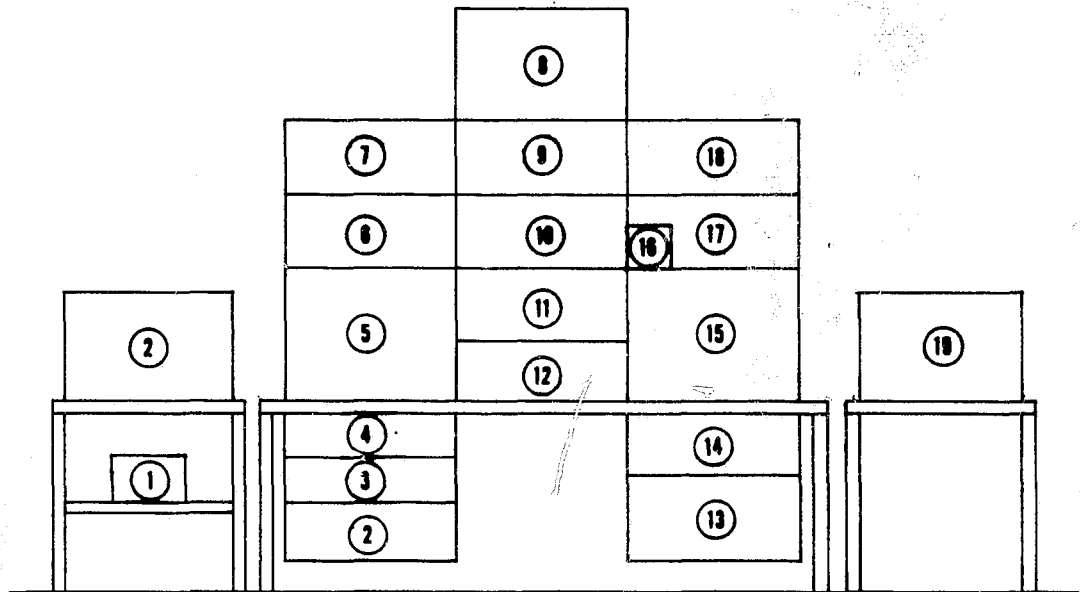


Figure 2.6. Centralized Console of the NASA-KSC-MILA  
RF Boresight Test Facility

- ① Monopulse Test Device Phase & Amplitude Control
- ② Radiation Distribution Printer
- ③ Test Positioner Programmer
- ④ Transmitter Tuning Unit
- ⑤ Wide-Range Receiver (20 MHz to 100 GHz)
- ⑥ Transmitter Height, Squint and Polarization Indicators
- ⑦ Transmitter Circularity Control Indicators
- ⑧ Remote Optical Boresight Display and Control Unit
- ⑨ Test Positioner  $\theta, \phi$  Offset Unit
- ⑩ Test Positioner  $\theta, \phi$  Indicators
- ⑪ Test Positioner  $\theta, \phi$  Digital Command and Readout Unit
- ⑫ Test Positioner  $\theta, \phi$  Control Unit
- ⑬ Storage Drawer
- ⑭ Transmitter Phase-Lock Unit
- ⑮ Rectangular Coordinate Antenna Pattern Recorder
- ⑯ Aperture Field Probe Polarization Control
- ⑰ Recorder Switch Panel
- ⑱ Test Positioner, Source Positioner, Transmitter Circularity and Aperture Field Probe Control Unit
- ⑲ Polar Coordinate Antenna Pattern Recorder

conventional model tower is employed. The full-scale RF model of the Gemini spacecraft, which is employed in boresight tests of the Gemini program, was employed as an extension bracket coincident with the upper azimuth axis of the test positioner. The spacecraft mockup is a semi-monocoque design chosen to provide high mechanical integrity; the mockup was designed by McDonnell Aircraft Corporation and fabricated by the 6549th Maintenance Squadron, Patrick Air Force Base, Florida. The inner skin, which provides nearly all of the structural strength, is thermally insulated from the outer skin. The interior of the mockup is cooled by air supplied from the air-conditioned control building to reduce structural deformations from stresses caused by non-uniform solar heating. As discussed in Chapter 3 of this document, the X-band and S-band monopulse test devices were designed to mount on the mockup in the same manner as the Gemini rendezvous radar package, and to utilize existing control- and RF-cabling routed to the devices via the mockup.

## 2.6 Integration of Delivered Equipment

In addition to X-band and S-band test devices, equipment delivered under Contract NAS10-2103 included phase-locked RF sources, transmitting antennas, and necessary cabling for operating in the ground-reflection and elevated modes at both X- and S-bands. The interconnections of the delivered hardware with the existing boresight range equipment are shown in the block diagrams of Figures 2.7 and 2.8.

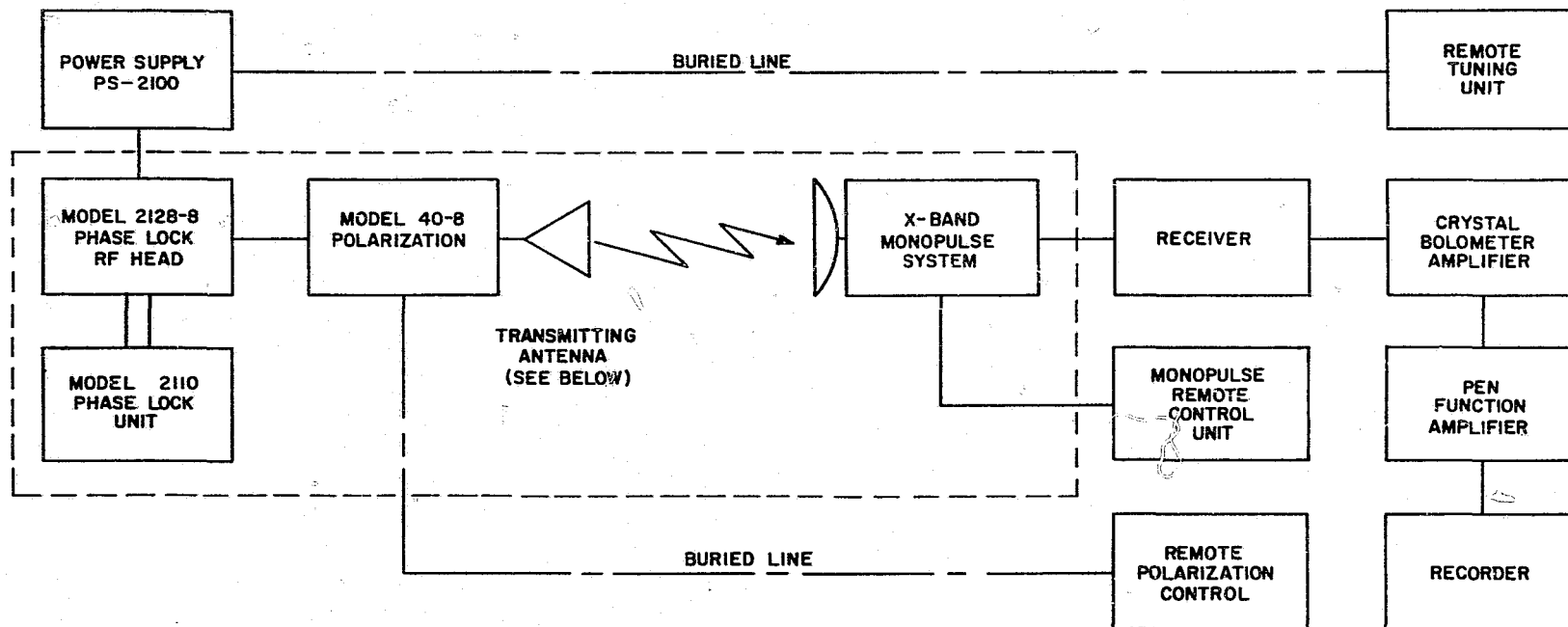


Figure 2.7 Block Diagram of MILA Boresight Range Instrumentation -- X-Band

For ground-reflection operation, a series 40-8/1 conical horn with corrective lens is used as the transmitting antenna. In the elevated mode, the transmitting antenna is a series 40-8/4 Cassegrain reflector which is fed by the standard feed horn of the series 40-8 Polarization Unit.



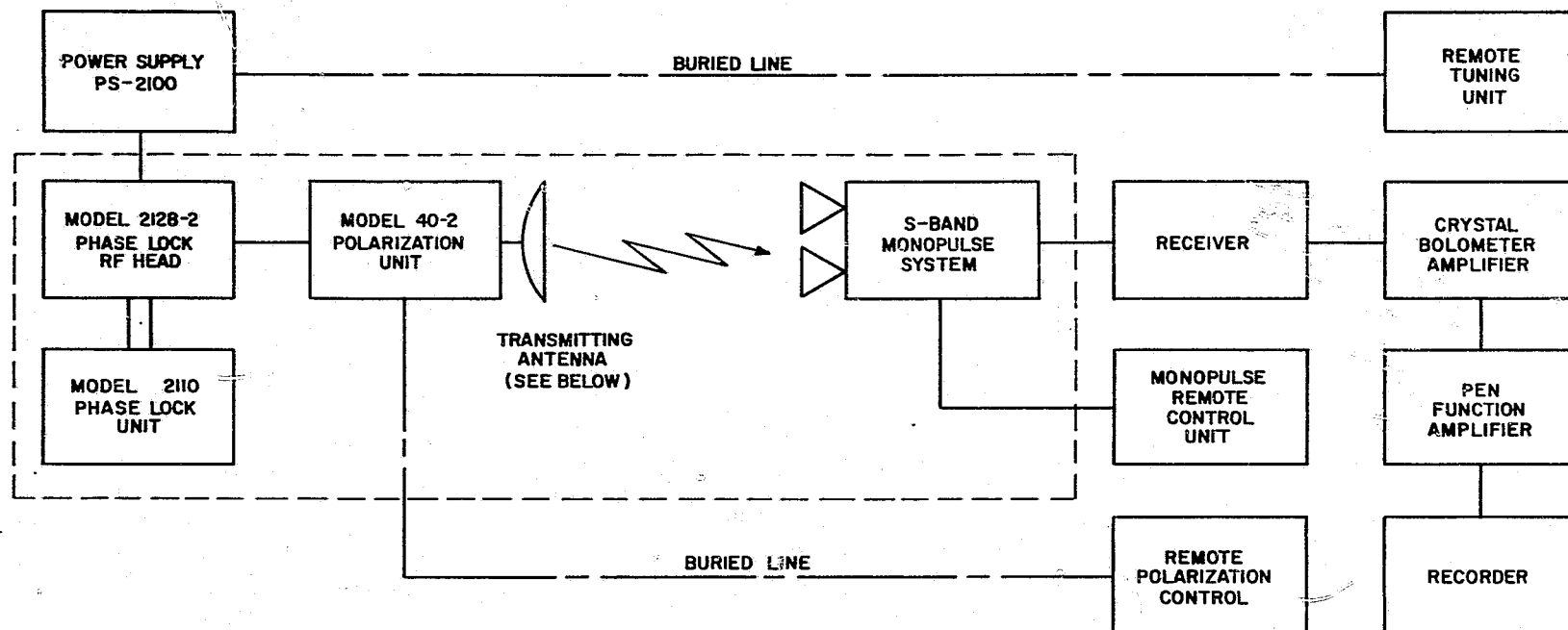


Figure 2.8 Block Diagram of MILA Boresight Range Instrumentation -- S-Band

A Model 22-4 reflector was supplied under this contract for use as a transmitting antenna in the ground-reflection mode. An existing 8-foot reflector was used as the transmitting antenna for elevated operation.

## CHAPTER 3

### RANGE EVALUATION TECHNIQUES AND DEVICES

As in any test problem, accurate antenna measurements require achievement of a test environment which adequately simulates the operational environment of the device under test. The specific environmental factor which will be considered in this section is the illumination of the test aperture.

Most antennas operate over ranges which are long in comparison with the aperture size, thus only a small solid angle of a transmitted radiation pattern\* is subtended by the antenna of interest. In its operating environment, the antenna will be illuminated by a direct-path spherical wave of very large radius so that the phase, amplitude, and polarization of the incident wave will be very nearly constant over the test aperture. If the antenna operates in a cluttered environment, as near the earth for example, it will receive energy by reflection or diffraction by extraneous paths, usually, but not always, through the sidelobe regions of its directivity pattern; measurements which take into account such sources are termed in situ measurements. The discussion here applies basically to free space measurements in which only a single path is desired between a source antenna and the antenna under test.\*\*

The NASA-MILA range has been evaluated under the current contract at X- and S-bands through a program of experimental measurements. In view of current and possible future test responsibilities of the MILA facility, the experimental program was directed in part toward the determination of the capability of the facility for obtaining high-accuracy boresight measurements at frequencies in these bands. Three measurement techniques were utilized in the evaluation:

- (1) Aperture field amplitude measurements,
- (2) Aperture field polarization measurements, and
- (3) Boresight comparison measurements.

---

\* This report will consider all antennas to be tested on receiving. The receiving characteristics thus obtained will be identical to the transmitting pattern, in accordance with the Rayleigh-Helmholtz reciprocity theorem, for all antennas except for those containing non-reciprocal components, such as ferrites.

\*\* In the Gemini and LEM radar problems, it is necessary to take into account effects of the spacecraft on the operation of the antenna. The problem of the effect of the spacecraft on the boresight measurements of the LEM rendezvous and landing radars is discussed in Chapter 6, the Gemini problem is discussed in Appendix K.

These techniques, which are discussed individually below, were employed to compare the quality of measurements obtained with several range configurations. Measurements were made in the ground-reflection mode and in the elevated mode with and without diffraction screens to determine the optimum range configuration for general antenna measurements and specifically for boresight testing at each frequency. Certain mechanical accuracy tests were conducted to supplement the standard measurements of the facility calibration program; results of these frequency-independent measurements are discussed in section 4.3.

### 3.1 Aperture Field Amplitude Measurements

#### 3.1.1 Discussion

The field in the test aperture consists of the sum of the field produced by direct-path radiation from the source antenna and the field produced by reflections from extraneous sources (see Appendix A). The total field is considered to consist of (1) the incident field, which includes the direct-path wave and the field produced by reflections from sources in front of the test aperture, and (2) the field caused by extraneous reflections from extremely wide angles and from the rear of the test aperture. The discussion here applies to measurement of the purity of the incident field. The effects of reflections from wide angles (and of perturbations of the incident field) were studied by means of boresight comparison measurements which are discussed in Appendix K.

#### 3.1.2 Amplitude Measurement Procedures

Measurements of the amplitude of the incident field were made with the field-probe mechanism shown schematically in Figure 3.1. The probe mechanism is basically a 16-foot beam along which a carriage supporting a probe antenna is driven to measure the incident field strength as a function of position. The probe carriage position is remotely controlled. A synchro signal indicating the position of the probe drives a position indicator and the angular coordinate of the rectangular recorder chart in the receiving console, permitting plots of the received field amplitude versus radial aperture position to be obtained. For these measurements, the probe mechanism was mounted on the front of the Gemini spacecraft mockup as shown. The line of exploration was selected by rotating the mockup about its roll axis, allowing measurements to be made along radial lines in the test aperture.

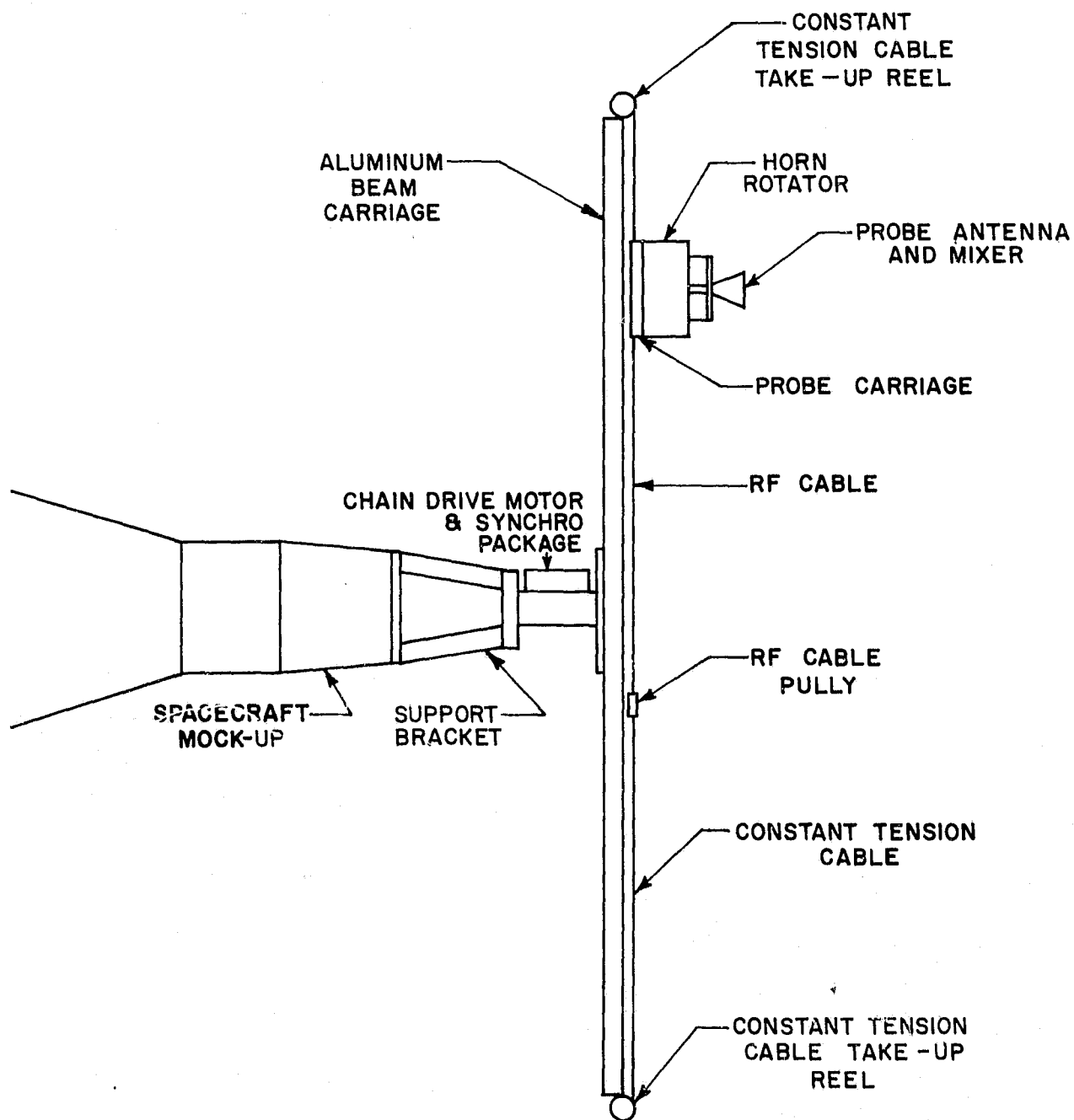


Figure 3.1. Schematic Diagram of Field Probe Mechanism

Test with the field probe device are limited to sampling the field incident on the test aperture from the forward direction. The presence of the probe mechanism presents a reflecting surface and distorts any energy distribution arriving from the rear of the test aperture (such as reflections from the positioner or control building). Horns with beamwidths of approximately 30x35 degrees were used as sampling antennas in order to suppress the reception of wide-angle and rearward signals.

Sets of aperture field probe measurements were made for X- and S-bands. The measurements were made for both the elevated and ground-reflection modes of range operation for horizontal and vertical polarizations. Measurements were included to document the effects of changing range parameters such as transmitter height, transmitter boresight direction, diffraction screen configurations, etc. Data obtained from these tests are presented and discussed in Chapter 4.

### 3.2 Polarization Measurements

#### 3.2.1 Discussion

In addition to the phase and amplitude requirements listed in the introduction to this section, simulation of far-field operation on a test range requires that the test aperture be illuminated by a wave possessing the proper polarization characteristics. Polarization errors at the test range can arise from three primary sources. The polarization characteristics of the transmitting antenna will vary somewhat over the solid angle which is subtended by the test aperture, and the polarization characteristics can be distorted by atmospheric inhomogeneities or by reflection from the range surface. It can be shown that atmospheric effects will generally be negligible on a 1000-foot range<sup>3-1</sup> such as the MILA facility. The results shown in Appendix A imply that upon reflection a wave will not identically maintain its original polarization characteristics even if the reflection is specular in nature except for vertical and horizontal transmitted polarizations. Any depolarization caused by the reflecting surface can cause degradation of the polarization in the receiving aperture.

<sup>3-1</sup>

Jack Chastain, et al., Investigation of Precision Antenna Pattern Recording and Display Techniques, Final Report, March 1963, AD415-912.

Thus, depolarization of the aperture field is associated with, although not solely dependent on, the amount of extraneous energy present.

When the polarization of a receiving-aperture field is explored by rotating a linearly polarized probe antenna about an axis which is coincident with the direction of propagation, the amplitude of the signal at the terminals of the probe antenna is proportional to  $(P_r)^{\frac{1}{2}}$ , where

$$P_r = \frac{P_o G G'}{2} \left( \frac{\lambda}{4\pi R} \right)^2 \left[ 1 + \frac{r^2 - 1}{r^2 + 1} \cos 2\alpha \right]. \quad (3-1)$$

In equation (3-1),

$P_r$  is the power received by the probe antenna,

$P_o$  is the input power at the terminals of the transmitting antenna,

$G$  is the gain of the transmitting antenna in the direction of the receiving antenna,

$G'$  is the gain of the receiving antenna in the direction of the transmitting antenna,

$R$  is the separation between antennas,

$r$  is the axial ratio of the transmitting antenna in the direction of the receiving antenna, and

$\alpha$  is the angle between the maxima of the polarization ellipses of the two antennas.

The polarization pattern of the incident field at the point of observation is given by the term in brackets in equation (3-1). It is seen that such a pattern will have maxima at  $\alpha=0$  or  $\pi$  and minima at  $\alpha=\pm\pi/2$ , and will define the tilt angle and the axial ratio of the polarization ellipse; determination of the sense of rotation requires supplemental measurements as discussed in Appendix G.

### 3.2.2 Polarization Measurement Procedures

The polarization characteristics of the field incident on the test aperture were measured at X- and S-bands for horizontal, vertical, and circular polarizations. The tests consisted of rotating a linearly polarized horn in the incident field to obtain polarization plots in accordance with the discussion of paragraph 3.2.1. The horn was mounted on a small polarization positioner which was in turn mounted on the carriage of the probe mechanism described in section 3.1. The polarization direction of the horn was read out by a synchro; recordings of the incident polarization could thus be made at any point in a 16-foot diameter

circular aperture. The frequency dependence of the aperture polarization was investigated by obtaining polarization plots as a function of frequency about the frequencies of interest in X- and S-bands. The results of these measurements are presented and discussed in Chapter 4.

### 3.3 Boresight Measurements

#### 3.3.1 Discussion

Boresight measurements are normally made to determine the capability of a tracking system or other direction sensor in locating the direction in space to a radiating or reflecting source. Most tracking devices, such as monopulse radars and conical scanning radars, perform this function in the operational case by sensing the direction of arrival as the direction of the normal to the approaching wavefront.

In boresight measurements on an antenna test range, boresight error of a system under test is determined by comparing the direction to a known source as indicated by the system under test with the same direction as indicated by the angle-readout of the measuring system taking into account parallax, which will almost always exist, between the center of parallax (see Appendix J) of the antenna under test and the origin of the range coordinate system.

The above procedure implies that the center of phase (i. e., the apparent location) of the source antenna is known. Although a unique center of phase does not generally exist for a practical antenna, a center of phase can be defined relative to a given test aperture, as discussed in Appendix J, if the phase variation across the test aperture is nearly spherical. This situation exists if the field incident on the test aperture is from a single direction; that is, if extraneous reflections do not exist. Calculations presented in Appendix J show that if a source antenna is designed to be symmetrical, as in the case of a paraboloid, and if it is made essentially symmetrical, the center of phase for almost all practical purposes can be taken as the geometrical center of the antenna if reflections are negligible. In the appendices, theoretical relationships are derived between the location of the apparent source of radiation and the field in the test aperture in the presence of reflections.

The measurements under this program were made to provide an evaluation of the accuracy of the range for making boresight measurements at X-band and S-band. In addition the measurements provide experimental correlation with the theory to permit extrapolation of the results of the measurements to other test situations. Measurements were performed at X- and S-bands using monopulse devices to sense the apparent location of the source antenna. The technique employed was essentially the same as that employed in validating the range for the Gemini program and described in Appendix K, page 33, except that measurements were made in only one plane at a time; (the monopulse sensor was rotated through 90 degrees to sense in orthogonal planes). X-band measurements were made with an amplitude-monopulse sensor which simulated the characteristics of the LEM rendezvous radar antenna. This permits the boresight data obtained to be related to the LEM measurement problem. Finally, since the accuracy of the monopulse measurements is affected by all of the system component errors such as positioner errors, frequency and amplitude instabilities, gravity and temperature effects, etc., rather than the extraneous signal level alone, these tests serve as a check on the total measurement system performance.

### 3.3.2 Description of the Monopulse Sensors

#### X-Band

The X-band sensor used for boresight measurements was a single-plane amplitude-monopulse system, shown schematically in Figure 3.2. The antenna utilized was a 2-foot diameter paraboloid with a Cassegrain sub-reflector. The feed and reflectors were designed to simulate, in a single plane, the LEM rendezvous radar antenna, operating at a center frequency of 10 GHz. The relative amplitudes and phases of the signals in the two channels are adjustable by means of a precision waveguide attenuator and a rotary vane phase shifter, as shown in Figure 3.2. The phase shifter and attenuator are motor driven and are controlled at the receiving console. The two signals are combined in a hybrid, and the output of one port is directed to the mixer of the measurements receiver, which acts as a null indicator.

The mechanical and electrical components are enclosed in a rigid drum which is insulated to reduce temperature effects. It was convenient to design the device to be mounted in the nose of the Gemini spacecraft mockup in the location normally occupied by the Gemini rendezvous radar. In effect,



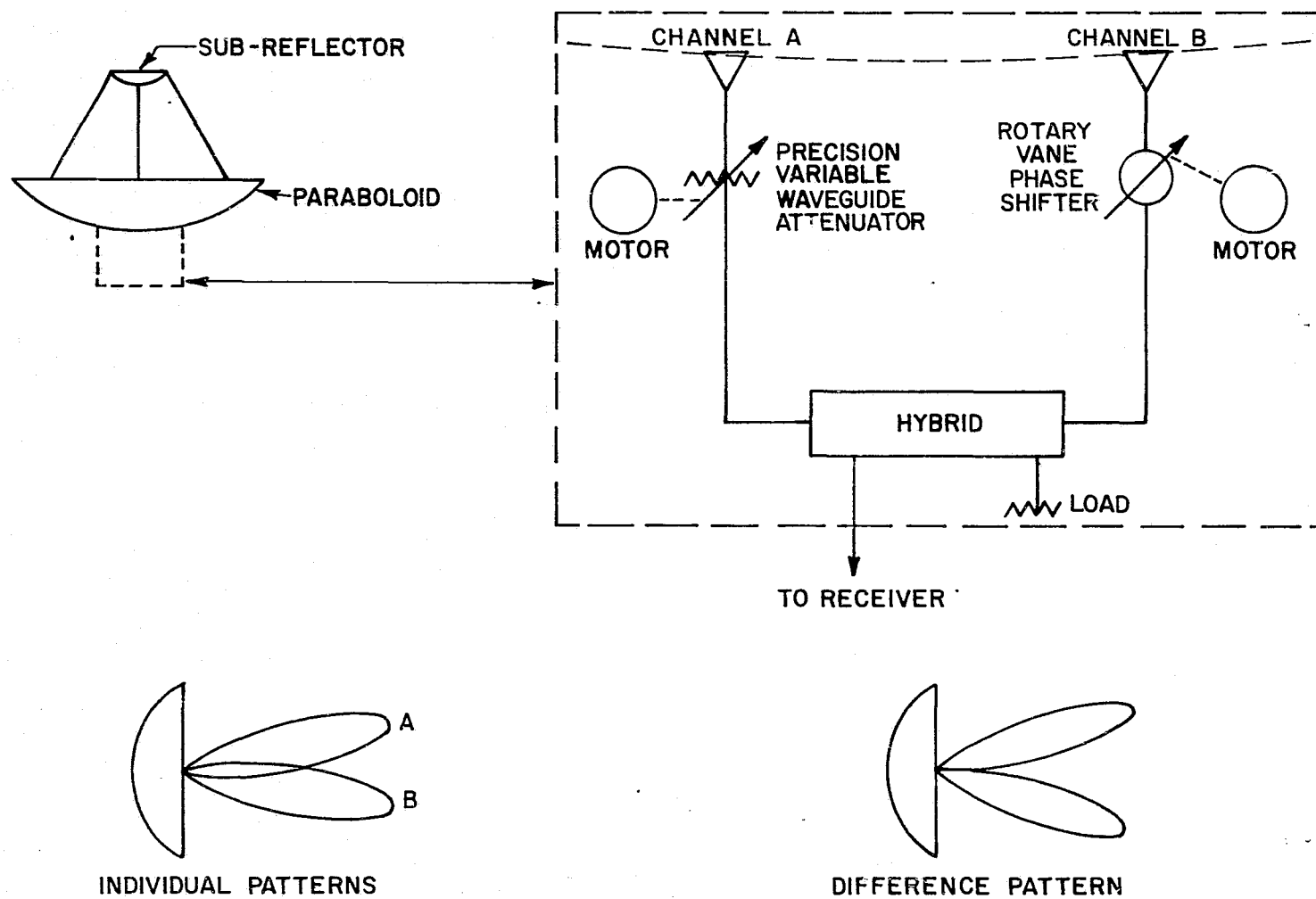


Figure 3.2. Schematic of X-Band Single-Plane Amplitude-Monopulse System

the Gemini mockup serves as a mounting bracket to position the monopulse sensor, shown in its operational configuration in Figure 3.3.

### S-Band

The S-band boresight sensing device is a single-plane phase-monopulse interferometer consisting of a pair of waveguide horn antennas and associated circuitry as illustrated schematically in Figure 3.4. The internal components differ from those of the X-band device in that they are coaxial, rather than waveguide, devices. The attenuator and phase shifter are remotely controlled by the same unit which is used with the X-band amplitude-monopulse device. The antenna system is mechanically rigid and the internal components are thermally insulated. As in the case of the X-band device, the interferometer is packaged to mount directly into the Gemini spacecraft mockup. A null, sensing zero phase difference between signals received by the two sampling antennas, is obtained for a given pointing direction by adjusting the phase shifter and attenuator to yield a minimum difference signal at the hybrid output. If a phase front is incident on the interferometer at an angle  $\theta$  as shown in Figure 3.4, the phase difference  $\phi$  between the A and B signals is

$$\phi = \frac{2\pi d}{\lambda} \sin\theta$$

where  $\lambda$  is the wavelength and  $d$  is the spacing between the antennas. The sensitivity of the interferometer for angular determination is dependent on the rate of change of  $\phi$  with respect to  $\theta$ . The sensitivity is thus given by

$$\frac{d\phi}{d\theta} = \frac{2\pi d}{\lambda} \cos\theta$$

The antennas in the phase monopulse device can be placed at separations of 8 and 24 inches, resulting in two possible sensitivity factors; the 24-inch separation was used for S-band boresight testing performed under this program. The interferometer sensitivity  $d\phi/d\theta$  at S-band (2.3 GHz) for this spacing is approximately  $30 \cos\theta$  electrical degrees per mechanical degree of boresight change. While the schedule of this program did not permit measurements with the 8-inch spacing, it is noted that this smaller separation between the interferometer pair would provide a sensitivity of approximately  $10 \cos\theta$  electrical degrees per mechanical degree of boresight change. Since this lower sensitivity represents a greater susceptibility to extraneous energy, it could be used in measurements designed to prove very high degrees of suppression of reflected and other extraneous signals.

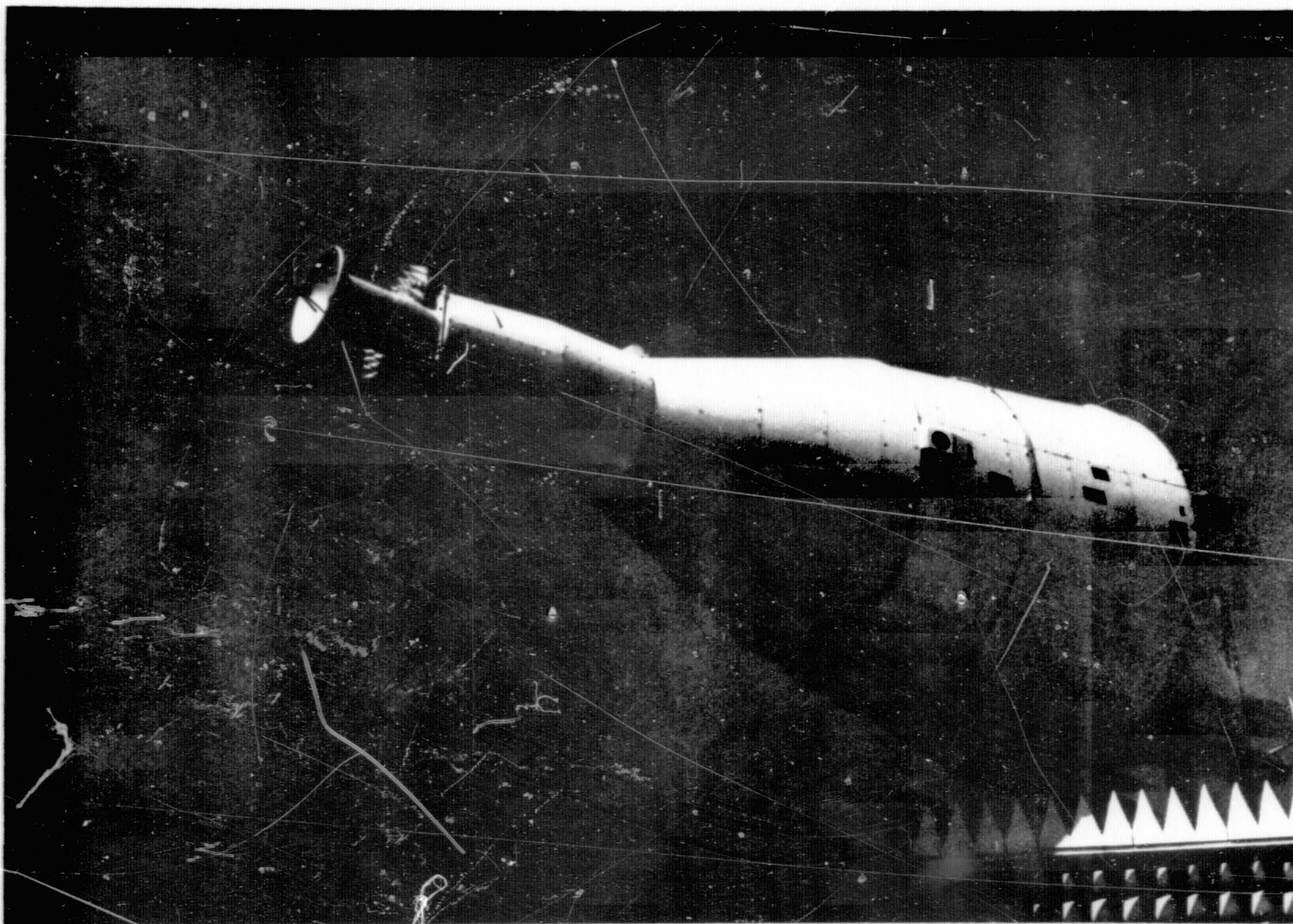


Figure 3.3. X-Band Monopulse Device Mounted on Gemini Spacecraft Mockup

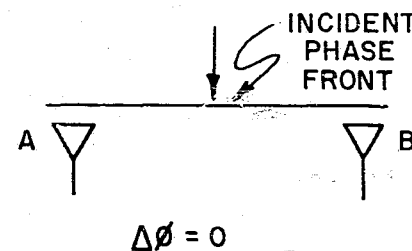
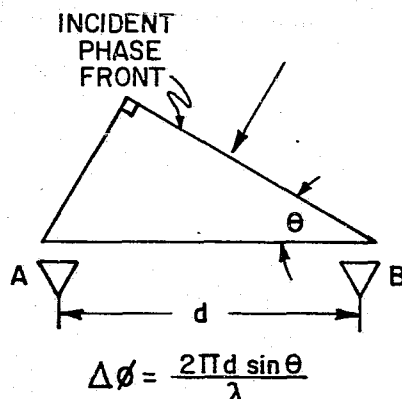
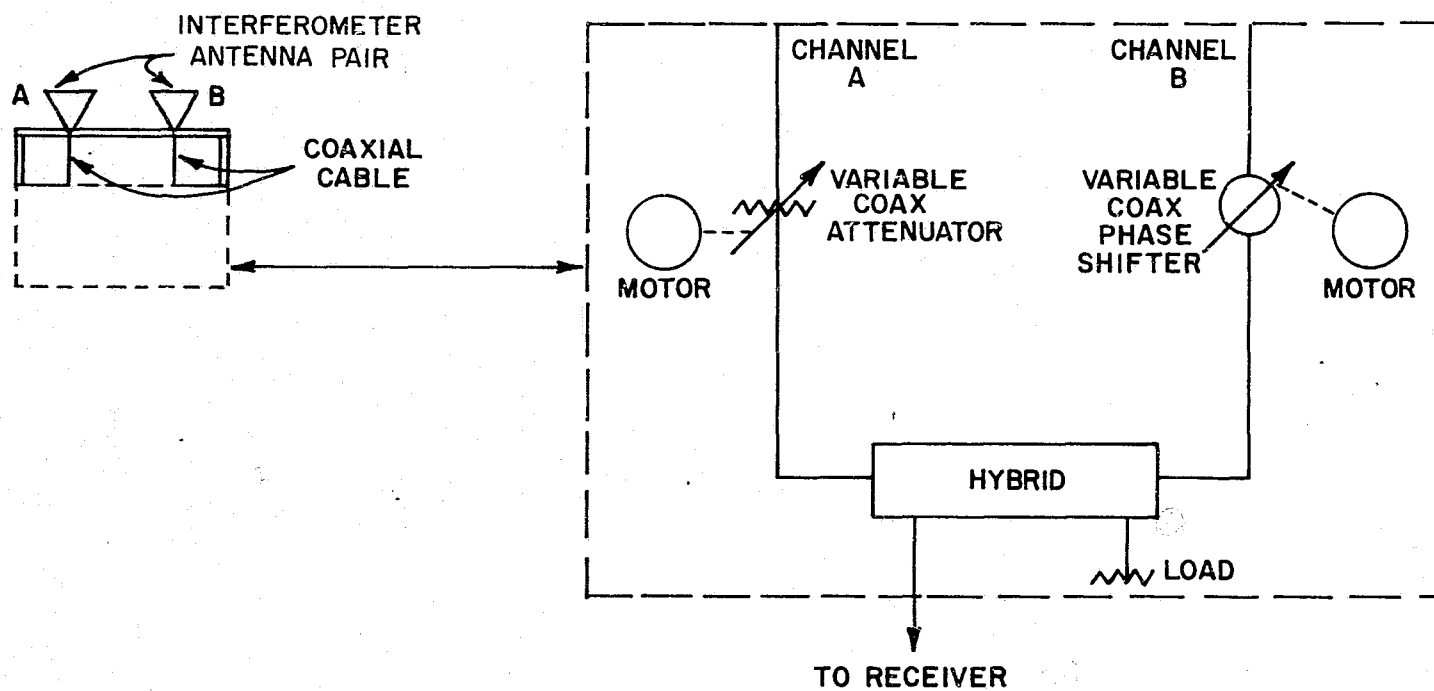


Figure 3.4. Schematic of S-Band Single-Plane Phase-Monopulse System

## CHAPTER 4

### MEASURED AND CALCULATED DATA

The capability of the NASA-MILA RF Boresight Test Facility for antenna measurements at X- and S-bands was evaluated in an experimental program involving the electrical measurements described in Chapter 3 and the mechanical measurements of positioner errors discussed in section 4.3. The range was investigated in the ground-reflection mode and in the elevated mode for both frequency ranges; the measurement program included experiments toward the determination of optimum range configurations and studies of the effects of diffraction screen and microwave absorbing material placements. Discussions of the measured data are presented here with representative patterns and calculations.

#### 4.1 X-Band Measurements

The MILA range was evaluated at X-band for use as a boresight test facility and as an antenna pattern measurement facility. Particular attention was directed toward the feasibility of utilizing the range for high-accuracy boresight measurements on the LEM Rendezvous Radar system and in evaluation tests of the LEM Landing Radar system. All X-band measurements described below were made at a frequency of 10 GHz unless otherwise specified.

##### 4.1.1 Ground-Reflection Mode

The following paragraphs present data pertinent to the performance of the MILA boresight test range as operated in the ground-reflection mode. Two transmitting antennas were used in this configuration: (1) a 1-foot paraboloidal reflector with linear polarization capability only, and (2) a conical horn with a 1-foot diameter aperture and dielectric lens operated in conjunction with a polarization adjusting system to obtain any required polarization of the transmitted wave. The 3-decibel beamwidth of each transmitting antenna is approximately 7 degrees.

4.1.1.1 Amplitude Measurements: The theoretical aperture field characteristics of a ground-reflection range are derived in Appendix A. Field amplitude

variations within the test aperture are of two types: (1) amplitude taper due to the directivity of the transmitting antenna and, in the ground-reflection case, due to the interference of the image of the transmitting antenna in the range surface with the direct-path wave from the transmitter; and (2) amplitude ripple due to signals caused by extraneous reflection and diffraction effects. As shown in Appendix A, the vertical amplitude taper over the test aperture for a ground-reflection range is determined by the ratio of the vertical dimension of the aperture to the height of the center of the aperture above the range surface, while the horizontal amplitude taper is essentially determined by the beamwidth of the transmitting antenna. If the transmitter height is optimum, the vertical taper will be symmetrical about the center of the aperture. The optimum transmitter height,  $h_t$ , which corresponds to a test aperture height of  $h_r$  for a theoretically perfect ground-reflection range of length  $R_o$ , is given by equation (A-31) of Appendix A,

$$h_t \doteq \frac{\lambda R_o}{4 h_r} \quad (4-1)$$

The pertinent parameters for the NASA-MILA range are:

$$h_r \doteq 30 \text{ feet}$$

and

$$R_o \doteq 1000 \text{ feet.}$$

At 10 GHz ( $\lambda \doteq 0.098$  foot), equation (4-1) yields

$$h_t \doteq 0.83 \text{ foot.}$$

Assuming proper adjustment of the transmitter squint angles, this height theoretically results in an in-phase condition for the direct-path and reflected signals at the center of the test aperture, so that the vertical amplitude taper of the aperture field is symmetrical about  $h_r$  for the conditions postulated in Appendix A (i. e., no phase difference between  $\bar{E}_D$  and  $\bar{E}_R$  due to the phase pattern of the transmitting antenna and exact 180-degree phase shift at the reflecting surface). If the phase characteristics of the transmitting antenna and the reflecting surface are not as postulated the optimum transmitter height will vary from that given by equation (4-1), although such variations will be insignificant for configurations which approach the theoretical model.

Vertical field amplitude plots for the ground-reflection mode are presented in Figure 4.1. Plots were made for horizontal and vertical linear polarizations with transmitter height as a parameter. For source heights between 0.79 and 0.83 foot, the patterns are all very nearly symmetrical about the center of the aperture. In other words, the quality of the field configuration for either polarization is relatively insensitive to fine adjustment of the source height about the theoretical value given in equation (4-1).

Horizontal amplitude patterns are also presented in Figure 4.1; for the ground-reflection mode, horizontal amplitude taper is almost entirely due to the directivity of the transmitting antenna. The taper in this plane is seen to be small due to the relatively broad 3-decibel beamwidth of the 1-foot paraboloidal source antenna at 10 GHz.

Consideration of the equations describing the aperture field for a ground-reflection range indicates that the vertical aperture-field taper should not be affected appreciably for small changes in the vertical squint direction of the transmitting antenna about the theoretical optimum. The vertical taper is primarily a result of the relative phases of the direct and reflected signals, rather than of the directivity factor of the transmitting antenna; thus the exact pointing direction of the transmitting antenna in the vertical plane is not as critical as is the case for the elevated range with respect to the amplitude of the aperture field.\* As stated above, horizontal amplitude taper is essentially dependent on the directivity of the source antenna, thus the taper is influenced by the azimuth squint angle. Typical field amplitude patterns illustrating these principles are reproduced in Figure 4.2. The vertical patterns are shown for elevation squint angles varying over a range of greater than four degrees. Very little change in the amplitude patterns is noted. Conversely, when the azimuth squint angle is varied from the optimum setting by as much as one degree, a tilt of the amplitude curves is noted. The optimum azimuth squint angle is seen to be about +0.1 degree for the particular antenna used to obtain the patterns of Figure 4.2. The slight deviation of this value from zero is due to small electrical and mounting misalignments.

---

\* See section A.5 and Appendix E for consideration of the phase of the aperture field and height of the apparent source of radiation as a function of elevation squint angle.

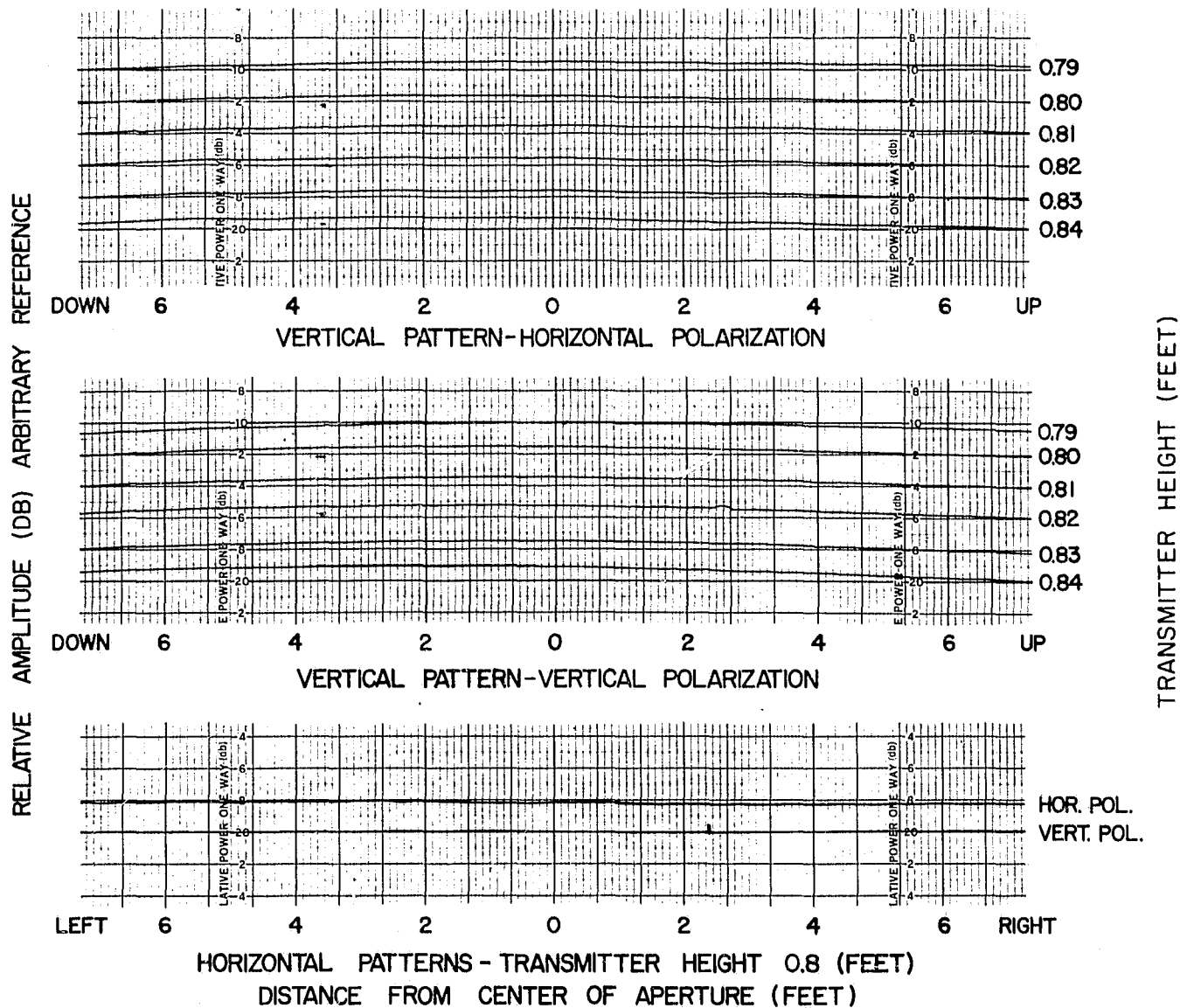


Figure 4.1. Aperture Field Patterns -- Ground Reflection Mode -- X-Band



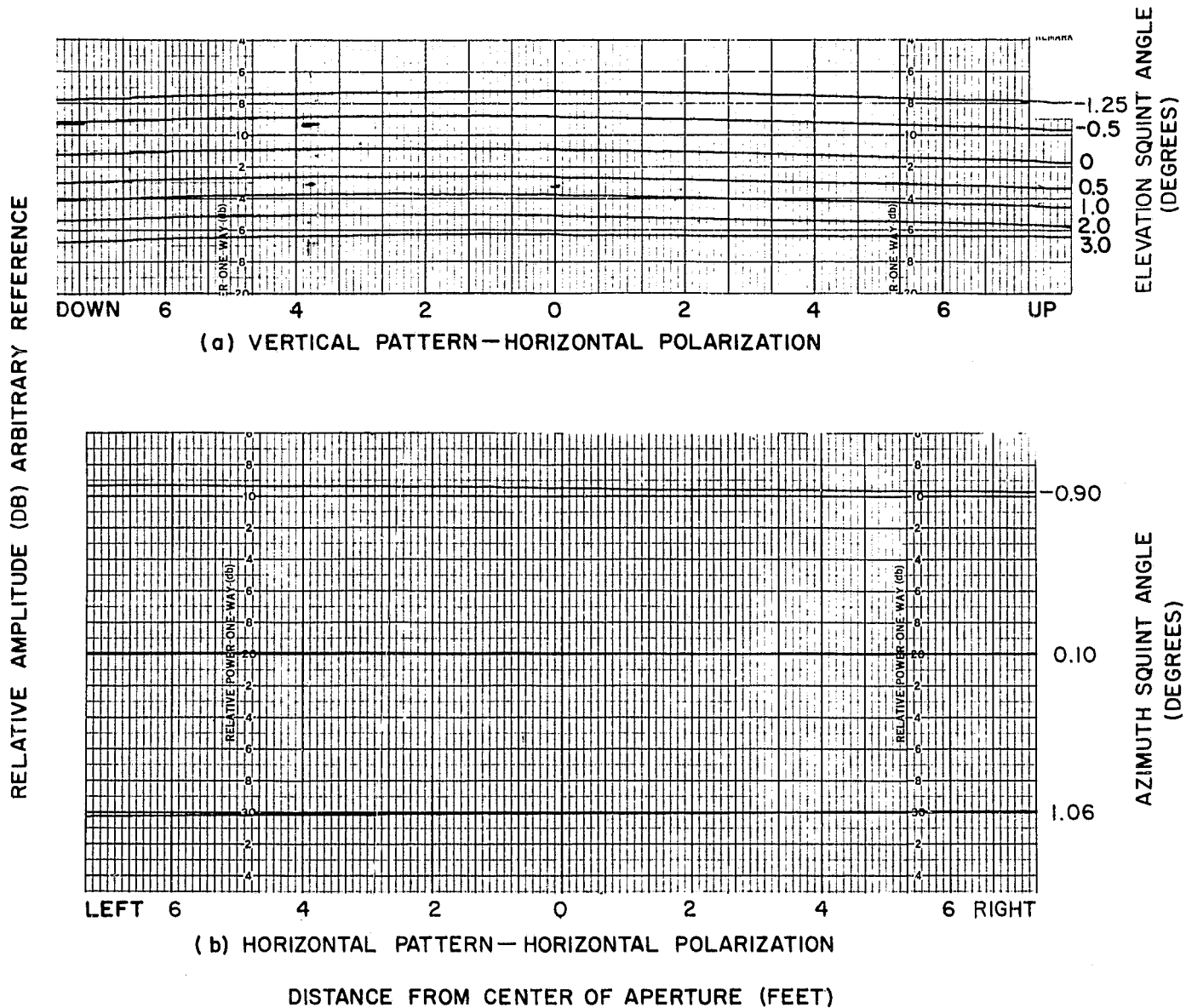


Figure 4.2. Aperture Field Patterns for Several Transmitter Squint Angles -- Ground Reflection Mode -- X-Band

The patterns of Figure 4.1 and Figure 4.2 are seen to be virtually free of amplitude ripple, indicating that the MILA range surface affords very nearly specular reflection for the ground-reflection mode at 10 GHz.

4.1.1.2 Polarization Measurements: The development of section A.3 implies that in a ground-reflection antenna range, the polarization of the field in the test aperture will not be identically the same as that of the transmitted field except for horizontal and vertical polarizations. The orientation and axial ratio of the field will be changed a small amount by the differential phase and amplitude of the reflection coefficients for the vertical and horizontal components of the wave reflected from the range surface. This effect will also result in some change in polarization with height in the test aperture because of the change in reflection coefficient of the vertical component with grazing angle. There will be an additional change in polarization with position in the test aperture because of the variation in the cross-polarization components of the transmitting antenna with direction over the portion of the beam pattern subtended by the test aperture. The measurements discussed below were made to investigate the magnitude of these effects.

Polarization measurements were made for vertical, horizontal, and circular polarizations as a function of aperture position as described in section 3.2.2. For vertical polarization, axial ratios of 35 decibels or greater were observed over an 8-foot diameter aperture and ratios of 30 decibels or greater were measured over a 16-foot diameter aperture. The horizontal polarization ratios were somewhat higher, being 40 decibels or greater over the 8-foot aperture and 35 decibels or greater over the 16-foot aperture. The improvement for horizontal polarization results from the fact that the surface affords a more constant phase shift due to reflection for horizontal polarization as the grazing angle varies,\* so that the reflected wave adds nearly in phase with the direct-path wave over a larger aperture than in the case of vertical polarization.

Circular polarization data as a function of aperture position are presented in Figure 4.3. The polarization of the received signal was adjusted to very nearly purely circular (axial ratio less than 0.1 decibel) at the center of the aperture. In addition to the points plotted in Figure 4.3, polarization measurements were

---

\* See for example, Jordan, E.C., Electromagnetic Waves and Radiating Systems, Prentice-Hall, 1950, pp. 612-613.

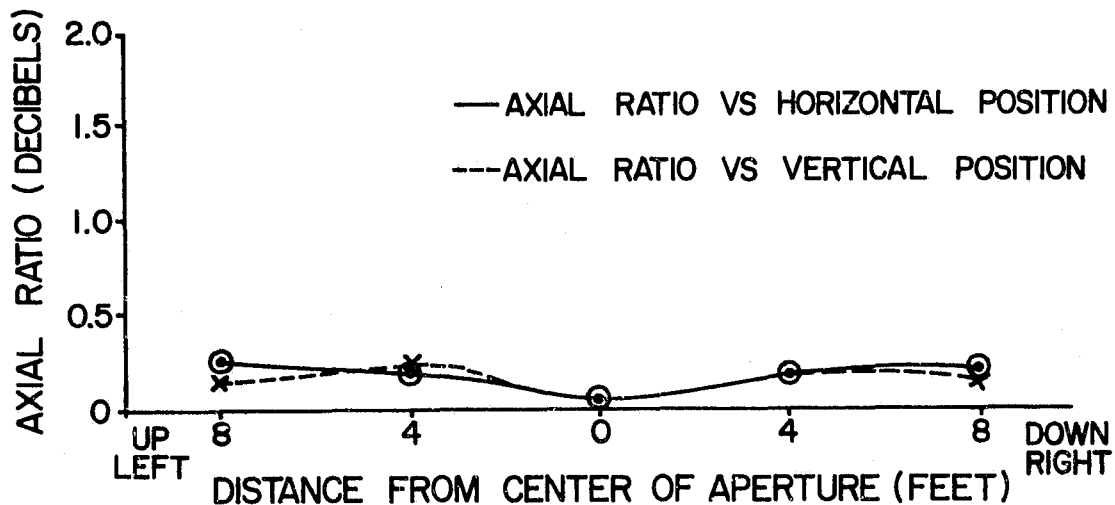


Figure 4.3. Circular Polarization Axial Ratio Versus Aperture Position -- Ground-Reflection Mode -- X-Band

made along diagonal lines across the aperture. The axial ratio remained less than 0.3 decibel for all points measured in a 16-foot diameter aperture.

The dependency of polarization on frequency was investigated about a center frequency of 10 GHz. The results of these measurements are typified by the data plotted in Figure 4.4. The maximum axial ratio observed in the frequency band between 8.5 and 12.0 GHz was less than 1.5 decibels when the polarization was adjusted to circular at 10.0 GHz. After changing frequencies, a near-circular axial ratio was found to be repeatable upon returning to a frequency of 10.0 GHz. The design of the conical horn transmitting antenna which was employed in these measurements is such that identically right- or left-circular polarization can be set at any frequency in the band.

**4.1.1.3 Boresight Measurements:** Boresight comparison measurements were made to determine the effects of small variations in the transmitting antenna orientation on the ground-reflection range performance. The measurements were made in accordance with the procedures described in section 3.3 and Appendix K.

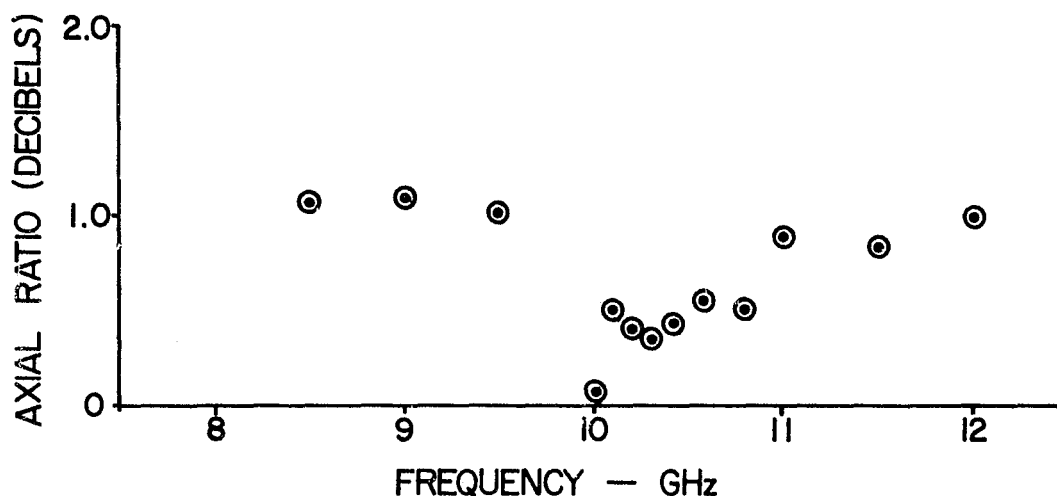


Figure 4.4. Circular Polarization Axial Ratio Versus Frequency -- Ground-Reflection Mode -- X-Band

Boresight measurement data obtained as a function of transmitter height, presented in Figure 4.5, indicate that the apparent source height is approximately 0.30 foot for actual transmitter heights in the neighborhood of the theoretically optimum height (0.82 foot). The apparent height is seen to be within 0.1 foot of this value for all transmitter heights up to 1.20 feet, indicating that small variations from the optimum transmitter height are not critical in their effects on the boresight measurement capability of the ground-reflection range at X-band.

The apparent source location for horizontal polarization is seen to be lower than that for vertical polarization. This can be explained by noting that the apparent height  $H$  for ground-reflection operation may be obtained from the equation

$$H \doteq \frac{1-k}{1+k} h_t \quad , \quad (E-17)$$

where  $k$  is ratio of the reflected signal to the direct-path signal (Appendix E). For an increasing coefficient of reflection, the apparent source height decreases. The lower measured heights for horizontal polarization indicate that the magnitude of the reflection coefficient is greater for horizontal polarization than for vertical polarization, a fact which was theorized to be true in Appendix E, and which was previously deduced from the field probe and polarization data discussed above.

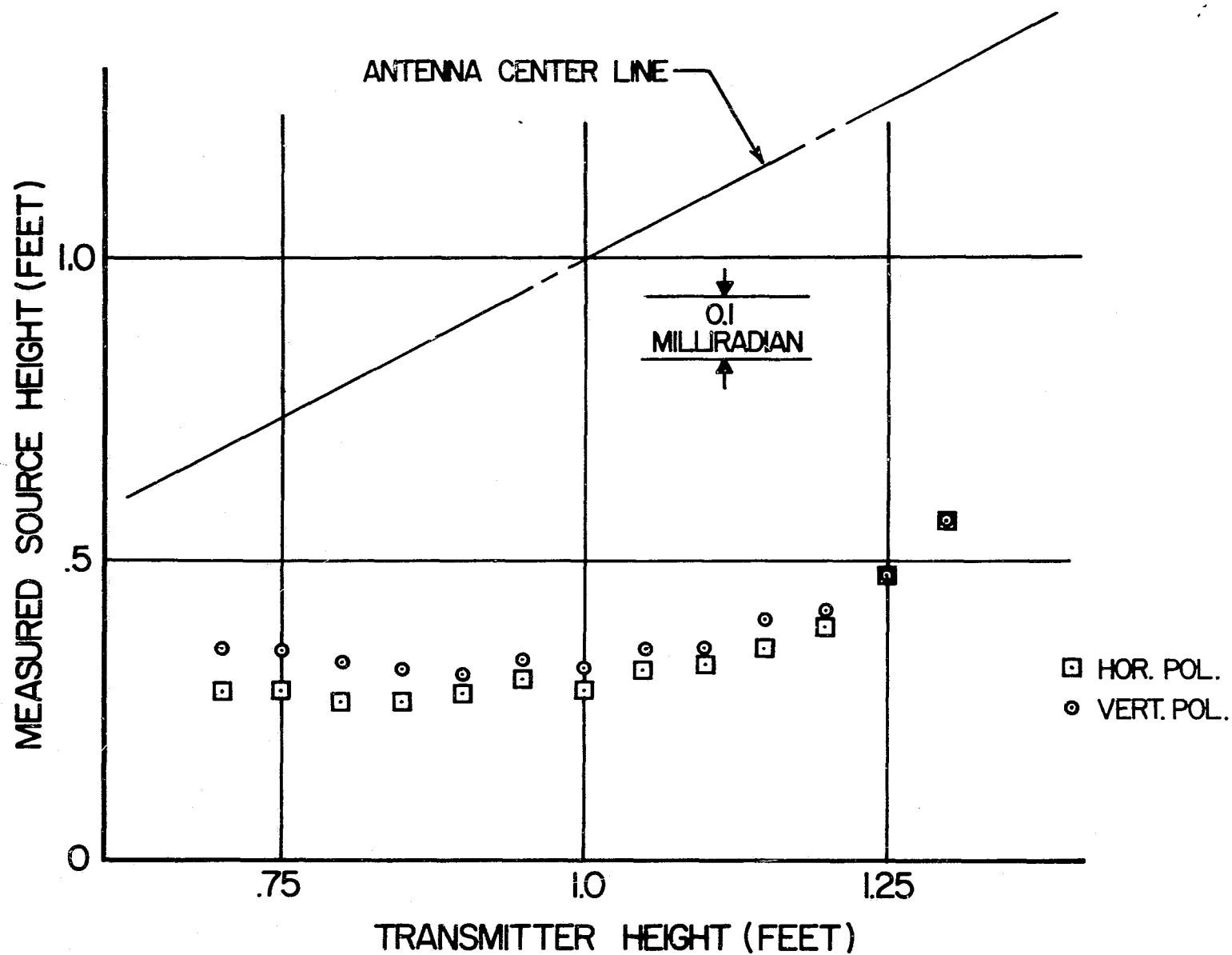


Figure 4.5. Apparent Source Height Versus Actual Source Height --  
Ground-Reflection Mode -- X-Band

The maximum difference in apparent height for the two polarizations is less than 0.1 foot, corresponding to a boresight ambiguity of  $\pm 0.05$  milliradian.\*

The effects of transmitter squint-angle variations on the apparent source location in the ground-reflection mode are discussed in Appendix E. Equation (E-14) of that derivation describes the theoretical apparent source height as a function of the transmitter elevation squint angle. The measured source height for the MILA ground-reflection range operating at 10 GHz, as a function of elevation squint angle, is presented in Figure 4.6. This Figure also includes a plot of the theoretical curve from equation (E-14). The measured variation parallels the theoretical curve with an offset of approximately 0.3 foot. The offset is probably due to a combination of the effects of imperfect reflection at the range surface (a unity reflection coefficient is assumed in the theoretical derivation) and a difference between the zero elevation squint references used for the theoretical and measured curves.

The data shown in Figure 4.6 represent the results of several sets of measurements made for both horizontal and vertical polarizations. The spread of measured height values is an indication of the repeatability and precision attainable in ground-reflection boresight measurements at X-band on the MILA range. The spread of  $\pm 0.05$  milliradian represents an envelope of measurements made on different days; data repeatability was somewhat better for measurements made in consecutive experiments.

The dependence of the horizontal location of the apparent source on azimuth squint angle is shown in Figure 4.7. The apparent source moves slightly clockwise as the indicated transmitter azimuth squint angle is increased. The total change in the horizontal source position is approximately 0.20 milliradian for an azimuth squint variation of  $\pm 3$  degrees. The angular spread for both horizontal and vertical linear polarizations is approximately 0.1 milliradian.

The beamwidth of the transmitting antenna is approximately 7 degrees. Displacement of the beam axis  $\pm 3$  degrees from the range axis produces a variation of the field of about 0.2 decibel over the two-foot aperture of the monopulse sensor and some small indeterminate phase variation over the aperture, which

---

\* For a range length of 1000 feet, a 1-foot movement in the transverse plane corresponds to an approximate angular movement of 1 milliradian; therefore, source location errors in feet may be interchanged with angular measurement errors in milliradians in the following discussions of boresight measurements.

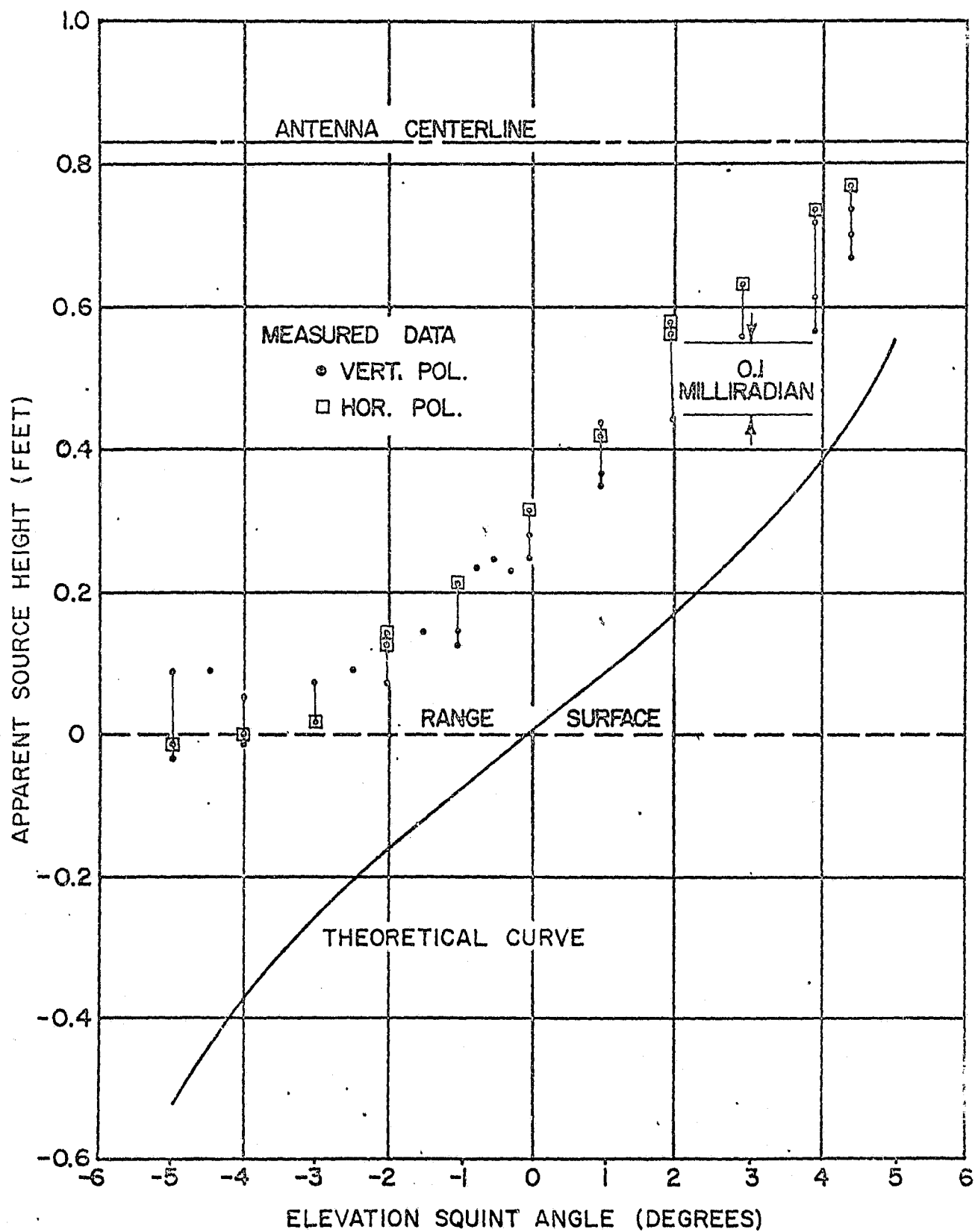


Figure 4.6. Apparent Source Height Versus Elevation Squint Angle -- Ground-Reflection Mode -- X-Band

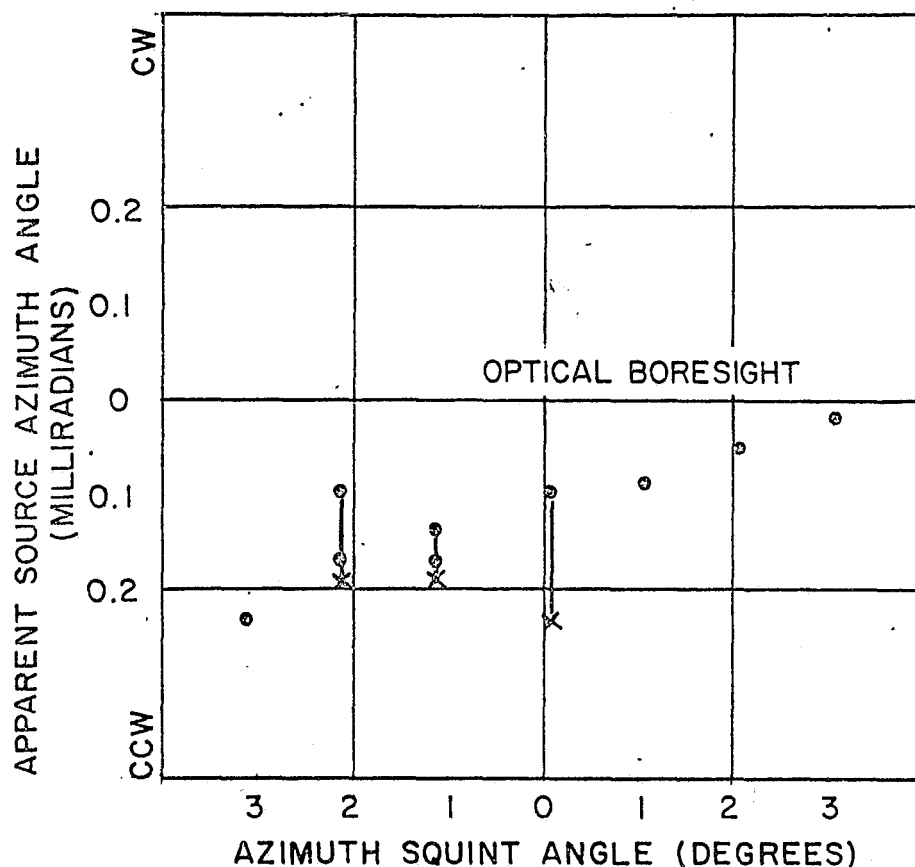


Figure 4.7. Apparent Source Location Versus Azimuth Squint Angle -- Ground-Reflection Mode -- X-Band

- o --- Vertical Polarization
- x --- Horizontal Polarization

depends on the focusing of the transmitting antenna. The conclusion which can be drawn from the results shown in Figure 4.7 is that the location of the apparent source of radiation of the transmitting antenna is relatively insensitive to the azimuth squint angle of the transmitting antenna.

#### 4.1.2 Elevated Mode With No Diffraction Fences

A discussion of the aperture-field perturbations which can result from propagation over a smooth reflecting surface in the elevated mode is presented in section A.6. The relatively smooth surface of the MILA range will allow specular reflection of microwave energy, with a reflection coefficient of nearly unity magnitude, for small grazing angles. Suppression of the effects of reflected energy



can be accomplished by reducing the illumination of the range surface with the use of diffraction fences or with the use of moderately directive source antennas, although the degree of suppression obtainable through the directivity of the source is limited by criteria which restrict the allowable amplitude taper in the vertical plane of the test aperture.\*

Elevated-mode X-band measurements were made (1) with no diffraction fences, to investigate and document the effects of reflections from the unscreened range surface, and (2) with various diffraction fence configurations in place, to determine and document the resulting improvements in the aperture field and the corresponding improvements in possible measurement accuracies. The following paragraphs present data taken with no diffraction fences in place; the effects of range-surface screening are discussed in section 4.1.3.

4.1.2.1 Amplitude Measurements: For the 30-foot height of the center of the MILA test aperture, the range surface in the vicinity of the specular point is illuminated primarily by the close-in sidelobes of the 4-foot source antenna. In addition to measurements with the 4-foot dish, data were recorded with a 1-foot source antenna for purposes of comparison. Patterns of the vertical aperture-field configuration are shown for the elevated mode at X-band in Figure 4.8. The patterns of Figure 4.8(a) represent the aperture-field variation for the case of a 1-foot diameter paraboloidal transmitting antenna with a 3-decibel beamwidth of approximately 7 degrees at the operating frequency of 10 GHz. The

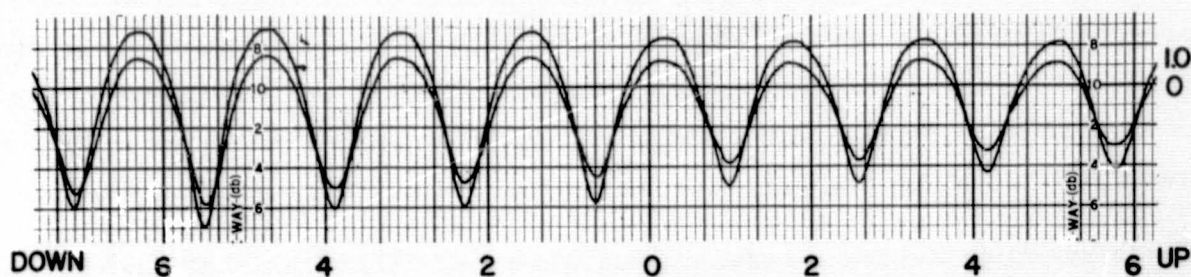
---

\*For example, a typical criterion applied for precise measurements which are designed to simulate semi-infinite separations between source and test antennas is to restrict the amplitude taper across the aperture of interest to the order of 0.25 decibel. This criterion can be shown (see Appendix E) to correspond to a restriction on the diameter (d) of the source antenna for a frequency of 10 GHz given by

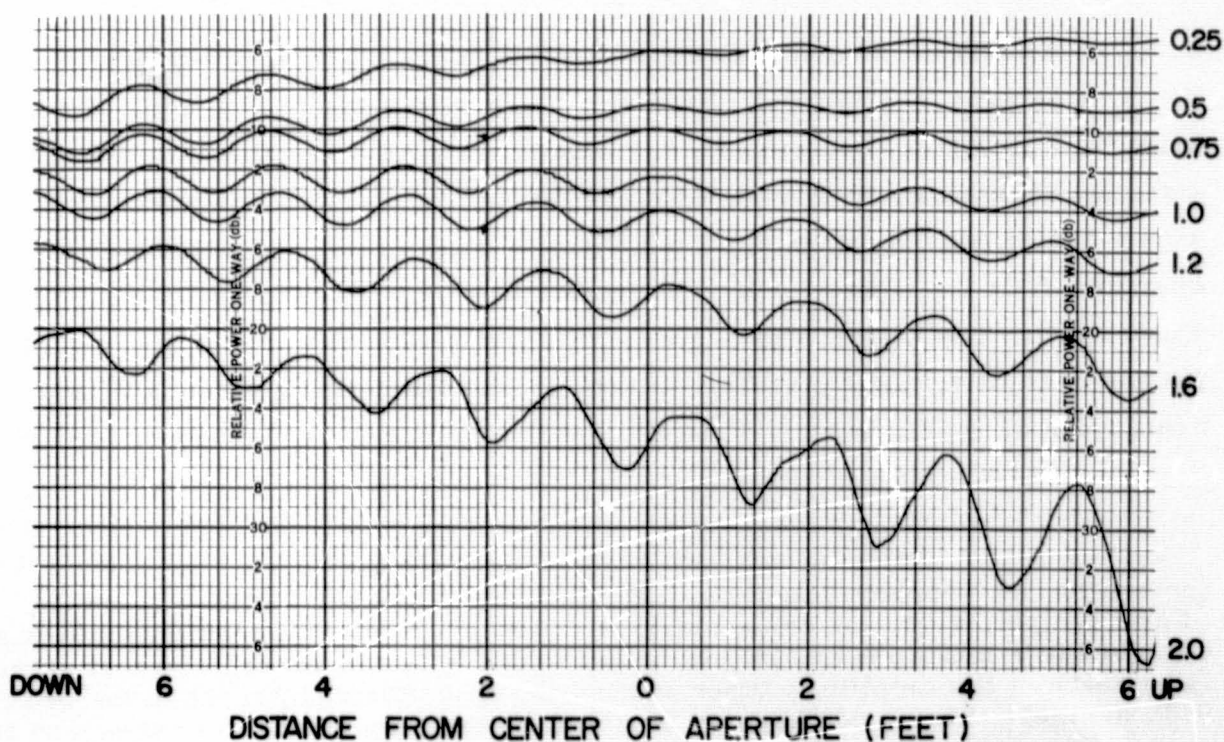
$$d_{\text{MAX}} \doteq \frac{40}{D} ,$$

where D is the maximum projection of the test aperture on the vertical normal to the direct-path propagation vector, and where  $d_{\text{MAX}}$  and D are measured in feet. Unless otherwise specified, the measurements discussed in this section employed a 4-foot diameter paraboloidal source antenna, which implies a maximum vertical dimension of the test aperture of approximately 10 feet which is illuminated within the 0.25-decibel taper criterion. It is noted that an approximate vertical test-aperture dimension of 20 feet would subtend the portion of the transmitted pattern between the 1-decibel points.

RELATIVE POWER (DB) - ARBITRARY REFERENCE



(a) 1-Foot Paraboloidal Transmitter  
3-Decibel Beamwidth  $\pm 7$  Degrees  
Horizontal Polarization



(b) 4-Foot Paraboloidal Transmitter  
3-Decibel Beamwidth  $\pm 1.7$  Degrees  
Vertical Polarization

Figure 4.8. Vertical Field Patterns -- X-Band Elevated Range

transmitter height is 30 feet and the angle to the point of specular reflection is approximately 3.5 degrees; the range surface is therefore illuminated by the main beam of the transmitter and, a relatively high extraneous signal level is predicted. The patterns of Figure 4.8(a) exhibit a peak-to-peak ripple of 6 to 8 decibels, corresponding to an extraneous field amplitude of approximately 0.4 times the field amplitude of the direct-path signal (see section A.6).

Amplitude probe patterns for the 4-foot paraboloidal transmitting antenna are shown in Figure 4.8(b). The 3-decibel beamwidth for this antenna is approximately 1.7 degrees at 10 GHz, and the 0.25 decibel beamwidth subtends a test aperture diameter of approximately 10 feet. The ripple caused by reflections from the range surface for this mode of operation is superposed on the amplitude taper. The increased directivity of the 4-foot dish results in a significant improvement in the extraneous signal level, as indicated by the pattern ripples of Figure 4.8(b). For elevation squint angles near the optimum, the ripple is of the order of 1 decibel, corresponding to an extraneous field of approximately 0.05 times the direct path field.

The patterns of Figure 4.8 also demonstrate the effects of changes in the transmitter elevation squint angle on the test-aperture field. As the transmitter beam axis is lowered, the surface illumination increases, and the extraneous signal level rises. The amplitude patterns indicate that the ripple component is small for elevation squint angles which direct the transmitted beam above the test aperture, but that the aperture field is asymmetrical for these values of elevation squint. The indicated optimum squint angle for the case shown in Figure 4.8(b) is approximately minus 0.75 degree; since the optimum should be at zero degrees (horizontal), the indicated value represents a misalignment error.

The derivation of section A.6 indicates that the approximate direction of arrival of the extraneous signal may be determined from the pitch of the aperture-field amplitude ripple. The variation of this pitch with the angle of arrival is illustrated in Figure 4.9 which shows vertical amplitude patterns with transmitter height as a parameter. For each pattern, the elevation squint angle was adjusted for symmetry of the amplitude taper about the center of the test aperture. The geometry for the measurements recorded in Figure 4.9 is shown in Figure 4.10. The ray labeled  $E_R$  is the ray which is reflected at the specular point, and  $E_D$  is the direct-path ray. The angle  $\theta_R$  between  $E_D$  and  $E_R$  is seen in Figure 4.10 to

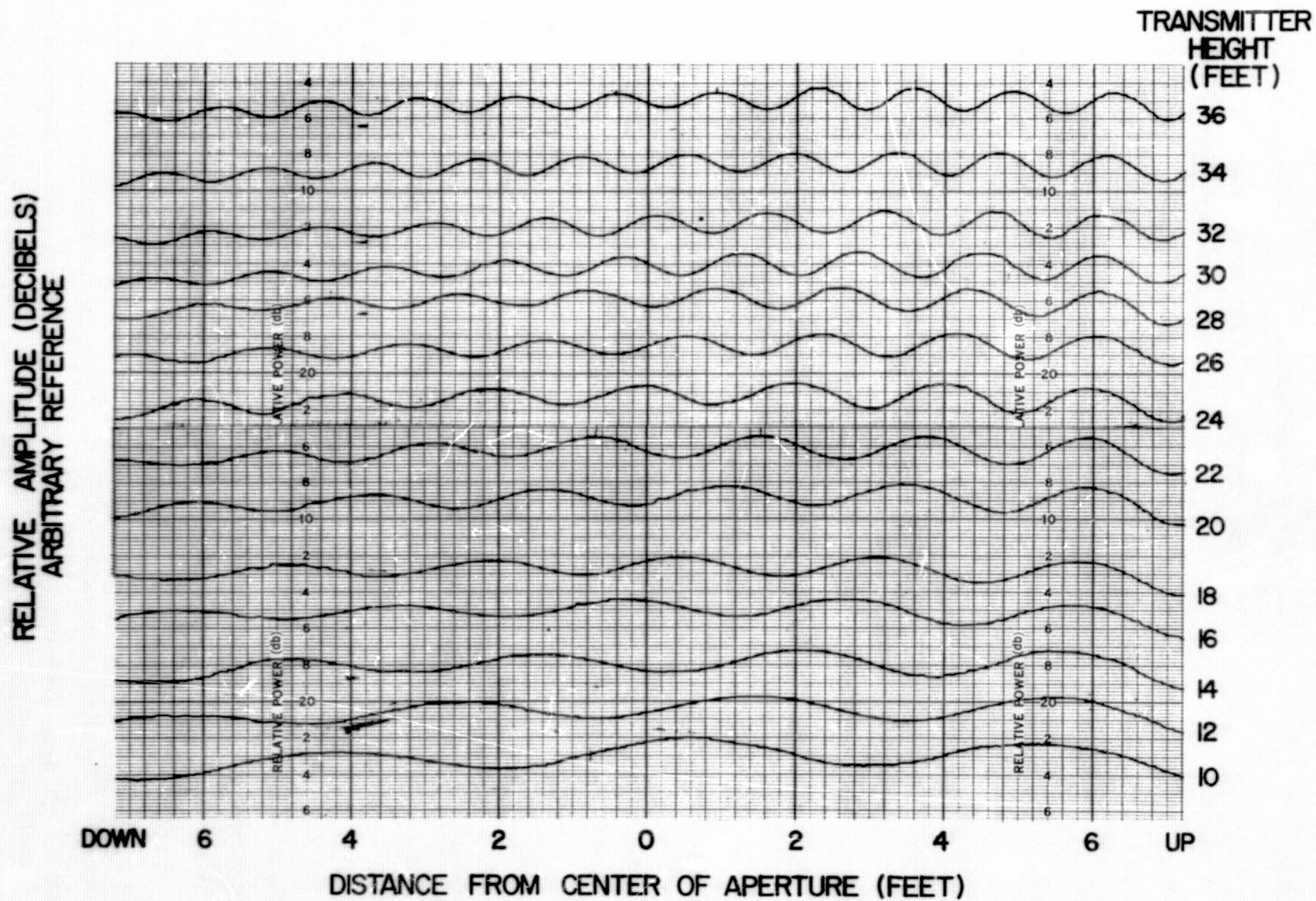


Figure 4.9. Vertical Aperture Field Amplitude Patterns --  
X-Band Elevated Range

be given by

$$\theta_R = \psi - \beta \doteq \frac{2h_t}{R_o} \quad \text{radians,} \quad (4-2)$$

where  $R_o \gg h_r$  and  $h_t$ . As shown in section A.6, the corresponding theoretical spatial periods of the aperture-field variations would be given by

$$P = \frac{\lambda}{\sin \theta_R} \doteq \frac{\lambda R_o}{2h_t} \quad (4-3)$$

The theoretical variation of  $P$  versus  $h_t$  is compared in Figure 4.11 to the measured pitches as determined from Figure 4.9. Although equation (4-3) is a result of plane wave approximations, it can be seen that the experimental data are in close agreement with the theoretical curve.

It is also of interest to correlate the relatively constant amplitudes of the aperture-field variations in Figure 4.9 to the theory. Note from Figure 4.10

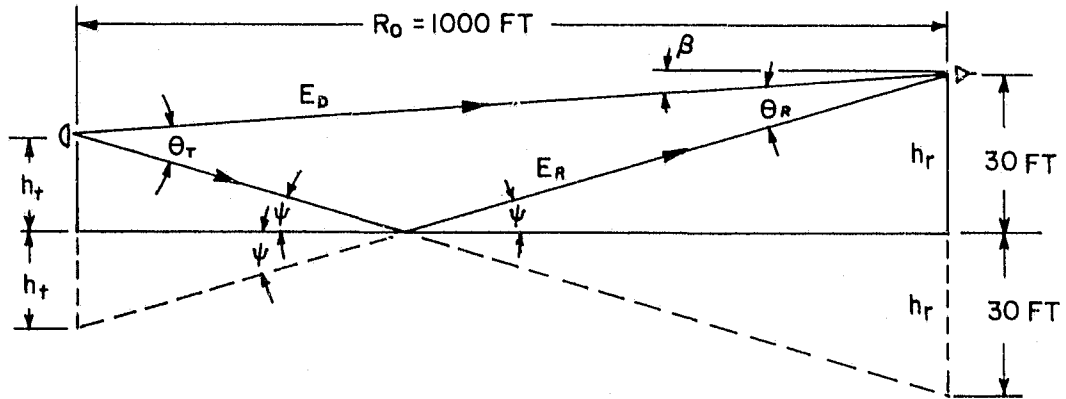


Figure 4.10. MILA Elevated Range Geometry

that the angle  $\theta_T$  between the direct-path ray and the ray incident on the specular point is given by

$$\theta_T = \psi + \beta \doteq \frac{2h_r}{R_o} \quad \text{radians,} \quad (4-4)$$

hence is essentially constant with variations in the transmitter height  $h_t$ . Assuming that the axis of the transmitted pattern is consistently directed toward the

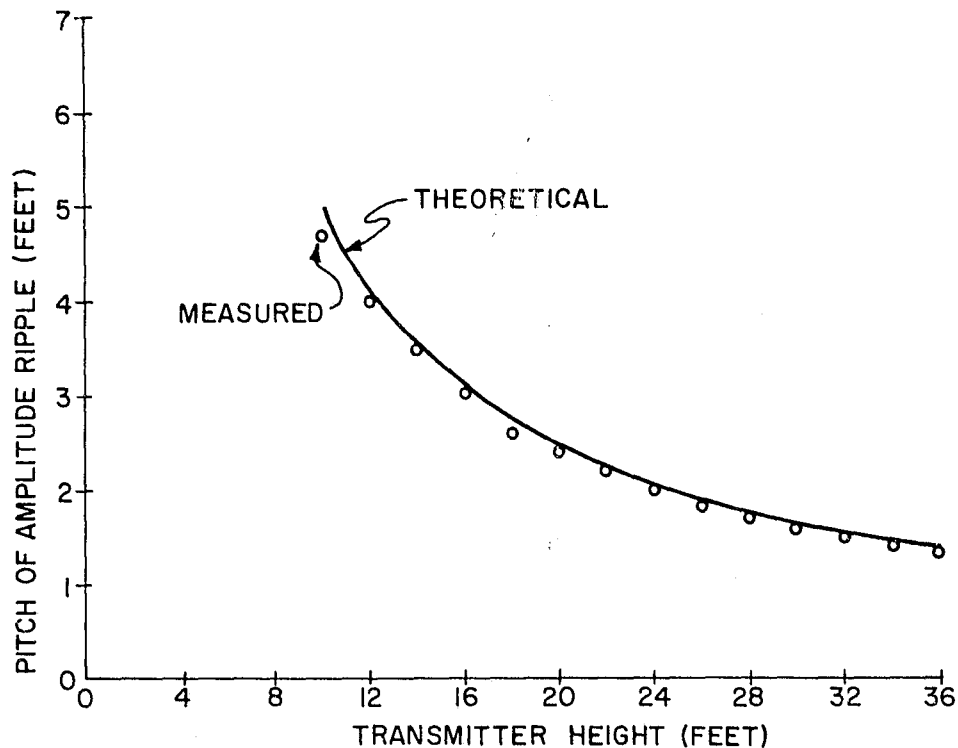


Figure 4.11. Theoretical and Measured Pitch of Vertical Amplitude Pattern Ripple -- Elevated Mode -- X-Band

center of the test aperture, the region of the range surface near the point of specular reflection will be illuminated by approximately the same sidelobe region of the transmitted pattern for all adjustments of the transmitter height. It follows that changes in the ratio of  $E_R$  and  $E_D$  would be due primarily to the slight change in reflection coefficient as a function of the differential grazing angles. Thus, the level of the extraneous signal should not vary significantly for practical excursions of the source antenna, and correspondingly the aperture-field fluctuations should be nearly constant. This theoretical prediction can be seen to agree with the experimental results shown in Figure 4.9, where the amplitude ripple of the patterns is approximately one decibel peak-to-peak for transmitter heights from 12 to 36 feet.

4.1.2.2 Boresight Measurements: The relatively large amplitude variations exhibited by the aperture-field patterns of Figure 4.9 indicate the presence of a significant extraneous signal level at the test aperture. As shown in section A.6, a peak-to-peak variation of 1 decibel in such patterns corresponds to an extraneous signal level of approximately -25 decibels with respect to the level of the direct-path signal. On the basis of the analysis of Appendix D, it is seen that extraneous signal levels of this magnitude can cause appreciable error



in boresight measurements made in the elevated mode with an amplitude-monopulse radar. For example, Figure D.5 shows that for an amplitude-monopulse system whose main reflector has a diameter of approximately 20 wavelengths (e.g., a 2-foot dish at 10 GHz), a relative extraneous signal level of -25 decibels can cause a one- to two-milliradian boresight error if this signal enters the monopulse device at more than approximately one degree from the optical boresight axis. Reference to equation (4-2) shows that an error of this order can occur for any transmitter height above 10 feet if the aperture-field variations are approximately 1 decibel peak-to-peak.

It is seen from the above discussion that data from probe measurements of the aperture field can be used to predict the approximate magnitudes of boresight errors which would be caused by a single specularly reflected extraneous signal in the elevated mode of range operation. A more quantitative correlation of experimental data with the theory can be based on the derivations of Appendices A, C and D and on the configuration of the monopulse patterns, as summarized below.

From Appendix A, it is seen that the pitch and amplitude of vertical amplitude patterns allow calculation of the approximate levels and locations of sources of extraneous energy. These calculations would provide values for the ratio of reflected to direct-path amplitudes,  $k = E_R / E_D$ , and for the angle of arrival of  $\bar{E}_R$  with respect to  $\bar{E}_D$ ,  $\theta_R$ .

From Appendix C, it is seen that, apart from the effects of the suppression of extraneous energy provided by the amplitude-monopulse pattern directivities, the apparent phase-center of the source antenna will exhibit oscillations of increasing amplitude about the actual source location as the transmitter height is increased. The spatial periods of these oscillations are shown to be essentially constant with variations in transmitter height. The amplitude of the oscillations is shown to be dependent on the transmitter height and on the ratio  $k$ , which is itself dependent on the transmitter height to some extent. (See Figures B.3 through B.5.)

From Appendix D, it is seen that the effect of the sidelobe suppression of the monopulse patterns can be related to  $\theta_R$ , the angle of arrival of the extraneous signal. This relation must be based on known or postulated pattern characteristics of the particular device of interest; for well-focused devices, the effect of the

directivities is generally a reduction in the amplitudes of the oscillations of apparent versus actual source height with increasing  $\theta_R$  (hence with increasing transmitter height, since, as shown above,  $\theta_R \doteq 2h_t/R_o$ ). The individual radiation patterns of the two channels of the X-band single-plane amplitude-monopulse device utilized in this study are shown in Figure 4.12, where the patterns were recorded at a frequency of 10 GHz. The theoretical curve of apparent versus actual source height shown in Figure 4.13 was generated by applying the above-mentioned derivations to the data of Figure 4.9, and modifying the resulting curve in accordance with an approximate envelope of the sidelobe regions of the patterns shown in Figure 4.12. It is noted that for the particular device discussed here, this modification was essentially a multiplication of the points of the original theoretical curve by the corresponding values of  $\sin K\theta_R/K\theta_R$  (see Appendix E).

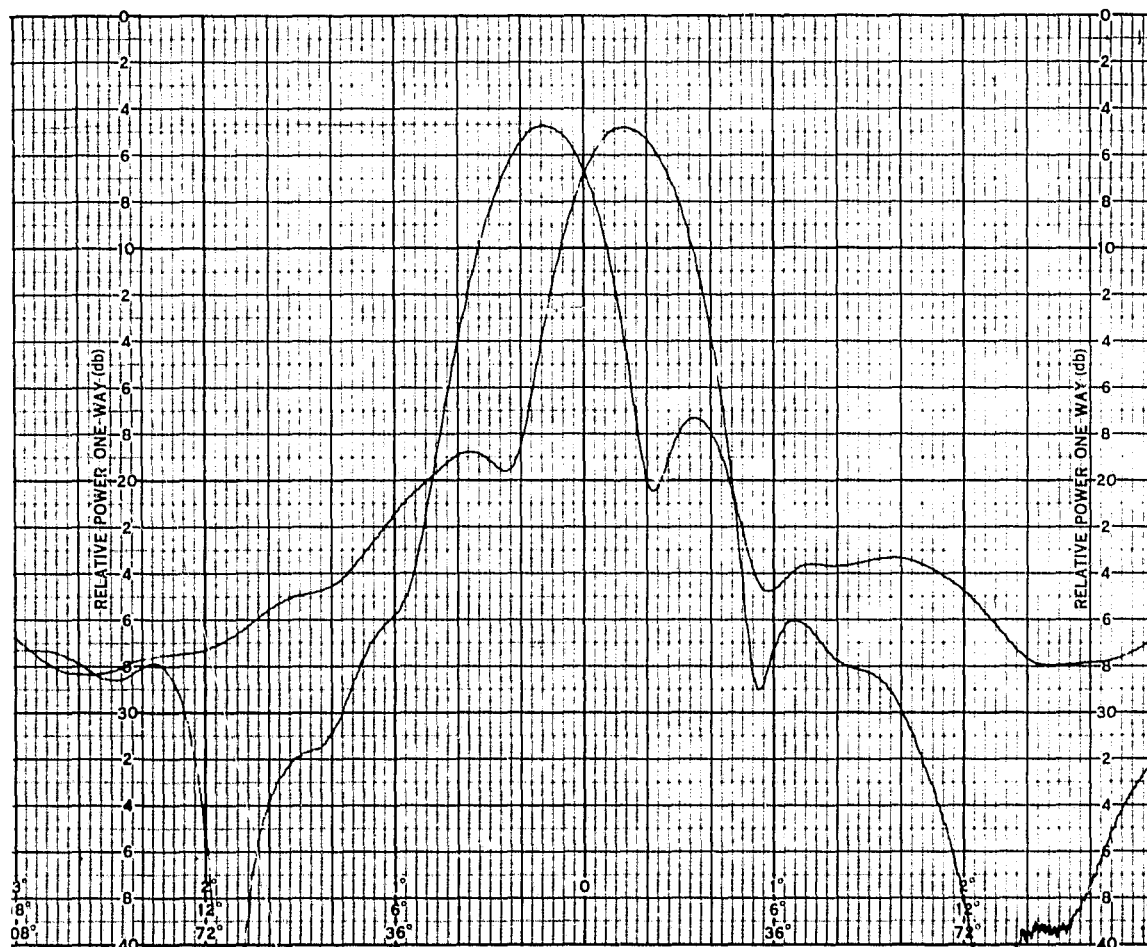


Figure 4.12. Typical A and B Channel Radiation Patterns for the X-Band Amplitude-Monopulse Test Device



The experimental data points shown on the best-fit curve in Figure 4.13 were obtained from boresight comparison measurements in the vertical plane of the test aperture with the X-band test device, following the procedures discussed in section 3.3. Note that boresight errors of the order of 2 milliradians are indicated at the successive maxima and minima of the experimental variation.

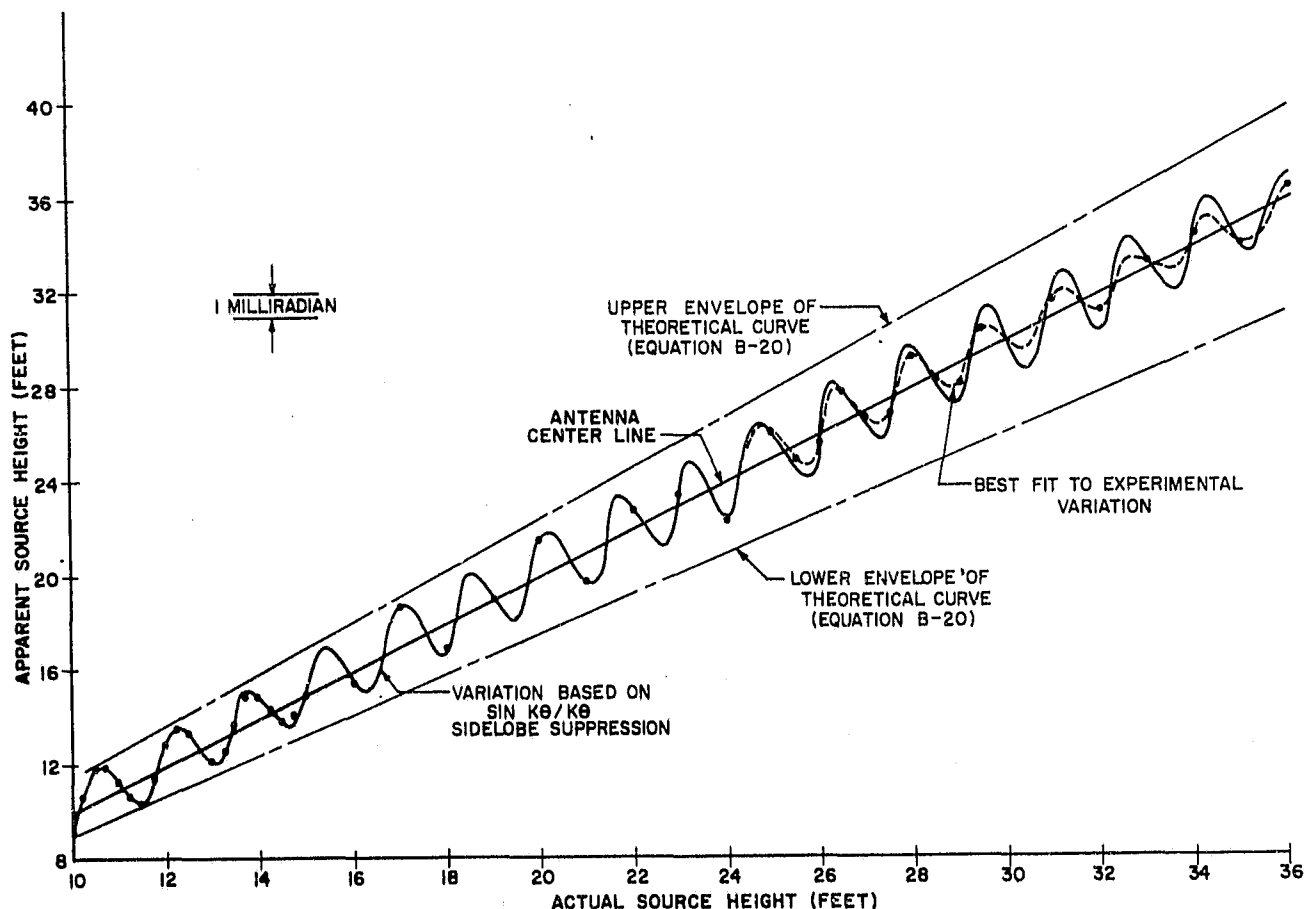


Figure 4.13. Theoretical and Measured Variation of Apparent Source Height with Actual Source Height.  
Elevated Mode -- X-Band  
No Diffraction Fences

The close correlation of experimental and theoretical variations in apparent source height as a function of actual transmitter height from 10 to 25 feet is obvious, indicating that the MILA range surface closely approximates a specularly reflecting surface at X-band frequencies as postulated in the theoretical developments.

It should be noted that the ambiguity between theoretical and experimental data for source heights above approximately 25 feet indicates that a more precise approximation to the effects of sidelobe suppression could perhaps be found. However, the emphasis of this study was on attempts to establish a range configuration which would permit boresight measurement accuracies to be improved by an order of magnitude over those indicated for the "no-fence" data in Figure 4.13, so that a more sophisticated approximation was not investigated.

#### 4.1.3 Elevated Mode with Various Diffraction Fence Configurations

In the absence of diffraction fences the relatively large aperture-field perturbations and resulting boresight ambiguity observed for the elevated mode at X-band render this configuration unsatisfactory for high-accuracy boresight measurements. In order to improve the aperture field purity and to effect a corresponding improvement in measurement accuracies, experiments were conducted with diffraction fence placements on the range surface. Theoretical aspects of reducing reflections with diffraction fences are presented in Appendix F. The theoretical studies resulted from the necessity of explaining the results of partial range-surface screening with diffraction fences and are supported by these test results.

The diffraction fences employed in this study were fabricated in 4' x 15' modular panels, permitting a variety of fence configurations to be evaluated. Multiple-fence configurations did not offer a significantly greater improvement in aperture field purity than did certain single-fence configurations. It was shown that under certain conditions, multiple reflections caused by a multiple-fence configuration could result in troublesome interference at the test aperture. A single-fence configuration which shielded 20 or more Fresnel zones was shown to be virtually as effective as the best multiple-fence configurations in reducing the extraneous signal level at the test aperture. Test data for both multiple-fence and single-fence configurations are presented in the following paragraphs to illustrate the comparative improvements in the test-aperture field and in boresight measurement accuracies.

4.1.3.1 Amplitude Data: Several fence configurations were investigated in the X-band study. The various arrangements are tabulated below, where the column headings have the following meanings:

S ... a fence located 250 feet from the source tower

C ... a fence located at the range center

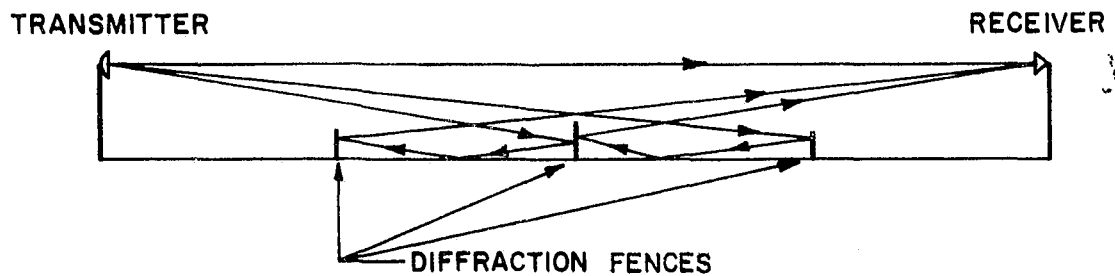
R ... a fence located 250 feet from the control building

The tabular entries give the fence heights; although the fence widths varied slightly in some configurations, a nominal width of 60 feet was employed.

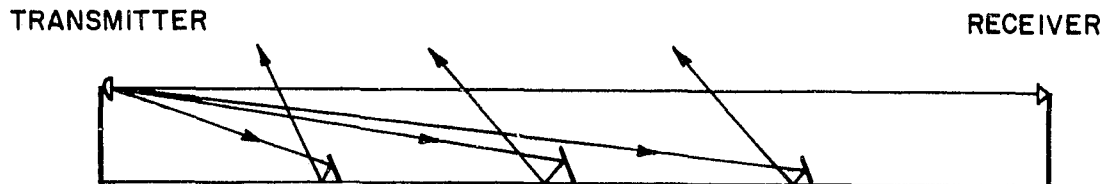
Configuration	S	C	R
(a)	8	8	8
(b)	8	12	8
(c)	8	15	8
(d)	8	15	-
(e)	8	12	-
(f)	-	15	-
(g)	-	12	-
(h)	-	8	-

When multiple-fence configurations such as (a) through (e) are employed, care must be exercised to suppress the effects of multiple reflections from the fences and the range surface. The mechanism by which such multiple reflections can produce a high extraneous signal level at the test aperture is illustrated schematically in Figure 4.14(a). A single multiple-reflection path may result in an extraneous signal level of the same order of magnitude as that caused by direct reflection from the range surface in the absence of diffraction fences; when more than one path is possible, as illustrated in Figure 4.14(a), random addition of the extraneous phasors can result in an extraneous signal level which is higher than that for the case of no diffraction fences. A straightforward method of suppressing multiple reflections is to tilt the fences as shown in Figure 4.14(b). For either tilted or vertical fence configurations, a residual extraneous signal level is likely to result from a combination of diffraction and reradiation effects introduced by the fences themselves; however, these effects will be second-order in magnitude if the fences are properly placed.

For purposes of comparison, and to illustrate the effect of multipath reflections on data repeatability, a set of vertical amplitude patterns recorded as a function of elevation squint angle with fence configuration (b) above is illustrated in



(a) Scattering by Vertical Fences



(b) Suppression Achieved by Tilting Fences

Figure 4.14. Multiple Scattering From Diffraction Fences

Figure 4. 15; the fences were all erected normal to the range surface for these measurements, and the patterns for each elevation squint-angle setting were repeated several times. The data for successive multiple-fence configurations were taken with the S and R fences tilted toward the source tower through an angle of approximately 20 degrees; as seen in Figure 4. 16 and 4. 17, these data indicated a relative freedom from multipath effects.

It was found that within measurable accuracies configuration (g), a single 12-foot fence at the range center, resulted in essentially the same improvement in aperture-field purity as did any of the more elaborate configurations (a) through (f). Some minor degradation of the aperture field was seen for configuration (h), a single 8-foot fence at the range center.

As an illustration of the effects of various fence installations, amplitude patterns for configurations (b), (e) and (h) are presented in Figures 4.16, 4.17 and 4.18, respectively. Comparison of these data with Figure 4.9 shows that the partial range-surface screening provided by the diffraction fence placements resulted in

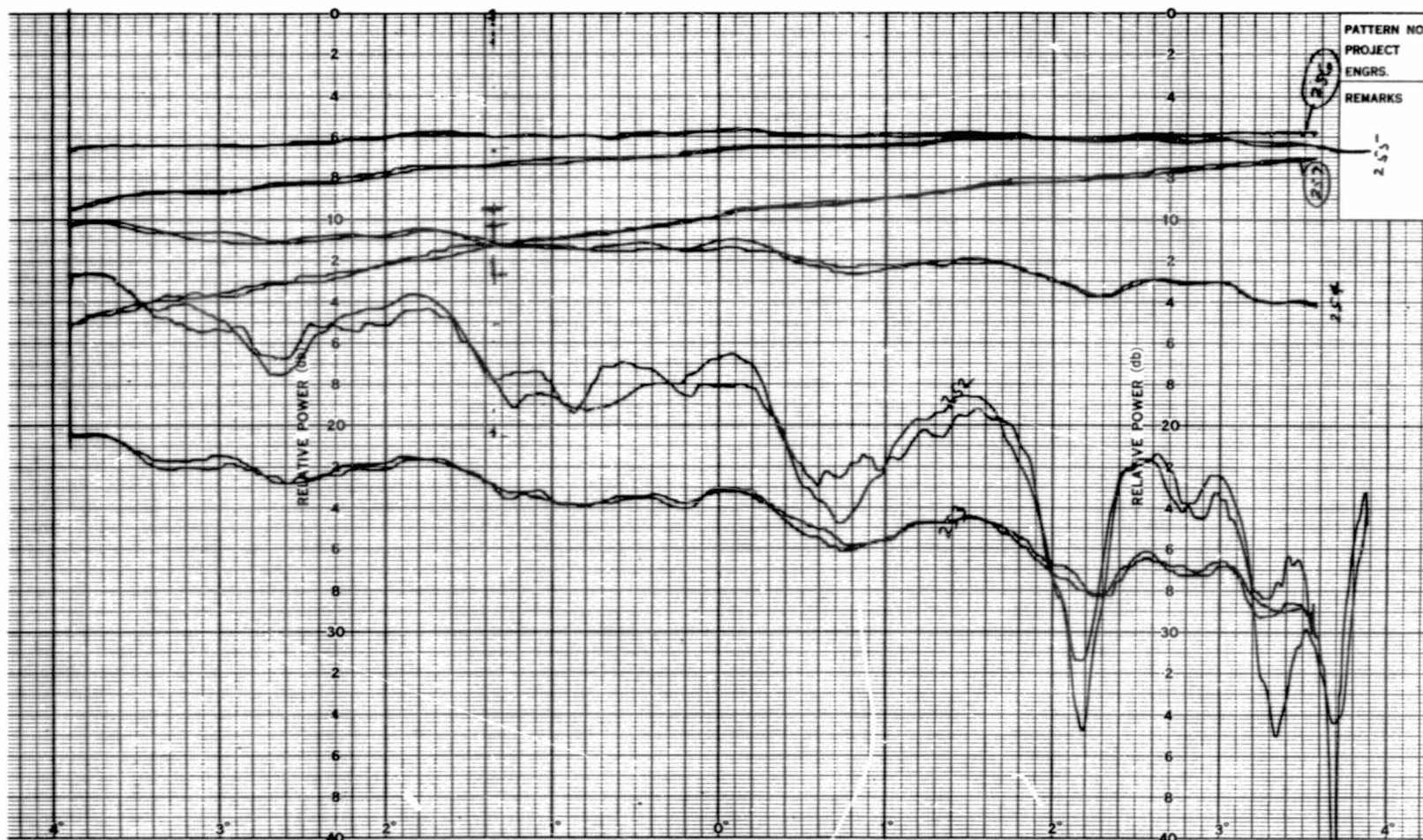


Figure 4.15 Effects of Multiple Scattering by Diffraction Fences on Vertical Aperture-Field Amplitude Patterns at X-Band --- Configuration (b)

The data above, which are vertical field patterns as a function of source elevation squint angle, illustrate the effects of randomly phased extraneous energy on pattern reproducibility. The effect is most noticeable for the traces numbered 252, where the source antenna was directed well below the horizontal so that the multiple (vertical) fences were heavily illuminated by the main lobe of the transmitted beam. Inclination of the secondary fences was found to suppress this effect. (see text)

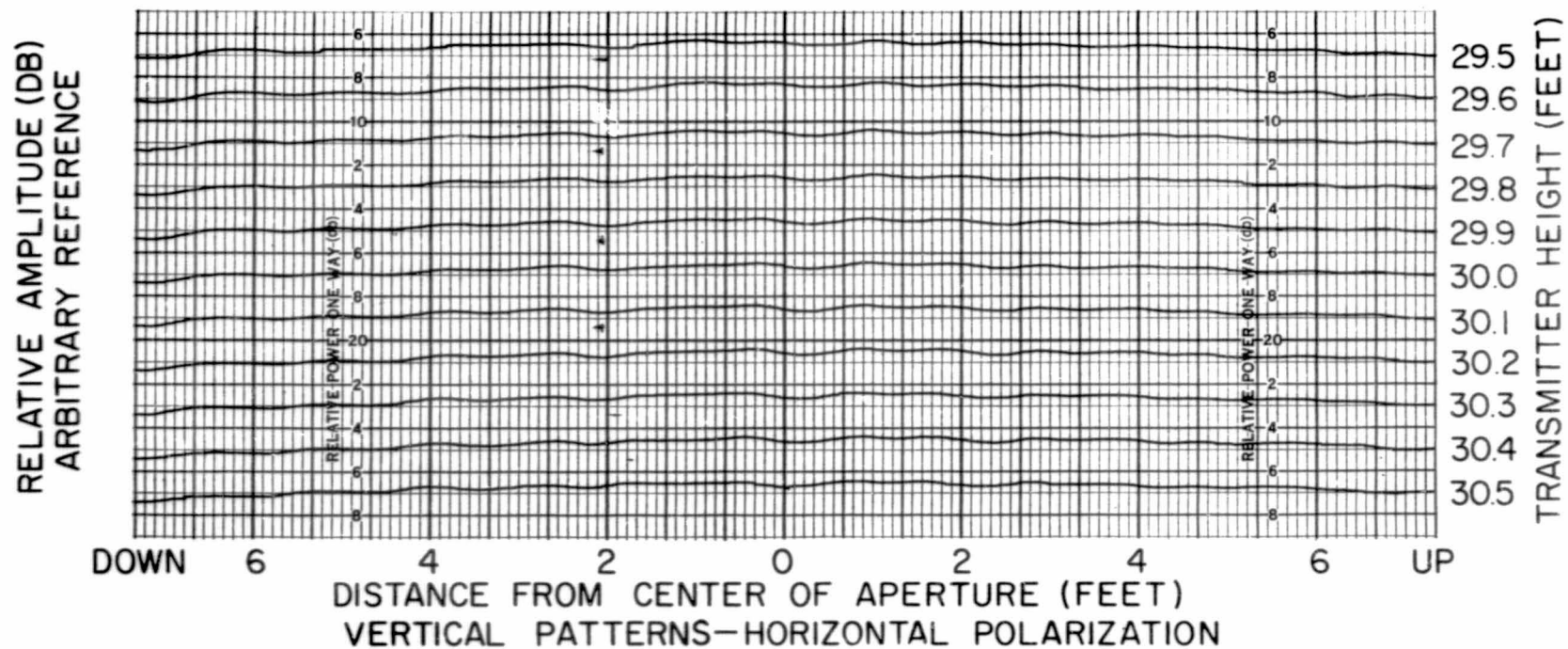


Figure 4.16. Vertical Aperture Field Patterns -- Elevated Mode With  
Three Diffraction Fences -- X-Band  
Configuration (b)

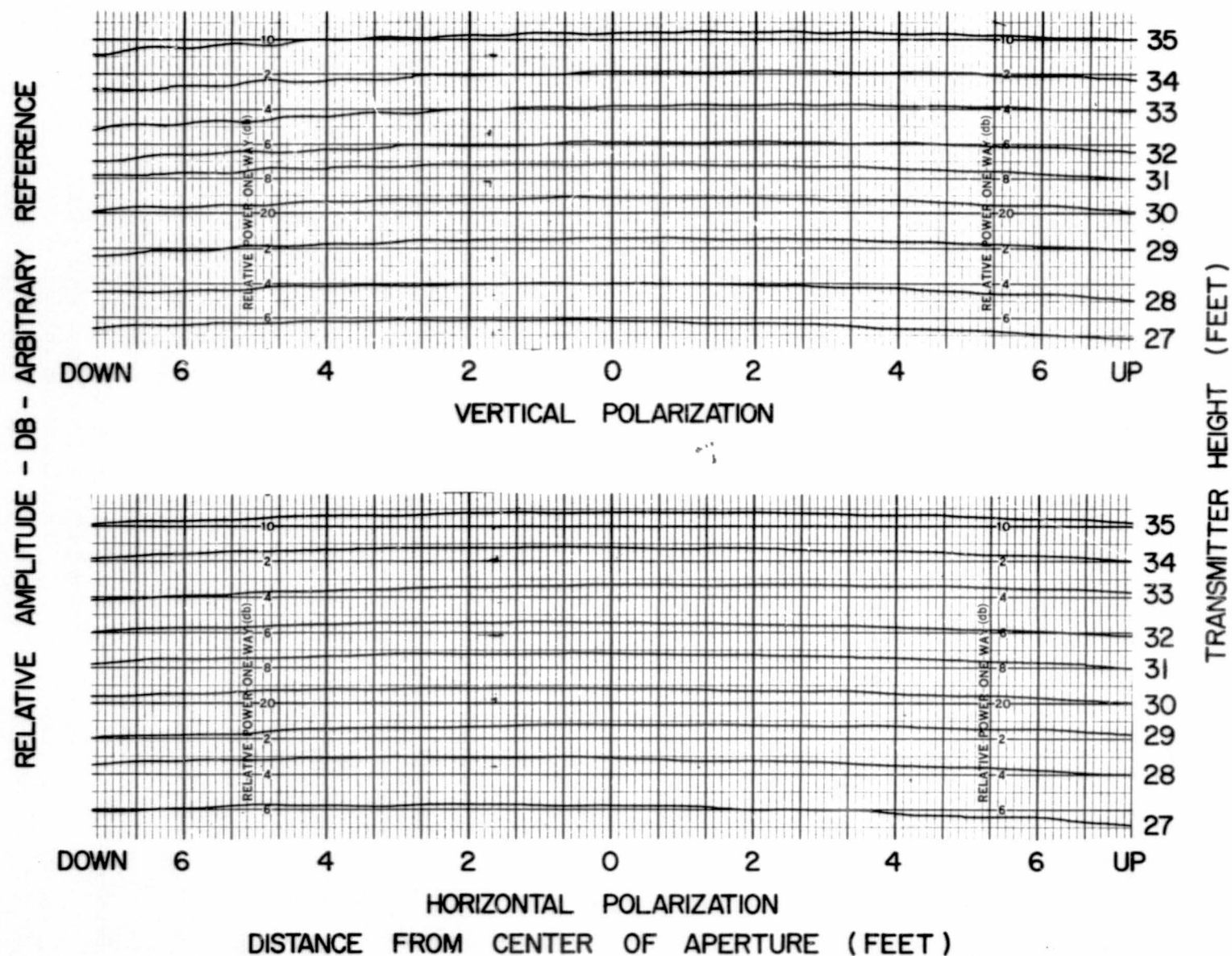


Figure 4.17. Vertical Aperture Field Patterns -- Elevated Mode With  
Two Diffraction Fences -- X-Band  
Configuration (e)



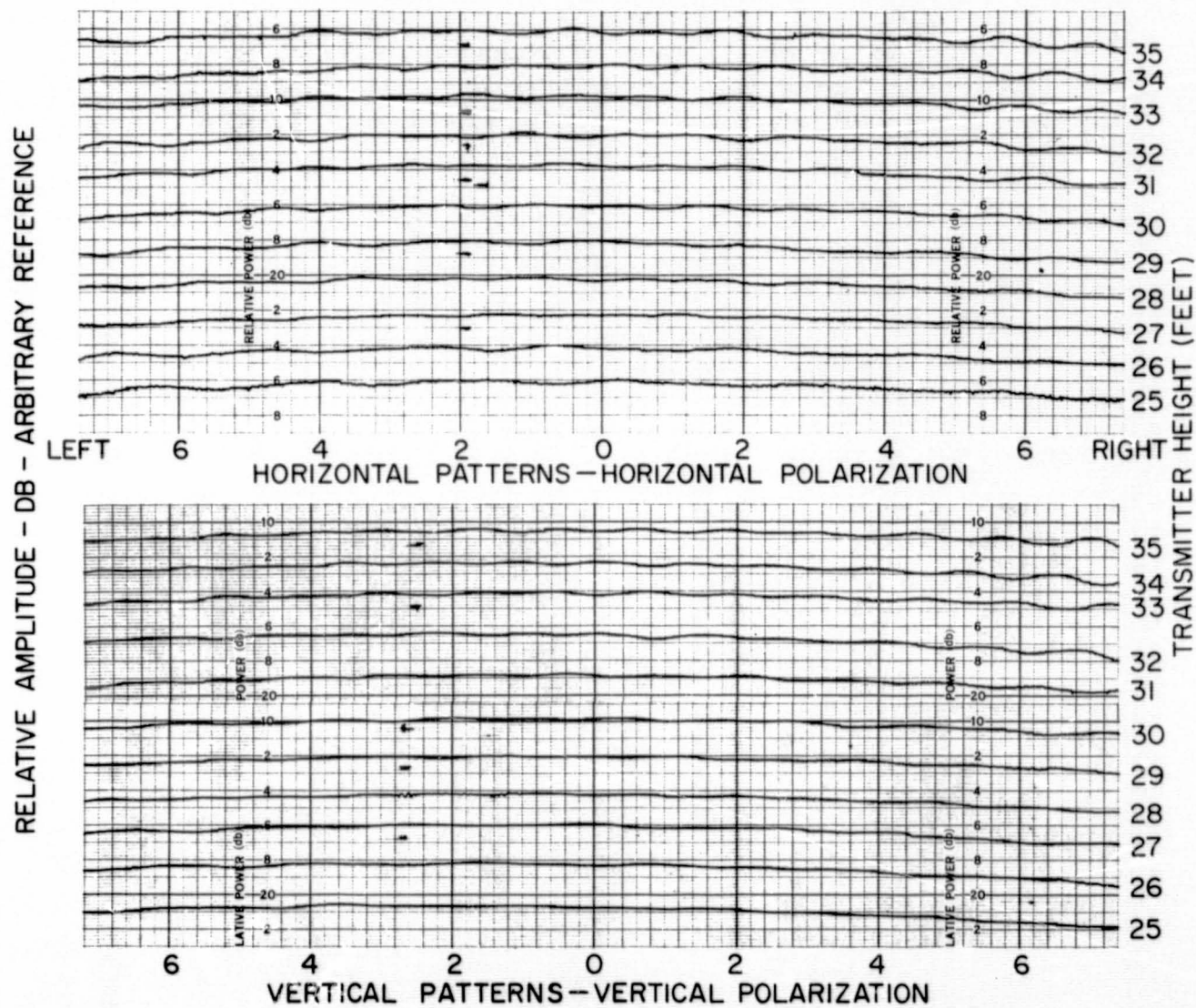


Figure 4.18. Aperture Field Patterns -- Elevated Mode With One 8-Foot Diffraction Fence -- X-Band Configuration (h)



a reduction of the ripple component in the aperture field from approximately 1 decibel to the order of 0.2 decibel. This improvement corresponds to a reduction in the relative level of extraneous energy of approximately 14 decibels. It was concluded that the use of a fence configuration which effectively screened approximately 20 Fresnel zones on the range surface, and was free from multipath effects, represented a reasonably optimum modification to the facility at X-band (see Figure F.9 of Appendix F).

The measurements reported herein are not considered to represent the ultimate improvement which can be obtained in the purity of the aperture field. The present study was limited by scheduling and the scope of the contract. A more exhaustive study which would continue the study of the effects of diffraction fences on aperture fields produced over a specular surface would be of value.

To investigate the possibility of reradiated energy from conduction currents excited on the fences, experiments were performed with microwave absorbing material attached to the tops of several fence configurations. No measurable reductions in the aperture-field ripple components were observed for the resulting data as compared to patterns for the same configurations with no absorbing material in place. It was concluded that reradiation effects were negligible at X-band.

The residual aperture-field amplitude ripple exhibited in the patterns of Figures 4.16 through 4.18 was considered to be due primarily to diffraction of the transmitted wavefront, as opposed to reradiation from the unscreened portions of the range surface. In order to investigate this assumption, vertical amplitude patterns were recorded for several transmitter heights such that the top of the diffraction fence was near the line-of-sight between the source antenna and the test aperture. These patterns, which are reproduced in Figure 4.19, are typical of the classical interference patterns which would theoretically result from diffraction over a straight-edge obstruction in the transmitted wavefront (see Appendix F).

Changes in the elevation squint angle with various fence configurations in place were found to affect the aperture field in much the same manner as for no diffraction screens (see Figure 4.8). Horizontal and vertical amplitude patterns, shown in Figure 4.20 for several elevation squint angles, indicate the magnitude of the aperture field asymmetry introduced by elevation squint errors.

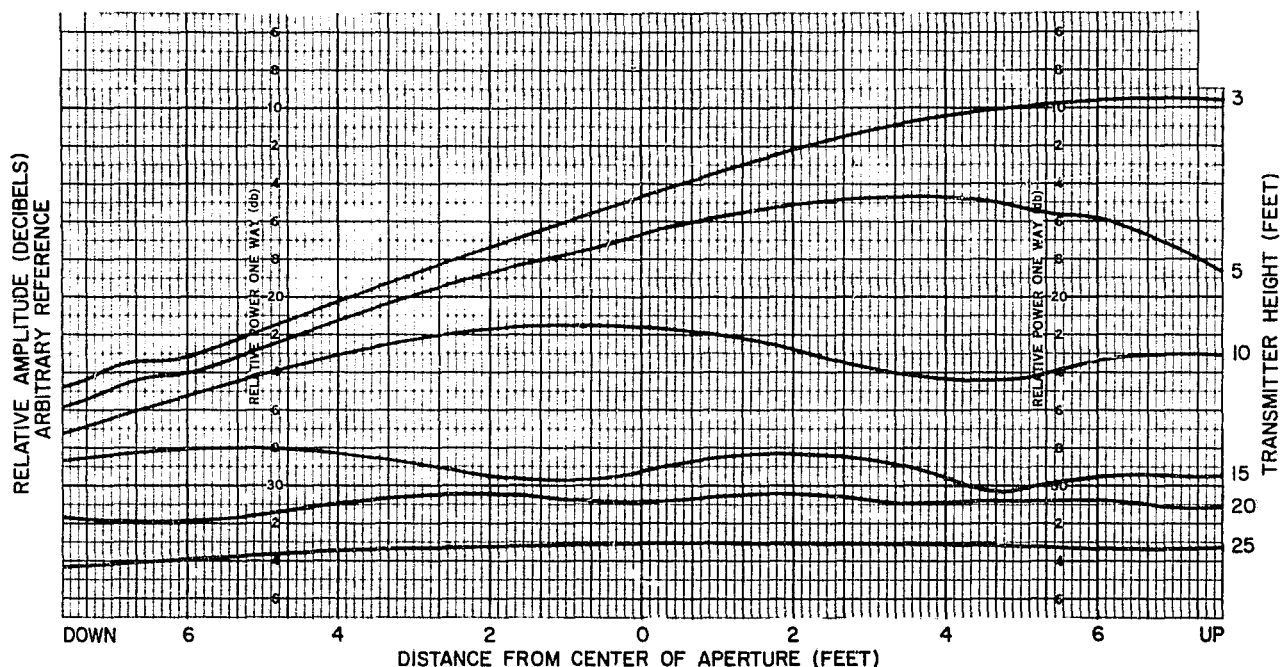


Figure 4.19. Effects of Diffraction Over a Fence --  
Vertical Patterns -- X-Band  
Configuration (g)

The patterns shown are for horizontal polarization;  
similar results were observed for vertical polarization.

As in the case of the elevated range with no diffraction fences, the amplitude ripple of the vertical patterns increases as the transmitter beam is lowered. The horizontal patterns are not significantly affected by the elevation squint angle, in accordance with the theory of section A.6.

4.1.3.2 Polarization Measurements: The polarization characteristics of the aperture field were investigated for the elevated mode with a single 8-foot diffraction fence in place at the center of the range. Axial ratio measurements were made at numerous points in a 16-foot diameter aperture for horizontal, vertical and circular polarizations of the transmitted energy. In each case, the transmitting antenna circuitry was adjusted until the appropriate polarization characteristics were observed at the center of the aperture, and the measurements of polarization versus aperture position were referenced to these results.

The measured axial ratio for the horizontal polarization tests was greater than

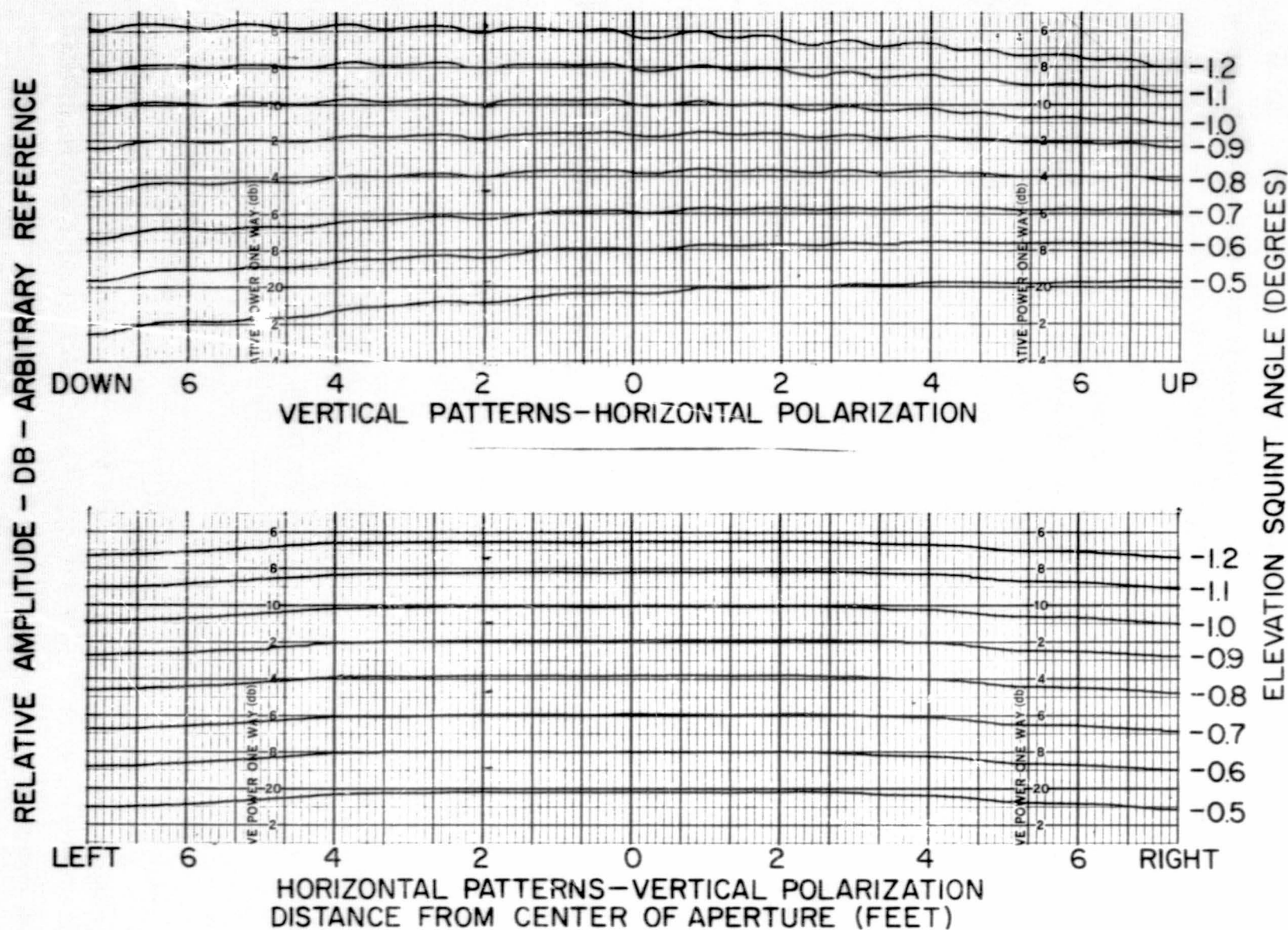


Figure 4.20. Effects of Elevation Squint Angle on Aperture Field Patterns --  
 Elevated Mode with Three Diffraction Fences -- X-Band

40 decibels for all points investigated in the 16-foot aperture. Axial ratios measured for vertical polarization tests exceeded 40 decibels except for three points observed on the periphery of the 16-foot aperture where the axial ratio fell to approximately 30 decibels.

Figure 4.21 shows the variation of the axial ratio with position in the test aperture for the case of circular polarization. The measured axial ratio was less than 0.8 decibel for all points investigated in the 16-foot aperture and changes in the axial ratio for an 8-foot aperture never exceeded 0.2 decibel.

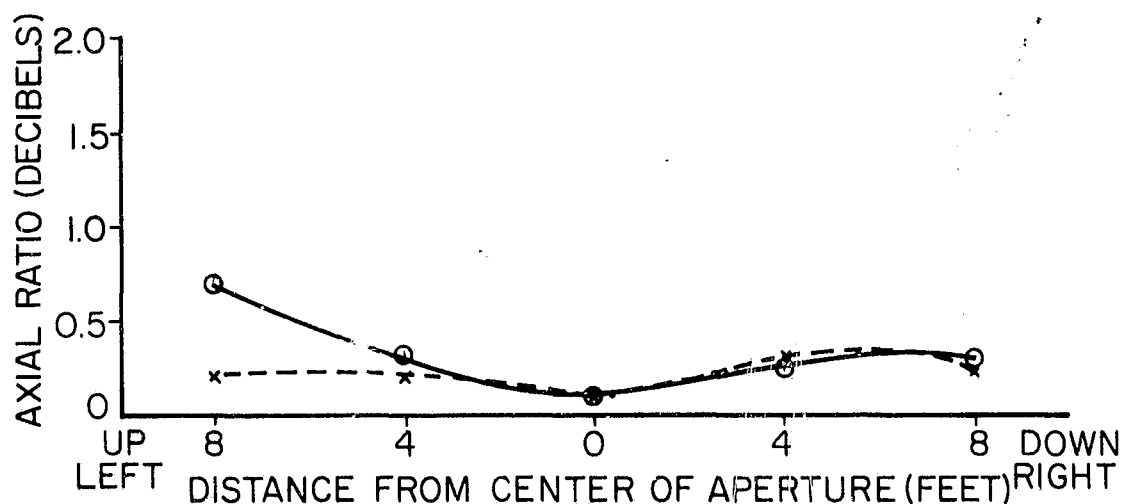


Figure 4.21. Axial Ratio as a Function of Aperture Position -- Elevated Mode with Single Diffraction Fence -- X-Band

o --- Up-Down  
x --- Left-Right

The frequency sensitivity of the aperture field polarization characteristics is graphed in Figure 4.22. The axial ratio for nominal circular polarization remained less than 2 decibels as the frequency was varied from 8 to 12 GHz. In the region of the center frequency of 10 GHz, the polarization variation with frequency was observed to be small.

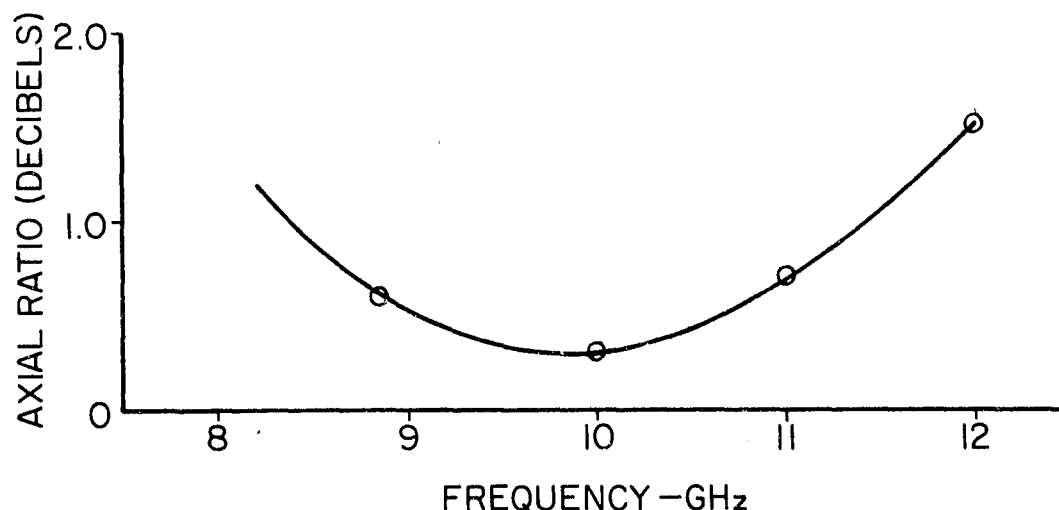


Figure 4.22. Axial Ratio Versus Frequency -- Elevated Mode with Single Diffraction Fence -- X-Band

4.1.3.3 Boresight Measurements: Boresight measurement error was reduced by an order of magnitude by the use of diffraction fences in the elevated mode at X-band. Typical plots of apparent source height versus actual source height are shown in Figures 4.23, 4.24 and 4.25 for three different linear polarizations and two fence configurations. The deviations from the true boresight direction are generally reduced to the order of 0.2 milliradian or less. The residual boresight error appears to be a combination of a cyclic variation, corresponding to the small amplitude ripple seen in the aperture-field amplitude patterns, a random error component caused by the random summation of various small system errors, solar heating effects, etc., and a small (approximately 0.1 milliradian) bias error which results in apparent source heights slightly above the actual source height.

The calculated average errors and standard deviations for 9 sets of boresight measurements comprising over 100 data points are shown graphically in Figure 4.26(a) for the elevated mode with diffraction fences. For comparison, calculated results are shown for 100 data points obtained in the elevated mode with no diffraction fences in Figure 4.26(b). In both cases a small positive bias of approximately 0.1 milliradian was calculated. Since the data summarized in Figure 4.26 represent the results of tests conducted on several days with two different transmitting antennas and with various polarizations, it is probable that the small residual bias error is associated with the optical reference system rather than the range configuration or sensing device.

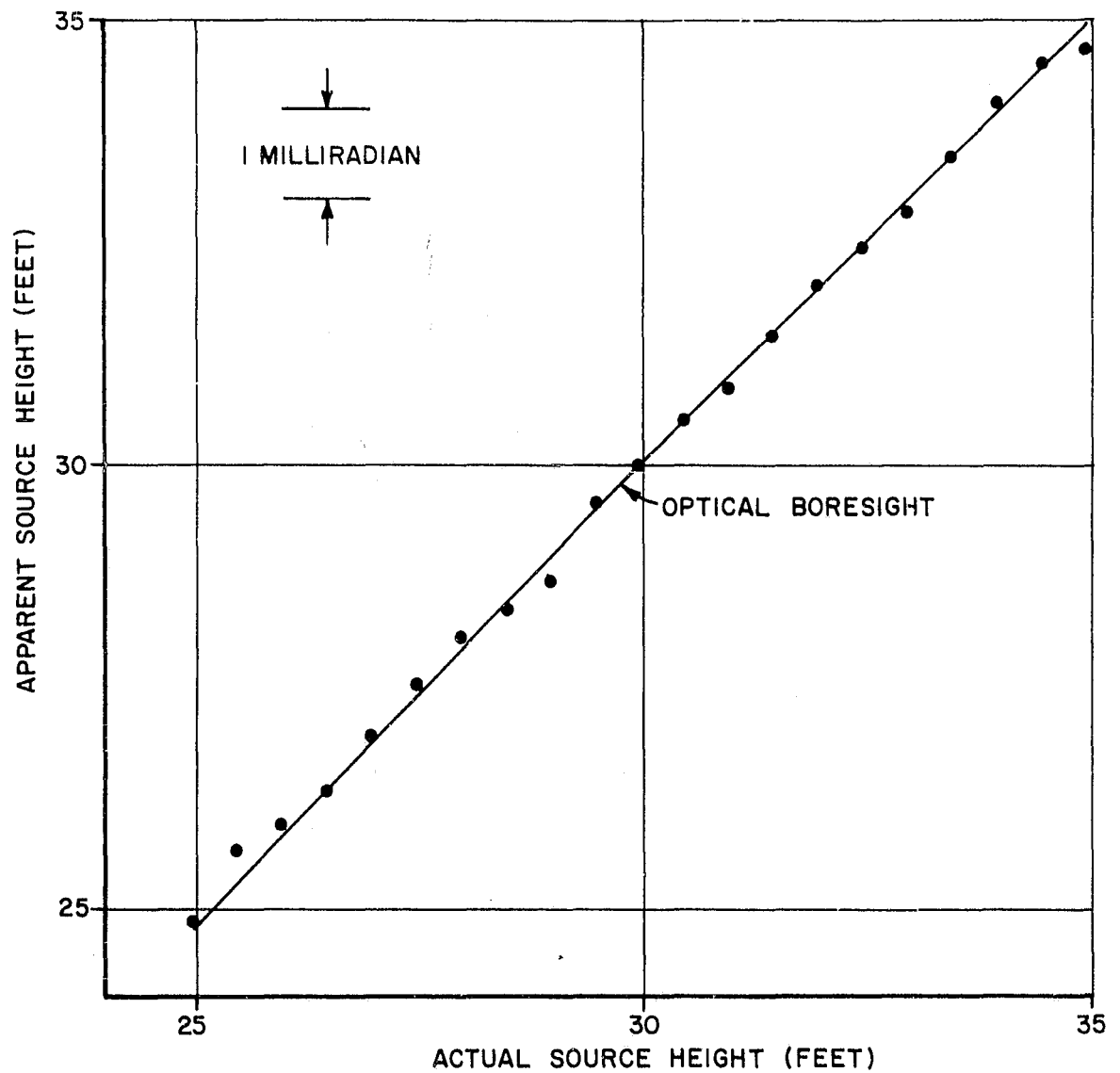


Figure 4.23. Apparent Source Height Versus Actual Source Height -- Elevated Mode with Diffraction Fences -- X-Band -- Vertical Polarization Configuration (h)

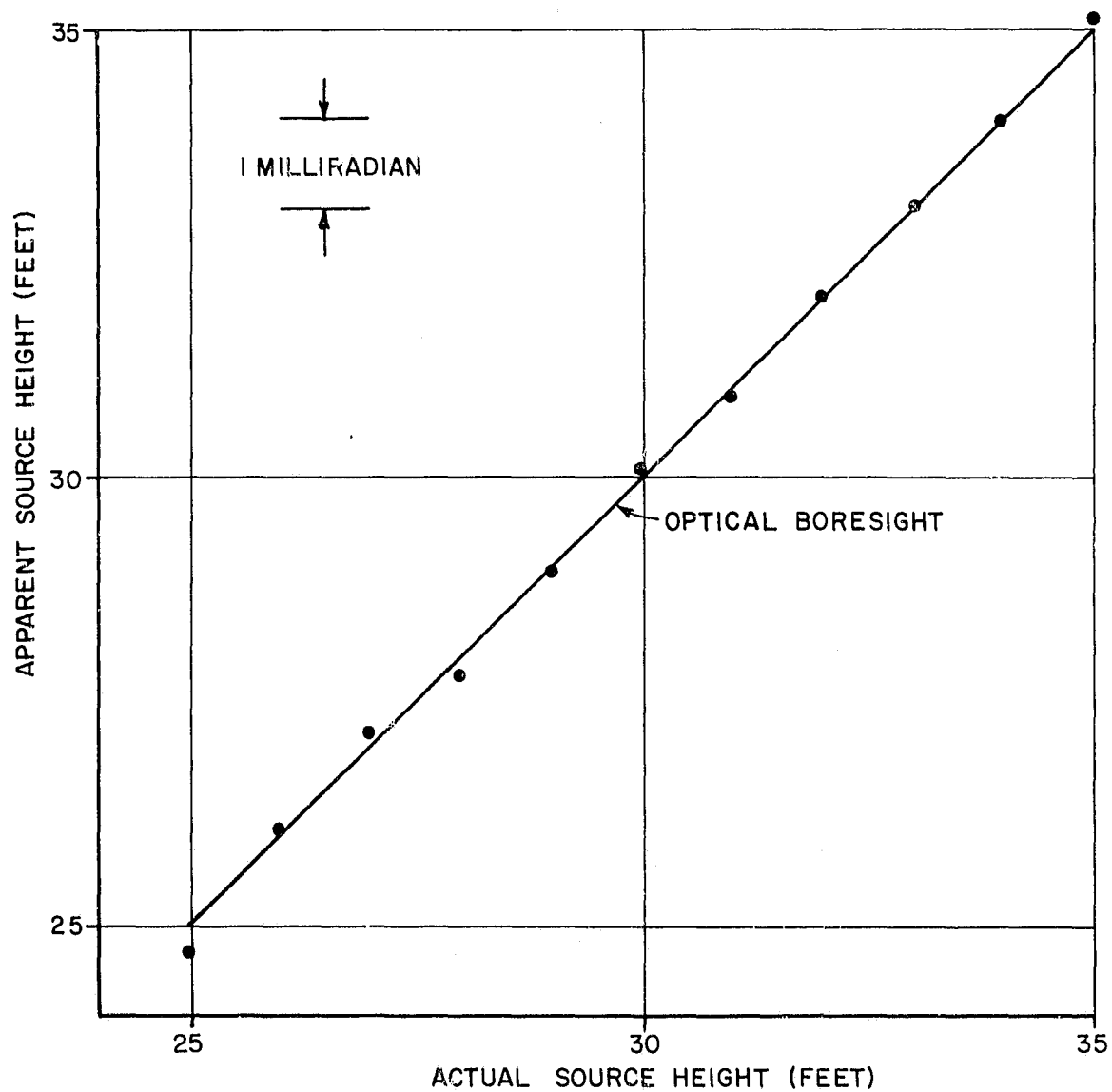


Figure 4.24. Apparent Source Height Versus Actual Source Height -- Elevated Mode with Diffraction Fences -- X-Band -- Horizontal Polarization Configuration (b)

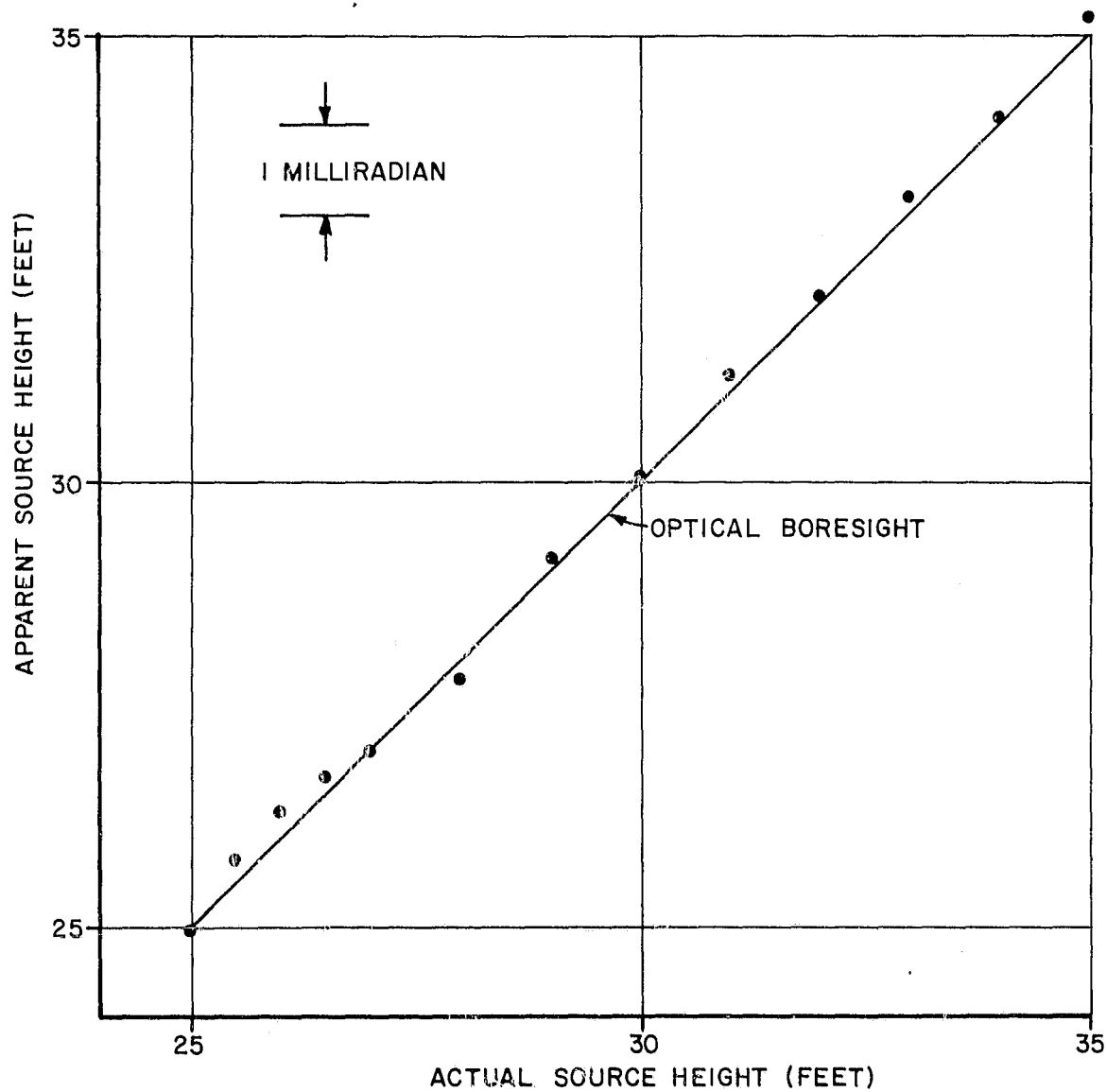
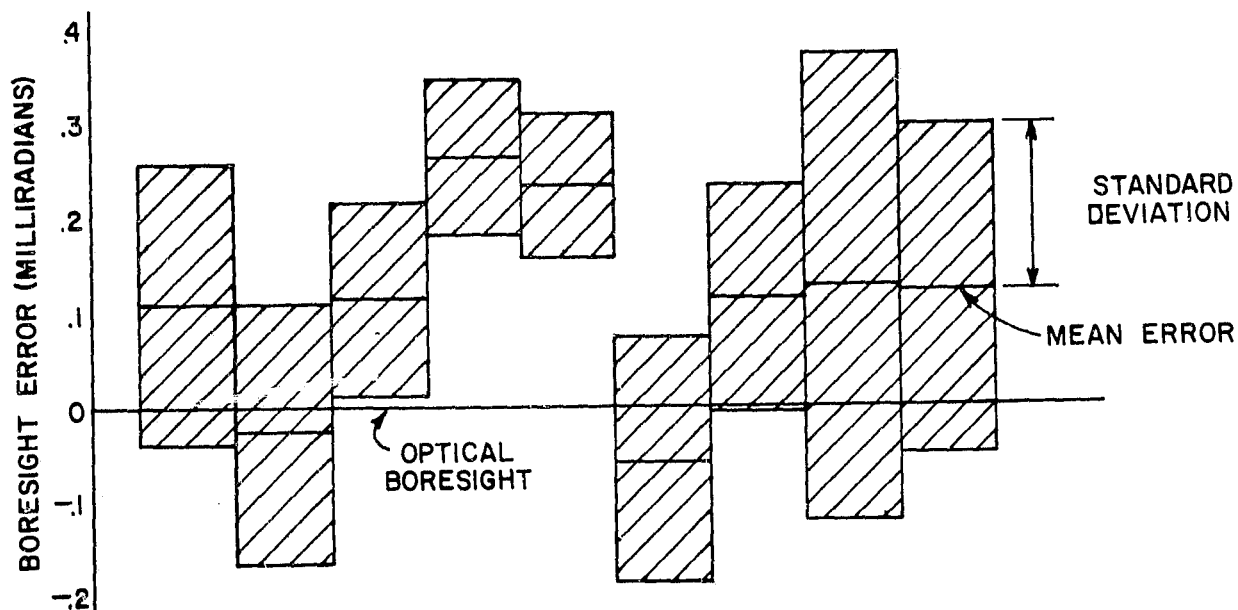
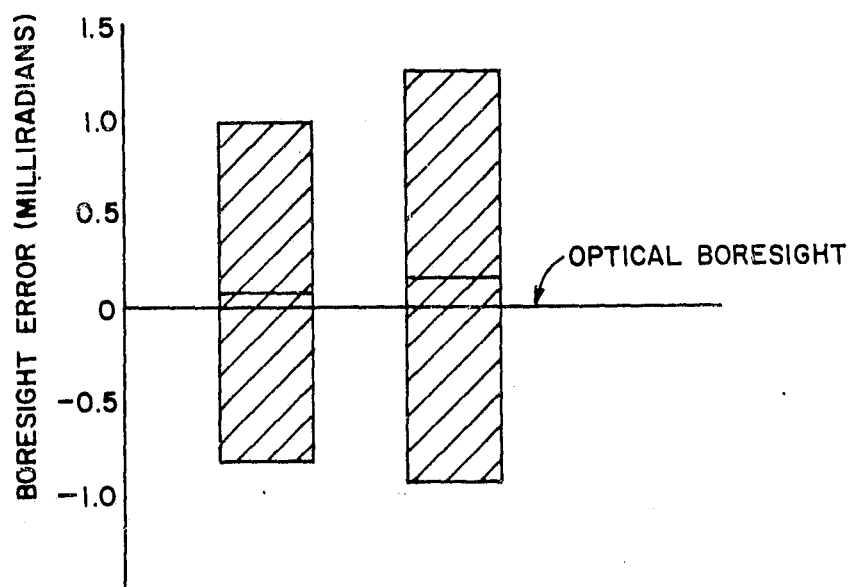


Figure 4.25. Apparent Source Height Versus Actual Source Height --  
 Elevated Mode with Diffraction Fences -- X-Band --  
 45-Degree Linear Polarization  
 Configuration (b)





(a) With Diffraction Fences



(b) Without Diffraction Fences

Figure 4. 26. Summary of X-Band Boresight Data for Elevated Mode -- Vertical Sensing

These graphs are included as an illustration of the total spread of boresight data obtained on widely separated dates, and with one or more of the following parameters varied in each data set: Elevation squint angle; azimuth squint angle; fence configuration; source height.

The results summarized in Figure 4.26 represent data obtained on two field trips by different personnel under a variety of climatic conditions; the data spreads are therefore indicative of the boresight accuracy which is likely to be obtained in the elevated mode with the use of diffraction fences. The standard deviations for measurements with diffraction fences do not exceed 0.15 milliradian except for two data sets; the standard deviation for all such boresight measurements is 0.14 milliradian with an average positive bias error of 0.09 milliradian. The overall standard deviation for boresight measurements in the absence of diffraction fences was 0.98 milliradian, with an average positive bias error of 0.11 milliradian.

The amplitude patterns of Figures 4.17 and 4.18 indicated very little variation in the aperture field as the probe was moved horizontally; this relative aperture-field purity implies that greater boresight measurement accuracy may be obtained for sensing in the horizontal (azimuth) plane than for the case of vertical (elevation) sensing. Typical azimuth boresight data are shown for several spacecraft orientations in Figure 4.27. The roll axis orientation angle is the angle between the spacecraft's roll axis and the reference coordinate axis OT as defined in Appendix H. The standard deviation of the data of Figure 4.27 is 0.03 milliradian about a mean value of  $-0.03$  milliradian, indicating that the azimuth sensing capability is superior to that for the case of elevation sensing.

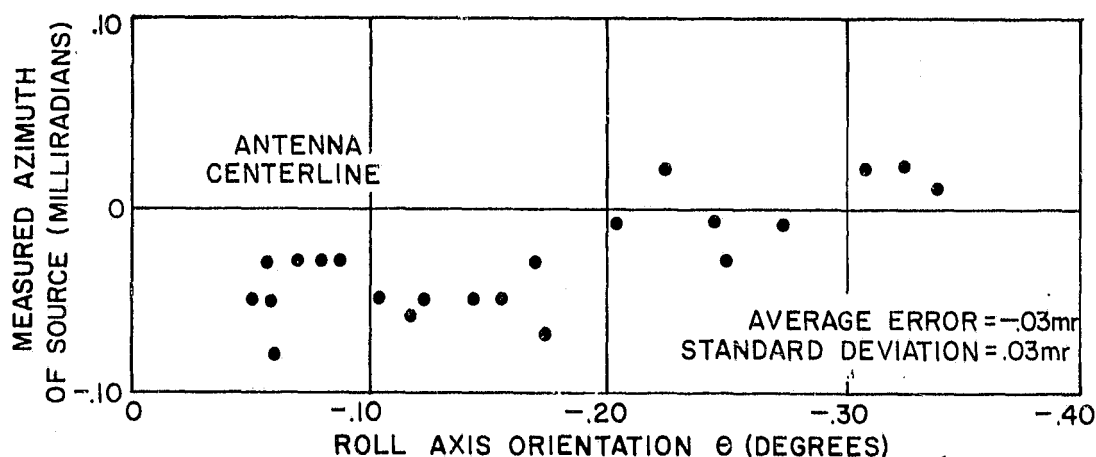


Figure 4.27. Measured Azimuth of Source Versus Azimuth Null Offset Angle -- Elevated Mode with Diffraction Fences -- X-Band

The effects of misalignments in the elevation and azimuth transmitter squint angles on boresight accuracy are shown in Figures 4.28 and 4.29. The apparent source height is seen to be somewhat sensitive to changes in the elevation squint angle, varying by approximately  $\pm 0.5$  milliradian as the squint angle changes by  $\pm 0.5$  degree about its experimentally optimum value. As the transmitter beam is lowered, relatively large errors result due to increased illumination of the diffracting edges, as seen for the large negative squint angles of Figure 4.28.

The setting of the azimuth squint angle is less critical than that of the beam axis in the vertical plane, as can be seen from the data of Figure 4.29. For azimuth squint variations of  $\pm 0.6$  degree about the range centerline the measured azimuth of the apparent source varied less than  $\pm 0.02$  milliradian for the typical data shown in this Figure.

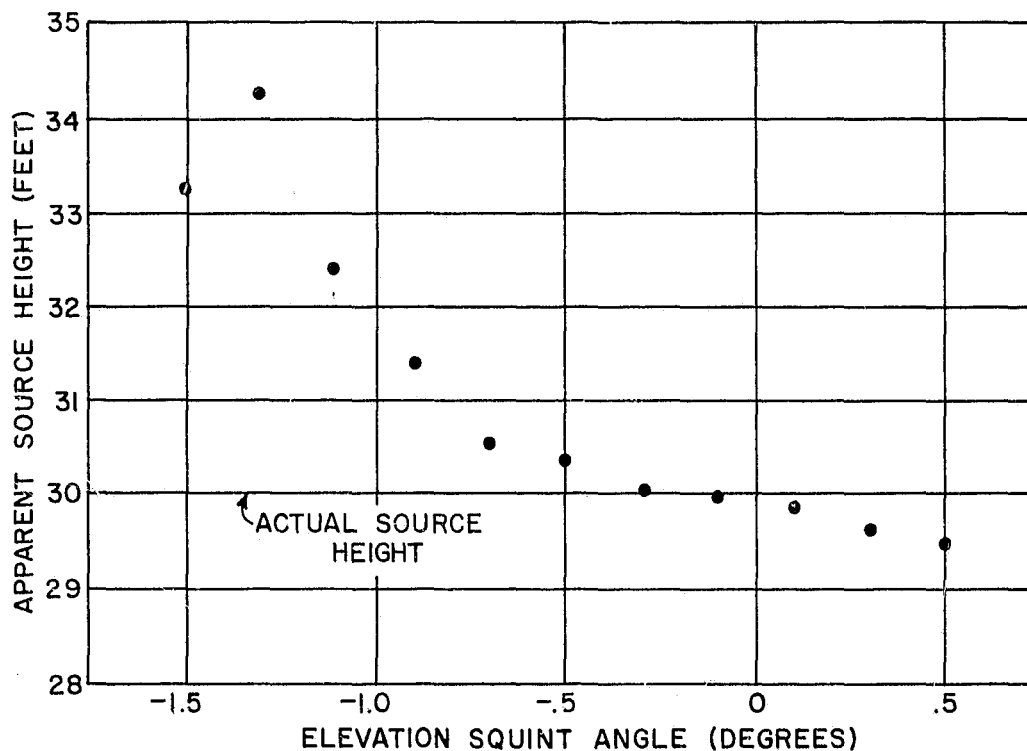


Figure 4.28. Effect of Varying Elevation Squint Angle on Apparent Source Height -- Elevated Mode with Diffraction Fences -- X-Band

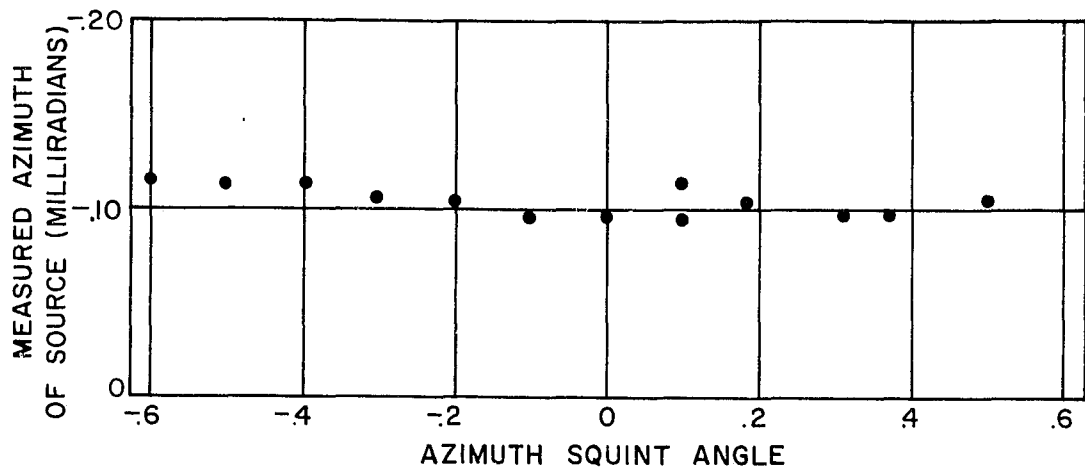


Figure 4.29. Measured Azimuth of Source Versus Azimuth Squint Angle -- Elevated Mode with Diffraction Fences -- X-Band

## 4.2 S-Band Measurements

The MILA boresight test range was evaluated at S-band for use as a precision boresight test facility and for use as a general purpose radiation pattern test facility. The S-band program generally paralleled the X-band program described in section 4.1, including boresight, polarization, and aperture-field amplitude measurements for the ground-reflection and elevated modes of operation. Details of the measurement techniques and equipment are included in Chapter 3. Unless otherwise specified, all S-band data presented in the following paragraphs were obtained at a frequency of 2.3 GHz.

### 4.2.1 Ground-Reflection Mode

The following paragraphs present data describing the performance of the MILA range when operated in the ground-reflection mode at 2.3 GHz. The transmitting antenna used for this mode of operation was a 4-foot paraboloidal reflector with a remotely adjustable feed allowing any desired polarization characteristic to be obtained. The 3-decibel beamwidth for this antenna is approximately 7.5 degrees; thus the free-space 0.25-decibel beamwidth subtends a test aperture diameter of

approximately 39 feet at a range length of 1000 feet. The wavelength  $\lambda$  corresponding to a frequency of 2.3 GHz is approximately 0.43 foot. The theoretically optimum transmitter height for the ground-reflection mode at this frequency can be calculated from equation (4-1):

$$h_t \doteq \frac{\lambda R_o}{4h_r} \doteq 3.57 \text{ feet},$$

where  $h_t$ ,  $h_r$ , and  $R_o$  are the transmitter height, receiver height (30 feet) and range length (1000 feet), respectively.

4.2.1.1 Amplitude Measurements: Vertical amplitude patterns of the aperture field are shown in Figure 4.30 as a function of transmitter height for the S-band ground-reflection range. The transmitter height which results in optimum pattern symmetry for the 18-foot test aperture is seen to be approximately 3.37 feet for both vertical and horizontal polarizations. The field asymmetry introduced in the central 10-foot test aperture for transmitter height variations of  $\pm 0.2$  foot from the optimum value of 3.37 feet is approximately  $\pm 0.2$  decibel; the transmitter height adjustment is thus less critical than for the X-band ground-reflection case where similar asymmetry is introduced by changing the transmitter height by a few hundredths of a foot from the optimum value as would be expected from equation (4-1).

Horizontal-plane amplitude patterns are shown for several transmitter heights in Figure 4.31. At S-band, as for X-band, the horizontal taper and ripple characteristics are seen to be virtually unaffected by changes in transmitter height, in accordance with the theory of section A.6.

Both the horizontal and vertical field patterns exhibit a high degree of purity. In each case the ripple component is essentially negligible within measurement accuracies over a 16-foot diameter aperture for the patterns taken at the optimum transmitter height. The amplitude taper is less than 0.25 decibel in the vertical plane for a 10-foot aperture and less than 0.8 decibel in the vertical plane for the 16-foot aperture. The horizontal taper of the pattern formed by the source antenna and its image in the range surface is negligible over a 16-foot aperture.

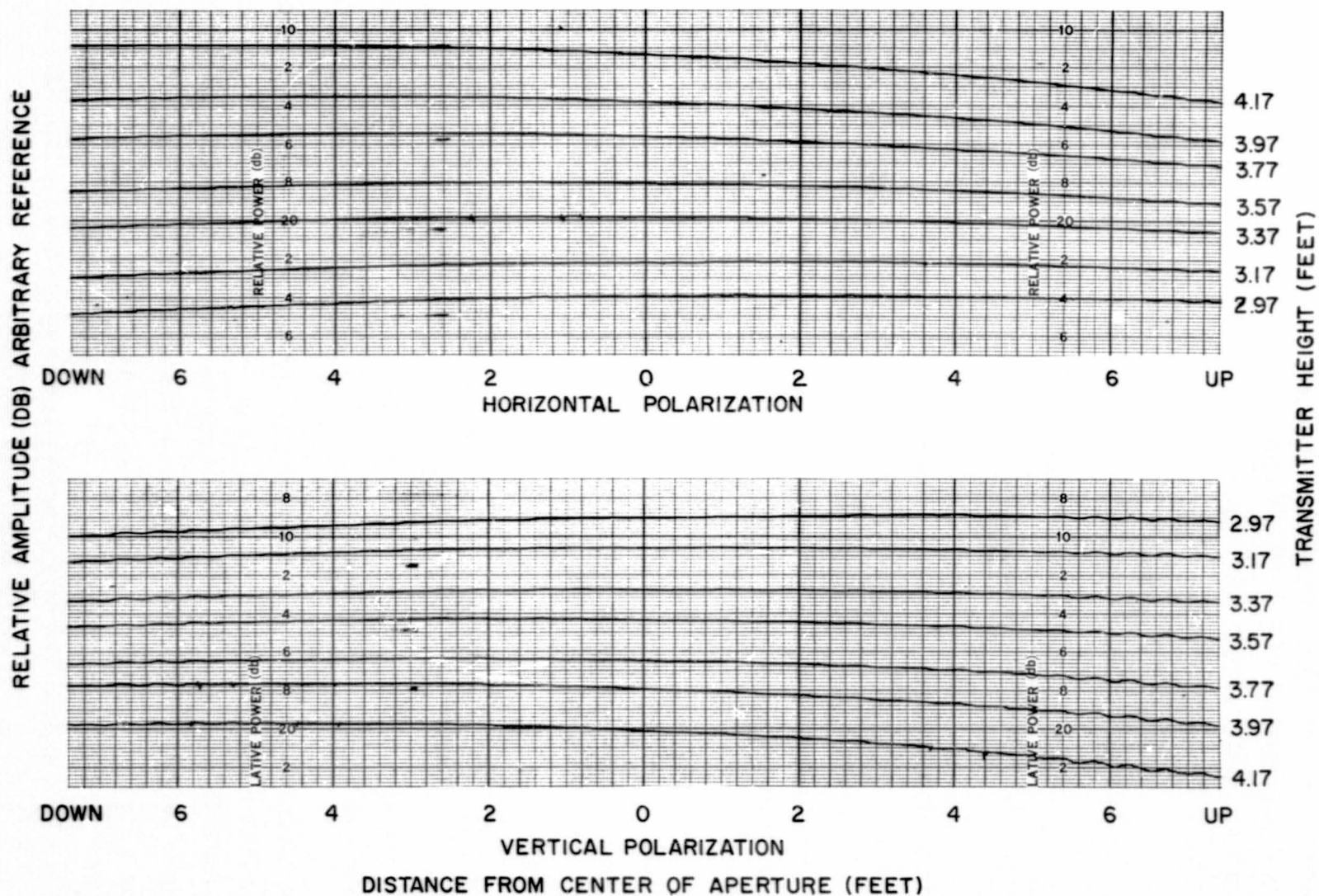


Figure 4.30. Vertical Aperture Field Patterns -- Ground-Reflection Mode -- S-Band

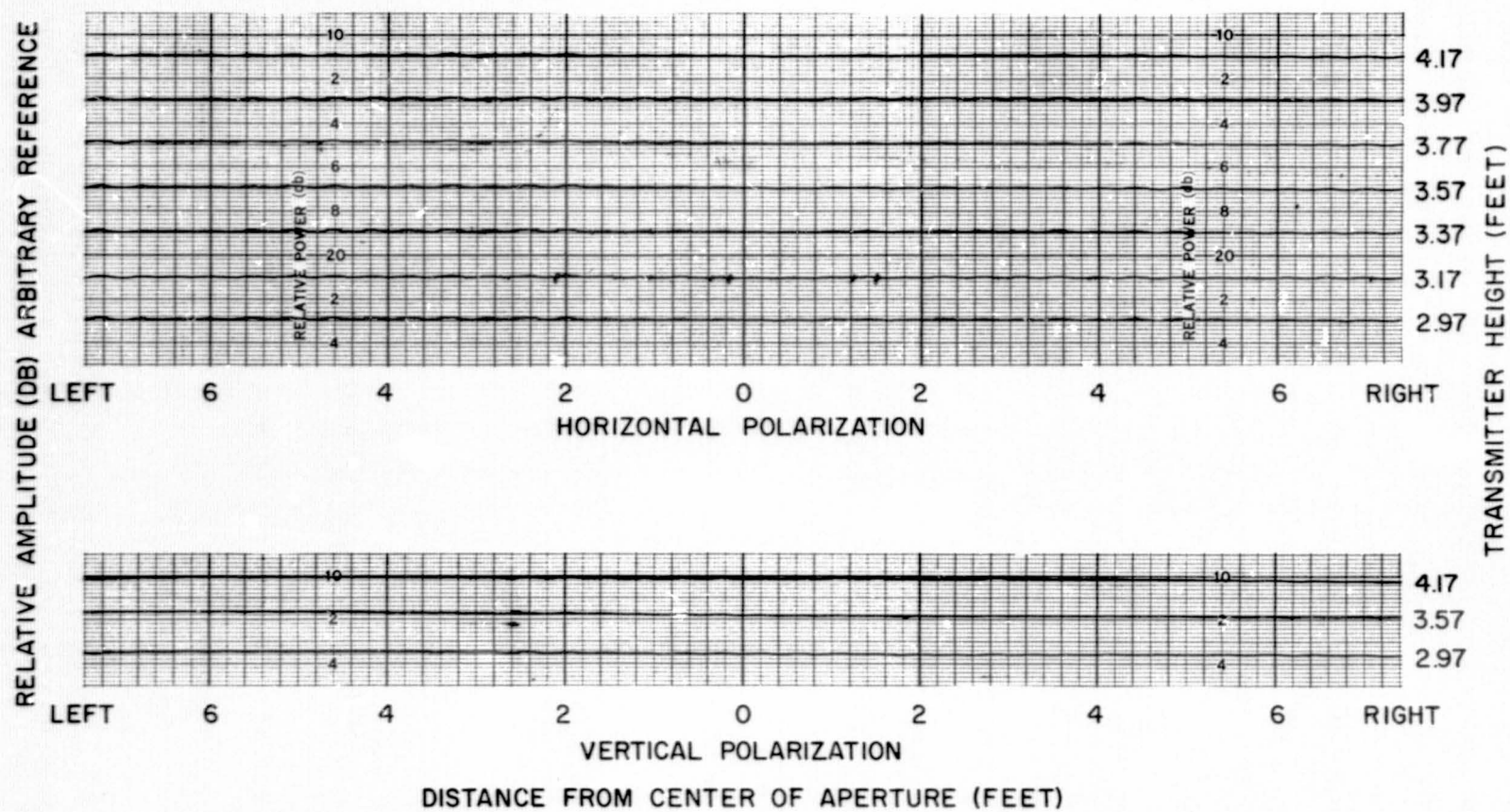


Figure 4.31. Horizontal Aperture Field Patterns -- Ground-Reflection Mode -- S-Band

4.2.1.2 Polarization Measurements: The measured polarization characteristics, of the aperture field in the ground-reflection mode were relatively constant over a 16-foot diameter test aperture. Polarization patterns obtained for vertical polarization maintained an axial ratio of greater than 40 decibels for all points measured in the 16-foot aperture. Similar plots for horizontal polarization exhibited axial ratios varying between 31 and 40 decibels for points in the 16-foot test aperture when the axial ratio was adjusted to 36 decibels at the center of the aperture.

The variation of the axial ratio with position in the test aperture for circular polarization is shown in Figure 4.32.\* The axial ratio as measured at several points in the test aperture varied less than 0.2 decibel from that of the reference polarization at the center of the aperture.

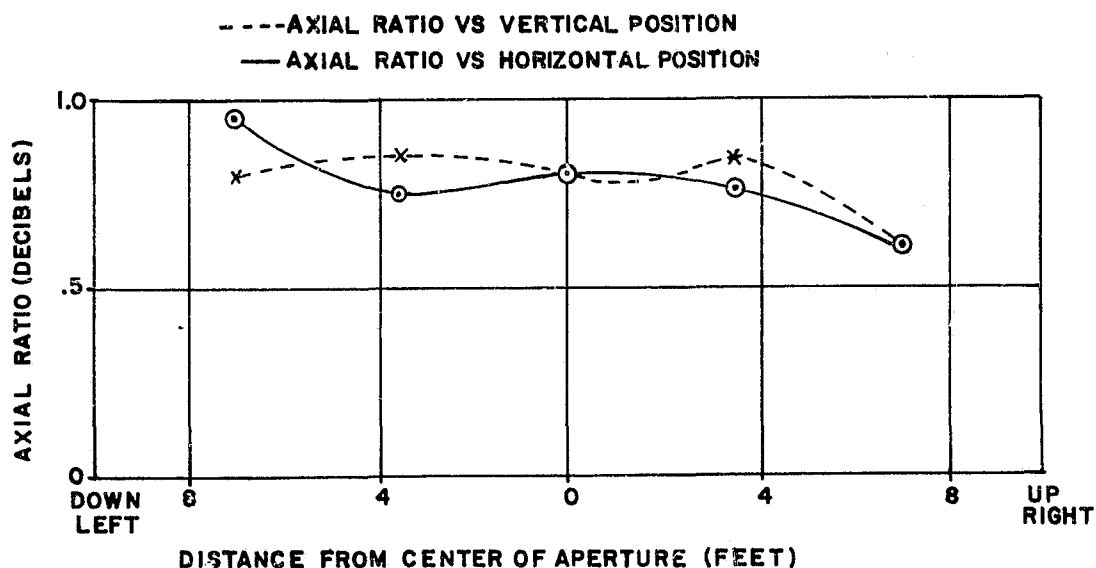


Figure 4.32. Axial Ratio Versus Aperture Position -- Ground-Reflection Mode -- S-Band

\* Difficulties were encountered in adjusting the axial ratio of the transmitted polarization due to a faulty connector in the phase-amplitude unit. Thus the reference polarization at the center of the test aperture exhibited an axial ratio of approximately 0.8 decibel rather than being "pure circular" polarization. The faulty connector was subsequently replaced, and laboratory measurements performed at Scientific-Atlanta indicate that the performance of the S-band phase-amplitude unit is comparable to that of the X-band unit.



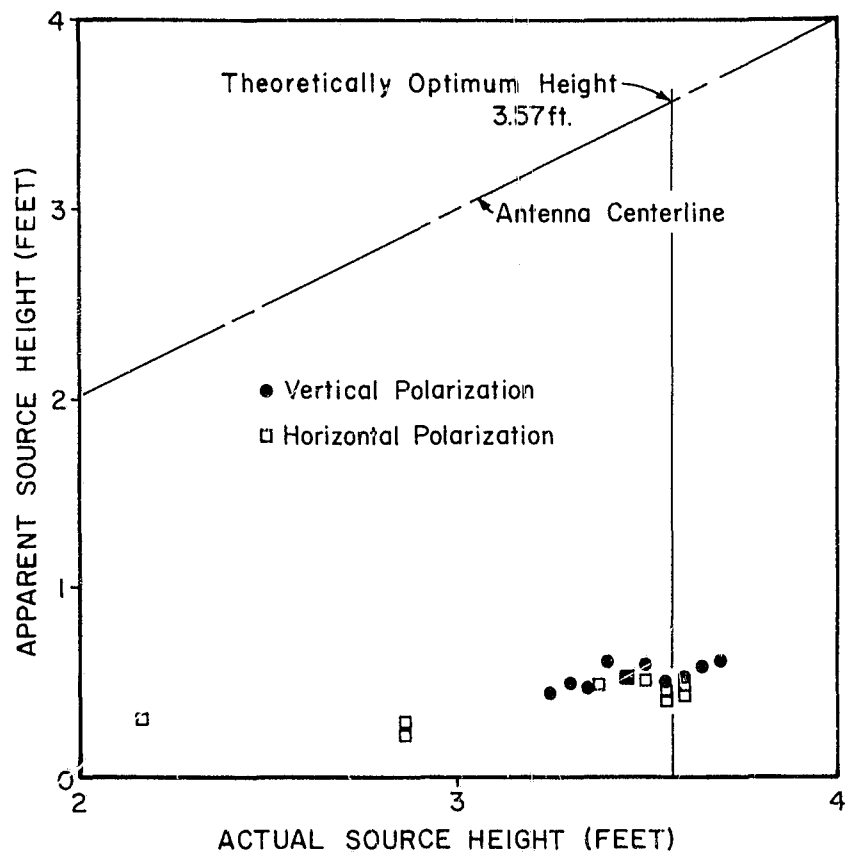
4.2.1.3 Boresight Measurements: The S-band boresight measurements utilized the phase-monopulse sensor described in Chapter 3 to measure the direction to the apparent source of radiation. The measurement techniques and data analysis were essentially identical to those used for the X-band program.

The effect on boresight measurements of varying the source height is shown in Figure 4.33(a). The data are shown plotted against an expanded vertical scale in Figure 4.33(b). When the actual source height varies near the theoretical optimum height of 3.57 feet, the measured source height values fall within  $\pm 0.15$  foot of 0.5 foot. The variation of the average apparent source height is less than 0.1 foot for actual source height variations of several inches; as for X-band operation, precise adjustment of the transmitter height is not critical for accurate boresight measurements in the ground-reflection mode.

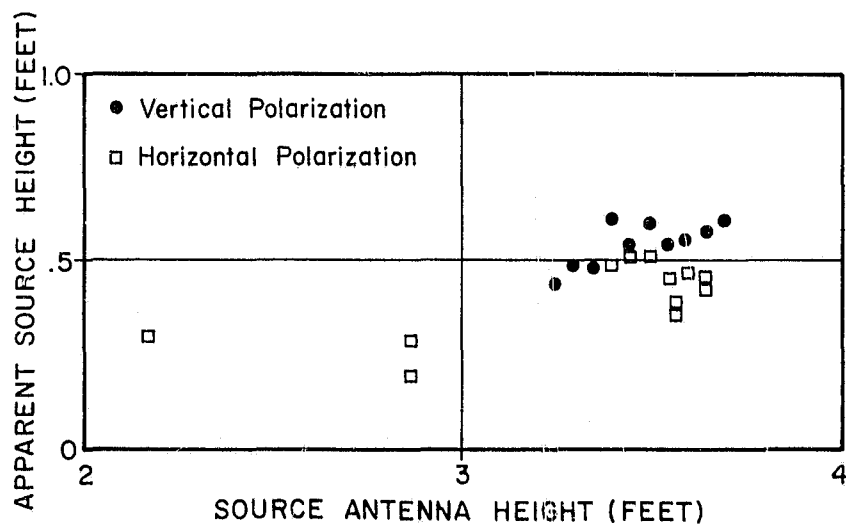
With the transmitter squint and height parameters optimized, boresight measurements were made for several orientations of the spacecraft roll axis. The roll axis was displaced from the range axis OT\* by an angle  $\theta$  and the monopulse circuitry was adjusted to obtain a null. The spacecraft was then rotated 180 degrees about the roll axis, and the direction to the apparent source was sensed. The two roll-axis position readings were averaged and the result compared to the optical boresight reference direction. As discussed in section 6.3 of Appendix K, the effects of parallax, reflections from the spacecraft, etc., are cancelled by averaging the two readings, and the deviation of the averaged result from the optical boresight direction represents a boresight measurement error of the antenna range, rather than the sensing device. These tests simulated typical boresight calibration tests in which the direction to the source antenna, is sensed as the spacecraft is changed in orientation. The results are shown in Figures 4.34 and 4.35; Figure 4.34 shows the apparent source height as the roll axis is displaced in the vertical plane, and Figure 4.35 shows results for measurements made as the roll axis is displaced in the horizontal plane. In both cases, the average source height is approximately 0.5 foot with maximum variations of the order of 0.15 foot.

---

\*See Appendix K, Figure 5.2.



(a) Vertical Scale -- 1 inch equals 1 milliradian



(b) Vertical Scale -- 1 inch equals 0.5 milliradian

Figure 4.33. Variation of Apparent Source Height with Actual Source Height -- Ground-Reflection Mode -- S-Band

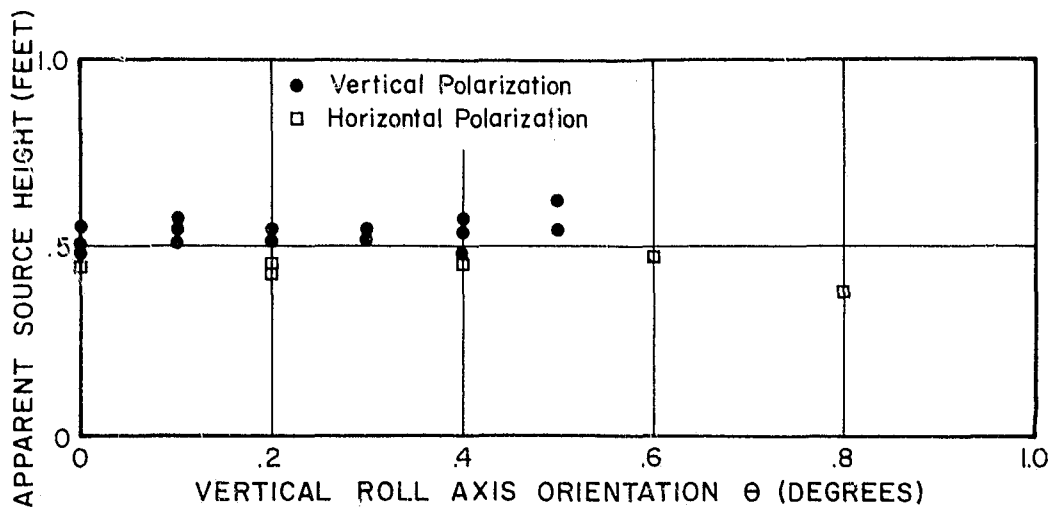


Figure 4.34. Variation of Apparent Source Height with Vertical Null Offset Angle -- Ground-Reflection Mode -- S-Band

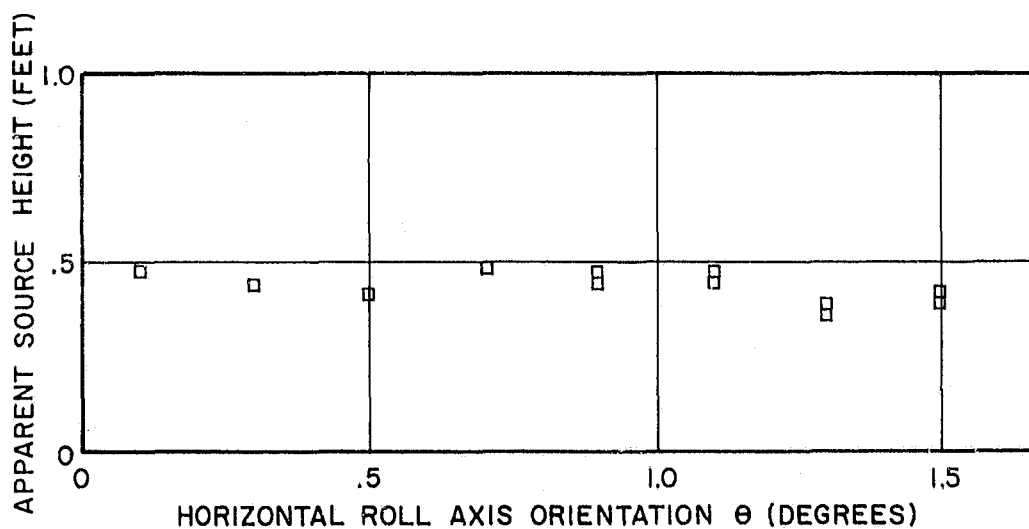


Figure 4.35. Variation of Apparent Source Height with Horizontal Null Offset Angle -- Ground-Reflection Mode -- S-Band

#### 4.2.2 Elevated Mode

For elevated operation at 2.3 GHz, the polarization adjusting system and feed were used with an 8-foot paraboloidal reflector as a transmitting system. The 3-decibel beamwidth of this antenna at 2.3 GHz is approximately 3.7 degrees. The transmitter height was nominally 30 feet, although measurements were made for other heights between 25 and 35 feet. The angle between the peak of the main lobe, and the first null of the transmitting-antenna beam was slightly greater than 4 degrees, and the angle to the point of specular reflection for a transmitter height of 30 feet was approximately 3.4 degrees; therefore more than half of the length of the range surface was illuminated by the main lobe.

Aperture-field amplitude patterns are shown in Figure 4.36 for operation at S-band in the elevated mode with no diffraction fences in place. The relatively low directivity of the transmitting antenna resulted in a high extraneous signal level at the test aperture; the vertical patterns of Figure 4.36 exhibit amplitude ripple magnitudes greater than 3 decibels. The horizontal patterns are virtually free of ripple, indicating the absence of extraneous signals arriving from sources other than the range surface. Amplitude taper due to the directivity of the transmitting antenna is negligible, as evidenced by the horizontal patterns.

As confirmed by the patterns of Figure 4.36, illumination of the range surface by the 8-foot transmitting antenna results in an unacceptable extraneous signal level at the test aperture; the theoretical developments of Appendices A, B, and D and the X-band measurements indicate that this mode of operation is not useful for precise boresight and pattern measurements.

The results of placing an 8-foot fence on the range surface are shown in Figures 4.37 and 4.38. The fence reduces the amplitude ripple to slightly less than 1 decibel for the vertical patterns corresponding to an extraneous signal magnitude of approximately 0.05 times that of the direct path signal.

Further reduction of the extraneous signal level could probably be accomplished by the use of a multiple fence configuration; it is not probable, however, that the high degree of suppression obtainable at X-band can be realized in the S-band case. The problem of diffraction from the tops of the fences is more severe at the lower frequencies, and the largest transmitting antenna currently available\*

---

\*At the time of publication, the largest antenna available at the MILA range is an 8-foot paraboloidal reflector.

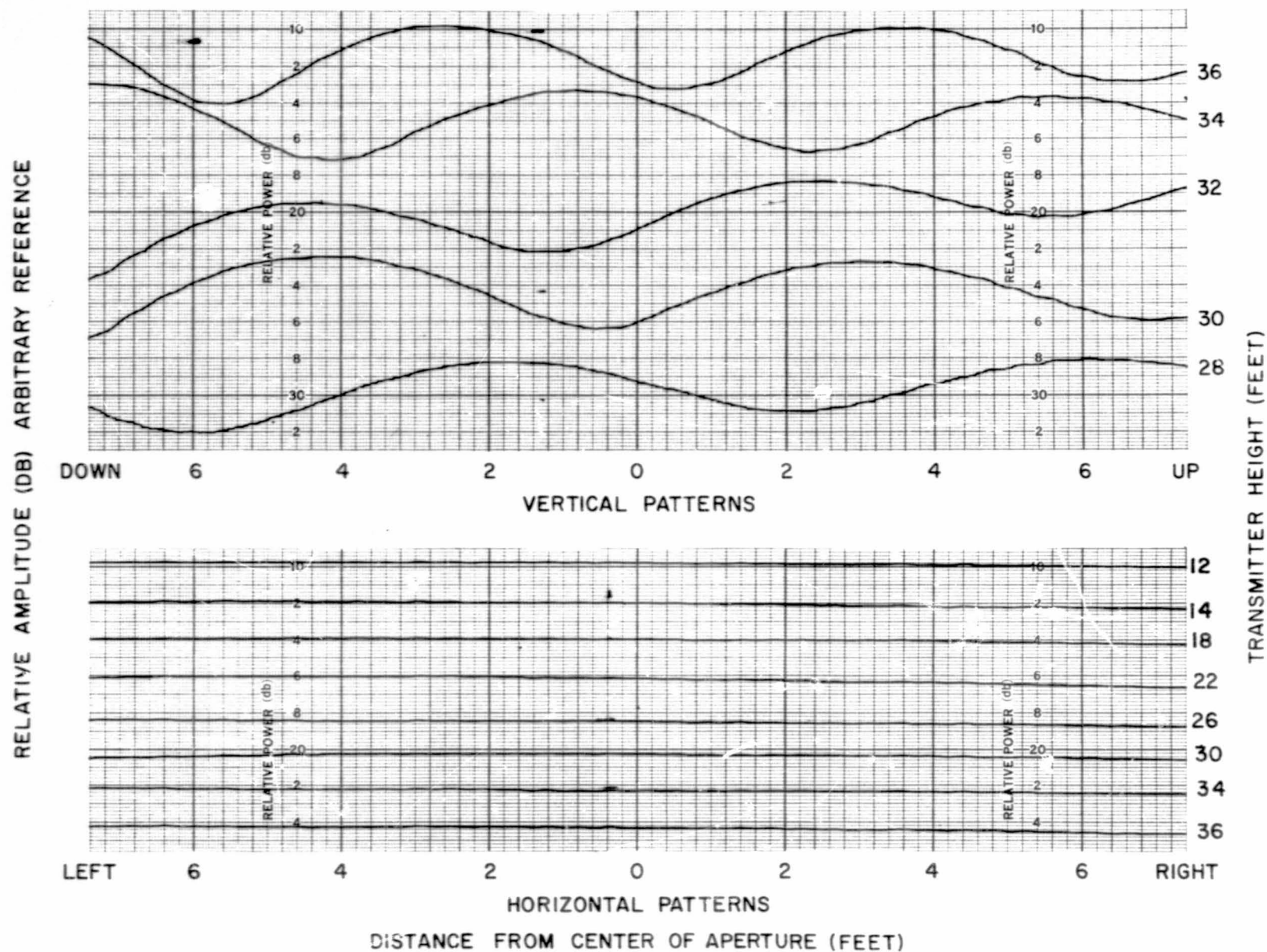


Figure 4.36. Aperture Field Patterns --  
Elevated Mode -- S-Band

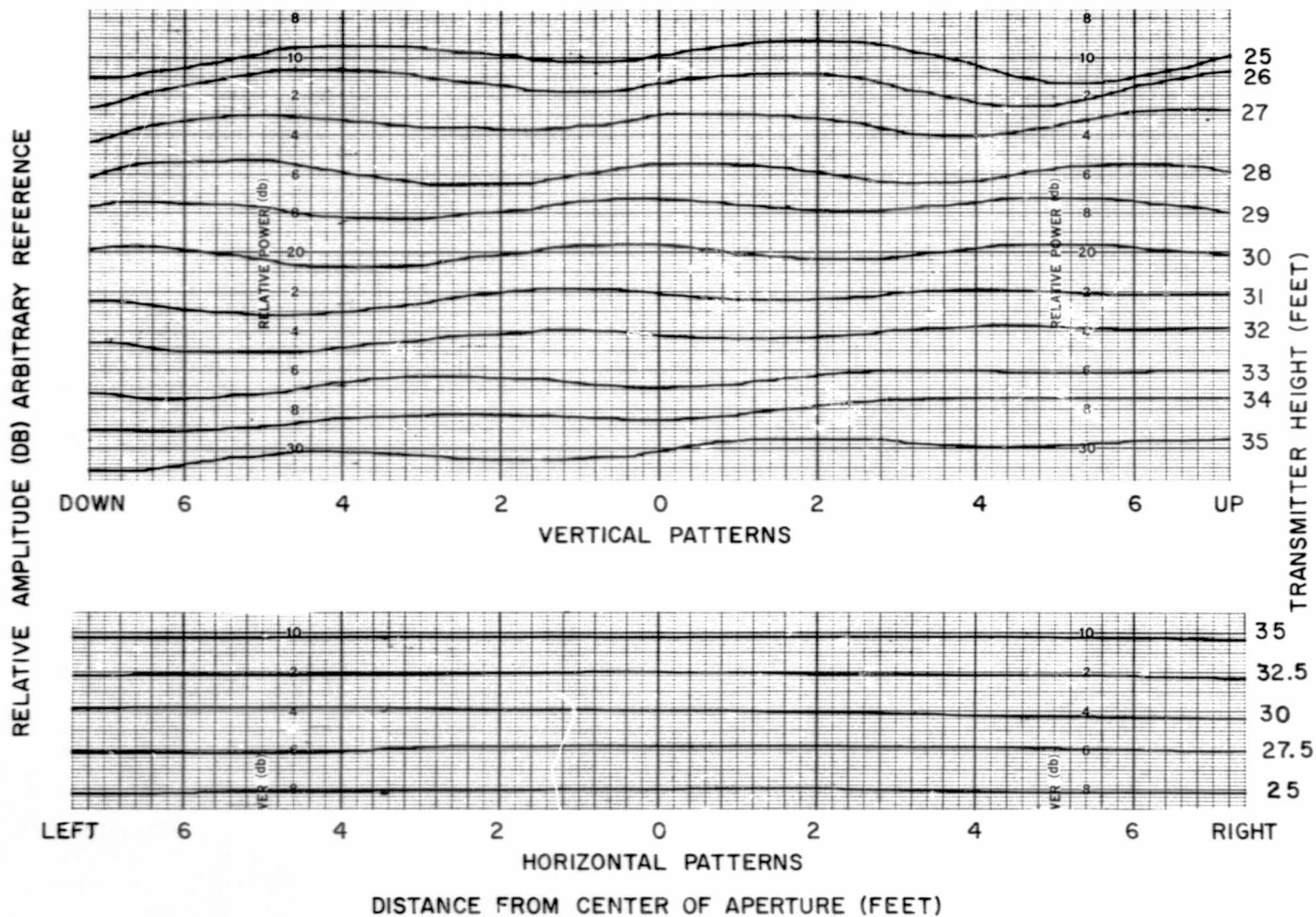


Figure 4.37. Aperture Field Patterns -- Elevated Mode with Diffraction Fence -- S-Band -- Horizontal Polarization

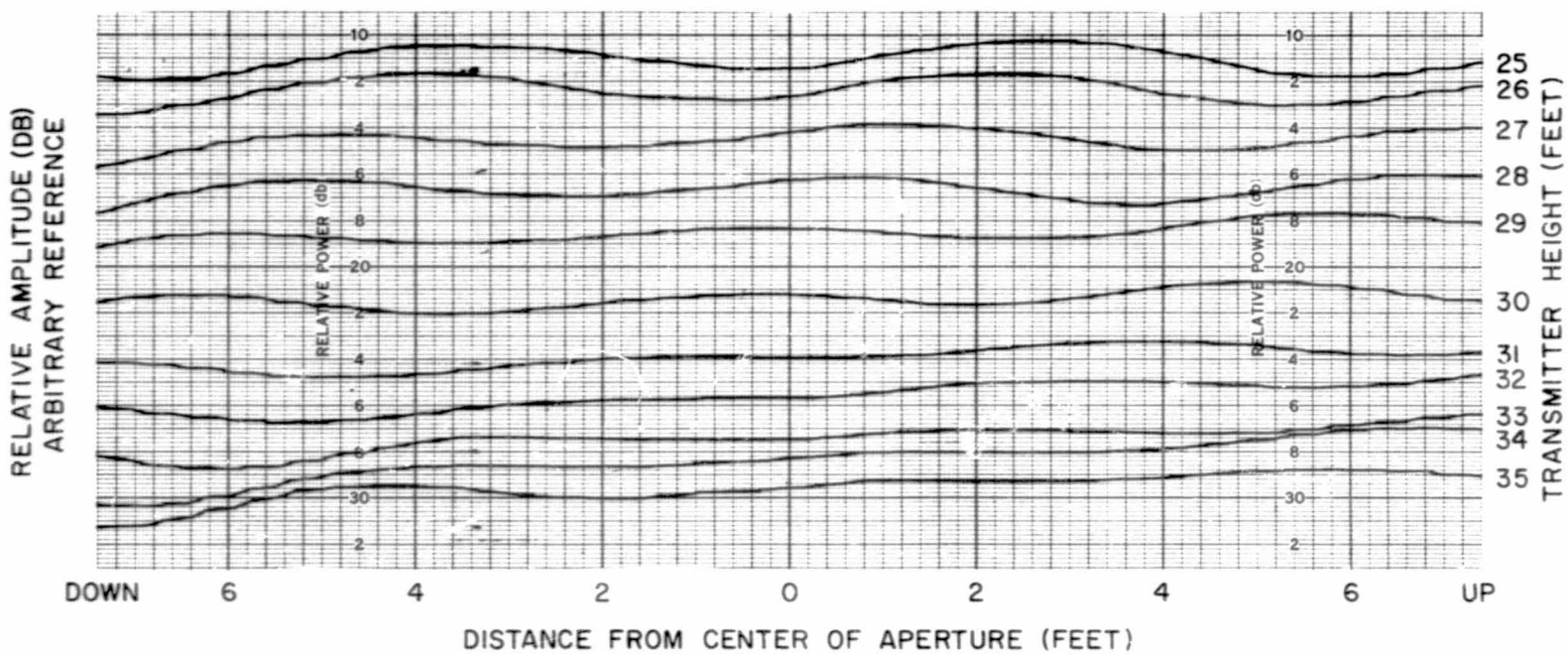


Figure 4.38. Vertical Aperture Field Patterns -- Elevated Mode with Diffraction Fence -- S-Band -- Vertical Polarization

at the MILA facility is not sufficiently directive for optimum S-band operation in the elevated mode.

4.2.2.2 Polarization Measurements: The polarization purity of the aperture field for the S-band elevated range was impaired by the relatively high extraneous signal level observed in the aperture field amplitude measurements. When the transmitting antenna circuitry was adjusted to obtain vertical polarization with an axial ratio of 40 decibels at the center of the aperture, the axial ratios measured at points in the 16-foot diameter aperture varied from a high value of 42 decibels to a low value of 30 decibels on the aperture periphery.

The effects of extraneous signals on circularly polarized transmission were investigated by comparing the axial ratios as measured at several points in the 16-foot diameter aperture to a reference at the center of the test aperture. As shown in Figure 4.39 the axial ratio deviated from the center value of 0.9 decibel (see footnote, page 4-44) by as much as 0.9 decibel at some points in the test aperture.

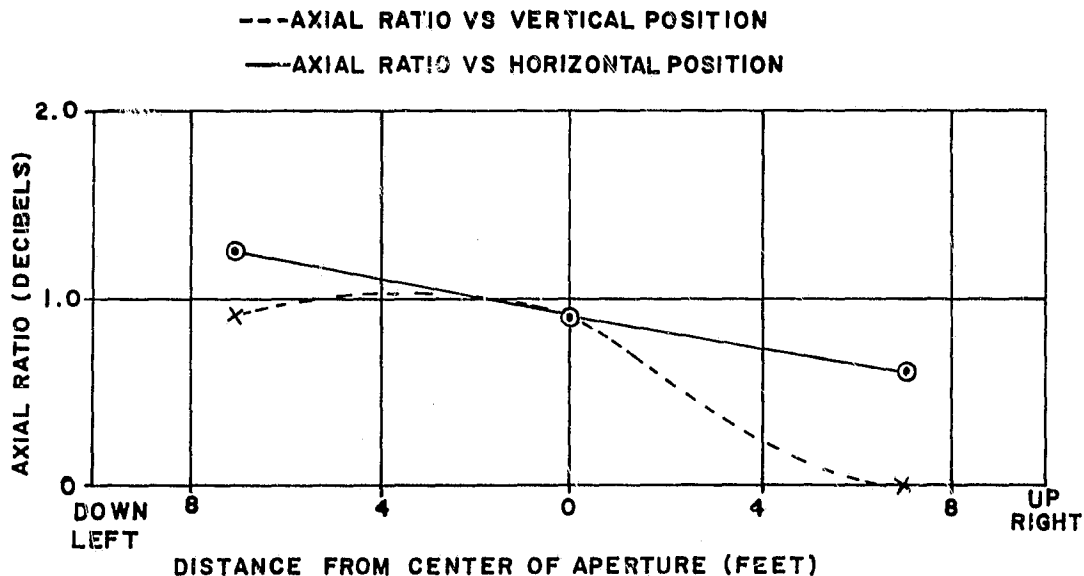


Figure 4.39. Axial Ratio Versus Aperture Position -- Ground-Reflection Mode -- S-Band



4.2.2.3 Boresight Measurements: Boresight measurements were made in accordance with the procedures outlined in Chapter 3 utilizing the phase-monopulse device described therein. The high extraneous signal level indicated by the patterns of Figures 4.37 and 4.38 caused large boresight errors as indicated in Figures 4.40 and 4.41. The cyclic nature of the theoretical boresight error curve as derived in Appendix B is evident in the plots of Figures 4.40 and 4.41.

#### 4.3 Mechanical Accuracy Measurements

A theoretical discussion is given in Appendix H of possible errors which can enter into boresight measurements where the MILA test positioner is employed as a direction instrument. For these measurements the upper-azimuth (roll) axis of the positioner was established as the direction axis, and the elevation and lower-azimuth axes were utilized to orient the direction axis to required positions ( $\phi, \theta$ ) in an earth-fixed coordinate system. Optical boresight references for various orientations of the source antenna were established via the remote closed-circuit television system mounted in the Gemini mockup (see Chapter 2). Inaccuracies in either the positioner alignment or the positioner synchro-readout system will thus introduce error both in the optically and electrically sensed boresight directions; at the same time, differential deflections of the television camera mounting frame for various direction-axis orientations can produce a bias error in the optical reference data. The results of measurements performed to assess the magnitudes of possible mechanical errors are discussed in the following paragraphs.

##### 4.3.1 Positioner Geometric Errors

The positioner geometric errors of interest here are orthogonality error and collimation error, which are defined in Appendix H, paragraphs H.3.1.2 and H.3.1.3, respectively. In particular, the contributions of such errors to elevation-angle error or to azimuth-angle error in boresight measurements was of direct importance in the present study. In addition, misalignments between the positioner coordinate system and the test-range coordinate system can contribute to such errors. Misalignment of the positioner and Gemini mockup coordinate systems contributed negligible error in the measurements of this program.

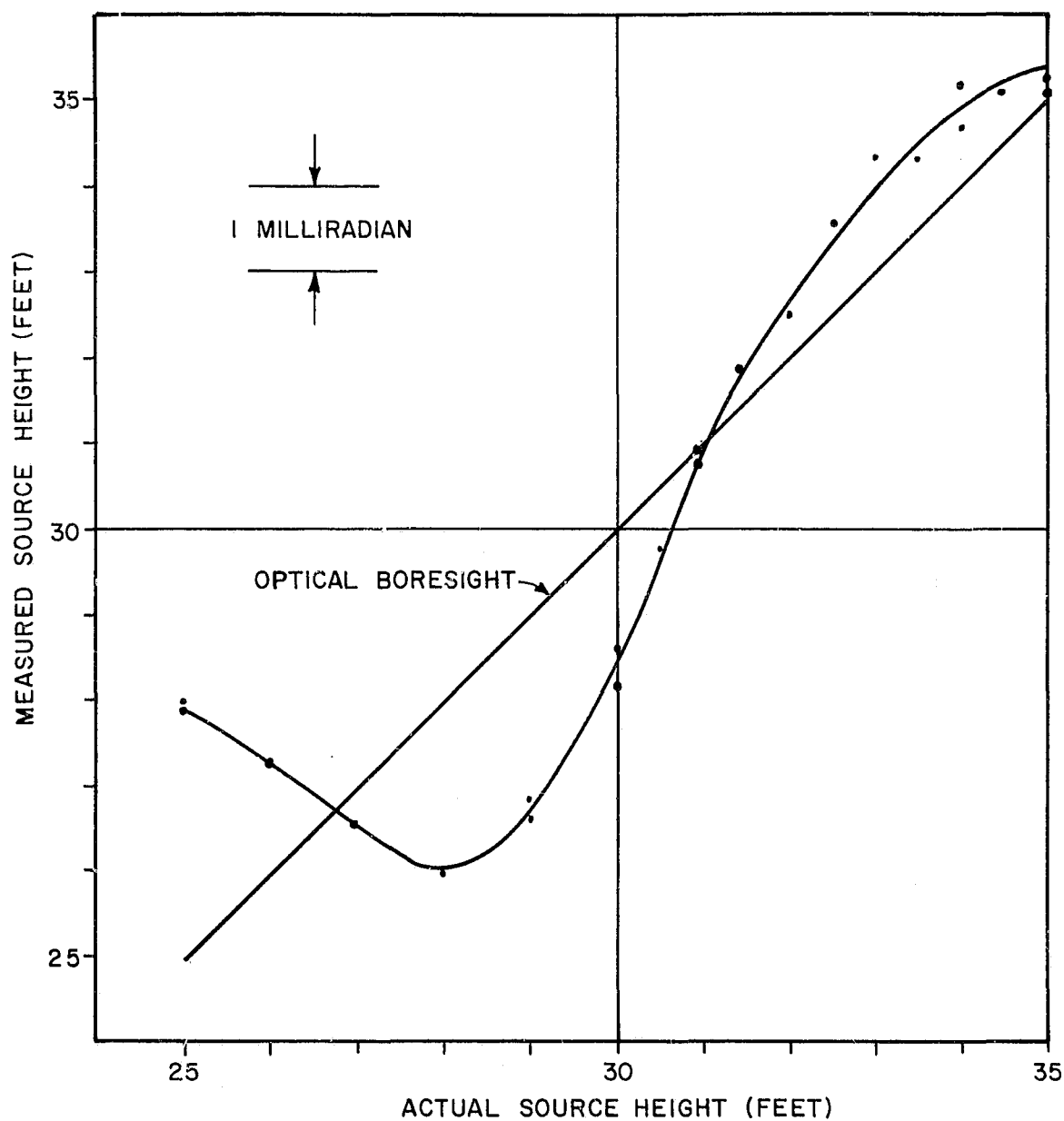


Figure 4.40. Measured Height of Apparent Source Versus Actual Source Height -- S-Band Elevated Range with a Single 8-Foot Fence -- Vertical Polarization

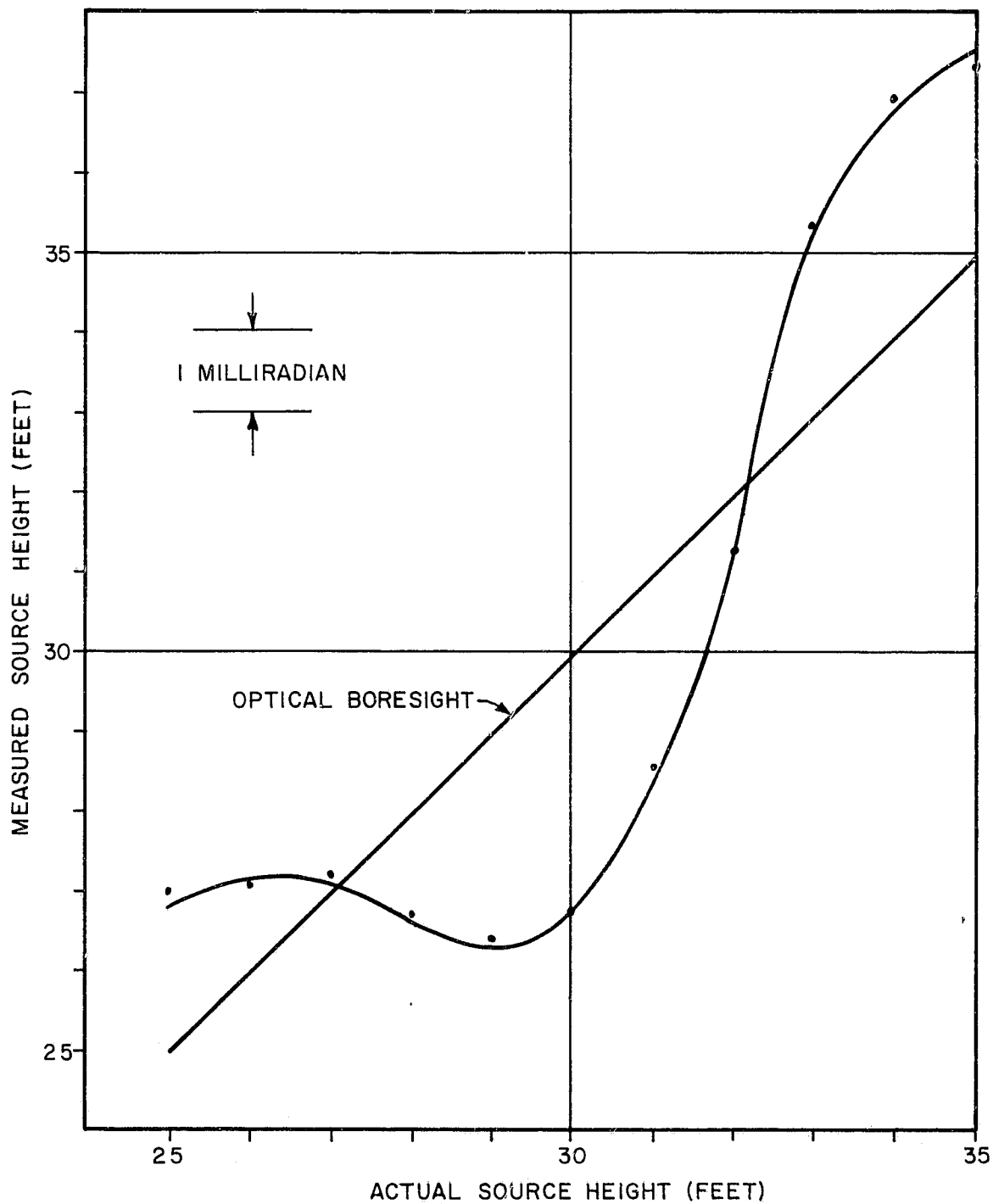


Figure 4.41. Measured Height of Apparent Source Versus Actual Source Height -- S-Band Elevated Range with a Single 8-Foot Fence -- Horizontal Polarization

Tests performed in August 1965 under Contract No. NAS10-1852 showed that the magnitudes of such misalignment errors were less than 1 minute of arc. Reference to paragraph H.3.1 shows that the resulting errors in  $\phi$  and  $\theta$  were negligibly small.

When an orthogonality error  $\delta$  exists between the elevation and lower-azimuth axes of the MILA test positioner (see Figure H.10), the possible elevation-angle error  $\Delta\theta_b$  can be defined with respect to two directions, say  $\overrightarrow{OP_1}$  and  $\overrightarrow{OP_2}$ , as

$$\Delta\theta_b = (\theta_1 - \theta_2) - (\bar{\theta}_1 - \bar{\theta}_2) \quad (4-5)$$

where

$\Delta\theta_b$  = elevation angle error due to orthogonality error

$\theta_1$  = elevation of  $P_1$  in the XYZ coordinate system

$\theta_2$  = elevation of  $P_2$  in the XYZ coordinate system

$\bar{\theta}_1$  = elevation of  $P_1$  indicated by instrument axis

$\bar{\theta}_2$  = elevation of  $P_2$  indicated by instrument axis

In terms of the orthogonality error  $\delta$  and the angle  $\bar{\theta}_1$  indicated by the positioner elevation axis, the  $\theta_i$  are given by equation (H-3):

$$\theta_i = \cos^{-1} (\cos\delta \cos\bar{\theta}_i) \quad (H-3)$$

Results of tests made on the MILA positioner in 1964 showed that  $\delta$  was less than 1 milliradian, which would correspond to negligible elevation-angle error. This orthogonality was not measured during the current program, thus an example calculation is given here using a conservative value of 10 milliradians for  $\delta$ .

Assume that the positioner elevation axis indicates a reading for  $\overrightarrow{OP_1}$  of  $\theta_1 = \pi/2$  radians and a reading for  $\overrightarrow{OP_2}$  of  $\theta_2 = 1.52$  radians. The resulting elevation-angle error is calculated from (4-5) to be

$$\Delta\theta_b = (\cos^{-1}[0] - \cos^{-1}[\cos(0.01) \cos(1.52)]) - (\frac{\pi}{2} - 1.52)$$

or

$$\Delta\theta_b \doteq 0.025 \text{ milliradian.}$$

It is seen that even for a 10-milliradian orthogonality error, the small elevation angles (near  $\theta = \pi/2$ ) which were employed in the boresight comparison measurements had negligible error.

Reference to Figure H.12 and equation (H-10) shows that the effect of a collimation error  $\epsilon$  between the line-of-sight and the positioner elevation axis is analogous to the effect of orthogonality error insofar as elevation-angle errors are concerned. That is, since for a collimation error  $\epsilon$  we have

$$\theta_1 = \cos^{-1}(\cos \epsilon \cos \bar{\theta}_1), \quad (\text{H-10})$$

then for  $\epsilon$  less than 10 milliradians the corresponding elevation-angle error in boresight measurements will be less than 0.025 milliradian for small elevation angles near  $\theta = \pi/2$ . As stated above, the boresight measurements under this program utilized the upper-azimuth axis as the direction line, so that collimation error for sensing in the elevation plane results from non-orthogonality of the positioner upper-azimuth and elevation axes. Measurements conducted on the MILA positioner in 1964 showed that these axes were orthogonal to within less than 1 minute of arc. Therefore an assumed value of 10 milliradians for  $\epsilon$  is quite conservative for the MILA facility, and it is seen that collimation error contributed negligibly to elevation-angle error in the boresight comparison tests.

In addition to the geometric errors discussed above, deflections of the positioner due to differential temperature effects and wind loading effects can cause boresight measurement errors. In the horizontal (azimuth) plane, the compliance of the lower-azimuth axis of the test positioner is such that a 20 mph wind can cause a deflection of approximately 0.003 degree if the wind velocity is normal to the roll axis of the Gemini mockup. As discussed in Appendix H, differential temperature effects can be expected to induce deflections of up to 0.008 degree in the positioner structure between the concrete mounting pad and the upper-azimuth turntable.

#### 4.3.2 Positioner Synchro-Readout Errors

The resolution of the digital readout indicators for the MILA test positioner axes is 0.002 degree. Calibration tests were performed to determine the readout accuracy of the lower-azimuth system in August 1965 under Contract NAS10-1852, and the readout accuracy of the elevation system was measured under the present contract in December 1965. Results of these tests are summarized in the following tables.

LOWER-AZIMUTH ( $\phi$ ) READOUT ACCURACY			
Degrees			
Indicated Angle ①	Surveyed Angle	Difference Angle	Error ②
4.542	4.552	0.010	+0.005
2.262	2.276	0.014	+0.001
0.558	0.569	0.011	+0.004
0.268	0.284	0.016	-0.001
0.096	0.113	0.017	-0.002
-0.018	-0.000	0.018	-0.003
-0.126	-0.113	0.013	+0.002
-0.298	-0.284	0.014	+0.001
-0.582	-0.569	0.013	+0.002
-2.296	-2.276	0.020	-0.005
-4.570	-4.552	0.018	-0.003

① Negative angles are counterclockwise rotation.

② Based on a mean difference angle of 0.015 degree.

ELEVATION (θ) READOUT ACCURACY			
Degrees			
Indicated Angle	Surveyed Angle	Difference Angle	Error ①
87.839	87.839	0.000	-0.001
88.059	88.062	0.003	-0.004
88.261	88.259	-0.002	+0.001
88.340	88.338	-0.002	+0.001
88.415	88.413	-0.002	+0.001
88.472	88.468	-0.004	+0.003
88.545	88.542	-0.003	+0.002
88.664	88.661	-0.003	+0.002
88.735	88.730	-0.005	+0.004
88.995	88.990	-0.005	+0.004
89.115	89.111	-0.004	+0.003
89.286	89.281	-0.005	+0.004
89.377	89.373	-0.004	+0.003
89.653	89.648	-0.005	+0.004
89.781	89.777	-0.004	+0.003
89.862	89.857	-0.005	+0.004

① Reference shifted to balance maximum positive and maximum negative difference angles.

#### 4.3.3 Optical Reference Errors

Measurements were made to determine the stability of the optical boresight television system upon rotation of the Gemini mockup about its roll axis, and to assess the capability of the television system for determining the alignment of the roll axis relative to a distant visual target. The optical axis of the camera would in the ideal case be parallel to the roll axis, but the weight of the instrument can cause differential sighting errors for various orientations of the mockup due to deflection of the camera mount.

The magnitudes of the optical reference errors due to deflection of the existing camera mount were determined as follows. A series of sightings to a fixed target for several roll-axis orientations was obtained with the camera mounting frame rigidly supported by angle braces in two orthogonal places. The angle braces were then removed, and the sightings were repeated with the existing mounting frame providing the only camera support. Azimuth- and elevation-angle data recorded in these experiments are tabulated below.

##### Target angles with TV camera braced.

Roll Axis	Azimuth	Elevation
000	359.944	89.665
180	359.994	89.762
Mean	359.969	89.713
090	359.923	89.732
270	360.021	89.677
Mean	359.972	89.704
Average Mean	359.970	89.708

##### Target angles with TV camera not braced.

Roll Axis	Azimuth	Elevation
000	360.000	89.715
180	359.967	89.735
Mean	359.984	89.725
090	359.945	89.720
270	359.964	89.750
Mean	359.955	89.735

The difference between the mean angles for the braced condition as compared to the unbraced condition is defined to be the camera differential boresight error. The relatively large difference between the two mean azimuth angles (000-180



and 090-270) for the unbraced condition indicates that the camera deflections vary with respect to the roll axis orientation. The differences between the average mean angles for the braced condition and the mean angles for the unbraced condition are tabulated below as correction factors. These correction factors were applied to the experimental boresight data presented in sections 4.1 and 4.2.

Bias correction for optical boresight directions.

Roll Axis Position	Azimuth	Elevation
000 - 180	-0.014°	-0.017°
090 - 270	+0.015°	-0.027°

## CHAPTER 5

### SUMMARY OF THEORETICAL AND EXPERIMENTAL PROGRAM

#### 5.1 Theoretical Developments

##### 5.1.1 Characterization of the MILA Range

It is shown in Appendix A that the close-tolerance surface of the MILA RF boresight test facility will approximate a specular reflector for microwave energy through X-band frequencies. The reflection coefficients for energy normal to and parallel with the plane of incidence are given by equations (A-14) and (A-15), respectively. General expressions for the direct-path and reflected waves which would be present at a test aperture are given in terms of these reflection coefficients and parameters of the range geometry in equations (A-22) and (A-23).

##### 5.1.2 Ground-Reflection Operation of the MILA Facility

Criteria are developed in section A.5 for optimum settings of the height of the source antenna and the orientation of the axis of the transmitted beam in the vertical plane (the elevation squint angle) for ground-reflection operation. These criteria are given in equations (A-31) and (A-26), respectively. The angular orientation criterion is specialized in Appendix E to fit the particular range parameters of the MILA facility. It is shown that the initial settings of the source height and elevation squint angle should be

$$h_t \doteq \lambda R_o / 4h_r \quad (A-31)$$

and

$$\theta_S \doteq - \lambda / 4h_r \text{ radians} \quad (E-16)$$

respectively, where

- $h_t$  is the height of the source antenna,
- $h_r$  is the height of the center of the receiving aperture,
- $R_o$  is the range length,
- $\lambda$  is the wavelength, and
- $\theta_S$  is the elevation squint angle.

Effects of violations of these criteria on the phase and amplitude of the aperture field are discussed and illustrated in section A.5 in terms of the MILA range geometry at X-band. It is indicated that minor misadjustments in the height or elevation squint angle of the source antenna will not cause severe distortions of the aperture field. For settings in agreement with the criteria, it is shown that the calculated theoretical taper of the aperture-field amplitude in the vertical plane at X-band will be approximately 0.25 decibel over a 10 foot aperture and 1 decibel over a 20 foot aperture.

### 5.1.3 Elevated Operation of the MILA Facility

Section A.6 presents developments which relate the magnitudes and periodicity of aperture-field variations to the approximate locations and relative strengths of sources of extraneous energy. The field incident on the test aperture is considered to consist of the direct-path wave  $\bar{E}_D$  and a single specularly reflected wave  $\bar{E}_R$ , which arrives at an angle  $\theta_R$  from  $\bar{E}_D$ . Equations are derived for the aperture field configuration along lines normal to the direction of propagation of  $\bar{E}_D$ . For typical logarithmic plots of the aperture-field amplitude, the theory predicts a spatial period for the amplitude variations given by

$$P \doteq \frac{\lambda}{\sin \theta_R} \doteq \frac{\lambda R_o}{2h_t} \quad (A-58)$$

and a relation between the relative level of the extraneous signal and the peak-to-peak decibel variation ( $\sigma$ ) of the patterns given by

$$\frac{E_R}{E_D}(\text{db}) \doteq 20 \frac{-1 + \text{antilog}(0.05 \sigma)}{1 + \text{antilog}(0.05 \sigma)} . \quad (A-54)$$

### 5.1.4 Height of the Apparent Source of Radiation

It is shown in Appendices B and C that a theoretical expression for the apparent source height as a function of actual source height can be based on the location

of the normal to the phasefront created by a direct-path wave  $\bar{E}_D$  and an extraneous wave  $\bar{E}_R$ , as long as the angle between the directions of propagation of these waves is small. The theory indicates that for such cases both phase-monopulse and amplitude-monopulse systems would sense the apparent source height as an oscillatory function of actual source height, where the amplitude of the oscillations would increase with increasing source height. The amplitudes of the oscillations also depend on the ratio  $k = E_R/E_D$ , as shown in equation (B-20).

Appendix D presents more generalized considerations of the effects of extraneous signals on boresight measurement accuracies, where the extraneous wave  $\bar{E}_R$  is assumed to take on arbitrary orientations with respect to the direct-path wave  $\bar{E}_D$ . Figure D. 5 gives the required suppression of  $E_R$  relative to  $E_D$ , as a function of the angle between the two signals, which will restrict the maximum theoretical boresight error of an amplitude-monopulse system to a specified value. The data of Figure D. 5 were calculated for the single-plane X-band amplitude monopulse test device utilized in the range evaluation program, which was designed to provide a general simulation of a single channel of the LEM/RR. Similar data for a single-plane phase-monopulse system are given in Figure D. 7. The S-band single-plane phase-monopulse test device used in the range evaluation employed a pair of low-directivity antennas, so that this system was somewhat more susceptible to extraneous signals than the X-band device.

As an example of the theoretical error which could be caused in these systems, Figure D. 5 shows that an extraneous signal level of the order of -45 decibels with respect to the direct-path signal could cause a boresight error of approximately 0.25 milliradian in the X-band amplitude monopulse device, while this same extraneous signal level could result in a boresight error of approximately 0.4 milliradian in the S-band phase-monopulse device with a spacing between antennas of approximately 4.7 wavelengths. For the closer spacing available with the S-band device ( $\sim 1.75$  wavelengths), the added sensitivity to extraneous signals could result in an error greater than 1 milliradian for this same level of extraneous energy.

The effect of variations in the elevation squint angle on the apparent height of the source of radiation in the ground-reflection mode is discussed in Appendix E.

The developments there are based on the results of Appendices A through C, and include an explanation of the conversion from physical angles to pattern angles of typical  $\sin K\theta/K\theta$  radiation patterns. Plots of the theoretical variations of the apparent source height  $H$  and of the ratio of reflected to direct-path fields  $k$  are shown in Figure E. 2 as a function of elevation squint angle. Appendix E also discusses the theoretically predicted difference in apparent source height which would result for propagation of horizontal and vertical polarizations; an implicit result of this discussion is the prediction of some depolarization of elliptically polarized energy upon reflection from the range surface.

#### 5. 1. 5. Use of Diffraction Fences on a Smooth Surface

The problem of placement of diffraction fencing for operation in the elevated mode over a smooth, planar range surface is discussed in Appendix F. Developments in this appendix are based on the quasi-geometrical optics approach, in accordance with the results of Appendix A.

Reflections from a surface such as that of the MILA range are the result of reradiation of energy which illuminates the surface; this reradiation is conveniently studied on the basis of the half-period (Fresnel) zones formed on the range surface by the loci of points which represent path lengths differing by successive integral values of half-wavelengths. It is shown that the Fresnel zones on a planar surface describe a set of expanding ellipses whose major axes lie along the center line of the range. Expressions are derived for the pertinent parameters of the Fresnel zones, and a set of computer calculations are included for these parameters at X-band and S-band in terms of the MILA range geometry.

When diffraction fences are erected on an antenna test range, a combination of effects must be considered. The fence configuration will partially or totally screen a number of Fresnel zones, dependent on the parameters of the range and fence geometries and on the frequency of operation; this screening will suppress the effects of reradiated energy. At the same time, however, the interception of energy by the fences will result in perturbations of the test-aperture field due to diffraction effects. The theoretical approach to the diffraction problem in Appendix F is based on the Cornu spiral, which is a plot of the Fresnel integrals. Computer calculations are summarized for the effects of diffraction fences in terms of

the MILA range geometry in Figures F.4 through F.10. The illustrated data cover frequencies in L-, S-, and X-band.

Quantitative examples which are particularly pertinent to test situations at the MILA facility are presented, based on the theoretical calculations. It is shown that proper placement of diffraction fences could theoretically reduce aperture-field variations by more than an order of magnitude in comparison to the variations which could result from reflections if the range were operated in the elevated mode with no diffraction fences.

#### 5.1.6 Measurements of the Aperture-Field Polarization

A brief discussion of the polarization measurement problem as it relates to the test requirements of the MILA facility is presented in Appendix G. Expressions are given which relate the polarization ellipse, which would be recorded by rotation of a linear probe antenna about an axis parallel to the propagation vector of the incident field, to the polarization pattern parameters  $r$  (axial ratio) and  $\tau$  (tilt angle). It is shown that a complete characterization of the incident-field polarization would require supplemental measurements to determine the sense of rotation of elliptically or circularly polarized energy. A discussion is included in Appendix G of an alternative method of polarization measurement, called the multiple component method, which provides complete polarization characterization by the measurement of a minimum of four components of the received field.

#### 5.1.7 Angular Measurement Accuracies

In most antenna measurement situations, it is necessary to determine the direction of the line-of-sight from a source antenna to the antenna under test. Such determination is of particular significance in high-accuracy boresight measurements, where correlation of a mechanical and an electrically sensed line-of-sight is mandatory. Appendix H describes basic antenna-range coordinate systems, and relates the LEM coordinate system to two configurations of the MILA boresight test positioner.

A section of this appendix discusses possible errors in angle measurement, where the errors are classified as

- (1) Geometric Error,
- (2) Shaft-Position Error, and
- (3) Deflection Error.

Equations are derived which allow calculation of each type of error. Certain of these derivations employ spherical coordinate transformations by Euler angles, which are described in Appendix I.

#### 5.1.8 Effects of Parallax in Boresight Measurements

Appendix J presents theoretical studies of the effects of parallax in testing asymmetrical antennas. These studies were based on the aperture-field equivalent-slit method, and utilized digital-computer calculations of beam directions. To describe the effects of asymmetry two terms are defined, center-of-phase and center-of-parallax, which affect the accuracy of boresight measurements in related but different manners. These effects can be seen with reference to Figure 5.1. Assume that an asymmetrical antenna  $A_T$  is to be tested in a configuration where the source antenna is also asymmetrical. In the measurements it is required that the direction to the source antenna be determined from the antenna under test. Parallax error enters into such measurements basically because of the relatively small test separation which is likely to be employed compared with the operational separations which are to be simulated. The radiation from the source antenna appears to emanate from its center of phase, which is shown located a distance  $\Delta$  from its geometrical center. Similarly, the operation of the antenna under test is such that it appears to be centered at a point which has been defined as the center of parallax; this point is shown located a distance  $\delta$  from the geometrical center of the antenna under test. If the center of parallax and the center of phase are not in the boresight plane,  $\Delta$  and  $\delta$  have projections  $\Delta_p$  and  $\delta_p$  on this plane given respectively by

$$\Delta_p = \Delta \cos \chi_T$$

and

$$\delta_p = \delta \cos \chi_R.$$

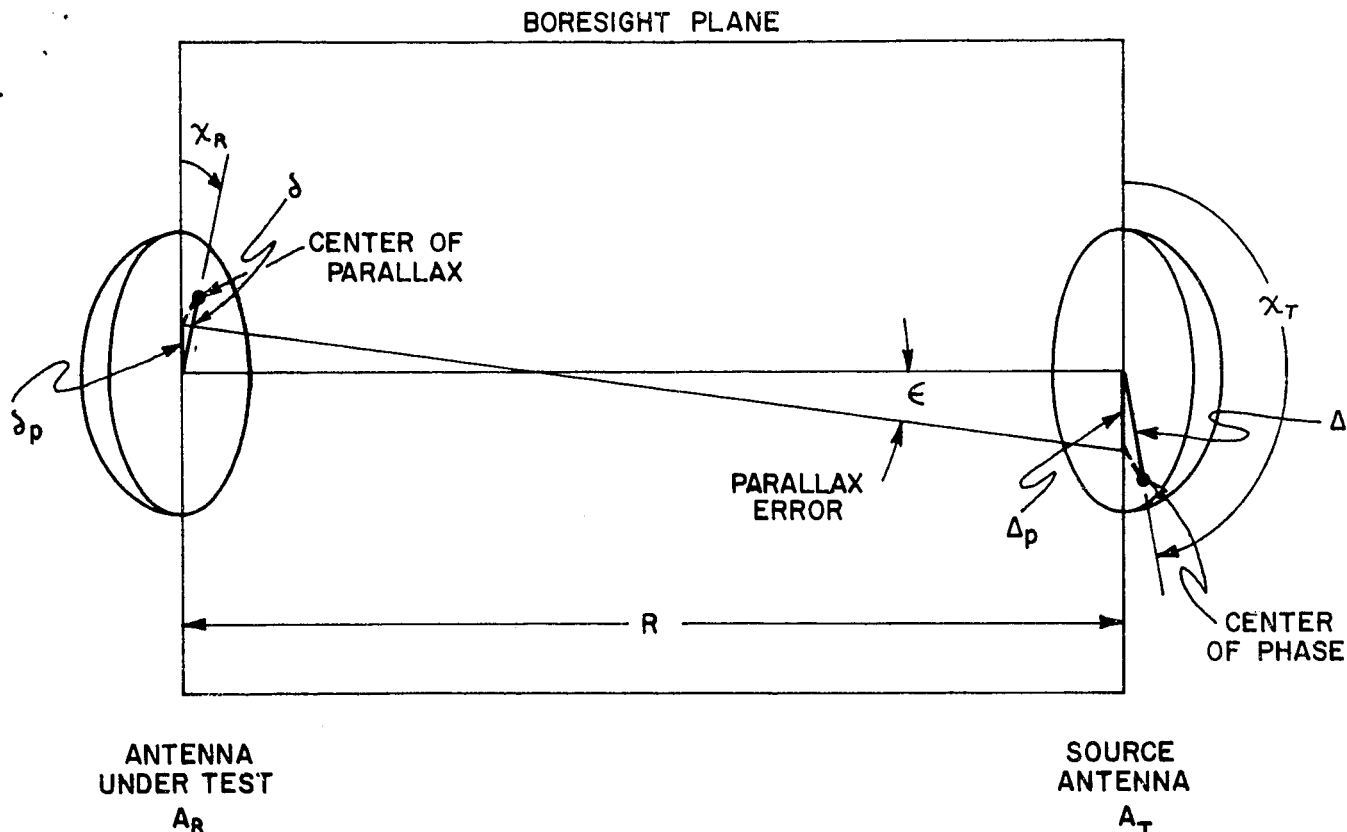


Figure 5.1. Illustration of Parallax Error in Testing an Asymmetrical Antenna with an Asymmetrical Source Antenna.

The parallax error  $\epsilon$  in the boresight plane results from assuming the source antenna's center-of-phase and the test antenna's center-of-parallax to be coincident with their geometrical centers.

At typical operational separations the parallax error angle in the sensing plane caused by the ratio  $(\delta_p - \Delta_p)/R$  approaches zero. In contrast, at typical test ranges the magnitude of this angle may become significant in comparison to the boresight error specification of the antenna under test. The calculations presented in Appendix J indicate magnitudes of the deviations of the center-of-phase and the center-of-parallax of antennas from their geometrical centers for assumed conditions of asymmetry.

With relation to the LEM/RR and LEM/LR boresight problems, it is difficult to draw quantitative conclusions concerning parallax error because the magnitude of the errors which are produced depend on the degree of asymmetry of the antenna under test. It is possible, however, to draw some general conclusions:

- (1) If a source antenna is designed to be symmetrical and is made essentially symmetrical, its center-of-phase can be considered to lie at the geometrical



center of the antenna with error which is so small that it can almost always be neglected unless measurements of the utmost precision are required. If the required precision is such that it is necessary to take into account the deviation of the center-of-phase from the center of the source antenna, the antenna can be rotated about its axis through 180 degrees between measurements and an average of the measured boresights taken. If this procedure is followed, meaningful results will only be obtained if extraneous reflections are adequately suppressed.

- (2) Extreme asymmetry of the source antenna is not likely to cause its center of phase to lie greater than  $0.2 D$  from its physical center, where  $D$  is the maximum dimension of the antenna in the plane of asymmetry, but the deviation may approach this magnitude.
- (3) The center of parallax of an asymmetrical antenna under test can result in a boresight error of as much as  $1/20$  times the half power beamwidth in tests made at separations of  $\leq 2D^2/\lambda$ .
- (4) The mirror symmetry of the rendezvous radar tends to provide cancellation of parallax error, so that boresight measurements should be possible at ranges as small 1000 inches.
- (5) The landing radar does not possess specific symmetry so that some error from parallax is likely to be present in boresight measurements.
- (6) The separation of 1000 feet provided by the existing MILA range is favorable from the viewpoint of controlling parallax error in comparison with ranges which have lengths of the order of 1000 inches.

## 5.2 Experimental Investigations

The evaluation program which was conducted at the NASA - KSC - MILA RF boresight test facility was directed primarily toward an assessment of the capability of this facility in making high-accuracy boresight measurements in either the ground reflection or elevated mode at S-band and X-band frequencies. While the measurement results are generally indicative of the facility's capability in more general antenna tests, such as pattern measurement, it is noted that the interest of this study led to the documentation primarily of the electromagnetic field incident on the test aperture.

The incident field is considered to consist of the direct-path wave from the source antenna and the field produced by reflections from sources in the region between the source antenna and the test aperture. This distinction is made in comparison to the total aperture field, which is considered to consist of the incident field and the field caused by extraneous reflections from extremely wide angles and from the rear of the test aperture.

An evaluation program which would document the general measurement capability of the facility would necessarily include a series of tests designed to document the effects of such possible sources of extraneous reflections as the control building, the test positioner, etc. on the total aperture field. One approach to such documentation is the pattern comparison technique, in which a series of measurements are made with a nominally low-directivity sensor for various orientations in which the source-sensor geometry is maintained constant while the sensor-scatterer geometry is made variable. While these geometrical relations were employed in the boresight comparison tests reported herein, the effects of rearward energy was suppressed both by the directive nature of the test devices and by the use of the Gemini spacecraft mockup as a mounting fixture for the test devices. It was recognized that the presence of the mockup altered the contribution of rearward scattered energy to the total aperture field, and it would have been desirable to make measurements to assess errors from this source; however, the schedule of the Gemini program made removal of the mockup impractical. In light of the control building configuration and the high-quality microwave absorber covering the building and screening the positioner base, it is felt that the documentation of high-accuracy boresight capabilities represents documentation of at least adequate capabilities for general antenna measurements.

Four types of measurements were performed in the evaluation program, including positioner mechanical accuracy tests and the three types of radiation measurements listed below:

- (1) Aperture-field amplitude measurements,
- (2) Aperture-field polarization measurements, and
- (3) Boresight comparison measurements.

The radiation tests were performed at X-band and S-band frequencies. Conclusions drawn from these measurements are summarized in the following paragraphs.

### 5.2.1 Mechanical Accuracy Tests

An assessment of the probable maximum errors which were contributed by the positioner-mockup-television system to boresight measurements under this program was obtained as described in Section 4.3. The optical reference errors due to deflection of the television camera mounting frame were measured as discussed in paragraph 4.3.3, and the corresponding calculated correction factors were applied to all boresight data obtained at X-band and S-band.

Tests of the positioner accuracies reported in paragraphs 4.3.1 and 4.3.2 were performed in part under Contract No. NAS 10-1852 and in part under the current contract. The results of these tests indicate possible maximum errors in the boresight measurements due to mechanical inaccuracies as shown in the following tabulated summaries.

#### AZIMUTH-ANGLE ERROR DEGREES

Source of Error	Magnitude
Misalignment Errors	Negligible
Orthogonality Error	Negligible
Collimation Error	Negligible
Wind-loading (20 mph Wind)	$\pm 0.003$
Thermal Deflection	Negligible
Syncho Readout	$\pm 0.005$
PROBABLE MAXIMUM (RSS)	<u>0.0054</u>

#### ELEVATION-ANGLE ERROR DEGREES

Source of Error	Magnitude
Misalignment Errors	Negligible
Orthogonality Error	Negligible
Collimation Error	Negligible
Wind-loading	Negligible
Thermal Deflection	$\pm 0.008$
Synchro Readout	$\pm 0.005$
PROBABLE MAXIMUM (RSS)	<u>0.0086</u>

## 5.2.2 X-Band Measurements in the Ground-Reflection Mode

5.2.2.1 The Aperture Field: Amplitude patterns of the receiving-aperture field were recorded at 10 GHz over a 16-foot circular planar aperture centered at a receiver height of 30 feet. These patterns indicate that the symmetry of the field and its relative freedom from amplitude variations are affected very little by slight variations in the source height or the source elevation squint angle about their theoretically optimum values. Misalignment of the source azimuth squint angle produces an asymmetry in the aperture field along lines parallel to the range surface, due to the directivity of the source antenna. The indicated procedure for establishing an optimum field for ground reflection operation at 10 GHz is as follows:

- (a) Set the source height at

$$h_t = \frac{\lambda R_c}{4h_r} = \frac{(0.98)(1000)}{4(30)} \doteq 0.82 \text{ foot}$$

- (b) Set the source elevation squint angle at a declination below the horizontal of

$$57.3 \left( \frac{-\lambda}{4h_r} \right) = -57.3 \left( \frac{0.098}{120} \right) = -0.05 \text{ degree}$$

- (c) Set the source azimuth squint angle at zero.
- (d) Make final adjustments using vertical and horizontal amplitude patterns recorded with the aperture field probe to document the settings which produce the desired degree of symmetry in the aperture field. This "fine tuning" should be effected for both horizontal and vertical polarizations of the transmitted pattern.

It was found that final settings of these parameters at the mean of the values determined for the two linear polarizations produced an excellent aperture-field configuration, and allowed subsequent tests such as boresight comparison measurements to be conducted for either polarization with no readjustment in the orientation of the source antenna.

It is noted that the use of the aperture field probe for fine adjustments of the source parameters is indicated only for measurements involving relatively large test apertures, that is, the aperture field probe should be employed in cases where either an antenna of large dimensions is to be tested or a small antenna is to be

tested over a sizable excursion in elevation and/or azimuth, or where tests of a vehicle-mounted antenna must document the effects of the spacecraft on the antenna characteristics. In other cases, it will be sufficient to mount a probe antenna at a fixed location in the center of the test aperture and to adjust the source parameters so that the peak of the transmitted beam is centered on the aperture.

The above procedures presuppose that the required settings of the transmitter polarization circuitry to produce vertical and horizontal polarizations have been documented. A discussion of the X-band polarization unit and a recommended procedure for establishing reference polarizations is given in the following paragraphs.

The polarization unit employed at X-band was a Scientific-Atlanta Series 40 Polarization Adjusting System. This unit includes a rectangular waveguide input, a rectangular-to-circular waveguide transition, a dielectric-loaded circular waveguide section and a conical output horn. Appropriate rotary joints and dc motor drive systems are provided which permit separation of the input signal into two orthogonal components and allow (1) amplitude adjustment by rotation of the rectangular waveguide input relative to the dielectric slabs, and (2) phase adjustment by variation of the spacing between the parallel dielectric slabs in the circular waveguide section. These adjustments are remotely controlled and indicated at the centralized control-room console. A schematic representation of the operation of the polarization unit is given in Figure 5-2.

For ground-reflection operation, a 1-foot conical horn is used on the output; a dielectric lens provides the required beam shaping by compensation for the phase error at the periphery of the output horn. For the elevated mode of range operation the polarization unit is designed for use with a small feed horn and a paraboloidal reflector and a Cassegrain sub-reflector.

A recommended procedure for establishing reference polarizations with the Series 40 unit is outlined below. For clarity, assume that horizontal polarization is to be established as a starting point.

- (a) Mount a linear probe antenna and a polarization positioner on the mounting plate available on the rear of the test positioner, with proper cabling for the control, synchro and RF signals.
- (b) Connect the receiver output signal and the polarization positioner synchro signal to the polar pattern recorder, and establish a zero

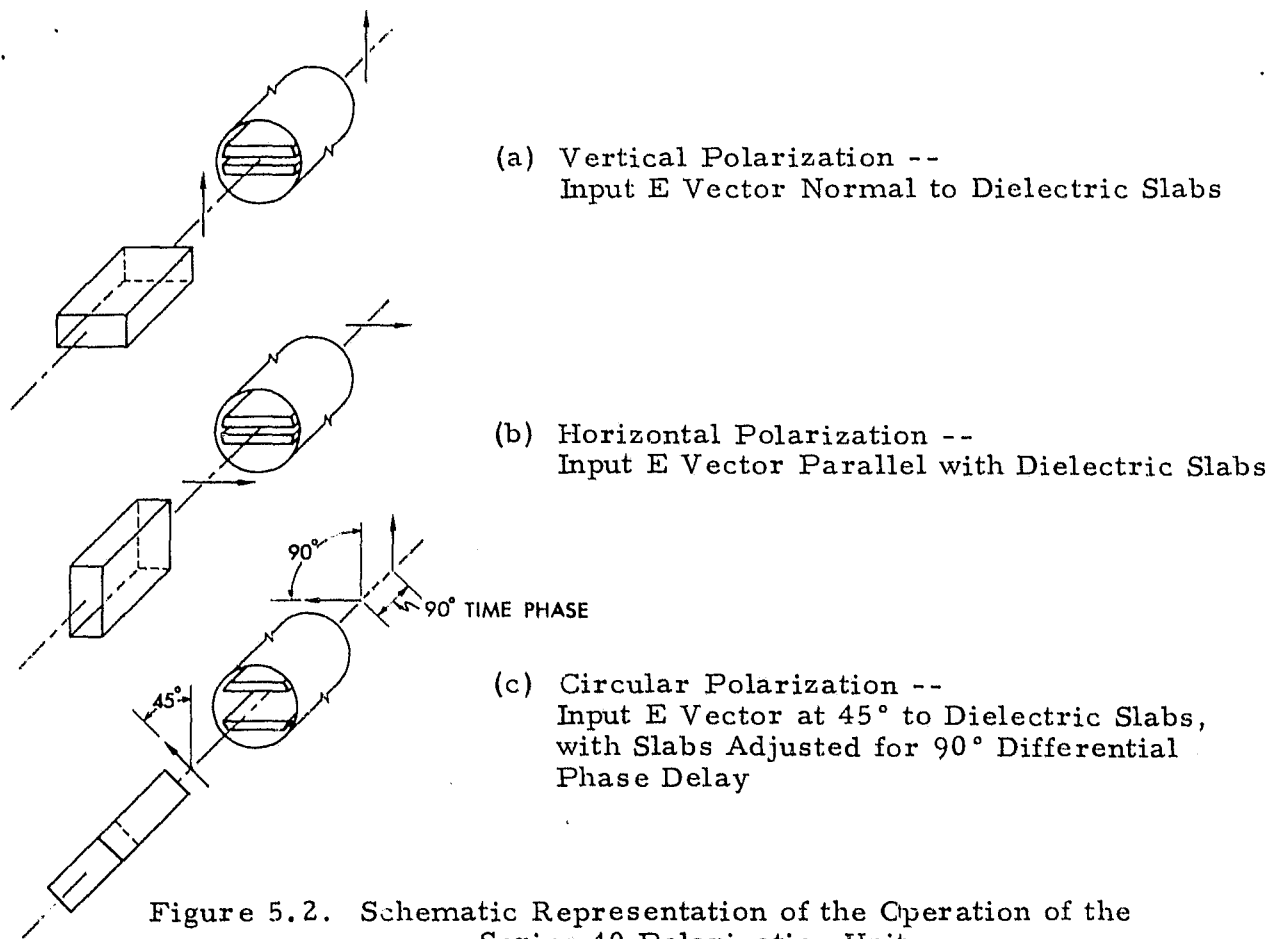


Figure 5.2. Schematic Representation of the Operation of the Series 40 Polarization Unit

The broad dimension of the dielectric slabs is assumed to be parallel to the range surface.

degree pattern reference for the vertical orientation of the probe horn E-plane.

- (c) Visually align the broad dimension of the dielectric slabs of the polarization unit, in their fully closed position, parallel with the range surface. Record the readout of the transmitter "phase" and "polarization" indicators for this orientation.
- (d) Adjust the "amplitude" control of the transmitter polarization unit until a null is indicated in the receiver output. Record a polarization pattern for these settings by rotating the probe antenna; the probable result at this stage will approach the classical figure-eight pattern of Figure 6.5, Appendix K, with the nulls slightly filled and displaced from the vertical.
- (e) Fine-tune the transmitter polarization adjustment to bring the pattern nulls into the vertical plane. Make final adjustments of the three controls to establish the desired degree of linearity, and record the indicator readings.

- (f) To establish vertical polarization, the primary adjustment will be rotation of the rectangular waveguide input of the polarization unit through an angle of  $90^\circ$ . Orient the E-plane of the probe horn to the horizontal position and adjust the amplitude control of the polarization unit until a null is indicated in the receiver output, noting the excursion of the amplitude indicator. Make final adjustments of the amplitude and phase controls for the desired degree of linearity, and record the indicator readings.
- (g) To establish circular polarization, adjust the amplitude control to a setting midway between the vertical and horizontal values, and record a polarization pattern by rotating the probe antenna. The result will be the characteristic dumbbell shaped polarization pattern as in Appendix K, Figure 6.4, with the major axis at some arbitrary orientation. Adjust the phase control of the polarization unit to align the major axis of the recorded pattern with either the  $0^\circ - 180^\circ$  or  $90^\circ - 270^\circ$  reference axis on the recorder. Equalize the amplitudes of the polarization pattern along these axes by adjusting the amplitude control of the polarization unit. Since the phase and amplitude controls are not completely independent, a few trial patterns should be recorded as the axial ratio is reduced to the desired degree of circularity. Record the indicator readings for the optimum settings.

The polarization tests conducted at X-band indicated that these reference polarization measurements at the center of the aperture will be sufficient to ensure generally acceptable polarization characteristics over an aperture of 16-foot diameter. The Series 40 polarization unit is a relatively broadband device for axial ratios of less than approximately 1 decibel; for precise circular polarization measurements the circularity should be set at the operating frequency.

5.2.2.2 Boresight Measurement Accuracies: Boresight comparison measurements were made as a function of source parameters including polarization (horizontal and vertical linear), height and squint angles. Several sets of measurements were obtained by different operating personnel and under varying climatic conditions, so that the measurement results represent a valid estimate of the probable error to be expected in boresight measurements. The test device was a

single-channel amplitude-monopulse system employing a Cassegrain reflector assembly. This device, which provided a general simulation of a single plane of the LEM/RR, and the boresight measurement procedures are described in Chapter 3 of this document.

It was found that for small deviations of the transmitter height and squint angles about their theoretically optimum values (See paragraph 5.2.2.1), the average apparent source height was approximately 0.3 foot. For these measurements, the monopulse beams were aligned in the vertical (elevation) plane; the measured source height was found to be relatively insensitive to slight variations in source height or azimuth squint angle, but approximated the theoretically predicted variation as a function of elevation squint angle (See Appendix E and Section 4.1.1.3). For sensing of the apparent source location in the horizontal (azimuth) plane, a slight dependence on the azimuth squint angle of the source was noted. The maximum spread of redundant data in the ground-reflection mode for any specific setting of the source parameters was 0.1 milliradian.

The intrinsic boresight bias error for elevation sensing in the ground-reflection mode can be interpreted in two ways, depending on whether the optical reference is established on the geometrical center of source antenna or at the theoretical (essentially zero) height of the center of the source-image array. The recommended optical reference is a point on the range surface directly below the source antenna. The predicted RF bias error employing the current optical reference system is then approximately 0.3 milliradian.

On the basis of the measurement results shown in Chapter 4 and discussed above, it is concluded that the MILA range can be utilized as a high-accuracy boresight test facility in the ground-reflection mode at X-band. Maximum errors in this mode can be restricted to the order of 0.25 to 0.35 milliradian with reasonable care employed in establishing the test geometry.

### 5.2.3 X-Band Measurements in the Elevated Mode with No Diffraction Fences

5.2.3.1 The Aperture Field: Elevated mode measurements at 10 GHz with no diffraction screens in place showed that the MILA range surface appears smooth to energy at X-band frequencies for grazing angles up to approximately



4 degrees, the maximum grazing angle encountered in the measurements. Aperture amplitude patterns exhibited direct correlation with the theory of Section A.6, in that the extraneous energy incident on the test aperture appeared to originate at the image of the source antenna. The pitch of the aperture-field variations was basically dependent on the height of the source antenna, the amplitude on the directivity and orientation (squint-angle) of the source antenna; the ripple component of logarithmically recorded field variations was of the order of 1 decibel for source heights from 10 to 36 feet, where the elevation squint angle was set for aperture-field symmetry at each height.

These measurements were conducted with a 4 foot paraboloidal source antenna which, in the absence of extraneous signals, would illuminate a test aperture of approximately 10 foot diameter within the 0.25 decibel points of its main lobe for a range length of 1000 feet. A more directive source antenna would suppress the effects of reflections from the range surface, but would increase the amplitude taper of the aperture field. Since the emphasis of the study was on the establishment of aperture fields with amplitude variations an order of magnitude less than those obtained with this configuration (i. e., without fences), no polarization experiments were performed other than reference measurements at the center of the aperture. However, for purposes of comparison, boresight measurements were obtained as discussed below.

5.2.3.2 Boresight Measurement Accuracies: The results of several sets of boresight measurements in the elevation plane were summarized in Figure 4.13. The cyclic variations in measured source height as a function of actual source height corresponded to boresight deviations of approximately  $\pm 2$  milliradians with reference to the center of the source antenna. While this magnitude of possible deviation makes the elevated mode with no diffraction fences unacceptable for high-accuracy boresight measurements, it is significant that the data from 100 typical measurements for this configuration exhibited an average error of approximately 0.1 milliradian and a standard deviation of approximately 1 milliradian.

#### 5.2.4 X-Band Measurements in the Elevated Mode with Various Diffraction Fences

5.2.4.1 The Aperture Field: A total of eight diffraction fence configurations were investigated at X-band, as discussed in Section 4.1.3.1. This investigation

led to the establishment of sufficient aperture-field purity to allow high-accuracy boresight measurements, but is not considered to represent a determination of the optimum aperture-field improvement which could be accomplished with the use of diffraction fences. It was found that a single fence 12 feet in height and 60 feet in width placed at the center of the range provided essentially the same improvement in the aperture-field configuration as did any of the multiple-fence installations investigated. Use of this single fence reduced the ripple component of aperture-field vertical amplitude patterns to approximately 0.2 decibel, corresponding to a reduction in the extraneous signal level relative to the direct-path signal of some 14 decibels as compared to the level observed for the elevated mode in the absence of diffraction fences. The 12-foot fence essentially screens the first 20 Fresnel zones on the range surface from illumination by the transmitted pattern, and the residual extraneous energy appears to be due primarily to diffraction effects. Budgetary and scheduling constraints prevented any experimentation directed toward reduction of diffraction effects by such means as serrated fence edges. The single straight-edge 12-foot fence represents a practical and acceptable modification to the MILA facility for operation in the elevated mode at X-band.

Polarization measurements as a function of aperture position indicate that in the elevated mode with an 8-foot fence at the range center reference measurements at the center of the aperture will be sufficient to ensure generally acceptable polarization characteristics over a 16-foot diameter test aperture.

5.2.4.2 Boresight Measurement Accuracies: Boresight measurements in the elevation plane with various fence configurations in place showed that, as compared to the ground-reflection mode, the elevated mode with diffraction fences is likely to produce a greater spread in redundant data (measured results were  $\pm 0.2$  milliradian vs  $\pm .05$  milliradian) but is likely to produce a smaller bias error (measured results were 0.1 milliradian vs 0.3 milliradian). Calculations for over 100 data samples indicated an average error in elevation sensing of approximately 0.1 milliradian and a standard deviation of the same order; these results show that in comparison to the elevated mode with no diffraction fences, the average errors are comparable, but the fences reduce the standard deviation by an order of magnitude.

Measurements in the azimuth plane indicated extremely high accuracy capabilities; the spread in data from such measurements was less than 0.1 milliradian for

various boresight offset angles. Virtually no effect was seen in the apparent location of the source in azimuth for slight variations in the transmitter azimuth squint angle.

The most critical parameter in the elevated mode was the transmitter elevation squint angle. For a fixed source height, misalignment of the peak of the transmitted pattern from the center of the aperture by 0.5 degree produced a variation in apparent source height of 0.5 milliradian; this was primarily due to the change in diffraction from the fence.

In summary, operation of the range in the elevated mode at X-band should include the placement of a 12-foot fence at the range center, and the peak of the transmitted beam should be carefully aligned to center the beam on the test aperture.

#### 5.2.5 S-Band Measurements in the Ground-Reflection Mode

5.2.5.1 The Aperture Field: The field produced by the source-image array at 2.3 GHz was investigated over a 16-foot diameter aperture centered at a receiver height of 30 feet. Amplitude patterns recorded for both horizontal and vertical polarizations exhibited negligible ripple components, indicating that the range surface appeared very nearly specularly reflecting to S-band energy. The character of the aperture field was relatively insensitive to slight variations of the source height or squint angles about their theoretically optimum values. The same comments apply to the adjustments of the source parameters and documentation of the aperture-field purity at S-band as for X-band (See paragraph 5.2.2.1), where the initial settings at 2.3 GHz should be

$$\text{height} = \frac{\lambda R_o}{4h_r} \doteq \frac{(0.43)(1000)}{4(30)} \doteq 3.6 \text{ feet,}$$

$$\text{elevation squint} = 57.3 \left( \frac{-\lambda}{4h_r} \right) \doteq -57.3 \left( \frac{0.43}{120} \right) \doteq -0.2 \text{ degree,}$$

and

$$\text{azimuth squint} = 0.$$

With proper adjustment of the source parameters, less than 1 decibel of amplitude taper will exist over the vertical plane of a 16-foot test aperture, and the amplitude taper in the horizontal plane will be negligible. Although a faulty connector developed in the course of polarization measurements, so that optimum reference polarizations could not be established, it was shown that the constancy of

the aperture-field polarization was very good for linear polarizations and for nearly circular elliptical polarization. Subsequent replacement of the faulty connector in the S-band polarization unit and laboratory tests showed that the performance of the S-band unit is comparable to the X-band Series 40 unit. As for the X-band ground-reflection case, reference polarization measurements at the center of the test aperture will be sufficient to ensure generally acceptable polarization characteristics over a minimum aperture of 16-foot diameter.

5.2.5.2 Boresight Measurement Accuracies: Boresight comparison measurements were made at S-band as a function of source parameters including linear polarization, height and squint angles, and as a function of roll axis offset in both the elevation and azimuth planes. The test device was a single-plane phase-monopulse sensor employing an interferometer-pair feed assembly as described in Chapter 3. As at X-band, the sensor was employed in a test procedure which cancelled the boresight error of the sensor itself. The maximum spread of redundant data for any specific setting of the source parameters was of the order of 0.1 milliradian, and the apparent location of the source of radiation was relatively insensitive to slight deviations in the source parameters from their optimum values. Summary calculations for over 50 redundant data points showed that the average apparent source height was 0.49 foot and the standard deviation of the data was 0.06 milliradian. The half-milliradian bias error represented by the average source height is of little consequence for most measurement problems and may be reduced by more precise optical reference techniques.

#### 5.2.6 S-Band Measurements in the Elevated Mode

Results of radiation measurements at 2.3 GHz in the elevated mode indicate that this mode of range operation is not advisable for high-accuracy measurements in general, and is particularly poor for boresight applications in comparison to the ground-reflection mode. The source antenna employed for these measurements was an 8-foot paraboloidal reflector, which is presently the most directive source antenna available at the MILA range. While some added suppression of extraneous signal effects could be realized with a more directive source, it is noted that the existing source positioning equipment will accommodate a maximum antenna of 10-foot diameter. On the basis of current test responsibilities of the MILA

facility, the investment which would be required to establish an acceptable capability for elevated mode measurements at S-band for the existing range length does not appear to be justified, since a high-accuracy ground-reflection mode capability already exists.

#### 5.2.7 Operation of the MILA Range at C-Band Frequencies

The results of the current evaluation program and of the original Gemini validation program have documented the performance of the MILA facility at L-band (1.428 GHz), S-band (2.3 GHz) and X-band (10 GHz). Operation of the range in the ground-reflection mode has been shown to provide excellent test-aperture field configurations at each of these frequencies, and to allow for high accuracies in such specialized tests as boresight comparison measurements. The existing facility can generally be operated satisfactorily in the elevated mode at X-band frequencies only if proper diffraction-fence placements are employed. The available line-of-sight heights are not acceptable for elevated-mode measurements in the absence of diffraction fences at frequencies up to X-band, except for such specialized test requirements as those employing extremely narrow-beam antennas.

From these results, the following conclusions are drawn concerning operation of the MILA range in its existing configuration at C-band. The MILA range will provide excellent ground-reflection operation at C-band frequencies for general antenna measurement problems and for tests of direction-sensing systems such as phase-monopulse or amplitude-monopulse radars. Unless future test responsibilities specifically require operation in the elevated mode, the existing facility should be operated in the ground-reflection mode at C-band. If measurements must be made in the elevated mode, it is recommended that a shorter separation between source and test antennas be provided than the existing 1000 feet. A feasible approach to such a requirement would be the use of a mobile source tower with complete remotely controlled capabilities for adjusting and indicating the height, squint angles, and rotation of source antennas. The mobile source tower would preferably be located on a graded-surface or railed track whose axis would lie at a diagonal with respect to the axis of the existing range. For high-accuracy tests employing the diagonal range, consideration should be given to the use of diffraction fences for all but the closest spacings between source and test antennas.

### 5.2.8 Tabular Summary of Range Parameters

Settings of the test parameters for operation of the 1000-foot MILA range in the ground-reflection mode from L-band through X-band, and in the elevated mode at X-band, for receiver heights of 30 feet and 45 feet are tabulated below. For properly adjusted source antennas, the azimuth squint angle should be set at zero for all configurations.

Operating Frequency (GHz)	Receiver Height (feet)	Mode of Operation* --	Source Size (feet)	Source Height (feet)	Elevation Squint (degrees)
1.428	30	GROUND	8	5.74	-0.33
1.428	45	GROUND	8	3.82	-0.22
2.3	30	GROUND	4	3.56	-0.20
2.3	45	GROUND	4	2.37	-0.13
5.8	30	GROUND	2	1.41	-0.08
5.8	45	GROUND	2	0.94	-0.05
10	30	GROUND	1	0.82	-0.05
10	45	GROUND	1	0.55	-0.03
10	30	ELEVATED*	4	30	0
10	45	ELEVATED*	4	45	0

\*With reference to the table on page 4-23, the suggested diffraction fence configurations are (g) for the 30-foot test height and (c) for the 45-foot test height. The aperture field probe should be utilized as discussed in previous paragraphs to optimize all range parameters for critical test situations. (See section 5.2.2.1.)

## CHAPTER 6

### CAPABILITY OF THE MILA RF TEST FACILITY IN RELATION TO THE LEM RENDEZVOUS RADAR AND LANDING RADAR BORESIGHT PROBLEMS

#### 6.1 Introduction

A major portion of the effort under this program has been either directly or indirectly concerned with the problem of making pre-launch boresight measurements of the LEM rendezvous radar (LEM/RR) and landing radar (LEM/LR). The purpose of the discussions presented in this chapter is to relate the requirements of the LEM/RR and the LEM/LR test problems to the capabilities of the existing MILA RF boresight test facility.

The problem can be stated as follows: Given a precision L-band ground-reflection boresight test facility, which was designed specifically for making boresight measurements of the Gemini rendezvous radar,

- (1) what are the capabilities and limitations of this antenna test range in making boresight measurements of the LEM rendezvous radar and landing radar, and
- (2) what alterations are required by the LEM test problem?

The discussions of this chapter have been divided into separate considerations of the rendezvous radar and the landing radar.

#### 6.2 Rendezvous Radar Boresight Test Problem

The study of the LEM/RR boresight test problem is broken into the following basic categories:

- (1) The boresight accuracy specifications of the LEM/RR.
- (2) The overall measurements program at RCA, GAEC, WSMR, NASA - MSC, and NASA - KSC.
- (3) The boresight capability of the existing MILA range in comparison with the requirements indicated by the LEM/RR problem.

These elements of the LEM/RR problem are considered in the following paragraphs.

### 6.2.1 Boresight Accuracy Specifications of the LEM Rendezvous Radar

The LEM/RR is an X-band, four-horn, amplitude-monopulse sensor utilizing a 2-foot diameter Cassegrain antenna. The specifications which are discussed in this section apply during the free-fall portion of the landing and rendezvous phases of the lunar-landing mission, with emphasis on the rendezvous phase.

The study reported herein has been conducted prior to development of rigorously definitive specifications of the boresight requirements of the rendezvous radar. Accordingly it has been necessary to interpret the intent of the preliminary specifications. Information has been obtained from documents which have been available and by conferences with engineers and/or scientists at NASA-KSC, NASA-MSC, MIT Instrumentation Laboratory, Grumman, RCA-Burlington, RCA-Moorestown, and North American Aviation. The discussion of this section is believed to interpret the intent of the specifications as it was at the time of the study. The discussion is based on the writers' understanding of statements made in conferences with cognizant personnel in the Apollo program in connection with the specifications and their implications, and is not an official statement of these specifications.

Specifications describing allowable errors between the angle readout of the LEM/RR and the true line of sight (LOS) to the CSM transponder (TR) have been broken into two categories in documents describing the rendezvous radar. These two categories are BIAS ERRORS and RANDOM ERRORS. While these categories are not entirely descriptive of the character of the errors which can exist, their intent is believed to be as described in the following statements and as illustrated in Figure 6.1.

#### (a) BIAS ERRORS

- (1) FIXED BIAS ERROR is the mean, non-varying component of the error between the indicated LOS and the true LOS. The terminology implies constancy of both the magnitude and the space direction of the error.
- (2) BIAS DRIFT. Bias drift error is the low-frequency component of any variation which may occur in the radar boresight error. The specifications, as written, limit the bias drift to a magnitude of 0.5 milliradian in any 10-minute operational interval. This specification



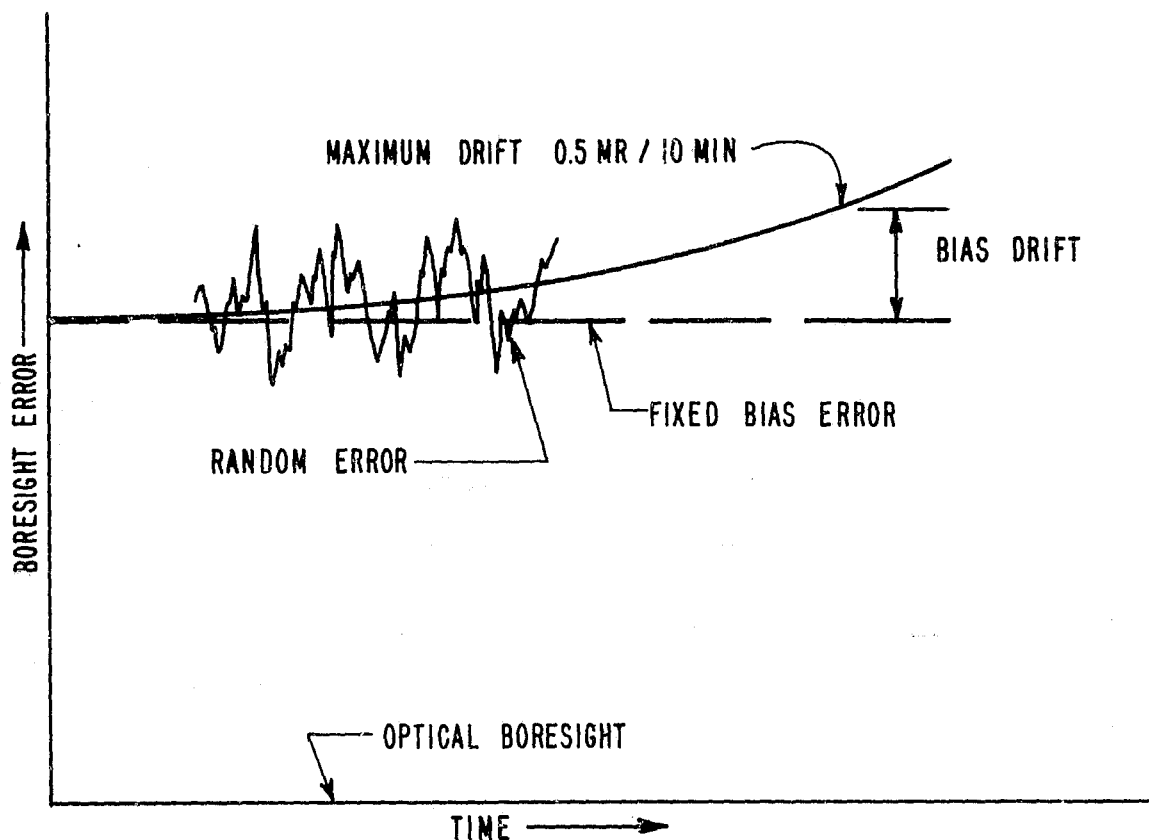


Figure 6.1. Interpretation of Rendezvous Radar Boresight Specifications

does not imply a maximum drift rate of 0.05 milliradian/minute, but a maximum change between the running mean of readings taken over some operational time interval at 10-minute spacings in time.

The specification limiting bias drift is imposed to permit determination of the magnitude and direction of the fixed bias error from calculations which are based on (1) an initial estimate of the direction to the CSM from the LEM based on independent data and (2) on the manner in which the difference between the measured direction and the estimated direction changes over a 10-minute interval during the rendezvous phase. This can be accomplished only if the bias error (1) remains fixed, or (2) varies in a known manner with time. The latter is considered to be impossible or impracticable; therefore, it has been specified that the bias be fixed within a suitable criterion (0.5 milliradian in 10 minutes).

The bias drift is specified as a function of time, but it is implicitly a function at least of (1) the polarization of the incident wave from the CSM/TR, (2) the orientation of the LEM relative to the LOS, and (3) the temperature of the antenna, which is a function of the orientation and rate of change of the orientation of the LEM relative to the sun and the lunar surface.

(b) RANDOM ERROR

The term random error as applied to the RR problem means the "short term alternating component" of the radar boresight error. It is not actually random, but is at least partially correlated with the orientation of the LOS relative to the LEM. For example, the magnitude of a component of the envelope of the so-defined "random error" is related to directions of the LOS relative to the LEM. Although reflections from the LEM will not be random in the rigorous sense, the short term alternating component of the error caused by such reflections is so considered because there has been no other defined category in which to place it. In addition to the short term alternating component of this error there will be a longer term component which is lumped into the bias drift category. The specified limit on random error is of the order of 3 milliradians.

Other short term errors from sources such as servo noise, etc., are more likely to have a zero mean than are those due to spacecraft reflections.

6.2.2 Discussion of the Specifications

During the early stages of this study program two meetings were held with cognizant personnel of the MIT Instrumentation Laboratory in an effort to obtain a better understanding of the intent of the specifications. The interpretation of errors indicated in the following paragraphs is intended to reflect the results of these meetings.

With regard to bias drift the following assessment was made: The specification of 0.5 milliradian in a 10-minute operating interval does not represent a specific limit per se, but is intended to imply a very small allowable variation in a parameter which could cause serious error if it should be allowed to become excessive.

The boresight accuracy implied by these specifications<sup>4</sup> has been recognized as representing critical requirements in the radar system in view of (1) the diameter of the antenna, (2) the weight requirements, (3) the hostile operating environment, (4) the problem of reflections from the spacecraft, and (5) the requirement on polarization, and has received considerable attention from LEM project personnel at the several activities involved.

With respect to the actual program of evaluation of the MILA range, the LEM/RR specifications did not particularly alter the approach to the problem, because the program was directed toward determination of the boresight capability of the existing range. The specifications did, however, affect the recommendations which were made in an interim presentation which was presented at NASA-KSC by Scientific-Atlanta on June 16, 1965. This presentation included tentative recommendations for modification to the MILA facility which would permit measurement accuracies approaching those implied by the specifications.

In the fall of 1965 a directive was sent from NASA-MSC to NASA-KSC to the effect that compliance with the 0.5 milliradian bias-drift specification would not have to be verified at the MILA facility. NASA-KSC is at present formulating plans to verify that the radar complies with a maximum boresight error specification of 8 milliradians between the indicated LOS and the true LOS referred to the RADAR BASE and 7 milliradians between the RADAR BASE and the NAV BASE. The recommendations presented in Chapter 7 are based on these requirements.

#### 6.2.3 Effect of Orientation of the Spacecraft Relative to the Line of Sight

In this section the problem of reflection of energy from the LEM into the RR antenna will be discussed qualitatively to demonstrate the manner in which the spacecraft reflections contribute to the "random" and "bias drift" error categories. The reflection problem can be visualized from consideration of the general characteristics of the radar, its location on the LEM, and the shape of the LEM. The problem has been considered theoretically at GAEC in choosing

the location of the radar on the LEM.<sup>6-1</sup> The detailed structure of the errors caused by reflections from the LEM in the boresight of the rendezvous radar will be virtually impossible to determine, for reasons discussed below.

Electromagnetic energy from the CSM transponder will illuminate the radar antenna and portions of the LEM structure. The nominal projected area of the antenna on the plane normal to the LOS is  $\pi$  square feet, while the projected area of the LEM is of the order of 200 square feet. Thus the level of the total energy incident on the LEM is of the order of 20 decibels higher than that incident on the radar antenna.

Energy incident on the LEM will be largely scattered because the surface is generally non-absorbent to microwave radiation. The scattered energy will be distributed in a complex lobe structure because of the angular character of the LEM configuration. The approximate directions and magnitudes of major specular-reflection lobes can be predicted to some degree by geometrical-optics approximations to the scattering problem, but the directions and levels of minor reflection lobes cannot be predicted to any degree of accuracy. Energy which is scattered from the LEM in the direction of the rendezvous radar will be partially suppressed by the directivity pattern of the radar. Generally, the reflected energy will enter the antenna through the minor-lobe regions of the antenna patterns, although for certain relative orientations of the LOS and the LEM energy will enter through the main lobes.

At this point it is important to emphasize that energy scattered from the LEM into the radar will be from scatterers which are in the near-zone of the radar antenna. Thus measurement of the far-zone, wide-angle patterns of the antenna does not provide an accurate measure of the lobe structure as it applies in the actual near-zone scattering problem. However, it has been shown that the average directivity to energy arriving from wide angles into a narrow beam antenna is roughly predicted by the envelope of the far-zone, wide-angle patterns.\*

---

<sup>6-1</sup>R. Ellis, GAEC LEM Engineering Memorandum, Subject: Rendezvous Radar Antenna Location, LMO-350-14, 29 May 1963.

\*Private communications with Dr. R. C. Johnson, Engineering Experiment Station, Georgia Institute of Technology in discussion of reports under preparation.

The scattering problem is complicated by a number of factors, including:

- (1) The multiplicity of directions of energy arrival and resulting radar pointing angles represented by the coverage sector of the rendezvous radar,
- (2) The range of polarizations represented by the relative orientations which occur between the LEM and the CSM,
- (3) The short wavelength of 10-GHz radiation,
- (4) The lack of infinite rigidity of the LEM structure, and
- (5) The physical size of the LEM, which makes it impractical to make measurements of the effects of reflections from the spacecraft in a true far-zone environment. (If the complete LEM is considered to scatter energy into the radar antenna, a separation of the order of 10,000 feet is required for achievement of far-zone conditions within generally accepted criteria.)

The mechanism by which reflections from the spacecraft perturb the indicated line-of-sight is such that, over any measuring interval, the perturbation will consist of an alternating (zero-mean-value) component and a bias component.

The indicated line-of-sight is a function of the shaft angle  $\alpha$  and the trunnion angle  $\beta$ , but is implicitly a function of time because the direction  $(\alpha, \beta)$  is itself a function of time. The spectral distribution of the alternating component of the indicated LOS is related to the rate of change of the true LOS with respect to the LEM spacecraft, the configuration of the spacecraft, and the wavelength of the 10-GHz incident energy.

For orientations of the LEM relative to the CSM such that the LOS moves relatively rapidly, the spectrum of the alternating component will be such that most of the resulting error can be considered in the random category. Unfortunately, as the rate of change of the LOS is reduced the frequency range of the perturbation becomes lower, and the component which must be considered in the bias-drift category tends to increase until at very slow LOS rates the entire perturbation may be in the bias-drift category.

One cannot, without knowledge of the manner in which the LEM may be programmed

relative to the LOS, properly categorize the effects caused by spacecraft reflections between random and bias drift errors. Therefore, evaluation of the effect of the spacecraft on the indicated LOS should take into consideration the expected rates of change of the LOS during the free-fall operational portion of the mission profile.

Study of the effect of the LEM configuration on the indicated LOS is being pursued at NASA-MSC as an R&D effort, utilizing an antenna range which is specifically designed for this purpose. The concern for this problem in the investigation reported herein is in relation to the practicability of and techniques for measuring the free-space boresight error of the radar in the presence of reflections from the LEM, and because of the uncertainty in the types of measurements which will be required at MILA.

#### 6.2.4 Effect of Polarization on Bias-Drift Error

The investigated design of the LEM/RR-CSM/TR system includes the capability for arbitrary orientation of the attitude of the CSM relative to the LEM within the constraint imposed by the radiation pattern of the CSM transponder antenna. This capability could be accomplished by any of three choices of polarization of the RR-TR antennas with certain resulting trade-offs:

	RR	TR
(1)	Linear	Circular
(2)	Circular	Linear
(3)	Circular	Circular

Of these three possibilities, number (2) represents the selected design; i.e., the rendezvous radar is designed to be circularly polarized, and the transponder is designed to be linearly polarized.

The polarization problem is acute because of the specification that the boresight bias error drift be not greater than 0.5 milliradian in any 10-minute operational period. This drift requirement implicitly includes change in boresight direction with polarization unless constraints were to be imposed on the relative polarization of the transponder antenna and the rendezvous radar during critical tracking intervals. Information to date has indicated that such a constraint could not be imposed. The problem of boresight change with polarization requires precise control of the axial ratios of the individual channels of the monopulse

network. In view of the critical nature of the bias drift specification it appears necessary to make measurements of the boresight direction versus polarization in tests at NASA-KSC.\*

#### 6.2.5 Outline of the LEM/RR Boresight Error Measurement Program

The tests which have been indicated for the LEM/RR program are summarized below. This summary is based on information obtained from the various participating activities, and is not an official statement of the test schedule.

<u>Activity</u>	<u>Range Length Where Applicable</u>	<u>Systems Tested</u>
RCA-Moorestown	1000 Inches	RR Antenna
(a) Standard gain comparison, power output, and other standard microwave tests.		
(b) Sum- and difference-channel pattern measurements.		
(c) Pattern polarization measurements on-axis and at 3-decibel points.		
(d) Alignment of RF and optical boresight directions.		
(e) Variation of RF boresight with orientation of linear polarizations.		

<u>Activity</u>	<u>Range Length Where Applicable</u>	<u>Systems Tested</u>
RCA-Burlington	90 Feet	RR Section and Subsection
(a) Gyro platform stability.		
(b) Point-by-point LOS motion tests.		
(c) Base motion angle track tests.		
(d) Acquisition angle tests.		
(e) (Simulated) range and range-rate tests.		

---

\* As stated above, NASA-KSC is not presently required to demonstrate compliance with the 0.5 milliradian bias drift specification. The 8-milliradian specification which must be verified could be interpreted to permit a possible boresight variation of 16 milliradians with polarization; such a variation is believed to be untenable in view of the weight which has been given to the bias drift component of boresight error in the specifications. Clarification of the NASA-KSC test requirements should be obtained to resolve this ambiguity.

<u>Activity</u>	<u>Range Length Where Applicable</u>	<u>Systems Tested</u>
GAEC Bethpage	1000 Inches	LEM/RR/TR Assembly

- (a) Engineering model (1/3 scale) measurements.
- (b) Test-point input checks of electrical and electro-mechanical loops.

<u>Activity</u>	<u>Range Length Where Applicable</u>	<u>Systems Tested</u>
WSMR	Variable (Fly-Over)	LEM/RR-CSM/TR

- (a) Range and range-rate.
  - (b) General assessment of simulated lunar surface effects and spacecraft reflections.
- (These tests are designed to provide "confidence factors" and are not specification compliance tests.)

<u>Activity</u>	<u>Range Length Where Applicable</u>	<u>Systems Tested</u>
NASA-MSC	2500 Feet	TM7/RR

- (a) R&D program for assessment of the effects of spacecraft reflections and simulated operational environments (in evacuation chamber).
- (b) Design validity tests.

<u>Activity</u>	<u>Range Length Where Applicable</u>	<u>Systems Tested</u>
NASA-KSC	1000 Feet (Existing)	TM7/RR

- (a) Boresight accuracy tests to show compliance with RADAR BASE and NAV BASE specifications.
- (b) LOS motion tests.
- (c) Acquisition tests.
- (d) Electrical and electro-mechanical loop check-out (in MILA O&C Building).
- (e) Pre-launch check-out (flight LEM) in stacked configuration.

#### 6.2.6 Capability of the MILA Range for Making Boresight Measurements of the LEM Rendezvous Radar

The capability of the MILA range for making measurements at X-band was investigated in a series of theoretical studies and in a program of experimental



measurements. These studies were directed toward (1) determination of the general capability of the range at X-band and (2) the specific problem of making boresight accuracy measurements of the LEM rendezvous radar, and are reported in other sections of this document. In this section implications of the investigations are discussed in relation to the LEM/RR problem.

The capabilities and limitations of the range for making boresight measurements of the LEM/RR are based on the following factors:

- (1) The range configuration (range length, line-of-sight, height, etc.).
- (2) Effects of extraneous signals.
- (3) Characteristics of the test positioner and range instrumentation (load-bearing capability, mechanical and electrical errors, control characteristics, data rates, adaptability to automation, etc.).
- (4) The physical environment (problems related to wind, temperature effects, atmospheric contamination, etc.).

6.2.6.1 Range Configuration: The physical configuration of the MILA range is described in section 2.1. The range is 1000 feet long and can be operated at X-band in either the ground-reflection mode or in the elevated mode. The test positioner is located on top of the control building at such a height that the line-of-sight of the upper-azimuth axis of the test positioner is nominally 30 feet above the range surface. For elevated operation the height of the source antenna would be set between 25 feet and 35 feet, nominally at 30 feet. The height of the line-of-sight of the LEM/RR mounted in place on the ascent stage of the LEM or a full-scale mockup would be nominally about 43 feet but would vary from approximately 44 feet to 33 feet with changes in orientation of the LEM.

(a) Range Length

The length of the MILA range was set at 1000 feet in the design of the range, which was based on the requirements of the Gemini/RR boresight test problem (see Appendix K, page 11). This range length provides less than a  $\pi/8$  radian phase deviation of the incident field over the maximum projection of the Gemini spacecraft on the plane which is normal to the line-of-sight, and at the same time provides a favorable grazing angle for ground-reflection operation of the range.

The optimum separation between the source antenna and the LEM/RR during boresight tests is difficult to specify because considerable latitude exists in choice of a range length; however, some observations can be made which indicate that the existing range length of 1000 feet represents a favorable compromise. The diameter of the radar antenna is two feet. Based on the commonly employed criterion,  $R \geq 2D^2/\lambda$ , where  $D$  is the diameter of the antenna under test,  $\lambda$  is the wavelength, and  $R$  is the separation, a minimum separation of about 80 feet is indicated for a nominal wavelength of 0.1 foot (frequency, 10 GHz). The adequacy of this criterion is determined by the required accuracy of the measurements and by the precision with which the radar is fabricated. Measurements which are being made at RCA-Moorestown and RCA-Burlington are made at separations of this order. Investigations reported in Appendix J indicate that such a separation is adequate unless measurements of extreme precision are required and unless other factors influence the separation. The two other major factors which can influence the separation are (1) errors from parallax and (2) the effects of reflections from the spacecraft.

The parallax problem is considered in Appendix J. The problem is complicated by a number of factors and cannot be argued in detail without definition of a specific set of tests. It is generally true, however, that the parallax problem decreases as range length increases and that a range length of 1000 feet represents a desirable separation from the viewpoint of parallax in the LEM/RR test problem; in any event, no parallax advantage appears to result from decreasing the range length from its existing value of 1000 feet.

In the evaluation of the effects of reflections from the spacecraft, it might appear that a range length of the order of 10,000 feet would be required. Such a range length would provide a large test aperture which would satisfy the  $R \geq 2D^2/\lambda$  criterion. (For  $\lambda \doteq 0.1$  foot, the resulting aperture diameter  $D$  would be about 22 feet for a maximum phase deviation of  $\pi/8$  radian.) A number of factors argue against such a range length, however. Primarily, as has been discussed in section 6.2.3, it is not possible to make precise quantitative measurements of the effect of the spacecraft on the radar boresight at any range length because of the nature of the problem.

A ground-reflection range with a length of 3000 feet was proposed by GAEC in a preliminary report<sup>6-2</sup> dated 15 March 1965. While such a length provides a

---

<sup>6-2</sup>"LEM-Facilities--Plan Apollo Requirements for the MSC-RF Systems Facility at MILA, Florida," GAEC LPL-1B, Appendix 14, Preliminary, 15 March 1965.

favorable grazing angle for ground-reflection operation and a reduction of the parallax problem, an antenna range of this length does not appear to be warranted by the present interpretation of the test requirements, and is not believed to be a currently proposed range configuration.

In its 16 June 1965 interim presentation at NASA-KSC, Scientific-Atlanta proposed a 1600-foot range which would be capable of both ground-reflection and elevated-mode operation. This proposed modification was based on two factors, (1) achievement of an adequate physical separation between the LEM and Gemini test sites to permit simultaneous measurements under the Gemini program and the Apollo program, (2) essential retention of the present grazing angle for ground-reflection operation while providing an increase in aperture test height to approximately 50 feet, which was indicated for the LEM/RR tests. At the time of the interim report, these tests were expected to employ the full LEM flight vehicle including ascent and descent stages, and verification of compliance with the 0.5 milliradian bias-drift specification was considered a test responsibility of NASA-KSC. Although a range length of 1600 feet would provide a more favorable grazing angle for a 45-foot test-aperture height, it is predicted that satisfactory operation of the range will result with this test height at the present separation of 1000 feet.

(b) Range Surface and LOS Height

The primary range surface of the MILA facility is graded to close tolerance and planted in Bermuda grass (see Chapter 2). Measurements reported in Chapter 4 show that this surface is sufficiently smooth at X-band for the existing range to possess excellent ground-reflection mode characteristics. The effects of alterations in the range length, height, or surface roughness can be interpreted in terms of the Rayleigh criterion of roughness (see equation (A-1), section A. 2). While the grazing angle would be increased by a factor of approximately 1.5 for an increase in the maximum test aperture elevation from 30 feet to 45 feet, elevated-mode measurements in the absence of diffraction fences indicated that the range surface will appear smooth for increases in grazing angle up to a factor 2. Thus, no problem is foreseen in ground-reflection operation for LEM/RR boresight test. However, the range should be re-evaluated for operation in the ground-reflection mode if the grazing angle is increased by increasing the height of the test aperture without increasing the range length.

This can be accomplished simply by probing the aperture field, since measurements made under this program show that direct correlation is achievable between the magnitudes of measured aperture field variations and measured deviations of the RF boresight direction from optical boresight.

Assuming that the TM7 LEM mockup will be mounted on the existing test positioner, the maximum LOS height available in the elevated mode will be less than optimum.\* However, boresight measurements of this study which were conducted under similar circumstances indicate that sufficient redundancy of data to provide random phasing of extraneous signals will allow the elevated mode to be employed with probable standard deviations of the order of 0.1 milliradian.

6.2.6.2 Error from Extraneous Signals: Analyses and measurements to determine the effects of extraneous signals on the probable boresight error in making measurements of the LEM/RR have constituted a major part of the program reported in this document. Analyses to determine the magnitude of effects of extraneous signals on the measured boresight of phase-monopulse or amplitude-monopulse radars and specifically of the LEM/RR are presented in Appendices A through F. The results of measurements which were made to determine the boresight capability of the range are presented in Chapter 4. The reader is referred to section D.2 for a detailed discussion of the effect of extraneous signals on the boresight measurement accuracy of the LEM rendezvous radar and to Chapter 5 for a detailed summary of the material which is presented in the appendices.

Measurements described in Chapter 4 were made with an amplitude-monopulse sensor which simulated the boresight characteristics of the LEM/RR. Thus the measurements can be interpreted directly in terms of the error which should result in tests of the LEM rendezvous radar in the modes of range operation which were employed in the evaluation measurements.

---

\* This conclusion is based on the developments of Appendix D and on the experimental investigations reported in Chapter 4. As shown in Figure D.5, the LEM/RR will likely be most sensitive to extraneous energy which arrives at the radar aperture from 2 to 4 degrees off the boresight axis. If the source antenna height is set at about 35 feet, the declination angles from the LOS to the top of a single diffraction fence located at the range center will lie in the 2 to 4 degree range for various orientations of the LEM/RR.

If one ignores the 0.5 milliradian bias drift specification which is discussed in section 6.2.1, the conclusion can be drawn that the range can be employed in either the ground-reflection or elevated mode, and will introduce negligible measurement error in relation to the 8 milliradian boresight accuracy specification which NASA-KSC is currently committed to verify in pre-launch tests.

Verification of compliance with the 0.5 milliradian bias-drift specification with any degree of confidence would call for meticulous verification of the range performance at every step and a large quantity of redundant data. The resulting measurement program and adaptation of the range to the automation that would be required would almost certainly be impracticable in light of the significance of the data which would be obtained.

In assessing the results of the measurements it is necessary to recognize that the boresight sensor, while generally simulating the characteristics of the LEM rendezvous radar, was mounted on a mockup of the Gemini spacecraft. Thus the effects of extremely wide-angle reflections will not be identical in tests of the LEM radar which is mounted on the TM7 mockup of the LEM ascent stage. However, because of the suppression afforded by the directivity patterns of the radar and the shielding provided by the mockup, and because the control building is covered with microwave absorbing material, it is predicted that wide-angle reflections from the test building will introduce negligible measurement error. If the boresight measurements are made on a support which does not provide the shielding afforded by a mockup of the LEM ascent stage, the test positioner should be covered with X-band absorbing material.

6.2.6.3 Positioner and Instrumentation: The existing MILA multi-axis test positioner and its associated instrumentation are described briefly in Chapter 2 of this document. Basic considerations of the angular measurement accuracies of this equipment are presented in Appendix H, with discussions of possible configurations which might be employed for LEM/RR tests utilizing a LEM spacecraft mockup. Specific measured and calculated elevation-angle and azimuth-angle accuracies of the positioning equipment as employed in the evaluation program reported in this document are summarized in Chapter 5.

In order to assess the adaptability of the positioner and instrumentation to the LEM/RR test problem, the following factors were considered:

- (1) Positioner load-bearing capability.

- (2) Axis-drive system characteristics.
- (3) Angle measurement accuracies.
- (4) Maximum data rates.

#### (1) Positioner Load-Bearing Capability

The concrete structure supporting the MILA test positioner was designed to withstand a 30,000-pound maximum vertical load and to withstand bending moments up to 30,000 pound-feet. The boresight positioner has an actual load rating of 40,000-pound vertical load and 75,000 pound-feet bending moment. The higher rated positioner was procured for the Gemini program to insure conservative loading for accuracy and stability. It is possible that the concrete support structure will safely support a much larger load than 30,000 pound-feet bending moment, however, before using larger loads a design review and testing for deflection and strength of the concrete support structure is required.

At present, the LEM/RR test program at MILA is expected to utilize the TM7 LEM ascent-stage mockup, which GAEC reports to weigh approximately 2500 pounds with a center of mass near the center of its approximate 10' x 10' cross-section. With this mockup mounted as depicted in Figure H. 4 through H. 6 (the X axis of the LEM parallel to the positioner lower-azimuth axis), the positioner and support structure will provide adequate safety factors in the load-bearing capabilities for all required orientations of the mockup. The two modes of sector coverage for the LEM/RR will require a 130° swing about the positioner elevation axis (+60°, -70°). The maximum resulting torque or bending moment will thus be approximately 15,000 pound-feet.

An alternate mounting configuration could be employed as depicted in Figure H. 7; this configuration would provide increased positioning accuracy but would require full counterbalancing due to the relatively low torque rating of the positioner's upper-azimuth axis.

#### (2) Axis-Drive-System Characteristics

The drive system for the three motion axes of the MILA test positioner has both a rate mode and a position mode of operation (see Appendix K, paragraph 5. 2. 2). The rate mode provides selectable constant rates of rotation about the positioner  $\phi$  and  $\theta$  axes which may be set by individual controls or programmed for automatic operation. This mode is applicable to rapid recording of large quantities of pattern data in standard chart form or in radiation distribution tables, and to

automated directivity calculations via the antenna pattern integrator. The position mode of positioner control will probably be employed for the bulk of the LEM/RR measurements. In the position mode, the appropriate  $\phi$  and  $\theta$  motions of the positioner are servo-driven in response to command settings of the position controls. This mode is appropriate for such measurements as point-to-point checks of the LEM/RR boresight accuracy, acquisition angle tests and LOS motion tests for various selected LEM orientations.

### (3) Angle Measurement Accuracies

In the LEM/RR measurement program, several sources of possible angle measurement error will exist, including parallax, positioner deflections, vehicle deflections, synchro readout errors, coordinate system misalignments and geometric errors of the test positioner. Once a specific mounting configuration for the TM7 mockup is selected and definite test procedures are formulated, the following assessments can be made of the above sources of error:

Parallax can be eliminated from the experimental data by appropriate computerized data reduction, with the exception of a small residual component which results from the ambiguity in the location of the test antenna's center-of-parallax.

The effects of positioner and vehicle deflections and of synchro readout errors can be largely eliminated or accounted for by optical calibration techniques. Such calibrations would be performed at each required orientation of the LEM vehicle.

Coordinate system misalignments and positioner geometric errors will always exist, however small. The effect of such intrinsic imperfections in the test configuration can be made negligible, particularly in light of the 8-milliradian boresight accuracy specification which must be verified at MILA, if precise optical boresight references are obtained for each spacecraft orientation and if the RF boresight measurements are restricted to differential sectors in the neighborhood of the optical references.

### (4) Maximum Data Rates

The data rate capability of the existing positioner-drive and angle-readout system is best suited for point-to-point boresight comparison tests. Accurate angle calibration during dynamic tracking tests is impractical with the present geared synchro readout system. Calibration methods employing high-speed data readout would require the addition of direct-drive digital-bit encoders to all positioner

axes, or alternatively a synchro-to-encoder conversion system, and a digital computer.

6.2.6.4 Environment of the MILA Facility: Modifications to the MILA facility will be required in order to provide an acceptable test environment for the LEM/RR. Operation of the radar is not permissible in winds over 4 knots or in an atmosphere containing the relatively high saline water-vapor levels common to the MILA environment. A suitable protective cover, as described in Chapter 7, can be employed to alleviate both the wind and moisture problems.

In addition to the above environmental factors, the effects of solar radiation and ambient temperatures must be considered. The maximum ambient temperature permissible for the LEM/RR is of the order of 100°F, and this limiting temperature can only be tolerated for relatively short operational intervals. Since it is required that the radar be totally enclosed as mentioned above, it is logical to provide adequate cooling to the conditioned air supply to protect the radar system. It is noted that even with a cooled-air atmosphere, the insulation of the LEM/RR circuitry against low lunar temperatures causes an internal heat problem which will still restrict the allowable operational intervals during pre-launch tests.

It appears impractical to totally shield either the LEM-TM7 or the test positioning equipment from solar radiation. However, if the solar heat problem warrants it, proper design of the required protective cover can largely eliminate errors from this source. For example, a dual-layer thin wall radome could be employed which has an outer skin which is highly reflective to sunlight and has an absorptive inner skin. The residual solar radiation which penetrates the radome will be sufficiently attenuated and diffuse to prevent significant deflections of the positioner or vehicle due to differential temperature effects. Such means would only be appropriate if the flow-time of required tests prevents the exclusive scheduling of experiments during hours when solar radiation is not problematical.

### 6.3 The LEM Landing Radar Test Problem

The problem of testing the LEM landing radar (LEM/LR) at the MILA RF test facility has been studied with attention directed to determining the range capability for obtaining boresight measurements to the accuracies specified for the landing radar. The study included consideration of the following factors:

- (1) The radar specifications for parameters which are related to the boresight measurement problem,



- (2) The test program for the landing radar, and
- (3) The capability of the existing MILA range for making the necessary measurements.

The following paragraphs discuss the factors listed above. In certain cases, conclusions and recommendations regarding the LEM/RR test problem are shown to apply to the LEM/LR problem, and material from the rendezvous radar section is cited.

#### 6.3.1 The LEM Landing Radar and Boresight Specifications

The LEM/LR consists of a three-beam (Janus) doppler velocity sensing system and a frequency-modulated doppler altimeter system, both of which operate at X-band. The system is required to deliver accurate velocity and altitude information during the powered descent, hover, and landing phases of the LEM mission.

The velocity sensing antenna system consists of a four-beam, slot-array transmitting antenna and three slot-array, receiving antennas. The 3-decibel beamwidths of the transmitting antennas in the E and H planes are approximately 4 degrees and 7 degrees, respectively, and their boresight directions form the corners of a pyramid as shown in Figure 6.2. The pyramid is centered on a reference axis, the beam group normal, which is normal to the transmitting array and to the spacecraft Y axis.

The three receiving beams, which have somewhat broader beamwidths than those of the transmitting antenna, are directed along three of the edges of the pyramid; since the velocity vector can be completely specified by inputs of three sensors<sup>6-3</sup>, information from the fourth beam is not required, and a corresponding receiving antenna is omitted. The approximate angular dimensions of the pyramid are  $\pm 20$  degrees from the beam group normal in the fore-and-aft direction and  $\pm 15$  degrees in the lateral direction.

The radar altimeter system consists of a two-beam, slot-array transmitting antenna, which is interlaced with the velocity sensor transmitting system, and a separate receiving array which is similar to those of the velocity sensing system.

---

<sup>6-3</sup> For a general discussion of the operation of typical doppler radar systems, see Airborne Radar, D.J. Povejsil, R.S. Raven, P. Waterman, D. Van Nostrand Co., pp. 726-759; 1961.

The receiving beam and one beam of the transmitting antenna are directed along the aft side of the pyramid of Figure 6.2 midway between velocity sensor beams 1 and 2. The second transmitter beam, which falls slightly outside the pyramid, is extraneous, and no corresponding receiver exists.

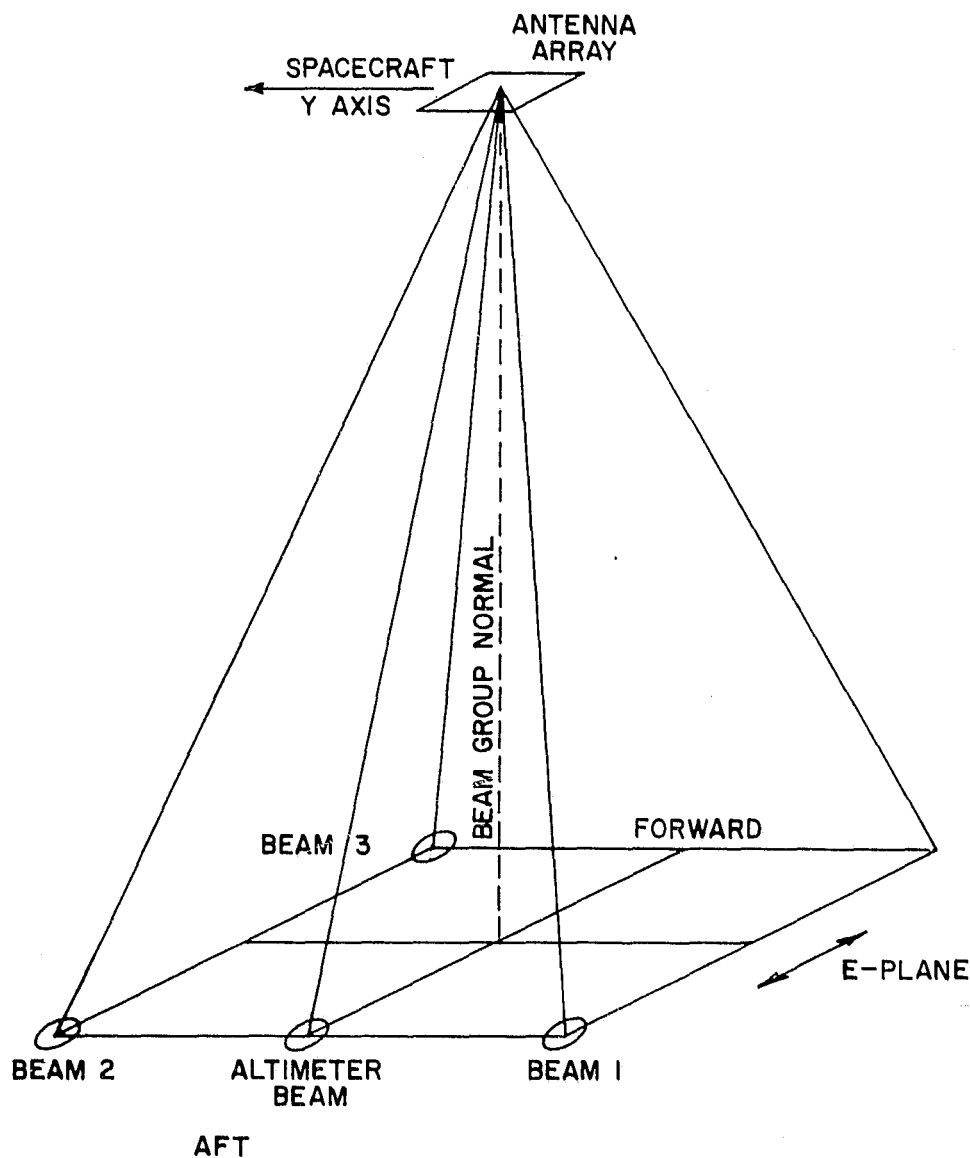


Figure 6.2. LEM Landing Radar Beam Geometry

The receiving beamwidths for both the velocity-sensing system and the altimeter system are somewhat broader than the transmitting beamwidths; the E-plane two-way 3-decibel beamwidths for each system are slightly less than 4 degrees and the H-plane beamwidths are slightly less than 7 degrees. The velocity sensing system operates in the CW mode while the altimeter system employs FM-CW modulation.

The boresight directions for the velocity sensor and altimeter beams are specified with angular tolerances of  $\pm 4$  minutes (approximately 1.2 milliradians) in the E-plane and  $\pm 7$  minutes (approximately 2 milliradians) in the H-plane.

### 6.3.2 LEM Landing Radar Boresight Test Program

Prior to arrival at NASA-KSC flight models of the landing radar will have undergone acceptance tests at Ryan and will have been integrated into the LEM at GAEC. During the development of the radar, in addition to tests of developmental models at Ryan, a research and development program will be conducted at NASA-MSC by NASA and GAEC personnel to determine the effects of the LEM vehicle on the landing radar performance. In addition, the radar system will be flight-tested in helicopters and aircraft at White Sands Missile Range. Final acceptance tests of the flight radar will be performed at Ryan immediately prior to delivery.

For acceptance tests at Ryan the boresight direction is defined as the direction determined by the mean of the directions of the half-power points of the two-way pattern measured in two defined orthogonal directions. The measurements are made at a separation of approximately 250 feet in two-way measurements which are made using a single sideband (SSB) modulator to tag the signal intercepted by a target. These tests will be made without use of a mockup of the LEM.

The total development program and test program as carried out at Ryan, NASA-MSC, and White Sands, is directed toward ensuring the capability of the radar to perform under the anticipated environmental conditions. The goal of pre-launch testing performed at NASA-KSC should then be to demonstrate that the radar is flight worthy, and to verify that the boresight directions have remained within the prescribed tolerances after shipment from Ryan. This might imply duplication of the test procedures employed at Ryan in the acceptance tests of the radar. However, it is not convenient to exactly duplicate the test set-up at Ryan because of the 1000-foot length of the MILA range. Before a specific recommendation is made relative to the method which should be employed at NASA-KSC it is necessary to consider basic factors which relate to the measurement problem. These are indicated and discussed below.

### 6.3.3 Implications of the Boresight Specifications with Respect to Pre-Launch Tests

The specifications indicated in paragraph 6.3.1 are the specifications with which Ryan is required to comply in acceptance measurements of the radar. The tolerances indicated by these specifications are extremely small and are probably set more for repeatability of results made on a specific antenna range than for absolute accuracy. For example, differences in geometry between the Ryan test range and the MILA range, which would result in a difference in parallax and differences in the precise mounting of the antennas as compared with that employed at Ryan, would produce a measurable difference in the absolute values of the beam directions measured on the two ranges.

Proof of the accuracy indicated on page 6-20 in pre-launch measurements would be costly in terms of instrumentation and man-power. Such measurements are not believed to be indicated by the nature of the problem, since error in beam separation produces only a velocity calibration error which is proportional to spacecraft velocity and which goes to zero at zero velocity. If the specifications include a safety factor and allowance is made for some absolute difference in the beam directions from the values measured on acceptance, then it should be possible to relax the tolerance which can be set for pre-launch measurements. In this event the MILA range can be employed in its present configuration for the measurement.

However, in the event that highly accurate measurements should be required, the measurements should be made in a technique which would determine the separations between the power centroids of the patterns. In operation the doppler system senses velocity from the doppler shift of the frequency spectrum produced by energy returned from the lunar surface through the complete portion of the radiation patterns which look at the surface. This return is weighted by the two-way power patterns of the beams and by the radar cross-section of the lunar surface for the angles of incidence involved. Thus the effective beam separations as interpreted by the radar are complicated by the operating environment, and no measurements under simulated conditions will precisely define the beam separation; however, measurements which are made to determine the beam directions as defined by the power centroids of the two-way patterns or a weighted power centroid will provide a more nearly correct indication of beam separation than does a separation defined by specific reference levels on the patterns. It is understood that investigations will be made at NASA-MSC under the R and D phase

of the program to determine the power centroid of the two-way beam patterns. These measurements will be made on a 2500-foot elevated range using engineering models of the radar. In addition, the difficulty of the measurement problem is reduced significantly if this method is employed. It can be shown by an analysis similar to that of Appendix D that received extraneous signals arriving from wide angles relative to the beam axis must be reduced to a level of the order of 50 decibels below the level of the beam maximum to limit the maximum error from extraneous signals to 0.2 milliradian in measurement of the direction of a beam whose half-power width is 4 degrees if the measurements are made by sensing the direction of the half-power points in orthogonal planes. This magnitude of error represents a high order of extraneous signal suppression, and is still only one error component of a total error budget.

Determination of the direction of the power centroid of a pattern requires integration over the portion of the pattern which contributes significantly to the total received energy. This process automatically provides redundancy of data which produces an RMS averaging of the effects of wide-angle extraneous signals so that suppression of such extraneous signals is not nearly as critical as it is in the measurement procedure which is based on definition of the beam-direction as the intersection of planes defined by half-power beamwidths.

#### 6.3.4 Capability of the MILA RF Test Facility for Making Boresight Measurements of the LEM/LR

Evaluation of the MILA boresight range for performing pre-launch boresight testing of the landing radar involves consideration of mechanical, electrical and environmental requirements. The capability of the MILA RF test facility in comparison with those requirements is discussed in the following paragraphs.

6.3.4.1 Test Positioner: In measurements of the altimeter and velocity sensor systems two types of measurements are indicated: (1) boresight measurements and (2) pattern measurements. As discussed in section 6.3.2, the boresight directions of the velocity sensor and altimeter beams are defined for purposes of measurements at Ryan by the means of the directions of the 3-decibel points of the two-way patterns in two orthogonal planes through the beams. The planes in which these measurements are made are defined by the sides of the pyramid of Figure 6.2. The boresight range positioning equipment should allow planar (i. e., great circle) cuts to be obtained along the four sides of the cone.

Boresight measurements require that the test positioner have capability for precise control of the orientation of the axes and precision readout of the axis orientation so that static measurements can be made to define the beam directions. Pattern measurements require continuous motion of the positioner axes and provisions for recording signal levels as a function of direction.

If boresight measurements should be made to an accuracy of the order of 0.3 milliradian, the total positioning error including load and solar effects, and positioning and readout errors should be of the order of 0.1 milliradian or less. Digital angle readout is indicated to permit readout of data into an incremental computer-compatible tape recorder.

The discussion of the capability of the MILA positioning equipment and instrumentation for the rendezvous radar boresight measurements, as presented in section 6.2.6.3, also applies to the landing radar problem. Additional theoretical considerations concerning the positioning system are contained in Appendix H.

The present positioner angle measurement accuracy is indicated in paragraph 2.3. However, precision, 16-bit digital encoders are recommended, which if installed will increase the wide angle measurement accuracy of the positioner essentially to the accuracy of the encoders. These will be installed directly on the axes of the positioner. The recommended encoders are described in Chapter 7.

#### 6.3.4.2 Electrical Considerations:

##### (a) Range Configuration

A discussion of the range configuration with regard to the rendezvous radar tests is contained in section 6.2.6. The frequencies and two-way beamwidths of the landing radar velocity and altimeter sensors are approximately the same as those of the rendezvous radar; hence the discussion of 6.2.6 applies to both measurement problems.

The landing radar will be tested on a 250-foot range at Ryan and on a 2500-foot range at MSC; the 1000-foot MILA range therefore represents a compromise with respect to range length. The amplitude taper over the test aperture will be much less than 0.25 decibel for ground-reflection operation (see section 4.1). The range surface and LOS height afford excellent ground-reflection properties at X-band.

### (b) Two-Way Measurement Capability

The boresight directions of the velocity sensor and altimeter beams are required to be measured in two-way pattern tests.

Tests can be accomplished in the following manner. The radar altimeter must be disabled when the velocity sensor system is tested, and vice versa. The altimeter must be tested in the CW mode by disabling the frequency modulation circuits. The transmitted signal is tagged at the target antenna by single-sideband (SSB) modulation. This technique provides an audio modulation signal and at the same time prevents scattered signals from producing error unless the reflected energy enters the target antenna or unless energy from the target antenna reaches the antenna under test by reflection.

The operation of a SSB modulator which can be employed is as follows. The amplitude of the signal received by the target is proportional to  $g_t^{\frac{1}{2}}$ , where  $g_t$  is the gain of the transmitting antenna of the system under test. The SSB modulator consists of a rotary vane phase shifter<sup>6-4</sup> and a short circuit, as shown in Figure 6.3. The rotary-vane phase shifter is modified for continuous rotation at a speed of, say, 2175 revolutions per minute.\*

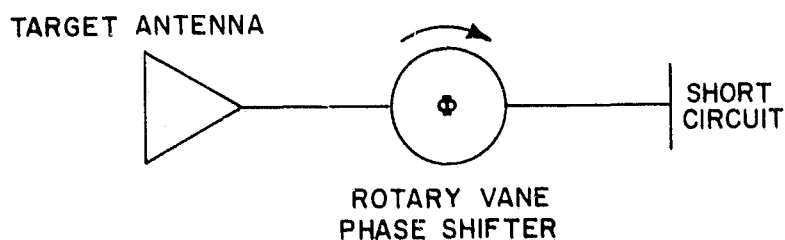


Figure 6.3. Single-Sideband Modulator for Two-Way Boresight Measurement System

After modulation and reradiation from the target antenna, the signal is received at the receiving antenna and is processed by the circuit shown in Figure 6.4, which is a symbolic representation of the applicable circuitry of the landing radar

<sup>6-4</sup>A.G. Fox, "Adjustable Waveguide Phase Changer," Proc. IRE, December 1947, pp. 1489-1498. Also see commercial literature, e.g., Hewlett-Packard Model X-382A.

\*This rate of rotation gives a modulation frequency of 145 cps, which provides low probability of interference with harmonics of 60 cps.

velocity sensor or altimeter. The received signal amplitude  $E_D$  is proportional to  $g_t^{\frac{1}{2}} g_r^{\frac{1}{2}}$ , where  $g_r$  is the gain of the receiving antenna of the system under test. Energy is also coupled from the transmitter to the receiver, at a level such that the direct-coupled signal drives the detector into its linear operating region. Under this condition the system can be analyzed with the aid of the phasor diagram

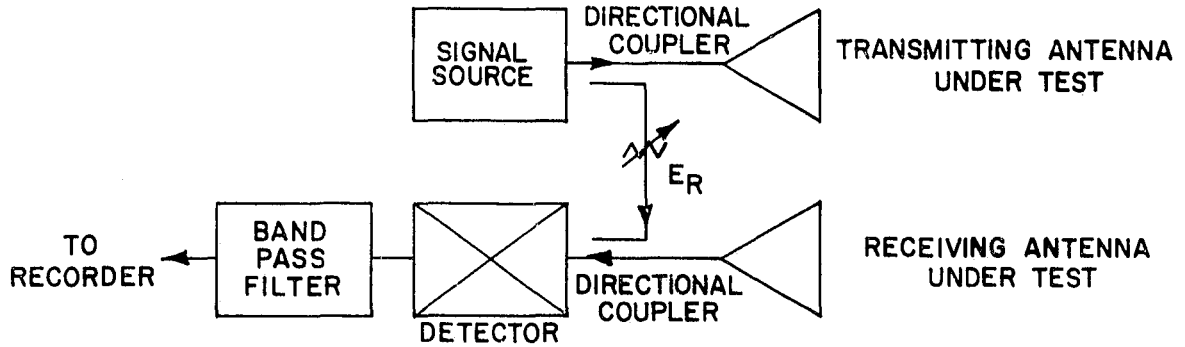


Figure 6.4. Symbolic Diagram of Two-Way Antenna Test System Using SSB Modulation for Making Boresight and Pattern Measurements of the Landing Radar

of Figure 6.5. The total signal incident on the detector is given by

$$\bar{E}_T = \left( E_R + \sum_{n=1}^N E_{S_n} e^{j\phi_n} \right) e^{j\omega t} + E_D e^{j(\omega + \omega_m)t} \quad (6-1)$$

where  $\omega_m$  is the phase modulation radian frequency, which we have set to correspond to 145 cps for convenience. Equation (6-1) can be written

$$\bar{E}_T = \left( E_F + E_D e^{j\omega_m t} \right) e^{j\omega t} \quad (6-2)$$

where  $E_F$  is the amplitude of the first term of equation (6-1) consisting of the sum of the directly coupled reference signal  $E_R$  and the scattered signals, all of frequency  $\omega$ . Then

$$\bar{E}_T = \left[ E_F + E_D (\cos \omega_m t + j \sin \omega_m t) \right] e^{j\omega t} \quad (6-3)$$

$$\bar{E}_T = \left[ (E_F + E_D \cos \omega_m t)^2 + E_D^2 \sin^2 \omega_m t \right]^{\frac{1}{2}} e^{j(\omega t + \alpha)} \quad (6-4)$$

$$\bar{E}_T = \left[ E_F^2 + 2E_F E_D \cos \omega_m t + E_D^2 \right]^{\frac{1}{2}} e^{j(\omega t + \alpha)}, \quad (6-5)$$



where

$$\alpha = \tan^{-1} \frac{E_D \sin \omega_m t}{E_F + E_D \cos \omega_m t}.$$

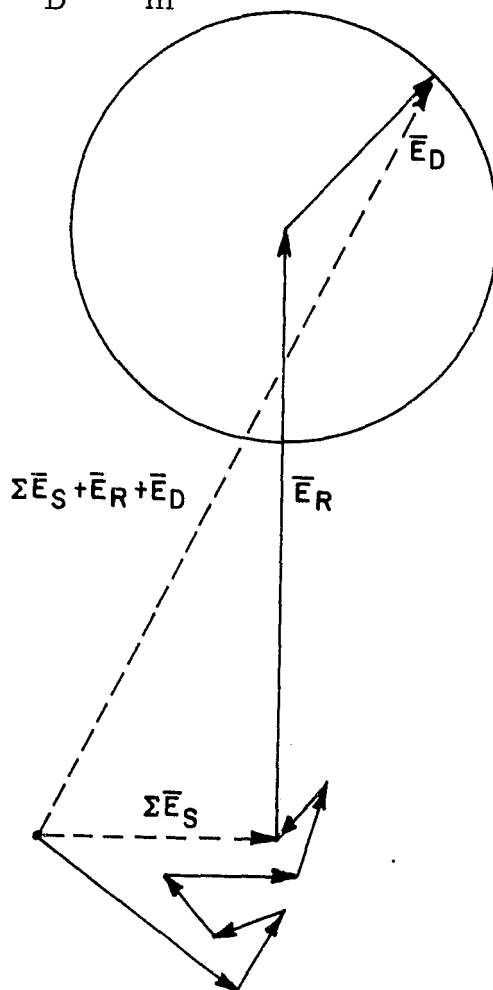


Figure 6.5. Phasor Diagram of Signal Incident on Detector of Two-Way Pattern Measurement System Employing Single-Sideband Modulation

Now if  $E_D$  is small compared with  $E_F$ ,  $E_D^2 \ll E_F^2$  and can be neglected with small error.

Then

$$\overline{E}_T \doteq \left[ E_F^2 + 2 E_F E_D \cos \omega_m t \right]^{\frac{1}{2}} e^{j(\omega t + \alpha)}, \quad (6-6)$$

but if  $E_D$  is small compared with  $E_F$ , the maximum value of  $E_F E_D \cos \omega_m t$  will be small compared with  $E_F^2$ , and  $E_T$  can be written, again with small error, using the first two terms of the binomial expansion,

$$\overline{E}_T \doteq [E_F + E_D \cos \omega_m t] e^{j(\omega t + \alpha)} \quad (6-7)$$

The linear detector of the system under test operates on  $\bar{E}_T$  to give an alternating term of frequency  $\omega_m$  and amplitude  $E_D$ , which is independent of  $E_F$ . Thus the output signal  $E_D$  is independent of the level of the coupled signal  $E_R$  and the scattered signal,  $\Sigma E_S$ . \*

Since  $E_D$  is linearly proportional to the product  $(g_t g_r)^{\frac{1}{2}}$ , it is a measure of the amplitude of the two-way pattern of the radar. In discussions with cognizant personnel of Ryan, it has been indicated that the linear dynamic ranges of the detectors of the altimeter and velocity sensors are in excess of 80 decibels. \*\*

### (c) Suppression of Extraneous Reflections

Specific specification for the requirements for suppression of extraneous reflections depends on the method which is employed for determining the LR boresight directions (see paragraph 6.3.2.2). If the power centroid method of boresight determination is employed, the level of extraneous reflections from angles near boresight are adequately suppressed. In paragraph 7.3, it is recommended that measurements be made in the ground-reflection mode of operation. If a mockup is not employed, a shield should be employed to block the radar from extraneous signals arriving from the rear. The shield could act as a support fixture and would be covered with a cone of absorbing material. Parallax introduced by the support fixture can be eliminated from the data by calculation as is done in tests of the Gemini radar.

---

\* This analysis implies that  $\Sigma \bar{E}_S$  is constant in magnitude, that is, it has only the frequency  $\omega$ . Actually  $\Sigma \bar{E}_S$  will fluctuate in magnitude and phase. However, the only component of this fluctuation which will add error is that which is within the pass band of the filter of Figure 6.4, centered at  $\omega_m$ . This component will normally be small compared with  $E_D$ .

\*\* In recording or reading the level of  $E_D$  the fact that the detector has a linear characteristic must be taken into account. Conventional antenna pattern recording equipment (including the instrumentation at MILA) is calibrated on the assumption that the detector operates in the square law region. Thus a recorder or meter calibrated on this basis will indicate a decibel level of one-half the true level change (i. e., a level change of 3 decibels will be indicated as a level change of  $1\frac{1}{2}$  decibels and a chart which is calibrated to read 40 decibels full scale will actually represent an 80-decibel level change).

## CHAPTER 7

### RECOMMENDATIONS

The recommendations presented in this chapter are directed toward establishing compatibility of the NASA-KSC-MILA RF boresight test facility with the requirements of pre-launch tests of the LEM/RR and LEM/LR systems. Recommended procedures and modifications to the facility are based on results of the X-band portion of the evaluation program reported herein, and on the existing KSC test responsibilities as indicated by cognizant personnel of the MILA Ground Support Systems Branch. Conclusions and recommendations relating to the general capability and operation of this facility are presented in Chapters 4 through 6 of this document, and will not be restated here.

#### 7.1 Facility Modifications

##### 7.1.1 Environmental Control

The environmental specifications of the LEM radar systems require that an air-conditioned protective enclosure be provided during tests at the MILA range. Such an enclosure must accomplish isolation of the radar systems from wind, ambient temperatures and the local untreated atmosphere, and must be fabricated of a material as transparent to X-band microwave energy as practicable. An inflatable, thin-wall plastic radome is recommended for these purposes.

The large radome configuration depicted in Figure 7.1 provides isolation of the complete control building-positioner-test system configuration. This radome consists of a hemispheric section of 30-foot radius above a 24-foot cylindrical section of 30-foot radius, providing a protected area nominally 60 feet in diameter and 54 feet in height. A positive internal pressure differential of approximately 0.5 inch  $H_2O$  gage pressure compared to the local atmospheric pressure will sustain such a thin-wall radome. This low pressure requirement alleviates the sealing problem, and allows for a practical blower system to produce the required pressure differential.

As shown in Figure 7.1, access to the radome interior would be through an air-lock entrance, which would preferably be located in a temporary building of

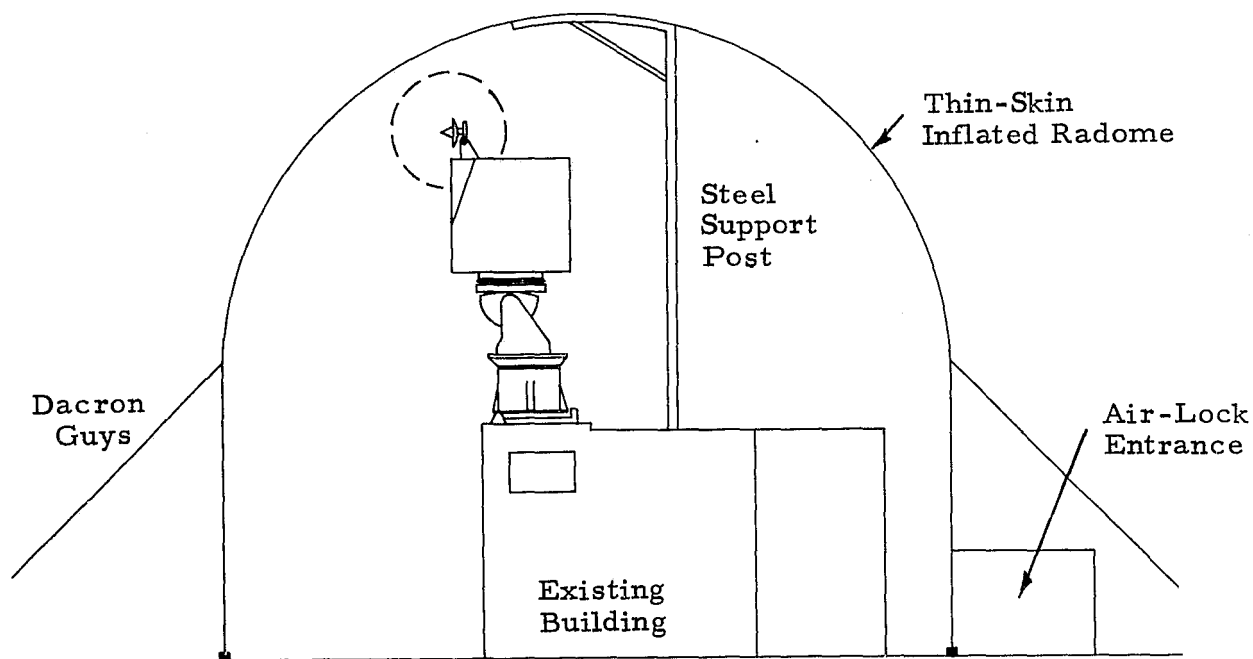


Figure 7.1. Air-Conditioned, Inflated Radome to Provide Environmental Control During Radar Testing

sufficient size to house the required blowers and air conditioning equipment. As a protective and stabilizing measure, a vertical support beam anchored to the roof of the existing control building would be installed. Dacron ropes attached to this beam would be used to prevent excessive motion of the radome walls due to the gusty wind conditions prevalent at the MILA site.

The material recommended for the fabrication of the radome is nylon-reinforced polyethylene.\* This material is available in a laminate, with two thin sheets of polyethylene bonded together with a net of nylon thread between the two layers. The resultant laminate is very resistant to tearing and ripping. Accidental punctures by sharp objects will not propagate due to the nylon net, and even a relatively large number of small holes will not significantly affect the protective nature of the cover; untreated air will be prevented from entering any punctures by the positive internal pressure.

An alternate radome configuration is shown in Figure 7.1 as a dashed "bubble" of approximate 5-foot diameter surrounding the LEM/RR. This smaller radome could probably be sustained by conditioned air from the existing control building system. The bubble would provide protection of the radar itself from the local environment, but would not suppress differential temperature effects which could cause deflections of the mockup, positioner and supporting structures.

#### 7.1.2 Data Rate and Readout Accuracies

A capability for high-speed, high-accuracy dynamic tests is not provided by the existing positioner angle readout systems. In light of expected test schedules, and in particular to accommodate dynamic tests of the LEM/LR beam structures, it is recommended that digital shaft position encoders be installed on each axis of the boresight positioner. Sixteen-bit Wayne-George Type BD-16 encoders will provide a readout resolution of approximately 20 arc seconds with a BCD output that is adaptable to computer analysis. The accuracy specified for the encoder is somewhat better than the resolution. Conversion systems and angle readouts of each shaft position in degrees are also recommended.

The existing drive system for the boresight positioner cannot simultaneously drive the lower-azimuth and the elevation axes as required for the LEM/LR tests (see section 7.3). The present system has one control unit for the upper-azimuth axis and one control unit that is shared by the lower-azimuth and elevation axes. The required control function and an added degree of system versatility can be achieved by adding a third control and servo amplifier system so that each axis can be driven simultaneously with any other axis.

---

\* Available from Griffolyn Co., Inc., Houston, Texas.

### 7.1.3 Validation Capabilities

The current test procedures at the MILA boresight test facility require validation of the purity of the incident field before each series of Gemini rendezvous radar tests as well as a periodic calibration of the range instrumentation. A similar schedule of range validation and equipment calibration is recommended during the LEM tests. In order to provide the capability of erecting the field probe to investigate the incident field at any required time, a bracket should be employed to mount the field probe behind the LEM mockup. With the field probe thus mounted, a 180-degree rotation of the lower azimuth axis will put the probe into position for use without requiring the demounting of either the mockup or the radar.

## 7.2 LEM Rendezvous Radar

Pre-launch tests of the LEM/RR at the MILA facility will include (1) boresight accuracy tests, (2) acquisition-angle tests and (3) line-of-sight motion tests. Once the modifications recommended in section 7.1 are accomplished, the MILA facility will be compatible with the requirements of the boresight accuracy and acquisition-angle tests; additional positioning and signal source equipment will be required for the line-of-sight motion tests. Brief discussions of these tests are given in the following paragraphs, with applicable recommendations.

### 7.2.1 Boresight Accuracy Tests

Boresight accuracy tests of the LEM/RR at MILA must confirm compliance with an 8-milliradian accuracy specification to the RADAR BASE. These tests are expected to be point-to-point comparisons of the RF boresight, as indicated by the LEM/RR, with precisely established optical references. It is recommended that the TM7 mockup of the LEM ascent stage be mounted on the boresight positioner as indicated in Figure 7.1 (LEM X axis parallel to positioner upper-azimuth axis). For this configuration, the point-to-point orientations of the vehicle would be accomplished with the positioner lower-azimuth and elevation axes.

In light of the straightforward approach to establishing excellent test-aperture field configurations in the ground-reflection mode and the corresponding boresight

accuracies attainable in this mode, it is recommended that the bulk of the bore-sight accuracy tests be performed with the facility employed as a ground-reflection range. If the schedule permits, redundancy checks can be obtained in the elevated mode using proper diffraction fencing. (see Section 5. 2. 8)

#### 7.2.2 Acquisition-Angle Tests

Acquisition-angle tests must confirm the capability of the LEM/RR to acquire over a  $2^\circ$  cone about the boresight direction. These tests can be performed in either the ground-reflection or elevated mode of range operation.

In the ground-reflection mode, a test would be initiated with the vehicle oriented to a fixed reference position and with the radar RF boresight aligned with the optical boresight reference. The radar tracking loop would then be disabled and the vehicle reoriented to an appropriately displaced position by rotation about the positioner elevation and lower-azimuth axes. The radar is again energized in the tracking mode to verify acquisition capability. Determination of the total acquisition angle can be accomplished by repeatedly disabling the tracking loop, orienting the vehicle to successively larger displacements from the reference position, and then closing the tracking loop, until the radar fails to lock on to the apparent source.

Redundancy checks could be made in the elevated mode utilizing the mobile source tower and moving-target source equipment discussed in paragraph 7.2.3.

#### 7.2.3 LOS Motion Tests

The objective of LOS motion tests is to verify that the rendezvous radar system maintains track under prescribed conditions of motion of the line-of-sight relative to the stationary RADAR BASE. In order to perform these tests, it is recommended that a mobile source tower and a moving-target waveguide horn antenna system be employed as depicted in Figure 7.2, with a separation between the source and test antennas of approximately 90 feet. It is recommended that the mobile source tower be mounted on a rubber-tired cart which can be towed into the required position. Support jacks should be provided to give the tower stability.

The recommended moving-target system is basically a polarization positioner

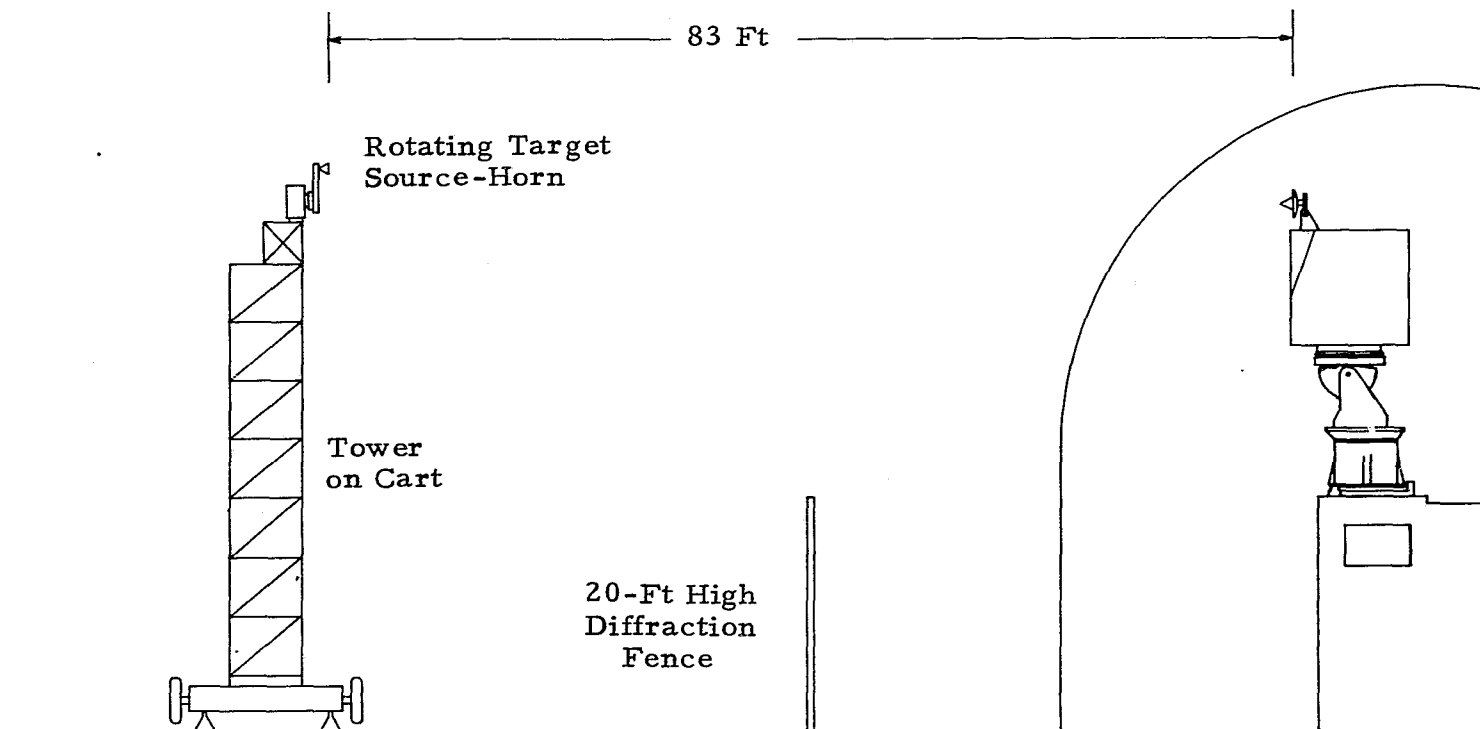


Figure 7.2. Moving Target for Line-of-Sight Tracking Tests



with an attached horn support arm and epicyclic mechanism. The target horn is mounted on the support arm which is mounted to the turntable of the polarization positioner. The horn is mounted so that it can be made to rotate about its polarization axis on a shaft and bearing assembly located in the mounting arm. A second bearing-mounted tubular shaft is located in the mounting arm coincident with the positioner turntable axis. These two shafts are connected at a one-to-one ratio by a miniature precision chain and sprocket system, so that the polarization of the horn is fixed relative to the concentric shaft. The concentric shaft extends through the center hole of the positioner turntable and is provided with an anchoring means by which the shaft may be anchored to either the positioner housing or the positioner turntable. With this arrangement it can be seen that, by selecting the proper anchor, the horn polarization may be fixed relative to either the positioner housing or the positioner turntable as the turntable is rotated. This anchoring system is adjustable so as to provide initial polarization of the horn at any desired angle.

In the LOS motion tests, the rendezvous radar is energized to lock-on and track the moving source horn. The radar line-of-sight moves in a conical excursion when tracking the rotating horn. This conical motion of the line-of-sight requires both the shaft and trunnion axes of the radar to stop, reverse direction and accelerate to a certain maximum tracking rate. For a given separation of target and radar, the angular acceleration and the maximum velocity required to continuously track the source is determined by the radius-arm and the rotational rate of the moving horn. For a 90-foot separation as recommended, a support arm of about 25 inches in length rotating at 10 rpm requires of both the shaft and trunnion axes an acceleration of approximately 1.4 degrees per second squared and a velocity of 1.4 degrees per second. Other maximum velocities and accelerations can be achieved with different support arm lengths and rotational rates.

To analyze the performance of the LEM/RR while it is tracking the moving horn it is necessary to compare the actual location of the target horn with the pointing direction of the rendezvous radar. The location of the horn is indicated as a function of the encoder readout of the moving-target system's polarization positioner. The pointing direction and the angular excursions of the radar are indicated by the shaft and trunnion axis resolvers. For a complete definition of radar tracking performance, a recording of all data on tape and a computer

program are necessary. A partial evaluation may be obtained by spot checking the actual radar shaft velocity against a calculated velocity.

### 7.3 LEM Landing Radar

The facility modifications described in paragraph 7.1 provide the environmental control and positioner digital readout which are required for boresight tests of the LEM/LR.

If measurements are to be made to determine the boresight directions of the LEM/LR by the separations of the means of the half-power points of the two-way patterns, the range can be used without major modification, except for addition of a single sideband modulator (SSB) as described in Section 6.3.4. Except for parallax error and perturbation of the boresight direction by the mockup or mounting structure, it is estimated that measurement accuracies of the order of 0.3 milliradian can be achieved with sufficient redundancy of data.

If measurements should be made by the power-centroid method, additional facility requirements for making these tests would be:

- (1) An incremental computer-compatible tape recorder.
- (2) A single sideband (SSB) modulator.
- (3) A test programmer.
- (4) Minor ancillary items.

The measurements as described below are two-way measurements made in azimuth using the ground-reflection or elevated mode of operation, preferably the ground-reflection mode. The SSB modulator is attached to the terminals of the target antenna, the four-foot diameter antenna for elevated operation or the one-foot diameter circular horn with correcting lens if the ground-reflection mode is employed.

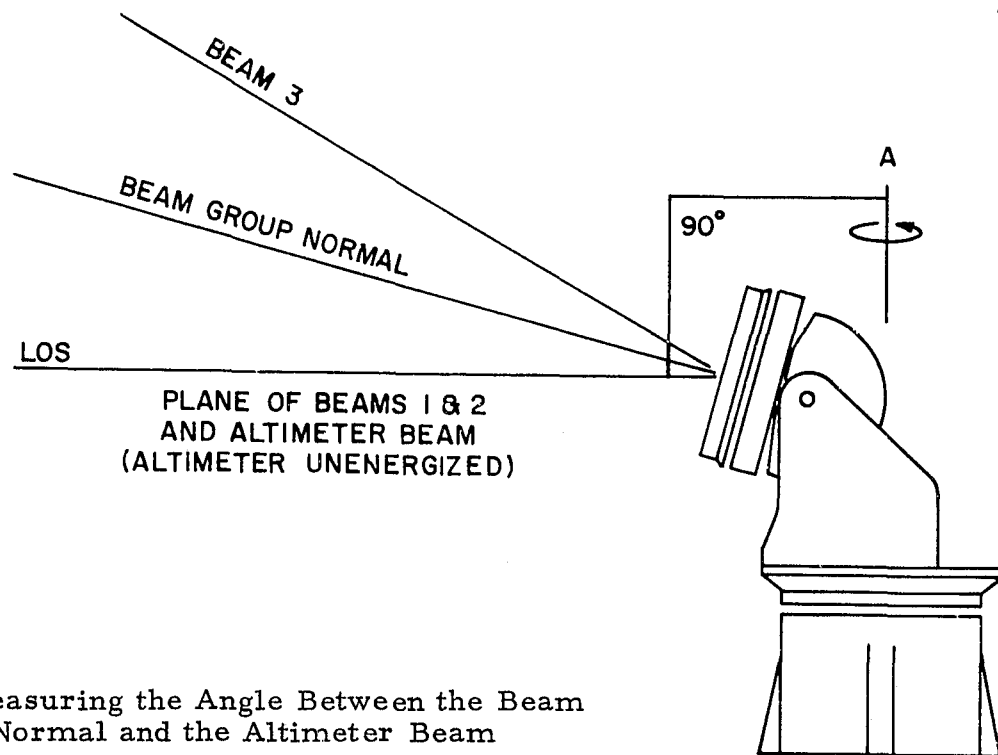
---

\* The pyramid defined by the radar beams is shown with its apex at the upper azimuth turntable in Figure 7.3, implying that the radar is mounted directly to the positioner. Actually, the radar is on a fixture or on a mockup of the descent stage, which removes it from the positioner by a few feet. The fixture or mockup does not alter the coordinate system as discussed here, but produces a parallax which must be compensated for by calculation. An additional component of parallax caused by uncertainty in the location of the center of parallax of the transmitter-receiver array cannot be accounted for.

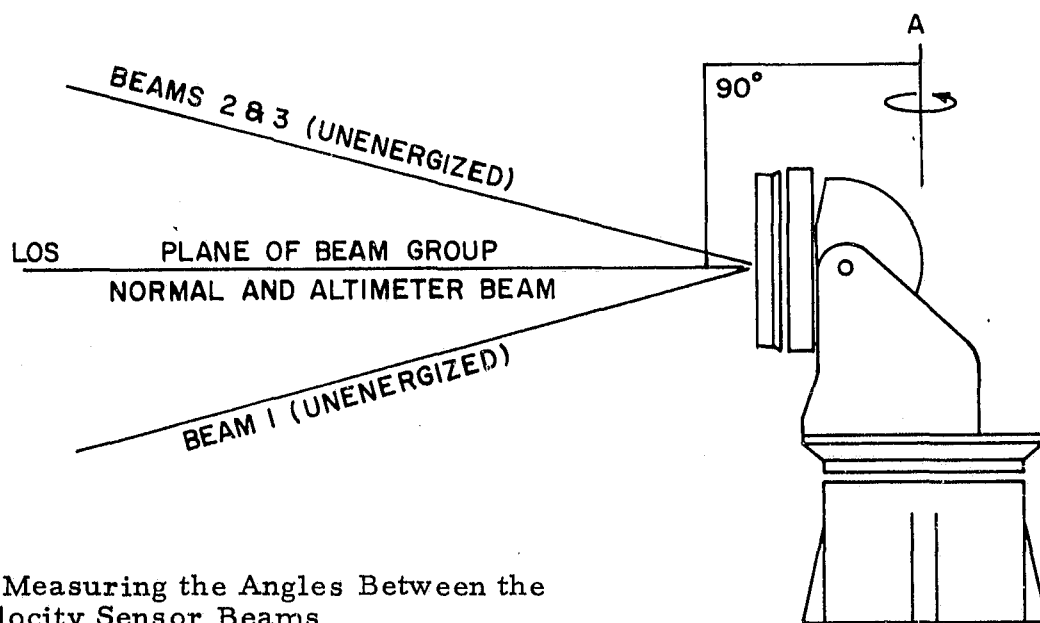
The landing radar is mounted with the beam group normal parallel with the upper-azimuth axis of the test positioner as shown in Figure 7.3.\* The tilt axis of the positioner is employed to orient the lower-azimuth axis A normal to the LOS to the target antenna. The upper-azimuth axis is employed to orient the desired side of the pyramid of Figure 6.2 parallel with the elevation axis of the positioner. The elevation axis is employed to set the elevation angle of the side of the pyramid in increments so that great-circle cuts can be made through the desired beam. In Figure 7.3(a) the plane of the side of the pyramid containing beams 1 and 2 is shown coincident with the LOS. Thus in the absence of boresight error rotation about axis A would produce a great-circle cut through the peaks of beams 1 and 2.

To determine the direction of the centroid of the two-way power pattern of a beam, incrementally spaced cuts are made over a pyramidal region of solid angle which is large enough to subtend the significant portion of the two-way power pattern.

The output data and the positioner directions are stored on tape and are processed by a digital computer to calculate the direction of the plane containing the power centroid. The orthogonal plane containing the centroid of the same beam is determined in a similar manner after rotation of the pyramid through 90 degrees by means of the upper-azimuth axis. The boresight direction is then defined as the intersection of the two planes. Measurement of the boresight direction of the altimeter beam is determined in a similar manner except that one series of cuts is made about the plane containing the altimeter beam and the beam group normal, as shown in Figure 7.3(b).



(a) Method of Measuring the Angle Between the Beam Group Normal and the Altimeter Beam



(b) Method of Measuring the Angles Between the Velocity Sensor Beams

Figure 7.3. Test Positioner Geometry for LEM/LR Tests  
Axis A is the Lower Azimuth Axis.

## APPENDIX A

### THE RECEIVING-APERTURE FIELD OVER A REFLECTING SURFACE

#### A.1 Introduction

A primary consideration in the design or control of antenna test range environments is the effect of reflected energy on measurement accuracies. Several specific examples of the contributions of extraneous energy to measurement error are presented in subsequent appendices. The purpose of the current appendix is to present a brief treatment of the reflections which can occur for propagation over a range surface of finite size which has random surface irregularities, and to specialize the general results to fit the specific case of an essentially smooth, planar range surface such as that of the MILA facility. Although reflections can be caused by any object or surface in the vicinity of the test range, the subject of this development will be reflections from the range surface in the region near the range axis as opposed to possible sources of reflection lying at large horizontal angles from the line of sight. For many test sites, and for the MILA range in particular, wide angle sources of reflection will be of little concern due to the decreased probability of specular reflection from such points and the discrimination provided by the directivities of typical test antennas.

#### A.2 Surface Irregularities

For a general range surface, reflections may be classified in two groups, specular reflection and diffuse scattering. Specular reflection obeys well known optical principles and is characterized by phase coherence. If the reflecting surface is sufficiently smooth and lossless, the coefficient of specular reflection can approach unity for a plane surface and can exceed unity for concave surfaces. When path lengths much longer than a wavelength are involved, a single specularly reflected wave can interact with the direct-path wave to produce an interference pattern whose amplitude and periodicity are to some extent predictable. (See paragraph A.6.)

Diffuse scattering results from the summation of wavelets scattered from all points of a rough surface. If the surface is periodically rough, regular cancellation and enforcement will result and a set of grating lobes will be formed. If the surface is randomly rough with variations spaced less than a wavelength apart,

diffuse scattering will radiate energy in all directions. The scattering pattern becomes increasingly omnidirectional as the magnitudes of surface variations increase.

The transition from diffuse to specular reflection is a gradual change; several authors have established surface "roughness" criteria which define the difference between the two states. The well-known Rayleigh criterion, proposed by Lord Rayleigh, is given by

$$\Delta h < \frac{\lambda}{m \sin \psi} \quad , \quad (A-1)$$

where  $\Delta h$  (Figure A.1) represents the height of a surface irregularity,  $m$  is a constant, and  $\psi$  is the grazing angle. This criterion is based on the quasi-geometrical optics approach, which is often employed in problems of this type where the wave is assumed to propagate by means of rays even though the wavelength is not vanishingly short as required by geometrical optics.

The derivation of the criterion is illustrated by Figure A.1(b). Consider two rays from a plane wave front,  $F_1$ , which approach a surface on which a pedestal of height  $\Delta h$  is located. Let the ray a strike the top of the pedestal and let the ray b strike the plane surface near the pedestal. Let the two rays be reflected in accordance with Fermat's laws of reflection<sup>A-1</sup> from the two surfaces and proceed to form part of a second front at  $F_2$ . The Rayleigh criterion is based on the geometrical difference in path length traversed by the rays in travelling from  $F_1$  to  $F_2$  (Figure A.1(b)). Let the distance traversed by ray a be  $d_1 + d_2$ . From inspection it can be seen that ray b will travel the distance  $d_1 + d_2 - c + c + 2\Delta h \sin \psi$  and that the difference in path length  $\Delta d$  is given by

$$\Delta d = 2\Delta h \sin \psi \quad . \quad (A-2)$$

Setting  $\Delta d < 2\lambda/m$  gives the criterion of (A-1).

For values of  $\Delta h$  less than  $\lambda/m \sin \psi$  the surface is regarded as smooth and essentially specularly reflecting, while for larger surface perturbations, the surface is assumed to be rough and, hence, a diffuse scatterer. Lord Rayleigh suggested a value of 8 for  $m$ , which corresponds to a phase difference of  $\pi/2$ ,

---

<sup>A-1</sup> Silver, S., Microwave Antenna Theory and Design, Radiation Laboratory Series, Volume 12, pp. 122-128, McGraw-Hill Co., 1949.

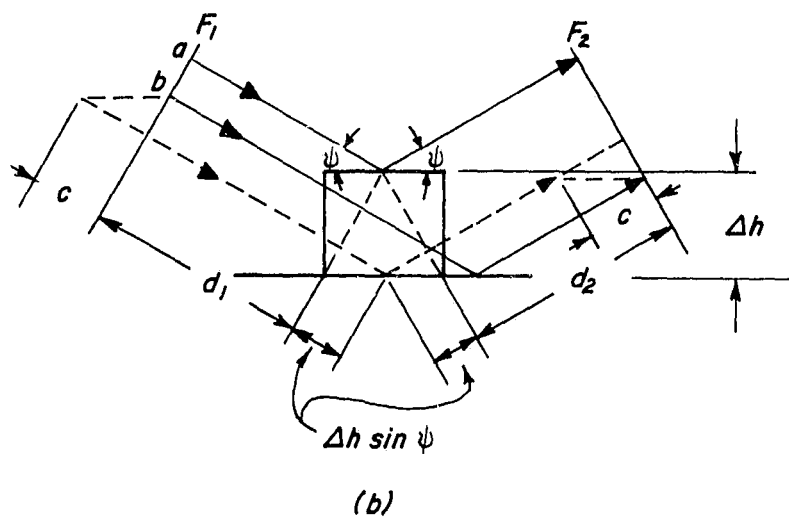
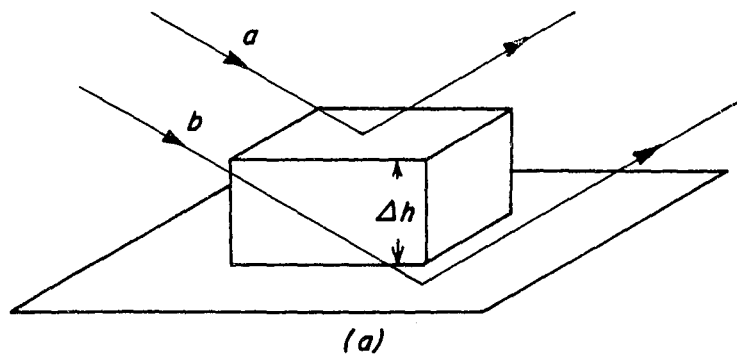


Figure A.1. Phase Difference Between Rays Reflected From Two Levels

while other authors<sup>A-2</sup> have suggested values ranging as high as 32, corresponding to a difference of  $\pi/8$ .

Another approach is to regard reflected energy as the sum of a specularly reflected component and a diffuse component; the two types of reflection can then be treated separately. The following section summarizes the theoretical development of the problem of reflections from a random rough surface. The resulting expressions are applied in paragraph A.4 to the specific problem of determining the expressions for the aperture-field components at the MILA range, and in paragraph A.5 to the development of criteria for operation of the MILA facility as a ground-reflection antenna test range. The effects of specularly reflected energy in the elevated mode of range operation are discussed in paragraph A.6.

### A.3 Theoretical Development of a General Reflection Coefficient

The problem of reflection from a rough surface involves determining the magnitude and polarization of the reradiated energy. Rigorous treatment of the problem includes consideration of cross polarization effects, requiring that the reflections be analyzed as a vector problem. The investigation may be simplified by considering the individual orthogonal components of the reflected field separately. This approach reduces the vector problem to a scalar problem where the reflected signal is assumed to possess the same polarization as the transmitted signal. The three-dimensional, scalar scattering problem is one of determining a function,  $E_r$ , interior to a surface,  $S$ , enclosing a source-free volume which is a solution of the scalar Helmholtz equation

$$(\nabla^2 + \kappa^2) E_r = 0, \quad (A-3)$$

where  $\kappa$  is the wave number, and which satisfies the boundary conditions imposed by Maxwell's equations at  $S$ . The problem has been treated by numerous authors<sup>A-3</sup>, and the detailed mathematics will not be presented here. The following paragraphs summarize the more pertinent parts of the theory.

---

<sup>A-2</sup> Kerr, D.E., Propagation of Short Radio Waves, Radiation Laboratory Series, Volume 13, McGraw-Hill Co., 1951, p. 411 and footnote, p. 416.

<sup>A-3</sup> Clarke, R.H., and G.O. Hendry, "Prediction and Measurement of the Coherent and Incoherent Power Reflected from a Rough Surface," IEEE Transactions on Antennas and Propagation, Volume AP-12, No. 3, May 1964; pp. 353-363.

(Continued on Page A-5.)



Consider a surface,  $S$ , which encloses a source-free volume,  $V$ , as illustrated in Figure A.2. A transmitting antenna,  $T$ , and an observation point,  $P$ , are located exterior to the surface. The point  $P$  is surrounded by a sphere,  $S'$ , of radius  $R$ , which is connected to the outside of the surface by a tubular surface,  $S''$ . The point  $P$  represents a point in the aperture of the test antenna,

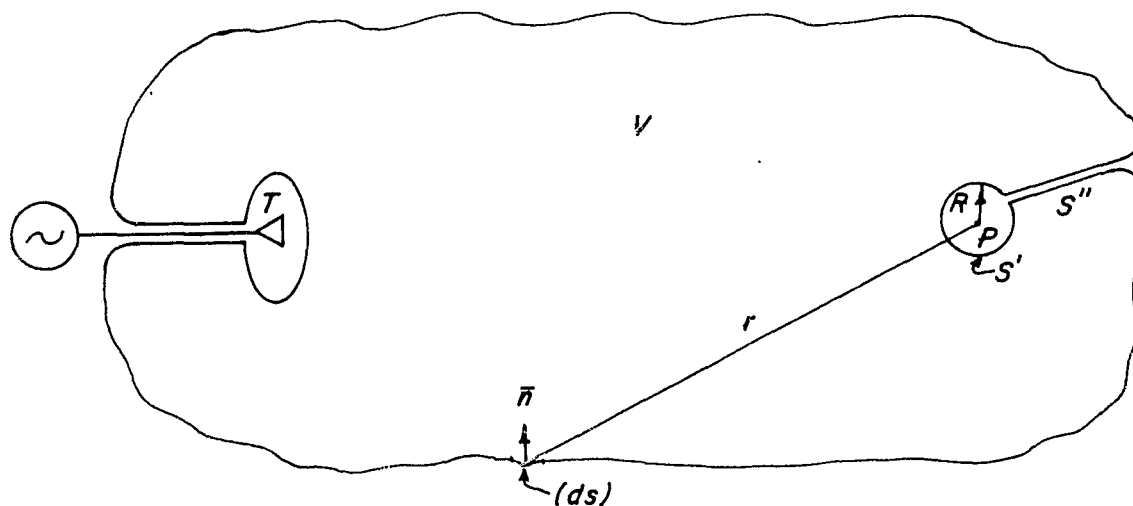


Figure A.2. Sketch of the Geometry Relating to the Helmholtz Integral

while the surface  $S$  includes the antenna range surface and an imaginary surface in the atmosphere above the test range. If  $E$  is a solution to (A-3) which is

#### A-3 (continued)

Beckmann, Petr, "Shadowing of Random Rough Surfaces," IEEE Transactions on Antennas and Propagation, Volume AP-13, No. 3, May 1965; pp. 384-388.

Twersky, Victor, "Signals, Scatterers, and Statistics," IEEE Transactions on Antennas and Propagation, November 1963; pp. 668-680.

Twersky, Victor, "On Scattering and Reflection of Electromagnetic Waves by Rough Surfaces," IRE Transactions on Antennas and Propagation, January 1957; pp. 81-90.

Beckmann, Petr, and Andre Spizzichino, The Scattering of Electro-Magnetic Waves from Rough Surfaces, The MacMillan Company, 1963; pp. 9-10.

Silver, op cit, Chapter 5.

Kerr, op cit, Chapter 5.

regular at infinity, and if the radius  $R$  is allowed to go to zero, then the value of the integral<sup>A-4</sup>

$$I(P) = \iint_S \left[ \frac{e^{jkr}}{r} \frac{\partial E}{\partial n} - E \frac{\partial}{\partial n} \frac{e^{jkr}}{r} \right] dS \quad (A-4)$$

is given by

$$I(P) = -4\pi E(P) \quad . \quad (A-5)$$

Here,  $\partial/\partial n$  denotes differentiation along a normal direction into the closed surface, and  $r$  represents the distance from  $P$  to a surface increment,  $dS$ . This integral, which follows directly from the divergence theorem and Green's theorem, is known as the Helmholtz integral; it gives the value  $E(P)$  for points interior to  $S$  in terms of the values of  $E$  and its normal derivatives over  $S$ .

The surface  $S$  can be considered to be the sum of several surface regions  $S_i$  such that

$$S = \sum_{i=1}^n S_i \quad . \quad (A-6)$$

The contribution of any surface region to the field at  $P$  is given by

$$E(P) = \frac{1}{4\pi} \iint_{S_i} \left[ \frac{e^{jkr}}{r} \frac{\partial E}{\partial n} - E \frac{\partial}{\partial n} \frac{e^{jkr}}{r} \right] dS_i \quad (A-7)$$

A typical surface region,  $s$ , where  $s$  is some  $S_i$  illuminated by a plane wave,  $E_1$ , is shown in Figure A.3. The surface is defined by the function  $\zeta(x, y)$  and its projected area in the  $xy$  plane is equal to  $A$ . The incident wave arrives from the direction defined by the propagation vector  $\bar{\kappa}_1$ , at an angle  $\theta_1$  from the  $z$  axis in the  $xz$  plane; the propagation vector  $\bar{\kappa}_2$  is a vector in the direction of the reflected wave. The magnitudes of  $\bar{\kappa}_1$  and  $\bar{\kappa}_2$  are  $2\pi/\lambda$ . The direction of  $\bar{\kappa}_2$  toward the point of observation  $P$  is defined by elevation and azimuth angles  $\theta_2$  and  $\phi_2$ , respectively. Equation (A-7) can be used to determine the contribution of a given  $s$  to the field at  $P$ ; the total field will be given by the summation of all such contributions.

---

<sup>A-4</sup>Baker, B.B., and E.T. Copson, The Mathematical Theory of Huygen's Principle, Oxford University Press, London, 1950; pp. 23-32.

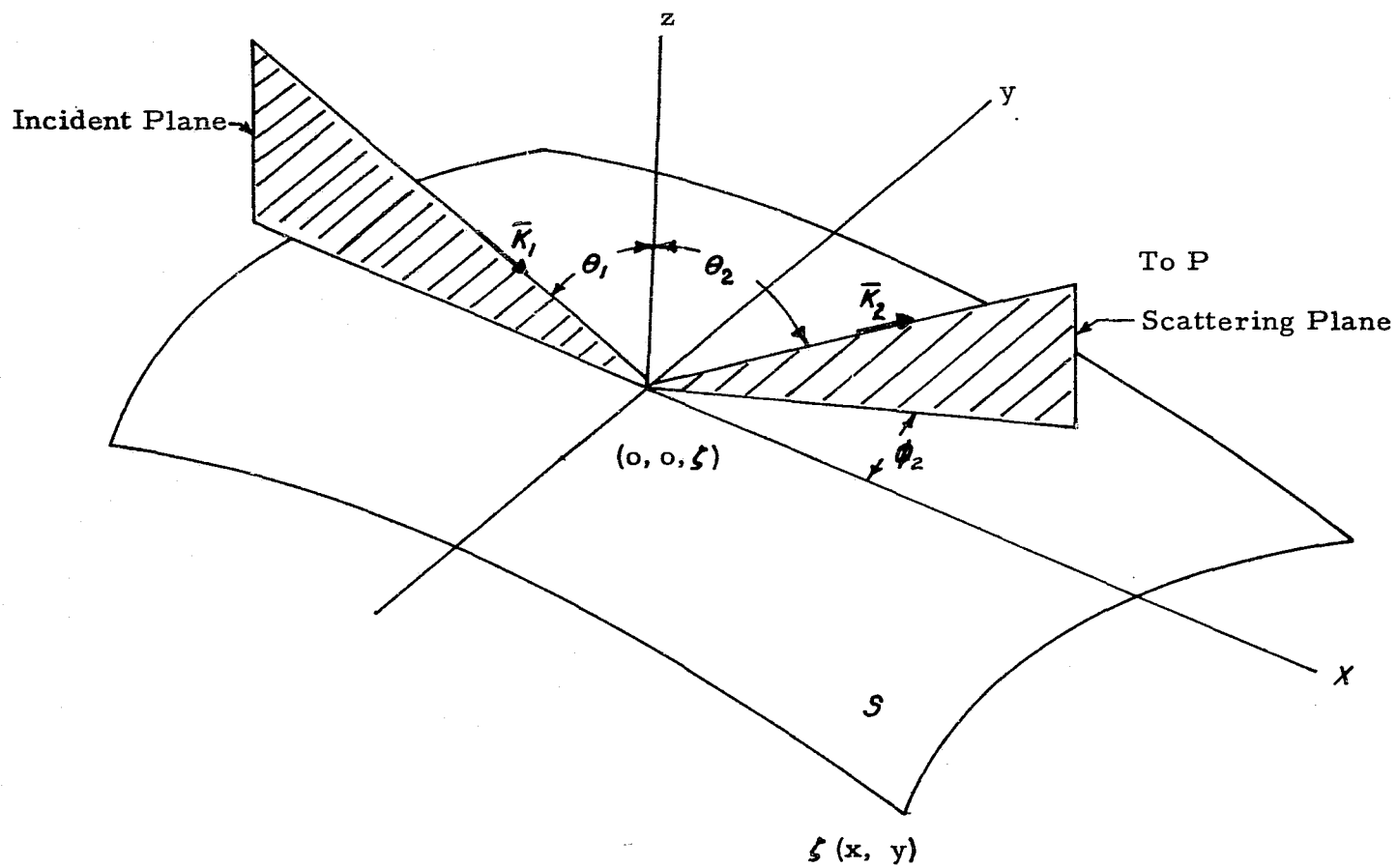


Figure A.3. Coordinate System for Scattering From a Surface

In order to solve equation (A-7), the boundary values for  $E$  and  $\partial E/\partial n$  must be known over  $S$ . Exact determination of the boundary conditions is impossible for a random rough surface; hence approximations are necessary. Beckmann takes the field at any point to be equal to the field that would be present on a tangential, smooth plane at that point. This approximation is quite good for slowly varying surfaces and less valid for rough surfaces with sharp edges. With this approximation, the boundary values are

$$E_s = (1 + \rho_o)E_1 \quad (A-8)$$

and

$$\frac{\partial E}{\partial n_s} = (1 - \rho_o)E_1 \bar{\kappa}_1 \cdot \bar{n} \quad , \quad (A-9)$$

where  $\bar{n}$  is the unit vector normal to the surface, and  $\rho_o$  is the coefficient of reflection of a smooth surface.

The value of  $\rho_o$  is dependent on the polarization of  $E_1$  and on the dielectric properties of the range surface. It can be shown that the reflection coefficients for components of the incident field which are normal to and parallel with the plane of incidence, respectively, are given by

$$\rho_{o,n} = \frac{\cos\theta - \left[ (\nu_R - \sin^2\theta) - j\nu_I \right]^{\frac{1}{2}}}{\cos\theta + \left[ (\nu_R - \sin^2\theta) - j\nu_I \right]^{\frac{1}{2}}} \quad (A-10)$$

and

$$\rho_{o,p} = \frac{\left[ (\nu_R - \sin^2\theta) - j\nu_I \right]^{\frac{1}{2}} - (\nu_R - j\nu_I) \cos\theta}{\left[ (\nu_R - \sin^2\theta) - j\nu_I \right]^{\frac{1}{2}} + (\nu_R - j\nu_I) \cos\theta} \quad (A-11)$$

where

$$\nu_R = \frac{(\epsilon'_r \mu'_r + \tan\delta \mu''_r)}{(\mu'^2_r + \mu''^2_r)} \quad (A-12)$$

and

$$\nu_I = \frac{(\tan\delta \mu'_r - \epsilon'_r \mu''_r)}{(\mu'^2_r + \mu''^2_r)} \quad (A-13)$$

The parameters in (A-12) and (A-13) are as defined below:

$\epsilon'_r - j\tan\delta = \epsilon_r$ , the complex relative permittivity of the range surface

and

$\mu_r' - j\mu_r'' = \mu_r$ , the complex relative permeability of the range surface.

For this special smooth-surface case,  $\theta = \theta_1 = \theta_2$  is the "local" angle of incidence and reflection. For most test ranges, it can be assumed with negligible error that  $\mu_r$  is equal to unity and that the loss tangent,  $\tan\delta$ , is small compared to the "relative dielectric constant"  $\epsilon_r'$ . For a smooth surface satisfying these assumptions, the reflection coefficient for normal energy becomes

$$\rho_{o,n} = \frac{\cos\theta - \sqrt{\epsilon_r' - \sin^2\theta}}{\cos\theta + \sqrt{\epsilon_r' - \sin^2\theta}} \quad (A-14)$$

and that for parallel energy becomes

$$\rho_{o,p} = \frac{\sqrt{\epsilon_r' - \sin^2\theta} - \epsilon_r' \cos\theta}{\sqrt{\epsilon_r' - \sin^2\theta} + \epsilon_r' \cos\theta} \quad (A-15)$$

Equation (A-7) is modified to solve for the general coefficient of reflection rather than the reflected field by dividing both sides by the field which would be reflected in the specular direction by a smooth plane of the same area as the  $S_1$  of interest. If the reflecting surface is given by  $\zeta(x, y)$  as measured from a fixed arbitrary coordinate origin, then the radius vector  $\bar{r}$  from the origin to a given point on  $\zeta(x, y)$  is defined as

$$\bar{r} = x\bar{x}_0 + y\bar{y}_0 + \zeta\bar{z}_0, \quad (A-16)$$

where  $\bar{x}_0$ ,  $\bar{y}_0$ , and  $\bar{z}_0$  are unit orthogonal vectors defined by the coordinate system. Note that the phase retardation due to the distance from the point defined by  $\bar{r}$  to the observation point P is accounted for in the process of division by the "smooth-plane" field mentioned above. The general coefficient of reflection of the total surface is then<sup>A-5</sup>

$$\rho = \frac{F}{A} \iint_S e^{j\bar{v} \cdot \bar{r}} dS \quad (A-17)$$

where A is the projected area of the surface,

$$F = \rho_o \left[ \frac{1 + \cos\theta_1 \cos\theta_2 - \sin\theta_1 \sin\theta_2 \cos\phi_2}{\cos\theta_1 (\cos\theta_1 + \cos\theta_2)} \right] \quad (A-18)$$

<sup>A-5</sup> Beckmann and Spizzichino, op cit, p. 27.

and

$$\begin{aligned}\bar{v} &= \bar{\kappa}_1 - \bar{\kappa}_2 \\ &= \frac{2\pi}{\lambda} [(\sin\theta_1 - \cos\phi_2 \sin\theta_2)\bar{x}_0 - (\sin\theta_2 \sin\phi_2)\bar{y}_0 + (\cos\theta_1 + \cos\theta_2)\bar{z}_0]\end{aligned}\tag{A-19}$$

Equation (A-17) neglects second-order terms called "edge effects" which result from the finite size of the surface  $s$ . However, these are small when  $A$  is large compared to  $\lambda^2$ , which condition is satisfied for typical antenna test range geometries.

The discussion of this section provides a background for predicting the distribution of scattered energy from a reflecting surface, but requires definition of the character of the reflecting surface before (A-17) can be applied to the solution of practical problems. This equation gives a value of reflection coefficient for an arbitrary rough surface if one can describe the detailed character of the surface. The accuracy of the result depends on the degree to which the physics of the actual problem adheres to the restrictions which have been made.

Several approximations were required to arrive at the form expressed in (A-17). The more significant assumptions are:

- A. The reflection coefficient,  $\rho_0$ , is assumed to be constant over the region of integration. This case may be realized in practice by dividing a given range surface into areas over which the terrain and ground cover will produce essentially constant reflection characteristics.
- B. Shadowing and multiple scattering effects are ignored. This approximation is valid if the surface is gently varying. Extremely rough surfaces require the introduction of a "shadowing factor" in the expression for  $\rho$  which will account for the fact that all of the surface is not illuminated. Such a factor has been derived by Beckmann<sup>A-6</sup>.
- C. The incident wave is linearly polarized with the  $\bar{E}$  vector either in the incident plane or perpendicular to it. No prediction is made concerning the polarization of the scattered energy. A rough reflecting surface is known to cause depolarization, but the problem of a random

---

<sup>A-6</sup> Beckmann, op cit.

rough surface has not been solved or even extensively studied. Little can be said, consequently, except that the degree of depolarization would be expected to be less for relatively smooth surfaces than for rougher surfaces.

- D. The transmitter and the point of observation P are sufficiently far removed from the surface S that plane wave approximations can be employed. At first thought, this might seem to imply that the analysis is not valid for transmitter and point of observation separations of distances such as those employed in antenna ranges. This is not so, however, because, while the definition of  $\rho$  in (A-17) is such that  $\rho$  is equal to  $\rho_0$  for a planar surface its definition does not require an identically plane wave.

The above approximations do not seriously impair the theoretical results. The analysis stands or falls on the validity of the boundary conditions which are applied; hence discretion must be used in application of equation (A-17) to a specific surface. Generally, one would expect the coefficient of reflection for the specular direction to be somewhat less for a surface composed of sharp edges than for a smoother surface with the same heights of perturbations.

#### A.4 Aperture-Field Components for the MILA Range Configuration

While the maximum deviation,  $\Delta h$ , of the surface of the MILA range is not precisely measurable in that the surface is gross, a conservative estimate for the height of surface irregularities is two inches. (See Chapter 2 of this document.) The minimum grazing angle for a given frequency will be experienced for operation in the ground-reflection mode; for such cases an approximate value of  $\sin\psi$  is

$$\sin\psi_{\text{MIN}} \doteq \psi_{\text{MIN}} \doteq 0.03 \quad ,$$

calculated as the angle subtended at the base of the source tower by the 30-foot receiver height at a range of 1000 feet. Using these values in (A-1), paragraph A.1, it is seen that the value of the dimensionless number  $m$  is approximately equal to  $200\lambda$ , where  $\lambda$  is in feet, for the ground-reflection mode. For example,  $m$  is approximately 20 for operation at 10 GHz, and increases as the ratio of 200 to the frequency in GHz for lower frequencies. When the grazing angle is

doubled, which would correspond to operation in the elevated mode with the source antenna at a height of 30 feet,  $m$  becomes approximately 10 for X-band frequencies.

It is seen from (A-1) and the related discussion that on the basis of the Rayleigh criterion, the MILA range should approximate a smooth reflecting surface for operation in either the ground-reflection or elevated modes, for frequencies up to 10 GHz.

If the range can be considered smooth, both the incident and reflected waves can be considered to lie in the plane of incidence, with the angle of reflection equal to the angle of incidence. Equations (A-18) and (A-19) of paragraph A.3 become

$$\bar{F} = \rho_o \left[ \frac{1 + \cos^2 \theta - \sin^2 \theta}{2 \cos^2 \theta} \right] = \rho_o \quad (\text{A-18a})$$

and

$$\bar{V} = \frac{2\pi}{\lambda} \left[ 2 \cos \theta \bar{z}_o \right] = \frac{4\pi}{\lambda} \cos \theta \bar{z}_o, \quad (\text{A-19a})$$

respectively, so that

$$\bar{V} \cdot \bar{F} = \frac{4\pi \zeta(x, y)}{\lambda} \cos \theta. \quad (\text{A-20})$$

Since the range surface appears "smooth",  $\zeta(x, y)$  can be assumed to be equal to zero with small error, and the general reflection coefficient reduces to

$$\rho \doteq \frac{\rho_o}{A} \iint_S dS = \rho_o. \quad (\text{A-21})$$

When (A-21) is valid, the reflected wave which reaches an observation point at the center of the receiving aperture appears to originate at a single image of the source antenna. This image source lies directly below the source, a distance  $h_t$  below the range surface. Let the reflected wave be represented by  $\bar{E}_R$  and the direct-path wave by  $\bar{E}_D$  at the receiving aperture. Assume that the transmitted beam has a symmetrical amplitude and phase characteristic about the beam axis, and that the beam axis is pointed at a declination angle  $\Delta$  in the plane of  $h_t$  and  $h_r$ . (Figure A.4.) Setting the phase reference to be zero for the direct



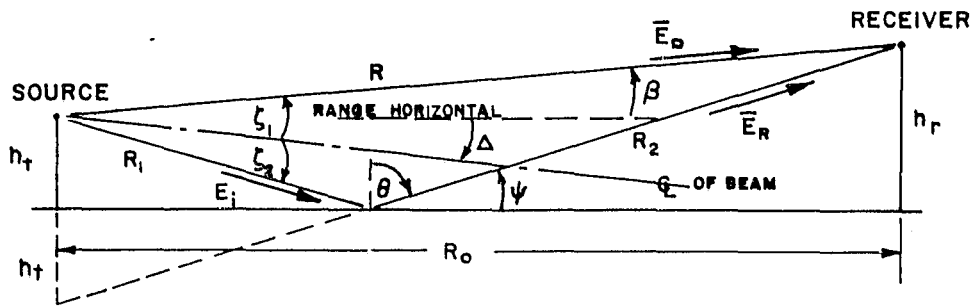


Figure A.4. Beam Angles Related to Range Geometry

path wave at the source antenna, and neglecting the slight difference in attenuation due to the unequal path lengths  $R$  and  $(R_1 + R_2)$ , the field components at the receiving aperture can be written

$$\bar{E}_D \doteq \left[ E_n(\zeta_1) + E_p(\zeta_1) e^{j\delta} \right] e^{j(\omega t - \frac{2\pi}{\lambda} R)} \quad (A-22)$$

and

$$\bar{E}_R \doteq \left[ E_n(\zeta_2) \rho_{o,n} e^{j\phi_n} + E_p(\zeta_2) \rho_{o,p} e^{j(\phi_p + \delta)} \right] e^{j(\omega t - \frac{2\pi}{\lambda} [R_1 + R_2])} \quad (A-23)$$

In (A-22) and (A-23), the indices  $n$  and  $p$  refer to field components normal to and parallel with the plane of incidence, respectively. The magnitudes of the reflection coefficients  $\rho_{o,n}$  and  $\rho_{o,p}$  are given by (A-14) and (A-15) of paragraph A.3, and the corresponding phase angles are written in (A-23) as  $\phi_n$  and  $\phi_p$ . The angle  $\delta$  is the phase angle by which  $E_p$  leads  $E_n$ , where the normal component is arbitrarily assigned zero phase at the source antenna.

#### A.5 Ground-Reflection Operation of the MILA Range

The operation of an antenna test range in the ground-reflection mode is based on the adjustment of the height and direction of the transmitting antenna to cause the direct-path signal and the reflected signal to arrive at the center of the receiving

aperture in phase. While the assumption of plane wave propagation for the relatively low transmitter heights involved would imply only qualitative results, it has been experimentally documented that criteria based on plane wave approximations are valid for ground-reflection operation.

Assume that equations (A-22) and (A-23) describe the field components at the receiving aperture in the general ground-reflection case, and consider the case where a single polarization is propagated. Omitting the polarization indices for simplicity, we have

$$\bar{E}_D + \bar{E}_R = \left[ E(\zeta_1) e^{-j\frac{2\pi}{\lambda}R} + E(\zeta_2) \rho e^{j(\phi - \frac{2\pi}{\lambda} [R_1 + R_2])} \right] e^{j\omega t} \quad (A-24)$$

If the source antenna is adjusted so that  $\bar{E}_D$  and  $\bar{E}_R$  are equal in amplitude and phase, it is seen from (A-24) that

$$\frac{E(\zeta_1)}{E(\zeta_2)} = \rho e^{j(\phi + \frac{2\pi}{\lambda} [R - R_1 - R_2])} \quad (A-25)$$

The left-hand side of (A-25) is a positive real, so that two conditions are implied:

$$\rho = \frac{E(\zeta_1)}{E(\zeta_2)} \quad (A-26)$$

and

$$\phi + \frac{2\pi}{\lambda} (R - R_1 - R_2) = 2N\pi, \quad N=0, 1, 2 \dots \quad (A-27)$$

Equation (A-27) leads to a criterion defining the proper height adjustment of the source. From the geometry of Figure A.4,

$$R_1 + R_2 = \left[ R_o^2 + (h_r + h_t)^2 \right]^{\frac{1}{2}} \quad (A-28)$$

and

$$R = \left[ R_o^2 + (h_r - h_t)^2 \right]^{\frac{1}{2}} \quad (A-29)$$

Substitution of (A-28) and (A-29) into (A-27) produces a quadratic in  $h_t$ , from

which

$$h_t = \frac{\lambda \phi}{4\pi} \left[ 1 + \frac{R_o^2}{h_r^2 - \left(\frac{\lambda \phi}{4\pi}\right)^2} \right]^{\frac{1}{2}} \quad (A-30)$$

for  $N=0$ . For the MILA range, the angle  $\phi$  for either horizontal or vertical polarizations differs very little from  $\pi$  radians assuming conservative values for the dielectric constant and conductivity of the range surface. Also, the parameters of the range geometry are such that

$$R_o \gg h_r \gg \frac{\lambda}{4}$$

Applying the above conditions to (A-30), the familiar expression for source-antenna height,

$$h_t \doteq \frac{\lambda R_o}{4h_r} \quad , \quad (A-31)$$

is obtained.

The remaining condition, given in (A-26), places a restriction on the orientation of the beam axis in the vertical plane. If (A-26) is violated, the phase of the resultant field about the center of the receiving aperture is degraded. This can be shown as follows.

Consider the  $\bar{E}_D$  and  $\bar{E}_R$  wavefronts which arrive at the center of the receiving aperture in phase as shown in Figure A.5. The angles  $\beta$  and  $\psi$  in the vertical plane are as defined in Figure A.4, and  $\alpha$  is some general angle measured from the vertical at  $h_r$  such that  $\psi > \alpha > \beta$ . Let  $\chi$  be a measure of distance along the line defined by  $\alpha$ , where  $\chi$  is zero at the center of the receiving aperture and positive  $\chi$  is upward. We then have

$$\bar{E}(\chi) = \left[ E_D e^{-j\frac{2\pi}{\lambda} \left( \frac{R_o}{\cos\beta} - \chi \sin[\alpha - \beta] \right)} + E_R e^{-j\frac{2\pi}{\lambda} \left( \frac{R_o}{\cos\psi} + \chi \sin[\psi - \alpha] \right)} e^{j\phi} \right] e^{j\omega t} \quad (A-32)$$

or

$$\bar{E}(\chi) = E_D \left[ e^{-j\phi_D} + k e^{-j\phi_R} \right] e^{j\omega t} \quad , \quad (A-33)$$

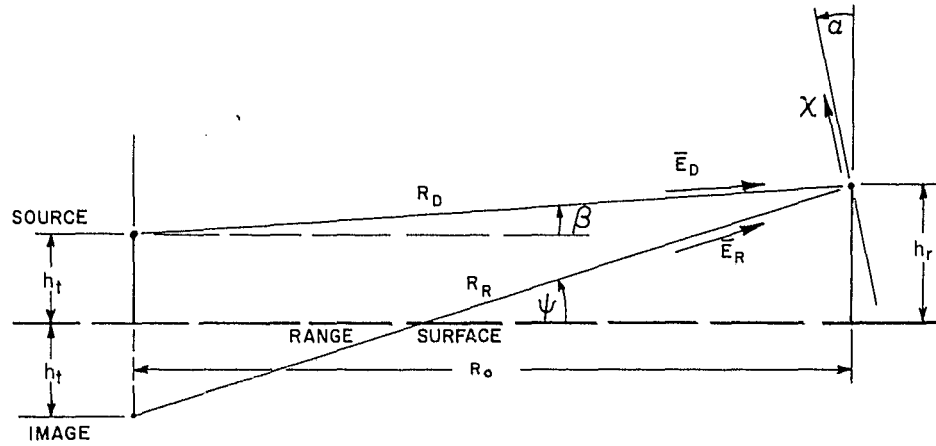


Figure A.5. Planar Wavefronts Related to Range Geometry

where

$$k = \frac{E_R}{E_D} \quad , \quad (A-34)$$

$$\phi_D = \frac{2\pi}{\lambda} \left[ \frac{R_o}{\cos\beta} - \chi \sin(\alpha - \beta) \right] , \quad (A-35)$$

and

$$\phi_R = \frac{2\pi}{\lambda} \left[ \frac{R_o}{\cos\psi} + \chi \sin(\psi - \alpha) \right] - \phi \quad . \quad (A-36)$$

Employing Euler's identity in (A-33), we have

$$\bar{E}(\chi) = E_D \left[ (\cos\phi_D - j \sin\phi_D) + k(\cos\phi_R - j \sin\phi_R) \right] e^{j\omega t} \quad (A-37)$$

or

$$\bar{E}(\chi) = E_D \left[ (\cos\phi_D + k \cos\phi_R)^2 + (\sin\phi_D + k \sin\phi_R)^2 \right]^{\frac{1}{2}} e^{j(\omega t - \Phi_\chi)} \quad (A-38)$$

where

$$\Phi_\chi = \tan^{-1} \frac{\sin\phi_D + k \sin\phi_R}{\cos\phi_D + k \cos\phi_R} \quad . \quad (A-39)$$

Expanding (A-38) and applying trigonometric identities, we have

$$\bar{E}(\chi) = E_D \left[ 1 + 2k \cos(\phi_R - \phi_D) + k^2 \right]^{\frac{1}{2}} e^{j(\omega t - \Phi_\chi)} \quad . \quad (A-40)$$

The optimum case is that for which  $\Phi_\chi$  is constant along  $\chi$ . We can examine the requirements on  $\alpha$  and  $k$  which would yield a constant  $\Phi_\chi$  by requiring the derivative of  $\Phi_\chi$  with respect to  $\chi$  to be equal to zero for all  $\chi$ , where from (A-39)

$$\frac{d\Phi_\chi}{d\chi} = \frac{2\pi}{\lambda} \left[ \frac{-\sin(\alpha - \beta) + k \cos(\phi_R - \phi_D) [\sin(\psi - \alpha) - \sin(\alpha - \beta)] + k^2 \sin(\psi - \alpha)}{1 + 2k \cos(\phi_R - \phi_D) + k^2} \right] \quad (A-41)$$

Since we demand this derivative to be zero for all  $\chi$ , we can arbitrarily choose the value  $\chi=0$  to compute the requirements on  $\alpha$  and  $k$ . For  $\chi$  equal to zero,

$$\cos(\phi_R - \phi_D) \Big|_{\chi=0} = \cos \left[ \frac{2\pi}{\lambda} \left( \frac{R_o}{\cos\psi} - \frac{R_o}{\cos\beta} \right) - \phi \right] = 1 \quad (A-42)$$

(By the postulation that the waves are in phase at the center of the receiving aperture, this cosine term is equal to unity.) Setting  $d\Phi_\chi/d\chi$  equal to zero at  $\chi$  equal to zero then yields, from (A-41) and (A-42),

$$-\sin(\alpha - \beta) + k [\sin(\psi - \alpha) - \sin(\alpha - \beta)] + k^2 \sin(\psi - \alpha) = 0 \quad (A-43)$$

Solving for  $k$  by the quadratic formula, we have

$$k = \frac{-[\sin(\psi - \alpha) - \sin(\alpha - \beta)] \pm \sqrt{[\sin(\psi - \alpha) - \sin(\alpha - \beta)]^2 + 4 \sin(\psi - \alpha) \sin(\alpha - \beta)}}{2 \sin(\psi - \alpha)} \quad (A-44)$$

which is seen to simplify to

$$k = \frac{-[\sin(\psi - \alpha) - \sin(\alpha - \beta)] \pm \sqrt{[\sin(\psi - \alpha) + \sin(\alpha - \beta)]^2}}{2 \sin(\psi - \alpha)} \quad (A-45)$$

Since  $k$  is a positive number (the ratio of two magnitudes) and by postulation  $\psi > \alpha > \beta$ , only the positive sign is of interest for the radical term in (A-45). Thus

$$k = \frac{\sin(\alpha - \beta)}{\sin(\psi - \alpha)} \quad (A-46)$$

Now,  $\beta$  and  $\psi$  are fixed angles determined by the range geometry, and  $\alpha$  has some value between  $\beta$  and  $\psi$ , so that the unique non-trivial condition for the ratio of the two sine functions to be constant is that the arguments of the sine functions be equal. Thus, (A-46) gives the required relations for both  $k$  and  $\alpha$  which will cause

$d\Phi_\chi/d\chi$  to be zero for all  $\chi$ . These conditions are

$$k = 1 \quad , \quad (A-47)$$

and

$$\alpha - \beta = \psi - \alpha$$

or

$$\alpha = \frac{\psi + \beta}{2} \quad . \quad (A-48)$$

A value of unity for  $k$  corresponds to the conditions of (A-26),  $\rho = E(\xi_1)/E(\xi_2)$ . For any  $k$  not equal to unity, the phase of the resultant field will be a function of  $\chi$ . For such cases, it is of interest to determine the angle  $\alpha$  for which the phase will have a space-rate-of-change equal to zero at the center of the receiving aperture. For  $\chi$  equal to zero, but  $k$  not equal to unity, equation (A-43) is then written

$$k(1+k) \sin(\psi - \alpha_0) - (1+k) \sin(\alpha_0 - \beta) = 0 \quad (A-49)$$

where we use the notation  $\alpha_0$  to indicate this angle applies only at the center of the aperture. Expanding the sine terms, we have

$$k \sin\psi \cos\alpha_0 - k \cos\psi \sin\alpha_0 - \sin\alpha_0 \cos\beta + \cos\alpha_0 \sin\beta = 0$$

or

$$\tan\alpha_0 = \frac{\sin\beta + k \sin\psi}{\cos\beta + k \cos\psi} \quad . \quad (A-50)$$

A set of computations for the values of  $\Phi_\chi$  versus  $\chi$  with  $k$  as a parameter were programmed for computer calculation using equations (A-31), (A-35), (A-36) and (A-39) with  $\alpha$  set equal to  $\alpha_0$  as defined by (A-50), and with  $R_0$ ,  $h_r$  and  $\lambda$  set equal to 1000 feet, 30 feet, and 0.098 foot ( $f=10$  GHz), respectively. Figure A.6 gives graphs of the change in  $\Phi_\chi$  as a function of  $\chi$  for  $k$  equal to 1.0, 0.9, 0.5 and 0. The field amplitude  $E(\chi)$  in the test aperture is given by (A-40). Figure A.7 gives graphs of  $E(\chi)$  corresponding to the values of  $k$  employed above, and Figure A.8 shows the normalized decibel taper of the function  $E(\chi)$  for values of  $k$  of 0.3, 0.5 and 1.0.

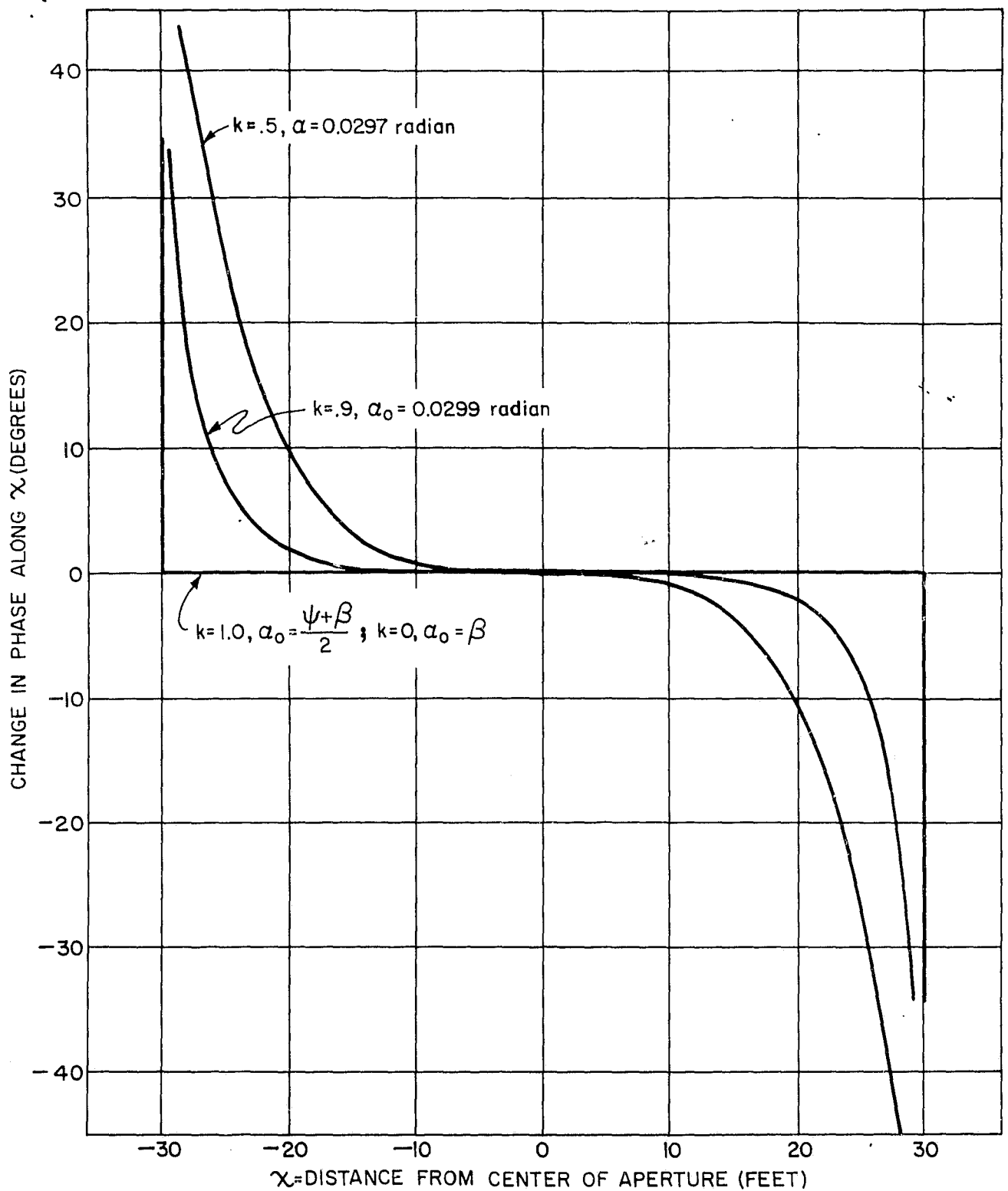


Figure A.6. Phase of the Aperture Field with  $k$  as a Parameter in the Ground Reflection Mode

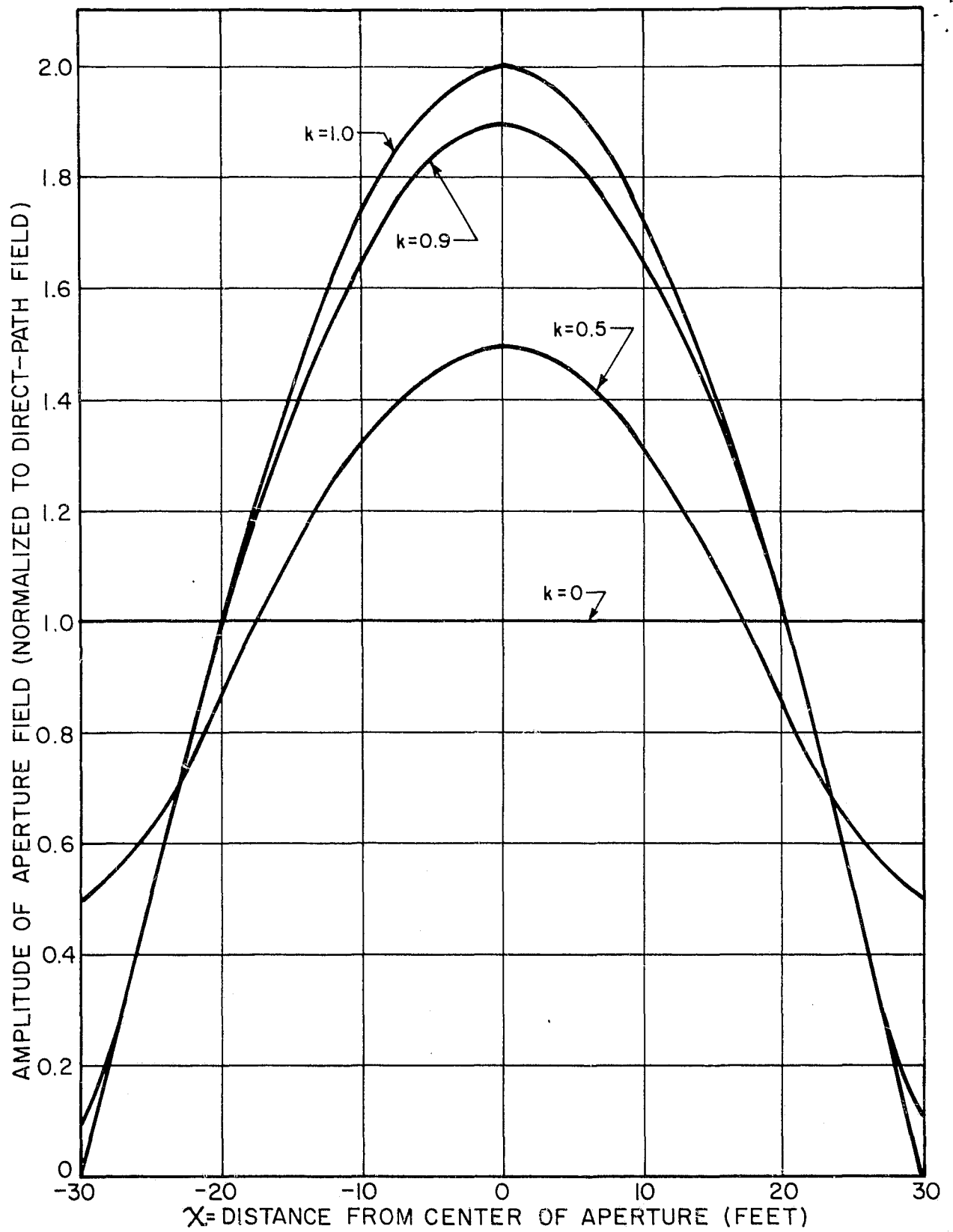


Figure A.7. Plot of the Aperture Field  $E(X)/E_D$  with  $k$  as a Parameter in the Ground-Reflection Mode



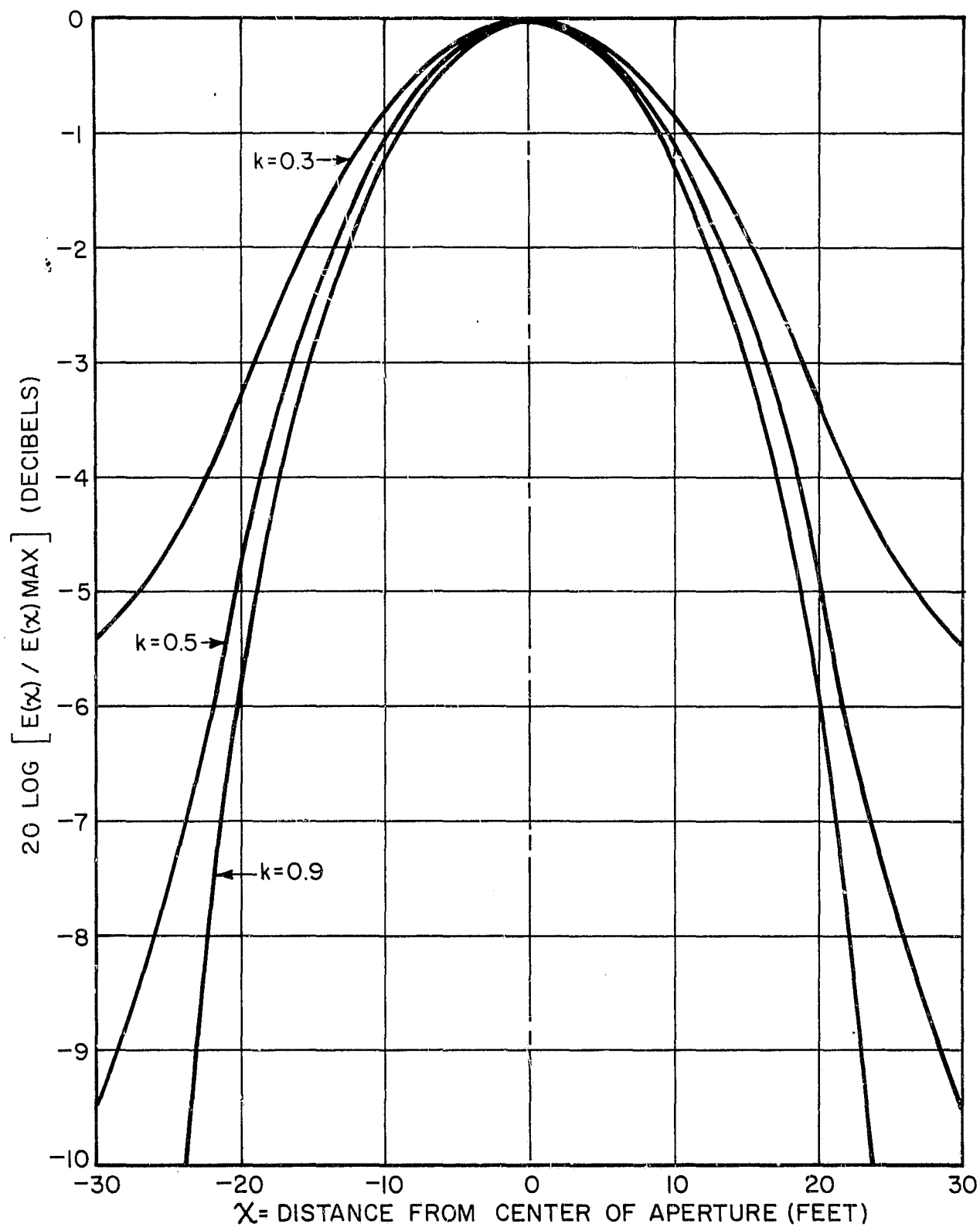


Figure A.8. Decibel Taper of the Normalized Aperture Field  $[E(x)/E(x)_{\text{MAX}}]$  with  $k$  as a Parameter in the Ground-Reflection Mode

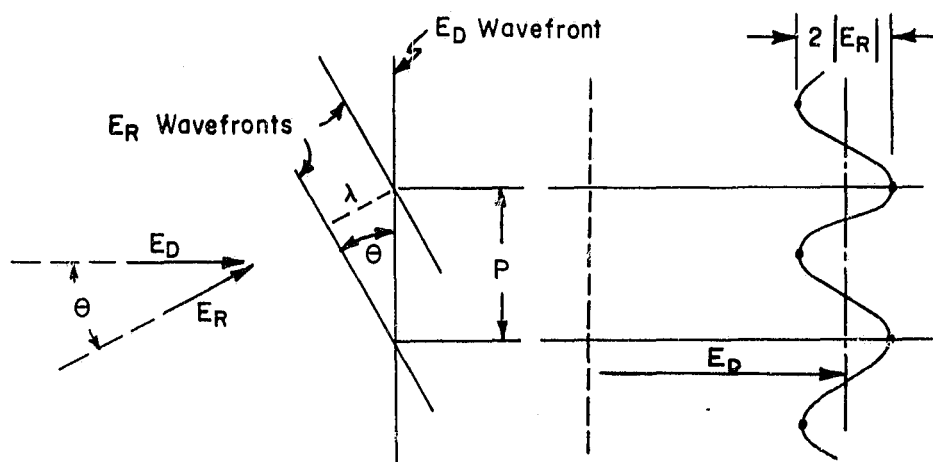
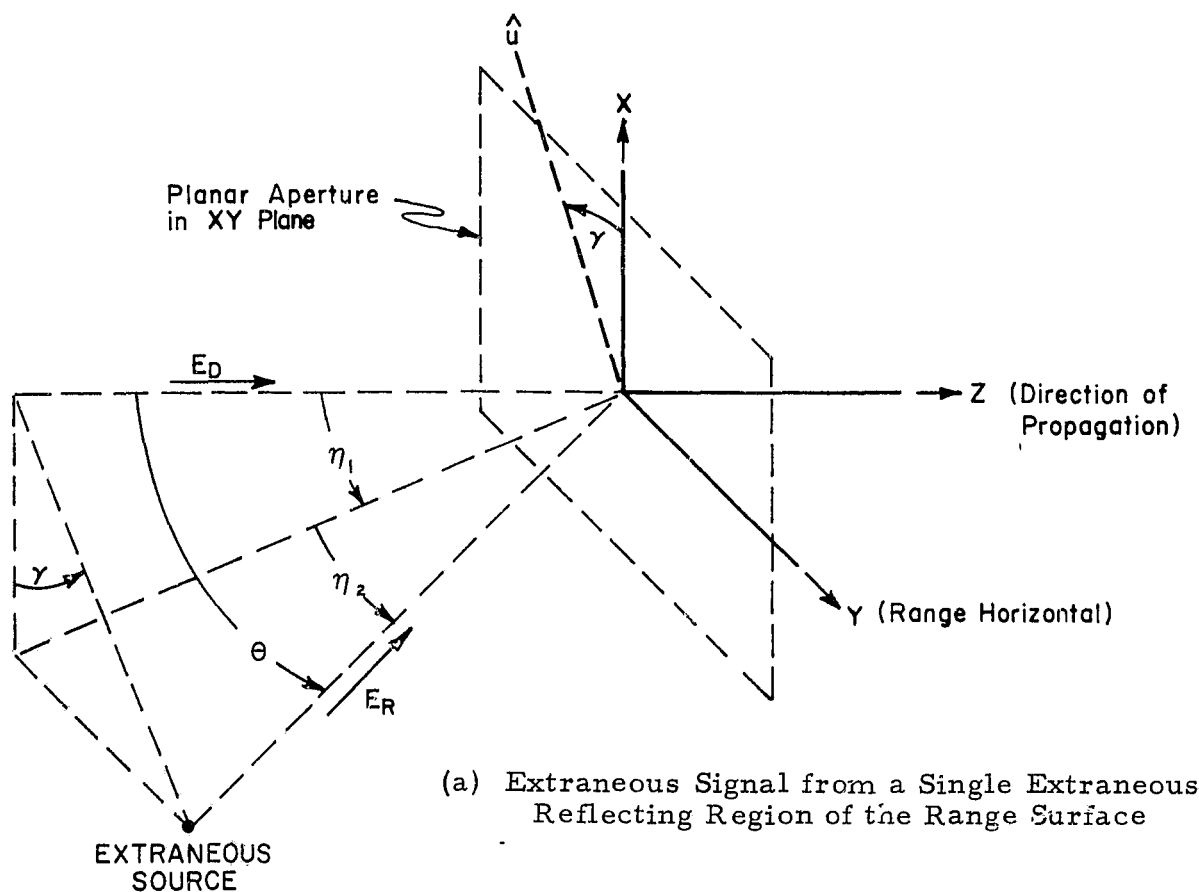
## A.6 Elevated Operation of the MILA Range

It has been shown in the preceding paragraphs of this appendix that the MILA range surface should approximate a smooth reflector for microwave energy up to a frequency of 10 GHz. Further, it was stated that this property of the range would allow some prediction to be made of the configuration of the receiving-aperture field when the range is operated in the elevated mode. The following analysis is directed toward the development of equations which describe the predicted incident field at the test aperture of the MILA facility for elevated operation (see paragraph 3.1.1). The incident field is considered to be centered on a receiving aperture at height  $h_r$ , and is investigated along lines which are normal to the direction of propagation of the direct-path wave from the source antenna. The source is allowed to assume some arbitrary height  $h_t$ .

When extraneous signals are incident on the test aperture from several regions of the range surface between the transmitter and receiver, the resultant aperture field is the phasor summation of components which include the direct-path signal and all extraneous signals. Recorded patterns of such a field are complicated in nature and do not yield direct quantitative information as to the locations and strengths of individual sources of interference. However, for a range which is essentially planar, as postulated for the MILA facility, the primary sources of reflections are restricted to the general region of the range axis; the amplitude and periodicity of field fluctuations along radial lines within the planar test aperture are thus indicative of the general amplitudes and directions of incidence of high-level extraneous signals. This may be shown as follows, where we shall assume plane wave propagation (see the discussions of paragraph A.3) and restrict our attention to a single polarization.

Since the primary use of these derivations is in correlating the data obtained from probe measurements of the aperture field, we will establish general relations, and then specialize the results to apply to the MILA configuration. Consider an aperture field which is the summation of the direct-path signal  $\bar{E}_D$  which is incident normally on the aperture, and a single extraneous signal  $\bar{E}_R$  as indicated in Figure A.9(a). If the field is measured as a function of distance  $u$  along the particular radial line  $\hat{u}$  in the aperture defined by the angle  $\gamma$  in Figure A.9(a), where  $\gamma$  is uniquely defined by  $\bar{E}_D$  and  $\bar{E}_R$ , the measured field will be proportional to

$$E(u) = E_D + E_R \sin(2\pi u \frac{\sin\theta}{\lambda}) \quad . \quad (A-51)$$



(b) Spatial Period and Amplitude of Resulting Aperture Field Fluctuation in Plane of  $E_D$  and  $E_R$

Figure A. 9. Relation of Range Coordinates and Aperture Field Components for a Single Extraneous Signal in the Elevated Mode of Operation

Note that the distance between successive peaks of the resultant field in the plane of  $\bar{E}_R$  and  $\bar{E}_D$  is

$$P = \frac{\lambda}{\sin\theta} , \quad (A-52)$$

as can be seen in Figure A.9(b). The spatial period indicated in (A-52) is the shortest possible period for this plane-wave case; if the unique radial line defined by  $\hat{u}$  is determined, then  $\theta$  (and consequently  $\eta_1$  and  $\eta_2$ ) can be calculated.

While the spatial periods of the measured field fluctuations are functions of the position of the radial line in the aperture for which a recording of the field is made, the peak-to-peak amplitude of these fluctuations is a constant proportional to

$$\Delta E = (E_D + E_R) - (E_D - E_R) = 2E_R . \quad (A-53)$$

Note that as the line of exploration approaches the direction defined by  $\gamma \pm 90^\circ$ , the period of the field variation approaches infinity for the simplified case under consideration. Thus, the measured variation in this direction over an aperture of practical size will approach zero.

For typical logarithmic patterns, the relation of  $E_R$  and  $E_D$  would be

$$\frac{E_R}{E_D} \text{ (db)} = 20 \log \frac{-1 + \text{antilog}(.05\sigma)}{1 + \text{antilog}(.05\sigma)} , \quad (A-54)$$

where  $\sigma$  is the difference in decibels between maxima and minima of the measured pattern. A plot of  $E_R/E_D$  versus  $\sigma$  is given in Figure A.10.

Measurements of the field incident on the test aperture were made at the MILA range within a 16-foot circular planar aperture employing the aperture field probe technique. This technique is discussed in Chapter 3 of this report, and representative sets of data are included in Chapter 4. For the MILA configuration, which approximates a specularly reflecting surface, the primary extraneous interference will appear to originate at the image of the source antenna and will be incident on the test aperture along the line  $\bar{Z}_O Q$  as shown in Figure A.11. Here  $Z_O$  is the point of specular reflection (see Appendix F), and  $Q$  is the geometrical center of the test aperture. In this case, the angle  $\theta$  between  $\bar{E}_D$  and  $\bar{E}_R$  becomes

$$\theta = \psi - \beta = \tan^{-1} \frac{h_r + h_t}{R_O} - \tan^{-1} \frac{h_r - h_t}{R_O} . \quad (A-55)$$

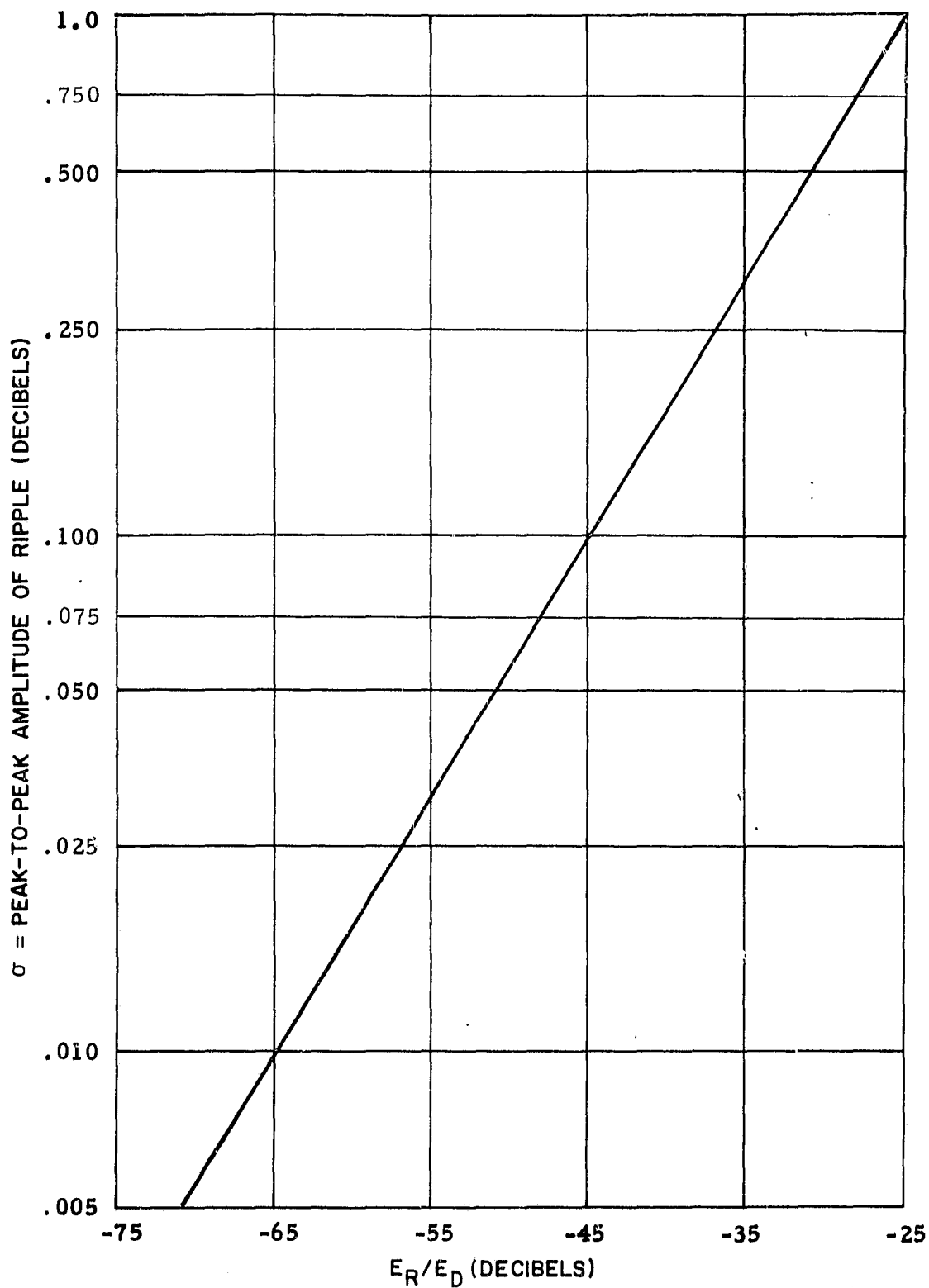


Figure A.10. Magnitude of Perturbed Field Variation Versus the Ratio of Reflected-Signal to Direct-Signal Strengths for a Plot in the Plane of  $\bar{E}_R$  and  $\bar{E}_D$ .

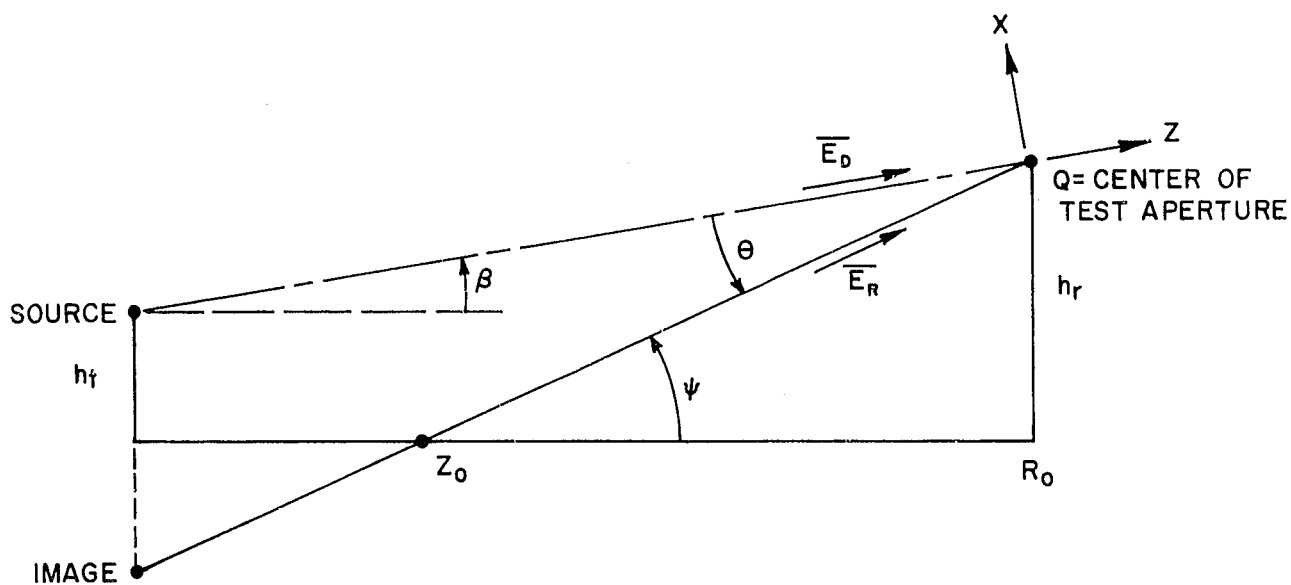


Figure A.11. Parameters of the Direct-Path and Specularly Reflected Waves Incident on the Test Aperture in the Elevated Mode

Since  $R_0$  is large compared to  $(h_r + h_t)$ , we can write

$$\theta \doteq \frac{2h_t}{R_0} \text{ radians.} \quad (\text{A-56})$$

For this case the extraneous source is in the XZ plane, thus the parameters of Figure A.9(a) reduce to

$$\eta_1 = \theta \quad (\text{A-57a})$$

$$\eta_2 = 0 \quad (\text{A-57b})$$

and

$$\gamma = 0 \quad (\text{A-57c})$$

It follows that the predicted aperture field is constant in  $y$  for any particular  $x$ ,

and is periodic in  $x$  with a physical period given by

$$P = \frac{\lambda}{\sin\theta} \doteq \frac{\lambda}{\theta} \doteq \frac{\lambda R_o}{2h_t} \quad (\text{A-58})$$

and a normalized peak-to-peak variation in amplitude about the direct-path level given by

$$\Delta E' = \frac{2E_R}{E_D} \equiv 2k \quad (\text{A-59})$$

# APPENDIX B HEIGHT OF THE APPARENT SOURCE OF RADIATION OVER A PLANAR REFLECTING SURFACE AS SENSED BY A PHASE-MONOPULSE RADAR

Phase-monopulse radars operate by sensing the direction of arrival of a wave as the direction of the normal to the approaching phase front on the assumption that the wave incident on the antenna arrives from a single distant source. In this case the incident phase front is a section of a sphere of such large radius that it is essentially planar. When monopulse measurements are made over a reflecting range surface, the phase front at the receiving aperture is produced by the summation of the direct path signal and all reflected signals, hence the phase will vary from spherical with position in the test aperture.

Let us assume that a phase-monopulse radar, whose antennas consist of an interferometer pair with antennas located at  $\chi=0$  and  $\chi=\chi_0$ , is employed to sense the vertical angle of arrival  $\alpha$  of the incident wave consisting of a direct path wave  $\bar{E}_D$  and a reflected wave  $\bar{E}_R$  as shown in Figure B.1. Let the distances to

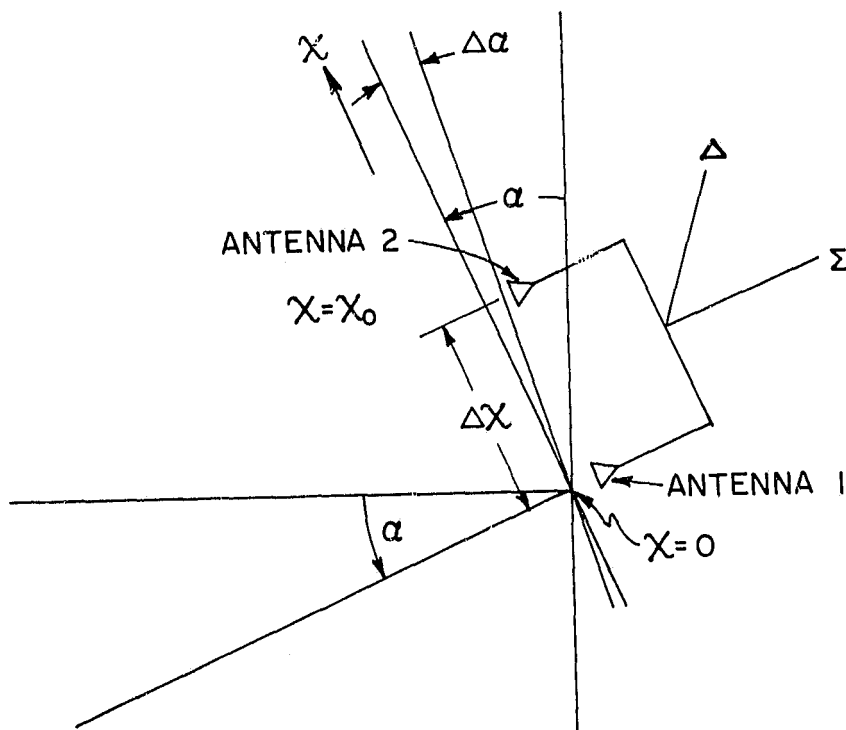


Figure B.1. Measurement Functions of a Single-Plane Interferometer Antenna Pair



the monopulse junction from the two antennas be equal so that a difference channel null indicates phase equality of the fields incident on antenna 1 at  $\chi=0$  and on antenna 2 at  $\chi=\chi_0$ . Let us further assume that antennas 1 and 2 are sufficiently small that the incident field is nearly constant over the aperture of each antenna. If antennas 1 and 2 are not oriented to coincide identically with equal phase points of the incident wave front, a phase difference  $\Delta\Phi$  will exist at the two antennas. This phase difference corresponds to a physical distance in the direction of propagation of  $\lambda\Delta\Phi/2\pi$  and a physical angle

$$\Delta\alpha = \frac{\lambda}{2\pi} \frac{\Delta\Phi}{\Delta\chi} \quad . \quad (B-1)$$

Phase equality, indicating the apparent direction of arrival of the wave, is achieved by sensing the condition that

$$\Delta\alpha = \frac{\lambda}{2\pi} \frac{\Delta\Phi}{\Delta\chi} = 0 \quad . \quad (B-2)$$

If the reflected energy which has been postulated to exist comes from the specularly smooth surface of an antenna range such as that at MILA, the phase and amplitude of the incident field will be cyclic with elevation, as shown in section A.6. The discussion given here applies to the height of the apparent source of radiation as sensed by a phase-monopulse radar for which the separation between antennas is small compared with the period  $P$  (equation A-52) of the vertical interference pattern, say for  $\Delta\chi < P/8$ . For the MILA range, this condition is satisfied for phase-monopulse radars which have a separation of less than  $\lambda$  between phase centers as in the case of the Gemini rendezvous radar.\* For this case  $\Delta\chi$  can be considered to approach zero,  $\Delta\Phi/\Delta\chi$  will be approximated by  $d\Phi/d\chi$  with small error, and the analyses of Appendix A, paragraphs A.4 and A.5 apply. On the assumption of plane wave propagation for both the direct-path and reflected signals, the phase of the receiving aperture field along some line defined by the angle  $\alpha$  is given by (A-39):

$$\Phi_{\chi} = \tan^{-1} \frac{\sin\phi_D + k \sin\phi_R}{\cos\phi_D + k \cos\phi_R} \quad , \quad (A-39)$$

---

\*Consideration of the effects of larger values of  $\Delta\chi$  is given in Appendix D.

where

$$\phi_D = \frac{2\pi}{\lambda} \left[ \frac{R_o}{\cos\beta} - \chi \sin(\alpha - \beta) \right] \quad , \quad (A-35)$$

and

$$\phi_R = \frac{2\pi}{\lambda} \left[ \frac{R_o}{\cos\psi} + \chi \sin(\psi - \alpha) \right] - \phi \quad . \quad (A-36)$$

For convenience, the parameters are redefined in Figure B.2.

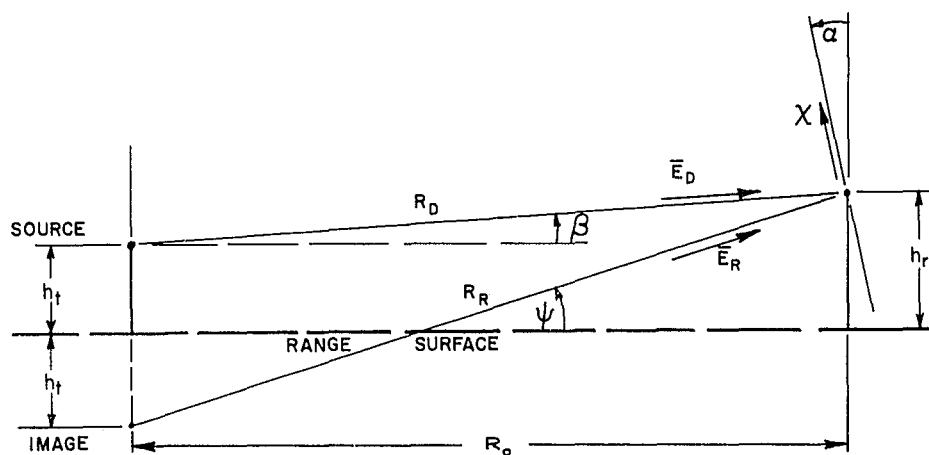


Figure B.2. Parameters for the Study of the Receiving-Aperture Phasefront

The derivative of  $\Phi_\chi$  with respect to  $\chi$  is given by (A-41); setting  $d\Phi_\chi/d\chi$  equal to zero at  $\chi=0$  requires that the numerator of (A-41) be equal to zero, which yields\*

$$\cos(\phi_R - \phi_D) \Big|_{\chi=0} = \frac{\sin(\alpha - \beta) - k^2 \sin(\psi - \alpha)}{k [\sin(\psi - \alpha) - \sin(\alpha - \beta)]} \quad (B-3)$$

\*Equation (B-3) is identical with (A-43) except that in (A-43) the term  $\cos(\phi_R - \phi_D)$  at  $\chi=0$  has been forced to equal unity by requiring that the phases of the direct and reflected waves be identical at the center of the test aperture. (See (A-42) and discussion.) This condition was imposed for proper operation of the antenna test range in the ground-reflection mode and implies a specific source height; it is not assumed to exist in the present analysis, which is for the case of reflections from a planar range surface for an arbitrary source height.

If we write

$$F = \cos(\phi_R - \phi_D) \Big|_{\chi=0} = \cos \left[ \frac{2\pi R_o}{\lambda} \left( \frac{1}{\cos\psi} - \frac{1}{\cos\beta} \right) - \phi \right] \quad (B-4)$$

and apply the identity

$$\sin(a-b) = \sin a \cos b - \cos a \sin b$$

to (B-3) we obtain

$$\tan\alpha = \frac{(1+kF)\sin\beta + k(k+F)\sin\psi}{(1+kF)\cos\beta + k(k+F)\cos\psi} \quad (B-5)$$

The normal to the line defined by  $\alpha$  will intersect the normal to the range surface at the transmitting site at a height H given by

$$H = h_r - R_o \tan\alpha \quad , \quad (B-6)$$

where H is measured from the range surface. From the geometry of Figure B.2,

$$\sin\beta = \frac{(h_r - h_t)}{R_D} \quad , \quad \cos\beta = \frac{R_o}{R_D} \quad (B-7a)$$

$$\sin\psi = \frac{(h_r - h_t)}{R_R} \quad , \quad \cos\psi = \frac{R_o}{R_R} \quad (B-7b)$$

$$\frac{\cos\beta}{\cos\psi} = \frac{R_R}{R_D} \quad (B-7c)$$

Substitution of (B-7a) and (B-7b) into (B-5) gives

$$\tan\alpha = \frac{(1+kF)(h_r - h_t) / R_D + k(k+F)(h_r + h_t) / R_R}{(1+kF)R_o / R_D + k(k+F)R_o / R_R} \quad ,$$

which can be written as

$$\tan\alpha = \frac{(1+kF)(h_r - h_t)R_R / R_D + k(k+F)(h_r + h_t)}{(1+kF)R_o R_R / R_D + k(k+F)R_o} \quad (B-8)$$

Multiplication of this expression by  $R_o$ , and substitution of (B-7c) into the result,

gives

$$R_o \tan \alpha = \frac{(1+kF)(h_r - h_t) \frac{\cos \beta}{\cos \psi} + k(k+F)(h_r + h_t)}{(1+kF) \frac{\cos \beta}{\cos \psi} + k(k+F)} \quad (B-9)$$

Substitution of (B-9) into (B-6) and simplification yields

$$H = h_t \left[ \frac{(1+kF) \frac{\cos \beta}{\cos \psi} - k(k+F)}{(1+kF) \frac{\cos \beta}{\cos \psi} + k(k+F)} \right] \quad (B-10)$$

As discussed in Appendix A,  $\phi$  can be set equal to  $\pi$  with negligible error for small grazing angles. In this case,

$$F = -\cos \frac{2\pi}{\lambda} (R_R - R_D) \quad (B-11)$$

so that

$$F = \begin{cases} 1, & R_R - R_D = \frac{n\lambda}{2} ; \quad n \text{ odd} \\ 0, & R_R - R_D = \frac{n\lambda}{4} ; \quad n \text{ odd} \\ -1, & R_R - R_D = n\lambda ; \quad n = 1, 2, 3, \dots \end{cases} \quad (B-12)$$

If we can express  $h_t$  in terms of the fixed parameters  $R_o$ ,  $h_r$  and  $\lambda$  and the integral variable  $n$ , then (B-10) and (B-12) will allow  $H$  to be plotted as a function of  $k$ . From the geometry of Figure B.1,

$$R_D^2 = R_o^2 + (h_r - h_t)^2 \quad (B-13)$$

and

$$R_R^2 = R_o^2 + (h_r + h_t)^2, \quad (B-14)$$

so that

$$R_R^2 - R_D^2 = 4h_r h_t \quad (B-15)$$

We may write (B-15) as

$$R_R^2 - R_D^2 = (R_R - R_D)(R_R + R_D + 2R_D) = 4h_r h_t \quad (B-16)$$

which yields, for  $R_R - R_D = N\lambda/4$ ,

$$R_D = \frac{8}{N\lambda} h_r h_t - \frac{N\lambda}{8}, \quad N=1,2,3,4,\dots \quad (B-17)$$

Squaring (B-17) and equating the result to (B-13) gives

$$h_t^2 = \left[ \frac{R_o^2 + h_r^2 - (\frac{N\lambda}{8})^2}{h_r^2 - (\frac{N\lambda}{8})^2} \right] (\frac{N\lambda}{8})^2 \quad (B-18)$$

For the case of interest, the range of values for N will be such that  $(\frac{N\lambda}{8})^2 \ll h_r^2$ . Also,  $R_o^2 \gg h_r^2$ , so that we have

$$h_t \doteq \frac{N\lambda}{8} \frac{R_o}{h_r} \quad (B-19)$$

Applying (B-12) and (B-19) to (B-10), the following results are obtained for the minima, inflection points, and maxima of the apparent source height versus actual source height as sensed at the center of the receiving aperture:

$$H \doteq \begin{cases} (\frac{\cos\beta}{\cos\psi} - k) / (\frac{\cos\beta}{\cos\psi} + k) \frac{N\lambda R_o}{8h_r}; & N = 2, 6, 10, \dots \\ (\frac{\cos\beta}{\cos\psi} - k^2) / (\frac{\cos\beta}{\cos\psi} + k^2) \frac{N\lambda R_o}{8h_r}; & N = 1, 3, 5, \dots \\ (\frac{\cos\beta}{\cos\psi} + k) / (\frac{\cos\beta}{\cos\psi} - k) \frac{N\lambda R_o}{8h_r}; & N = 4, 8, 12, \dots \end{cases} \quad (B-20)$$

The following figures are graphs of H versus  $h_t$  with k as a parameter for  $R_o = 10^3$  feet,  $h_r = 30$  feet, and for frequencies in L-, S- and X-bands.

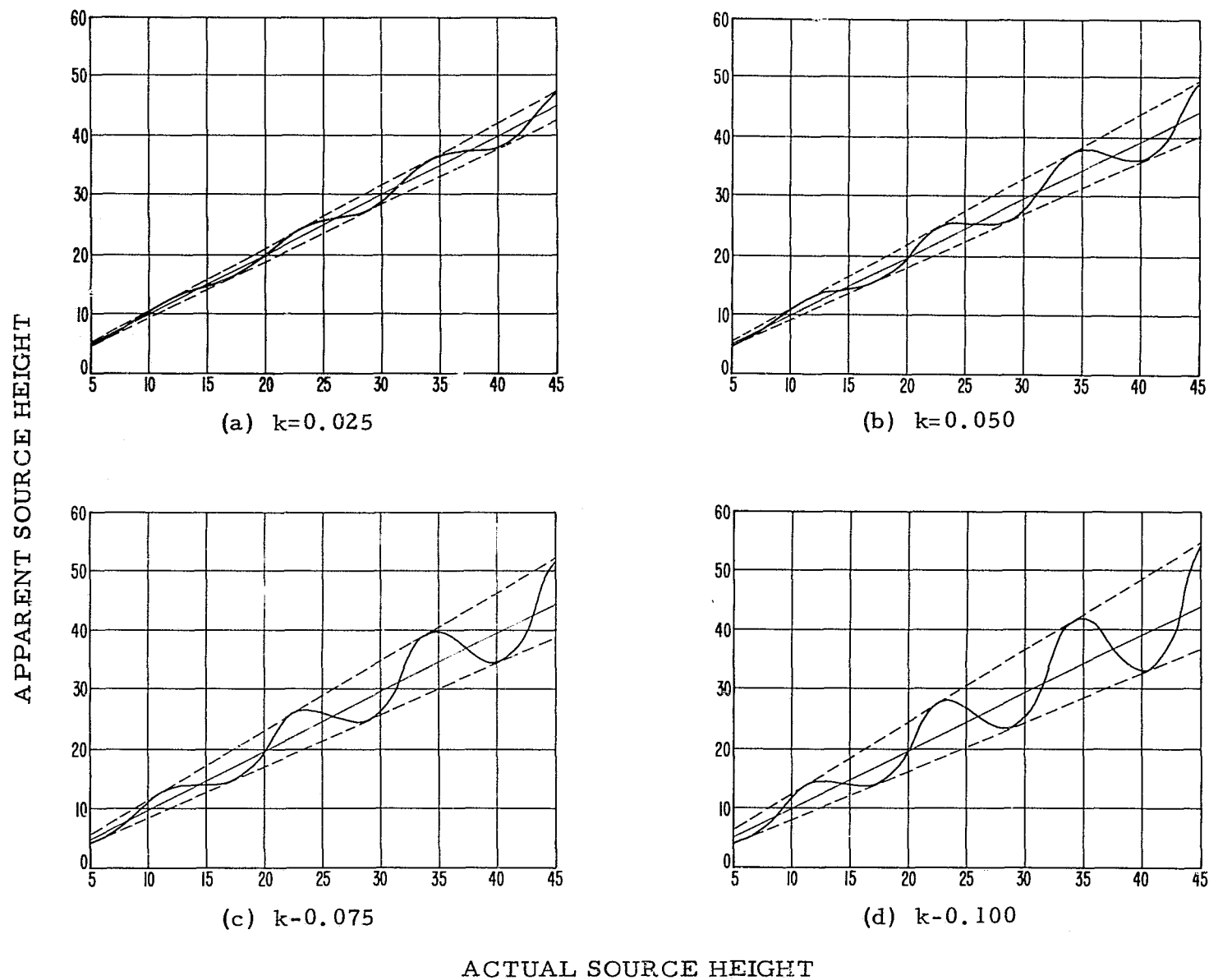
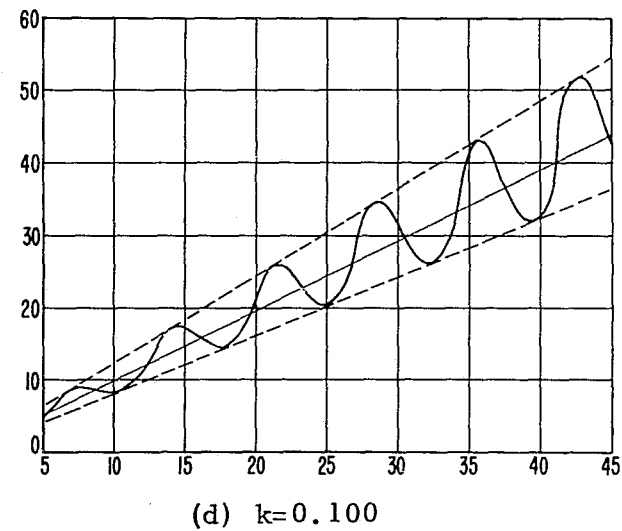
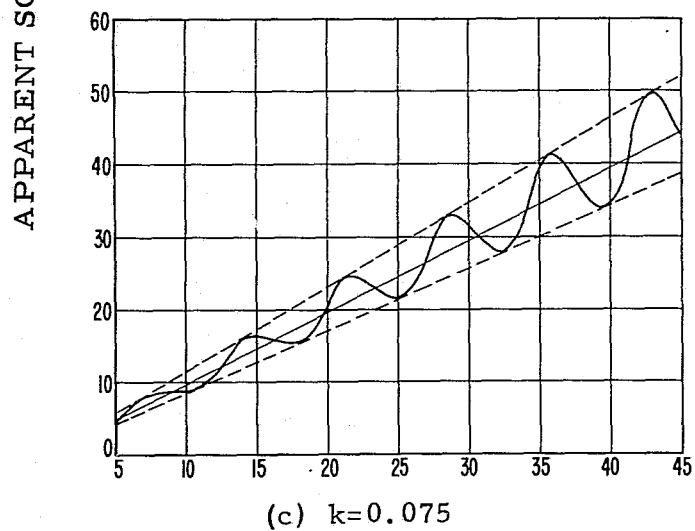
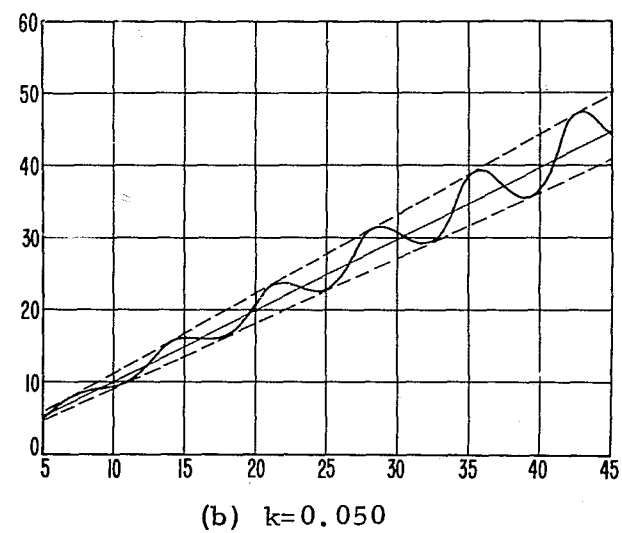
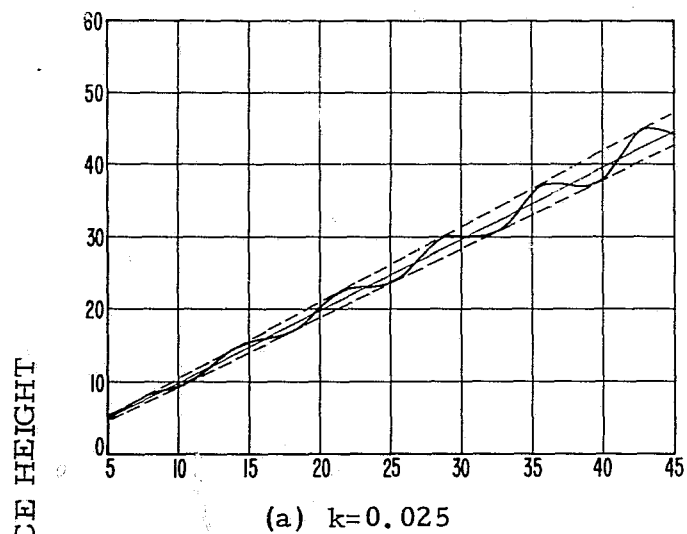
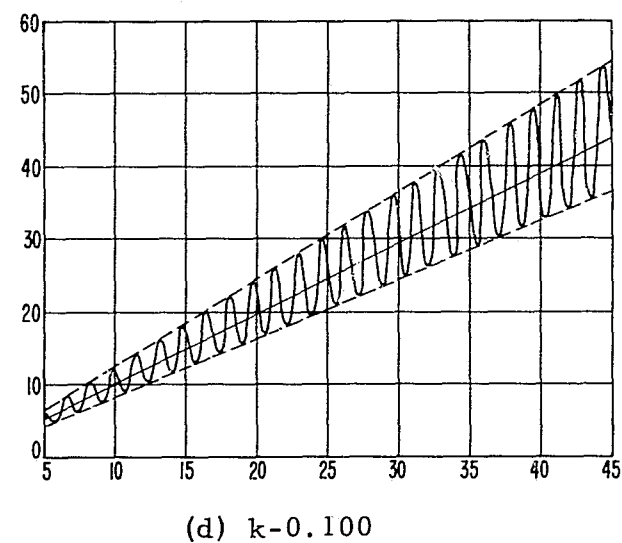
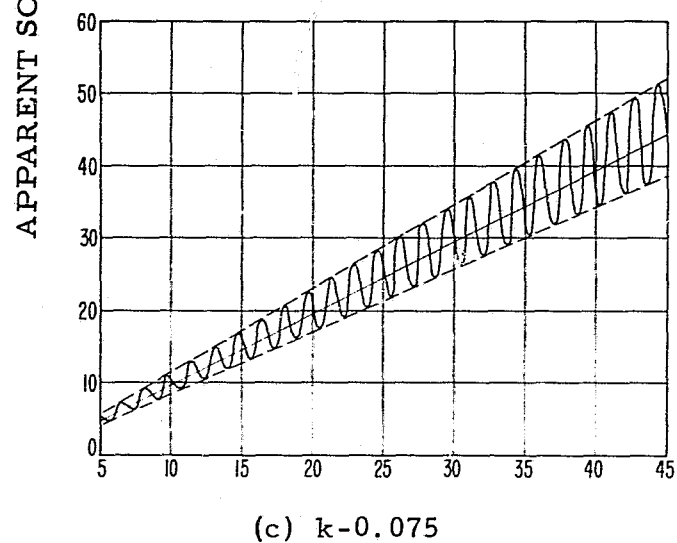
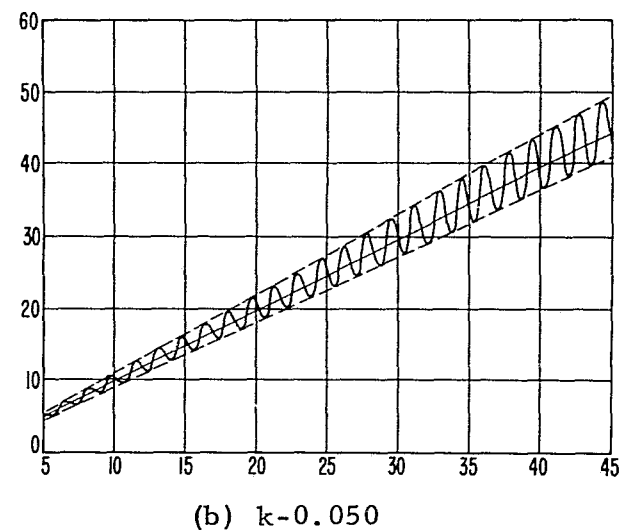
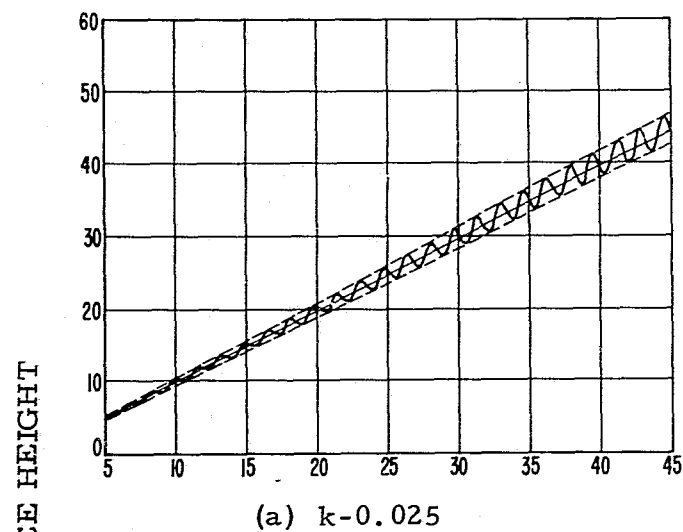


Figure B.3. Apparent Versus Actual Source Height With  $k$  as a Parameter as Sensed by a Phase-Monopulse Radar at 1.428 GHz on the MILA Range



ACTUAL SOURCE HEIGHT

Figure B.4. Apparent Versus Actual Source Height With  $k$  as a Parameter as Sensed by a Phase-Monopulse Radar at 2.3 GHz on the MILA Range



ACTUAL SOURCE HEIGHT

Figure B.5. Apparent Versus Actual Source Height With  $k$  as a Parameter as Sensed by a Phase-Monopulse Radar at 10 GHz on the MILA Range



## APPENDIX C

### HEIGHT OF THE APPARENT SOURCE OF RADIATION OVER A PLANAR REFLECTING SURFACE AS SENSED BY AN AMPLITUDE-MONOPULSE RADAR

#### C.1 Introduction

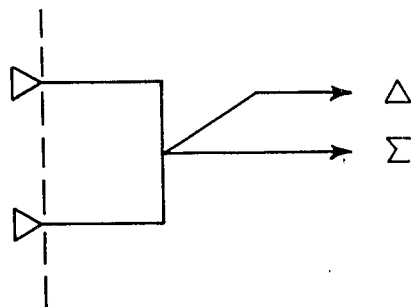
In Appendix B an analysis was made of the height of the apparent source of radiation as sensed by a phase-monopulse radar over a planar range surface. In this appendix a similar analysis is made to determine the height of the apparent source as sensed by an amplitude-monopulse radar, such as that employed by the LEM rendezvous radar system. The problem is physically different in the manner in which the radar samples the incident field. While the phase-monopulse radar (Figure C.1a) consists of two antennas which are physically separated so that each antenna samples a different area of the incident field (although with some degree of mutual coupling between the antennas), the amplitude-monopulse radar consists of a single aperture (Figure C.1b), usually a paraboloidal reflector with two feeds which are displaced to produce two displaced directivity responses to the incident field (see Chapter 5 and Appendix J). The amplitude-monopulse radar samples the same incident field but processes the data with two separate feeds. Thus a different analysis is required to determine the direction to the apparent source as sensed by an amplitude-monopulse radar.

#### C.2 Apparent Versus Actual Source Height

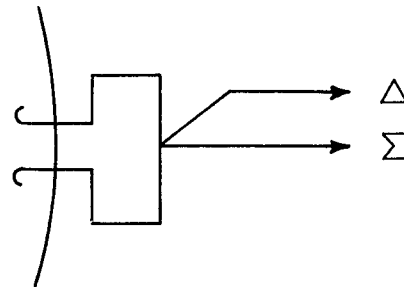
Assume that an amplitude-monopulse radar having  $\sin K\theta/K\theta$  lobe structures (see Appendix E) is illuminated by a direct-path signal  $\bar{E}_D$ , and a single extraneous signal  $\bar{E}_R$  which arrives at the radar at an angle  $\theta_R^*$  from  $\bar{E}_D$ . The orientation of the angles of incidence of these signals with respect to the monopulse lobes is indicated schematically in Figure C.2(a), and the resulting difference channel phasor diagram is sketched in Figure C.2(b).

---

\*This analysis assumes that the extraneous signal enters the directivity patterns of both feeds at some point on their main lobes. The effects of wide-angle interference are discussed in Appendix D.

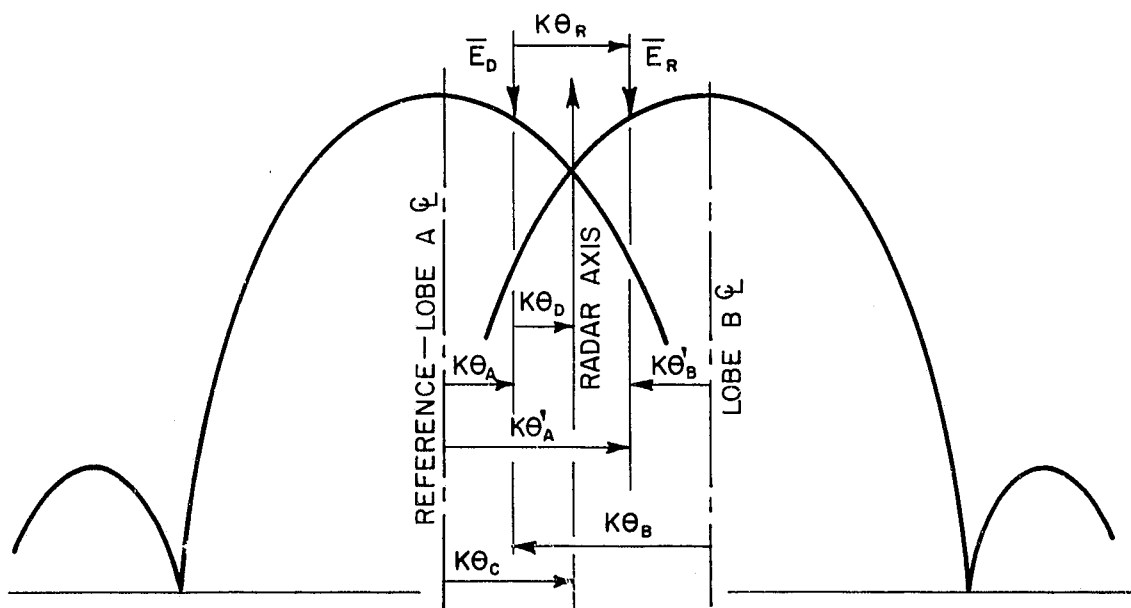


(a) Phase-Monopulse Device

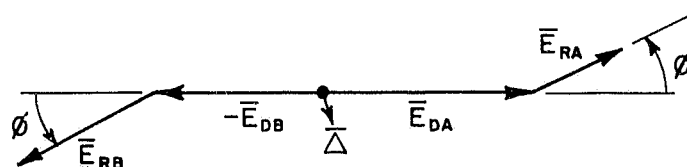


(b) Amplitude-Monopulse Device

Figure C.1. Schematic Representations of Monopulse Devices for Single-Plane Direction Sensing



(a) Pattern Angles Related to Incident Signals



(b) Direct-Path and Reflected Signals in  $\Delta$  Channel

Figure C.2. Relation of Difference-Channel Phasors to Points of Incidence of  $\bar{E}_D$  and  $\bar{E}_R$  on the Monopulse Directivity Patterns

The respective pattern angles in radians as measured from the lobe centers are given by

$$K\theta_A = K\theta_C - K\theta_D \quad (\text{Direct Signal in Lobe A}) \quad (C-1)$$

$$K\theta'_A = K\theta_A + K\theta_R \quad (\text{Extraneous Signal in Lobe A}) \quad (C-2)$$

$$K\theta_B = K\theta_C + K\theta_D = 2K\theta_C - K\theta_A \quad (\text{Direct Signal in Lobe B}) \quad (C-3)$$

$$K\theta'_B = K\theta_B - K\theta_R = 2K\theta_C - K\theta_A - K\theta_R \quad (\text{Extraneous Signal in Lobe B}) \quad (C-4)$$

If we write the extraneous signal in terms of the direct signal as

$$\bar{E}_R = k e^{j\phi} \bar{E}_D, \quad (C-5)$$

then the difference signal,  $E_A - E_B = \Delta E$ , is written

$$\Delta E = A_o E_D \left[ \left( \frac{\sin K\theta_A}{K\theta_A} + k e^{j\phi} \frac{\sin K\theta'_A}{K\theta'_A} \right) - \left( \frac{\sin K\theta_B}{K\theta_B} + k e^{j\phi} \frac{\sin K\theta'_B}{K\theta'_B} \right) \right] \quad (C-6)$$

Now, for small  $K\theta_i$ , the function  $\sin K\theta_i / K\theta_i$  can be approximated from its power series by

$$\frac{\sin K\theta_i}{K\theta_i} \doteq 1 - \frac{(K\theta_i)^2}{3!} \quad (C-7)$$

It is noted that (C-7) represents a valid approximation only over the major portion of the main  $\sin K\theta_i / K\theta_i$  lobe of each pattern. If either  $\bar{E}_D$  or  $\bar{E}_R$  is received in the region of a first pattern null or through a sidelobe, a modification of (C-7) is required which would be based on recorded patterns for the A and B channels. (See Chapter 4 and Appendix D of this document.) For cases where (C-7) is applicable, (C-6) can be written

$$\frac{6\Delta E}{K^2 A_o E_D} \doteq -\theta_A^2 - k e^{j\phi} (\theta_A + \theta_R)^2 + (\theta_A + 2\theta_D)^2 + k e^{j\phi} (\theta_A + \theta_R - 2\theta_C)^2 \quad (C-8)$$

where we have used (C-2) through (C-4). Employing Euler's identity in (C-8), we obtain

$$\left| \frac{6\Delta E}{4K^2 A_o E_D} \right| = \left\{ \left[ \theta_D(\theta_A + \theta_D) + k \cos \phi \theta_C(\theta_C - \theta_A - \theta_R) \right]^2 + \left[ k \sin \phi \theta_C(\theta_C - \theta_A - \theta_R) \right]^2 \right\}^{\frac{1}{2}}$$

which simplifies to

$$\left| \frac{6\Delta E}{4K^2 A_o E_D} \right| = \left\{ (\theta_C - \theta_A)^2 + k^2 (\theta_C - \theta_R - \theta_A)^2 + 2k \cos \phi (\theta_C - \theta_A)(\theta_C - \theta_A - \theta_R) \right\}^{\frac{1}{2}} \quad (C-9)$$

Recalling that the angle  $\theta_R$  is fixed by the range geometry while the angle  $\theta_A$  is established by the operator via the pointing direction set for the radar axis, it is seen that solution for the particular  $\theta_A$  which will cause the derivative of (C-9) with respect to  $\theta_A$  to become zero determines the pointing direction for which the radar exhibits a minimum difference signal. This situation represents orthogonality between the sum-channel signal and the difference-channel signal of an amplitude-monopulse radar; while (C-9) could be examined for the various combinations of conditions which would produce an absolute null ( $\Delta E=0$ ), the resulting criteria would not likely be met in an antenna test range environment.

Consider the derivative of (C-9) with respect to  $\theta_A$ :

$$\frac{d}{d\theta_A} \left| \frac{6\Delta E}{4K^2 A_o E_D} \right| = \frac{k\theta_R(k + \cos \phi) - (\theta_C - \theta_A)(1 + 2k \cos \phi + k^2)}{\left[ (\theta_C - \theta_A)^2 + k^2(\theta_C - \theta_R - \theta_A)^2 + 2k \cos \phi (\theta_C - \theta_A)(\theta_C - \theta_A - \theta_R) \right]^{\frac{1}{2}}} \quad (C-10)$$

Setting this derivative equal to zero yields

$$\theta_C - \theta_A = \frac{\theta_R k(k + \cos \phi)}{1 + 2k \cos \phi + k^2}$$

or, using (C-1),

$$\theta_D = \frac{k(k + \cos \phi)}{1 + 2k \cos \phi + k^2} \theta_R \quad (C-11)$$

This value of  $\theta_D$  may be interpreted in terms of the range geometry to indicate the apparent height of the source of radiation. Consider Figure C.3 below.

For  $R_o \gg h_t$  and  $h_r$ , we have the following expressions for the angular parameters

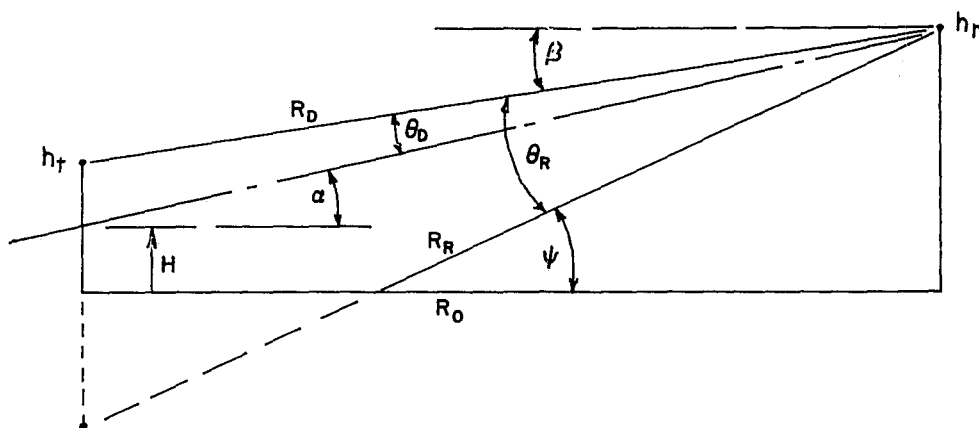


Figure C.3. The Apparent Height (H) of the Source of Radiation Related to the Test Range Geometry

in radians:

$$\psi = \tan^{-1} \frac{h_r + h_t}{R_o} \doteq \frac{h_r + h_t}{R_o}, \quad (C-12)$$

$$\beta = \tan^{-1} \frac{h_r - h_t}{R_o} \doteq \frac{h_r - h_t}{R_o}, \quad (C-13)$$

$$\theta_R = \psi - \beta \doteq \frac{2h_t}{R_o}, \quad (C-14)$$

$$\alpha = \tan^{-1} \frac{h_r - H}{R_o} \doteq \frac{h_r - H}{R_o}, \quad (C-15)$$

and

$$\theta_D = \alpha - \beta \doteq \frac{h_t - H}{R_o}. \quad (C-16)$$

Substitution of (C-14) and (C-16) in (C-11) gives

$$h_t - H \doteq 2h_t \frac{k(k + \cos\phi)}{1 + 2k\cos\phi + k^2} \quad (C-17)$$

or

$$H \doteq \frac{1 - k^2}{1 + 2k \cos \phi + k^2} h_t , \quad (C-18)$$

where H is the apparent height of the source of radiation.

Note that for cases where (C-7) is valid, the above result is independent of the beamwidths of the symmetrical lobes, since the factor  $K = 2.78/(\text{beamwidth in radians})$  does not appear in (C-11) or (C-18). While some dependence on K could be introduced by approximating  $\sin X_i/X_i$  by the first three terms of its power series rather than the first two terms as in the above analysis, the resulting equation in X for minimizing  $\Delta E$  would be in terms of fifth powers of X. The relative accuracies inherent in any correlation of data by employing experimental values for  $\phi$  and k do not warrant the use of such an unwieldy expression.

Comparison of (C-18) with equation (B-10) of Appendix B shows that the results of the current analysis are analogous to the results of Appendix B, which had no relation to the beam structures of sensing antennas.

## APPENDIX D

### EFFECT OF EXTRANEOUS SIGNALS ON BORESIGHT MEASUREMENT ACCURACIES

#### D.1 Introduction

The height of the apparent source of radiation as sensed by a phase-monopulse or an amplitude-monopulse device under test over a planar range surface was shown in Appendices B and C to be affected by the presence of energy reflected from the range surface. The context there was that of an extraneous signal entering the test aperture from a small angle relative to the direct-path signal direction. The analyses presented in Appendices B and C do not apply for angles of incidence  $\theta_R$  of the reflected-path signals greater than  $C_1\lambda/D$  radians where, (1)  $D$  is the diameter of the aperture of an amplitude-monopulse radar and  $C_1$  is approximately 1.5 or (2)  $D$  is the spacing between the antennas of a phase-monopulse pair and  $C_1$  is approximately 0.5. In terms of the aperture field variation, Appendices B and C are not valid for spatial periods  $P$  of the aperture field variation (see section A.6) which are less than  $C_2D$  where (1)  $C_2$  is 2/3 for the amplitude monopulse case or (2)  $C_2$  is 2 for the phase-monopulse case.

This appendix considers the effect on boresight measurement accuracies of extraneous signals which enter the test aperture from arbitrary angles of incidence.

#### D.2 Errors in Amplitude-Monopulse Systems

Consider a single-plane amplitude-monopulse system as shown schematically in Figure D.1(a). The phasors which correspond to the sum ( $\Sigma$ ) and difference ( $\Delta$ ) channel signals are depicted in Figure D.1(b) for the condition where an extraneous signal is present in both the A and B channels of the monopulse system. (The  $e^{j\omega t}$  time dependence of all phasors will be suppressed in this analysis.) In Figure D.1(b),

$\bar{A}_0 = A_0$  is the phasor in channel A due to the direct-path signal  $\bar{E}_D$  ,

$\bar{B}_0 = B_0$  is the phasor in channel B due to the direct-path signal  $\bar{E}_D$  ,

$\bar{a} = a e^{j\phi_1}$  is the phasor in channel A due to the extraneous signal  $\bar{E}_R$ ,

and

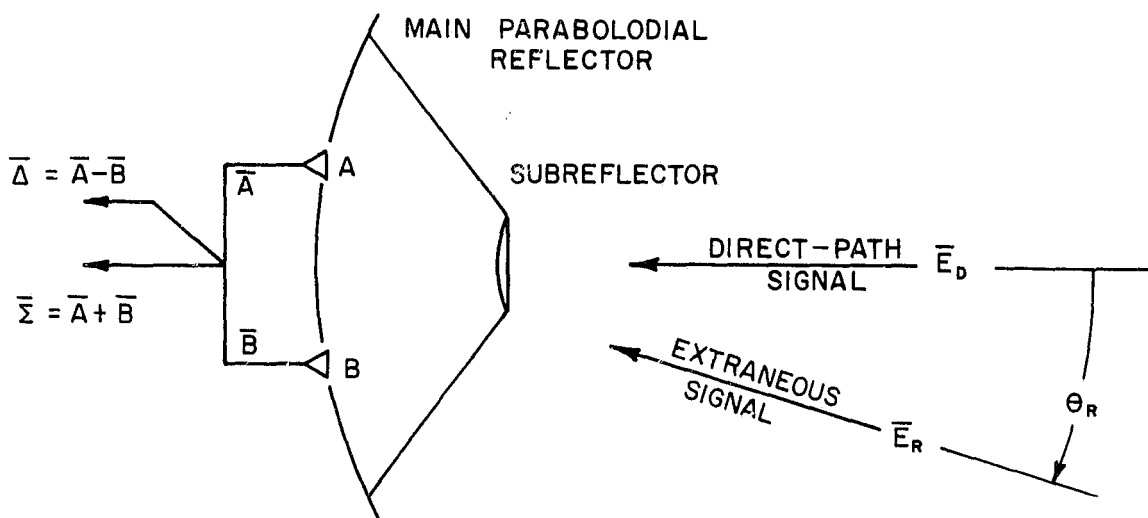
$\bar{b} = b e^{j\phi_2}$  is the phasor in channel B due to the extraneous signal  $\bar{E}_R$ ,

thus the phasors in channels A and B, respectively, are

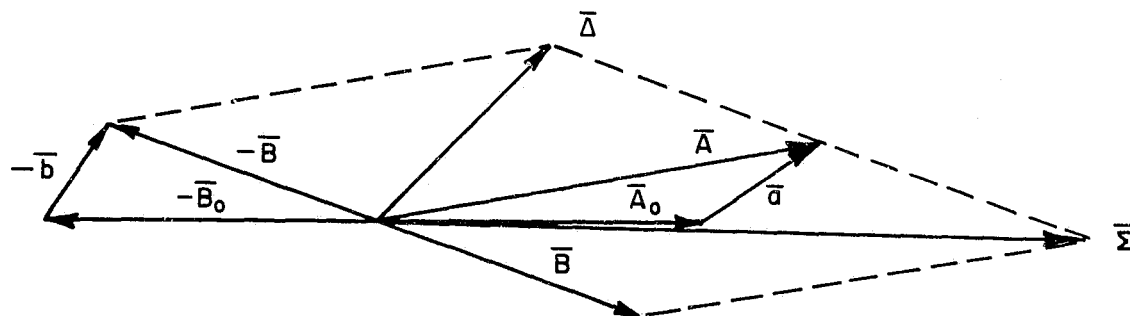
$$\bar{A} = (A_o + a e^{j\phi_1}) \quad (D-1)$$

and

$$\bar{B} = (B_o + b e^{j\phi_2}) \quad (D-2)$$



(a) Single-Plane Cassegrain Amplitude-Monopulse Radar



(b) Phasor Diagram of Signals in Monopulse Circuits

Figure D.1. The Effects of Wide-Angle Extraneous Signals on the Sum- and Difference-Channel Phasors of an Amplitude-Monopulse Radar



Assuming the monopulse system has identical  $\sin K\alpha/K\alpha$  main lobes with peak amplitudes  $M$  for the A and B patterns, and has been aligned so that the lobe axes are equally displaced from the reflector axis (optical boresight axis), then for the orientation of the radar which causes the direct-path signal to arrive along the reflector axis  $A_0$  will be equal to  $B_0$ . In this case, the sum and difference signals become

$$\bar{S} = (\bar{A} + \bar{B}) = (2A_0 + a e^{j\phi_1} + b e^{j\phi_2}) \quad (D-3)$$

and

$$\bar{\Delta} = (\bar{A} - \bar{B}) = (a e^{j\phi_1} - b e^{j\phi_2}) \quad (D-4)$$

The relative amplitudes and phases of the phasors  $\bar{a}$  and  $\bar{b}$  cannot be precisely predicted for arbitrary angles of incidence of the extraneous signal. It is of interest, therefore, to examine the effect of the extraneous energy under the worst case of phasing between  $\bar{a}$  and  $\bar{b}$ . It is seen that, regardless of the relative amplitudes, the phase condition which will cause the greatest error is given by  $\phi = \phi_1 = \phi_2 \pm \pi$  radians; this situation causes the phasors  $\bar{a}$  and  $\bar{b}$  to add in the difference channel. Applying this condition in (D-4), we have

$$\bar{\Delta}_{MAX} = (a + b) e^{j\phi} \quad (D-5)$$

Typical composite patterns of an amplitude-monopulse system are shown in Figure D.2(a). In keeping with the LEM/RR configuration, we have assumed that the crossover level on each pattern is at -3 decibels with respect to the beam maximum. The slope  $S$  of the patterns will approximate straight lines in the region of the crossover point, where

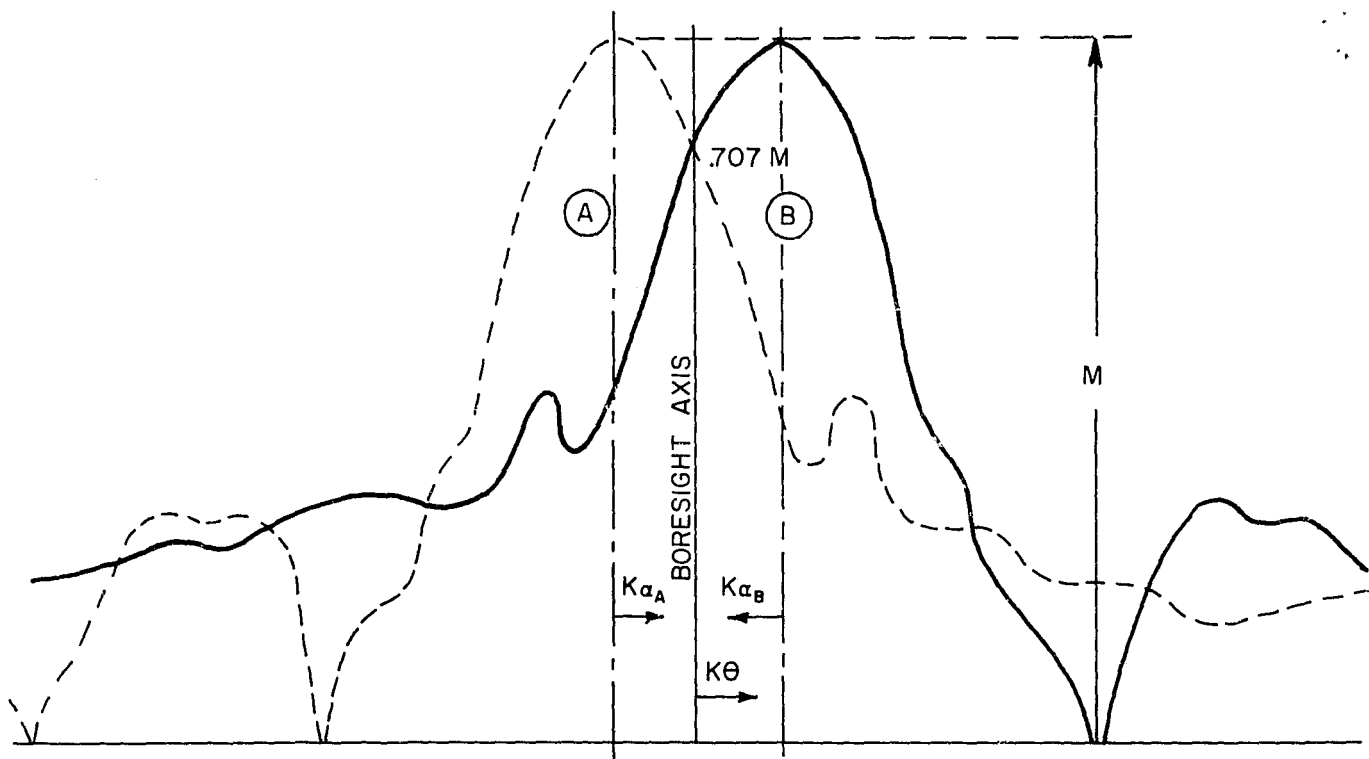
$$S = \frac{d(M \sin K\alpha / K\alpha)}{dK\theta} = \frac{d(M \sin K\alpha / K\alpha)}{dK\alpha} \cdot \frac{dK\alpha}{dK\theta} \quad (D-6)$$

Since  $\alpha_A = \theta + \gamma = 2\gamma - \alpha_B$ , where  $\gamma$  is one-half times the half-power beamwidth of the patterns, then

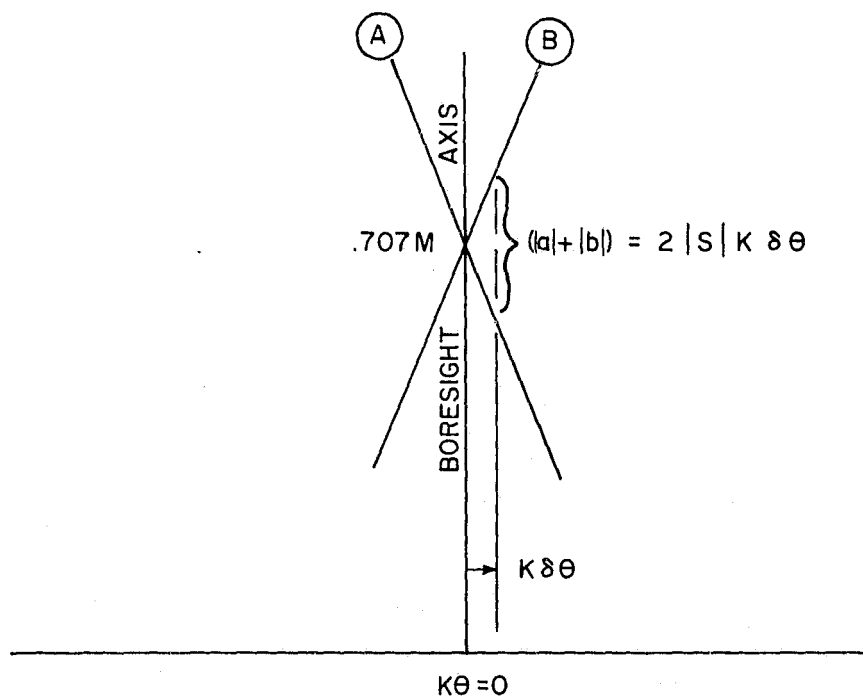
$$\frac{dK\alpha_A}{dK\theta} = -\frac{dK\alpha_B}{dK\theta} = 1, \quad (D-7)$$

and we have equal and opposite slopes for the patterns at the crossover point with the magnitude of the slopes given by

$$|S(\text{crossover})| = \frac{M(K\alpha \cos K\alpha - \sin K\alpha)}{(K\alpha)^2} \quad (D-8)$$



(a) Individual Patterns



(b) Straight-Line Approximation-Expanded Scale

Figure D.2. Amplitude-Monopulse Radiation Patterns About the Crossover (Boresight) Axis

As shown in Appendix E, the factor K is given by

$$K \doteq 2.28 D/\lambda \quad (D-9)$$

where D is the diameter of the main paraboloidal reflector and  $\lambda$  is the wavelength, and the half-power points of the patterns correspond to a value of approximately 1.39 radians for  $K\alpha$ . Thus, the slopes of the patterns in the region of the crossover point have magnitudes of

$$|S(\text{crossover})| \doteq M(1.39 \cos 1.39 - \sin 1.39)/(1.39)^2$$

or

$$|S(\text{crossover})| \doteq 0.38M \quad (D-10)$$

Assuming that the amplitude-monopulse system senses boresight as the condition of orthogonality between  $\bar{\Delta}$  and  $\bar{\Sigma}$ , the error in boresight direction is represented by the pattern angle  $K(\delta\theta)$  shown in Figure D.2(b), at which the patterns differ in magnitude by  $(a+b)$ . The difference phasor  $\bar{\Delta}$  at the physical angle  $\delta\theta$  off the optical boresight axis is given by

$$\bar{\Delta}_{\delta\theta} = \bar{\Delta}_{\text{MAX}} - 2S(K\delta\theta)$$

or

$$\bar{\Delta}_{\delta\theta} = (a+b)e^{j\phi} - 2S(K\delta\theta) \quad (D-11)$$

This change in the difference phasor causes  $\bar{\Delta}$  and  $\bar{\Sigma}$  to be orthogonal, as indicated in the phasor diagram of Figure D.3.

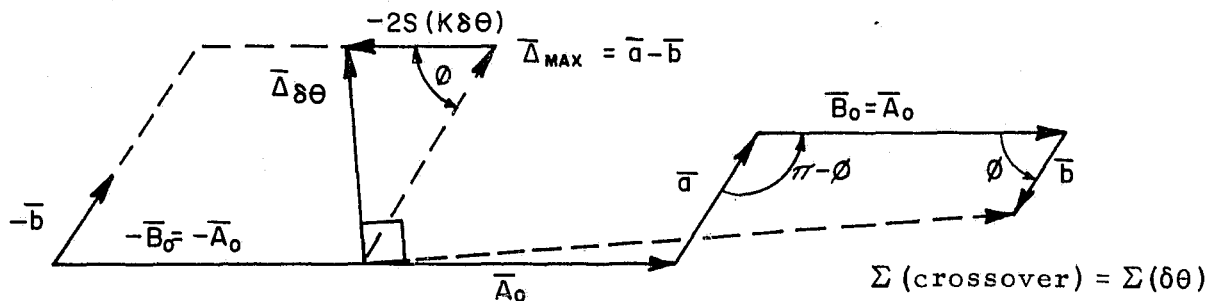


Figure D.3. Orthogonality of  $\bar{\Sigma}$  and  $\bar{\Delta}$  Phasors at Corrected Boresight

Solution for the angle  $\delta\theta$  which will produce this orthogonality for a general phase angle  $\phi$  is straightforward, but tedious. Only the result will be given here, where the procedure was to obtain the arguments of the  $\bar{\Delta}$  and  $\bar{\Sigma}$  phasors at the point  $K\delta\theta$  on the patterns, and to force  $\text{ARG}(\bar{\Delta}_{\delta\theta})$  to equal  $\text{ARG}(\bar{\Sigma}_{\delta\theta}) + \pi/2$ . It can be shown that this leads to

$$\delta\theta = \frac{1}{2SK} \frac{(a^2 - b^2) \cos 2\phi + (a+b) \cos \phi \sqrt{2} M}{(a-b) \cos \phi + \sqrt{2} M} \quad (D-12)$$

The purpose here is not an exhaustive analysis based on approximations, but rather an indication of the order of error one might expect for boresight measurements. Thus we will examine (D-12) only for the case which would produce maximum boresight error. This condition can be shown from equation (D-11) to occur for  $\phi$  equal to zero or  $\pi$  radians. Setting  $\phi$  equal to zero or  $\pi$  radians in (D-12), we have

$$|\delta\theta_{\text{MAX}}| = \frac{1}{2SK} \frac{(a^2 - b^2) + (a+b)\sqrt{2} M}{(a-b) + \sqrt{2} M} = \frac{a+b}{2SK} \quad (D-13)$$

Employing (D-9) and (D-10), this expression can be written

$$|\delta\theta_{\text{MAX}}| = \frac{0.577}{D/\lambda} \left[ \frac{a+b}{M} \right] \quad (D-14)$$

It is emphasized that the magnitude  $(a+b)/M$  represents a signal in the monopulse circuitry. For the LEM/RR, the ratio  $D/\lambda$  is approximately 20 and boresight errors of the order of one milliradian are of interest. Figure D.4 gives plots of the required suppression of extraneous energy in terms of the decibel level of  $(a+b)$  referenced to the individual pattern peaks  $M$  as a function of maximum allowable boresight error, with  $D/\lambda$  as a parameter. For these plots, equation (D-14) is used in the form

$$20 \log \frac{a+b}{M} = 20 \log (\delta\theta_{\text{MAX}}) (1.73 D/\lambda) \quad (D-15)$$

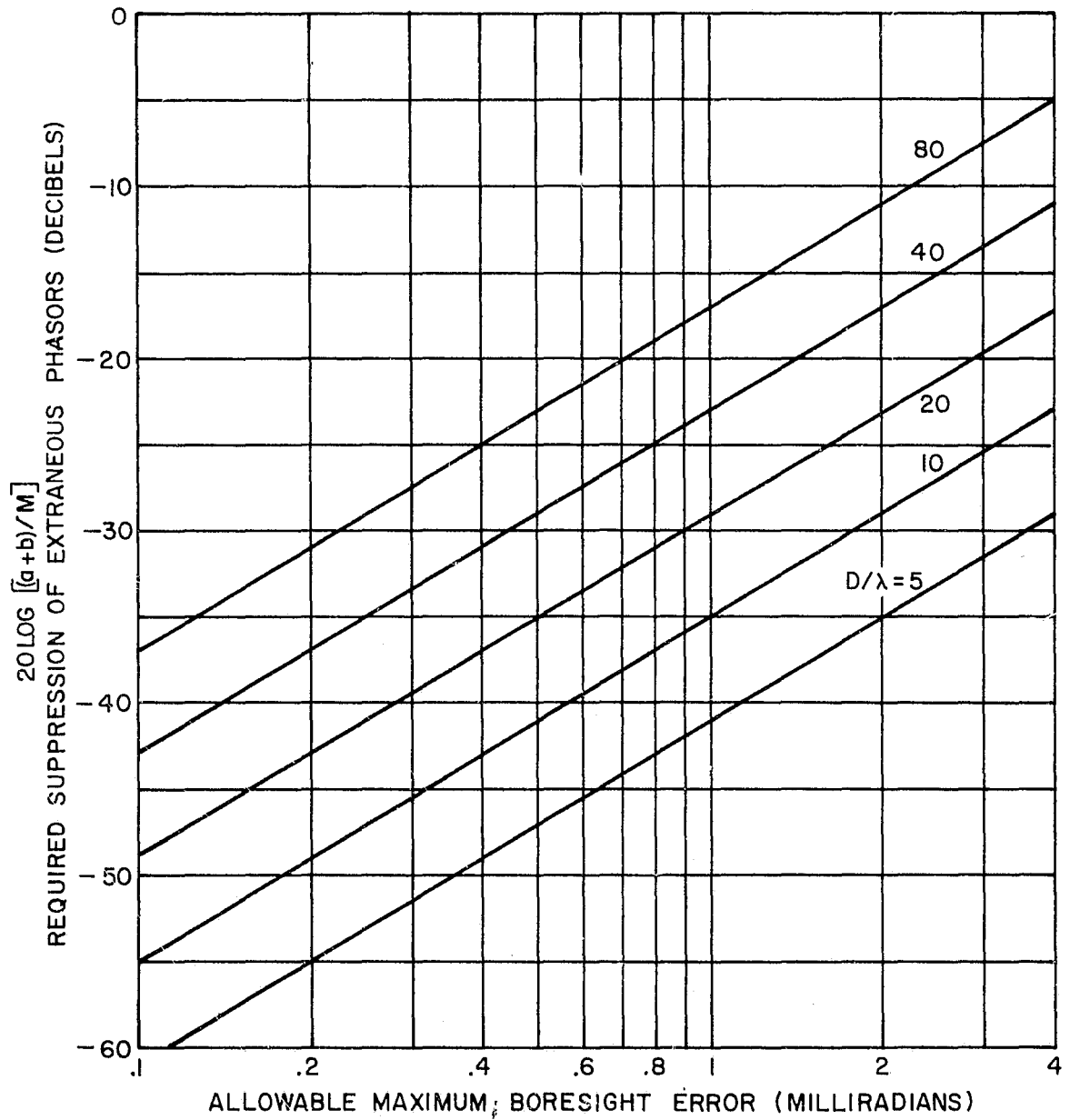


Figure D.4. Maximum Allowable Level of Extraneous Phasors in an Amplitude-Monopulse Circuit Versus Specified Maximum Boresight Errors

Equation (D-14) must be rewritten to determine boresight errors which can result from given magnitudes and angles of incidence of extraneous signals in terms of the ratio of the extraneous field  $\bar{E}_R$  to the direct path field  $\bar{E}_D$  incident on the test aperture (see paragraph A.6). Also the investigator must have rather detailed knowledge of the actual pattern structures of the monopulse device. In terms of the direct-path signal  $\bar{E}_D$  and the extraneous signal  $\bar{E}_R$ , the phasors of equations (D-1) and (D-2) can be written

$$\bar{A}_O = C E_D d_x^{\frac{1}{2}} = \bar{B}_O \quad , \quad (D-16)$$

$$\bar{a} = C E_R d_a^{\frac{1}{2}} e^{j\phi_1} \quad , \quad (D-17)$$

and

$$\bar{b} = C E_R d_b^{\frac{1}{2}} e^{j\phi_2} \quad , \quad (D-18)$$

where C is a constant which accounts for the intrinsic impedance of free-space, the efficiency of the antenna and the waveguide impedance. The directivity terms (d) are defined as follows:

$d_x$  is the directivity of the A and B patterns at the crossover point, which is postulated as before to be the point of incidence of  $\bar{E}_D$  ,

$d_a$  is the directivity of the A pattern at the point of incidence of  $\bar{E}_R$  ,

and

$d_b$  is the directivity of the B pattern at the point of incidence of  $\bar{E}_R$  .

It is noted that when both patterns intercept  $\bar{E}_R$  within their main lobes, the phases of  $\bar{a}$  and  $\bar{b}$  are constrained to be approximately equal. Since  $\bar{E}_D$  is postulated to arrive at the crossover point, then  $\bar{a}$  and  $\bar{b}$  are very nearly in phase with each other and with  $\bar{A}_O$  and  $\bar{B}_O$  , and  $\bar{A}_O$  is equal to  $\bar{B}_O$  . For this case the difference phasor

$$\bar{\Delta} = (\bar{A}_O + \bar{a}) - (\bar{B}_O + \bar{b}) = \bar{a} - \bar{b}$$

can be written, from (D-17) and (D-18) with  $\phi_1 = \phi_2 \doteq 0$  ,

$$\bar{\Delta} \doteq C \bar{E}_R (d_a^{\frac{1}{2}} - d_b^{\frac{1}{2}}) \quad .$$

Thus as  $d_a$  approaches  $d_b$ ,  $\bar{\Delta}$  approaches zero for any practical amplitudes of  $\bar{E}_R$ , however large. This means that extraneous signals which arrive at the test aperture from virtually the same direction as the direct path signal have little effect on the boresight direction.

The developments which follow apply to relatively large angles of incidence for the signal  $\bar{E}_R$ , which presents a high probability of the greater errors which occur for the assumed worst-case phasing  $\phi_1 = \phi_2 \pm \pi$  radians. The difference phasor at the crossover point is then written

$$\bar{\Delta}_{MAX} = C \bar{E}_R (d_a^{\frac{1}{2}} + d_b^{\frac{1}{2}}) , \quad (D-19)$$

and the difference phasor at the angle  $K\delta\theta$  is written as before as

$$\bar{\Delta}_{\delta\theta} = \bar{\Delta}_{MAX} - 2SK\delta\theta .$$

Since  $M = \sqrt{2} A_o$  by postulation, the above expression can be written

$$\bar{\Delta}_{\delta\theta} = \bar{\Delta}_{MAX} - 2(0.38/\sqrt{2} \bar{A}_o)(2.28 D/\lambda)\delta\theta . \quad (D-20)$$

The terms of (D-20) are all in phase with the phasor  $\bar{A}_o$ , so that there is a particular value for  $\delta\theta$  which will produce an absolute null for  $\bar{\Delta}_{\delta\theta}$ . (Since we have assumed worst case phasing for the extraneous signals and ideal phasing for the direct path signals, the boresight correction will result in an absolute null for  $\bar{\Delta}_{\delta\theta}$ .) In practice some quadrature component of  $\bar{\Delta}$  will always exist at boresight. The monopulse circuitry senses zero magnitude of the component of  $\bar{\Delta}$  which is in phase with  $\bar{\Sigma}$  (by sensing the condition of orthogonality between  $\bar{\Delta}$  and  $\bar{\Sigma}$ ). For the idealized conditions of the present analysis, this is tantamount to setting  $\bar{\Delta}_{\delta\theta} = 0$ ; the results of the analysis are thus applicable to the practical case in which a residual quadrature component of  $\bar{\Delta}$  exists at boresight.

Setting  $\bar{\Delta}_{\delta\theta}$  equal to zero in (D-20), and employing (D-16) and (D-19), we have

$$C_1 E_R (d_a^{\frac{1}{2}} + d_b^{\frac{1}{2}}) = 1.73\sqrt{2} C_1 E_D d_x^{\frac{1}{2}} (D/\lambda)\delta\theta . \quad (D-21)$$

Since  $d_o$  (the directivity at the peak of each pattern) is equal to  $2d_x$ , we can write (D-21) as

$$\frac{E_R}{E_D} = 1.73 (D/\lambda) \frac{d_o^{\frac{1}{2}}}{d_a^{\frac{1}{2}} + d_b^{\frac{1}{2}}} \delta\theta . \quad (D-22)$$

Equation (D-22) contains the same information as (D-14), where it is seen that

$$\frac{a+b}{M} = \frac{E_R (d_a^{\frac{1}{2}} + d_b^{\frac{1}{2}})}{E_D d_o^{\frac{1}{2}}} \quad (D-23)$$

Application of (D-22) to a particular problem requires that the ratio  $d_o^{\frac{1}{2}}/(d_a^{\frac{1}{2}} + d_b^{\frac{1}{2}})$  be either postulated or approximated from experimental pattern data; if we represent this ratio by the term  $\rho$ , then we can write (D-22) in decibel form as

$$20 \log \frac{E_R}{E_D} = 20 \log \delta \theta + 20 \log 1.73 D/\lambda + 20 \log \rho \quad (D-24)$$

The X-band amplitude-monopulse device employed in boresight comparison tests on the MILA range was designed to give a general simulation of a single-plane channel of the LEM/RR. The individual patterns of this antenna are illustrated in Chapter 4, Figure 4.12. Note that for angles of incidence  $\theta_R$  of the signal  $\bar{E}_R$  greater than approximately 2.5 degrees as measured from the boresight axis,  $\bar{E}_R$  enters one or both of the patterns through the sidelobes, and the effects of the sidelobes must be approximated in some way if a prediction is to be made of possible boresight error resulting from extraneous energy entering the aperture from angles greater than this value. For any similar amplitude-monopulse device whose patterns have the general character of a  $\sin x/x$  amplitude variation over the main lobes, we can define an angle  $\theta_R^1$  at which the sidelobe approximations must be applied in terms of the aperture ratio  $D/\lambda$ . That is, since the first null of typical  $\sin x/x$  patterns occurs at  $x \approx 2.5 x_{3\text{-db}}$ , then for  $\theta_R$  to correspond to main lobe reception of  $\bar{E}_R$  in both patterns we must have (see Figure D.2(a))

$$K\theta_R^1 \doteq 2.5K\alpha_{3\text{-db}} - K\alpha_{3\text{-db}} = 1.5K\alpha_{3\text{-db}} \quad (D-25)$$

or

$$\theta_R^1 \doteq 1.5\alpha_{3\text{-db}} \quad (D-26)$$

Since the beam angle in degrees at the half-power points is given by  $\alpha_{3\text{-db}} \doteq 35\lambda/D$  for such patterns, then

$$\theta_R^1 \doteq 1.5(35\lambda/D) = 52.5\lambda/D \text{ degrees} \quad (D-27)$$



One approach to the approximation of the pattern effects for  $\theta_R > \theta_R^1$  is to obtain an envelope of the sidelobe regions of the composite patterns. This approach was used to produce the qualitative data in the sidelobe reception portion of Figure D.5. This portion of Figure D.5 is a plot of equation (D-24) for an assumed boresight error of one milliradian, with the ratio  $\rho = d_o^{\frac{1}{2}} / (d_a^{\frac{1}{2}} + d_b^{\frac{1}{2}})$  approximated from the sidelobe envelope. It is emphasized that this plot is not intended to represent a quantitative comparison to the LEM/RR configuration. However, since the experimental device did provide a generalized simulation of a single channel of the LEM/RR, it is reasonable to assume that the envelope represents a useful estimate of the region of high probability for the effects of signals  $\bar{E}_R$  incident from angles greater than  $\theta_R^1$  off the boresight axis. The portion of Figure D.5 for  $\theta_R < \theta_R^1$  is also plotted from equation (D-24), but with the ratio  $\rho = d_o^{\frac{1}{2}} / (d_a^{\frac{1}{2}} - d_b^{\frac{1}{2}})$  calculated directly from  $\sin x/x$  tables. (See discussion following (D-18).)

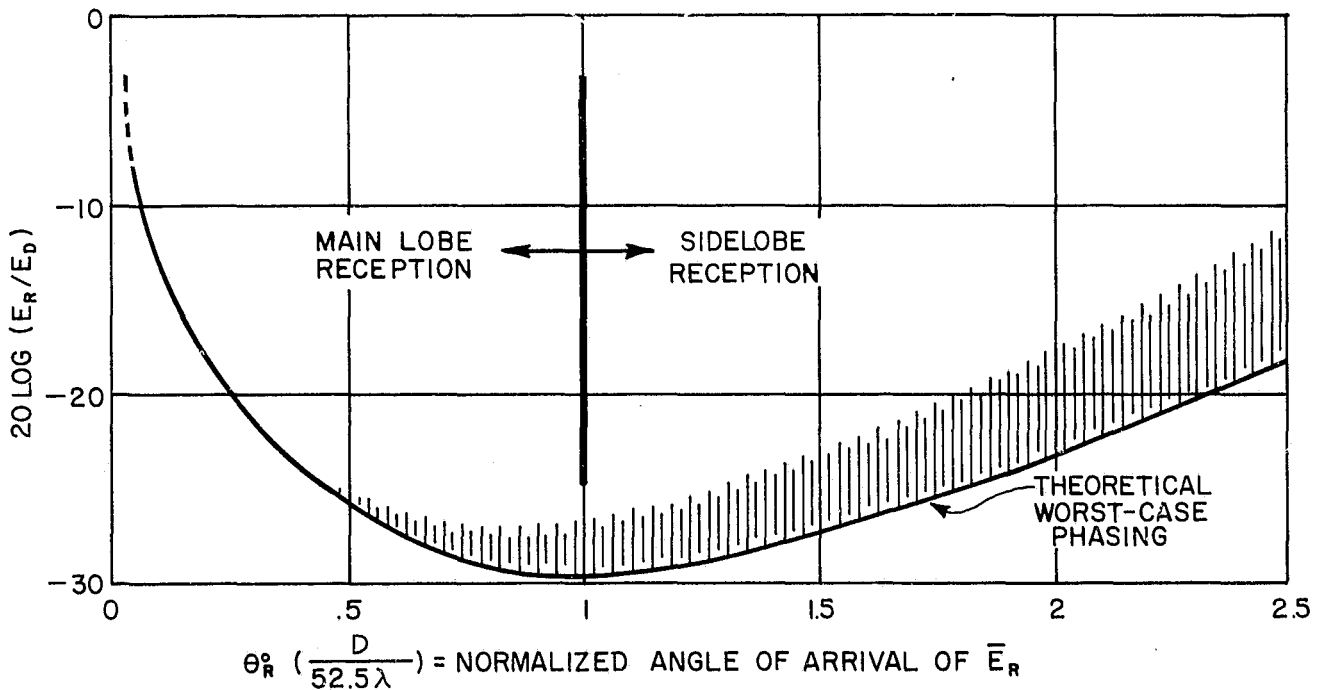


Figure D.5. Extraneous Signal Level Referenced to Direct-Path Signal Which Can Cause a One Milliradian Boresight Error. The curve is plotted versus the normalized angle of arrival of  $\bar{E}_R$ , and represents an approximation to the quantitative effect of signals  $\bar{E}_R$  which enter the the aperture from regions such that  $\theta_R > \theta_R^1$ .

To use Figure D.5 for other values of boresight error, the ordinates should be changed by a factor of  $+(-) 6$  decibels for each increase (decrease) in the boresight error by a factor of 2. (See Figure D.4.) As mentioned above, the aperture ratio for the LEM/RR is approximately 20, so that  $\theta_R'$  is very nearly 2.6 degrees. Although the information shown in Figure D.5 is based on approximations, useful qualitative conclusions can be drawn from the curves. For example, in the case of the LEM/RR, a reflected wave which arrives at an angle of greater than one-half degree from the boresight axis can cause a 0.25 milliradian boresight error if it is of the order of 30 to 40 decibels below the direct signal level. The most sensitive angle is between 2 and 4 degrees from the boresight axis. In this region, the reflected wave has a maximum effect on one channel and may have a minimum or additive effect on the other, resulting in the possibility of maximum error in the indicated boresight direction. Reflected signals entering this region of the patterns of the order of 45 decibels below the direct signal level can cause a 0.25 milliradian boresight error.

### D.3 Errors in Phase-Monopulse Systems

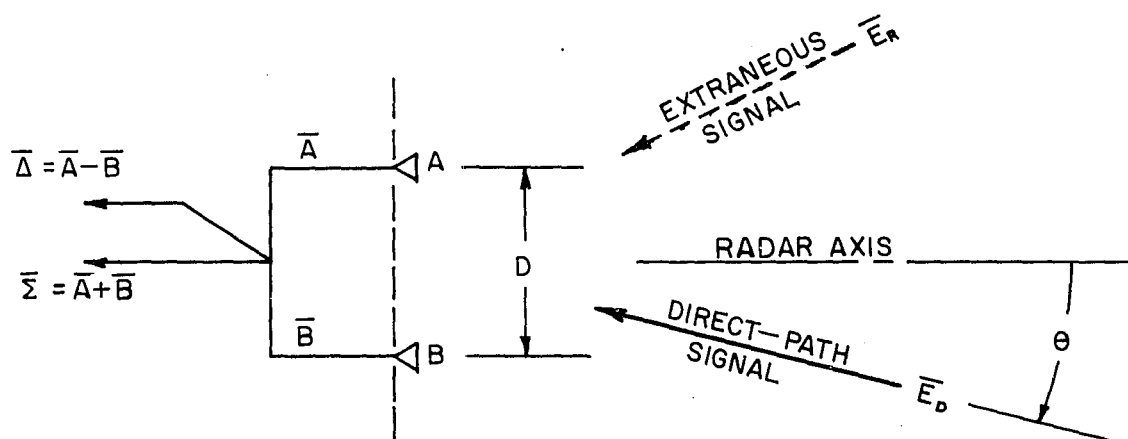
Consider a single-plane phase-monopulse system as shown schematically in Figure D.6(a). For direction sensing in the plane of the antenna pair, a typical procedure is to insert a calibrated phase shift into one signal channel of proper magnitude to cause the relative signal phases to be zero at a summation point. Assuming plane wave propagation, the angle  $\theta$  to the source of radiation would then be calculable from the equation

$$\sin\theta = \frac{\lambda}{2\pi D} \phi, \quad (D-25)$$

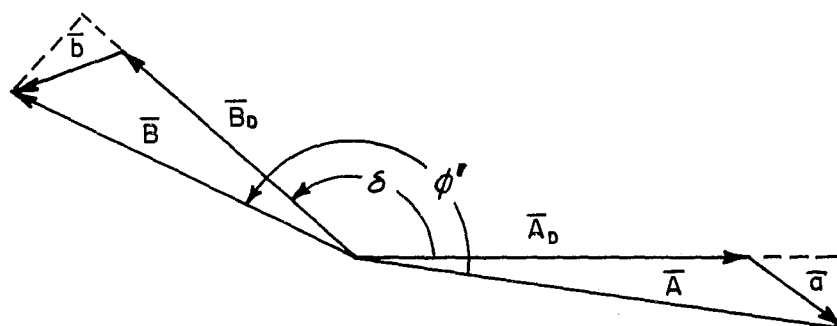
where  $D$  is the separation between the antennas,  $\phi$  is the measured differential phase and  $\lambda$  is the wavelength.

If an extraneous signal at the frequency of the direct-path signal is incident on the radar, the signal at the summation point of the monopulse circuitry will be a combination of phasors as depicted in Figure D.6(b). (As for the amplitude-monopulse analysis, the assumed  $e^{j\omega t}$  time dependence of all phasors is suppressed.) The individual phasors are as defined below.

$$\bar{A}_D = C \bar{E}_D d_A^{\frac{1}{2}} \text{ is the phasor in channel A due to the direct-path signal } \bar{E}_D,$$



(a) Single-Plane Phase-Monopulse Radar



(b) Alteration of the Monopulse-Circuit Phasors due to an Extraneous Signal

Figure D.6. The Effects of Wide-Angle Extraneous Signals on the Phasors of a Phase-Monopulse Radar Circuit

$\bar{B}_D = C \bar{E}_D d_B^{\frac{1}{2}} e^{j\delta}$  is the phasor in channel B due to the direct-path signal  $\bar{E}_D$ ,

$\bar{a} = C \bar{E}_R d_a^{\frac{1}{2}} e^{j\phi_a}$  is the phasor in channel A due to the extraneous signal  $\bar{E}_R$ ,

and

$\bar{b} = C \bar{E}_R d_b^{\frac{1}{2}} e^{j\phi_b}$  is the phasor in channel B due to the extraneous signal  $\bar{E}_R$ .

The directivity terms are defined as follows:

$d_A$  and  $d_B$  are the directivities of the A and B patterns, respectively, at the point of incidence of  $\bar{E}_D$ , and

$d_a$  and  $d_b$  are the directivities of the A and B patterns, respectively, at the point of incidence of  $\bar{E}_R$ .

The constant C accounts for the intrinsic impedance of free-space, the assumed identical antenna efficiencies, and the effects of the transmission paths of the monopulse circuitry.

To investigate the boresight error caused by the extraneous signal, we assume the monopulse to be adjusted so that  $\delta = \phi$ .\* In this case, the phase difference

$$\Delta\phi = \phi' - \phi \quad (D-26)$$

is proportional to the boresight error. From Figure D.6(b), with  $\delta$  set equal to  $\phi$ , we have

$$\Delta\phi = \phi' - \phi = \tan^{-1} \frac{-a \sin \sigma_a}{A_D + a \cos \sigma_a} + \tan^{-1} \frac{b \sin(\sigma_b - \phi)}{B_D + b \cos(\sigma_b - \phi)} \quad (D-27)$$

As in the amplitude-monopulse analysis of paragraph D.2, we will examine the effects of  $\bar{E}_R$  for worst-case phasing of  $\bar{a}$  and  $\bar{b}$ . It is seen from (D-27) that  $\Delta\phi$  will take on its maximum value for  $\sigma_a = (4n-1)\pi/2$  and  $\sigma_b = \phi + (4n-3)\pi/2$ , where  $n=1,2,3,\dots$ , for any particular set of magnitudes for the phasors. The maximum phase difference due to  $\bar{E}_R$  is thus

$$\Delta\phi_{MAX} = \tan^{-1} a/A_D + \tan^{-1} b/B_D \quad (D-28)$$

Typical phase-monopulse systems employ antennas of low directivity, so that a highly probable condition is one for which

$$|\bar{A}_D| \doteq |\bar{B}_D|, \quad |\bar{a}| \doteq |\bar{b}| \quad (D-29)$$

Assuming that these approximations apply, (D-28) becomes

$$\Delta\phi_{MAX} \doteq 2 \tan^{-1} \frac{a}{A_D} \doteq 2 \tan^{-1} \frac{b}{B_D}, \quad (D-30)$$

---

\*For  $\delta = \phi$ , the monopulse would indicate true boresight in the absence of  $\bar{E}_R$ .

or

$$\Delta\phi_{MAX} \doteq 2 \frac{E_R d_a^{\frac{1}{2}}}{E_D d_A^{\frac{1}{2}}} \doteq 2 \frac{E_R d_b^{\frac{1}{2}}}{E_D d_B^{\frac{1}{2}}} \quad (D-31)$$

for the wide angles of interest where  $E_R d_a^{\frac{1}{2}}$  will be small in comparison to  $E_D d_A^{\frac{1}{2}}$ .

For the purpose of this analysis it is logical to assume that the initial setting of  $\delta=\phi$  was accomplished with the direct-path signal incident near the boresight axis, so that equation (D-25) may be written

$$\sin\theta \doteq \theta \doteq \frac{\lambda}{2\pi D} \Delta\phi$$

or

$$\Delta\theta \doteq \frac{\lambda}{2\pi D} \Delta\phi \quad (D-32)$$

From (D-31) and (D-32) we can express the maximum boresight error  $\Delta\theta_{MAX}$  as

$$\Delta\theta_{MAX} \doteq \frac{\lambda}{2\pi D} \cdot \frac{2E_R d_a^{\frac{1}{2}}}{E_D d_A^{\frac{1}{2}}} \text{ radians.} \quad (D-33)$$

Let the ratio  $(d_A/d_a)^{\frac{1}{2}}$  be equal to  $\rho'$ . Then from (D-33) we have

$$20 \log \frac{E_R}{E_D} = 20 \log \left( \frac{\pi D}{\lambda} \right) + 20 \log \rho' + 20 \log \Delta\theta_{MAX} \quad (D-34)$$

If the ratio  $\rho'$  is known or can be approximated, equation (D-34) will allow calculation of the required suppression of extraneous energy to satisfy a specification of maximum allowable boresight error.

As an example of particular interest for the MILA facility, consider a test situation at 2.3 GHz with  $D=24$  inches. Assume an effective peak gain for each antenna of 10 decibels, and an approximate gain of 0 decibel at the point of incidence of  $\bar{E}_R$ . Then

$$20 \log \frac{E_R}{E_D} = 20 \log (14.7) + 10 + 20 \log \Delta\theta_{MAX} \text{ decibels,}$$

or

$$20 \log \frac{E_R}{E_D} \doteq 33 + 20 \log \Delta\theta_{MAX} \text{ decibels.}$$

For a one milliradian allowable error, this example case would require the extraneous signal to be suppressed to a level of the order of -27 decibels with respect to the direct-path signal. Accuracies of the order of 0.2 milliradian would allow a maximum extraneous signal level of only -41 decibels with respect to  $\bar{E}_D$ .

Figure D.7 gives plots of equation (D-34) as a function of boresight error for  $20 \log \rho'$  equal to 10 decibels, with the ratio  $D/\lambda$  as a parameter. To apply Figure D.7 to other directivity ratios  $\rho'_1$ , one would change the ordinate scale by a factor  $(20 \log \rho'_1) - 10$  decibels.

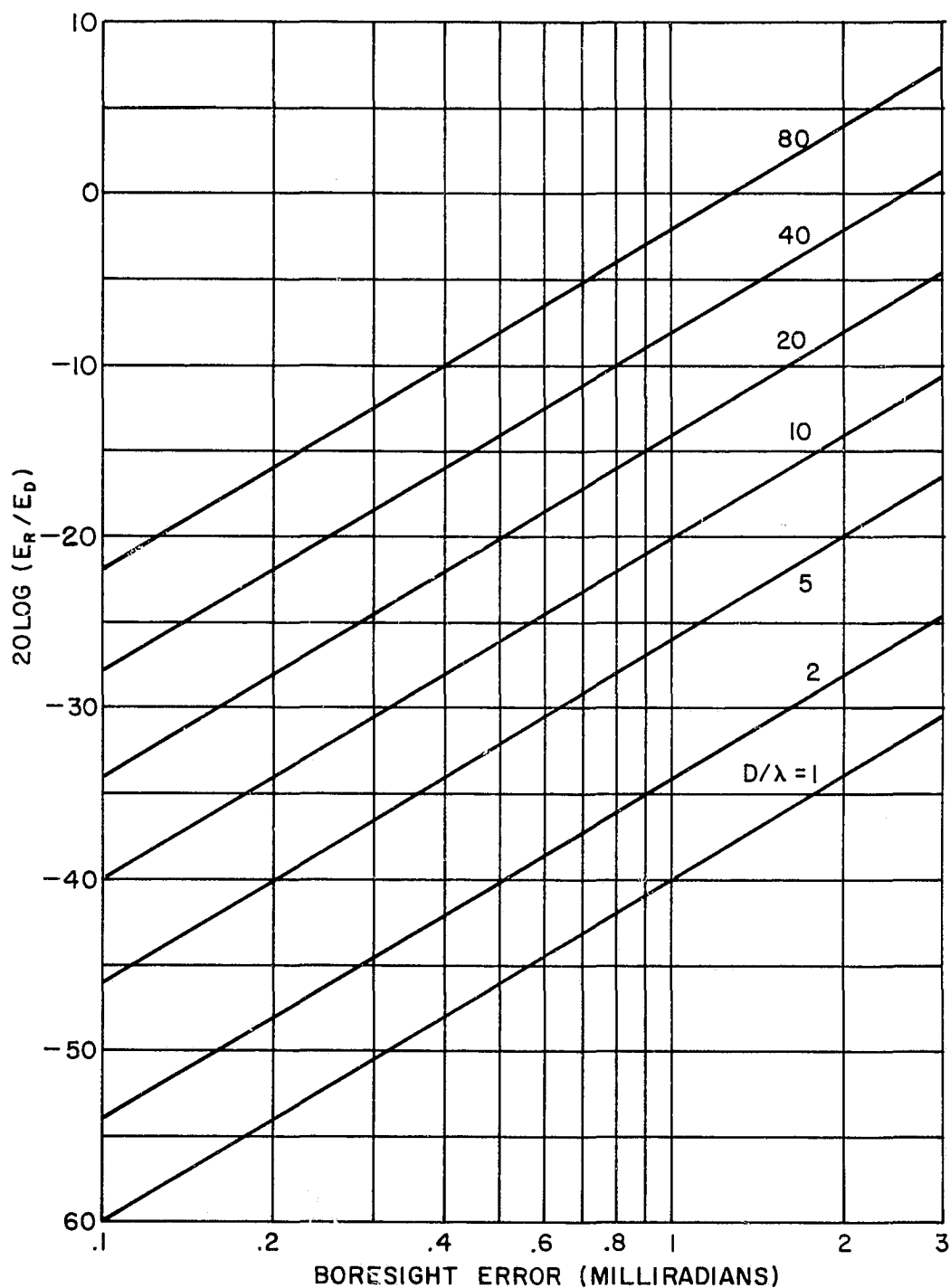


Figure D.7. Required Suppression of Extraneous Energy Incident on a Phase-Monopulse Radar Versus Boresight Error for Worst-Case Phasing at the Summation Point.

The curves are plotted for  $20 \log(d_A^{1/2}/d_a^{1/2}) = 10$  decibels.

# APPENDIX E APPARENT SOURCE HEIGHT VERSUS ELEVATION SQUINT ANGLE\* FOR THE GROUND-REFLECTION MODE

As shown in Appendix A, the magnitude and phase of the reflection coefficient for either horizontal or vertical polarizations of the transmitted wave are very nearly 1.0 and  $\pi$  radians, respectively. In paragraph A.5, it was shown that operation in the ground-reflection mode requires the source antenna to be located at a height given by (see Figure E.1)

$$h_t \doteq \frac{\lambda R_0}{4h_r} \quad , \quad (E-1)$$

and that for optimum phase conditions over the test aperture, the axis of the radiated pattern should be oriented in the vertical plane such that the direct-path

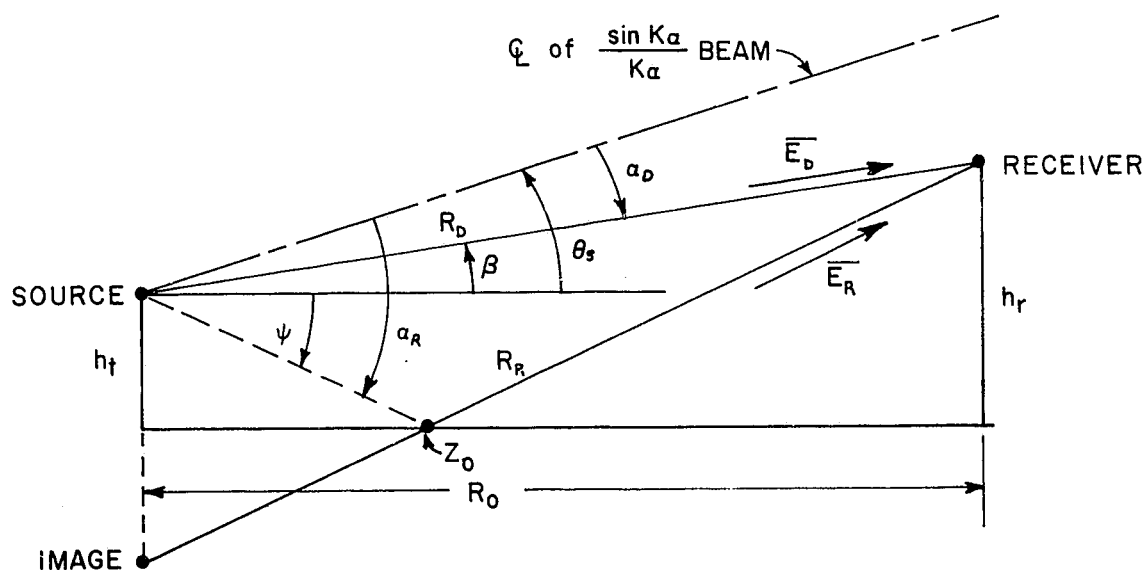


Figure E.1. Parameters for Consideration of the Effect of Variations in Elevation Squint Angle on the Operation of a Ground-Reflection Antenna Test Range

signal  $\bar{E}_D$  and the reflected signal  $\bar{E}_R$  are equal in amplitude. If all the above conditions are satisfied, the results of Appendices B and C indicate that the apparent height of the source of radiation will be given by (see for example

\*See section 2.2 for definition of "squint angle".



equation (B-20)

$$H \doteq \left[ \frac{\cos\beta - \cos\psi}{\cos\beta + \cos\psi} \right] \frac{\lambda R_o}{4h_r} \quad (E-2)$$

Ground reflection antenna test ranges are designed with  $h_t$  and  $h_r \ll R_o$ , so that  $R_R \doteq R_D \doteq R_o$ . Therefore the cosine terms in (E-2) will be approximately equal to unity, and H will be approximately zero for the ratio  $k = E_R/E_D$  equal to unity. If an improper elevation squint angle is employed, k will not be unity, and (E-2) must be replaced by the expression

$$H = \left[ \frac{\cos\beta - k \cos\psi}{\cos\beta + k \cos\psi} \right] \frac{\lambda R_o}{4h_r} \quad (E-3)$$

The object of the following derivation is to express the ratio k in terms of the elevation squint angle  $\theta_s$ , in order to provide a theoretical basis for correlation of experimental boresight comparison measurement data as discussed in Chapter 4. The transmitted radiation pattern is assumed to be symmetrical about the axis of the source antenna, with an amplitude A which varies as

$$A = \frac{A_o \sin(K\alpha)}{K\alpha} \quad , \quad (E-4)$$

and the half-power beamwidth of the main lobe in radians is assumed to be given by the familiar expression for typical microwave antennas of diameter d,

$$BW(-3 \text{ db}) = \frac{1.22\lambda}{d} \quad (E-5)$$

The reflected wave  $\bar{E}_R$  is assumed to be produced by specular reflection from the point of specular reflection in accordance with the quasi-geometrical optics approach as discussed in paragraph A.2.

The proportionality constant K in (E-4) is found as follows. If  $\alpha_i$  is an angle measured in radians from the axis of the main lobe, then at  $A = 0.707 A_o$ ,

$$\alpha_i = \alpha_{3 \text{ db}} = \frac{1}{2} (BW(-3 \text{ db})) = \frac{0.61\lambda}{d} \quad (E-6)$$

For this same amplitude, we find from  $\sin x/x$  tables that the product  $K\alpha_{3 \text{ db}}$  must be given in radians by

$$K\alpha_{3 \text{ db}} = 1.39 \quad (E-7)$$

From (E-6) and (E-7) it follows that,

$$K = \frac{2.28d}{\lambda} \quad (E-8)$$

where  $d$  and  $\lambda$  are expressed in the same units.

Referring to Figure E.1, and still on the assumption of a unity reflection coefficient, the ratio of the reflected signal to the direct-path signal is given by

$$k = \frac{\frac{A_o \sin K \alpha_R}{K \alpha_R}}{\frac{A_o \sin K \alpha_D}{K \alpha_D}} \quad (E-9)$$

From the geometry,

$$\alpha_R = \theta_s + \psi \quad (E-10)$$

and

$$\alpha_D = \theta_s - \beta \quad (E-11)$$

Since  $R_o$  is large compared to  $(h_r + h_t)$ ,

$$\psi = \tan^{-1} \frac{h_r + h_t}{R_o} \approx \frac{h_r + h_t}{R_o} \quad (E-12)$$

and

$$\beta = \tan^{-1} \frac{h_r - h_t}{R_o} \approx \frac{h_r - h_t}{R_o} \quad (E-13)$$

We can now write (E-3) in terms of the range parameters  $R_o$ ,  $h_r$ ,  $\psi$  and  $\beta$ , the source parameters  $d$  and  $\theta_s$ , and the wavelength  $\lambda$  as

$$H = \frac{\lambda R_o}{4h_r} \left[ \frac{(\theta_s + \psi) \sin\left(\frac{2.28d}{\lambda} [\theta_s - \beta]\right) - (\theta_s - \beta) \sin\left(\frac{2.28d}{\lambda} [\theta_s + \psi]\right)}{(\theta_s + \psi) \sin\left(\frac{2.28d}{\lambda} [\theta_s - \beta]\right) + (\theta_s - \beta) \sin\left(\frac{2.28d}{\lambda} [\theta_s + \psi]\right)} \right] \quad (E-14)$$

As an example of particular interest for the MILA range, consider the case where

$d = 1$  foot (paraboloid)

$R_o = 1000$  feet

$$\lambda = 0.098 \text{ foot (f = 10 GHz)}$$

$$h_r = 30 \text{ feet}$$

$$h_t = \frac{\lambda R_o}{4h_r} \doteq 0.82 \text{ foot.}$$

We then have

$$\beta \doteq 0.0292 \text{ radian}$$

$$\psi \doteq 0.0308 \text{ radian}$$

and

$$K \doteq 23.3$$

Substitution of these values into (E-14) yields the theoretical curve of apparent source height  $H$  versus elevation squint angle  $\theta_s$  which is shown in Figure E.2. The ratio  $k = E_R/E_D$  is also plotted versus  $\theta_s$  in Figure E.2. A comparison of the theoretical and experimental values of  $H$  versus  $\theta_s$  is given in Chapter 4, Figure 4.6.

It is emphasized that in the ground-reflection mode the apparent source height is not critically dependent on fine adjustments of  $\theta_s$ . Although the optimum case is represented by a  $\theta_s$  that causes  $k$  to be equal to unity, Figure E.2 shows that insofar as boresight comparison measurements are concerned,  $k$  could vary from approximately 0.6 to 1.6 with only a 0.4 milliradian change in the indicated boresight direction between these extremes. This variation in  $k$  corresponds approximately to a  $\pm 2.3$  degree excursion in  $\theta_s$ . Since the assumption of a unity reflection coefficient is quite good for the MILA range, the indicated procedure for ground-reflection operation is to set the source height at  $\lambda R_o/4h_r$  and adjust the elevation squint angle to a declination below the horizontal so that the beam axis bisects the angle  $(\psi + \beta)$ , which will cause  $k$  to be very nearly unity. It is seen from Figure E.1 that the latter adjustment is accomplished by setting  $\theta_s$  equal to

$$\theta_{s_o} = \frac{1}{2}(\psi + \beta) - \psi \quad . \quad (E-15)$$

Using (E-12) and (E-13), it is seen that

$$\theta_{s_o} \doteq \frac{1}{2} \left[ \frac{h_r + h_t}{R_o} + \frac{h_r - h_t}{R_o} \right] - \frac{h_r + h_t}{R_o} = \frac{-h_t}{R_o}$$

which can be written

$$\theta_{s_o} \doteq \frac{-\lambda}{4h_r} \quad \text{radian.} \quad (E-16)$$

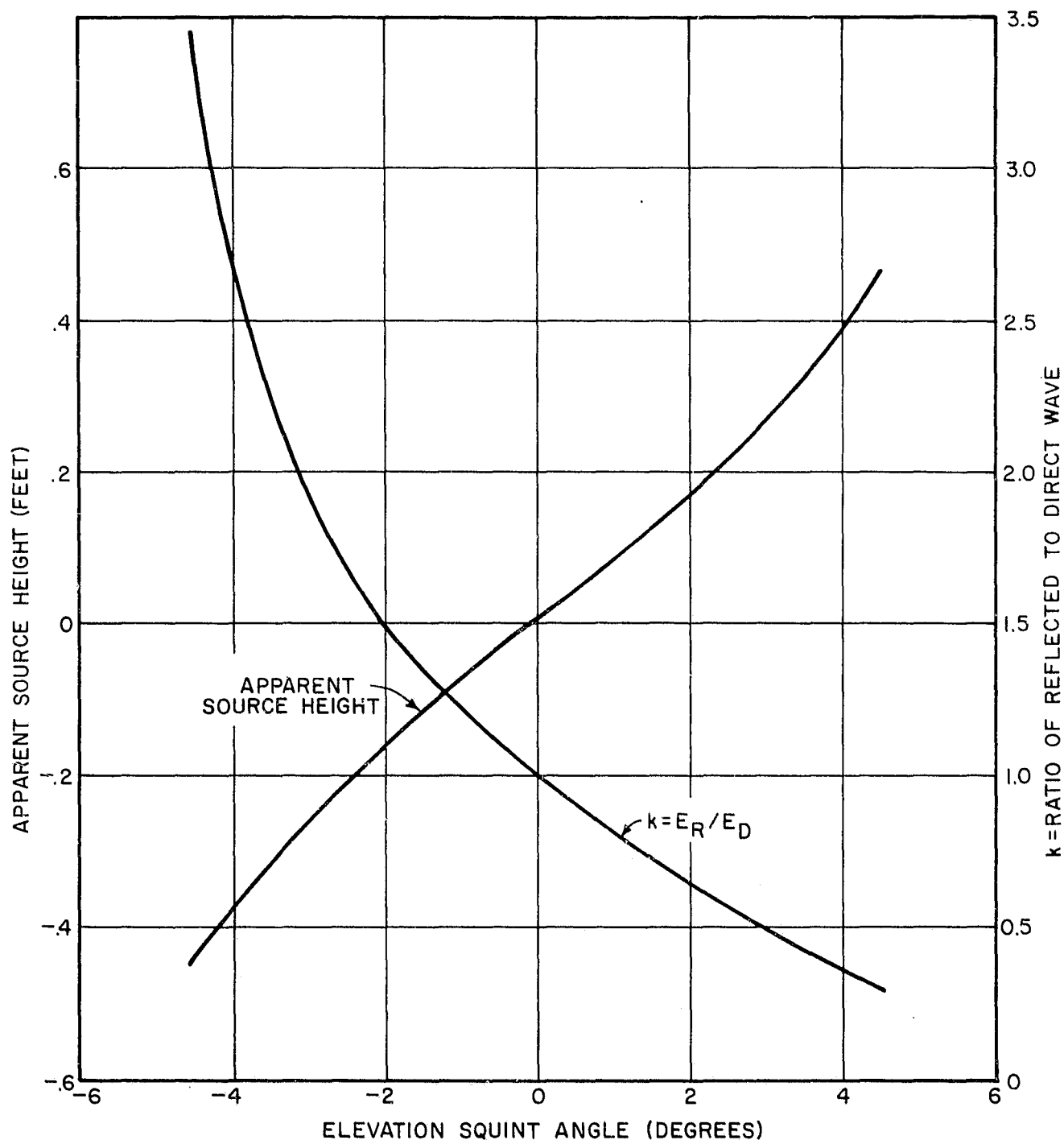


Figure E.2. Apparent Source Height and the Ratio of Reflected- to Direct-Wave Amplitude as a Function of Elevation Squint Angle in the Ground-Reflection Mode. (Curves are for a 1-foot paraboloidal source antenna operating at a frequency of 10 GHz, with  $R_o = 1000$  feet and  $h_r = 30$  feet.)

For the example above, this corresponds to  $\theta_{s_0} \doteq -0.05$  degree. Figure E.3 gives a plot of  $\theta_{s_0}$  in degrees versus frequency from L-band to X-band.

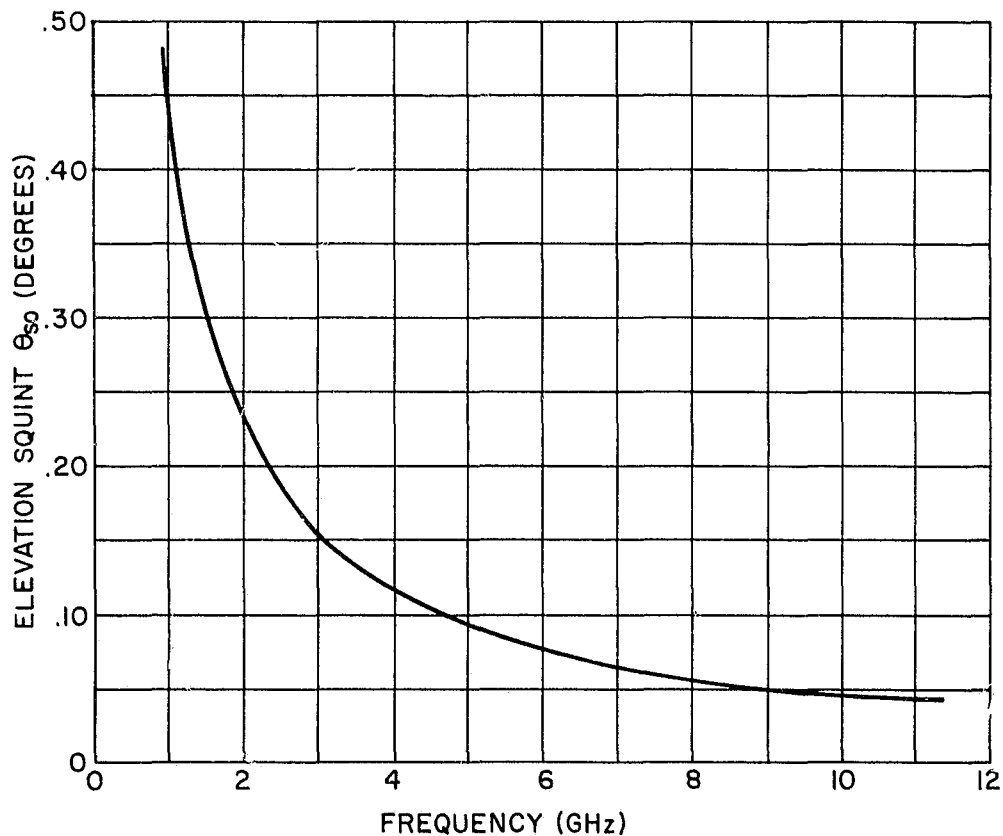


Figure E.3. Elevation Squint Settings Versus Frequency Ground-Reflection Operation of the MILA Range. (The calculated squint settings are for an assumed unity reflection coefficient and for  $h_t = \lambda R_0 / 4h_r$ .)

It is emphasized that the indicated procedure will result in slightly different apparent heights of the source for horizontal and vertical polarizations. The apparent heights depend on both the coefficients of reflection of the surface and

on the directivities of the transmitted pattern for the two polarizations. While it is possible for these effects to work in opposition and cancel each other, in practical cases one or the other is likely to predominate resulting in a small difference in the apparent source height for the two polarizations. However, for a practically symmetrical transmitted pattern and a close-tolerance surface such as the MILA range, the measurable difference in the apparent source location for the two polarizations will be due primarily to the change in reflection coefficient, and will represent only a small bias error in boresight comparison measurements. (See paragraph 4.1.1.3.) A further implication here is that some depolarization of general elliptically polarized energy will always occur upon reflection from practicable antenna test range surfaces.

The very small but non-zero shift in apparent height for the two linear polarizations can be explained from consideration of the relation of the factor  $k = E_R / E_D$  to the reflection coefficients for a smooth surface. From (E-12) and (E-13), we see that (E-3) can be written for the MILA range at X-band frequencies as

$$H \doteq \left( \frac{1-k}{1+k} \right) h_t \quad , \quad (E-17)$$

since  $h_r \gg h_t = \lambda R_o / 4h_r$  so that  $\cos \beta \doteq \cos \psi \doteq 1$ . Assuming that the elevation squint angle  $\theta_s$  has been adjusted as discussed in connection with equation (E-16), any change in  $k$  as one goes from one linear polarization to another depends primarily on the resulting change in reflection coefficient magnitude. Referring to equations (A-14) and (A-15) of Appendix A, we see that the magnitude of the ratio of the reflection coefficients for horizontal (normal) and parallel (vertical) components of the transmitted field is given by

$$\left| \frac{\rho_{o,n}}{\rho_{o,p}} \right| = \left| \frac{1 + \cos \theta \sqrt{\epsilon'_r - \sin^2 \theta} - \cos^2 \theta}{1 - \cos \theta \sqrt{\epsilon'_r - \sin^2 \theta} - \cos^2 \theta} \right| \quad (E-18)$$

Since  $\epsilon'_r$  will be greater than unity, we see that this ratio is always greater than unity for any  $\theta$  less than  $\pi/2$  radians. It follows that the factor  $k$  in equation (E-17) will be slightly larger for horizontal polarization than for vertical polarization. Since  $k$  is equal to or less than unity for practical test configurations, the indicated apparent source height will be slightly lower for horizontal polarizations than for vertical polarizations.

## APPENDIX F

### DIFFRACTION FENCE PLACEMENTS ON A PLANAR RANGE SURFACE

#### F.1 Introduction

In this appendix an analysis is presented of the problem of placement of diffraction fencing for operation in the elevated mode over a smooth, planar range surface. A range surface such as that at MILA can be considered to be a lossy dielectric. Several authors<sup>F-1</sup> have treated the problem of reflection from lossy dielectric surfaces; the bulk of such work deals with theoretical approximations to solutions of complex boundary value problems. When the reflecting surface is essentially smooth and planar, as is the MILA range, it has been shown that the energy which reaches a receiving point via the reflecting surface appears to originate primarily at a single image of the source. This image is located along the line from the receiving point through the "point of specular reflection"\* (see Figures A.4 and F. 1) in the range surface. Screening of a portion of the range surface by diffraction fencing will produce a reduction in the contribution of

---

<sup>F-1</sup> Clarke, R.H., and G.O. Hendry, "Prediction and Measurement of the Coherent and Incoherent Power Reflected from a Rough Surface," IEEE Transactions on Antennas and Propagation, Volume AP-12, No. 3, May 1964; pp. 353-363.

Beckmann, Petr, "Shadowing of Random Rough Surfaces," IEEE Transactions on Antennas and Propagation, Volume AP-13, No. 3, May 1965; pp. 384-388.

Twersky, Victor, "Signals, Scatterers, and Statistics," IEEE Transactions on Antennas and Propagation, November 1963; pp. 668-680.

Twersky, Victor, "On Scattering and Reflection of Electromagnetic Waves by Rough Surfaces," IRE Transactions on Antennas and Propagation, January 1957; pp. 81-90.

Beckmann, Petr, and Andre Spizzichino, The Scattering of Electro-Magnetic Waves from Rough Surfaces, The MacMillan Company, 1963; pp. 9-10.

Silver, S., Microwave Antenna Theory and Design, Radiation Laboratory Series, Volume 12, Chapter 5, McGraw-Hill Co., 1949.

Kerr, Donald E., Propagation of Short Radio Waves, McGraw-Hill Book Company, 1951; Volume 13, Chapter 5.

\*The term "point of specular reflection" applies literally only in the case of geometrical optics where the wavelength approaches zero. Specular reflection at wavelengths in the microwave frequency region is actually the superimposed effect of elemental contributions reradiated from all illuminated regions of the surface. The relative amplitudes and phases of such contributors can be examined by dividing the surface into Fresnel zones, discussed in the following paragraphs.

reflected energy to the field at the receiver, but simultaneously introduces variations in the receiving-aperture field due to diffraction effects. A discussion of diffraction effects is presented in terms of the MILA range geometry in paragraph F.3. Tabulations and plots of Fresnel zone and diffraction fence parameters of specific importance to the MILA facility are given in this appendix.

## F.2 Fresnel Zones on a Planar Range Surface

Consider Figure F.1, which represents an elevated antenna range having a source antenna at height  $h_t$ , a receiving antenna at height  $h_r$ , and a separation between the bases of the antenna support structures of  $R_o$ . The shortest path between the source and receiver via the range surface is given by

$$r_o = \left[ (h_t + h_r)^2 + R_o^2 \right]^{\frac{1}{2}} \quad (F-1)$$

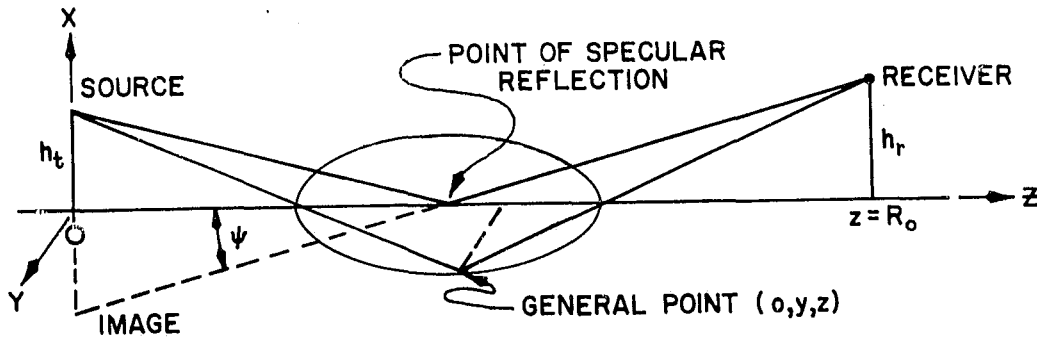


Figure F.1. Sketch of Fresnel Zone Boundary on a Planar Range Surface

This path defines the point of specular reflection, which is the center of the region of constant phase, at which the grazing angle  $\psi$  is given by

$$\sec \psi = \frac{r_o}{R_o} = \left[ \frac{(h_t + h_r)^2 + R_o^2}{R_o^2} \right]^{\frac{1}{2}} \quad (F-2)$$

For any other point  $(o, y, z)$  on the range surface, the path length via the surface



is given by

$$r = \left[ h_t^2 + y^2 + z^2 \right]^{\frac{1}{2}} + \left[ h_t^2 + y^2 + (R_o - z)^2 \right]^{\frac{1}{2}} . \quad (F-3)$$

Since  $r > r_o$ , the phase of the wave traveling along  $r$  will lag behind that of the wave traveling along  $r_o$  by  $\Delta\Phi$  radians, where

$$\Delta\Phi = \frac{2\pi}{\lambda} (r - r_o) , \quad (F-4)$$

and  $\lambda$  is the wavelength of propagation.

By definition, the locus of points  $(o, y_i, z_i)$  for which

$$\Delta\Phi_i = N\pi \quad (F-5)$$

or

$$r_i - r_o = \frac{N\lambda}{2} , \quad N = 1, 2, 3, \dots \quad (F-6)$$

determines the outer boundary of the Nth Fresnel zone.\* The inner boundary of the Nth zone is given by

$$r_i - r_o = (N - 1) \frac{\lambda}{2} ; \quad (F-7)$$

energy arriving at the receiving point from the outer bound of a Fresnel zone lags in phase by  $\pi$  radians that energy arriving from the inner bound of the zone. The pertinent parameters of a given Fresnel zone are the center, length and width of its outer bound, and the area enclosed by its bounds. These parameters can be calculated from (F-6), which is written in terms of the range dimensions and coordinates, the wavelength and the Fresnel zone number as

$$\left[ h_t^2 + y^2 + z^2 \right]^{\frac{1}{2}} + \left[ h_r^2 + y^2 + (R_o - z)^2 \right]^{\frac{1}{2}} - \left[ (h_t + h_r)^2 + R_o^2 \right]^{\frac{1}{2}} = \frac{N\lambda}{2} . \quad (F-8)$$

Equation (F-8) shows that the successive outer bounds of the Fresnel zones describe a set of expanding ellipses whose major axes lie on the range axis. The algebraic manipulations of the solution of (F-8) for the pertinent parameters will not be given here; the solution and resulting expressions are simplified by the

---

\* Although Fresnel zones are strictly defined for point source radiators, for practical antenna range geometries Fresnel zones for a point in the receiving aperture can be defined by regarding the transmitting antenna to be a point source located at the center-of-phase of its aperture.

introduction of the following definitions:

$$F_1(N, \lambda, \psi) = \left( \frac{N\lambda}{2R_o} + \sec\psi \right) \quad (F-9)$$

$$F_2(N, \lambda, \psi) = \frac{(h_r^2 - h_t^2)/R_o^2}{F_1^2 - 1} \quad (F-10)$$

and

$$F_3(N, \lambda, \psi) = \frac{(h_r^2 + h_t^2)/R_o^2}{F_1^2 - 1} \quad (F-11)$$

It can be shown that (F-8) through (F-11) yield the following expressions for the parameters of the outer-bound ellipse of the Nth Fresnel zone:

$$\text{Center:} \quad z_N = \frac{R_o}{2} (1 - F_2) \quad (F-12)$$

$$\text{Length:} \quad \ell_N = R_o F_1 (1 + F_2^2 - 2F_3)^{\frac{1}{2}} \quad (F-13)$$

$$\text{Width:} \quad w_N = \left[ \frac{F_1^2 - 1}{F_1^2} \right]^{\frac{1}{2}} \ell_N \quad (F-14)$$

$$\text{Area:} \quad A_N = \frac{\pi}{4} \ell_N w_N \quad (F-15)$$

The area enclosed within adjacent zone boundaries is then given by

$$S_N = A_N - A_{N-1} = \frac{\pi}{4} (\ell_N w_N - \ell_{N-1} w_{N-1}), \quad (F-16)$$

which is a slowly decreasing function of N.

If the illumination were truly isotropic, contributions to the received field from successive Fresnel zones near the point of specular reflection would be essentially constant in amplitude. However, for practical directive microwave antennas, the relative illumination of the various zones depends on both the height and pointing-angle of the source of radiation. For example, consider the particular case of the 18th Fresnel zone on the 1000-foot MILA range, with  $h_t = h_r = 30$  feet

and  $\lambda = 0.098$  foot (10 GHz). This zone has the following parameters:\*

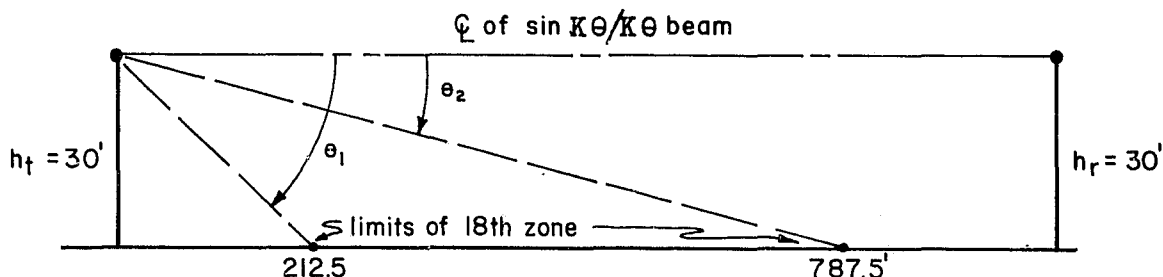
$$z_{18} = 500 \text{ feet}$$

$$\ell_{18} = 575 \text{ feet}$$

$$w_{18} = 42 \text{ feet}$$

The 18th zone for this case thus extends from 212.5 feet to 787.5 feet along the range axis, as measured from the source tower. Assume that a source antenna having a 3-decibel beamwidth of 0.122 radian has its main beam centered on the receiver, and that the beam has a typical  $\sin K\theta/K\theta$  amplitude characteristic.

The situation is as sketched below.



From the geometry,

$$\theta_1 = \tan^{-1} 30/212.5 \doteq 8 \text{ degrees}$$

and

$$\theta_2 = \tan^{-1} 30/787.5 \doteq 2 \text{ degrees.}$$

As shown in Appendix E, these physical angles correspond to values of  $K\theta$  of approximately 3.2 radians and 0.8 radian, respectively, referenced to the beam axis. From  $\sin x/x$  tables, it is seen that the illumination at the receiving-end point compared to the beam maximum will be approximately -1.1 decibel, and the source-end point will be in the region of the first null of the beam, or at some -30 decibels or less relative to the receiving-end point.

---

\*Tabulated parameters for the first twenty Fresnel zones are given for both X-band (10 GHz) and S-band (2.3 GHz), for source heights from 24 to 36 feet, at the end of this paragraph.

In the analysis of the MILA range, a computer program was written to calculate pertinent parameters of the first twenty Fresnel zones at X- and S-bands for transmitter heights between 24 and 36 feet. The tabulated results of these calculations are reproduced directly from the computer format on the following pages. The following definitions and nomenclature were employed in the computer program:

- H1 = the source height.
- Z0 = the point of specular reflection.
- S = the secant of the grazing angle at Z0.
- C = the center of the Nth Fresnel zone.
- Z1 = the source limit of the Nth Fresnel zone.
- Z2 = the receiver limit of the Nth Fresnel zone.
- W = the width of the Nth Fresnel zone.
- A = the area enclosed by the outer bound of the Nth Fresnel zone.
- N = the Fresnel zone number.

The range length was set at 1000 feet and the receiver height was set at 30 feet for all calculations. The formulae employed were those derived above. The X-band frequency was set at 10 GHz and the S-band frequency at 2.3 GHz for the calculations.

# X-Band Data

\* \* H1 = 24 \* \*

Z0 = 444.444

S = 1.00146

C	Z1	Z2	W	A
* N = 1	*			
446.253	356.438	536.069	9.84712	1389.25
* N = 2	*			
447.948	322.914	572.982	13.9291	2735.72
* N = 3	*			
449.54	298.727	600.352	17.0629	4042.15
* N = 4	*			
451.037	279.457	622.616	19.7061	5311.13
* N = 5	*			
452.448	263.358	641.538	22.0359	6545.17
* N = 6	*			
453.779	249.52	658.039	24.1431	7746.33
* N = 7	*			
455.039	237.396	672.682	26.0815	8916.58
* N = 8	*			
456.231	226.623	685.84	27.8864	10057.8
* N = 9	*			
457.363	216.948	697.777	29.5821	11171.5
* N = 10	*			
458.437	208.184	708.689	31.1864	12259.3
* N = 11	*			
459.458	200.19	718.726	32.7128	13322.5
* N = 12	*			
460.43	192.856	728.005	34.1716	14362.5
* N = 13	*			
461.357	186.093	736.622	35.571	15380.4
* N = 14	*			
462.242	179.829	744.655	36.9179	16377.3
* N = 15	*			
463.087	174.006	752.168	38.2178	17354.2
* N = 16	*			
463.895	168.575	759.215	39.4752	18312.1
* N = 17	*			
464.668	163.493	765.844	40.6941	19251.8
* N = 18	*			
465.409	158.725	772.094	41.8779	20174.2
* N = 19	*			
466.12	154.241	777.998	43.0294	21080.
* N = 20	*			
466.802	150.015	783.589	44.1511	21970.

# X-Band Data

\* \* H1 = 26 \* \*

Z0 = 464.286

S = 1.00157

C	Z1	Z2	W	A
* N = 1	*			
465.37	378.342	552.398	9.88253	1350.98
* N = 2	*			
466.39	345.121	587.658	13.9774	2662.54
* N = 3	*			
467.351	320.949	613.754	17.1203	3937.13
* N = 4	*			
468.26	301.556	634.963	19.7704	5177.03
* N = 5	*			
469.119	285.256	652.982	22.1056	6384.38
* N = 6	*			
469.933	271.169	668.697	24.2172	7561.07
* N = 7	*			
470.705	258.765	682.645	26.1593	8708.84
* N = 8	*			
471.439	247.694	695.183	27.9673	9829.33
* N = 9	*			
472.136	237.71	706.563	29.6657	10924.
* N = 10	*			
472.801	228.632	716.97	31.2723	11994.2
* N = 11	*			
473.434	220.321	726.548	32.8005	13041.2
* N = 12	*			
474.039	212.669	735.409	34.261	14066.2
* N = 13	*			
474.617	205.592	743.642	35.6618	15070.1
* N = 14	*			
475.17	199.018	751.322	37.01	16054.2
* N = 15	*			
475.699	192.889	758.509	38.3109	17019.2
* N = 16	*			
476.206	187.156	765.256	39.5692	17966.
* N = 17	*			
476.692	181.78	771.605	40.789	18895.4
* N = 18	*			
477.159	176.723	777.595	41.9735	19808.3
* N = 19	*			
477.608	171.957	783.259	43.1255	20705.3
* N = 20	*			
478.039	167.455	788.624	44.2478	21587.

# X-Band Data

\* \* H1 = 28 \* \*

Z0 = 482.759

S = 1.00168

C	Z1	Z2	W	A
* N = 1	*			
483.247	398.959	567.536	9.90194	1311.02
* N = 2	*			
483.709	366.152	601.267	14.0041	2585.98
* N = 3	*			
484.147	342.102	626.191	17.152	3827.02
* N = 4	*			
484.561	322.687	646.434	19.8059	5036.05
* N = 5	*			
484.954	306.28	663.628	22.1443	6215.04
* N = 6	*			
485.328	292.032	678.624	24.2585	7365.61
* N = 7	*			
485.683	279.431	691.936	26.2028	8489.23
* N = 8	*			
486.022	268.137	703.907	28.0127	9587.44
* N = 9	*			
486.345	257.914	714.777	29.7126	10661.5
* N = 10	*			
486.654	248.585	724.723	31.3206	11712.6
* N = 11	*			
486.949	240.017	733.881	32.85	12741.9
* N = 12	*			
487.231	232.105	742.357	34.3115	13750.4
* N = 13	*			
487.501	224.765	750.238	35.7133	14739.1
* N = 14	*			
487.761	217.927	757.594	37.0622	15709.
* N = 15	*			
488.009	211.536	764.482	38.3639	16660.8
* N = 16	*			
488.248	205.545	770.951	39.6229	17595.3
* N = 17	*			
488.477	199.911	777.043	40.8431	18513.3
* N = 18	*			
488.698	194.602	782.794	42.0281	19415.5
* N = 19	*			
488.91	189.587	788.234	43.1806	20302.5
* N = 20	*			
489.115	184.839	793.39	44.3032	21175.

# X-Band Data

\* \* H1 = 30 \* \*

Z0 = 500

S = 1.0018

C	Z1	Z2	W	A
* N = 1	*			
500	418.384	581.616	9.90828	1270.27
* N = 2	*			
500	386.071	613.929	14.0128	2507.71
* N = 3	*			
500	362.227	637.773	17.1624	3714.16
* N = 4	*			
500	342.873	657.127	19.8176	4891.3
* N = 5	*			
500	326.437	673.563	22.1571	6040.76
* N = 6	*			
500	312.101	687.899	24.2722	7164.
* N = 7	*			
500	299.372	700.628	26.2173	8262.29
* N = 8	*			
500	287.921	712.079	28.0278	9337.
* N = 9	*			
500	277.52	722.48	29.7284	10389.2
* N = 10	*			
500	267.999	732.001	31.3368	11420.
* N = 11	*			
500	259.227	740.773	32.8668	12430.4
* N = 12	*			
500	251.104	748.896	34.3287	13421.4
* N = 13	*			
500	243.548	756.452	35.7308	14393.6
* N = 14	*			
500	236.491	763.509	37.0801	15348.2
* N = 15	*			
500	229.88	770.12	38.382	16285.7
* N = 16	*			
500	223.667	776.333	39.6413	17206.8
* N = 17	*			
500	217.813	782.187	40.8618	18112.3
* N = 18	*			
500	212.285	787.715	42.047	19002.8
* N = 19	*			
500	207.052	792.948	43.1996	19878.9
* N = 20	*			
500	202.089	797.911	44.3225	20741.1



# X-Band Data

\* \* H1 = 32 \* \*

Z0 = 516.129

S = 1.00192

C	Z1	Z2	W	A
* N = 1	*			
515.727	436.705	594.75	9.90367	1229.33
* N = 2	*			
515.345	404.946	625.745	14.0066	2428.96
* N = 3	*			
514.981	381.373	648.589	17.1551	3600.37
* N = 4	*			
514.634	362.144	667.124	19.8094	4744.98
* N = 5	*			
514.302	345.743	682.861	22.1482	5864.23
* N = 6	*			
513.985	331.381	696.589	24.2627	6959.37
* N = 7	*			
513.682	318.583	708.781	26.2072	8031.52
* N = 8	*			
513.392	307.031	719.752	28.0174	9081.86
* N = 9	*			
513.114	296.506	729.722	29.7176	10111.3
* N = 10	*			
512.847	286.842	738.851	31.3257	11120.9
* N = 11	*			
512.59	277.915	747.266	32.8554	12111.4
* N = 12	*			
512.344	269.625	755.063	34.317	13083.8
* N = 13	*			
512.107	261.896	762.319	35.719	14038.7
* N = 14	*			
511.879	254.66	769.098	37.0681	14977.
* N = 15	*			
511.66	247.866	775.454	38.3699	15899.2
* N = 16	*			
511.448	241.468	781.428	39.629	16806.
* N = 17	*			
511.244	235.427	787.061	40.8494	17698.1
* N = 18	*			
511.047	229.711	792.384	42.0345	18576.
* N = 19	*			
510.857	224.29	797.424	43.1871	19440.2
* N = 20	*			
510.674	219.14	802.207	44.3099	20291.3

# X-Band Data

\* \* H1 = 34 \* \*

Z0 = 531.25

S = 1.00205

C	Z1	Z2	W	A
* N = 1	*			
530.518	453.999	607.038	9.89049	1188.81
* N = 2	*			
529.82	422.837	636.803	13.9883	2350.71
* N = 3	*			
529.153	399.586	658.72	17.1331	3487.01
* N = 4	*			
528.515	380.535	676.496	19.7847	4598.9
* N = 5	*			
527.905	364.222	691.588	22.1211	5687.63
* N = 6	*			
527.32	349.886	704.754	24.2337	6754.25
* N = 7	*			
526.759	337.068	716.449	26.1766	7799.73
* N = 8	*			
526.22	325.464	726.976	27.9853	8825.1
* N = 9	*			
525.703	314.859	736.546	29.6842	9831.21
* N = 10	*			
525.206	305.097	745.314	31.2913	10818.8
* N = 11	*			
524.727	296.056	753.398	32.82	11788.8
* N = 12	*			
524.267	287.641	760.892	34.2808	12741.9
* N = 13	*			
523.823	279.776	767.87	35.682	13678.7
* N = 14	*			
523.395	272.398	774.392	37.0304	14599.8
* N = 15	*			
522.982	265.455	780.509	38.3316	15506.
* N = 16	*			
522.584	258.904	786.263	39.5901	16397.7
* N = 17	*			
522.199	252.707	791.69	40.8101	17275.6
* N = 18	*			
521.827	246.833	796.821	41.9947	18140.1
* N = 19	*			
521.467	241.252	801.681	43.1469	18991.6
* N = 20	*			
521.119	235.942	806.296	44.2694	19830.7

## X-Band Data

\* \* H1 = 36 \* \*

Z0 = 545.455

S = 1.00218

C	Z1	Z2	W	A
* N = 1	*			
544.452	470.346	618.559	9.8698	1148.91
* N = 2	*			
543.493	439.809	647.178	13.9598	2273.6
* N = 3	*			
542.575	416.916	668.233	17.099	3375.06
* N = 4	*			
541.694	398.085	685.303	19.746	4454.33
* N = 5	*			
540.849	381.902	699.796	22.0787	5512.49
* N = 6	*			
540.038	367.634	712.441	24.1882	6550.45
* N = 7	*			
539.258	354.839	723.676	26.1284	7569.01
* N = 8	*			
538.508	343.223	733.792	27.9348	8569.08
* N = 9	*			
537.785	332.579	742.992	29.6316	9551.39
* N = 10	*			
537.09	322.757	751.423	31.2368	10516.6
* N = 11	*			
536.42	313.639	759.201	32.7639	11465.5
* N = 12	*			
535.773	305.133	766.413	34.2232	12398.7
* N = 13	*			
535.149	297.166	773.132	35.6231	13316.8
* N = 14	*			
534.546	289.678	779.415	36.9704	14220.3
* N = 15	*			
533.964	282.618	785.31	38.2705	15109.8
* N = 16	*			
533.401	275.944	790.858	39.5281	15985.7
* N = 17	*			
532.856	269.619	796.093	40.7472	16848.6
* N = 18	*			
532.329	263.613	801.044	41.9311	17699.
* N = 19	*			
531.818	257.899	805.737	43.0826	18537.2
* N = 20	*			
531.323	252.452	810.194	44.2044	19363.7

## S-Band Data

\* \* H1 = 24 \* \*

Z0 = 444.444

S = 1.00146

C	Z1	Z2	W	A
* N = 1	*			
451.565	273.234	629.896	20.5924	5768.4
* N = 2	*			
457.068	219.419	694.717	29.1418	10878.6
* N = 3	*			
461.449	185.431	737.467	35.7108	15483.1
* N = 4	*			
465.02	161.218	768.822	41.2539	19686.9
* N = 5	*			
467.986	142.848	793.124	46.1411	23565.5
* N = 6	*			
470.489	128.335	812.642	50.5619	27174.7
* N = 7	*			
472.629	116.534	828.724	54.6291	30557.
* N = 8	*			
474.48	106.722	842.238	58.4162	33745.5
* N = 9	*			
476.097	98.4211	853.772	61.9742	36766.4
* N = 10	*			
477.521	91.2966	863.746	65.3405	39640.9
* N = 11	*			
478.786	85.1081	872.464	68.543	42386.2
* N = 12	*			
479.916	79.6775	880.154	71.6037	45016.8
* N = 13	*			
480.932	74.8696	886.994	74.5399	47544.7
* N = 14	*			
481.85	70.5799	893.12	77.3658	49980.1
* N = 15	*			
482.684	66.7266	898.642	80.0929	52331.6
* N = 16	*			
483.445	63.2441	903.646	82.731	54606.8
* N = 17	*			
484.142	60.0796	908.205	85.2884	56812.1
* N = 18	*			
484.783	57.1897	912.376	87.7719	58953.2
* N = 19	*			
485.374	54.5389	916.21	90.1879	61035.2
* N = 20	*			
485.921	52.0975	919.745	92.5414	63062.4

## S-Band Data

\* \* H1 = 26 \* \*

Z0 = 464.286

S = 1.00157

C	Z1	Z2	W	A
* N = 1	*			
468.581	295.266	641.896	20.6588	5624.23
* N = 2	*			
471.955	240.264	703.645	29.2247	10636.
* N = 3	*			
474.675	204.899	744.45	35.8018	15171.5
* N = 4	*			
476.914	179.368	774.46	41.3492	19326.
* N = 5	*			
478.79	159.798	797.782	46.2384	23168.8
* N = 6	*			
480.384	144.207	816.561	50.6602	26752.
* N = 7	*			
481.756	131.441	832.071	54.7276	30115.2
* N = 8	*			
482.948	120.766	845.131	58.5144	33289.8
* N = 9	*			
483.995	111.689	856.301	62.0718	36300.7
* N = 10	*			
484.92	103.866	865.975	65.4373	39168.1
* N = 11	*			
485.745	97.0457	874.444	68.6389	41908.8
* N = 12	*			
486.484	91.0415	881.927	71.6986	44536.4
* N = 13	*			
487.151	85.711	888.591	74.6338	47062.7
* N = 14	*			
487.755	80.9434	894.566	77.4587	49497.6
* N = 15	*			
488.305	76.6515	899.958	80.1848	51849.4
* N = 16	*			
488.807	72.7652	904.849	82.8219	54125.7
* N = 17	*			
489.249	69.2278	909.309	85.3782	56332.5
* N = 18	*			
489.693	65.9927	913.394	87.8608	58475.7
* N = 19	*			
490.086	63.0213	917.151	90.2757	60560.
* N = 20	*			
490.45	60.2814	920.619	92.6283	62589.8

## S-Band Data

\* \* H1 = 28 \* \*

Z0 = 482.759

S = 1.00168

C	Z1	Z2	W	A
* N = 1	*			
484.708	316.366	653.05	20.6956	5472.58
* N = 2	*			
486.261	260.533	711.989	29.2712	10378.8
* N = 3	*			
487.528	224.045	751.012	35.8533	14839.
* N = 4	*			
488.582	197.381	779.783	41.4035	18938.7
* N = 5	*			
489.471	176.744	802.199	46.2945	22741.3
* N = 6	*			
490.232	160.173	820.291	50.7171	26294.6
* N = 7	*			
490.891	146.515	835.267	54.7849	29635.6
* N = 8	*			
491.466	135.031	847.902	58.5719	32793.8
* N = 9	*			
491.974	125.219	858.728	62.1292	35792.5
* N = 10	*			
492.424	116.728	868.12	65.4945	38651.1
* N = 11	*			
492.827	109.299	876.354	68.6958	41385.5
* N = 12	*			
493.189	102.738	883.639	71.7551	44008.9
* N = 13	*			
493.516	96.8968	890.135	74.6899	46532.5
* N = 14	*			
493.813	91.6598	895.967	77.5144	48966.
* N = 15	*			
494.085	86.9351	901.234	80.24	51317.5
* N = 16	*			
494.333	82.6485	906.018	82.8767	53594.2
* N = 17	*			
494.562	78.74	910.384	85.4325	55802.2
* N = 18	*			
494.773	75.16	914.386	87.9147	57947.
* N = 19	*			
494.968	71.8673	918.069	90.3292	60033.4
* N = 20	*			
495.149	68.8274	921.471	92.6813	62065.5

## S-Band Data

\* \* H1 = 30 \* \*

Z0 = 500  
S = 1.0018

C	Z1	Z2	W	A
* N = 1	*			
500	336.549	663.451	20.7078	5316.7
* N = 2	*			
500	280.188	719.812	29.2868	10112.2
* N = 3	*			
500	242.806	757.194	35.8709	14491.9
* N = 4	*			
500	215.18	784.82	41.4223	18532.2
* N = 5	*			
500	193.605	806.395	46.314	22290.3
* N = 6	*			
500	176.153	823.847	50.7372	25810.
* N = 7	*			
500	161.677	838.323	54.8054	29125.6
* N = 8	*			
500	149.441	850.559	58.5925	32264.5
* N = 9	*			
500	138.939	861.061	62.1501	35248.7
* N = 10	*			
500	129.814	870.186	65.5154	38096.4
* N = 11	*			
500	121.802	878.198	68.7168	40822.8
* N = 12	*			
500	114.705	885.295	71.7762	43440.5
* N = 13	*			
500	108.369	891.631	74.711	45960.3
* N = 14	*			
500	102.675	897.325	77.5355	48391.3
* N = 15	*			
500	97.5258	902.474	80.2611	50741.6
* N = 16	*			
500	92.8454	907.155	82.8977	53018.
* N = 17	*			
500	88.5704	911.43	85.4536	55226.4
* N = 18	*			
500	84.6485	915.352	87.9357	57372.3
* N = 19	*			
500	81.0362	918.964	90.3502	59460.2
* N = 20	*			
500	77.6969	922.303	92.7023	61494.4

## S-Band Data

\* \* H1 = 32 \* \*

Z0 = 516.129

S = 1.00192

C	Z1	Z2	W	A
* N = 1	*			
514.51	355.841	673.179	20.6993	5159.02
* N = 2	*			
513.186	299.209	727.164	29.2761	9840.17
* N = 3	*			
512.084	261.136	763.032	35.859	14135.2
* N = 4	*			
511.151	232.706	789.596	41.4099	18111.9
* N = 5	*			
510.352	210.315	810.388	46.3013	21821.7
* N = 6	*			
509.659	192.076	827.243	50.7244	25304.4
* N = 7	*			
509.054	176.859	841.248	54.7926	28591.4
* N = 8	*			
508.519	163.929	853.109	58.58	31708.3
* N = 9	*			
508.045	152.784	863.305	62.1377	34675.5
* N = 10	*			
507.62	143.062	872.177	65.5033	37510.3
* N = 11	*			
507.237	134.497	879.978	68.7049	40226.8
* N = 12	*			
506.892	126.886	886.897	71.7646	42837.2
* N = 13	*			
506.577	120.074	893.08	74.6997	45351.6
* N = 14	*			
506.29	113.937	898.644	77.5244	47779.
* N = 15	*			
506.027	108.376	903.679	80.2503	50126.9
* N = 16	*			
505.785	103.31	908.26	82.8873	52402.
* N = 17	*			
505.562	98.6757	912.448	85.4434	54610.
* N = 18	*			
505.355	94.4171	916.293	87.9258	56756.3
* N = 19	*			
505.163	90.489	919.837	90.3406	58845.2
* N = 20	*			
504.984	86.853	923.116	92.693	60880.8



# S-Band Data

\* \* H1 = 34 \* \*

Z0 = 531.25  
S = 1.00205

C	Z1	Z2	W	A
* N = 1	*			
528.288	374.273	682.302	20.6736	5001.48
* N = 2	*			
525.838	317.585	734.091	29.243	9566.09
* N = 3	*			
523.778	279.001	768.555	35.8219	13773.4
* N = 4	*			
522.023	249.911	794.134	41.3703	17683.
* N = 5	*			
520.508	226.821	814.195	46.2603	21341.
* N = 6	*			
519.188	207.887	830.489	50.6825	24783.3
* N = 7	*			
518.027	192.001	844.053	54.7503	28038.8
* N = 8	*			
516.999	178.437	855.56	58.5375	31130.9
* N = 9	*			
516.081	166.696	865.467	62.0952	34078.8
* N = 10	*			
515.257	156.416	874.099	65.461	36898.3
* N = 11	*			
514.514	147.329	881.699	68.6629	39603.
* N = 12	*			
513.839	139.231	888.448	71.7229	42204.3
* N = 13	*			
513.224	131.963	894.486	74.6585	44711.9
* N = 14	*			
512.662	125.4	899.924	77.4836	47134.2
* N = 15	*			
512.145	119.44	904.85	80.21	49478.5
* N = 16	*			
511.668	114.001	909.336	82.8475	51751.2
* N = 17	*			
511.228	109.015	913.441	85.4041	53957.9
* N = 18	*			
510.819	104.427	917.212	87.887	56103.7
* N = 19	*			
510.439	100.189	920.69	90.3023	58192.8
* N = 20	*			
510.085	96.2605	923.91	92.6552	60229.2

# S-Band Data

\* \* H1 = 36 \* \*

Z0 = 545.455

S = 1.00218

C	Z1	Z2	W	A
* N = 1	*			
541.38	391.88	690.879	20.6335	4845.46
* N = 2	*			
537.974	335.318	740.631	29.191	9292.45
* N = 3	*			
535.086	296.381	773.792	35.763	13409.6
* N = 4	*			
532.606	266.762	798.45	41.3071	17249.3
* N = 5	*			
530.453	243.078	817.828	46.1943	20852.5
* N = 6	*			
528.566	223.537	833.596	50.6148	24251.6
* N = 7	*			
526.899	207.053	846.746	54.6814	27472.7
* N = 8	*			
525.416	192.914	857.918	58.468	30537.5
* N = 9	*			
524.087	180.625	867.55	62.0255	33463.4
* N = 10	*			
522.89	169.826	875.955	65.3912	36265.6
* N = 11	*			
521.807	160.249	883.364	68.5934	38956.5
* N = 12	*			
520.821	151.691	889.95	71.6537	41546.9
* N = 13	*			
519.92	143.99	895.85	74.5896	44045.9
* N = 14	*			
519.094	137.02	901.168	77.4153	46461.7
* N = 15	*			
518.333	130.676	905.989	80.1423	48801.1
* N = 16	*			
517.63	124.877	910.384	82.7803	51070.3
* N = 17	*			
516.98	119.551	914.408	85.3376	53274.6
* N = 18	*			
516.375	114.642	918.108	87.8212	55418.9
* N = 19	*			
515.812	110.101	921.523	90.2371	57507.3
* N = 20	*			
515.286	105.886	924.686	92.5907	59543.8

### F.3 Diffraction Effects of Fence Placements

From the above discussion, it can be seen that the primary use of diffraction fences on a planar range surface should be the screening of the receiver from energy which would, in the absence of the fences, be incident from points within the region of the range surface including the Fresnel zones which are illuminated by relatively high-level regions of the transmitted pattern. Such surface screening requires placement of the diffraction fences such that they intercept part of the energy from the source antenna; this results in perturbations of the receiving-aperture field due to diffraction effects. If such perturbations are not negligible, a compromise must be arrived at for a fence configuration which will afford an acceptable total field disturbance due to the combination of reflections and diffraction. The following development gives an indication of the effect of a single fence on the free-space field of the source antenna for the MILA range geometry.

Consider Figure F.2.

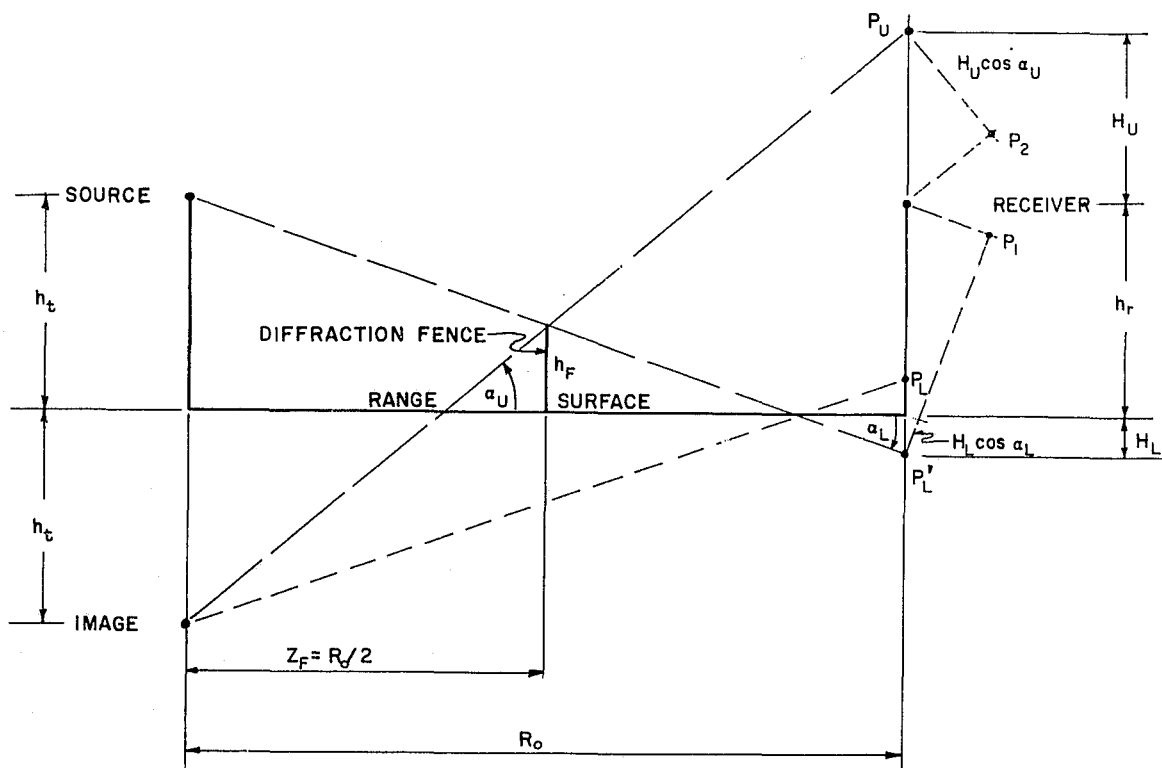


Figure F.2. Relation of Diffraction Parameters to Range Geometry for a Single Diffraction Fence at the Center of the Range

From the geometry,

$$H_L = h_t - 2h_F, \quad (F-17)$$

$$H_U = h_t + 2h_F - h_r, \quad (F-18)$$

$$\alpha_L = \tan^{-1} \frac{2(h_t - h_F)}{R_o} \quad (F-19)$$

and

$$\alpha_U = \tan^{-1} \frac{2(h_t + h_F)}{R_o}. \quad (F-20)$$

For  $R_o \gg 2(h_t + h_F)$ ,

$$\alpha_L \doteq \tan \alpha_L \doteq \sin \alpha_L \doteq \frac{2(h_t - h_F)}{R_o}; \quad \cos \alpha_L \doteq 1 \quad (F-21)$$

and

$$\alpha_U \doteq \tan \alpha_U \doteq \sin \alpha_U \doteq \frac{2(h_t + h_F)}{R_o}; \quad \cos \alpha_U \doteq 1. \quad (F-22)$$

For a point-source radiator, consider the superposition of the diffracted fields from the source and its image. If the fence of height  $h_F$  were infinitely wide, the Cornu spiral<sup>F-2</sup> would provide a solution to the calculation of the field at the receiving point.

The full development of the theoretical basis of the Cornu spiral and its application to the present problem is beyond the scope and intent of this analysis. The approach is essentially one of dividing a wavefront into incremental regions in a systematic fashion and computing the field at an observation point in terms of the relative phases of contributions from these "secondary" or "differential" sources. It is shown in the indicated references that this procedure leads to the Fresnel integrals

$$C(u) = \int_0^u \cos \frac{\pi(u')^2}{2} du'$$

---

<sup>F-2</sup>Rossi, Bruno, Optics, Addison-Wesley Publishing Co., 1965; pp. 184-196.

Longhurst, R.S., Geometrical and Physical Optics, John Wiley & Sons, Ltd., 1964; pp. 264-274.

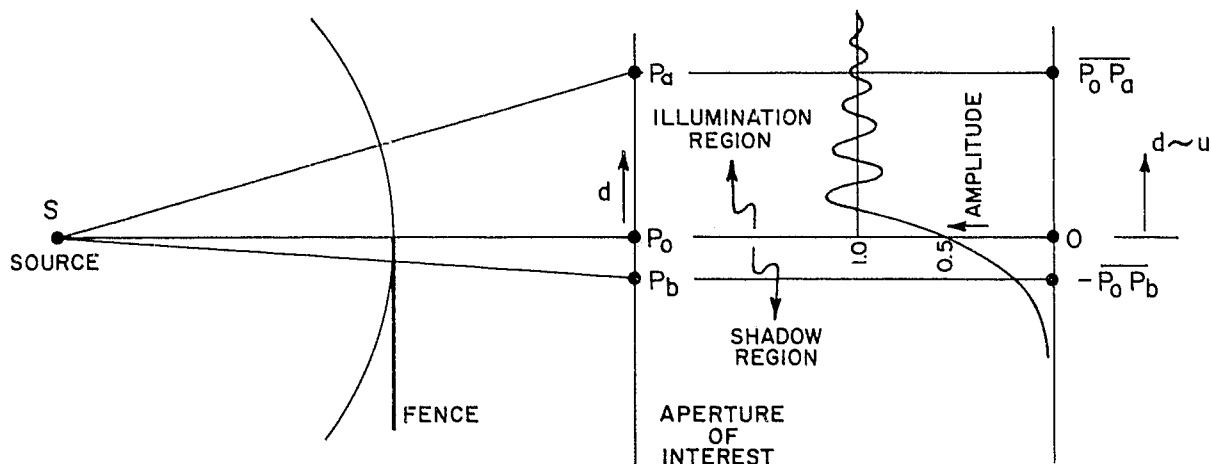
Jenkins, Francis A., and Harvey E. White, Fundamentals of Optics, McGraw-Hill Book Company, 1957; pp. 363-375.

and

$$S(u) = \int_0^u \sin \frac{\pi(u')^2}{2} du' ,$$

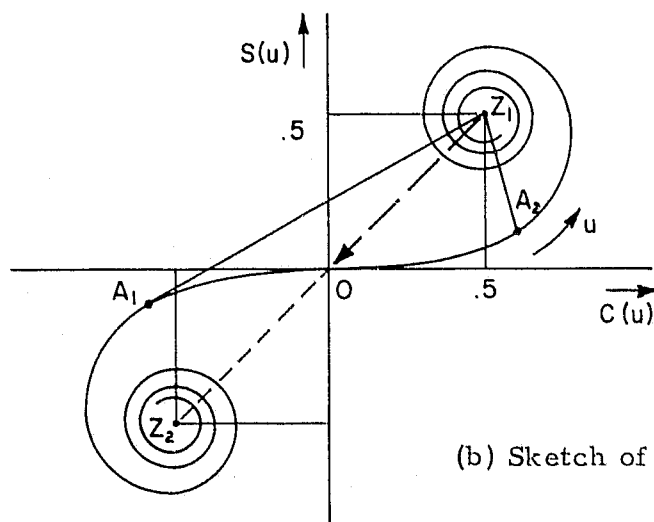
and to the Cornu spiral, which is a plot of  $S(u)$  versus  $C(u)$ .

Consider Figure F.3, which summarizes the application of the cryptically stated technique to the present problem. The point  $P_0$  of Figure F.3(a) receives energy



(a) Section Through Wavefront

(c) Resultant Field Amplitude



(b) Sketch of Cornu Spiral

Figure F.3. Illustration of the Application of the Cornu Spiral to the Straight-Edge Diffraction Problem

from only half of the transmitted wavefront. The magnitude of the field which would exist at  $P_0$  in the absence of the fence is represented by the line  $\overline{Z_1 Z_2}$  on the Cornu spiral sketched in Figure F.3(b). The presence of the fence makes the lower branch of the spiral ineffective as far as the field at  $P_0$  is concerned, thus the amplitude at  $P_0$ , normalized to the unobstructed case, is represented by the line  $\overline{Z_1 0}$ , thus is 0.5 as shown in Figure F.3(c).

For a point of observation such as  $P_a$ , the whole of the wave above  $\overline{SP_a}$  is unobstructed, so that the total upper branch of the spiral is effective. In addition, the portion of the wave between  $\overline{SP_a}$  and  $\overline{SP_0}$  is unobstructed, and the corresponding portion of the spiral between 0 and  $A_1$  is also effective. The field amplitude at  $P_a$  is thus represented by the line  $\overline{Z_1 A_1}$  on the spiral. As  $P_a$  moves away from  $P_0$ , the point  $A_1$  moves around the lower branch of the spiral toward  $Z_2$ , producing the successive maxima and minima indicated in the amplitude sketch.

For a point such as  $P_b$ , the whole of the wave below  $\overline{SP_b}$  is obstructed, as well as the portion of the wave between  $\overline{SP_b}$  and  $\overline{SP_0}$ . The corresponding effective portion of the Cornu spiral is thus between  $A_2$  and  $Z_1$ , and the amplitude at  $P_b$  is represented by the line  $\overline{Z_1 A_2}$  on the spiral. As  $P_b$  moves away from  $P_0$ , the point  $A_2$  moves around the upper branch of the spiral toward  $Z_1$ , producing the uniformly decreasing portion of the amplitude sketch for  $d < 0$ .

It is noted that even for ideal theoretical conditions (an isotropic source antenna and a knife-edge of infinite width and height), the Cornu spiral is somewhat inaccurate in the regions of its asymptotes ( $Z_1$  and  $Z_2$ ) due to certain approximations. Also, the finite source-fence distance and the nonuniform amplitude and phase of realizable transmitted wavefronts would contribute to error if this technique were applied to precise quantitative analyses. However, for the present purposes, this approach yields rapid and informative qualitative indications of the effects of diffraction fencing.

For the range configuration of Figure F.2, the point  $P_1$  is in the illumination region of the source, and is removed from the boundary of the shadow region of the source by a distance  $(h_r + H_L) \cos \alpha_L \doteq (h_r + H_L)$ . The field at  $P'_L$ , due to the source, is one-half that which would have existed if the fence were not present. Between  $P'_L$  and  $P_1$ , this field exhibits successive maxima and minima. The point  $P_2$  is in the shadow region of the image, and is removed from the boundary of the illumination region of the image by a distance  $H_U \cos \alpha_U \doteq H_U$ . The field at  $P_U$ , due

- to the image, is one-half that which would have existed if the fence were not present. Between  $P_U$  and  $P_2$ , this field decreases uniformly toward zero.

The fields may be plotted from the Cornu spiral, if the distances  $X_{OL}$  and  $X_{OU}$  from the top of the fence to the points  $P_L$  and  $P_U$ , respectively, are known.

From the geometry of Figure F.2,

$$X_{OL} = \left[ (h_F + H_L)^2 + \left( \frac{R_O}{2} \right)^2 \right]^{\frac{1}{2}} \quad (F-23)$$

and

$$X_{OU} = \left[ (h_r - h_F + H_U)^2 + \left( \frac{R_O}{2} \right)^2 \right]^{\frac{1}{2}} \quad (F-24)$$

If  $d_L$  and  $d_U$  are distances from  $P_L'$  to  $P_1$  and from  $P_U$  to  $P_2$ , respectively, the corresponding arc lengths on the Cornu spiral are

$$s_L = \left( \frac{2}{X_{OL}\lambda} \right)^{\frac{1}{2}} d_L \quad (F-25)$$

and

$$s_U = \left( \frac{2}{X_{OU}\lambda} \right)^{\frac{1}{2}} d_U \quad (F-26)$$

where the units of the spiral are chosen such that

$$s = \sqrt{2} \text{ for } d^2 = \left( X_O + \frac{\lambda}{2} \right)^2 - X_O^2 \doteq X_O \lambda \quad .$$

As stated above, the range dimensions are such that

$$d_L \doteq h_r + H_L \text{ (the distance from } P_L' \text{ to the receiver)} \quad (F-27)$$

and

$$d_U \doteq H_U \text{ (the distance from } P_U \text{ to the receiver)} \quad (F-28)$$

Employing these approximations and equations (F-17) and (F-18), equations (F-25) and (F-26) become

$$s_L \doteq \left( \frac{2}{\lambda} \right)^{\frac{1}{2}} (h_t - 2h_F + h_r) \left[ (h_t - h_F)^2 + \left( \frac{R_O}{2} \right)^2 \right]^{-1/4} \quad (F-29)$$

and

$$s_U \doteq \left( \frac{2}{\lambda} \right)^{\frac{1}{2}} (h_t + 2h_F - h_r) \left[ (h_t + h_F)^2 + \left( \frac{R_O}{2} \right)^2 \right]^{-1/4} \quad (F-30)$$

A sketch of the diffraction-field amplitude versus the Cornu spiral factor  $s$  is

given in Figure F.4 for a point-source radiator, where the amplitudes are normalized to that of the unobstructed free-space wave. Figure F.5 gives a graph of the envelope of the diffraction field amplitude about the free-space asymptote up to  $s = 25$ . Two alterations of the idealized curve of Figure F.4 are caused by the use of typical directive source antennas rather than point-source radiators. Since the fence is at some level of illumination below the level of the beam axis, the successive maxima and minima of the field will approach the free-space asymptote somewhat more rapidly than indicated in Figure F.4. Also, the asymptote will exhibit some concave curvature for relatively small displacements from the shadow-illumination boundary, so that both the relative amplitude and the peak-to-peak variations of the resultant field will be less than indicated by the theoretical curve. Figure F.4 thus represents a "worst-case" condition of diffraction in the antenna range situation. (Second-order reflections are not considered in this analysis.)

A computer program was employed for calculation of diffraction effects resulting from the placement of a single fence at the center of the MILA range. The calculations were based on equations (F-27) through (F-30), and were made for both an 8-foot fence and a 12-foot fence at X-band, S-band and L-band. The results of this computer analysis are summarized in Figures F.6 through F.8.

As an example of the use of these data in conjunction with Figures F.4 and F.5, consider a test situation at 10 GHz with the source and receiving heights set at 30 feet and a 12-foot fence in place at the center of the 1000-foot range. From Figure F.8(d), we see that the receiving point is approximately 24 feet into the shadow region of the image, and the corresponding Cornu spiral factor is 4.8. Referring to the portion of Figure F.4 illustrating the shadow region, the image is seen to contribute a negligible amount of energy to the field at the receiver. For the direct wave from the source antenna, Figure F.8(d) shows that the receiver is some 36 feet inside the illumination region, corresponding to a Cornu spiral factor of 7.3. The plotted envelope of Figure F.5 shows that for  $s = 7.3$ , a peak-to-peak variation of the order of 0.06 times the beam maximum will exist in the field near the receiver due to diffraction of the field from the source antenna. For typical logarithmic field amplitude plots, such a variation would produce a ripple component given by  $20 \log(1 + .03)/(1 - .03)$ , or about 0.5 decibel.

If an isotropic source antenna had been employed without the fence in place, the



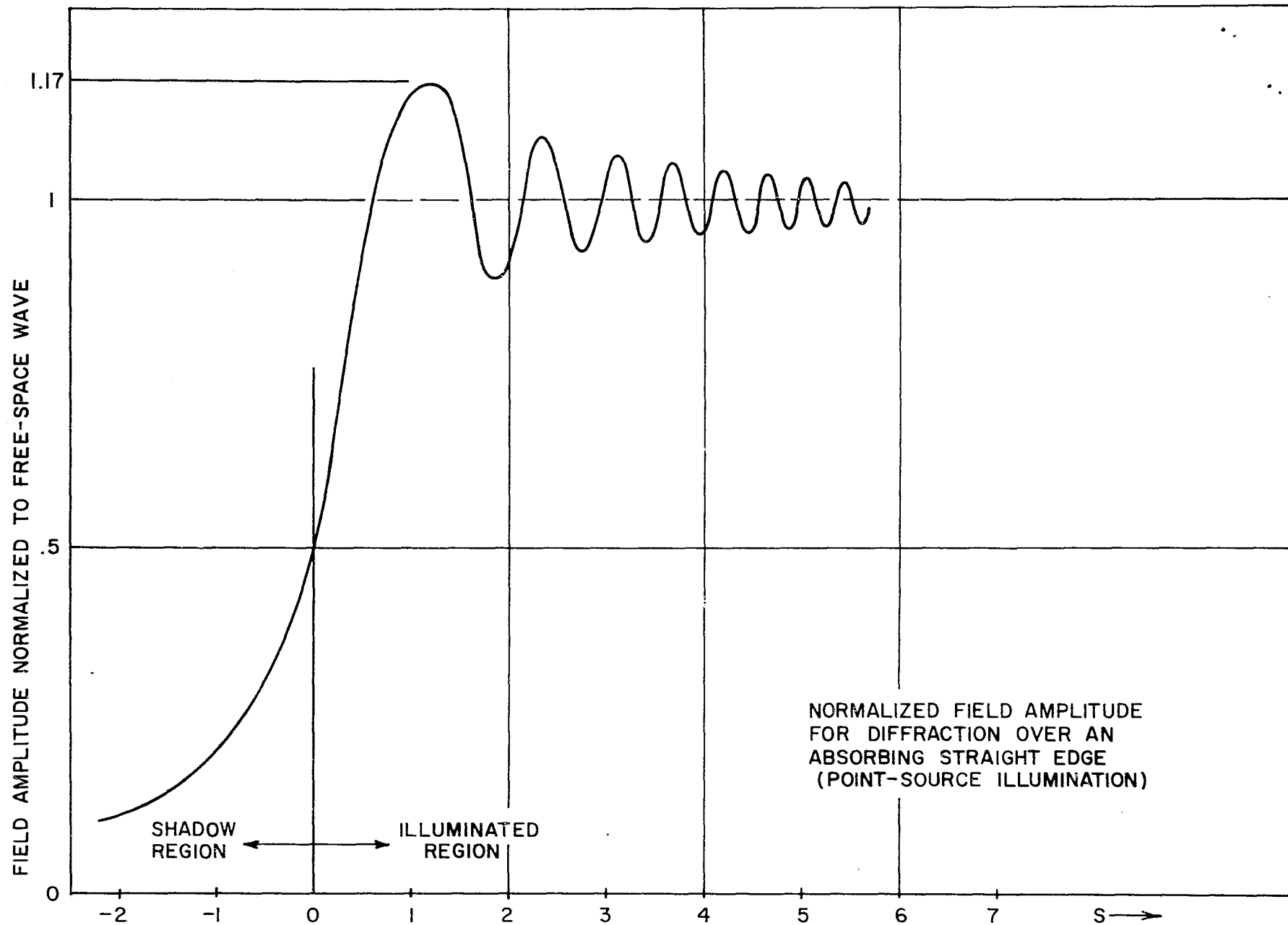


Figure F.4. Normalized Field Amplitude for Diffraction Over an Absorbing Straight Edge (Point-Source Illumination)

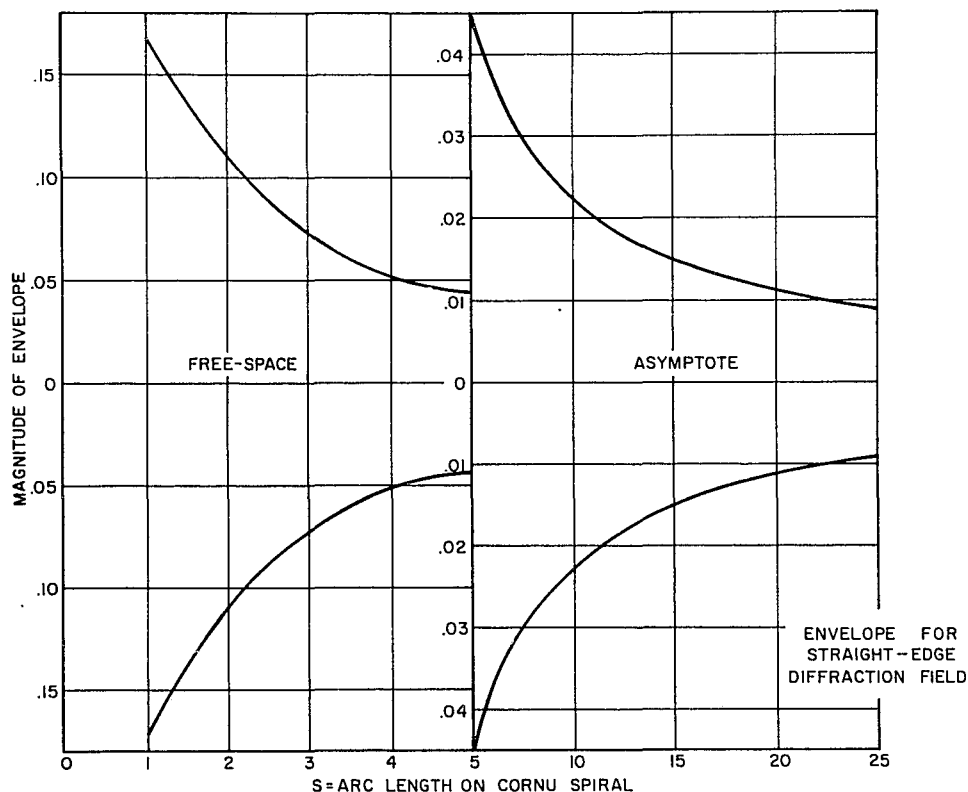
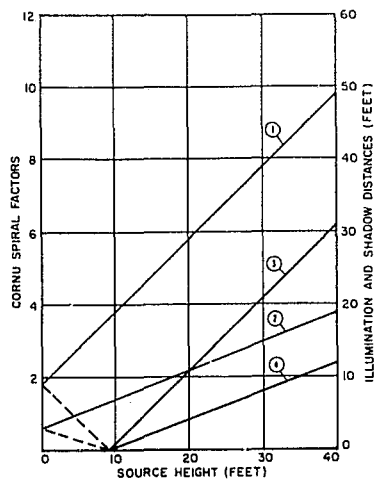


Figure F.5. Envelope and Free-Space Asymptote for the Straight-Edge Diffraction Field

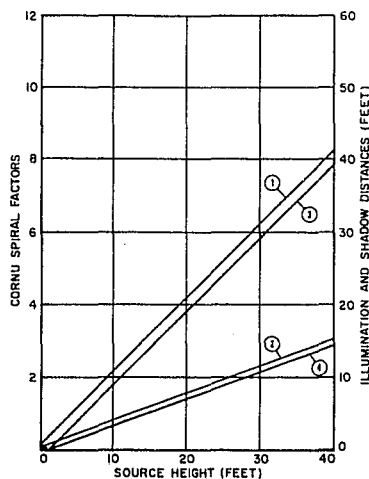
specular point would have been illuminated by energy at the level of the direct-path wave. Assuming the relatively large grazing angle for this example reduced the magnitude of the reflection coefficient to 0.5, the corresponding ripple component of a logarithmic aperture-field plot would be given by  $20 \log (1+.5)/(1-.5)$ , or about 9.5 decibels. For this theoretical example, then, a single 12-foot fence at the point of specular reflection would reduce the variational component of the receiving-aperture field from approximately 9.5 decibels to 0.5 decibel.

It is of interest to consider the effect of this same fence for the conditions of the above example with the exception that a typical directive source antenna is employed rather than a theoretical isotropic source. As a particular case, assume that a 1-foot diameter paraboloid is used, and that the main lobe of the transmitted beam is centered on the receiving aperture and has a  $\sin K\theta/K\theta$  amplitude characteristic. For such a pattern, the factor  $K$  is given by (see Appendix E)

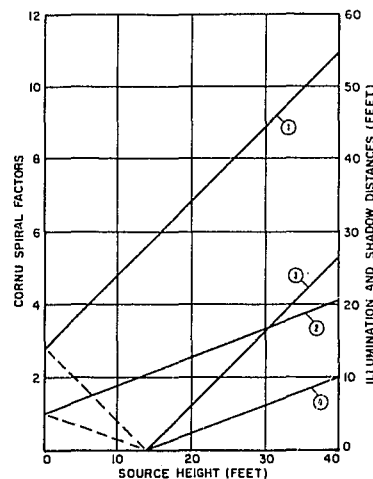
$$K \doteq 2.28D/\lambda$$



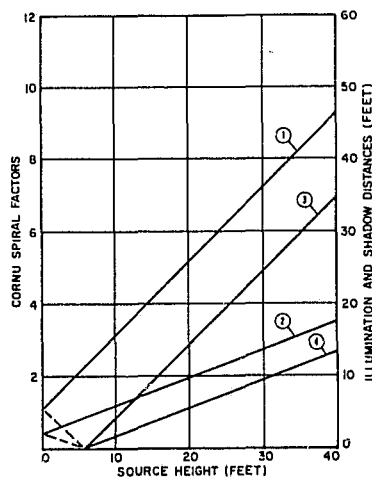
(a)  $h_r = 25$  feet  
 $h_F = 8$  feet



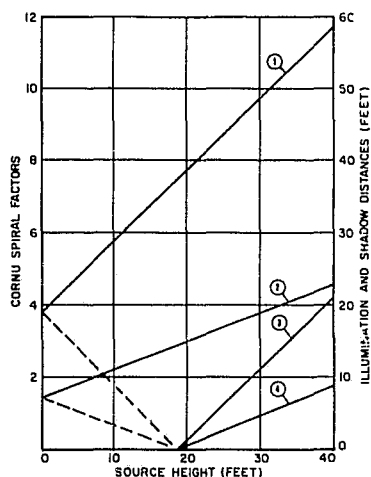
(b)  $h_r = 25$  feet  
 $h_F = 12$  feet



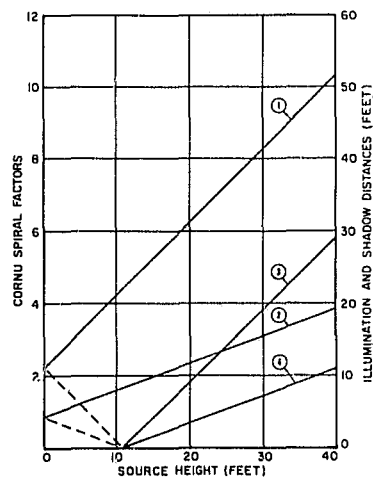
(c)  $h_r = 30$  feet  
 $h_F = 8$  feet



(d)  $h_r = 30$  feet  
 $h_F = 12$  feet



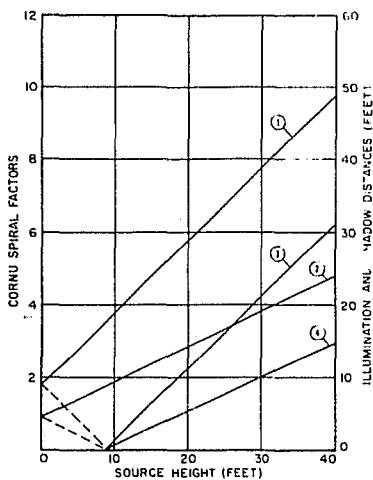
(e)  $h_r = 35$  feet  
 $h_F = 8$  feet



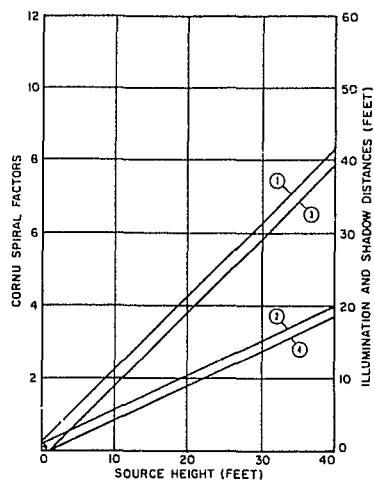
(f)  $h_r = 35$  feet  
 $h_F = 12$  feet

Figure F. 6 Diffraction Field Distances and Cornu Spiral Factors Versus Source Height at 1.428 GHz with Fence and Receiver Heights as Parameters. The numbered curves correspond to:

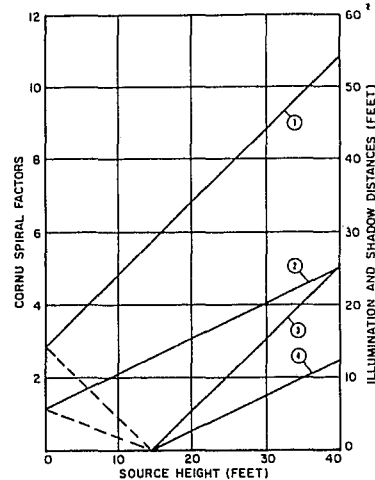
- (1) Illumination Distance
- (2) Illumination Spiral Factor
- (3) Shadow Distance
- (4) Shadow Spiral Factor



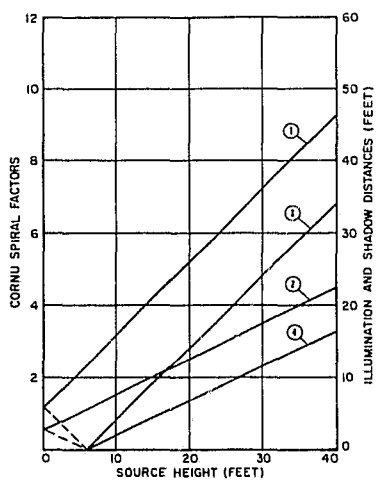
(a)  $h_r = 25$  feet  
 $h_F = 8$  feet



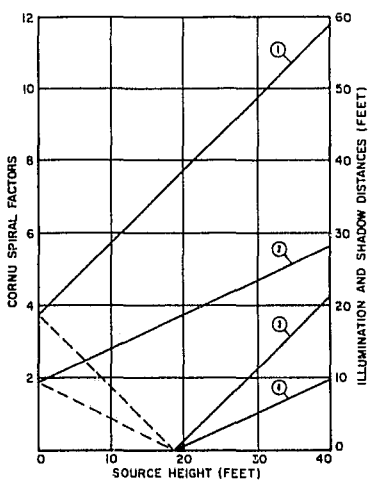
(b)  $h_r = 25$  feet  
 $h_F = 12$  feet



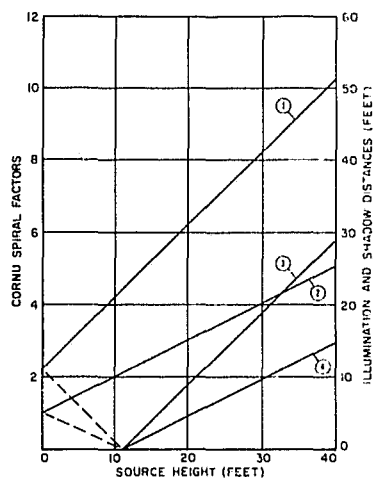
(c)  $h_r = 30$  feet  
 $h_F = 8$  feet



(d)  $h_r = 30$  feet  
 $h_F = 12$  feet



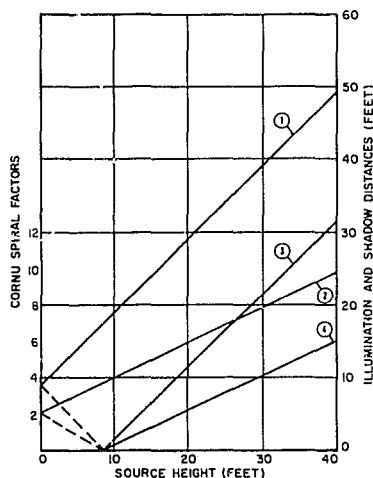
(e)  $h_r = 35$  feet  
 $h_F = 8$  feet



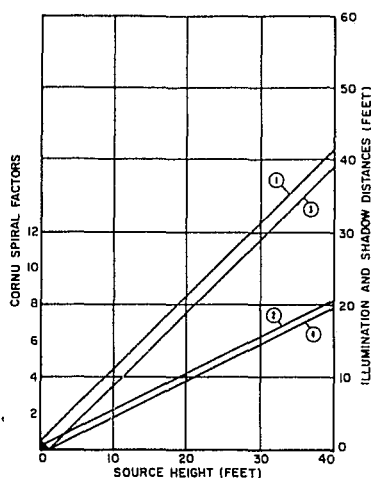
(f)  $h_r = 35$  feet  
 $h_F = 12$  feet

Figure F.7. Diffraction Field Distances and Cornu Spiral Factors Versus Source Height at 2.3 GHz with Fence and Receiver Heights as Parameters. The numbered curves correspond to:

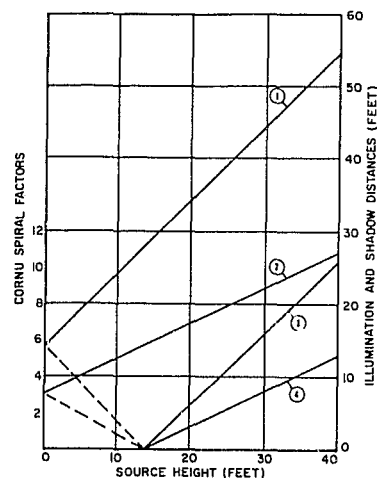
- (1) Illumination Distance
- (2) Illumination Spiral Factor
- (3) Shadow Distance
- (4) Shadow Spiral Factor



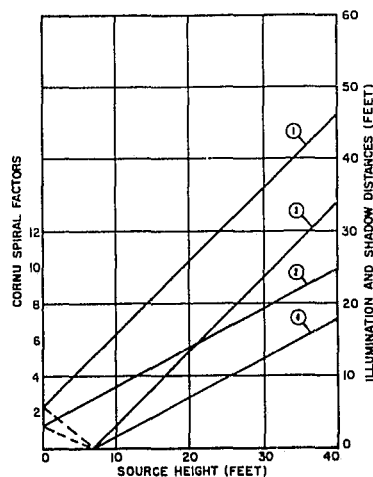
(a)  $h_r = 25$  feet  
 $h_F = 8$  feet



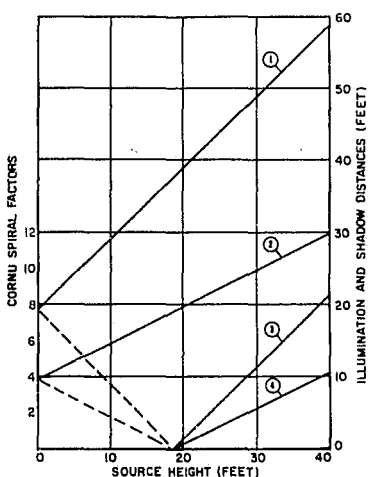
(b)  $h_r = 25$  feet  
 $h_F = 12$  feet



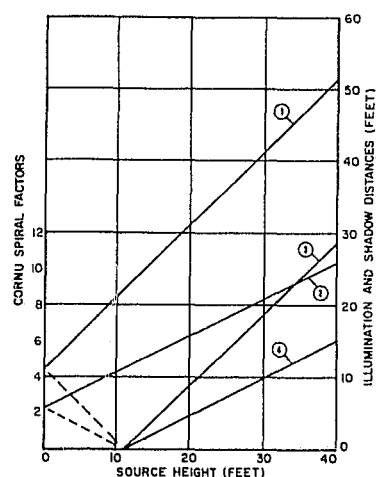
(c)  $h_r = 30$  feet  
 $h_F = 8$  feet



(d)  $h_r = 30$  feet  
 $h_F = 12$  feet



(e)  $h_r = 35$  feet  
 $h_F = 8$  feet



(f)  $h_r = 35$  feet  
 $h_F = 12$  feet

Figure F. 8 Diffraction Field Distances and Cornu Spiral Factors Versus Source Height at 10 GHz with Fence and Receiver Heights as Parameters. The numbered curves correspond to:

- (1) Illumination Distance
- (2) Illumination Spiral Factor
- (3) Shadow Distance
- (4) Shadow Spiral Factor

where  $D$  is the paraboloid diameter and  $\lambda$  is the wavelength. This form for  $K$  is used with angles  $\theta_i$  measured in radians from the axis of the main lobe. For the current example, the angle to the specular point is given by

$$\theta_s = \tan^{-1} \frac{2h_r}{R_0} \doteq \frac{2(30)}{1000} = 0.06 \text{ radian}$$

and the angle to the top of the 12-foot fence is given by

$$\theta_f = \tan^{-1} \frac{2(30-12)}{1000} \doteq 0.036 \text{ radian.}$$

Thus  $K\theta_s \doteq 1.39$  and  $K\theta_f \doteq 0.84$ ; from  $\sin x/x$  tables it is seen that the level of the wavefront at the top of the fence is some 1.1 decibels below the beam maximum, and that in the absence of the fence the specular point would have been illuminated by energy some 3 decibels below the beam maximum. Again assuming the reflection coefficient is only 0.5 due to the elevated source, the reflected wave would have an amplitude 0.354 times that of the direct wave if the fence were not used; this value corresponds to an aperture-field variation of 6.4 decibels. (See Figure 4.8 for an experimental plot of the aperture field under the conditions of this example.) When the fence is in place, the reduction of the illumination of the top of the fence to a level 1.1 decibels below the direct-path beam causes the resulting diffraction envelope to be reduced by a factor of approximately 0.9. The residual aperture-field variation due to diffraction should thus be very nearly  $20 \log (1 + .9[.03]) / (1 - .9[.03])$ , or about 0.4 decibel. Experimental verification of this theoretical value was not obtained, because the emphasis of the X-band program was on obtaining residual variations of less than 0.2 decibels.

A further reduction of the residual variation requires a more directive source antenna rather than a reduced fence height, since the fence must screen a significant portion of the range surface in the region of the specular point. Several sets of experimental aperture-field data are presented in Chapter 4 which illustrate the effect of diffraction fencing on the field purity in the elevated mode, employing directive source antennas. It is shown that once the first several Fresnel zones are screened from illumination by the source, additional fence placements provide very little improvement in the configuration of the field over the test aperture. Figures F.9 and F.10 show the relative Fresnel zone screening provided by an 8-foot fence and a 12-foot fence at X-band and S-band, respectively, as a function of source antenna height in the elevated mode.

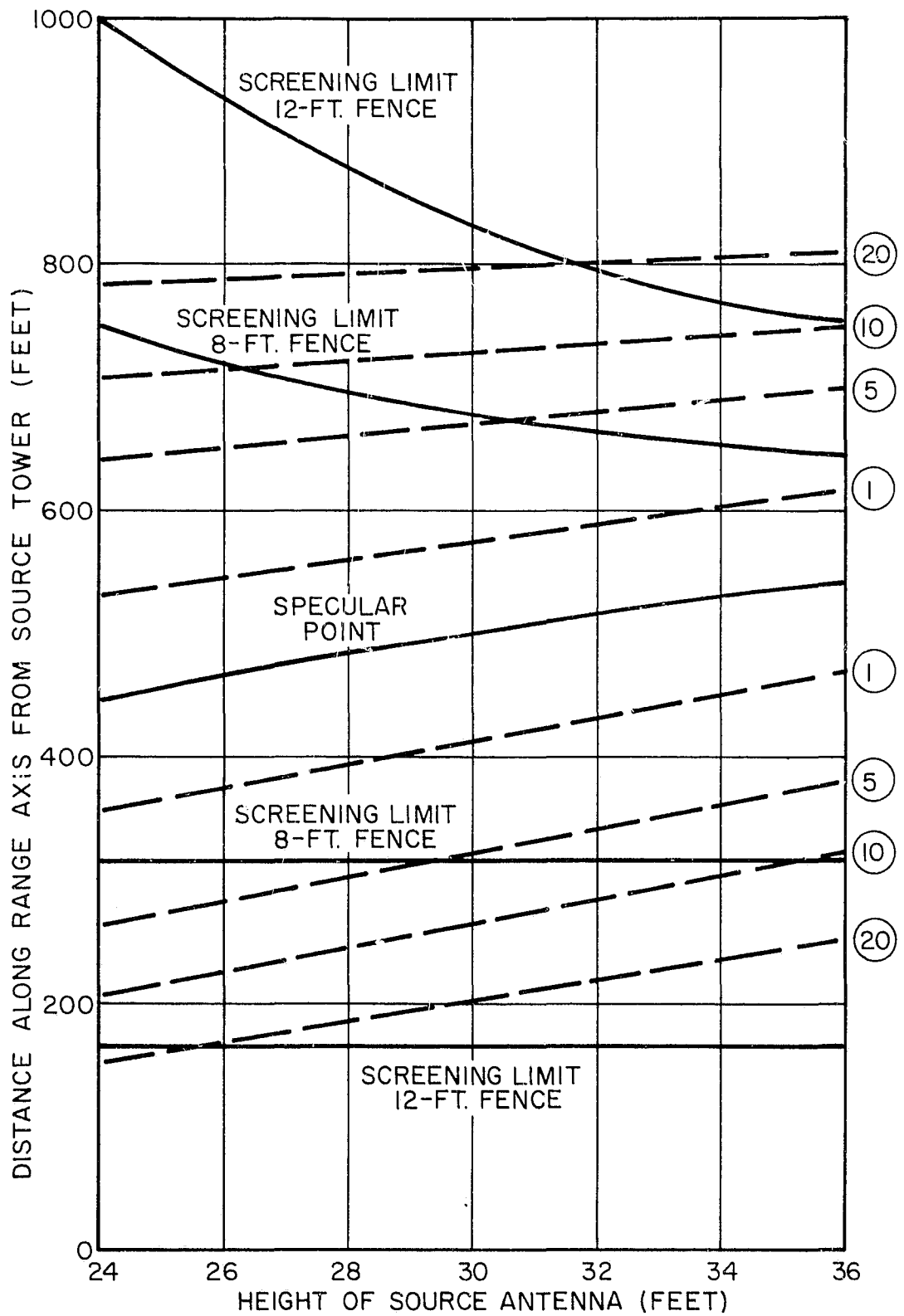


Figure F.9. Relative Fresnel Zone Screening on the MILA Range Provided by 8-Foot and 12-Foot Fences at 10 GHz. (The circled numbers at the right of the Figure indicate the Fresnel zone number.)

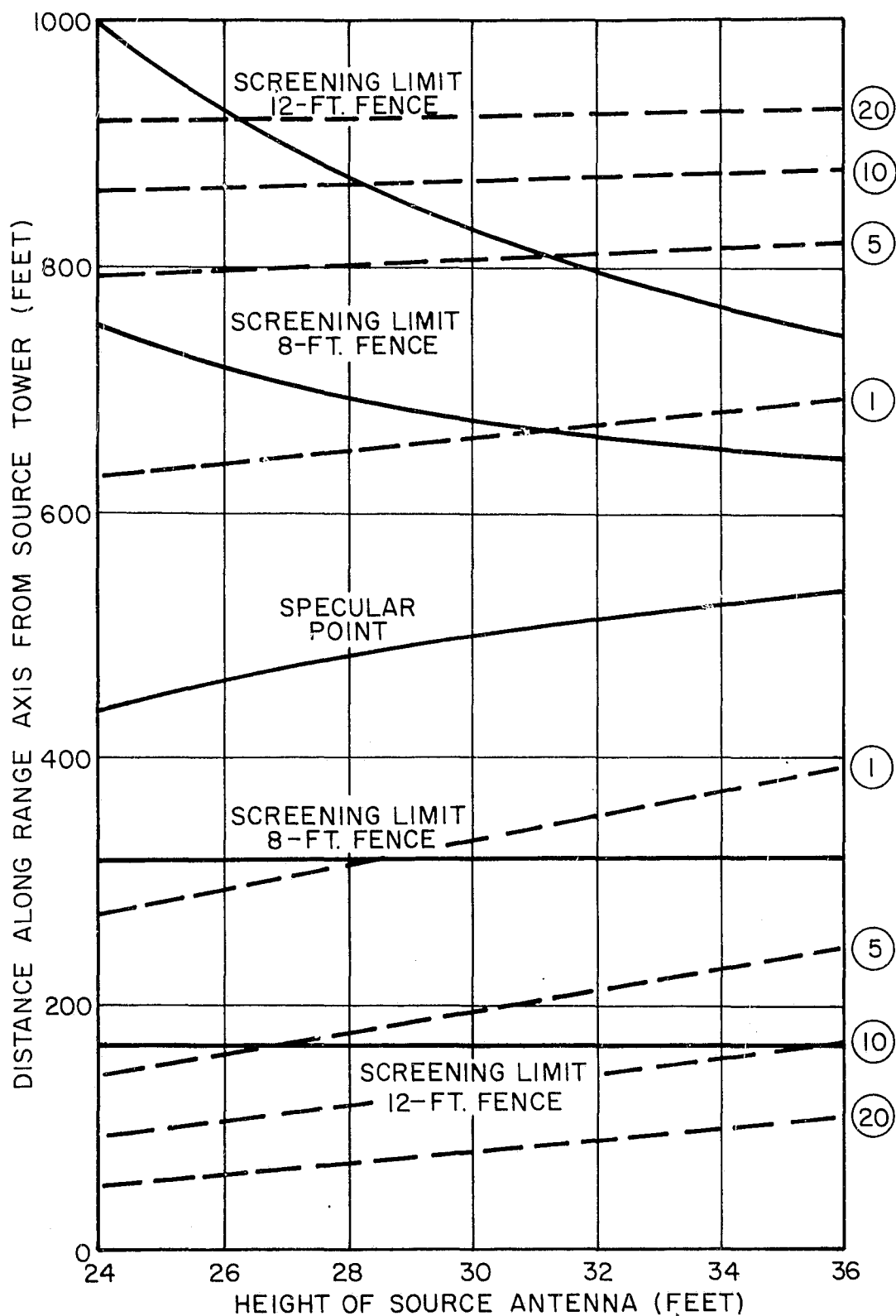


Figure F.10. Relative Fresnel Zone Screening on the MILA Range Provided by 8-Foot and 12-Foot Fences at 2.3 GHz. (The circled numbers at the right of the Figure indicate the Fresnel zone number.)



## APPENDIX G

### POLARIZATION MEASUREMENTS

Determination of the complete radiation characteristics of an antenna requires measurement of the polarization properties of the antenna. Polarization properties of antennas and polarization measurement techniques have been described in detail in the literature<sup>G-1</sup>. Only a brief discussion of polarization will be presented here as it relates to the KSC-MILA problem.

The polarization of an electromagnetic field at a point in space is defined as the direction along which the electric vector points, and the polarization of an antenna is described by the polarization of its radiated field. At large distances from an antenna the polarization of the radiated field is virtually independent of the distance from the antenna in the same manner that the radiation patterns are independent of distance.

The electric vector of a linearly polarized wave at a point in space oscillates in a single direction which is normal to the direction of propagation. In this case the total energy in the field is contained in a single polarization, represented by the electric field and its associated magnetic field. In the general case, however, the total energy in the field is the sum of the energy in two orthogonal polarizations. The electric vectors of these two orthogonal polarization components are in space quadrature, but are not necessarily equal in either magnitude or phase. In this event, the total field at a point in space represented by  $\vec{E}(t)$ , the vector summation of the two component electric vectors, does not oscillate in a single direction, but rotates in a plane which is normal to the direction of propagation; in the general case the instantaneous magnitude of the total field changes with time, and the tip of the electric vector representing the direction and magnitude of the field and plotted versus time describes an elliptical locus, which is the familiar polarization ellipse of Figure G.1.

The importance of the polarization in the analysis of system performance can be seen by consideration of the equation for power transfer between two arbitrarily

---

<sup>G-1</sup> L. Clayton and J.S. Hollis, Antenna Polarization Analysis by Amplitude Measurement of Multiple Components, presented at the Thirteenth Annual Symposium on USAF Antenna Research and Development, University of Illinois, 15-18 October 1963.

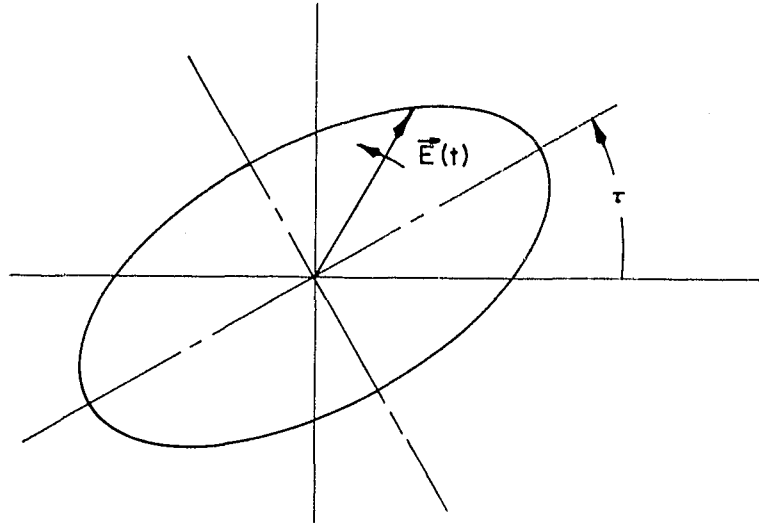


Figure G.1. Polarization Ellipse for Right-Hand Elliptical Polarization. Direction of propagation is out of paper. Rotation of  $\vec{E}(t)$  is counterclockwise in accordance with IEEE Standards.

polarized antennas<sup>G-2</sup>,

$$P_r = P_o G G' \left( \frac{\lambda}{4\pi R} \right)^2 \left[ \frac{(r^2 + 1)(r'^2 + 1) + 4 r r' + (r^2 - 1)(r'^2 - 1) \cos 2\alpha}{2(r^2 + 1)(r'^2 + 1)} \right] \quad (G-1)$$

where

$P_r$  is the power received,

$P_o$  is the input power at the terminals of the transmitting antenna,

$G$  is the gain of the transmitting antenna,

$G'$  is the gain of the receiving antenna,

$R$  is the separation between antennas,

$r$  is the axial ratio of the transmitting antenna in the direction of the receiving antenna,

$r'$  is the axial ratio of the receiving antenna in the direction of the transmitting antenna, and

$\alpha = (\tau - \tau')$ , the angle between the maxima of the polarization ellipses of the two antennas.

<sup>G-2</sup>V.H. Rumsey, G.A. Deschamps, M.L. Kales, and J.I. Bohnert, "Techniques for Handling Elliptically Polarized Waves with Special Reference to Antennas," Proceedings of the IRE 39, pp. 533-552 (1951); also the immediately following paper by M.G. Morgan and W.R. Evans, "Synthesis and Analysis of Elliptic Polarization Loci in Terms of Space-Quadrature Sinusoidal Components."

In accordance with IEEE standards, in (G-1)  $r$  and  $r'$  are taken as positive for right-hand circular polarization and negative for left-hand circular polarization. The quantity within the brackets is commonly referred to as the polarization efficiency of the antenna system. When  $r=r'$  and  $\alpha=0$ , the polarization efficiency becomes unity and (G-1) reduces to

$$P_r = P_o G G' \left( \frac{\lambda}{4\pi R} \right)^2 \quad (G-2)$$

In this case the antennas are said to be polarization matched.

If either of the antennas is linearly polarized,  $r$  or  $r'$  approaches infinity, and it is necessary to write (G-1) in the form

$$P_r = P_o G G' \left( \frac{\lambda}{4\pi R} \right)^2 \frac{\left(1 + \frac{1}{r^2}\right) \left(1 + \frac{1}{r'^2}\right) + \frac{4}{r r'} + \left(1 - \frac{1}{r^2}\right) \left(1 - \frac{1}{r'^2}\right) \cos 2\alpha}{2 \left(1 + \frac{1}{r^2}\right) \left(1 + \frac{1}{r'^2}\right)} \quad (G-3)$$

If the field of an antenna under test is explored by rotating a linearly polarized probe antenna ( $r'=\infty$ ) about an axis which is parallel with the direction of propagation, the received power is given by

$$P_r = P_o G G' \left( \frac{\lambda}{4\pi R} \right)^2 \left[ \frac{(r^2 + 1) + (r^2 - 1) \cos 2\alpha}{2(r^2 + 1)} \right] \quad (G-4)$$

The amplitude  $E_r$  of the signal at the terminals of the probe antenna is proportional to  $(P_r)^{\frac{1}{2}}$ .

Thus, from (G-4)  $E_r$  can be seen to be given by

$$E_r = K \left[ 1 + \left( \frac{r^2 - 1}{r^2 + 1} \right) \cos 2\alpha \right]^{\frac{1}{2}} \quad (G-5)$$

The quantity within the brackets of (G-5) is the polarization pattern of the antenna under test, shown in Figure G.2. The polarization pattern has maxima for  $\alpha=0$  or  $\pi$  and minima for  $\alpha=\pm\pi/2$ . The polarization pattern serves to define the axial ratio  $r$  and tilt angle  $\tau$  of the polarization ellipse.

Measurement of the polarization pattern of an antenna by rotation of a linearly polarized probe in the field serves to determine the tilt angle and axial ratio of the field radiated by the antenna in a given direction; it does not determine the

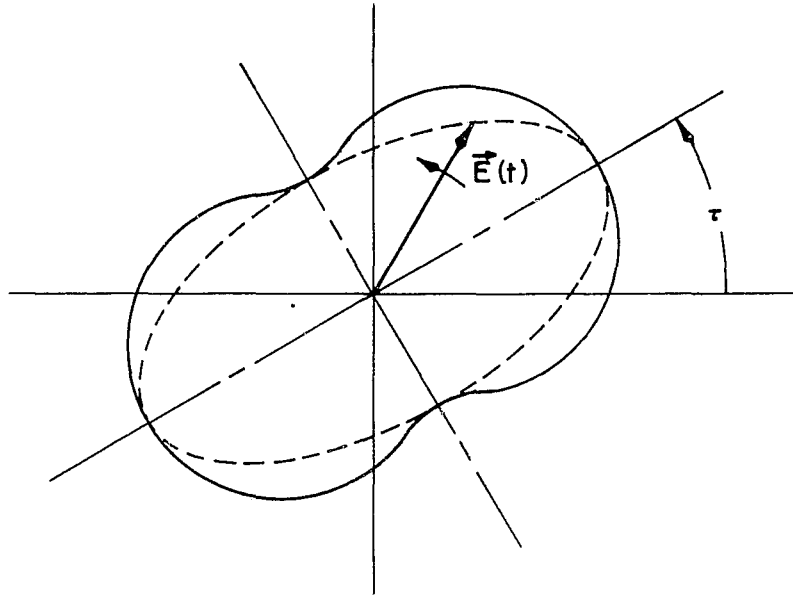


Figure G.2. Geometry Showing Relationship of Polarization Pattern to Polarization Ellipse

sense of the polarization. This can be accomplished by sampling the field successively with identical right circularly polarized and left circularly polarized antennas, and using the relation

$$r = \frac{E_R + E_L}{E_R - E_L} \quad (G-6)$$

where  $E_R$  and  $E_L$  are the amplitudes of the signals at the terminals of the right- and left-circularly polarized antennas, respectively.

An alternative method of polarization measurement is given by Clayton and Hollis<sup>G-1</sup>. This method, called the multiple component method, involves measurement of a minimum of 4 components of the received field, usually  $E_R$  and  $E_L$  and  $E_0$  or  $E_{90}$  and  $E_{45}$  or  $E_{135}$ , as shown in Figure G.3.

If all six components are measured, the complete polarization characteristics of an antenna can be determined by the simple equations:

$$r = \frac{E_R + E_L}{E_R - E_L} \quad , \quad (G-6)$$

and

$$\tau = \frac{1}{2} \tan^{-1} \frac{E_{45}^2 - E_{135}^2}{E_0^2 - E_{90}^2} \quad (G-7)$$

Additionally, measurement of all six components provides a check on the validity of the data through redundancy since

$$E_0^2 + E_{90}^2 = E_{45}^2 + E_{135}^2 = E_R^2 + E_L^2 \quad (G-8)$$

Use of (G-8) with (G-7) gives

$$\tau = \frac{1}{2} \tan^{-1} \frac{2E_{45}^2 - (E_R^2 + E_L^2)}{2E_0^2 - (E_R^2 + E_L^2)} \quad (G-9)$$

requiring measurement of only four components, but without the redundancy check provided by six measurements.

When antennas are employed in a system which detects energy scattered from a complex target, the polarization response of the system depends on the combined polarization characteristics of the transmitting and receiving antennas and of the target. A determination of the requirement for polarization measurements must be made for any particular test problem on the basis of the particular system characteristics and error specifications which apply.

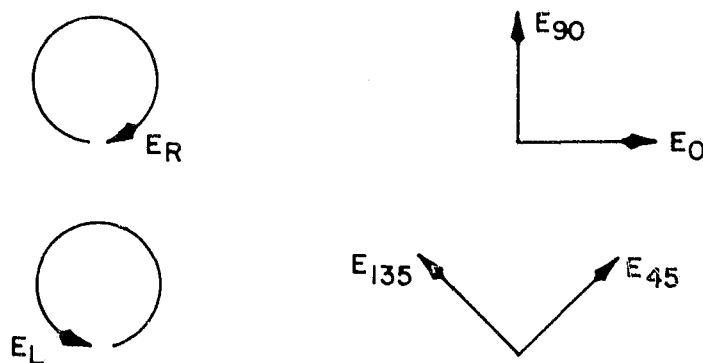


Figure G. 3. Field Components Used in Multiple Component Method of Polarization Analysis

APPENDIX H  
ANGULAR MEASUREMENT ACCURACY  
OF THE MILA RF BORESIGHT TEST FACILITY

H.1 Introduction

This appendix considers factors which affect the capability of the MILA RF Boresight Test Facility in measuring the direction of the line-of-sight from the source antenna to an antenna under test, usually a direction sensor, such as the Gemini or LEM rendezvous radars. The results also apply to angle measurement accuracy for making radiation pattern measurements, although extreme precision is not normally as critical in this application as in the boresight measurement problem.

To provide a background for the specific data and calculations which are presented in section 4.3, a theoretical discussion is included of antenna positioners and antenna positioner errors related to boresight measurements. Certain of this information was developed under Contracts AF30(602)-3425<sup>H-1</sup> and NAS10-817<sup>H-2</sup> and under Scientific-Atlanta sponsored research tasks.

H.2 Angle Measurements on a Boresight Range With Specific Reference to the Gemini and LEM Rendezvous Radars

An antenna boresight test range has as its primary function determination of the accuracy of a direction sensor; here we will consider the sensor to be located on an aircraft or space vehicle. A direction relative to the vehicle is usually described by two angles measured from reference coordinates of the vehicle's coordinate system. Figure H.1 shows the standard spherical coordinate system<sup>H-3</sup> which is employed for virtually all direction measuring systems.

---

<sup>H-1</sup> Investigation of Precision Antenna Pattern Recording and Display Techniques Phase II, Final Report, Vol. I, Contract No. AF30(602)-3425, Project No. 4506, Task No. 45064, Report No. RADC-TR-65-534.

<sup>H-2</sup> See A Precision Ground-Reflection Antenna Boresight Test Range, included as Appendix K of this document.

<sup>H-3</sup> IRIG Standard Coordinate System and Data Format for Antenna Patterns, Inter-Range Instrumentation Group, IRIG Document No. 102-61, AD 266697, September 1961, Chapter IV.

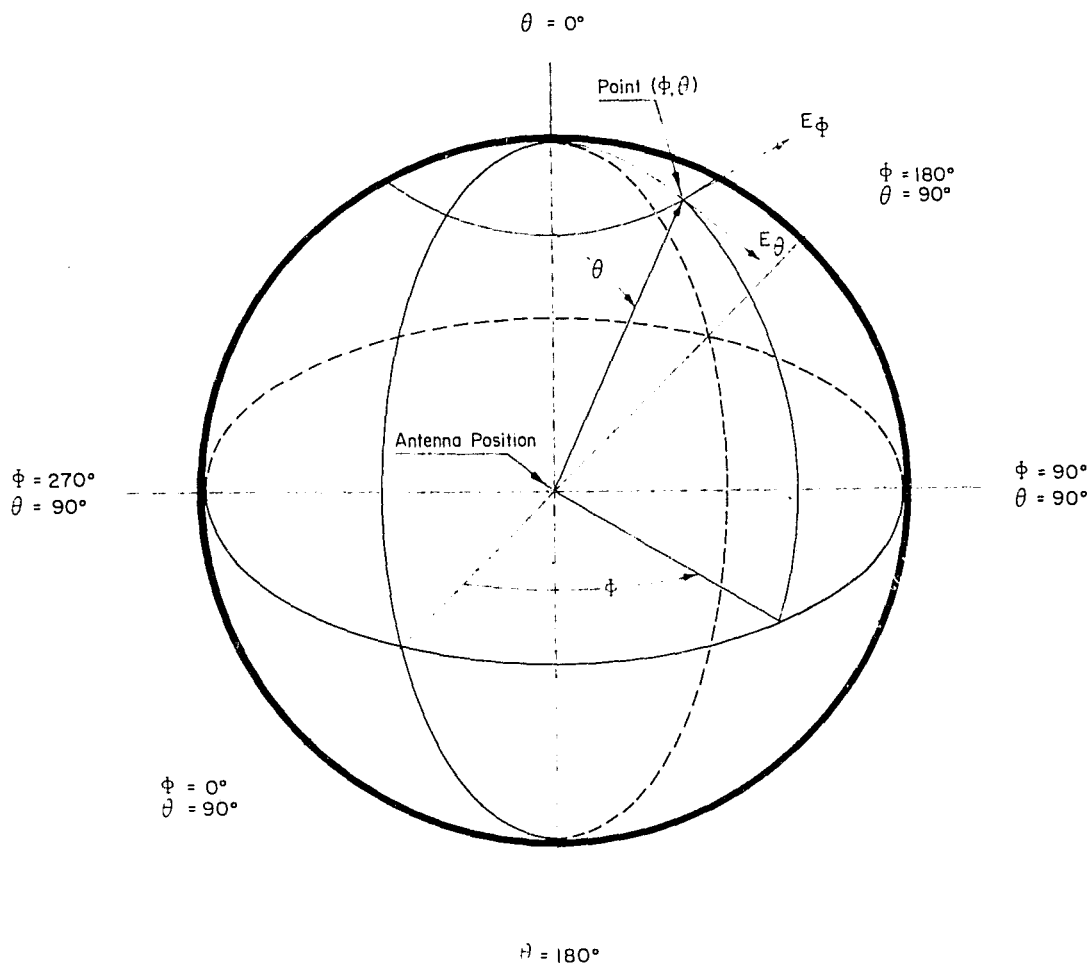


Figure H.1. Standard Antenna Coordinate System

The coordinate axes may be oriented with respect to the vehicle in any manner that is most convenient; the particular orientation usually is determined by the requirements of the vehicle's guidance system. The IRIG standard coordinate system for vehicle-mounted antennas is shown in Figure H.2.

Direction-measuring (boresight) accuracy may be determined in one-way or two-way measurements, sensing the direction to a source antenna in one-way tests or to a target antenna in two-way tests. The angle measuring problem is the same in both cases; here we will consider the measurements to be one-way measurements made with a source antenna with the understanding that the

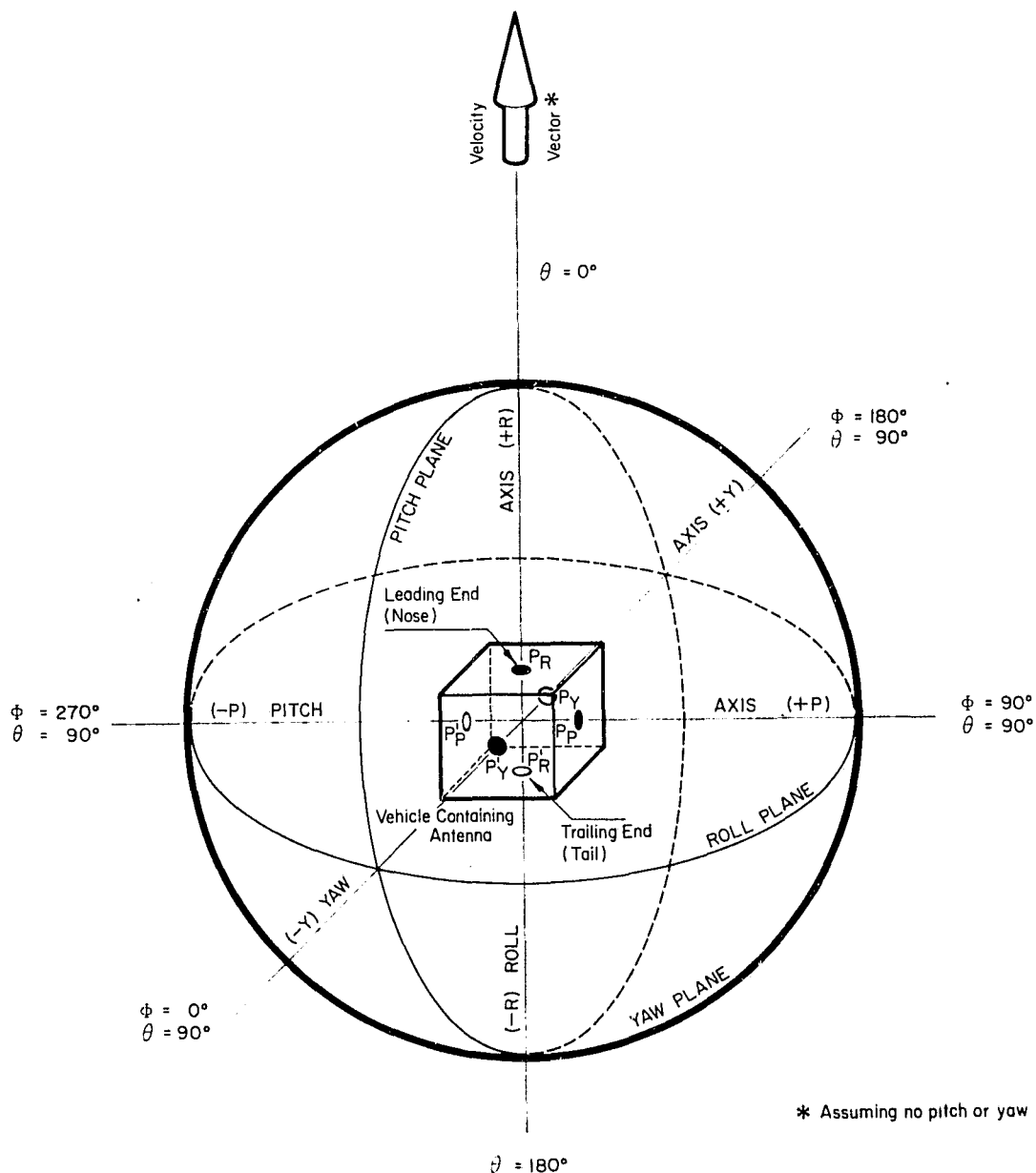


Figure H.2. IRIG Consolidated Vehicle and Antenna Coordinate System

discussion applies to both types of tests. In making tests of this type it is usually impracticable to move the source antenna over the wide range of angles which may be required, therefore the line-of-sight to the source antenna is maintained fixed or nearly-fixed in direction and a positioner, called a boresight positioner, is utilized to support and rotate the antenna system, with the vehicle if it is mounted, in relation to the source antenna. The boresight positioner should have such orientation capability as required by the using system,



and provide a position angle readout system whose output can be compared with the direction readout of the vehicle's measurement system.

#### H.2.1 Basic Consideration of the MILA Test Positioner for Mounting a LEM Mockup

Appendix K describes the coordinate systems and angle readout systems which are employed in the tests of the Gemini rendezvous radar. In this section two positioner orientations are described which are applicable to tests of the LEM rendezvous radar. The descriptions are idealized in nature in that parallax, misalignment, radar boresight and other errors are assumed to be zero. The effect of angular errors is considered in Section H.3.

Figure H.3 shows the LEM coordinate system and indicates a direction OT measured by the angles  $\alpha$  and  $\beta$  (the shaft and trunnion angles, respectively) of the rendezvous radar.\* Figures H.4 and H.5 show the LEM oriented on the bore-sight positioner in such a way that the lower azimuth and the elevation axes are utilized to rotate the LEM to the required test positions. Figure H.4 illustrates a zero reference position\*\* where

- (1) the rendezvous radar shaft axis is parallel to the LEM coordinate axis  $OY_L$
- (2) the rendezvous radar trunnion axis is parallel to the LEM coordinate axis  $OX_L$
- (3) the rendezvous radar RF boresight axis is parallel to the LEM coordinate axis  $OZ_L$ .

At these positions the shaft ( $\alpha$ ) and trunnion ( $\beta$ ) axis resolvers are to read zero.

---

\*The designations  $\alpha$  and  $\beta$  are employed in the LEM rendezvous radar coordinate system. These angles are related to the standard spherical coordinate system angles by the definitions

$$\alpha = \phi \quad (H-1)$$

$$\beta = \pi/2 - \theta \quad (H-2)$$

The LEM  $OY_L$  axis is the polar axis.

\*\*For simplicity it is here assumed that there are no misalignment errors in the rendezvous radar or the positioning system and that parallax error does not exist.

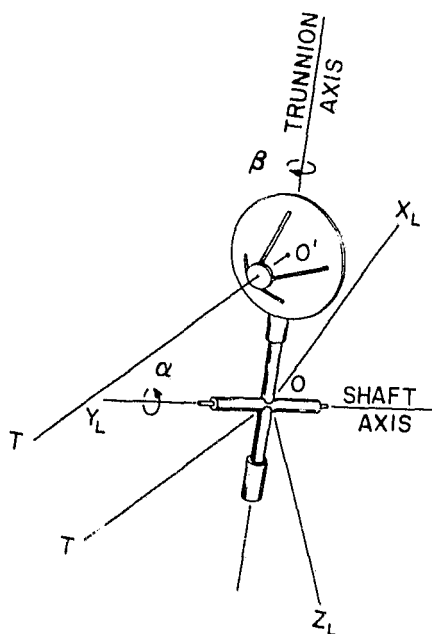
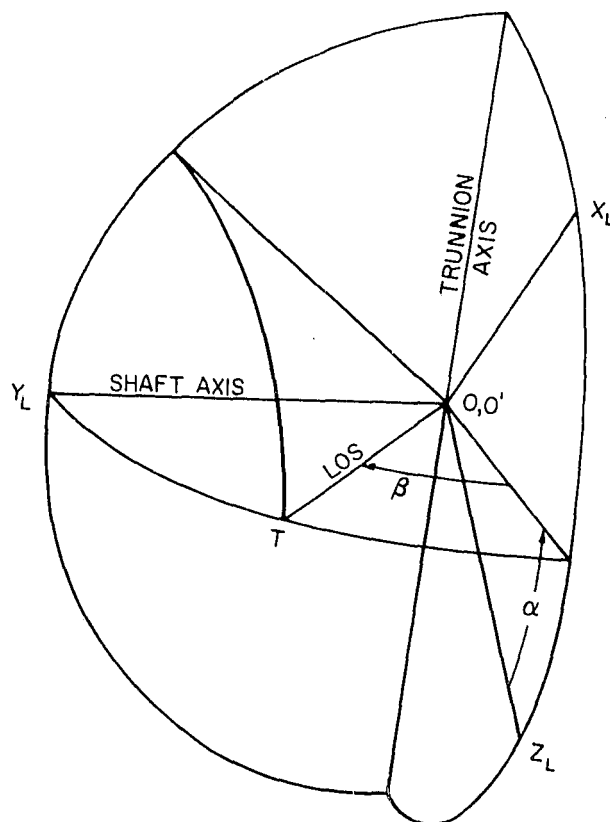


Figure H.3. LEM/RR Coordinate System

The shaft angle  $\alpha$  is measured in the right-hand direction in the  $X_L Z_L$  plane, from  $Z_L$  to the intersection of the  $X_L Z_L$  and  $Y_L T$  planes. The trunnion angle  $\beta$  is the latitude angle of the LOS (measured from the  $X_L Z_L$  plane) in the  $Y_L T$  plane. It is assumed that the distance  $OT$  is of sufficient magnitude that  $O$  and  $O'$  can be considered coincident.

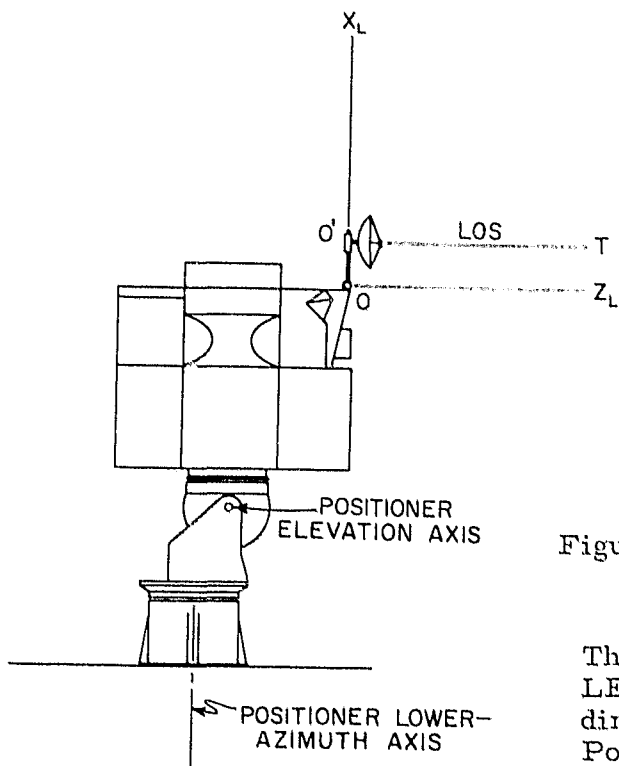


Figure H.4. View Along the LEM/RR  $OY$  Axis of a Partial LEM Mockup Mounted on a Three-Axis Boresight Positioner.

The LEM/RR  $OY_L$  (shaft) axis is orthogonal to the LEM/RR  $OX_L$  and  $OZ_L$  axes in a right-hand coordinate system, and is aligned parallel to the Positioner Elevation Axis. For the illustrated position of the radar,  $\alpha = \beta = 0$ .

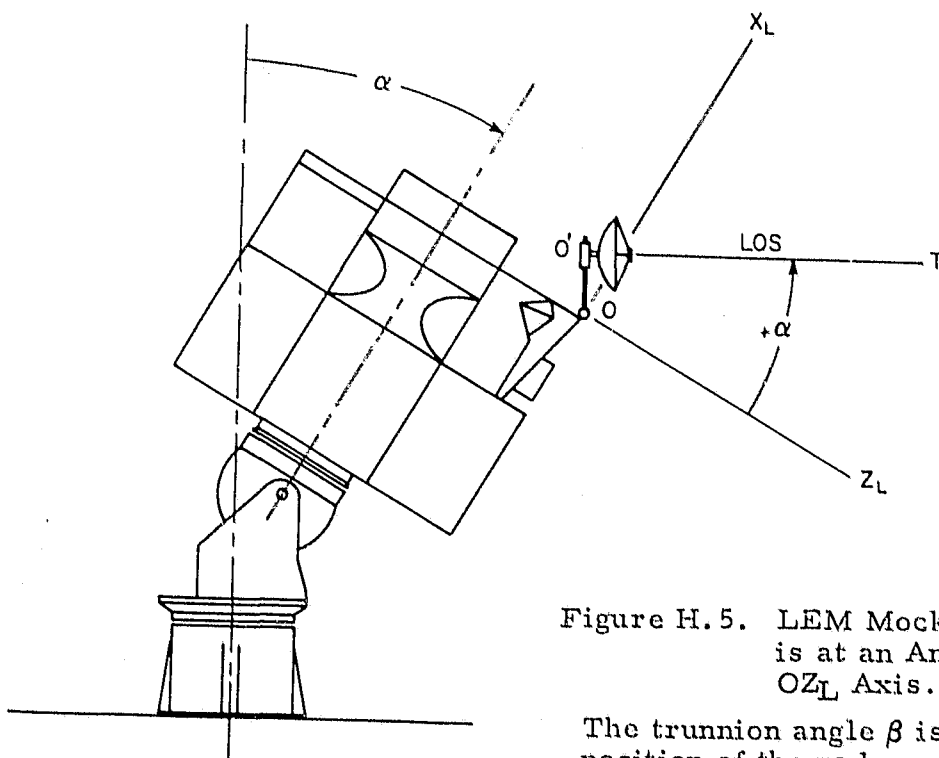


Figure H.5. LEM Mockup Inclined Such That the LOS is at an Angle of  $+\alpha$  From the LEM/RR  $OZ_L$  Axis.

The trunnion angle  $\beta$  is zero for the illustrated position of the radar, since the LOS is in the  $X_L Z_L$  plane of the LEM/RR coordinate system.

The zero reference position of Figure H.4 also shows that

- (1) the boresight positioner's elevation axis is parallel to the LEM coordinate axis  $OY_L$  and normal to the direction  $O'T$
- (2) the positioner's lower-azimuth axis is parallel to the LEM axis  $OX_L$  and normal to the direction  $O'T$ .

At these positions the shaft position readout of the boresight positioner corresponds to the zero position of the shaft and trunnion axes of the rendezvous radar.

Figure H.5 shows the boresight positioner elevation axis rotating the LEM and the LEM coordinate system to an inclination of  $+\alpha$  relative to the direction  $OT$ . The rendezvous radar is shown with its RF axis aligned with  $O'T$ , indicating that the shaft axis has rotated through a  $+\alpha$  angle equal to the angle of rotation made by the boresight positioner's elevation axis.

Examination of Figure H.5 shows that during the radar tracking tests (assuming no radar errors, misalignments or parallax) the rendezvous radar trunnion axis remains parallel to the boresight positioner's lower-azimuth axis. In either the orientation of Figure H.4 or the inclined position of Figure H.5, rotation of the positioner's lower-azimuth axis can be matched by rotation in the opposite direction by the radar trunnion axis to keep the RF boresight axis of the antenna aligned with the direction  $O'T$ .

Figure H.6 illustrates a front view of the LEM and positioner orientation shown in Figure H.4. The purpose of Figure H.6 is to indicate a LEM coordinate system and positioner axis orientation that may be directly compared to an alternate method of mounting the LEM mockup on a three-axis boresight positioner. In the alternate configuration of Figure H.7 the upper-azimuth axis of the boresight positioner is utilized to rotate the LEM coordinate system to selected angles  $\alpha$ . The elevation axis is used only to adjust the upper-azimuth axis to a position of perpendicularity with respect to the lower-azimuth axis. A major advantage provided by the mounting configuration of Figure H.7 is that of improved positioning accuracy. The upper- and the lower-azimuth axes can be counter-weighted so that the center of gravity of the turntable loads about each of these axes is very nearly on the axis of rotation. The resulting small shifts in weight due to axis rotations result in small deflection errors. A disadvantage of the mounting orientation of Figure H.7 is that the boresight positioner is closer to

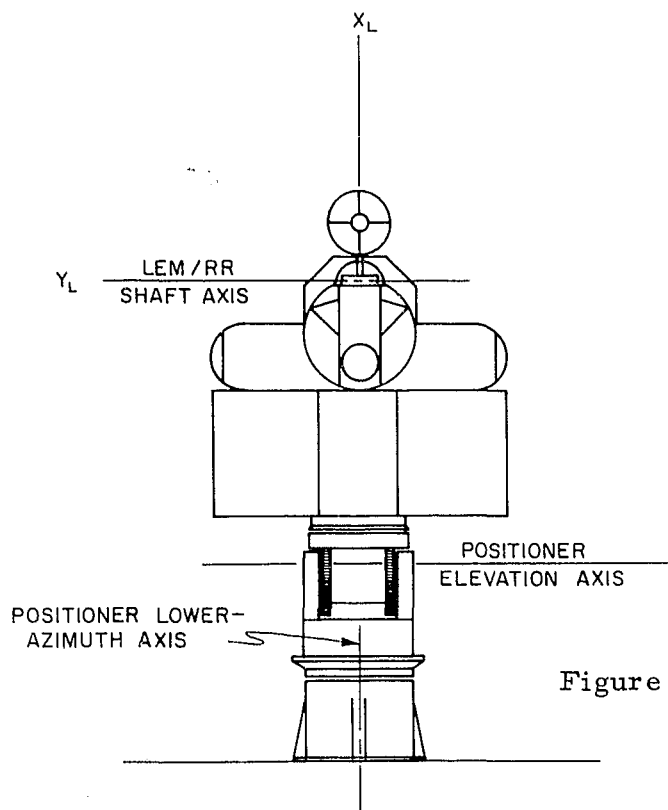


Figure H.6. View Along the LEM/RR  $OZ_L$  Axis of a Partial LEM Mockup Mounted on a Three-Axis Bore-sight Positioner. The LOS is out of the page, and  $\alpha = \beta = 0$ .

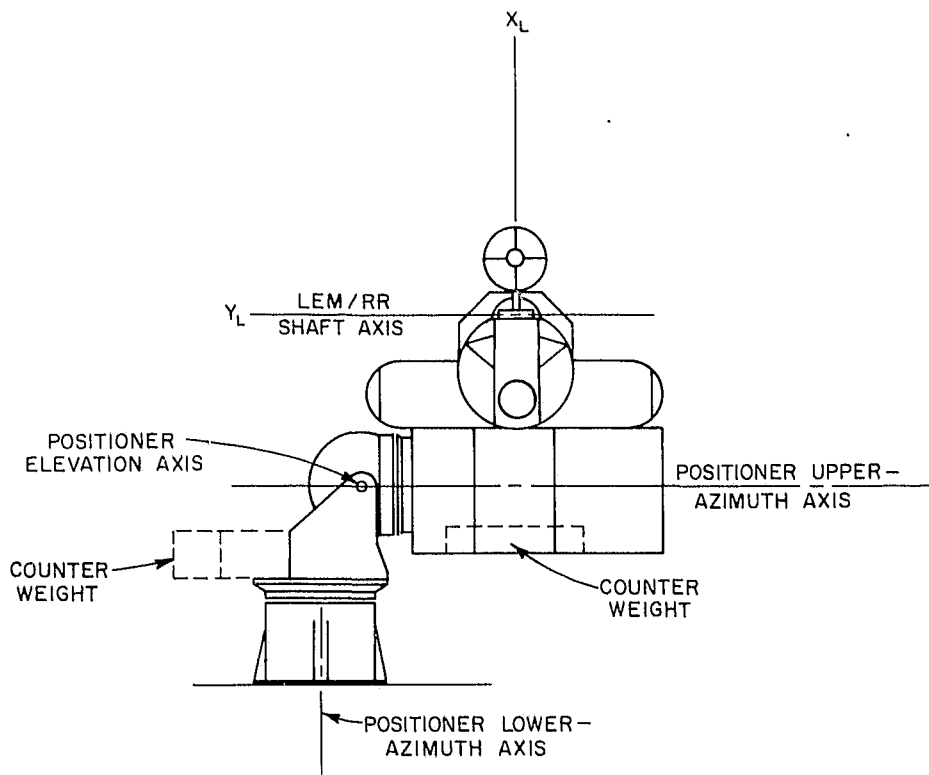


Figure H.7. View Along the LEM/RR  $OZ_L$  Axis of a Configuration Utilizing the Positioner Upper-Azimuth Axis for LEM/RR Shaft Motion. The LOS is out of the page, and  $\alpha = \beta = 0$ .

the rendezvous radar reflector than in the previous orientations. Although the LEM mockup can be designed to partially surround the positioner, parts of the positioner would likely be visible to the radar for certain test orientations.

### H.3 Angle Measurement Error on a Boresight Range

Angle measurement errors from a number of sources must be considered in determining the accuracy of a boresight range. For the purposes of this analysis, the error sources can generally be included in one of the following classifications:

- (1) Geometric Error
- (2) Shaft-Position Error
- (3) Deflection Error

Additional direction errors which can be caused by phase and amplitude variations in the field over the test aperture, reflections, and parallax are discussed in other sections of this report.

#### H.3.1 Geometric Error

If the boresight positioners of Figure H.8 were geometrically perfect, the earth-fixed positioner axis OA would be exactly normal to the positioner axis  $OZ_P$ , and the direction line OT from the positioner to the source antenna would be exactly normal to OA. The geometrically perfect boresight test system would also have the vehicle installed on the positioner turntable so that the coordinate system of the vehicle would be exactly aligned with the coordinate system of the positioner, as implied in Figure H.8.

An actual boresight range consists of physical components that may approach the above requirements, but geometric and mechanical errors will always exist. Every boresight measurement system will have three separate geometric errors, which can be identified and described as follows:

- (1) Coordinate axis alignment error--Improper alignment of the vehicle coordinate system with that of the antenna positioner.
- (2) Orthogonality error--Non-orthogonality of the two motion axes of the antenna positioner.

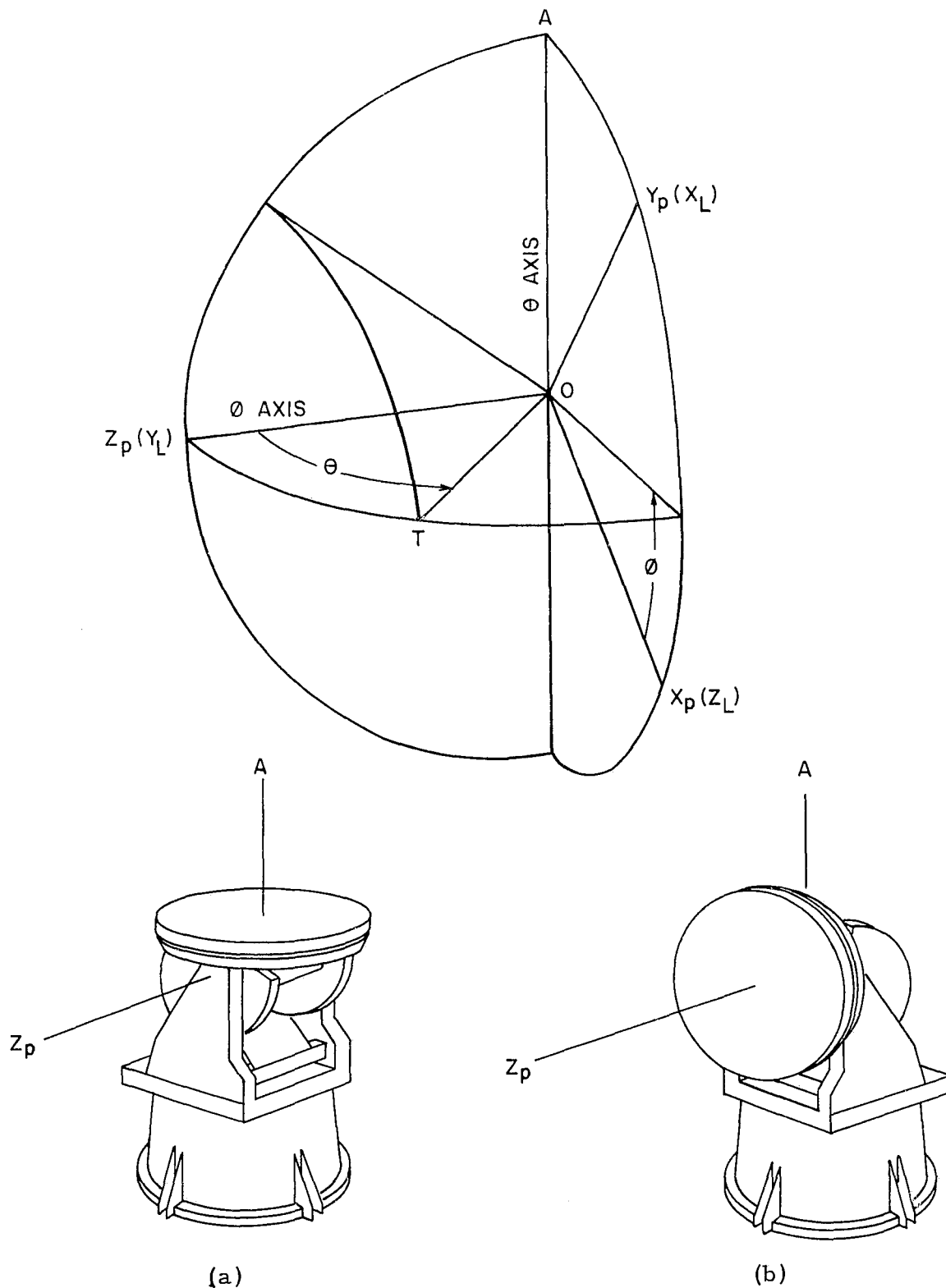


Figure H.8. Spherical Coordinate System Employed with Two Orientations of MILA Test Positioner. The configuration shown in (a) is that of Figures H.4, H.5 and H.6. The configuration of (b) is that of Figure H.7. Note that the same coordinate system applies to both test positioner arrangements. In (a) and (b) axis  $OA$  refers to the lower azimuth axis of the test positioner.

- (3) Collimation error--Non-orthogonality of the  $\theta$ -axis (OA) with the direction OT to the signal source antenna.

The analysis in this section will not present arguments relating to the interdependence of one geometric error upon the others; an analysis of the combined effect of simultaneous errors of the three types is beyond the scope of the present study. For most measurement applications sufficient accuracy will be achieved by calculating the three geometric-error effects separately, and the following calculations will treat them as if they were independent functions.

H.3.1.1 Coordinate Axis Alignment Error: In order to calculate the errors that are caused by coordinate axis misalignment it is convenient to stipulate that the positioner and range be mechanically perfect in all other respects. That is, it will be assumed that the two motion axes are exactly orthogonal and that the direction to the source antenna is exactly orthogonal to the OA axis.

Examination of Figure H.8 shows that the polar axis of the coordinate system is to be coincident with the  $\phi$  axis of the positioner. Since the vehicle coordinate system is defined with respect to a mechanical reference on the vehicle while the  $\phi$  axis is mechanically related to the positioner, some misalignment between the two will always exist in practice. The misalignment can be described and the errors analyzed by the use of Euler angles (see Appendix I).

Figure H.9 illustrates an antenna range installation in which a vehicle coordinate system (XYZ) is positioned and fixed to a positioner turntable such that a misalignment error exists. The direction  $\phi, \theta$  is the direction to the source transmitter in the vehicle coordinate system (XYZ).

The polar ( $\bar{\phi}$ ) axis of rotation is  $O\bar{Z}$  of the positioner turntable coordinate system  $\bar{X}\bar{Y}\bar{Z}$ , and the direction  $\bar{\phi}, \bar{\theta}$  is the direction of the source transmitter in the positioner coordinate system.\*

The vehicle coordinate system XYZ is misaligned from coordinate system  $\bar{X}\bar{Y}\bar{Z}$  by the Euler angles  $\alpha, \beta$ , and  $\gamma$ . (Not to be confused with the shaft and trunnion angles  $\alpha$  and  $\beta$  of paragraph H.2.)

---

\* In the context of paragraph H.2, the system (XYZ) would correspond to  $(Z_L X_L Y_L)$ , and the system ( $\bar{X}\bar{Y}\bar{Z}$ ) would correspond to  $(X_P Y_P Z_P)$ .



In the typical boresight measurements situation the boresight directions are required as a function of  $\phi, \theta$ . However, the boresight range equipment (positioner, position indicators, recorder) will measure the boresight directions as functions of  $\bar{\phi}, \bar{\theta}$ .

Given the Euler angles  $\alpha, \beta$ , and  $\gamma$  and the direction  $\bar{\phi}, \bar{\theta}$ , the direction  $\phi, \theta$  may be calculated by equations (I-9) and (I-2) of Appendix I:

$$\phi = \tan^{-1} \left[ \frac{\sin \bar{\theta} \sin(\bar{\phi} - \alpha)}{\sin \bar{\theta} \cos \beta \cos(\bar{\phi} - \alpha) - \cos \bar{\theta} \sin \beta} \right] - \gamma \quad (\text{I-9})$$

$$\theta = \cos^{-1} \left[ \cos \bar{\theta} \cos \beta + \sin \bar{\theta} \sin \beta \cos(\bar{\phi} - \alpha) \right] \quad (\text{I-2})$$

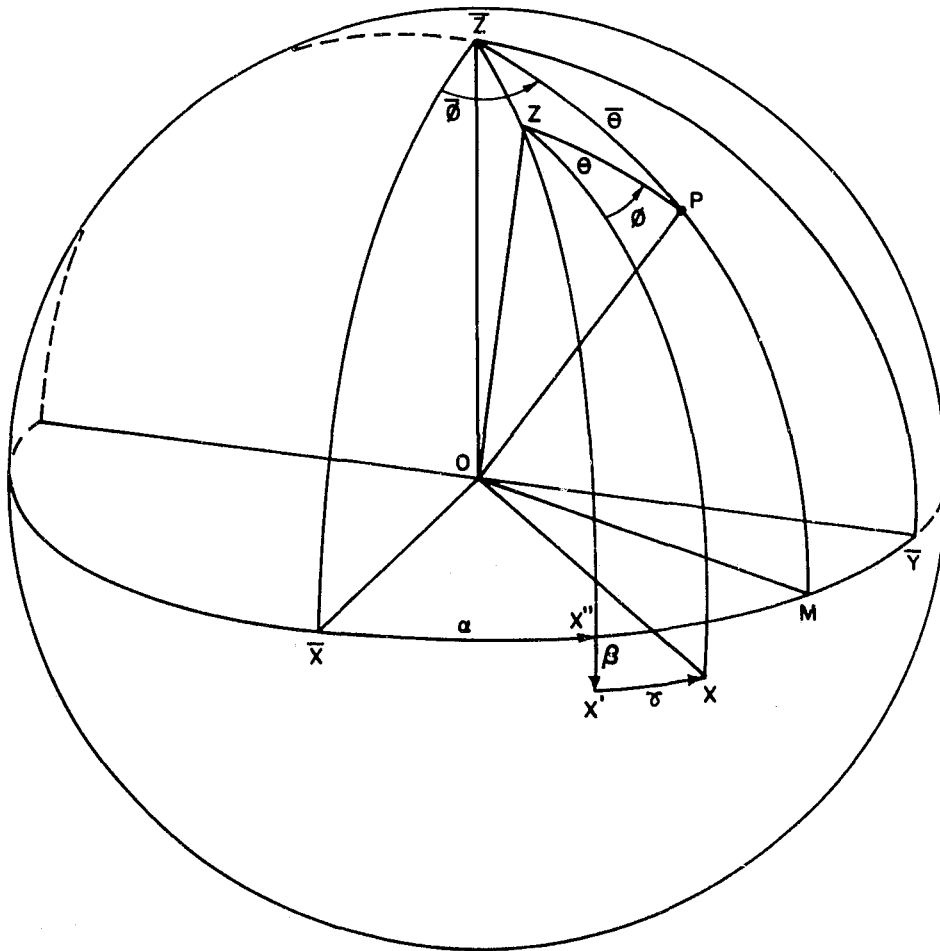


Figure H.9. A Direction Described in Two Coordinate Systems

H.3.1.2 Orthogonality Error: A positioner with an orthogonality error is diagrammed in Figure H.10. For this case it is stipulated that all other characteristics of the geometry of the system are perfect. The coordinate system of the vehicle coincides perfectly with the positioner coordinate system, and the direction to the source transmitter is exactly normal to the mechanical  $\bar{\theta}$ -axis, which will be designated OA'. The polar ( $\bar{\phi}$ ) axis of the antenna positioner is OZ. The mechanical  $\bar{\theta}$ -axis OA', which should be coincident with OA, is displaced by an angle  $\delta$  from the XY plane.

If the geometry were perfect, the vehicle coordinate system XYZ could be rotated about OA so that the direction OT to the source transmitter would be in the plane OMZ. However, due to the orthogonality error, rotation about the  $\bar{\theta}$  axis will position OT in the plane OMZ'.

The angles or directions which will be indicated by the instrumentation equipment are  $\bar{\phi}, \bar{\theta}$ , where  $\bar{\phi}$  is the rotation about the positioner polar ( $\bar{\phi}$ ) axis and  $\bar{\theta}$  is the rotation about the positioner  $\bar{\theta}$  axis.

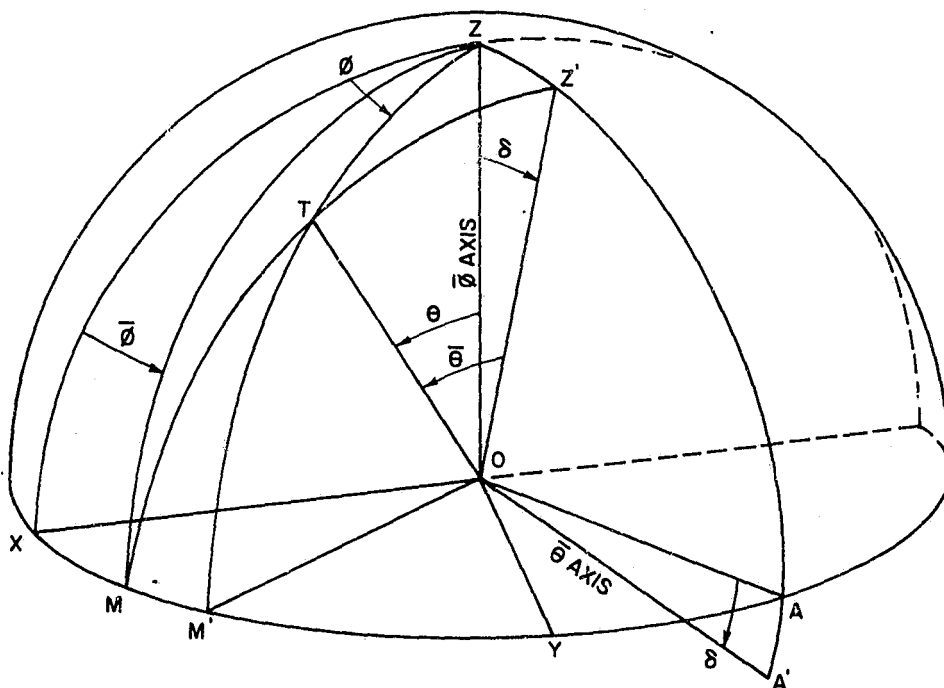


Figure H.10. Antenna Positioner With Orthogonality Error

In order to position the direction OT as shown in Figure H.10, OT can be considered to have moved from OX to OM by rotation about the OZ axis, then from OM to OT by rotation about the OA' axis. Therefore, the direction  $\bar{\phi}$  of OT is the angle between planes XOZ and MOZ.

Since  $\bar{\theta}$  is a measure of the mechanical rotation about OA' it is an angle in plane MOZ', which is the plane of the great circle that is normal to OA'.

The spherical triangles utilized in the solution are shown in Figure H.11. It can be seen that the spherical angles ZX, ZM, ZM' and Z'M are all equal to 90 degrees by definition or construction. Also the spherical angles ZZ'T and TM'M are equal to 90 degrees. Angle  $\delta$  is the orthogonality error.

From the right spherical triangle Z'ZT

$$\theta = \cos^{-1} (\cos \delta \cos \bar{\theta}) \quad (\text{H-3})$$

and

$$\sin^2 \theta = 1 - \cos^2 \delta \cos^2 \bar{\theta} \quad (\text{H-4})$$

From the right spherical triangle MM'T

$$\cos \Delta \phi = \frac{\cos(90^\circ - \bar{\theta})}{\cos(90^\circ - \theta)} \quad ,$$

or

$$\cos \Delta \phi = \frac{\sin \bar{\theta}}{\sin \theta} \quad (\text{H-5})$$

Substituting from equation (H-4) gives

$$\cos \Delta \phi = \frac{\sin \bar{\theta}}{(1 - \cos^2 \delta \cos^2 \bar{\theta})^{\frac{1}{2}}} \quad (\text{H-6})$$

It can be seen from Figure H.11 that

$$\phi = \bar{\phi} + \Delta \phi \quad ,$$

therefore

$$\phi = \bar{\phi} + \cos^{-1} \frac{\sin \bar{\theta}}{(1 - \cos^2 \delta \cos^2 \bar{\theta})^{\frac{1}{2}}} \quad (\text{H-7})$$

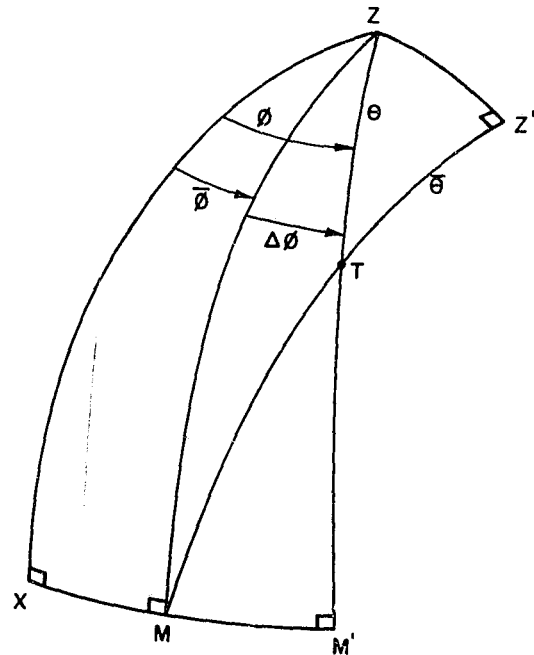


Figure H.11. Spherical Triangles of Figure H.10

The evaluation of equation (H-7) is difficult when  $\delta$  is small. By the substitution of identities a more convenient form can be derived. It can be shown that equation (H-7) is identical to

$$\phi = \bar{\phi} + \sin^{-1} \frac{\sin \delta \cos \bar{\theta}}{(1 - \cos^2 \delta \cos^2 \bar{\theta})^{\frac{1}{2}}} \quad , \quad (\text{H-7a})$$

thus for small  $\delta$  where  $\cos^2 \delta \doteq 1$ ,

$$\phi \doteq \bar{\phi} + \sin^{-1} [\sin \delta \cot \bar{\theta}] \quad . \quad (\text{H-7b})$$

H.3.1.3 Collimation Error: Collimation error is that error which exists when the direction to the source antenna is not normal to the  $\theta$  axis. The effect of collimation error is shown in Figure H.12. In this analysis the coordinate axes of the vehicle are coincident with the coordinate axes of the positioner turntable and the positioner  $\theta$  axis (OA) is exactly normal to the positioner  $\phi$  axis. Collimation error is identified in Figure H.12 as angle  $\epsilon$ . When the vehicle

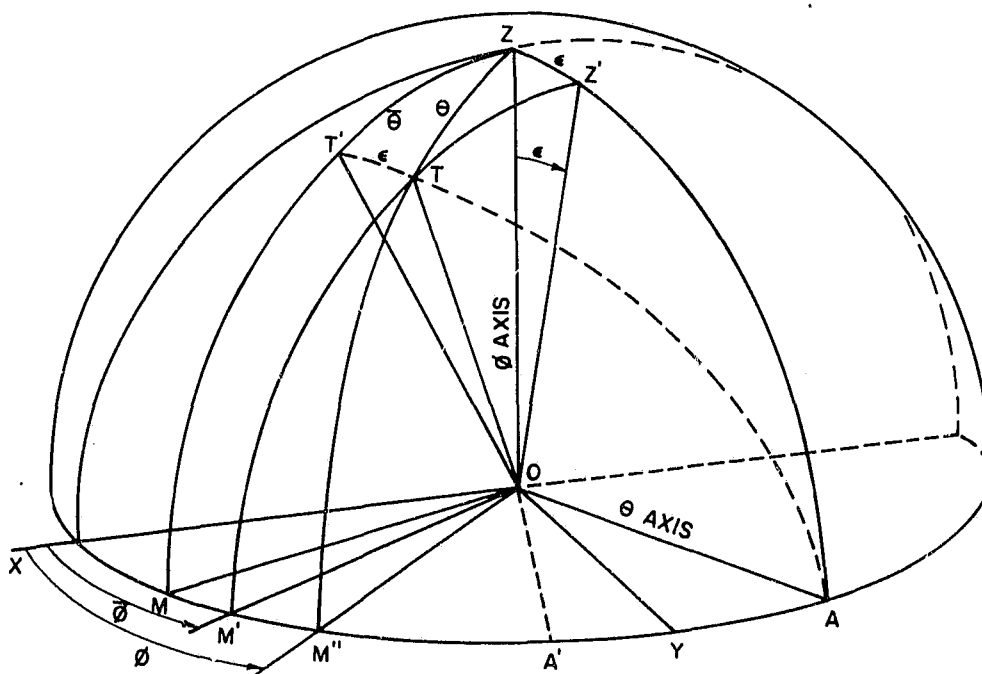


Figure H.12. Antenna Positioner With Collimation Error

coordinate system XYZ is moved by rotation of the  $\theta$  axis, OT sweeps a conical surface OZ'M'. The arc Z'M' is a portion of a small circle which is parallel to the great circle (ZM) of axis OA. Arc TT' is a portion of a great circle that intercepts point A. It can be seen that an antenna positioner with collimation error cannot position OT coincident with the OZ-axis; OZ' is the closest approach of OT to the OZ-axis.

The zero position for  $\bar{\phi}$  will be defined as that position of the mechanical  $\phi$ -axis that will align OT with the coordinate axis OX. This occurs when OA is at OA', an angle  $\epsilon$  from Y. The angle  $\bar{\theta}$  is again defined as rotation of the axis OA; the zero position for  $\theta$  is that position which establishes coincidence of OT with OZ'.

The spherical triangles of Figure H.12 which are utilized for the solution of angles  $\phi, \theta$  are redrawn in Figure H.13. By construction, TT'Z is a right spherical triangle with the 90-degree spherical angle at T', and MM''Z is a right spherical triangle with 90-degree spherical angles at both M and M''.

In Figure H.12 it can be seen that

$$\epsilon = ZZ' = TT' = MM'$$

and

$$\phi = \bar{\phi} + M'M''$$

or

$$\phi = \bar{\phi} + MM'' - \epsilon, \quad (H-8)$$

where  $\epsilon$  is positive when angle A'OT is less than  $90^\circ$ .

Further

$$\tan \sigma = \frac{\tan \epsilon}{\sin \bar{\theta}},$$

and since  $\sigma = MM''$ ,

$$MM'' = \tan^{-1} \frac{\tan \epsilon}{\sin \bar{\theta}}$$

which may be substituted in equation (H-8) to give

$$\phi = \bar{\phi} - \epsilon + \tan^{-1} \frac{\tan \epsilon}{\sin \bar{\theta}}. \quad (H-9)$$

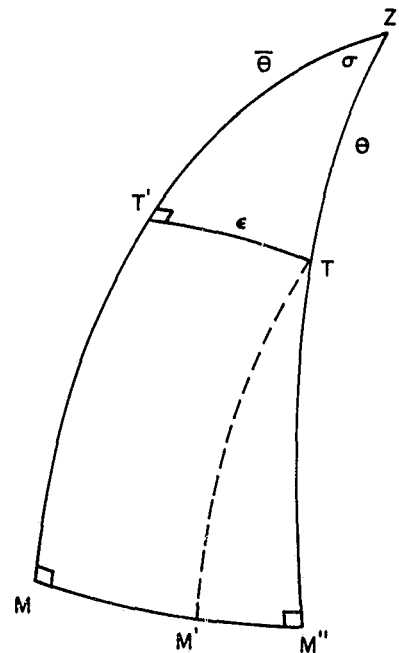


Figure H.13. Spherical Triangles of Figure H.12

From the conventional relation between the sides and the angles of the right spherical triangle TT'Z,

$$\theta = \cos^{-1} [\cos \bar{\theta} \cos \epsilon] \quad . \quad (H-10)$$

H.3.1.4 Summary of Geometric Error Calculations: The calculations for a direction  $\phi, \theta$  of a vehicle having geometric misalignment errors are summarized as follows:

(1) Coordinate Axis Misalignment

(Figure I.1, Appendix I, and section H.3.1.1):

$$\phi = \tan^{-1} \left[ \frac{\sin \bar{\theta} \sin(\bar{\phi} - \alpha)}{\sin \bar{\theta} \cos \beta \cos(\bar{\phi} - \alpha) - \cos \bar{\theta} \sin \beta} \right] - \gamma \quad (H-11)$$

$$\theta = \cos^{-1} [\cos \bar{\theta} \cos \beta + \sin \bar{\theta} \sin \beta \cos(\bar{\phi} - \alpha)] \quad (H-12)$$

(2) Orthogonality Error

(Figure H.10 and section H.3.1.2):

$$\phi = \bar{\phi} + \sin^{-1} \frac{\sin \delta \cos \bar{\theta}}{(1 - \cos^2 \delta \cos^2 \bar{\theta})^{\frac{1}{2}}} \quad (H-7a)$$

$$\theta = \cos^{-1} (\cos \delta \cos \bar{\theta}) \quad (H-3)$$

(3) Collimation Error

(Figure H.12 and section H.3.1.3):

$$\phi = \bar{\phi} - \epsilon + \tan^{-1} \frac{\tan \epsilon}{\sin \bar{\theta}} \quad (H-9)$$

$$\theta = \cos^{-1} [\cos \bar{\theta} \cos \epsilon] \quad (H-10)$$

## H.3.2 Shaft Position Error

The shaft position of a boresight positioner is usually determined by synchro transmitters, resolvers or digital encoders. Shaft position error is the difference between the true shaft angle and the shaft angle as indicated by the encoder or

synchro readout system. The angle measuring equipment of the MILA boresight positioner consists of geared synchro transmitters at ratios of 1:1 and 36:1 with respect to each axis. Over large angles of axis rotation the readout error is less than 0.01 degree (36 arc seconds) maximum for the upper and lower azimuth axes and 0.05 degree for the elevation axis. All three axes show an improvement in accuracy when a small angle is considered. Errors of less than 0.005 degree were recorded when axis angles of 2 to 5 degrees were calibrated. Additional information on shaft position error is given in section 4.3.

At the current state of the art, direct-drive digital encoder systems are more accurate than geared synchro systems. On the basis of recent measurements at Scientific-Atlanta of the accuracy of a positioner which employed 19-bit encoders, modification of the existing MILA boresight positioner by the addition of 19-bit encoders can improve the accuracy to about 10 arc seconds. (The total shaft position error with an encoder installed consists of the encoder error, encoder housing deflection, encoder coupling error, differential temperature effects, etc.)

### H.3.3 Deflection Error

Positioner deflection errors are caused principally by changes in the forces applied to the positioner turntables and by expansion and contraction of structural members due to differential temperatures. Measurements performed by Scientific-Atlanta on other recent projects and observations made at MILA indicate that temperature effects caused by uneven solar heating can be expected to induce deflections of up to 30 arc seconds in the positioner structure between the concrete mounting pad and the upper azimuth turntable.

To reduce the effect of errors due to solar deflection an insulated shield or barrier could be fabricated to cover the positioner support structure. In addition to the solar radiation shield a deflection monitoring system can be employed. The deflection monitor would be installed to indicate the inclination of the lower-azimuth axis relative to the local gravity vector. Electronic levels such as the Taylor-Hobson "Talyvel" or the Geotechnical Corporation Tilt Measuring System, Model 18279, could be utilized for this purpose. Both the Taylor-Hobson and the Geotec levels have remote-reading electronic indicators that could be installed in the antenna range control room.

Large changes in the positioner bending moment applied at the upper azimuth turntable will cause significant direction errors in a vertical plane. For example, if a 2000-pound model were supported so that the center-of-gravity was 10 feet above the upper-azimuth turntable and the model was rotated from the vertical to a horizontal position with the elevation axis, the change in bending moment would be 20,000 pound-feet. The MILA boresight positioner has a compliance in bending of approximately  $12 \times 10^{-8}$  radians per pound-foot, and the 20,000 pound-foot change would cause a structural deflection of approximately 0.1 degree.



# APPENDIX I

## SPHERICAL COORDINATE TRANSFORMATION BY EULER ANGLES\*

The relative orientation of two three-dimensional, orthogonal coordinate systems can be described by the three Euler angles  $\alpha$ ,  $\beta$  and  $\gamma$ . In the general case any relative orientation of the two coordinate systems can be achieved by three successive rotations about the coordinate axes. The rotations from a coordinate system  $\bar{X}\bar{Y}\bar{Z}$  to a system  $XYZ$  are (Figure I.1):

1. Rotation about the  $\bar{Z}$ -axis through an angle  $\alpha$  to  $X''Y''Z''$ .
2. Rotation about the  $Y''$ -axis through an angle  $\beta$  to  $X'Y'Z'$ .
3. Rotation about the  $Z'$ -axis through an angle  $\gamma$  to  $XYZ$ .

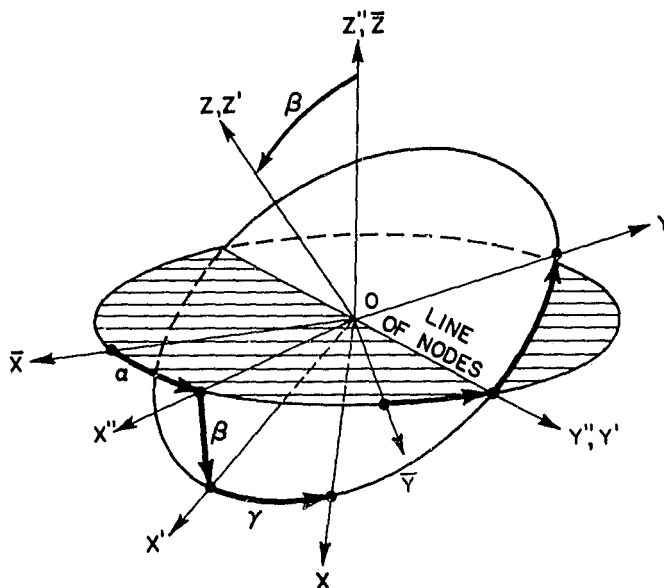


Figure I.1. Coordinate Axes Rotated Through the Euler Angles  $\alpha$ ,  $\beta$ ,  $\gamma$

\*The material presented in this appendix was developed under Contract AF 30-(602)-3425, and was contained in Rome Air Development Center Report RADC-TR-65-534 dated February 1966. It is presented here because of its direct use in Appendix H.

Let the spherical coordinates  $\phi, \theta$  designate a direction  $OP$  in the coordinate system  $XYZ$  of Figure I.2, and let the spherical coordinates  $\bar{\phi}, \bar{\theta}$  designate the direction  $OP$  in the coordinate system  $\bar{X}\bar{Y}\bar{Z}$ . The direction  $\phi, \theta$  may then be described in terms of  $\bar{\phi}, \bar{\theta}$  and the Euler angles  $\alpha, \beta$  and  $\gamma$ .

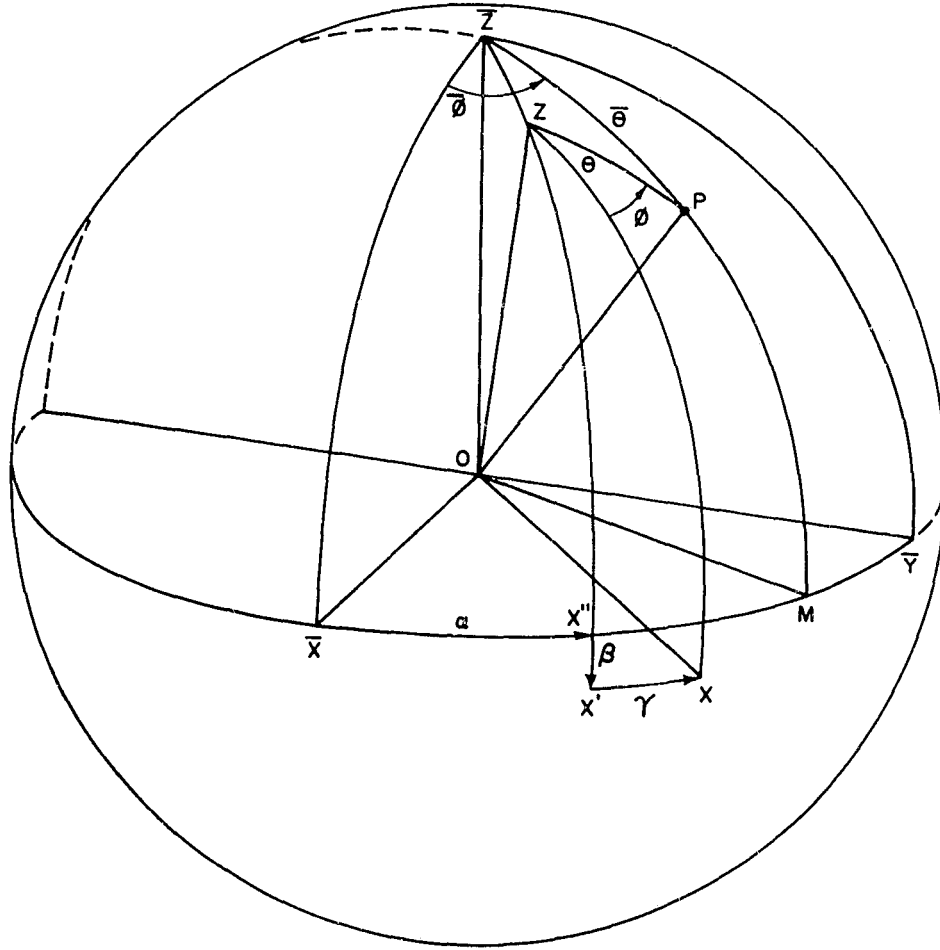


Figure I.2. A Direction Described in Two Coordinate Systems

Figure I.3 shows the spherical triangles which are used in the solution of

$$\phi, \theta = f(\bar{\phi}, \bar{\theta}, \alpha, \beta, \gamma) .$$

From the spherical triangle  $Z\bar{Z}P$  and the law of cosines,

$$\cos \theta = \cos \bar{\theta} \cos \beta + \sin \bar{\theta} \sin \beta \cos (\bar{\phi} - \alpha) , \quad (I-1)$$

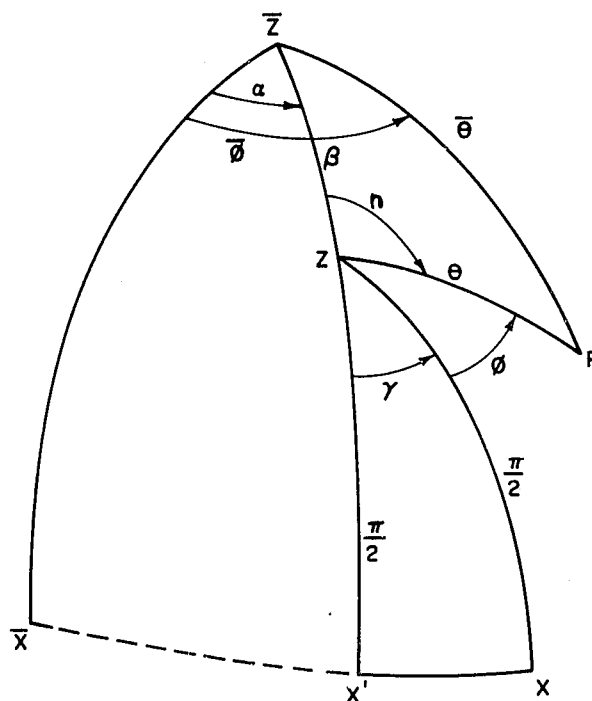


Figure I.3. Spherical Triangles From Figure I.2.

or

$$\theta = \cos^{-1}[\cos \bar{\theta} \cos \beta + \sin \bar{\theta} \sin \beta \cos (\bar{\phi} - \alpha)] . \quad (\text{I-2})$$

And also by the law of cosines

$$\cos \bar{\theta} = \cos \theta \cos \beta + \sin \theta \sin \beta \cos n . \quad (\text{I-3})$$

It can be seen that

$$n = \pi - (\phi + \gamma) ,$$

and

$$\cos n = \cos [\pi - (\phi + \gamma)] ,$$

or

$$\cos n = -\cos (\phi + \gamma) , \quad (\text{I-4})$$

and

$$\sin n = \sin (\phi + \gamma) . \quad (\text{I-5})$$

Equation (I-4) may be substituted into (I-3) to give

$$\cos \bar{\theta} = \cos \theta \cos \beta - \sin \theta \sin \beta \cos (\phi + \gamma) ,$$

or

$$\sin \theta \cos (\phi + \gamma) = \frac{\cos \theta \cos \beta - \cos \bar{\theta}}{\sin \beta} . \quad (\text{I-6})$$

From the spherical triangle  $Z\bar{Z}P$  and the law of sines,

$$\frac{\sin (\bar{\phi} - \alpha)}{\sin \theta} = \frac{\sin n}{\sin \bar{\theta}} .$$

Substituting from (I-5) and rearranging gives

$$\sin \theta \sin (\phi + \gamma) = \sin \bar{\theta} \sin (\bar{\phi} - \alpha) . \quad (\text{I-7})$$

Dividing (I-7) by (I-6) gives

$$\tan (\phi + \gamma) = \frac{\sin \bar{\theta} \sin \beta \sin (\bar{\phi} - \alpha)}{\cos \theta \cos \beta - \cos \bar{\theta}} . \quad (\text{I-8})$$

Substituting (I-1) into (I-8) and rearranging gives

$$\phi = \tan^{-1} \left[ \frac{\sin \bar{\theta} \sin \beta \sin (\bar{\phi} - \alpha)}{\cos \beta [\cos \bar{\theta} \cos \beta + \sin \bar{\theta} \sin \beta \cos (\bar{\phi} - \alpha)] - \cos \bar{\theta}} \right] - \gamma ,$$

which may be simplified to

$$\phi = \tan^{-1} \left[ \frac{\sin \bar{\theta} \sin (\bar{\phi} - \alpha)}{\sin \bar{\theta} \cos \beta \cos (\bar{\phi} - \alpha) - \cos \bar{\theta} \sin \beta} \right] - \gamma . \quad (\text{I-9})$$

APPENDIX J  
THE EFFECTS OF PARALLAX  
IN BORESIGHT MEASUREMENTS OF ASYMMETRICAL ANTENNAS\*

J.1     Introduction

The purpose of the investigations which are reported in this appendix is to obtain an understanding of the errors which are introduced in precision antenna bore-sight measurements by testing at typical antenna test-range separations between the antenna under test and the source antenna. The errors arise from three basic and interrelated sources (1) from the physical distance which almost always exists between the antenna under test and the origin of the coordinate system in which measurements are made, (2) by the uncertainty and lack of uniqueness in the definition of a specific point which can be used as the effective location of the antenna under test, and (3) by the distortion of the radiation pattern which results because the antenna is being tested in a spherical wavefront rather than in the virtually planar phase front in which the antenna normally operates, that is for large separations between the antenna and the source of radiation. The viewpoint in the investigations is related to direction measurements rather than to measurements of distortion of the complete radiation pattern; this viewpoint was taken for economy and because of the specific concern for boresight accuracy in the evaluation of the MILA range.

In the present study a Burroughs Datatron 5000 computer of the Rich Electronic Computer Center of the Georgia Institute of Technology was programmed to calculate antenna patterns as a function of the separation between the source antenna and an antenna under test for certain assumed asymmetrical antenna configurations. In the following paragraphs terms are defined, a summary is given of the technique which was employed in the calculations, and the resulting data are presented.

---

\*The investigations reported herein were supported jointly under Contracts NAS10-2103 and AF30(602)-3425. Except for the introduction to the investigations and minor differences, the material presented is the same as that reported in the final report under the latter contract (see Investigation of Precision Antenna Pattern Recording and Display Techniques, Phase II, Final Report, Vol. I, Contract No. AF30(602)-3425, Project No. 4506, Task No. 45064, Report No. RAD C-TR-65-534.)

## J.2 Definition of Terms

### J.2.1 Parallax

Parallax is defined as the difference in the apparent direction of a point or object as seen from two different station points which are not on a common straight line with the point or object under observation. In Figure J.1 let the directions to the point  $p$  be measured from station points which are the origins  $o$  and  $o'$  of two parallel coordinate systems. If the directions to  $p$  are defined by  $(\phi, \theta)$  and  $(\phi', \theta')$  respectively in the two coordinate systems, the  $\phi$  and  $\theta$  parallax angles are defined by  $(\phi' - \phi)$  and  $(\theta' - \theta)$ , as shown below.

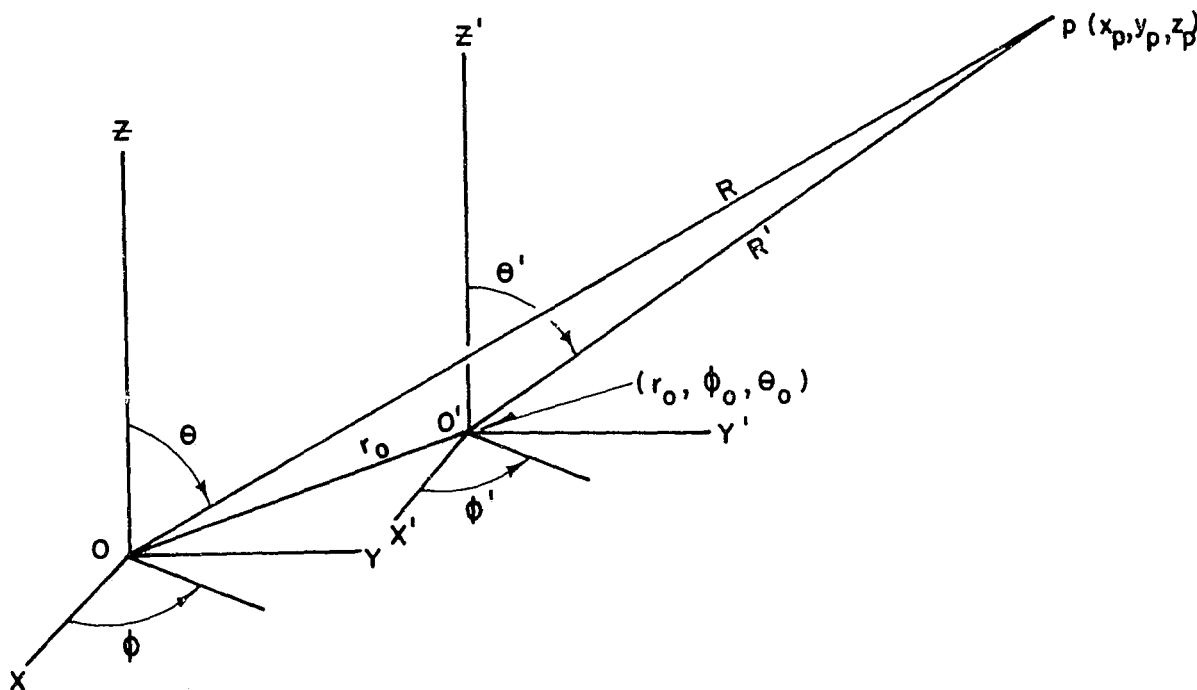


Figure J.1. Coordinate Systems Employed for Antenna Measurements, Showing Parallax

With reference to Figure J.1, the general expression for the magnitude of the radius vector in a Cartesian coordinate system is

$$r_i^2 = x_i^2 + y_i^2 + z_i^2 \quad . \quad (J-1)$$

Translation from a system whose origin is  $(x = 0, y = 0, z = 0)$  to a system whose origin is at the point  $(x_o, y_o, z_o)$  defines

$$r_o^2 = x_o^2 + y_o^2 + z_o^2 \quad . \quad (J-2)$$

If the point defined by (J-2) is to be the origin of a primed coordinate system  $(x', y', z')$ , then

$$\begin{aligned} x' &= x - x_o \\ y' &= y - y_o \\ z' &= z - z_o \end{aligned} \quad . \quad (J-3)$$

The general transformation equations for the changes of variable in going from Cartesian to spherical coordinate systems are (see Figure J-1)

$$x_i = r_i \sin\theta_i \cos\phi_i \quad (J-4)$$

$$y_i = r_i \sin\theta_i \sin\phi_i \quad (J-5)$$

$$z_i = r_i \cos\theta_i \quad . \quad (J-6)$$

From (J-4) and (J-5), we have  $r_i^2 \sin^2\theta_i = x_i^2 + y_i^2$ , and from (J-6),  $\cos\theta_i = z_i/r_i$ . The transcendental equations for  $\theta'$  are seen to be

$$\sin\theta' = \frac{1}{r'} \left[ (r \sin\theta \cos\phi - r_o \sin\theta_o \cos\phi_o)^2 + (r \sin\theta \sin\phi - r_o \sin\theta_o \sin\phi_o)^2 \right]^{\frac{1}{2}} \quad (J-7)$$

and

$$\cos\theta' = \frac{(r \cos\theta - r_o \cos\theta_o)}{r'} \quad (J-8)$$

where

$$r' =$$

$$\left[ (r \sin\theta \cos\phi - r_o \sin\theta_o \cos\phi_o)^2 + (r \sin\theta \sin\phi - r_o \sin\theta_o \sin\phi_o)^2 + (r \cos\theta - r_o \cos\theta_o)^2 \right]^{\frac{1}{2}} \quad (J-9)$$

Using (J-7) in (J-5) gives

$$\sin\phi' = \frac{(r \sin\theta \sin\phi - r_o \sin\theta_o \sin\phi_o)}{\left[ (r \sin\theta \cos\phi - r_o \sin\theta_o \cos\phi_o)^2 + (r \sin\theta \sin\phi - r_o \sin\theta_o \sin\phi_o)^2 \right]^{\frac{1}{2}}} \quad (J-10)$$

Using (J-8) in (J-4) gives

$$\cos\phi' = \frac{(r \sin\theta \cos\phi - r_o \sin\theta_o \sin\phi_o)}{\left[(r \sin\theta \cos\phi - r_o \sin\theta_o \cos\phi_o)^2 + (r \sin\theta \sin\phi - r_o \sin\theta_o \sin\phi_o)^2\right]^{\frac{1}{2}}} \quad (J-11)$$

Equations (J-7) and (J-8) yield

$$\theta' = \cot^{-1} \left\{ \frac{(r \cos\theta - r_o \cos\theta_o)^2}{(r \sin\theta \cos\phi - r_o \sin\theta_o \cos\phi_o)^2 + (r \sin\theta \sin\phi - r_o \sin\theta_o \sin\phi_o)^2} \right\}^{\frac{1}{2}} \quad (J-12)$$

and equations (J-10) and (J-11) yield

$$\phi' = \cot^{-1} \frac{r \sin\theta \cos\phi - r_o \sin\theta_o \cos\phi_o}{r \sin\theta \sin\phi - r_o \sin\theta_o \sin\phi_o} \quad (J-13)$$

for the primed angular parameters. The unprimed angular parameters are

$$\theta = \cot^{-1} \left[ \frac{z^2}{r^2 - z^2} \right]^{\frac{1}{2}} \quad (J-14)$$

and

$$\phi = \cot^{-1} \frac{x}{y} \quad (J-15)$$

The parallax angles are given by

$$\theta_p = \theta' - \theta \quad (J-16)$$

and

$$\phi_p = \phi' - \phi \quad (J-17)$$

The situation depicted in Figure J-1 is typical of practical antenna problems, but differs markedly in severity between operational and measurement situations. Let the direction to a target at p be measured in the unprimed coordinate system defined by the shaft orientations of, say, a two-axis positioner with origin at o, the intersection of the positioner axes. Let the center of the antenna be located in o' a distance  $r_o$  from o. In the typical operating environment the distance  $R'$  to the target is of the order of miles and therefore is so large compared with  $r_o$  that  $\phi$  and  $\theta$  can almost always be considered equal to  $\phi'$  and  $\theta'$  respectively without measurable error. When measurements are being made of the radiation characteristics of such antennas, on the other hand, the range  $R'$  is often not

C-4



sufficiently great compared with  $r_0$  that parallax can be neglected. We will be concerned with the effects of parallax at ranges which are of the order of  $D^2/\lambda$ , where  $D$  is the diameter of the antenna under test.

### J.2.2 Center of Parallax

In discussions related to measurement of the radiation patterns of symmetrical antennas parallax is sometimes discussed in terms of the center of radiation of the antennas.<sup>J-1</sup> This term may be used synonymously with center of phase. In considering parallax in testing asymmetrical antennas it is necessary to define terms more precisely, and in this discussion we will use the term center of parallax in contrast with center of phase, and we will not employ the term center of radiation.

Parallax error can be accounted for and removed in analyzing antenna pattern data, except for a component which exists because of lack of specific information concerning the location of  $o'$ , the center of parallax of the antenna under test. The center of parallax will be defined for our purpose as that location  $o'$ , in or near the aperture of an antenna under test, which can be employed as an origin such that the function  $g(R', \phi', \theta')$  describing the normalized radiation pattern of an antenna will be constant with  $R'$ .

Strictly speaking, of course,  $g(R', \phi', \theta')$  is not constant with  $R'$ ; thus a true center of parallax does not exist as defined. In pattern measurements of narrow-beam antennas, however, a major concern is that of determining the direction of the main lobe of the radiation pattern. It is of interest, therefore, to consider whether a center of parallax can be defined for practical use in locating the direction which the main beam of an asymmetrical antenna will have at large operational ranges when the measurements are made at distances that are typical in antenna test ranges.

For this study, the direction to the peak of the beam was computed in two ways:

- (a) A computer search was employed at given ranges  $R$  to determine the point at which the amplitude of the beam had zero slope. The corresponding direction angles to such points are termed  $\Phi_{MR}$ .

---

<sup>J-1</sup> Chastain, et al, Investigation of Precision Antenna Pattern Recording and Display Techniques, Final Report, 1 April 1962 to 29 March 1963, AD415-912.

- (b) The direction to the 3-decibel points on each side of the beam maximum was determined by computation at given ranges  $R$ , and the average of these angles was taken as the direction to the peak. These angles are termed  $\Phi_R$ .

The transverse displacement of  $o'$  as  $R$  was reduced from  $R = \infty$  to some finite range  $R$  was calculated in the computer program for case (b) above. The defining equation for this displacement can be obtained from Figure J.2.

$$\Delta Y = \frac{\ell}{\cos \Phi_R} \quad (J-18)$$

$$\ell \doteq R(\Phi_R - \Phi_\infty) \equiv R\Delta\phi \quad (J-19)$$

$$\Delta Y = \frac{R\Delta\phi}{\cos \Phi_R} \doteq R\Delta\phi \quad (\text{for small } \Phi_R) \quad (J-20)$$

Plots of  $\Delta\phi$ ,  $\Delta\phi_M$  and  $\Delta Y$  are presented for several combinations of phase and amplitude asymmetries as a function of range in paragraph J.4, where

$$\Delta\phi_M \equiv (\Phi_{MR} - \Phi_{M\infty}) \quad (J-21)$$

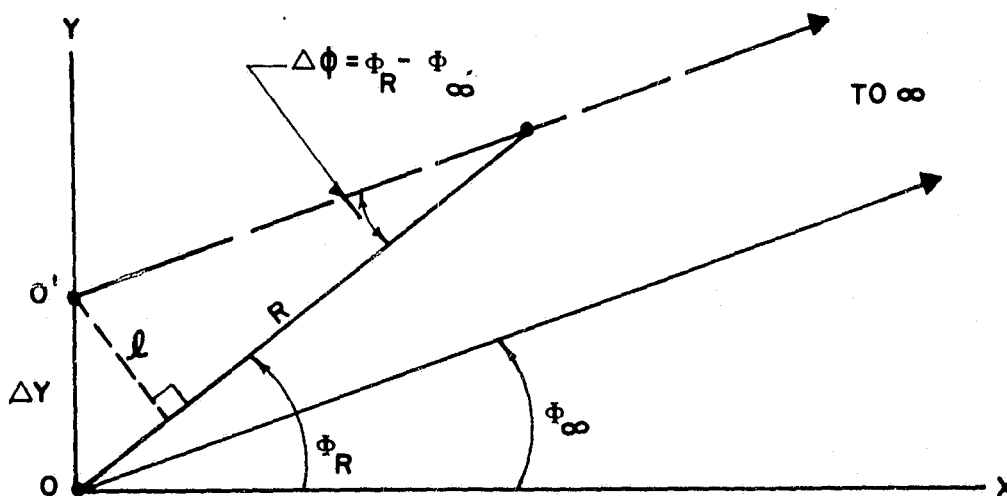


Figure J.2. Geometry Defining Center of Parallax

### J.2.3 Center of Phase

The center of phase of an antenna can be defined as the location of the center of a sphere of radius  $R'$  which is coincident with and of the same radius as the phase front produced by an antenna at a point in space  $p(R, \phi, \theta)$ . The location of the center of phase is of specific importance in measuring the boresight direction of phase-monopulse or amplitude-monopulse radars<sup>J-2</sup> because such radars operate by sensing the direction of arrival of a wave as the direction of the normal to the approaching phase front.

Morita has shown that a unique center of phase does not generally exist for the practical antenna. In analogy with the location of the center of curvature of a planar curve, the radius and the location of the center of phase of an antenna are not fixed, but vary with the location in space of the field point. Although the radius of curvature of the wavefront of a beam in space is not generally constant with rotation of a plane of exploration about the axis of the beam, the axial location of the center of phase is usually not of great importance in practical applications; therefore our concentration of attention will be directed toward the transverse location of the center of phase.

In the following investigations antennas will be considered which are symmetrical in  $\theta$  but asymmetrical in  $\phi$ . Considering only the transverse location of the center of phase, a coordinate system  $X''Y''Z''$  (see Figure J.3) will be defined which is parallel with a coordinate system  $XYZ$  in which a narrow-beam antenna radiates with its beam axis nearly parallel with the  $X$  axis.

Consider the sphere  $S_1$  centered at  $o$ , and the phase front  $S_2$  which intersects  $S_1$  at  $p_1$ . Let the phase of the field at  $p_1$  be  $\psi_1$ . Now call  $\psi_2$  the phase at  $p_2$  a distance  $R\Delta\phi$  from  $p_1$  in the  $\phi$  direction.

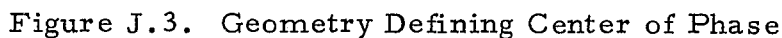
From the geometry, for  $\Delta R \ll R$ ,

$$\frac{\Delta R}{R\Delta\phi} \doteq \alpha, \quad (J-22)$$

where  $\alpha$  is defined as the angle at  $p_1$  between  $S_1$  and  $S_2$  in the  $XY$  plane.

---

<sup>J-2</sup> Tetsu Morita, Determination of Phase Centers and Amplitude Characteristics of Radiating Structures, Tech. Report No. 1, SR 1, Project 898, Stanford Res. Inst., Menlo Park, California, Contract DA04-200-ORD-273, AD68240; March 1955.



$$\alpha \doteq \frac{\Omega \cos \phi}{R} \quad \text{for } R \gg \Omega, \quad (\text{J-23})$$

$$\Delta R \doteq \frac{\lambda}{2\pi} (\psi_2 - \psi_1) \equiv \frac{\lambda}{2\pi} \Delta \psi \quad . \quad (J-24)$$

$$\mathcal{G} \doteq \frac{\lambda \Delta \psi}{2\pi \Delta \phi \cos \phi} \doteq \frac{\lambda}{2\pi} \frac{\Delta \psi}{\Delta \phi} \quad (\text{for small } \phi). \quad (\text{J-25})$$

Calculations were made in this study of  $\Omega(R)$  for certain assumed antenna asymmetries using  $p_2$  and  $p_1$  as the half-power points of the main lobe in the XY plane.\* Results of these calculations are presented in paragraph J.4.

\* The values of  $\Omega$  thus calculated were checked for several cases which are considered to be extreme by defining a third point  $p'$  as the peak of the beam and solving equation (J-25) for values of  $\phi$  and  $\psi$  related to the point pairs  $p_1, p'$  and  $p_2, p'$ . The average values of  $\Omega$  calculated in this manner were in close agreement with those presented here.

#### J.2.4 Boresight Deviation

Parallax is of importance in testing high-accuracy, amplitude-monopulse direction-of-arrival sensors and, specifically, in measuring the boresight error of the LEM rendezvous radar. Antennas of this type sense the direction of arrival of a wave as that direction for which the sum pattern signal  $\bar{\Sigma}$  and the difference pattern signal  $\bar{\Delta}$  at the terminals of each of the two channels (e.g., azimuth and elevation) of the monopulse network are in phase quadrature, assuming ideal data processing circuitry in the monopulse receiver. This is tantamount to the condition that

$$|A| = |B| , \quad |C| = |D|$$

where A and B are the magnitudes of the signals produced by the opposite lobes of the monopulse pattern for the crossover direction in one plane, and C and D are the magnitudes in the orthogonal plane. A problem of specific concern is that of the behavior of the boresight directions with the separation between the source antenna and the antenna under test.

If we consider sensing in only one plane (say the XY plane, Figure J.4, where we will assume the Z axis to be vertical) the monopulse antenna can be considered to consist of two asymmetrical antennas, one with its feed (A) on one side of the centerline of the reflector and the second with its feed (B) on the opposite side. The axis of the antenna is assumed to lie in the XZ plane. If the antenna possesses

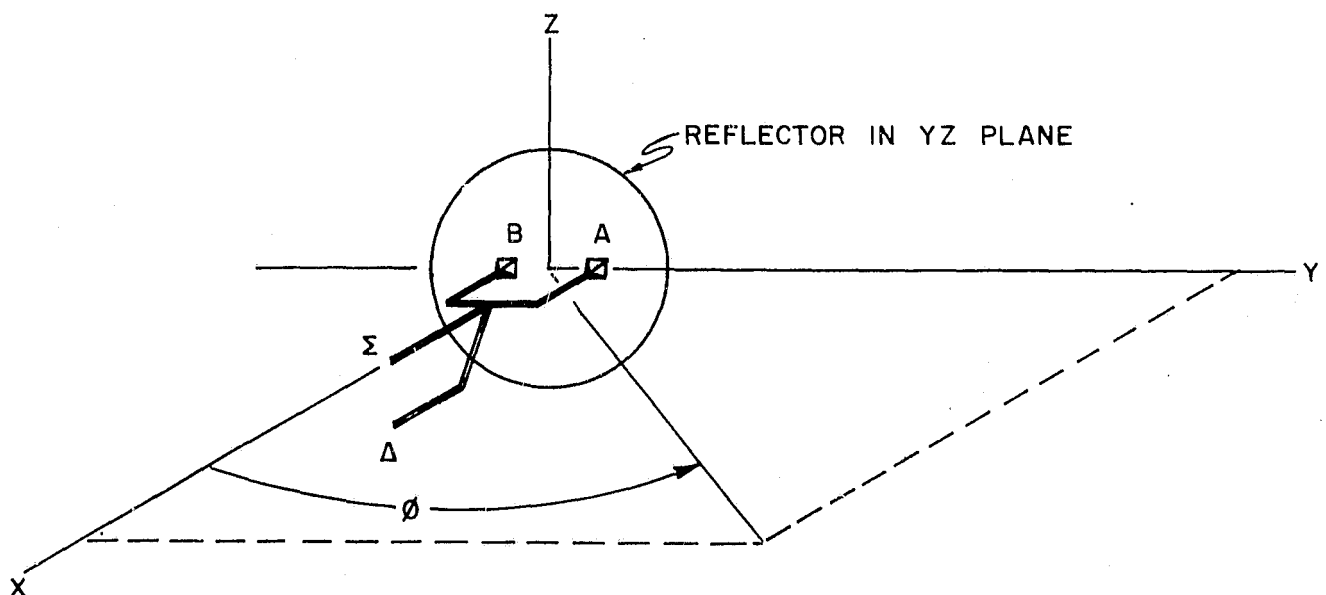


Figure J.4. Schematic Representation of Single-Plane Monopulse Sensor

mirror symmetry about the XZ plane, the asymmetry for channel A will be identical to that for channel B, and the boresight direction  $\phi_0$  defined by  $|A|=|B|$  will be in the XZ plane ( $\phi=0$ ).

Now, still assuming absolute symmetry, if the boresight direction is measured at a source antenna separation which is sufficient for the secondary pattern to have formed (for example at a separation of  $D^2/4\lambda$ , where D is the diameter of the reflector), the measured boresight direction must lie in the XZ plane because of the assumption of symmetry. In practical cases ideal symmetry will never exist and the purpose of the investigation of this section is to provide an insight into the variation of the boresight direction as measured at different source antenna separations for assumed degrees of differential symmetry between the two antennas of the monopulse pair.

In the following section the method is described which was employed in the calculations; in section J.4.2 and Figures J.16 through J.19 the input data and resulting calculations are presented. It is emphasized that these calculations are made to give an insight into the problem; the design and fabrication of the LEM rendezvous radar are directed toward achievement of as small a differential asymmetry as possible, and it is expected that the asymmetry which results will be much less than that employed in the calculations. Conclusions are drawn in Chapter 6 concerning the results of the calculations.

### J.3 Radiation Pattern Calculations

#### J.3.1 Theoretical Development

Radiation patterns were calculated for a number of simulated antenna configurations by the aperture-field method, assuming the total radiated energy to be contained in a single polarization. For this case the contribution by direct radiation from the aperture to the field at p is described by equation (A-7) where  $S_i$  is the active aperture of the antenna, which we will henceforth call simply S, and which is assumed to be a planar surface lying in the YZ plane of Figure J.5. This integral does not give the total field at p, but only the contribution from the aperture; however we will assume that almost all of the energy from the antenna passes through the aperture and that the contribution to the field at p of sources other than the field over S can be neglected.

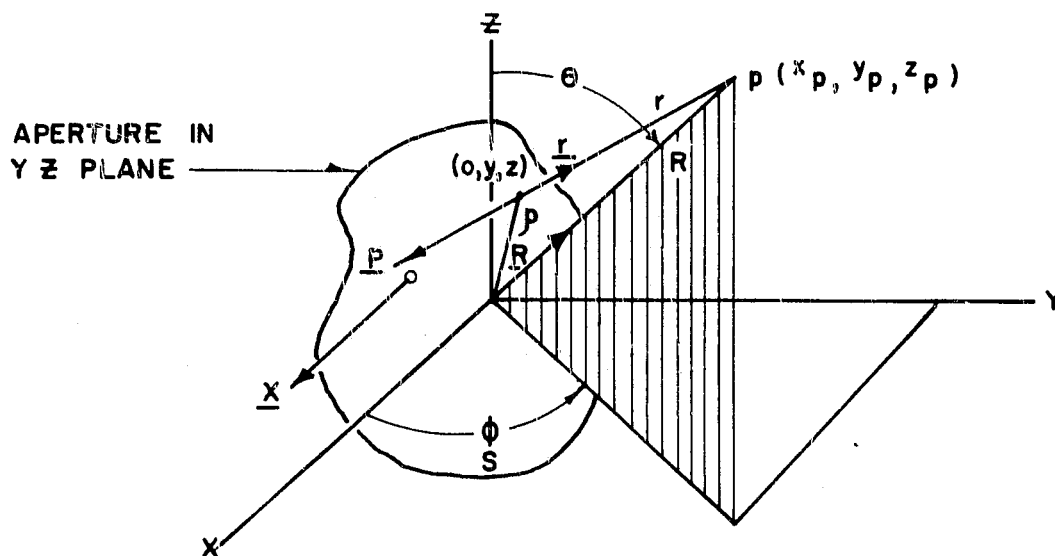


Figure J.5. Aperture Geometry for Theoretical Development of Aperture Field Method

Equation (A-7) leads to the scalar diffraction integral<sup>J-3</sup> under the assumptions which have been made:\*

$$\bar{E}_p \doteq K \int_S F(o, y, z) e^{j\psi(o, y, z)} \frac{e^{-jkr}}{r} \left[ \left( jk + \frac{1}{r} \right) \underline{x} \cdot \underline{r} + jk \underline{x} \cdot \underline{P} \right] ds, \quad (J-26)$$

where, with reference to Figure J.5,

K is a constant of proportionality,

$F(o, y, z)$  is the amplitude of the field distribution over S,

$\psi(o, y, z)$  is the phase of the field distribution over S,

r is the distance from a source point (o, y, z) to a field point  $p(x_p, y_p, z_p)$ ,

k is the wave number  $2\pi/\lambda$ ,  $\lambda$  being the wavelength,

$\underline{P}$ ,  $\underline{x}$ ,  $\underline{R}$  and  $\underline{r}$  are unit vectors, and

$\underline{P}$  denotes the direction of power flow through the aperture.

<sup>J-3</sup> Silver, Samuel, Microwave Antenna Theory and Design, RLS Volume 12, McGraw-Hill, 1949, p. 170.

\* In this section the exponential form  $e^{-jkr}$  will be employed. The choice is optional and has no bearing on the outcome of the argument. (See J. A. Stratton, Electromagnetic Theory, McGraw-Hill, 1941, page viii.)

For the problem at hand we can restrict  $p$  to the Fresnel and Fraunhofer regions, which are sufficiently removed from the aperture that

1.  $1/r$  is negligible compared with  $k$ ,
2.  $\underline{x} \cdot \underline{r} = \underline{x} \cdot \underline{R} = \sin\theta \cos\phi$ ,
3.  $r = R$  except in the phase term  $e^{-jkr}$ .

In addition we will postulate that the direction of power flow through the aperture is nearly enough parallel with the  $x$ -axis that  $\underline{x} \cdot \underline{P} = 1$  with negligible error.

If we designate the rectangular coordinates of  $p$  by  $(x_p, y_p, z_p)$ , the distance  $r$  from  $p$  to the point  $(0, y, z)$  in the aperture is given by

$$r = \left[ x_p^2 + (y_p - y)^2 + (z_p - z)^2 \right]^{\frac{1}{2}} \quad (J-27)$$

The transformation,

$$\begin{aligned} x_p &= R \sin\theta \cos\phi, \\ y_p &= R \sin\theta \sin\phi, \text{ and} \\ z_p &= R \cos\theta \end{aligned} \quad (J-28)$$

allows writing

$$r = \left[ (R \sin\theta \cos\phi)^2 + (R \sin\theta \sin\phi - y)^2 + (R \cos\theta - z)^2 \right]^{\frac{1}{2}}, \quad (J-29)$$

which through routine reduction gives

$$r = \left[ R^2 - 2R(y \sin\theta \sin\phi + z \cos\theta) + (y^2 + z^2) \right]^{\frac{1}{2}} \quad (J-30)$$

For our application symmetry will be postulated about the  $X$ -axis in  $\theta$ , so we will require  $p$  to move only in  $\phi$  in the  $XY$  plane. Further the region of exploration in  $\phi$  will be near the  $X$ -axis, and  $\sin\theta$  will be equal to unity and  $\cos\theta$  equal to zero. Under these conditions equation (J-30) becomes

$$r = \left[ R^2 - (2Ry \sin\phi - y^2 - z^2) \right]^{\frac{1}{2}} \quad (J-31)$$

and  $r$  can be approximated by the first two terms of the binomial expansion, giving

$$r = R - y \sin\phi + \frac{y^2 + z^2}{2R} \quad (J-32)$$

These approximations allow (J-26) to be written, since we are interested only in



relative phases and magnitudes at specific values of R,

$$\bar{A}_p = \int_S F(o, y, z) e^{j\left[\psi(o, y, z) + k(y \sin\phi - \frac{y^2 + z^2}{2R})\right]} ds \quad (J-33)$$

where

$$\bar{A}_p = \bar{C} \bar{E}_p, \text{ and}$$

$\bar{C}$  is an appropriate phasor.

The aperture S which was assumed for the simulated antenna configurations employed is shown in Figure J.6. The aperture is circular in shape, of radius a and is assumed to be illuminated by fields which are described by the functions,

$$F(o, y, z) = \left[K_1 + \cos \frac{\pi}{2} \rho\right] \left[1 + K_2 y\right] \quad (J-34)$$

and

$$\psi(o, y, z) = K_3 y + K_4 y^3 + K_5 \rho^2 \quad (J-35)$$

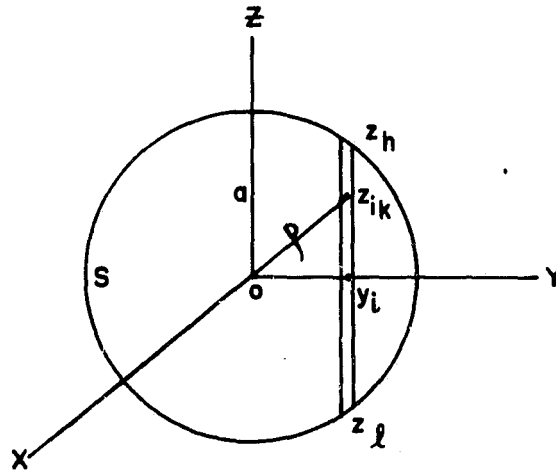


Figure J.6. Aperture Geometry Employed in Antenna Pattern Calculations

Equation (J-33) is accordingly written

$$\bar{A}_p = \int_{-a}^a \left[ \int_{z_l}^{z_h} F(y, z) e^{j(K_5 - \frac{k}{2R})z^2} dz \right] e^{j[K_3 y + K_4 y^3 + (K_5 - \frac{k}{2R})y^2 + ky \sin\phi]} dy \quad (J-36)$$

Since the integral within the brackets is not a function of  $\phi$ , the calculations can

be made by the equivalent slit method<sup>J-4</sup>. In programming the computer for achieving an approximation to (J-36) by a process of finite summation,  $F$  and  $\psi$  were approximated by 41 sample points along each axis.

#### J.4 Presentation of Data

In the computer calculations determining center of parallax and center-of-phase the following sets of input data were employed to represent typical asymmetries of  $F$  and  $\psi$  of equation (J-33).

$$K_1 = (0.462)$$

$$K_2 = (0), (0.5), (1.0)$$

$$K_3, K_4 = (0, 0), (1.4, 0), (0, 1.57), (1, 1)$$

$$K_5 = (0), (\pi/2), (-\pi/2)$$

$$\frac{R\lambda}{D^2} = (0.5), (1), (2), (4), (\infty)$$

Graphs of the functions  $F(o, y, z)$  employed in the calculations are shown in Figure J.7 showing rotational symmetry of  $F$  about the  $x$ -axis for  $K_2$  equal to zero and increasing asymmetry in the  $y$  direction for increasing values of  $K_2$ .

##### J.4.1 Center-of-Parallax and Center-of-Phase Calculations

In Figures J.8 through J.16 values of  $\Delta Y$ ,  $\Delta\phi$ ,  $\Delta\phi_M$  and  $\Omega$ , as defined in paragraphs J.2.2 and J.2.3, are presented as functions of  $R\lambda/D^2$  for the indicated values of the parameters listed above. For completeness certain graphs are included for cases for which the values of  $\Delta Y$ ,  $\Delta\phi$ ,  $\Delta\phi_M$  and  $\Omega$  are zero by symmetry.

For convenience, all curves are plotted upward, regardless of algebraic sign. Where a curve is actually a plot of negative values, a minus sign precedes the curve designator. In cases where the graphs become congested, some curves are dashed in order to make them more readable.

<sup>J-4</sup> L. Clayton and J.S. Hollis, "Calculation of Microwave Antenna Radiation Patterns by the Fourier Integral Method," Microwave Journal, September 1960.

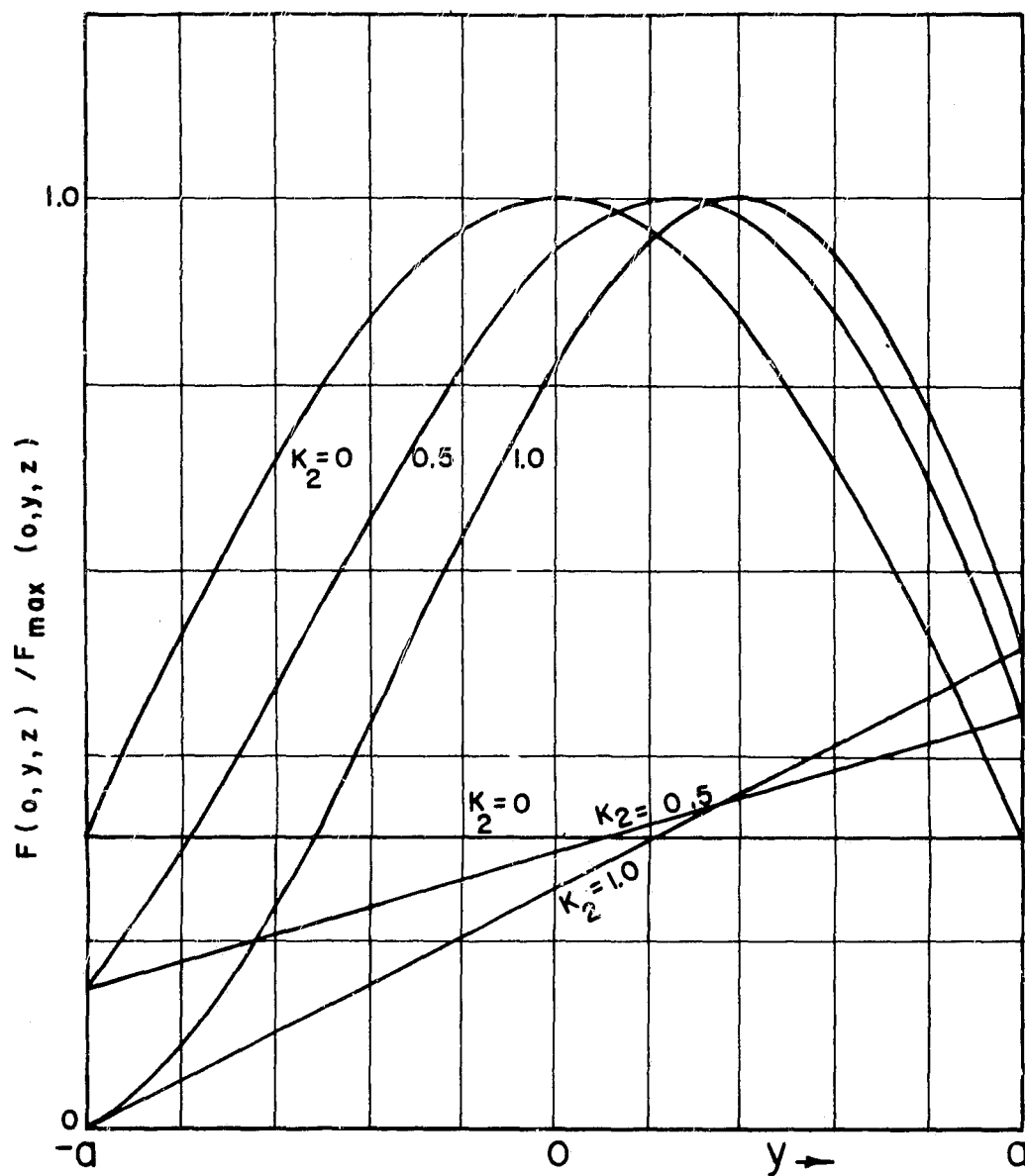
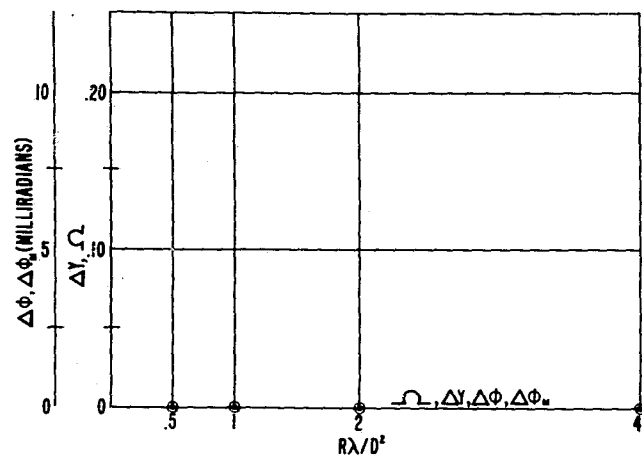
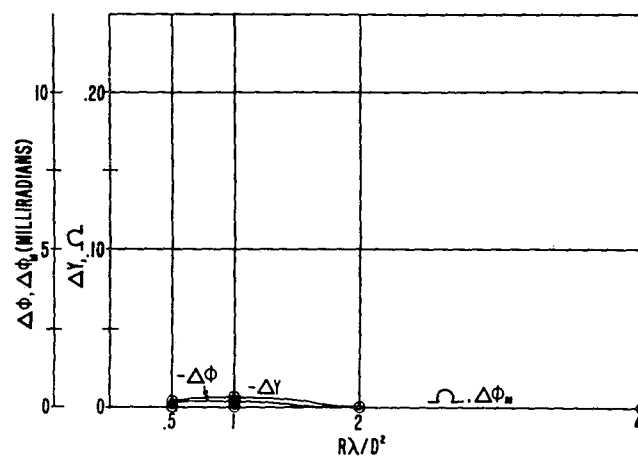


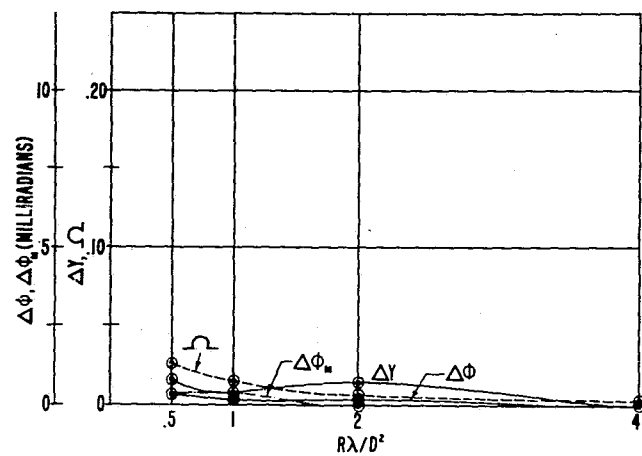
Figure J. 7. Functions  $F(o, y, z)$  Employed in Computer Calculations. Upper curves are cuts through aperture at  $z = 0$  [ $F(o, y, 0)$ ]. Lower curves (straight lines) show fields at periphery of aperture [ $F(o, y, z)/\rho = a$ ].



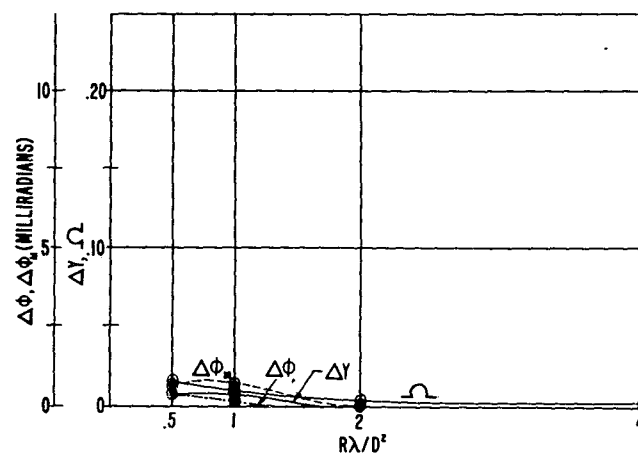
(a)  $K_3=0, K_4=0$



(b)  $K_3=1.4, K_4=0$

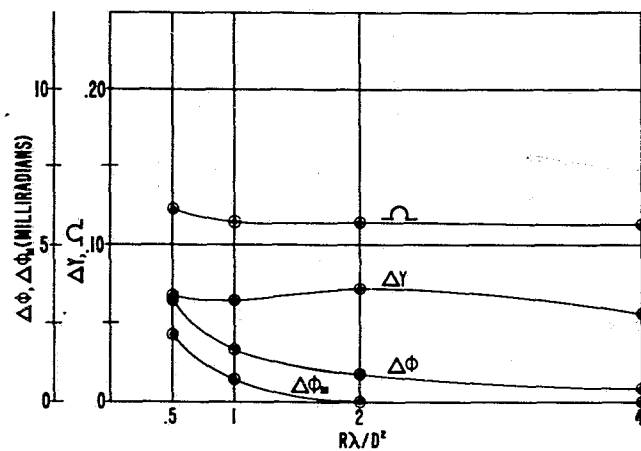
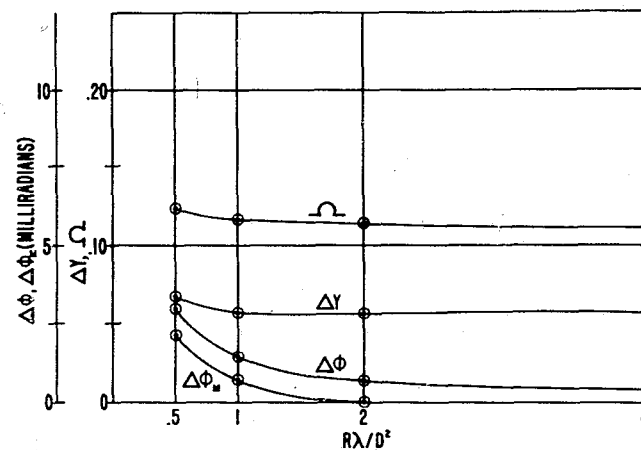
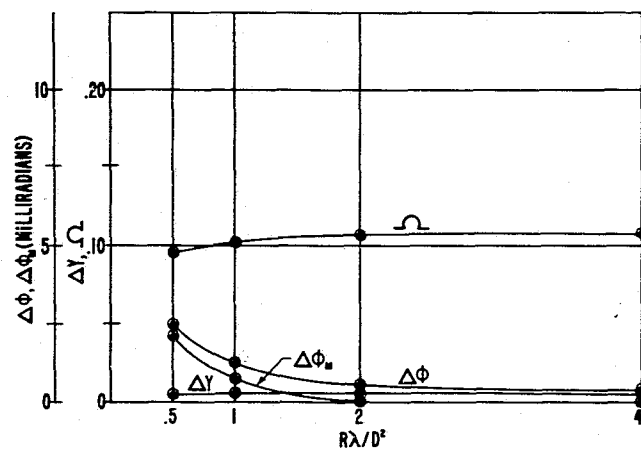
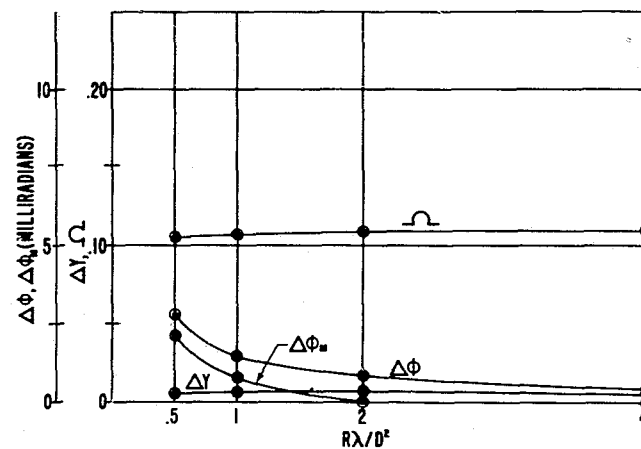


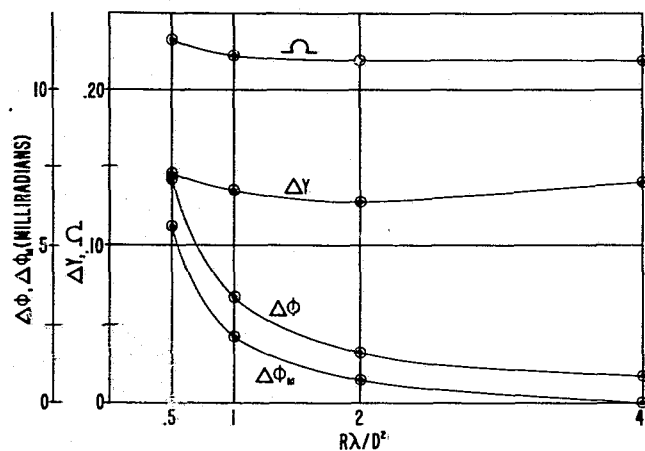
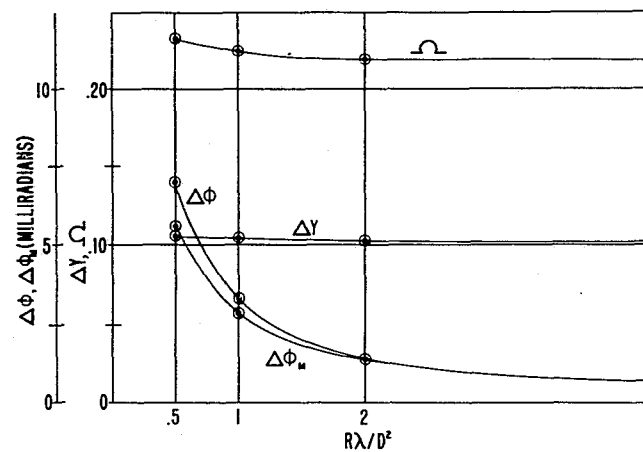
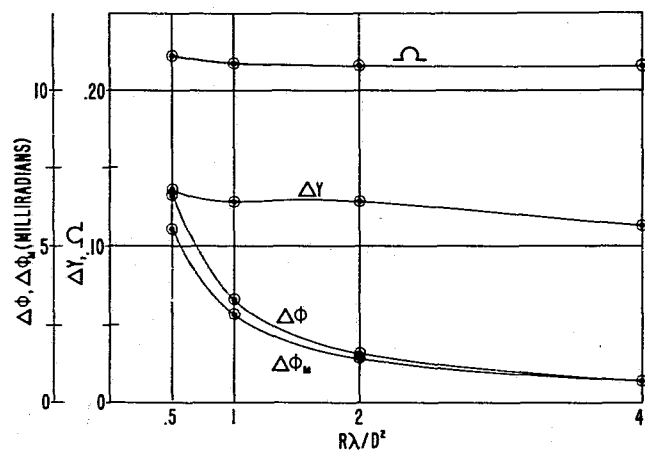
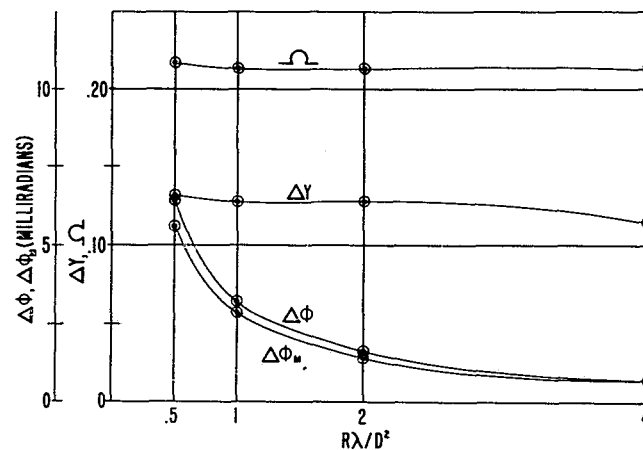
(c)  $K_3=0, K_5=1.57$

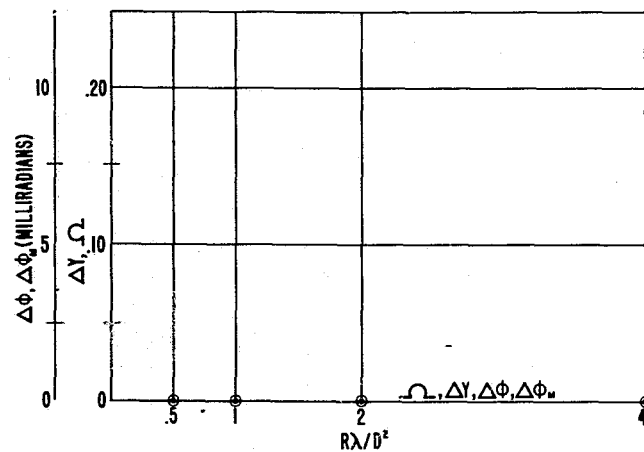
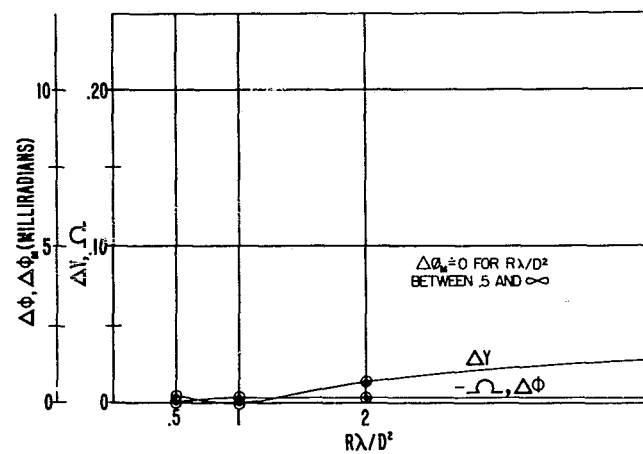
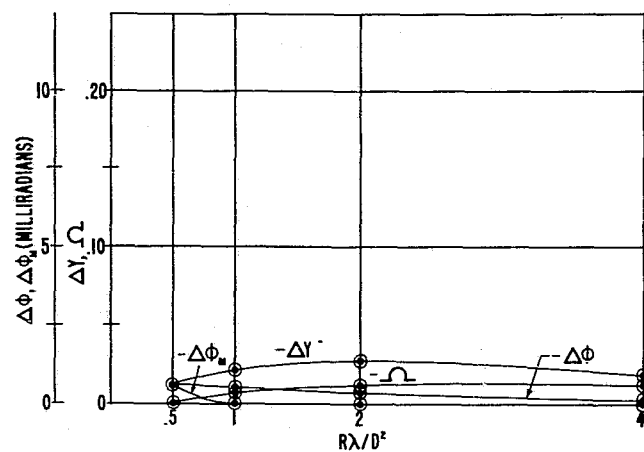
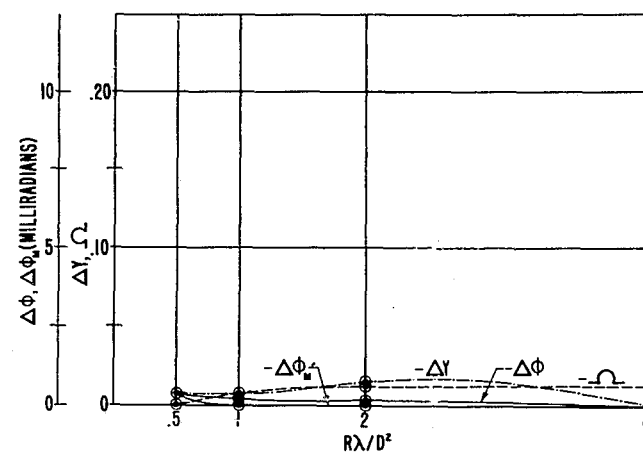


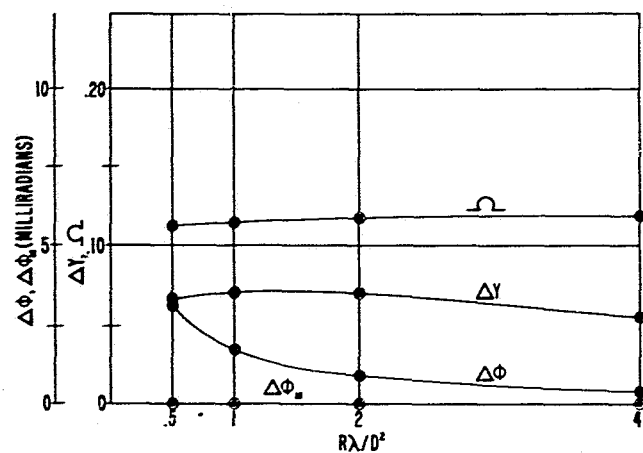
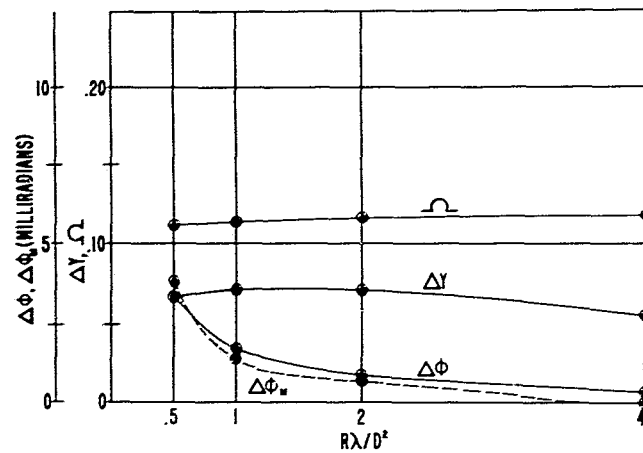
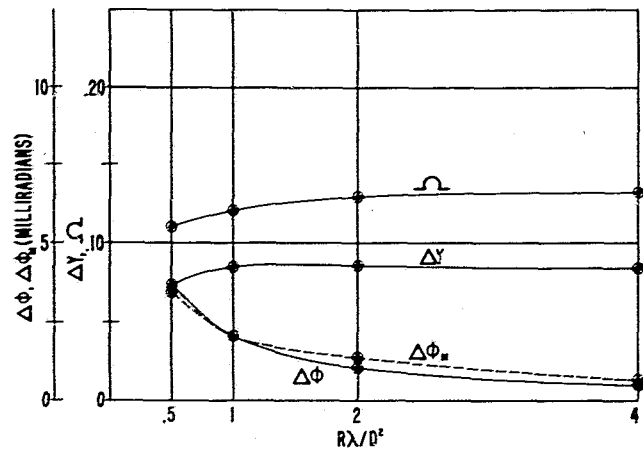
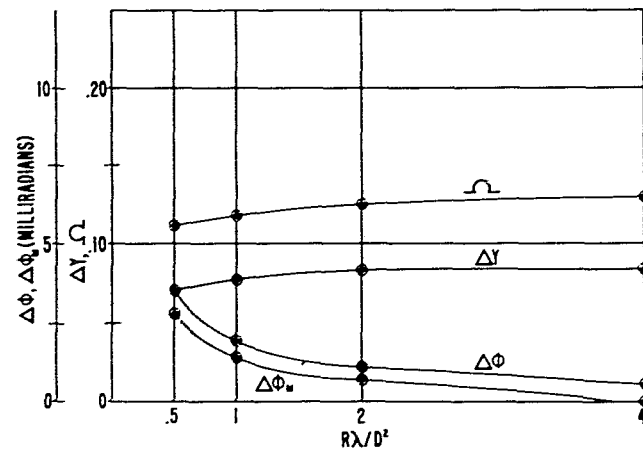
(d)  $K_3=1.0, K_4=1.0$

Figure J.8. Results of Parallax and Center-of-Phase Calculations,  $K_2=0, K_5=0$

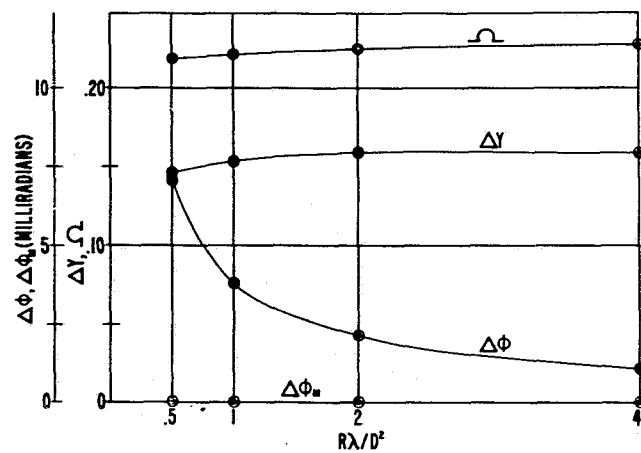
(a)  $K_3=0, K_4=0$ (b)  $K_3=1.4, K_4=0$ (c)  $K_3=0, K_5=1.57$ (d)  $K_3=1.0, K_4=1.0$ Figure J.9. Results of Parallax and Center-of-Phase Calculations,  $K_2=0.5, K_5=0$

(a)  $K_3=0, K_4=0$ (b)  $K_3=1.4, K_4=0$ (c)  $K_3=0, K_5=1.57$ (d)  $K_3=1.0, K_4=1.0$ Figure J. 10. Results of Parallax and Center-of-Phase Calculations,  $K_2=1.0, K_5=0$

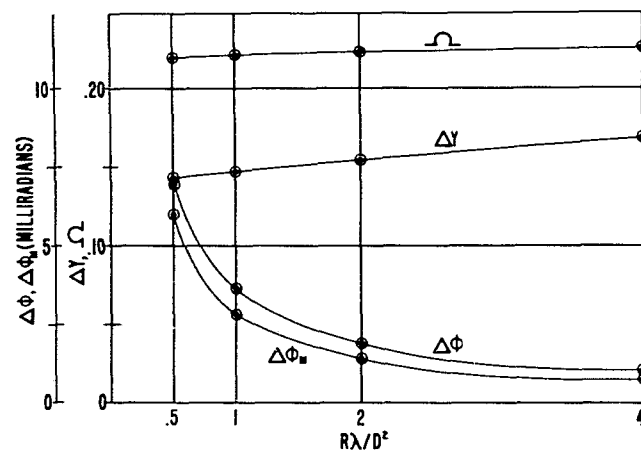
(a)  $K_3=0, K_4=0$ (b)  $K_3=1.4, K_4=0$ (c)  $K_3=0, K_5=1.57$ (d)  $K_3=1.0, K_4=1.0$ Figure J.11. Results of Parallax and Center-of-Phase Calculations,  $K_2=0, K_5=\pi/2$

(a)  $K_3=0, K_4=0$ (b)  $K_3=1.4, K_4=0$ (c)  $K_3=0, K_5=1.57$ (d)  $K_3=1.0, K_4=1.0$ Figure J.12. Results of Parallax and Center-of-Phase Calculations,  $K_2=0.5, K_5=\pi/2$

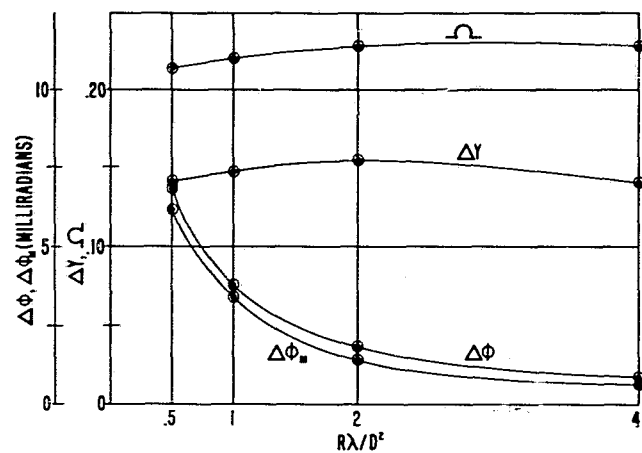




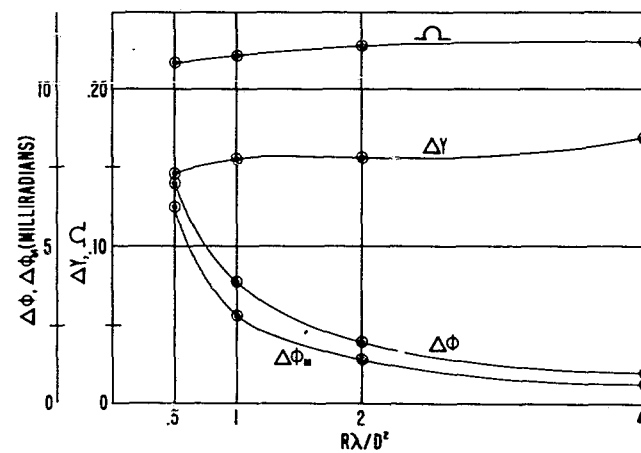
(a)  $K_3=0, K_4=0$



(b)  $K_3=1.4, K_4=0$

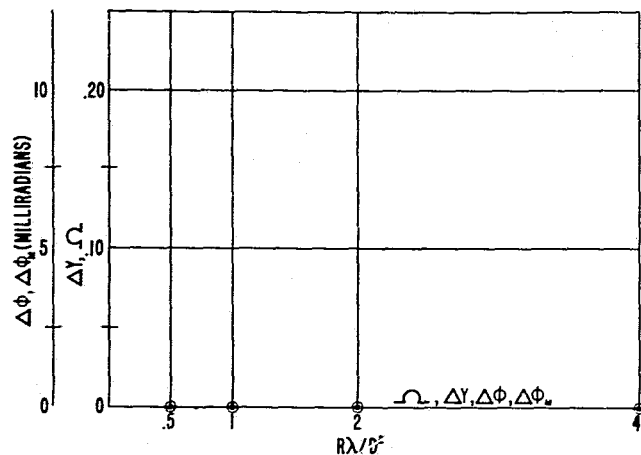


(c)  $K_3=0, K_5=1.57$

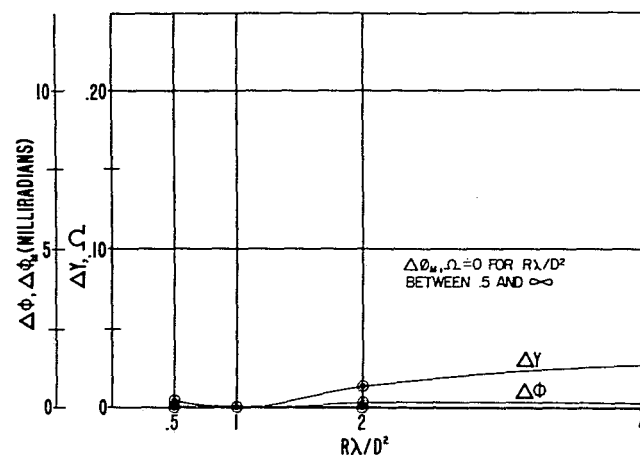


(d)  $K_3=1.0, K_4=1.0$

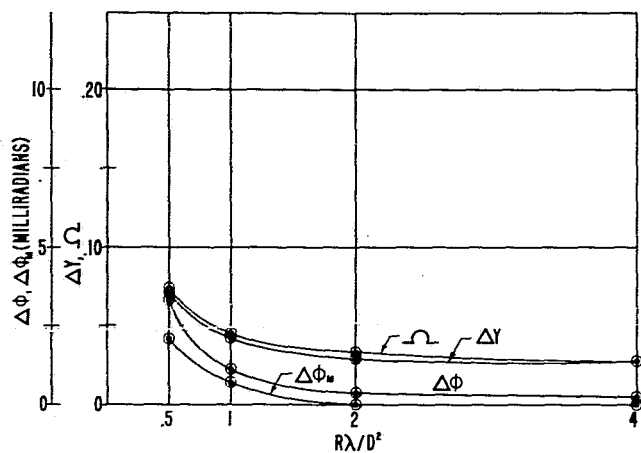
Figure J.13. Results of Parallax and Center-of-Phase Calculations,  $K_2=1.0, K_5=\pi/2$



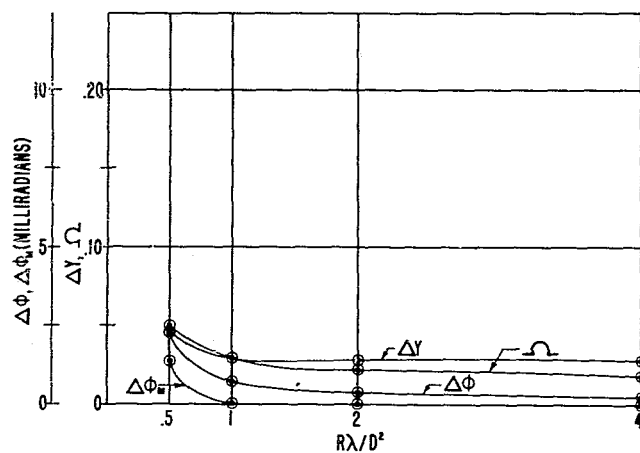
(a)  $K_3=0, K_4=0$



(b)  $K_3=1.4, K_4=0$

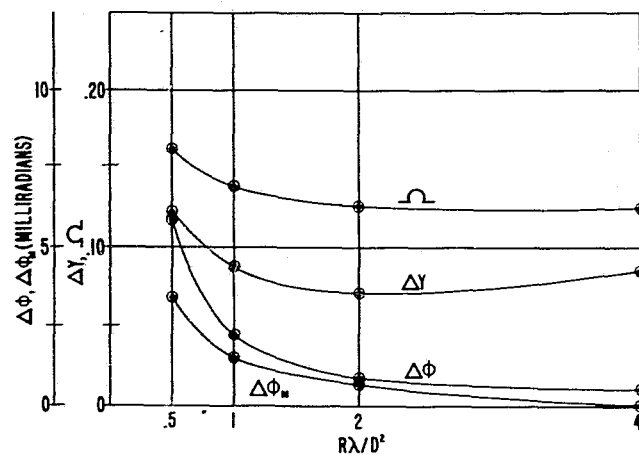
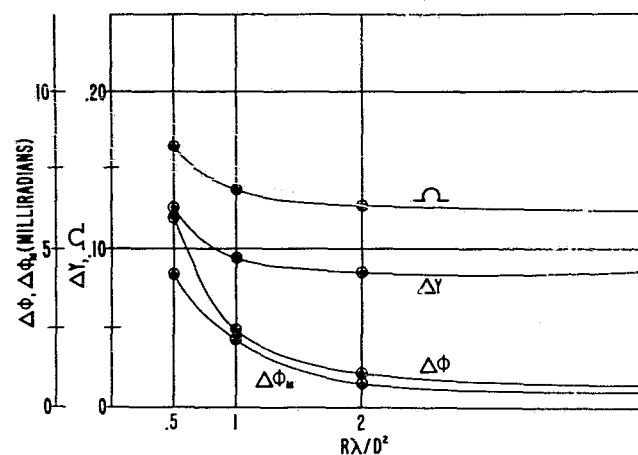
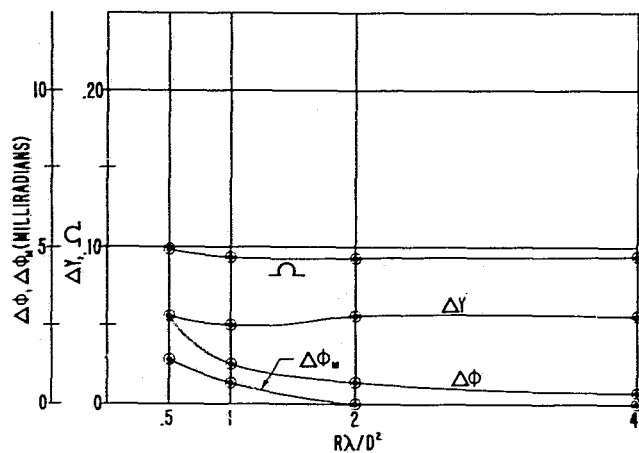
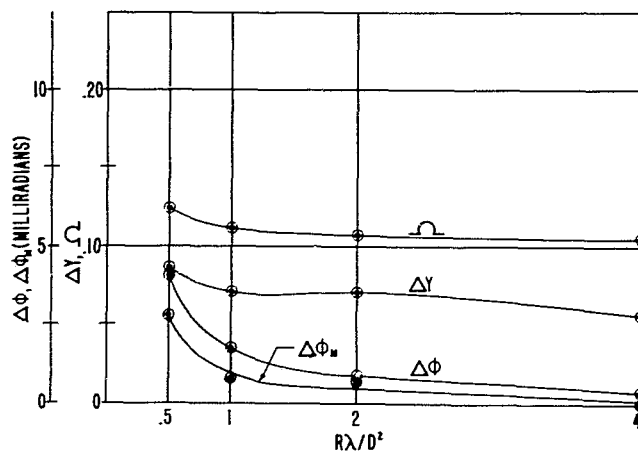


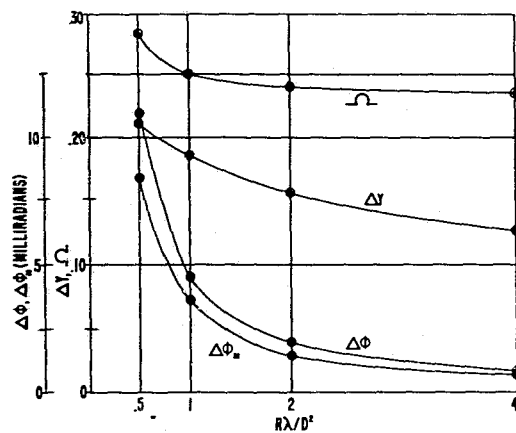
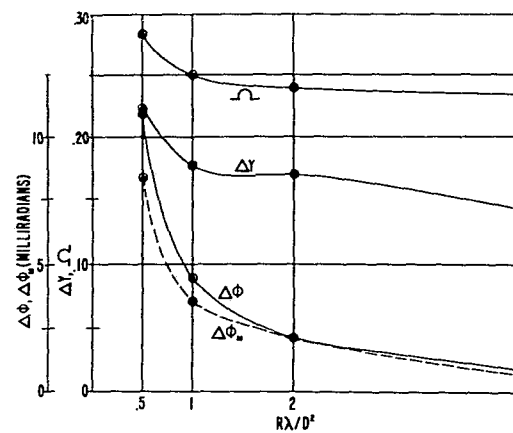
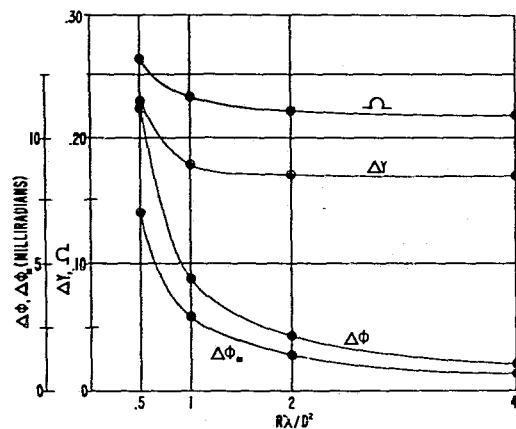
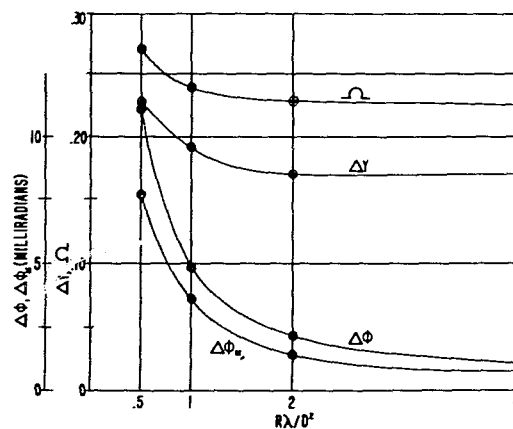
(c)  $K_3=0, K_5=1.57$



(d)  $K_3=1.0, K_4=1.0$

Figure J.14. Results of Parallax and Center-of-Phase Calculations,  $K_2=0, K_5=-\pi/2$

(a)  $K_3=0, K_4=0$ (b)  $K_3=1.4, K_4=0$ (c)  $K_3=0, K_5=1.57$ (d)  $K_3=1.0, K_4=1.0$ Figure J.15. Results of Parallax and Center-of-Phase Calculations,  $K_2=0.5, K_5=-\pi/2$

(a)  $K_3=0, K_4=0$ (b)  $K_3=1.4, K_4=0$ (c)  $K_3=0, K_5=1.57$ (d)  $K_3=1.0, K_4=1.0$ Figure J.16. Results of Parallax and Center-of-Phase Calculations,  $K_2=1.0, K_5=-\pi/2$

#### J.4.2 Boresight Deviation Calculations

Calculations were made of boresight directions  $\phi_0$  (section J.2.4), as functions of range for simulated amplitude-monopulse radar antennas. The aperture illumination functions employed were

$$F_L(o, y, z) = \left[ K_{1L} + \cos \frac{\pi}{2} \rho \right] \left[ 1 + K_{2L} y \right] , \quad (J-37)$$

$$F_R(o, y, z) = \left[ K_{1R} + \cos \frac{\pi}{2} \rho \right] \left[ 1 + K_{2R} y \right] , \quad (J-38)$$

$$\psi_L(o, y, z) = K_{3L} y + K_{4L} y^3 + K_5 \rho^2 , \quad (J-39)$$

and

$$\psi_R(o, y, z) = K_{3R} y + K_{4R} y^3 + K_5 \rho^2 , \quad (J-40)$$

where the subscripts L and R indicate left (+ $\phi$ ) and right (- $\phi$ ) lobe illumination functions. The following parameters were employed:

$$K_{1L} = (0.462)$$

$$K_{1R} = (0.462)$$

$$K_{2L} = (0)$$

$$K_{2R} = (0), (0.5), (1)$$

$$K_{3L}, K_{4L} = (-1.4, 0), (0, -1.57), (-1, -1)$$

$$K_{3R}, K_{4R} = (1.4, 0), (0, 1.57), (1, 1)$$

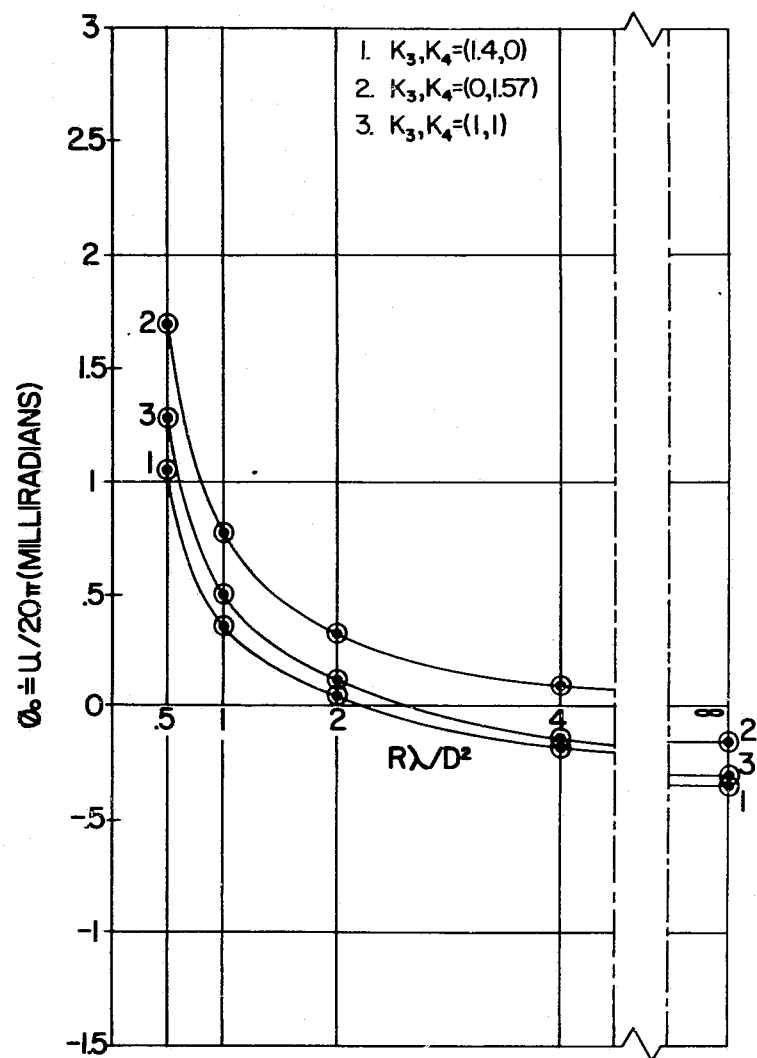
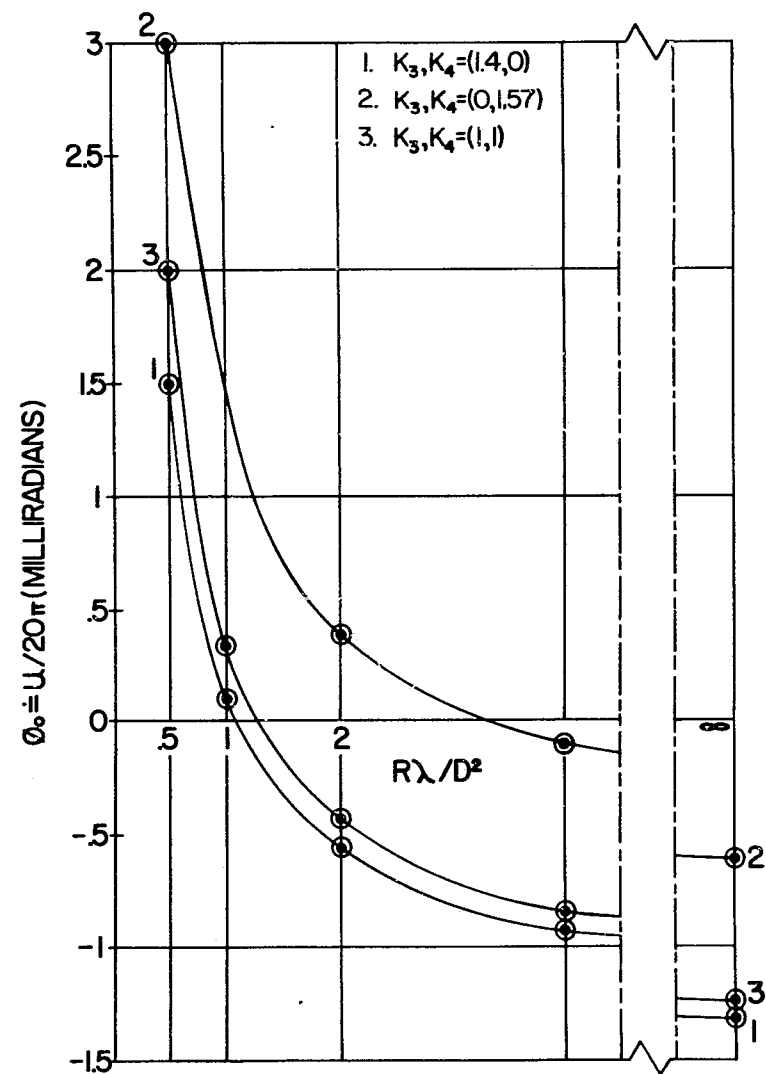
$$K_5 = (0), (\pi/2), (-\pi/2)$$

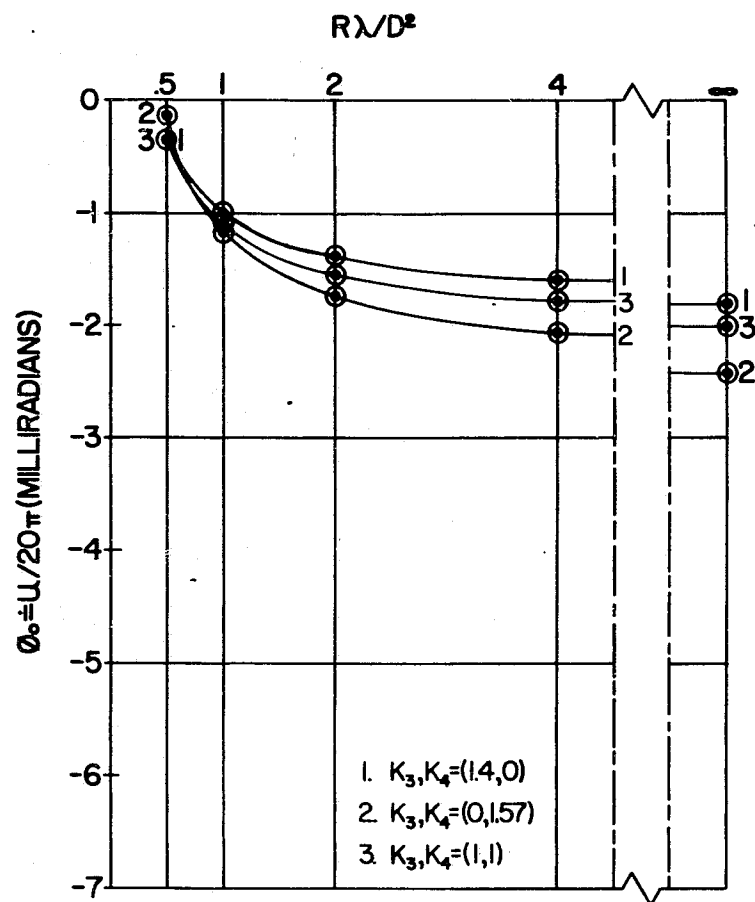
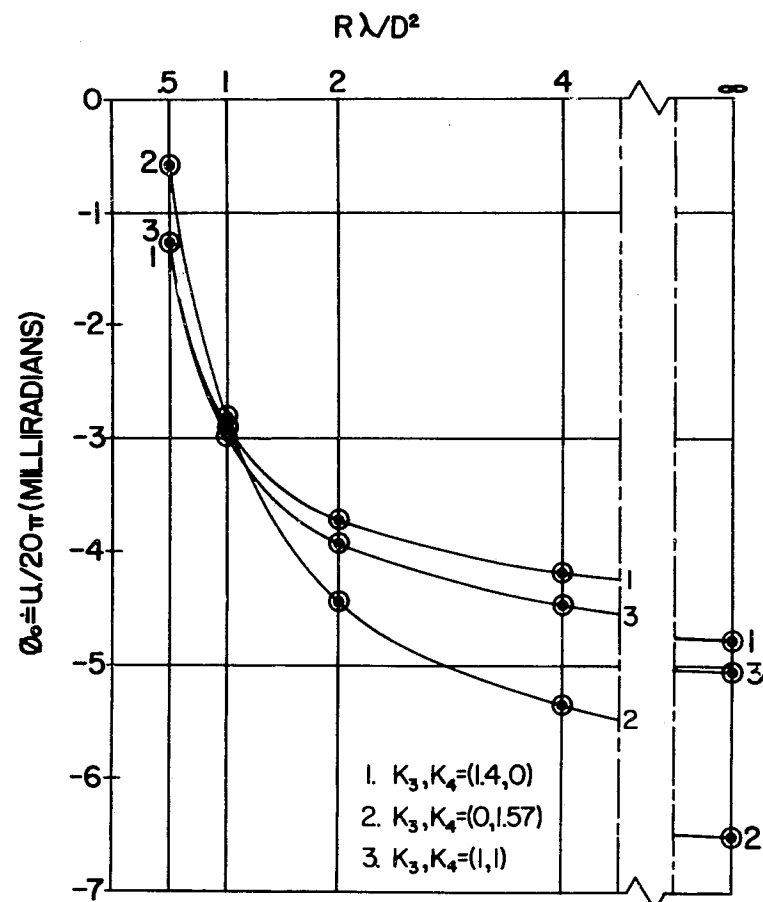
$$\frac{R\lambda}{D^2} = (0.5), (1), (2), (4), (\infty)$$

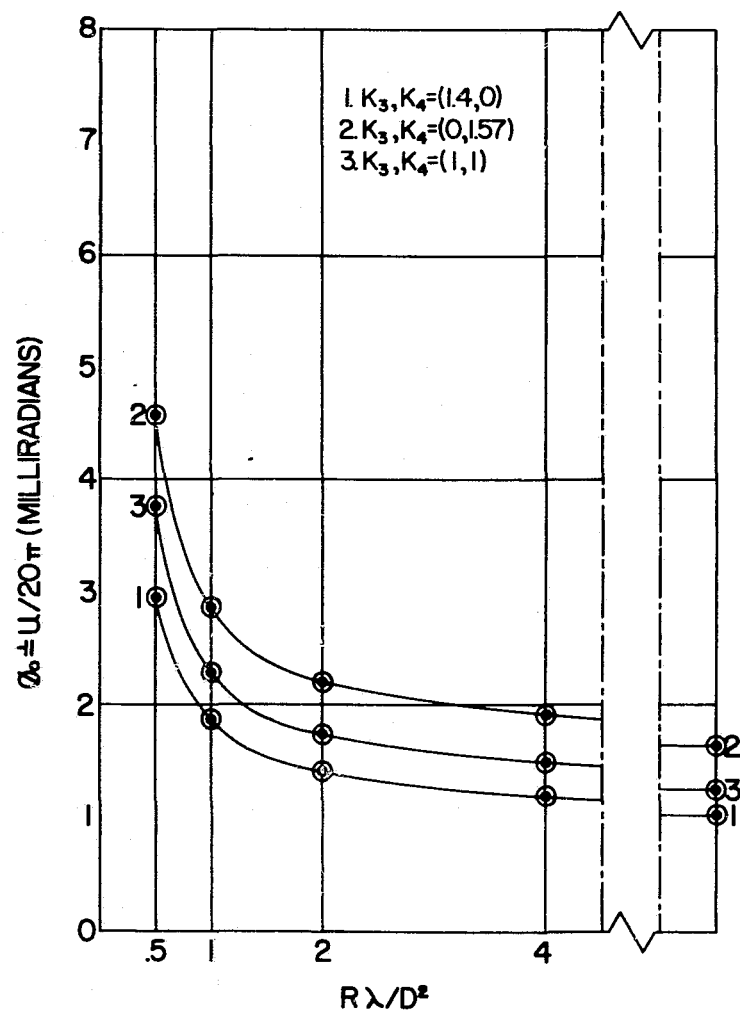
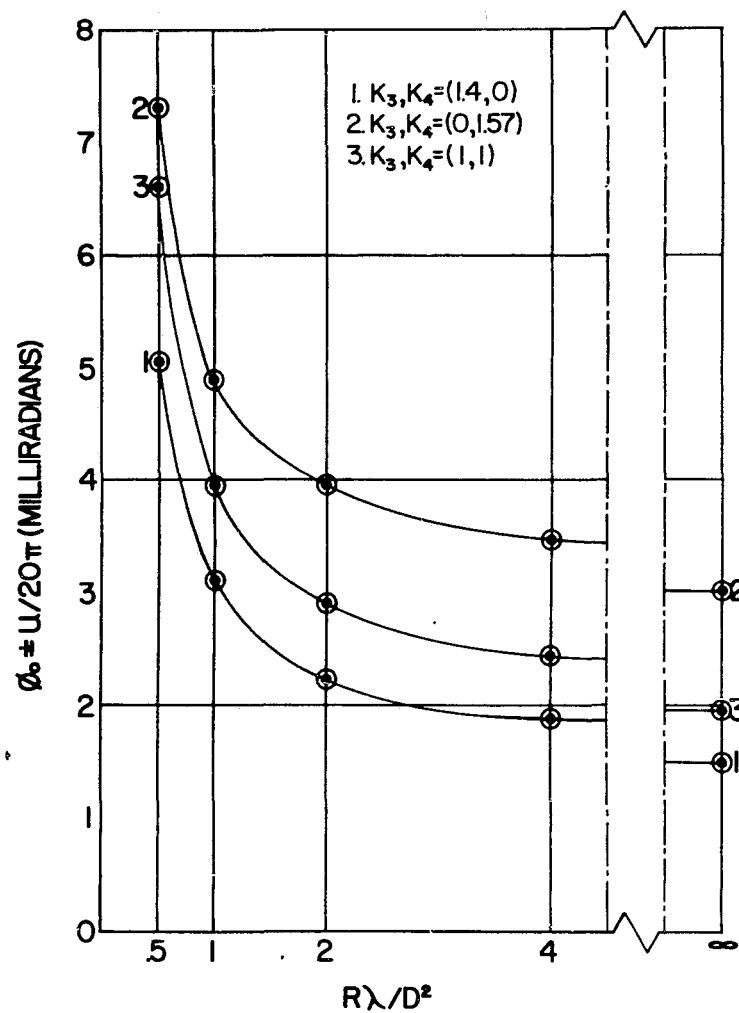
Calculated values of  $\phi_0$  versus  $R\lambda/D^2$  are plotted in Figures J.17 through J.19. The ordinates for these plots are given in terms of the parameter,

$$u = \frac{2\pi}{\lambda} a \sin \phi = \frac{2\pi}{\lambda} a \phi \quad (\text{for } \phi \ll 1) . \quad (J-41)$$

For the particular cases calculated, the aperture was very nearly 20 wavelengths in diameter, so that  $\phi_0 = u/20\pi$ . To use these curves for a general

(a)  $K_{2L} = 0, K_{2R} = 0.5$ (b)  $K_{2L} = 0, K_{2R} = 1.0$ Figure J.17. Calculated Boresight Direction,  $K_5 = 0$

(a)  $K_{2L}=0, \quad K_{2R}=0.5$ (b)  $K_{2L}=0, \quad K_{2R}=1.0$ Figure J.18. Calculated Boresight Direction,  $K_5=\pi/2$

(a)  $K_{2L}=0, K_{2R}=0.5$ (b)  $K_{2L}=0, K_{2R}=1.0$ Figure J.19. Calculated Boresight Direction,  $K_5=-\pi/2$



..aperture of diameter =  $n\lambda$ , the corresponding crossover point is

$$\phi_{on} = \frac{20\phi_o}{n}$$

(J-42)

APPENDIX K

A PRECISION GROUND-REFLECTION ANTENNA BORESIGHT  
TEST RANGE

**A PRECISION GROUND-REFLECTION ANTENNA BORESIGHT  
TEST RANGE**

by

**J. S. Hollis**  
Principal Engineer, Scientific-Atlanta, Inc.

**R. E. Pidgeon, Jr.**  
Senior Electronic Engineer, Scientific-Atlanta, Inc.

and

**R. M. Schutz**  
Design Engineer, McDonnell Aircraft Corporation

**Prepared for Presentation at**

**Fourteenth Annual Symposium on  
USAF Antenna Research and Development  
University of Illinois  
6-8 October 1964**

## ABSTRACT

The NASA-MSC-FO-MILA\* antenna boresight test facility is described and the results of measurements of the range characteristics are presented.

The antenna test facility, which is of the ground-plane type, was designed for making boresight accuracy tests of the 1428-Mc Gemini rendezvous radar and as a general purpose antenna test facility. It provides a separation of 1000 feet between transmitting and receiving antennas and is graded to a tolerance of one inch.

The requirements of the boresight problem dictated that far-zone, free-space conditions be simulated to a high degree of precision, and that extraneous reflections be suppressed to a minimum practicable level.

The radar is tested in a full-scale mockup of the Gemini spacecraft, which is mounted on a multi-axis antenna positioner capable of orienting and indicating the position of the test mockup to an accuracy of 0.01 degree. The polarization of the field at the test aperture, the transmitting antenna height, azimuth and elevation squint angles, and the frequency of the transmitter are remotely controlled from the operator's console.

During May and June of 1964 the range was validated for making boresight acceptance measurements of the Gemini rendezvous radar. Measurements were made of the amplitude and polarization of the test aperture field as functions of position, frequency, and environmental conditions. A number of measurements at different positions in the test aperture were made using a microwave interferometer to determine the location of the phase center of the composite array consisting of the transmitting antenna and its image in the range surface. In addition, measurements were made of the height of the source of radiation as a function of elevation squint angle of the transmitting antenna. With the axis of the antenna horizontal, the source appeared to lie within a circle less than one foot in radius and centered slightly above the midpoint of the line joining the antenna and its geometrical image.

---

\*National Aeronautics and Space Administration--Manned Spacecraft Center--Florida Operations--Merritt Island Launch Area.

# TABLE OF CONTENTS

SECTION		PAGE NO.
1	INTRODUCTION	1
2	THE GEMINI RENDEZVOUS RADAR	5
3	THE RENDEZVOUS RADAR BORESIGHT MEASUREMENT PROBLEM	8
	3.1 Suppression of Extraneous Reflections	9
	3.2 Range Length	11
	3.3 Gain of the Source Antenna	11
4	CONSIDERATION OF THE GROUND-REFLECTION ANTENNA TEST RANGE	12
	4.1 Height of the Apparent Source of Radiation	13
	4.2 Range Surface	15
5	RANGE INSTRUMENTATION	17
	5.1 Spacecraft Mockup	18
	5.2 Positioning and Indicating Equipment	18
	5.2.1 Coordinate System	18
	5.2.2 Positioner	20
	5.2.3 Alignment of Coordinate Systems	21
	5.3 Transmitting Equipment	22
	5.4 Receiving and Recording Equipment	23
6	MEASUREMENTS	25
	6.1 Introduction	25
	6.2 Aperture-Field Measurements	25
	6.2.1 Amplitude	25
	6.2.2 Polarization	26
	6.3 Boresight Measurements	33
	6.3.1 Discussion of the Measurement Problem	33
	6.3.2 Principle of Operation of the Interferometer	33
	6.3.3 Practical Considerations	37
	6.3.4 Interferometer Test Results	39
7	SUMMARY	43

Second Printing  
November 1964

# LIST OF ILLUSTRATIONS

FIGURE		PAGE NO.
1. 1	Aerial View of Radar Boresight Range	2
1. 2	Plan View of Radar Boresight Range	3
1. 3	Gemini Spacecraft Mockup on Control Building	4
2. 1	Rendezvous Radar Installed in Spacecraft Mockup	6
2. 2	Illustration of Relationship Between Electrical Phase and Space Angle in Interferometer	7
2. 3	Determination of Boresight Direction by Intersection of Cones of Constant Phase Delay	7
3. 1	Illustration of the Effect of Extraneous Reflections on Boresight Accuracy	10
4. 1	Illustration of the Principle of the Ground-Reflection Range	13
4. 2	Limits of Field Variation with Height Over the Test Aperture of a Ground-Reflection Antenna	14
5. 1	Range Operating Console	17
5. 2	Spherical Coordinate System	18
5. 3	Spherical Coordinate System Shown in Relationship to Range Geometry	19
5. 4	Rear View of Spacecraft Mockup and Multi-Axis Positioner	20
5. 5	Illustration of the Optical Reflection Technique for Aligning the Z and Z' Axes with the Line OT	21
5. 6	Transmitting Antenna, Positioner, and Hoist Viewed Looking Toward the Control Building	23
5. 7	Aperture Field Probe with Horn Antenna Mounted on Carriage	23
5. 8	Polarization Probe Mounted on Spacecraft Mockup	24
5. 9	Illustration of the Use of the Polarization Probe to Obtain Polarization Patterns as a Function of Position in Test Aperture	24
6. 1	Aperture Field Patterns	27
6. 2	Polarization Pattern Measured at Center of Test Aperture	29
6. 3	Family of Polarization Patterns as a Function of Relative Amplitude of Orthogonal Field Components	29
6. 4	Family of Polarization Patterns as a Function of Relative Phase Between Orthogonal Field Components	30
6. 5	Polarization Pattern of Linearly Polarized Field	31

# LIST OF ILLUSTRATIONS-continued

FIGURE		PAGE NO.
6. 6	Axial Ratio at Center of Test Aperture as a Function of Frequency	32
6. 7	Axial Ratio as a Function of Position in the Test Aperture	32
6. 8	Block Diagram of Interferometer	34
6. 9	Illustration of the Method Employed for Positioning the Spacecraft to Obtain Two Identical Orientations of the Spacecraft Relative to OT	36
6. 10	Illustration of the Method Employed for Positioning the Spacecraft Mockup to Make $T'$ Coincident with $T'$	38
6. 11	Measured Azimuth of the Apparent Source Versus $\theta$ at L-Band	40
6. 12	Measured Height of the Apparent Source Versus $\theta$ at L-Band	41
6. 13	Height of Apparent Source as a Function of Transmitting Antenna Squint Angle	42

# A PRECISION GROUND-REFLECTION ANTENNA BORESIGHT TEST RANGE

J. S. Hollis\*, R. E. Pidgeon, Jr.<sup>†</sup>, and R. M. Schutz<sup>‡</sup>

## 1. INTRODUCTION

The purpose of this paper is to describe the NASA-MS-C-FO-MILA\*\* antenna test facility and the results of measurements of the range characteristics. This antenna range, which is shown in Figure 1.1 and in the plan view of Figure 1.2, was designed specifically for making boresight-accuracy and calibration tests of the 1428-Mc Gemini Rendezvous Radar and secondarily as a general purpose antenna test facility.

The range has the dual capability of operating as a ground-reflection range and as a conventional elevated range. As can be seen from Figure 1.2, the surface of the range is graded plane. In the ground-reflection mode of operation the antenna under test, assuming that it is operated on reception, is illuminated by direct-path energy from the source antenna and by energy which is specularly reflected from the smooth range surface. In this manner reflections from the earth are used to advantage rather than being allowed to contribute to the received field in a random fashion. The ground-reflection mode of operation is the subject of this paper.

In the elevated mode, discrimination against extraneous reflections is achieved by the directional characteristics of both the transmitting antenna and the antenna under test and by the use of diffracting or absorbing materials. While the performance of the range has not been tested for the elevated mode, the planar range surface is advantageous for this mode because the location and size of the region of specular reflection can be calculated.

For the rendezvous radar boresight application the radar is tested in a full-scale mockup of the Gemini Spacecraft, shown in Figure 1.3. The mockup is mounted on a precision, multi-axis positioner on top of the range control building. To aid in suppressing reflections from the support structure, the building is oriented such that its sides make angles of 45 degrees with the axis of the range, and the two illuminated sides of the building are covered with weatherproof, high performance, microwave absorbing material.

---

\*Principal Engineer, Scientific-Atlanta, Inc.

<sup>†</sup>Senior Electronic Engineer, Scientific-Atlanta, Inc.

<sup>‡</sup>Design Engineer, McDonnell Aircraft Corporation.

\*\*National Aeronautics and Space Administration--Manned Spacecraft Center--Florida Operations--Merritt Island Launch Area. In this paper the range will be called the Gemini Rendezvous Radar Boresight Test Range or appropriate contractions.



The range was designed and validated for NASA as a co-operative effort between Scientific-Atlanta and McDonnell Aircraft Corporation, the prime contractor for the Gemini Spacecraft, and is instrumented with Scientific-Atlanta equipment. Architects were John J. Harte Associates, Architects and Engineers, and the facilities contractor was Williams Development Corporation. Equipment for making pre-installation acceptance tests of the radar was designed and fabricated by Westinghouse Aerospace Division, Baltimore, Maryland, the subcontractor for the radar.



Figure 1.1. Aerial View of Radar Boresight Range

The spacecraft mockup is shown mounted on the control building at the left. The source tower is at the right between two floodlight towers. This photograph was made before the grass cover was established. The sprinklers shown in the dark areas on the range are removed during range operation.

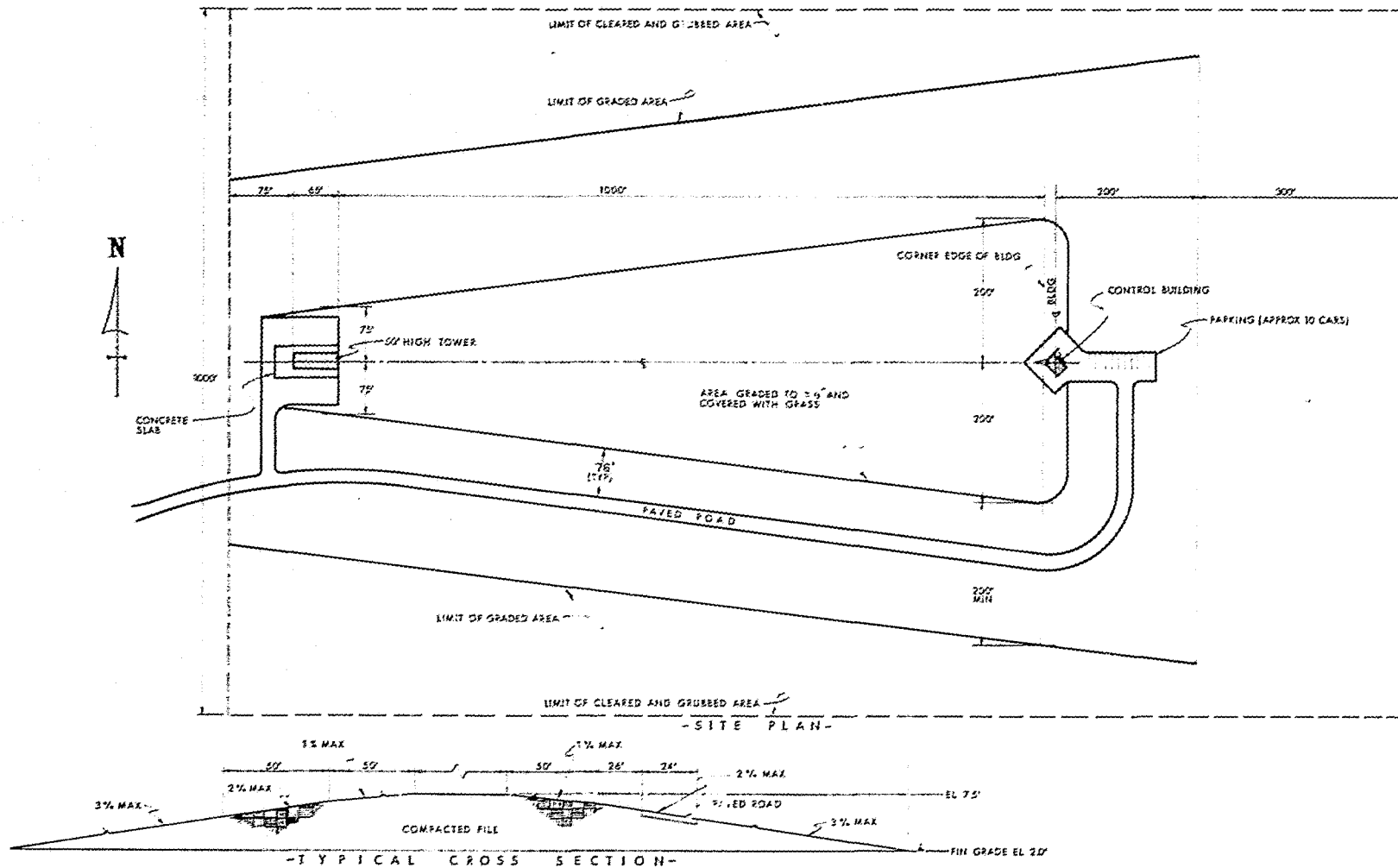


Figure 1.2. Plan View of Radar Boresight Range

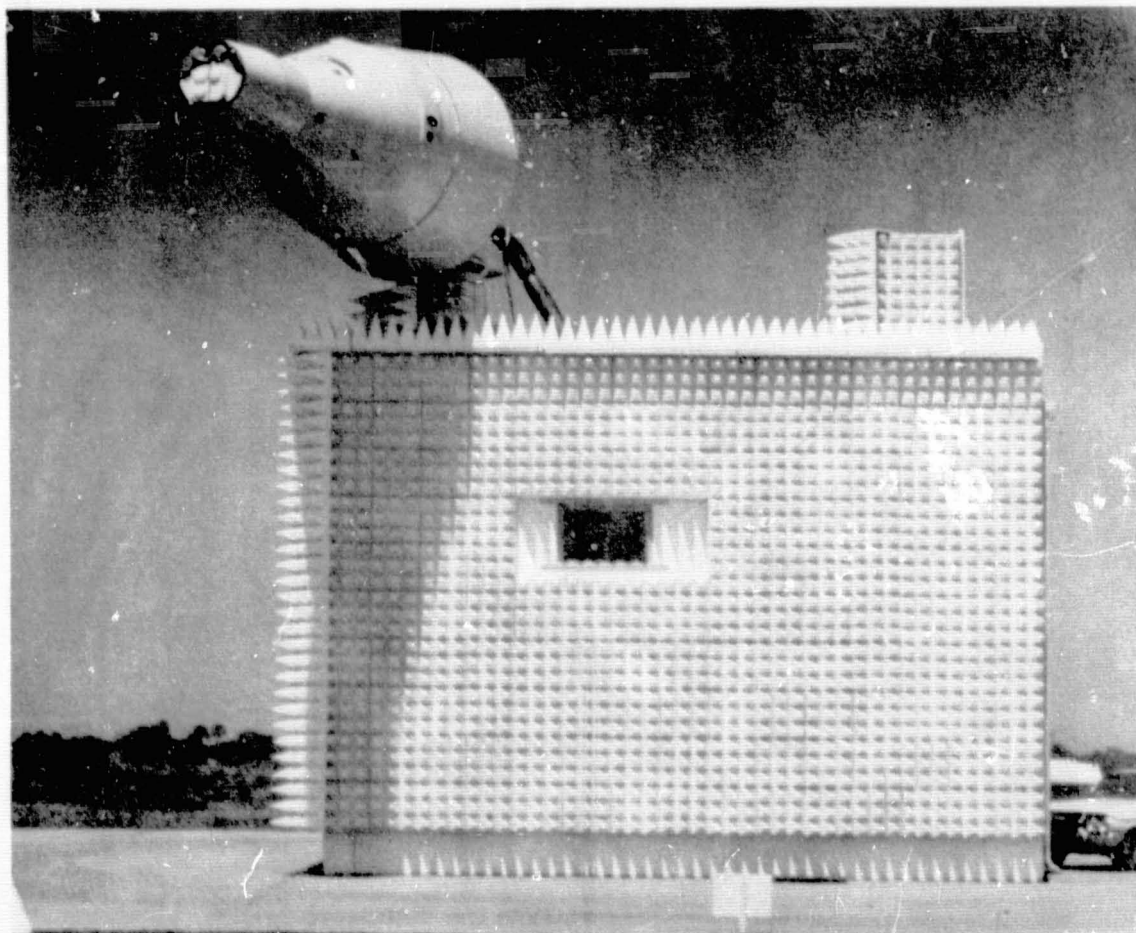


Figure 1.3. Gemini Spacecraft Mockup On Control Building

Absorber panels (B. F. Goodrich type VHP-18) on the control building can be removed in case of high winds. An absorber insert (not shown) is provided for the control building window. The small, absorber-covered structure on the roof to the right is a work stand for servicing the radar.

## 2. THE GEMINI RENDEZVOUS RADAR

A brief description of the Gemini rendezvous radar is given to provide an understanding of some of the major problems associated with establishing the specifications for the boresight test range.

The purpose of the rendezvous radar<sup>1</sup> is to measure the range and relative bearing from the Gemini spacecraft to the unmanned Agena target vehicle during the rendezvous of the two satellites in space.\* A co-operative radar system is employed in which an RF pulse is transmitted from the Gemini radar, received by a transponder in the target vehicle, and re-transmitted after a short delay at a different frequency. The range to the target vehicle is determined from the measured delay between transmission and reception of the signals. Readouts are provided for range, range rate, and direction to the Agena vehicle, and an on-board digital computer calculates the orbital corrections which are necessary to effect rendezvous.

The Gemini rendezvous radar operates as a two-channel phase-monopulse radar or interferometer to measure the direction of arrival of the received signal. Three antennas are incorporated in the interferometer with one antenna common to both channels. A fourth antenna is used as the transmitting antenna. The antennas are located on the spacecraft as shown in Figure 2.1.

The phase differences between the signals received by the two orthogonal pairs of antennas are measured by the radar. The electrical phase differences  $\phi_1$  and  $\phi_2$  are related to the space direction angles  $\alpha$  and  $\beta$  as illustrated in Figure 2.2 by the equations

$$\phi_1 = \frac{2\pi d}{\lambda} \cos \alpha; \quad \phi_2 = \frac{2\pi d}{\lambda} \cos \beta \quad (1)$$

where  $d$  is the spacing between the phase centers of each antenna pair,  $\lambda$  is the wavelength, and  $\alpha$  and  $\beta$  are measured from the yaw and pitch axes of the spacecraft, respectively. These angles are limited by the radar to the intervals of 90 degrees  $\pm 25$  degrees. The radar provides coverage for yaw and pitch angles up to  $\pm 25$  degrees.

Each channel of the interferometer locates the source of radiation on the surface of a cone. The spacing between the antennas is less than  $\lambda$ ; thus a unique cone is defined for each channel of the interferometer. The direction to the source of radiation is

---

<sup>1</sup>Vester, B. H., "Gemini Rendezvous Radar," The Westinghouse Engineer, Volume 24, Number 1; January 1964.

\* In the rendezvous mission the two-man Gemini spacecraft will be launched into an orbit which is approximately co-planar with that of an unmanned Agena target vehicle launched earlier. With the aid of guidance information furnished by the rendezvous radar, corrections will be made to the orbit of the Gemini vehicle to bring it into contact with the Agena vehicle.

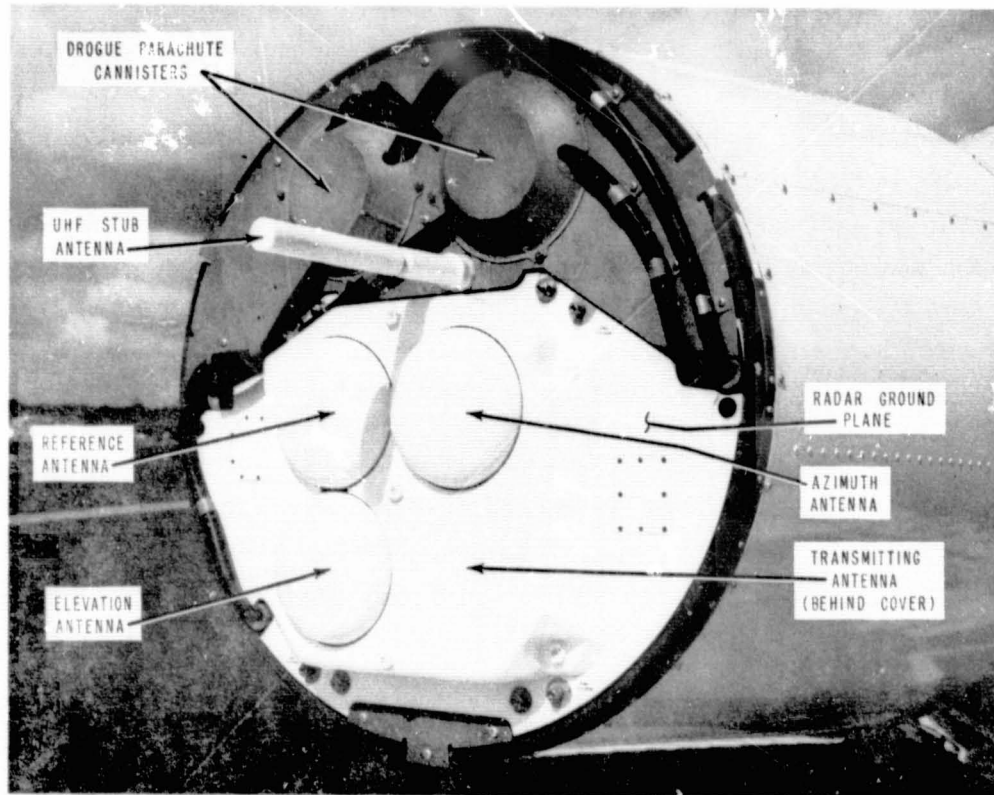


Figure 2.1. Rendezvous Radar Installed in Spacecraft Mockup

given by the intersection in space of these two cones as illustrated in Figure 2.3. Ambiguity results from the two lines of intersection of the cones, one in the hemisphere forward of the spacecraft and the other in the hemisphere to the rear of the spacecraft. The null in the rear hemisphere is discriminated against by the directivity of the radar antennas.

The circularly polarized radar antennas are printed-circuit Archimedian spirals located over a ground plane. The beamwidth of the interferometer antennas is approximately 70 degrees measured between the 3-db points on the pattern. Measurement of the phase differences between the antennas is achieved by rotating the antennas about their axes with servos to obtain nulls and measuring the angles of

rotation with shaft-position encoders. The phase delay thus introduced in each antenna is very nearly proportional to rotation of the antenna for small ellipticity ratios.

This paper is concerned with techniques and equipment employed for measuring the accuracy with which the radar determines the direction to the Agena, defined as the boresight accuracy. Equipment designed by Westinghouse and referred to previously is employed to measure the radar range accuracy.

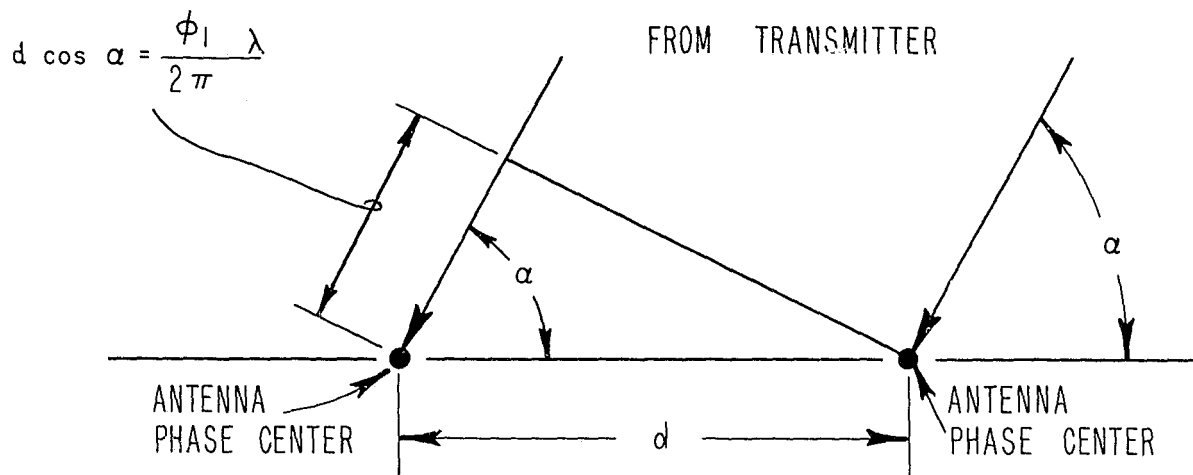


Figure 2.2. Illustration of Relationship Between Electrical Phase and Space Angle in Interferometer

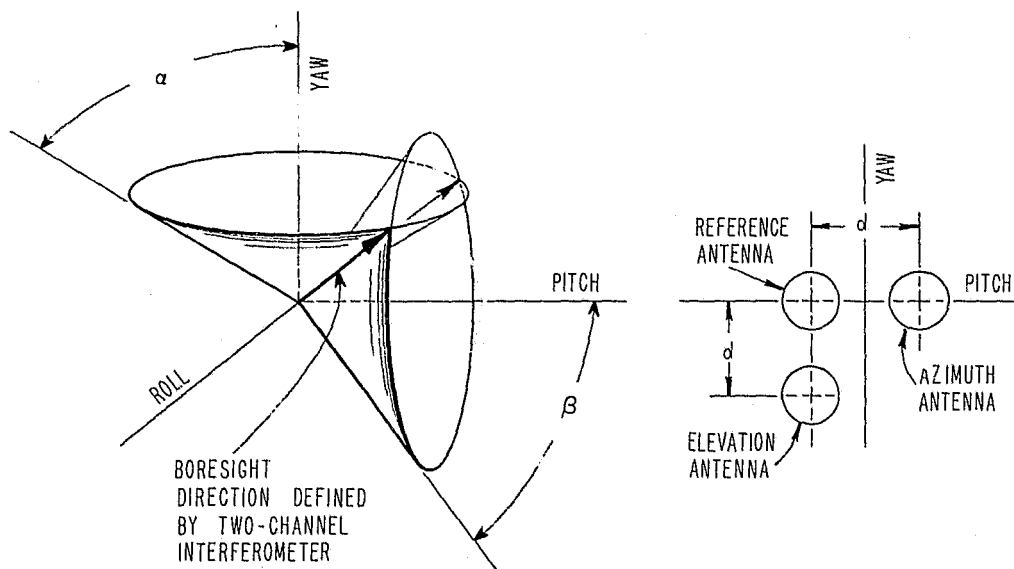


Figure 2.3. Determination of Boresight Direction by Intersection of Cones of Constant Phase Delay

### 3. THE RENDEZVOUS RADAR BORESIGHT MEASUREMENT PROBLEM

The Gemini rendezvous radar must function in a space environment of zero atmospheric pressure, increased solar radiation levels, and zero gravity. In establishing criteria for the acceptance tests of the boresight accuracy, it was considered impracticable to attempt to simulate a zero-pressure environment or to take into account in the measurements the effects of the increased level of solar radiation. The effect of gravity on the boresight directions measured by the radar was investigated in the manner described in Section 6.

The boresight-measurement problem can be divided into the following categories:

- (a) Establishment of an incident 1428-megacycle, circularly polarized field over the active aperture of the radar antennas which would adequately simulate an incident plane wave of constant amplitude,
- (b) Provision for supporting, positioning, and indicating the orientation of the radar,
- (c) Establishment of a frame of reference in which the measurements could be made,
- (d) Determination of the location of the source of radiation, and
- (e) Establishment of an optical line of sight from the source of radiation to the radar to permit its comparison with the line of sight indicated by the radar.

We will not dwell on a discussion of the various range configurations<sup>2</sup> that might have been employed for testing the rendezvous radar. The ground-reflection range was selected because of the high suppression required of extraneous signals, the low directivity of the radar antennas, and because this type of range is in keeping with the flat terrain which exists at Merritt Island.

A discussion of some of the basic problems involved in the establishment of the incident field over the test aperture and which influenced the selection of the range configuration is given in the following paragraphs.

---

<sup>2</sup>Hollis, J. S., and R. E. Moseley, "Siting Considerations in Microwave Antenna Measurements," Essay No. 3, Scientific-Atlanta, Inc.; August 1961.

Cumming, W. A., "Radiation Measurements at Radio Frequencies: A Survey of Current Techniques," Proc. IRE, Volume 47, No. 5, pp. 703-735; May 1959.

### 3.1 Suppression of Extraneous Reflections

The radar-boresight error specification for which the range was designed was 3 milliradians. In a typical measurement problem of this type it is customary to require that the measurement system error be an order of magnitude smaller than the tolerance of the quantity being measured. This criterion would have resulted in a measurement system overall accuracy of 0.3 milliradian and would have limited the error caused by extraneous reflections to the order of 0.1 milliradian.

Calculations showed, however, that this degree of accuracy would have demanded suppression of range reflections and tolerances on other measurement errors which were not considered practicable. A more realistic range accuracy goal appeared to be 1 milliradian with a maximum allowable contribution from extraneous reflections of 0.3 to 0.5 milliradian.

The required suppression of range reflections can be determined by considering the relationship of the radar electrical phase error to boresight error. Differentiation of equations (1) gives

$$\frac{d\phi_1}{d\alpha} = -\frac{2\pi d}{\lambda} \sin \alpha; \quad (2)$$

$$\frac{d\phi_2}{d\beta} = -\frac{2\pi d}{\lambda} \sin \beta .$$

The mechanical spacing  $d$  between antenna centers is 6.80 inches. Evaluation of equations (2) for the range of the variables  $\alpha$  and  $\beta$  gives the approximate relationship

$$d\phi_1 \doteq 5d\alpha ; \quad (3)$$

$$d\phi_2 \doteq 5d\beta .$$



Referring to Figure 3.1, let  $A$  be the amplitude of the phasor at the difference terminals of one of the interferometer summation networks caused by a direct-path signal impinging upon the antenna. If  $B$  is the amplitude of the phasor produced by an extraneous signal entering the same antenna, the maximum electrical phase deviation will occur when the two phasors are in quadrature. The error  $\epsilon$  will be  $(B/A) \times 10^3$  milliradians if  $B \ll A$ . For the worst-case condition, if equal and oppositely phased extraneous signals exist in each channel of an interferometer pair, the phase error will be  $2(B/A) \times 10^3$  milliradians, corresponding to a boresight error contribution of about  $0.4(B/A) \times 10^3$  milliradians in accordance with equations (3).

If the contribution of extraneous signals is to be, say, 0.4 milliradian, we must let

$$0.4(B/A) \times 10^3 \text{ mr} = 0.4 \text{ mr} , \quad (4)$$

giving

$$B/A = 10^{-3} . \quad (5)$$

These calculations indicate that the maximum level of the sum of all extraneous signals should be held to the order of 60 decibels below the level of the direct-path signal to meet the above criterion. It should be noted that the calculations give the maximum error contribution from one interferometer channel. The magnitude of the total boresight error is given by the rms sum of the errors in the two channels.

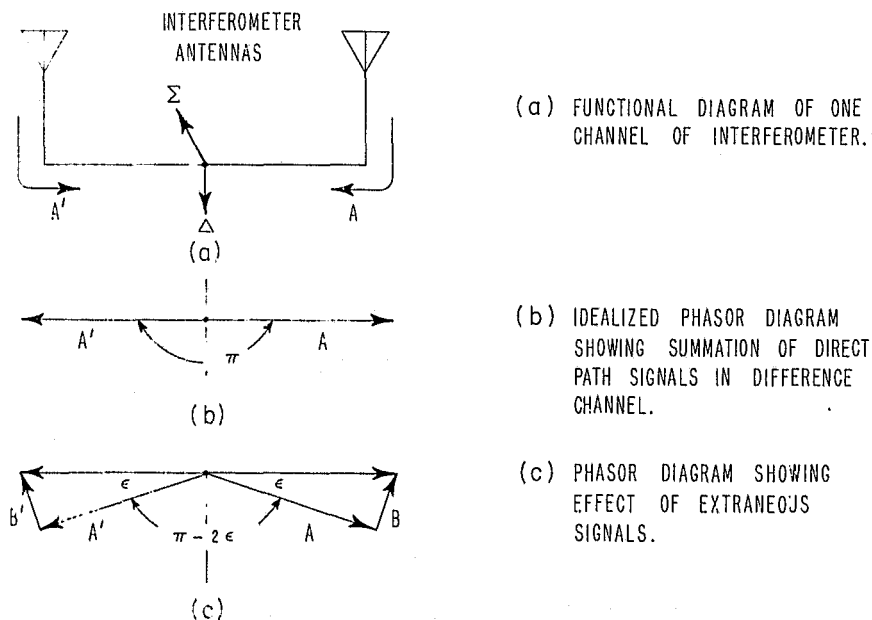


Figure 3.1. Illustration of the Effect of Extraneous Reflections on Boresight Accuracy  
( $A=A'$ ;  $B=B'$ )

### 3.2 Range Length

In order to establish the range length it was necessary to determine the extent of the active aperture of the radar antennas, that is, over how much of the spacecraft quasi constant-amplitude, constant-phase conditions must be provided. Upon consideration of the problem and after consultation with leading antenna authorities, it was concluded that one could not predict to any degree of certainty the contributions of currents flowing over the surface of the spacecraft to the indicated boresight angle. However, one can show easily that the contribution may be significant.\* It was therefore decided that the entire spacecraft would be mocked-up and that the phase error would be limited to less than  $\lambda/16$  over the aperture represented by the maximum projection of the spacecraft normal to the direction of incidence. This would have resulted in a range length of about 700 feet. The range length was set at 1000 feet because this length resulted in a lower grazing angle for the ground-reflection range configuration and at the same time provided a more desirable phase-variation limit.

### 3.3 Gain of the Source Antenna

The maximum gain of the source antenna (actually the directivity rather than gain) is limited because of one of two factors: (a) the requirement for a nearly constant field over the test aperture<sup>3</sup> and (b) the requirement for control of the circularity of the incident field at the test aperture. To adequately simulate far-zone conditions, a criterion was established that the taper of the field over the test aperture should not vary more than approximately 0.25 decibel.

The maximum projection of the spacecraft is 10 feet at nose-on incidence, but the horizontal projection increases to approximately 19 feet as the spacecraft is rotated in azimuth. The variation of the field in the vertical plane is determined by the ground-reflection range configuration discussed in Section 4. The variation of the field horizontally is determined directly by the directivity pattern of the source antenna. However, it became evident that the ground-reflection range configuration was the major factor in deciding the beamwidth since the maximum allowable height of the center of the source antenna was about five feet. An 8-foot diameter antenna was employed giving a beamwidth of about 5 degrees and a directivity of about 30 decibels.\*\* Estimates of the cross-polarization characteristics of a paraboloidal reflector with an axial ratio of 0.373 indicated that the change in circularity should not be excessive over the 19-foot test aperture. Aperture amplitude and polarization patterns are presented in Section 6.

<sup>3</sup>Chastain et al, Investigation of Precision Antenna Pattern Recording and Display Techniques, Final Report, Contract AF 30(602)-2737, Scientific-Atlanta, Inc., April 1963, AD415912.

\*Subsequent measurements have shown that currents on the spacecraft do contribute significantly to the boresight direction.

\*\*In the ground-reflection range this directivity is increased by about 5 decibels by the in-phase interference from the ground-reflected wave.

#### 4. CONSIDERATION OF THE GROUND-REFLECTION\* ANTENNA TEST RANGE

The ground-reflection antenna test range has been employed for a number of years and has been described in the literature.<sup>4</sup> A rigorous description of the theory of operation is exceedingly complex; however, its principle of operation can be explained in an elementary manner by the method of images of geometrical optics and by use of Rayleigh's criterion of roughness<sup>5</sup> of physical optics.

The range geometry is given by Figure 4.1. The range is plane and smooth within Rayleigh's criterion to provide for specular reflection of the incident energy. At frequencies above about 100 megacycles for nearly grazing angles of incidence and for both horizontal and vertical polarizations, the phase of the reflection coefficient for a plane incident wave is virtually 180 degrees.<sup>6</sup> Under this set of assumptions an image of the transmitting antenna appears to lie below the range surface, equidistant from the antenna, thus maintaining the angle of incidence  $i$  equal to the angle of reflection  $r$  at the range surface. It has been shown that for a unity reflection coefficient and, neglecting the vertical directivity pattern of the transmitting antenna, the field variation with height at the test antenna is approximated by

$$E = 2E_0 \sin \frac{2\pi h_1 h_2}{\lambda R}, \quad (6)$$

where  $E_0$  is the field produced by direct-path transmission.<sup>7</sup>  $E$  thus has a sinusoidal variation with height, with a value of zero for  $h_2 = 0$  and a first maximum for

$$\frac{2\pi h_1 h_2}{\lambda R} = \frac{\pi}{2}, \quad (7)$$

\*This type of range has been described by the terms ground-level and ground-plane. The term ground-reflection more specifically describes the principle of operation than do the alternate designations.

<sup>4</sup>Cutler, C. C., A. P. King, and W. E. Kock, "Microwave Antenna Measurements," Proc. IRE, Volume 35, No. 12, pp. 1462-1471; December 1947.

Hollis and Moseley, op cit.

Cohen, A., and A. W. Maltese, "The Lincoln Laboratory Antenna Test Range," The Microwave Journal, April 1961.

Campanella, A. J., C. F. Douds, and R. E. Wolfe, Feasibility Study of a High Performance Antenna Test Range (U), HRB Singer, Inc., Contract AF 30(602)-2445, Report No. RADC-TDR-62-301; 19 October 1962.

Christie, R. A., Antenna Testing Facilities, Bell Telephone Laboratories, Inc., Whippany, New Jersey.

Communications with Mr. George Dale, Bell Telephone Laboratories, Inc., Whippany, New Jersey.

<sup>5</sup>Kerr, D. E., Propagation of Short Radio Waves, Radiation Laboratory Series, Volume 13, McGraw-Hill; equation 19 and footnote page 16.

<sup>6</sup>Jordan, E. C., Electromagnetic Waves and Radiating Systems, Prentice-Hall, Inc., New York, p. 613; 1961.

<sup>7</sup>Cutler et al, op cit.

or

$$h_2 = \frac{\lambda R}{4h_1} \quad (8)$$

In consideration of the geometry of Figure 4.1, it is evident that, in the ground-reflection antenna test range, the incident wave produced by the transmitting antenna is not plane. Further, the antenna usually has a significant change in directivity with elevation angle. Experimental measurements have shown, however, that equation (6) predicts the field variation with height quite well near the region of the maximum. Although the field may depart from the predicted value in the vicinity of the nulls, this is of no consequence since the vertical aperture of the antenna under test must be limited to a height  $d$  such that the field variation predicted by equation (6) is small. A generally accepted criterion for the total variation is 0.25 decibel.

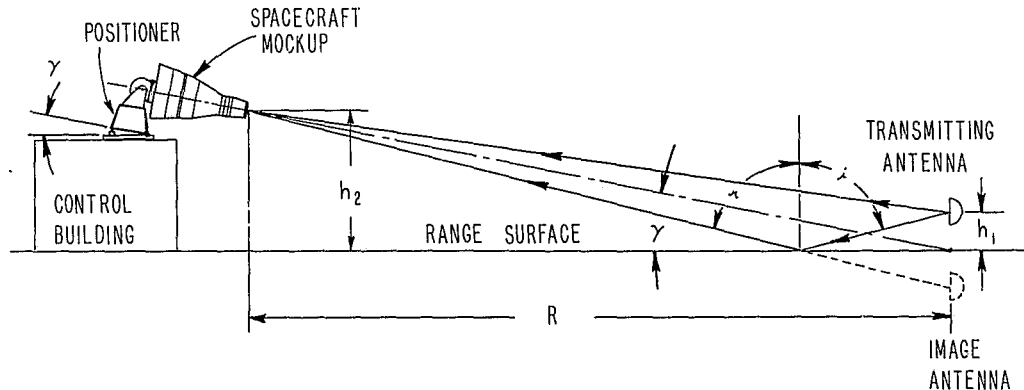


Figure 4.1. Illustration of the Principle of the Ground-Reflection Range

Figure 4.2 shows the limits of the field variation in decibels as a function of the normalized aperture height  $d/h_2$ . Here,  $h_2$  is the height of the center of the test aperture, which is assumed coincident with the maximum given by equation (8). The height  $h_1$  is predicted by equation (8) to be 5.75 feet for a range length of 1000 feet and height  $h_2$  of 30 feet, the nominal values for the rendezvous measurement problem.

#### 4.1 Height of the Apparent Source of Radiation

The apparent source of radiation for the ground-reflection range can be defined as the center of phase of the array formed by the transmitting antenna and its image in the reflecting surface of the range. Although it has been shown that a unique center of phase usually does not exist except over a small region of solid angle of the

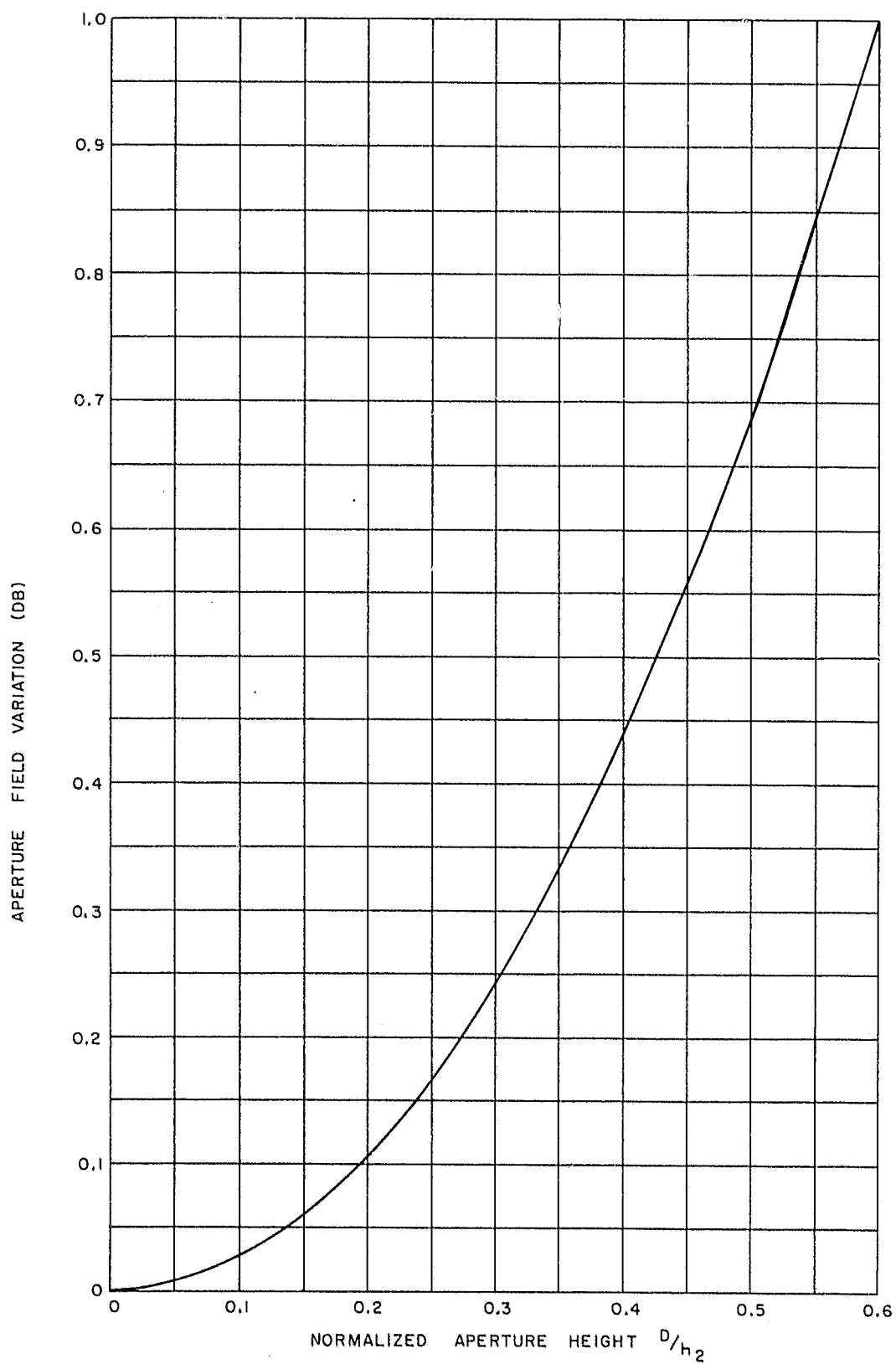


Figure 4.2. Limits of Field Variation with Height Over the Test Aperture of a Ground-Reflection Antenna

far-zone pattern of a directional antenna<sup>8</sup>, such a center of phase can be defined as it exists at the center of the test aperture. By the method of images it can be shown that the height of this center of phase is approximated by

$$h \doteq \frac{1-R}{1+R} h_1, \quad (9)$$

where R is the amplitude ratio of the specularly reflected wave to the direct-path wave. This approximation is based on 180-degree phase reversal of the incident wave at the range surface and constant phase of the transmitting antenna far-zone field with elevation.

In typical ground-reflection antenna range applications the phase center (hence the apparent source) is often assumed to be located at the intersection of the range surface with the vertical line joining the centers of the antenna and its image. While this assumption is satisfactory for many applications, the height of the apparent source can vary significantly; therefore it was necessary to determine its location. For example, a radar accuracy specification of 3 milliradians is represented by a circle which is 3 feet in radius at the test range of 1000 feet. It was necessary to determine that the location of the apparent source could be predicted with small error compared with this radar error specification. It was further required that a direction be assigned for the mean location of the apparent source, which would be used as a comparison standard in making the boresight measurements. The method employed to accomplish this and the results are described in paragraph 6.3.

#### 4.2 Range Surface

The primary requirements for the range surface are that it be graded smooth within Rayleigh's criterion and have a shape which produces a unique image of the transmitting antenna in the range surface for all orientations of the spacecraft mockup. These requirements are met by a plane surface over the major area of illumination, which is graded to the tolerances shown in the plan view of Figure 1.2.

Most of the reflected energy comes from within the first few Fresnel zones on the range surface<sup>9</sup>. These zones are bounded by ellipses for a plane range surface and a point source transmitting antenna. For the range constants at L-band, the first Fresnel zone has major and minor axes of approximately 495 feet and 22 feet and is centered 280 feet in front of the source antenna. The tenth Fresnel zone has major and minor diameters of 888 and 80 feet and is centered 447 feet from the source antenna.

<sup>8</sup>Tetsu Morita, Determination of Phase Centers and Amplitude Characteristics of Radiating Structures, Technical Report No. 1, SR 1, Proj. 898, Stanford Res. Inst., Menlo Park, California, Contract DA04-200-ORD-273, AD68240; March 1955.

<sup>9</sup>Campanella et al, op cit.

The range surface is controlled over the area indicated in Figure 1.2 in addition to the region of specular reflection to reduce errors from diffuse reflection.

The Rayleigh criterion<sup>10</sup> is given by

$$\eta \sin \psi < \lambda/k, \quad (10)$$

where  $\eta$  is the height of a surface irregularity,  $\psi$  is the grazing angle and  $k$  is usually set between 8 and 32, the constant 32 defining a very smooth surface.

Letting  $\lambda = 8$  inches ( $f \sim 1428$  Mc), and  $\psi \sim 2^\circ$ , the constants for the current problem, and letting  $k = 32$ , gives  $\eta < 7$  inches or  $\pm 3.5$  inches. However, because of the extreme accuracy requirements of the problem and because the antenna range is to be employed in higher frequency applications later, the surface was graded to a tolerance of  $\pm 1$  inch. Surveys of the range have since led to the conclusion that the graded surface probably has a  $\pm 1/2$ -inch tolerance exclusive of the Bermuda grass cover.

The question of the type of surface which would be employed was of some concern. Gravel in the form of graded, crushed aggregate would be a good choice, because it would allow rainwater to leach into the surface and yet would resist wind erosion. It was decided against, however, because of the cost.

Asphalt and concrete were considered but were discarded because of the cost and the drainage problem caused by their lack of perviousness. The cost of asphalt or concrete could have been reduced by use of a narrow strip of either material down the center of the range with grass on both sides. While this technique can be employed, it was rejected because of the high angular-accuracy requirement of the measurement problem, the consequent desire to have no linear discontinuities along the length of the range, and because of the drainage problem.

Grass has been criticized as a range surface because the blades can fill with water, which has a high dielectric constant, resulting in changes in the reflecting characteristics. However, grass was chosen because of the low initial cost, but with the specification that it be maintained closely mowed. In measurements which have been made to date the effect of moisture on the grass or of the moisture content of the range surface has been found to be insignificant. Specifically, polarization measurements have been made immediately before, during, and after a severe thunderstorm with a circularity change of less than 0.1 decibel from an axial ratio of 0.5 decibel. The measurement after the rain was made with large puddles of water on the range. Measurements have not been made at frequencies other than L-band, nor has it been possible to make precisely controlled measurements of the height of the apparent source immediately before and after a rain for comparison purposes.

---

<sup>10</sup>Kerr, op cit, equation (19) and footnote, page 416.

## 5. RANGE INSTRUMENTATION

Primary considerations in the design of the instrumentation system were accuracy of the boresight measurements, rapidity and ease of acquiring data, and flexibility of operation. The range can be used for making general antenna measurements as well as boresight measurements, and equipment is provided which makes possible detailed study of the characteristics of the range itself.

Operation of the range is conducted from the centralized console shown in Figure 5.1. Major items of equipment are identified, indicating the degree of control provided. Most of the units shown are standard items of range instrumentation and are not discussed in detail. The positioning system and other special items are described in the following paragraphs. Plans are currently being considered for incorporating the additional equipment necessary to extend the full capability of the range for operation through X-band.

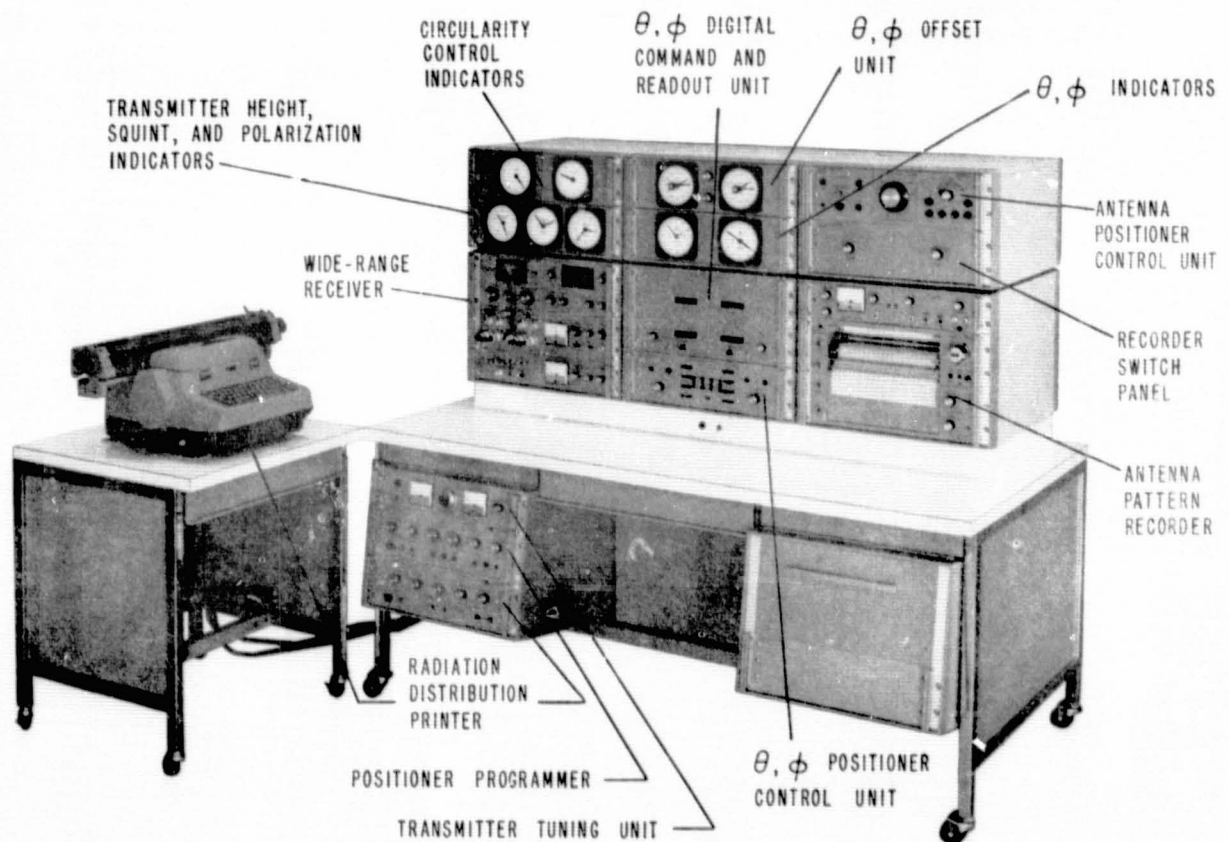


Figure 5.1. Range Operating Console. A polar recorder not shown is mounted on a removable wing normally located at the right of the console.



## 5.1 Spacecraft Mockup

The spacecraft mockup is a full-scale RF model of the Gemini Spacecraft in which the major details forward of the rear mounting structure are retained.\* Windows and large protuberances are included, but minor details, such as skin corrugations, are omitted. A semi-monocoque design was chosen to provide high mechanical integrity. The inner skin, which provides nearly all of the structural strength, is thermally insulated from the outer skin, which serves to electrically simulate the skin of the actual spacecraft. To reduce structural deformations from stresses caused by non-uniform solar heating, the interior of the mockup is cooled by air supplied from the air-conditioned control building.

## 5.2 Positioning and Indicating Equipment

The accuracy requirements of the Gemini rendezvous radar plus the weight and size of the spacecraft mockup dictated that the positioner for supporting the mockup have unusual positioning capabilities and accuracies. This equipment, the coordinate system which is employed in the boresight problem, and the method of optically aligning the positioner and radar in the coordinate system are described in the following paragraphs.

### 5.2.1 Coordinate System

The coordinate system shown in Figure 5.2 relates the spacecraft coordinates (roll, pitch, and yaw), radar coordinates, and positioner axes to the location of the source

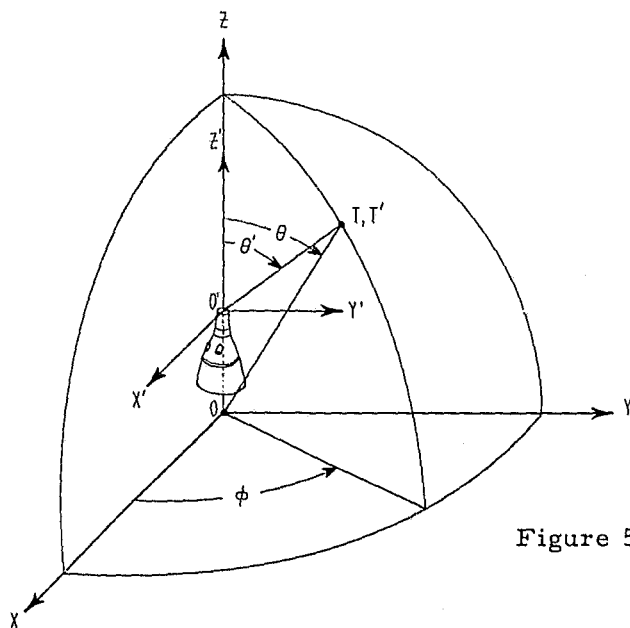


Figure 5.2. Spherical Coordinate System

\*The spacecraft mockup was designed by McDonnell Aircraft Corporation and fabricated by the 6549th Maintenance Squadron, Patrick Air Force Base, Florida.

of radiation in a composite coordinate system. This system is in agreement with standards established by the Inter Range Instrumentation Group (IRIG) for testing space-vehicle antennas.<sup>11</sup> The spacecraft mockup is fixed with respect to the XYZ coordinate system, and the source of radiation, defined by the point T', moves over the surface of the sphere.\*

The primed coordinate system is fixed relative to the radar; the X'Y' plane is located coincident with the phase centers of the radar antennas, assumed to be on the surface of the radar ground plane, and the Z' axis is adjusted coincident with the Z (roll) axis.

Figure 5.3 depicts the coordinate system as it is oriented in the test range, showing the relationship of the positioner axes to the spacecraft and radar coordinate system.

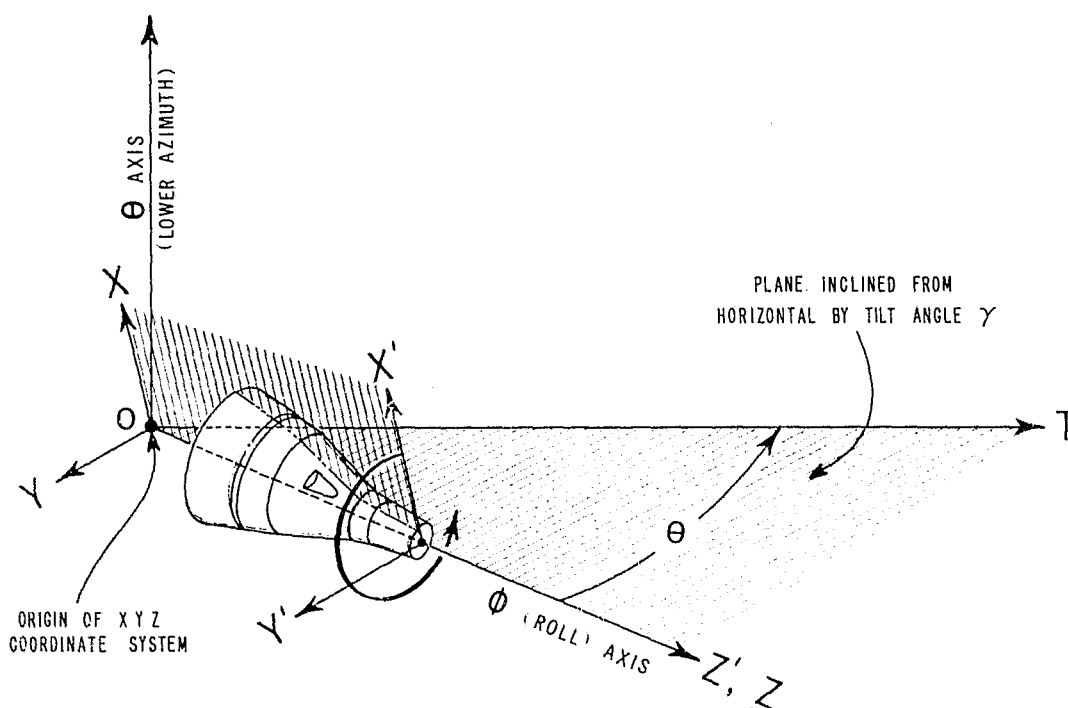


Figure 5.3. Spherical Coordinate System Shown in Relationship to Range Geometry. The spacecraft mockup is shown rotated clockwise in  $\theta$ .

Parallax between the angles  $\theta$  and  $\theta'$  exists because the spacecraft mockup is cantilevered over the edge of the control building to reduce reflections into the radar antennas from the control building and positioner. This parallax is accounted for in

<sup>11</sup>"IRIG Standard Coordinate System and Data Format for Antenna Patterns," IRIG Document No. 102-61.

\*Here, as in the usual antenna test range, the line OT' remains fixed relative to the earth. The coordinate system moves relative to the space-fixed line OT'.

computation of tables of the radar digital readout as a function of the  $\theta, \phi$  orientation of the mockup.\*

### 5.2.2 Positioner

The multi-axis positioner shown in Figure 5.4 supports and orients the full-scale Gemini mockup. The positioner, which is used here in the same manner that a conventional model tower is used for supporting antenna models, is an azimuth-over-elevation-over-azimuth antenna positioner. The upper-azimuth axis is the  $\phi$  (roll) axis, and the lower-azimuth axis is the  $\theta$  axis. The elevation axis enables the  $\phi$  and  $\theta$  axes to be adjusted orthogonal, and permits the spacecraft mockup to be mounted in a vertical position for ease of installation.

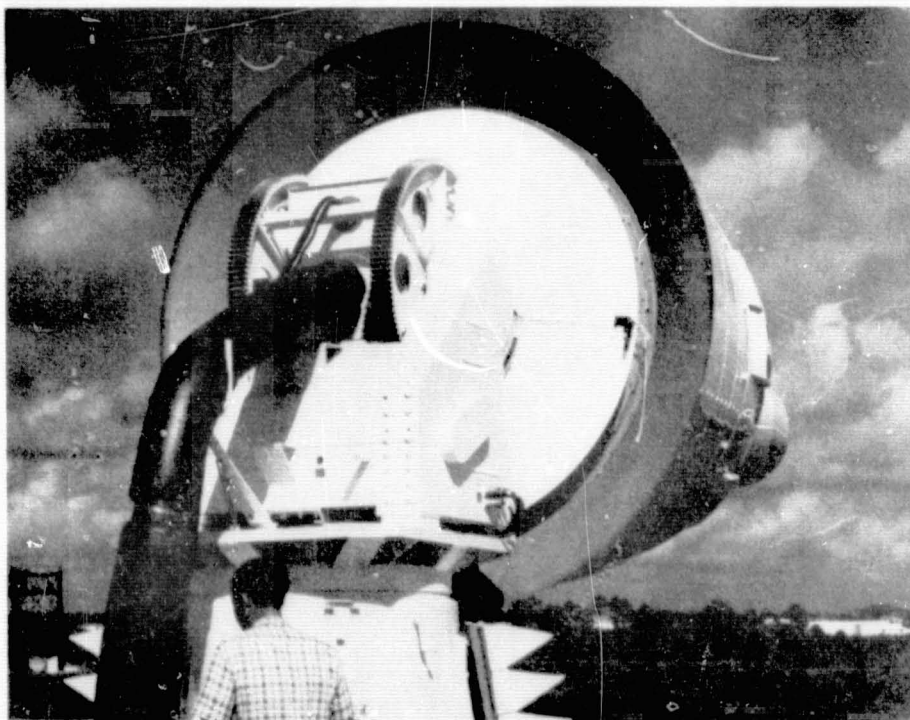


Figure 5.4. Rear View of Spacecraft Mockup and Multi-Axis Positioner

In testing the Gemini radar, static measurements\*\* are made in which the spacecraft mockup is oriented to successive positions, which are indicated to an accuracy of

---

\*An uncertainty in the parallax calculations is theoretically caused by lack of knowledge of the location of the phase centers of the radar antennas. A similar error would be introduced by the uncertainty in axial location of the phase center of the source antenna; however this source of error can be eliminated by squinting the antenna to direct its beam axis toward the radar antennas, and, in any event, both parallax errors are small.

\*\*A preliminary design study is being conducted to determine specifications for equipment modifications to permit dynamic accuracy measurements under conditions of controlled acceleration and velocity of the mockup.

0.01 degree, and the radar digital readout is compared with the calculated values. To facilitate making these measurements, the positioner is controlled by a high-performance two-channel servo system with independent operation of the  $\theta$  and  $\phi$  axes.

Two modes of operation of the servo system are provided, a rate mode and a position mode. In the rate mode of operation, the  $\theta$  and  $\phi$  axes of the positioner are driven at constant rates as set by individual rate controls. Antenna patterns may be recorded in the conventional manner in this mode. In the position mode of operation, the positioner is servo-driven to manually set angles of orientation. The  $\theta, \phi$  command angles and the digital readout of positioner orientation are displayed on direct-reading counters having a resolution of 0.002 degree. The high resolution of the positioning servo system makes it possible to position the spacecraft mockup smoothly to within a few thousandths of a degree.

In addition to the manual control capabilities, the positioner can be program-controlled to automatically generate a series of  $\phi$  cuts for examining the characteristics of an antenna over the sphere of radiation.

### 5.2.3 Alignment of Coordinate Systems

The  $Z$  and  $Z'$  axes\* are brought to within 0.1 milliradian of coincidence by means of a precision clinometer. The coordinate system is defined to measure  $\theta$  from the  $Z$  axis to the line  $OT$ . The line  $OT$  is defined as the line joining the origin  $O$  with a surveyed point  $T$  on the range surface directly beneath the center of the source antenna. The  $\theta$ -readout counter is set to zero when the  $Z$ -axis is aligned with  $OT$ . Alignment of the  $Z$ -axis and the line  $OT$  is accomplished by the optical reflection technique illustrated in Figure 5.5. The line  $OT$  is referred to as the optical boresight.

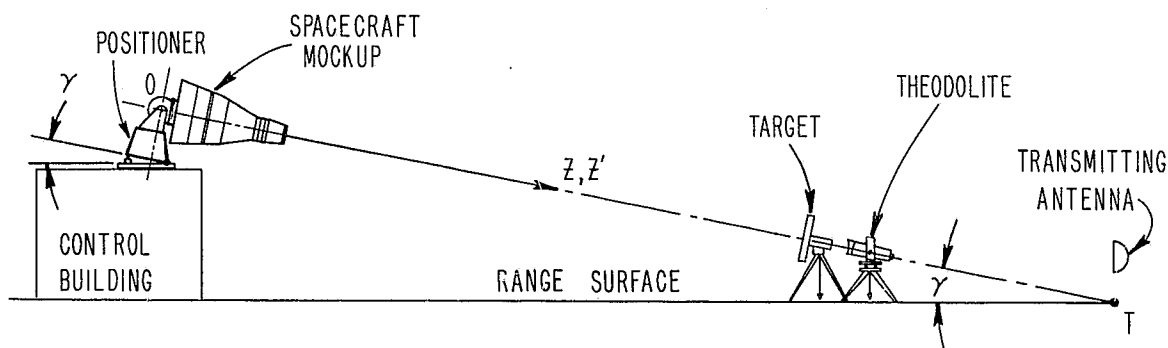


Figure 5.5. Illustration of the Optical Reflection Technique for Aligning the  $Z$  and  $Z'$  Axes with the Line  $OT$

\*The  $Z'$  axis is defined by a line passing through a reference point on the radar ground plane and normal to a plane which is defined by three flats on the ground plane.

In this procedure, an optically flat 4-inch diameter mirror is mounted on a fixture in front of the radar with the surface of the mirror parallel to the surface of the radar ground plane. A theodolite and target are located at surveyed bench marks such that the optical axis of these instruments is aligned with  $OT'$ . The distance from the origin  $O$  to the target is approximately 858 feet; this distance places the target and theodolite at a convenient eye level.

The positioner is oriented to center the target in the mirror, and the spacecraft mockup is then rolled to detect any misalignment of the  $Z$  and  $Z'$  axes. If required, the positioner can be reoriented slightly so that the center of the target rotates about the center of the mirror as the mockup is rolled. This procedure precisely aligns the  $Z$  axis with the line  $OT$ .

The direction to the source of radiation is defined by the line  $OT'$ . It is necessary to bring  $OT$  and  $OT'$  into coincidence, since  $T'$  is not necessarily located on the range surface but at a height  $h$ , approximated by equation (9). Because of extraneous reflections and other measurement errors, the location of  $T'$  cannot be determined as a unique point, but as the center of a small region of uncertainty. The direction  $OT'$  is measured by the interferometer procedure\* using the interferometer which has a resolution of about 0.1 milliradian, or the radar, which has a resolution of approximately 0.8 milliradian. The line  $OT'$  thus defined is aligned with  $OT$  either by moving  $OT'$  into coincidence with  $OT$  or by moving the  $Z$  axis into coincidence with  $OT'$  with the 0 readout counters set to zero.  $OT$  can be changed by varying the elevation squint angle of the transmitting antenna; the  $Z$  axis can be changed by tilting the positioner with the mechanism provided for this purpose.

It is planned to supplement the optical boresight alignment system with one in which a television camera with a telescopic lens is mounted in the front of the spacecraft mockup and aligned optically with the surveyed point  $T$ , using the previously described optical boresight procedure to establish an accurate reference. This system will provide a convenient monitoring capability for frequent checks of the boresight reference.

### 5.3 Transmitting Equipment

The transmitting equipment furnished for the radar boresight range includes signal sources, antennas, and associated equipment, antenna positioning equipment, and equipment for making polarization adjustments. All of the transmitting equipment is controlled remotely from the operating console.

The wooden source tower shown in Figure 1.1 was designed to permit antenna impedance, radio interference, and Gemini and Agena RF compatibility measurements to be made. The antenna positioner, shown in Figure 5.6, is raised by means of a hoist

---

\*See paragraph 6.3.

controlled from the operating console to the proper height for ground-reflection range operation, or to the top of the tower for operation of the range as an elevated range. The antenna positioner provides for  $\pm 4.5$  degrees of azimuth and elevation motion of the transmitting antenna and for rotation about the axis of the antenna.

The circularity of the received field is adjusted remotely by varying the relative amplitude and phase of the orthogonal components of the transmitted field.

This capability makes it convenient to obtain polarization data on the range characteristics or the system under test. For example, the circularity of the received field can be changed to determine the sensitivity of the rendezvous radar to polarization changes.



Figure 5.6. Transmitting Antenna, Positioner, and Hoist Viewed Looking Toward the Control Building



#### 5.4 Receiving and Recording Equipment

Antenna-range receiving and recording instruments include a 20-Mc to 100-Gc wide-range receiver, rectangular- and polar-coordinate antenna pattern recorders, and a radiation distribution printer.\*

Field probes are provided for sampling the incident RF field in front of the spacecraft mockup. The aperture field probe is shown in Figure 5.7; the horn antenna is mounted on a small remotely controlled carriage. With this device mounted on the front of the spacecraft mockup, the field amplitude distribution can be determined over a 16-foot diameter aperture.

Figure 5.7. Aperture Field Probe with Horn Antenna Mounted on Carriage

\*An instrument for numerically recording the relative antenna gain in decibels as sampled at discrete angular increments in  $\theta$  and  $\phi$ . See L. Clayton and J. S. Hollis, Polarization Analysis by Measurement of Multiple Components, 13th Annual Symposium, USAF Antenna Research and Development Program; October 14-18, 1963.

The polarization probe is shown in Figure 5.8 mounted on the front section of the spacecraft mockup. The polarization positioner can be mounted on the aperture field probe as shown in Figure 5.9 to permit measurements of polarization over the test aperture.

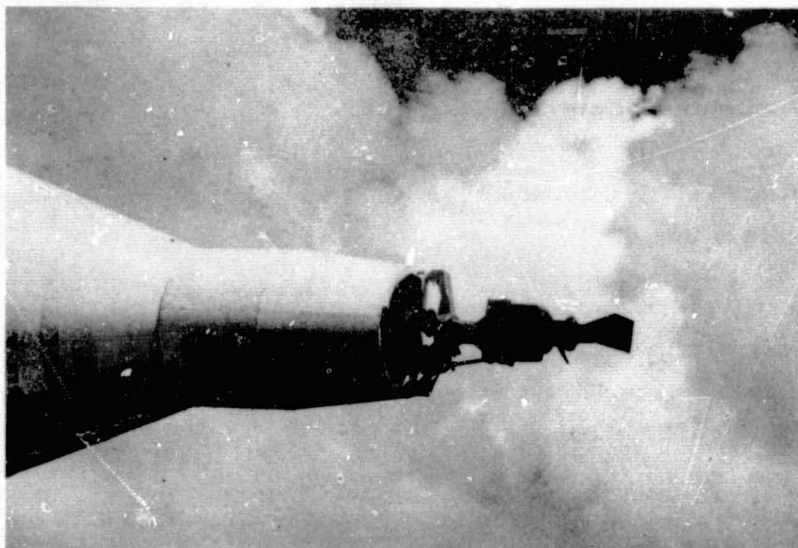


Figure 5.8. Polarization Probe Mounted on Spacecraft Mockup.  
The rendezvous radar is not shown in this photo.

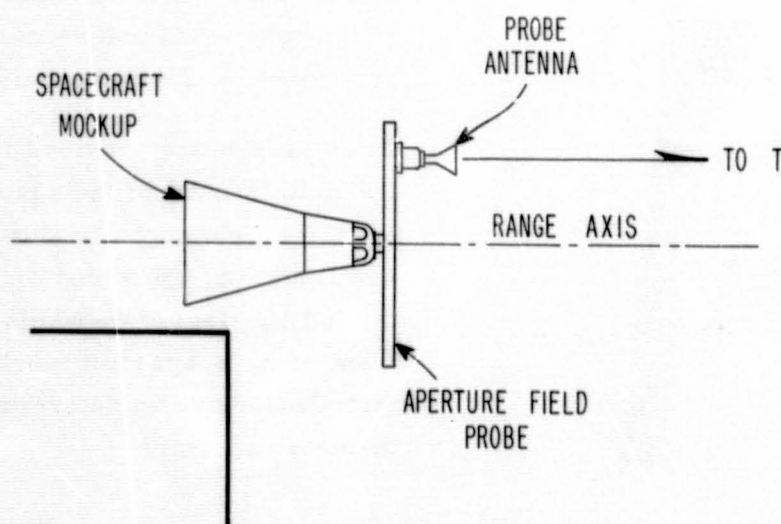


Figure 5.9. Illustration of the Use of the Polarization Probe  
to Obtain Polarization Patterns as a Function of  
Position in Test Aperture

## 6. MEASUREMENTS

### 6.1 Introduction

A field trip was made to validate the range in the ground-reflection mode for making acceptance measurements of the rendezvous radar boresight accuracy. To determine the performance of the range measurements were made (1) of the amplitude and polarization of the incident field over the test aperture, and (2) of the specific capability of the range for making boresight measurements. Samples of the data are presented in the following paragraphs.

While indicative of the performance of the range at L-band, the measurements are in no sense comprehensive and, in fact, raise many questions concerning the detailed mechanism of the range operation which are worthy of investigation and for which the instrumentation is already provided. Because the measurements to determine the boresight capability of the range are somewhat unusual, the procedure used in making the measurements is described in some detail.

### 6.2 Aperture-Field Measurements

#### 6.2.1 Amplitude

Field patterns were recorded over a 16-foot diameter aperture in front of the spacecraft mockup employing the aperture probe shown in Figure 5.7. The probe was mounted to the front of the mockup and parallel with the pitch axis. Measurements were made with the mockup oriented at zero degrees in  $\theta$ ; the mockup was rolled to successive  $\phi$  angles, and the field was explored by moving the sampling antenna radially across the center of the aperture.

A linearly polarized horn antenna with a gain of about 15 decibels and with 30-degree beamwidths was mounted to the probe carriage. The purpose of using a relatively high-directivity antenna was to minimize the effect of reflections from the probe-support structure and spacecraft mockup to give a measure of the incident field. The relative position of the horn on the carriage was adjusted for each  $\phi$  angle to obtain patterns of the vertical and horizontal polarization components as a function of radial distance from the roll axis. Aperture field patterns are given in Figure 6.1.

Figures 6.1(a) and 6.1(b) are patterns of the vertical and horizontal polarization components as a function of vertical position in the aperture. From equation (8), the calculated height  $h_1$  of the transmitting antenna which produces an interference maximum at the center of the receiving aperture is 5.75 feet. The corresponding



height of the transmitting antenna was determined experimentally to be approximately 5.1 feet. For these patterns the elevation squint angle of the transmitting antenna was  $-0.5$  degree (down). It was found that the height of the interference maximum does not vary appreciably with small changes in elevation squint angle, indicating that the phase of the far-zone pattern of the transmitting antenna is relatively constant with elevation angle. Additional measurements are required to explain the difference between the height  $h_1$  calculated by the simplified theory leading to equation (8) and that determined experimentally.

It is seen that the peak of the interference pattern for the horizontal component is approximately 1 foot lower than that of the vertical component. The height of the transmitting antenna could be readjusted for a best compromise for the two polarizations, although from a practical viewpoint this is a finer adjustment than is likely to be necessary.

The shapes of the vertical patterns are in virtual agreement with those predicted by equation (6) and Figure 4.2. The vertical taper of the field is approximately 0.25 decibel in 10 feet, which is the maximum diameter of the spacecraft. Because of the small difference in the height of the horizontal and vertical polarization maxima, the total vertical taper is approximately 0.35 decibel.

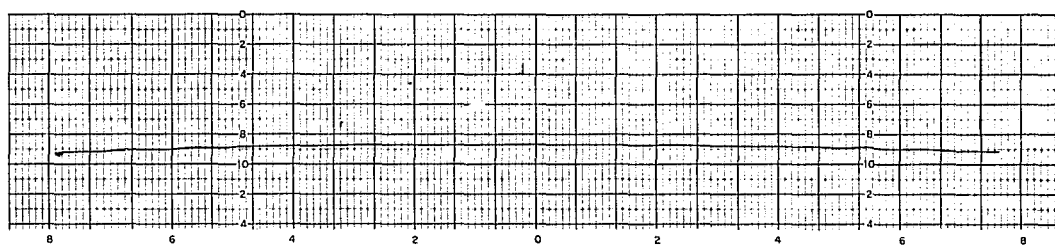
Figures 6.1(c) and 6.1(d) are patterns of the vertical and horizontal polarization components as a function of horizontal position in the aperture. The amplitude taper in the horizontal plane is a function of the beamwidth of the transmitting antenna. The horizontal dimension of the aperture represented by the mockup is 10 feet when the mockup is oriented to zero degrees in  $\theta$  and increases to approximately 19 feet as the mockup is positioned to the specified limits in  $\theta$ . Under these conditions the transmitting antenna beamwidth is sufficient to provide an illumination taper of less than about 0.25 decibel.

The vertical and horizontal field patterns provide an indication of the proper adjustment of the height and squint angles of the transmitting antenna, and confirm that the range operates in general accordance with the theory discussed in Section 4. The smoothness of the patterns indicates virtual freedom of interference from objects which are within the directivity pattern of the probe horn. The high degree of suppression of extraneous reflections required for the boresight measurement problem dictates a measurement technique of greater sensitivity and accuracy, as discussed in paragraph 6.3, to determine the range capabilities for this application.

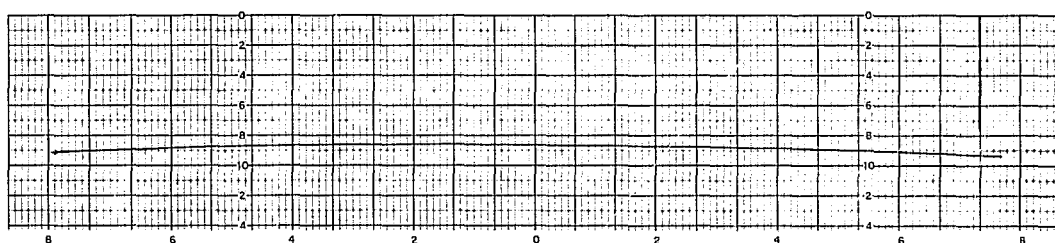
#### 6.2.2 Polarization

Polarization patterns of the incident field were made with the polarization prob. shown in Figure 5.8. The linearly polarized probe antenna shown in this photograph

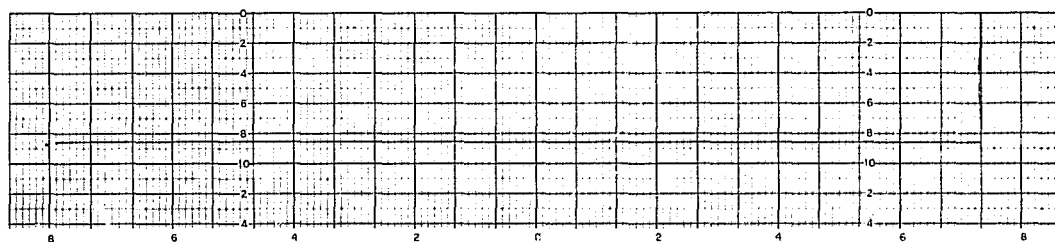
RELATIVE POWER (DECIBELS)



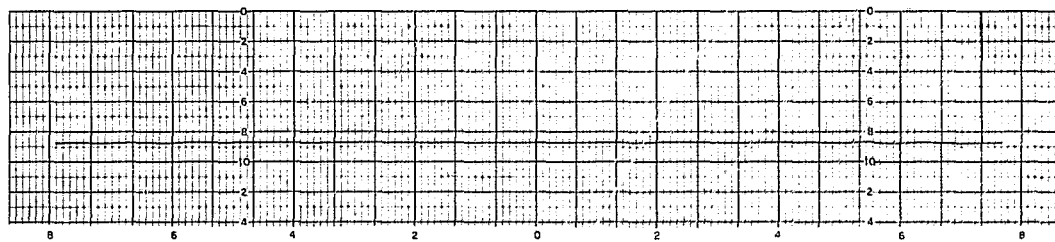
(a) Vertical Pattern, Vertical Polarization



(b) Vertical Pattern, Horizontal Polarization



(c) Horizontal Pattern, Vertical Polarization



(d) Horizontal Pattern, Horizontal Polarization

DISTANCE FROM CENTER OF TEST APERTURE (FEET)  
(DOWN, LEFT) (UP, RIGHT)

Figure 6.1. Aperture Field Patterns

was employed for these measurements. The circularity of the incident field at the center of the test aperture was adjusted from the operating console by varying the relative amplitude and phase of the vertical and horizontal field components of the source antenna. This adjustment capability permits compensation for the difference in reflection coefficient of the range surface for the horizontal and vertical field components and permits measurements to be made of the sensitivity of the measured boresight direction to the polarization of the incident field. The polarization pattern shown in Figure 6.2 illustrates that the axial ratio can be adjusted to less than 0.1 decibel at a given position in the test aperture.

Figures 6.3 and 6.4 indicate the range of adjustment provided by the circularity control unit. Figure 6.3 is a family of polarization patterns with relative amplitude as a parameter. The relative phase between the orthogonal components is approximately 90 degrees.

Figures 6.4(a) and 6.4(b) are polarization patterns recorded as a function of the relative phase angle between orthogonal field components. Figure 6.4(a) is recorded in decibels; Figure 6.4(b) is a linear voltage recording for approximately the same phase variations.

The circularity control unit may be employed to obtain precise linear polarization of the incident field after insertion of a fixed phase delay to increase the range of adjustment. The patterns of Figure 6.4 degenerate into the linearly polarized patterns shown in Figure 6.5 with a tilt angle of 45 degrees as the relative phase goes to zero. The linear-voltage pattern of Figure 6.5(b) has the predicted classic shape of two tangent circles. The tilt angle of the incident field can be set by rolling the transmitting antenna about the axis of the beam.

The axial ratio of the incident field at the center of the test aperture as a function of frequency is given in the graph of Figure 6.6. The change in axial ratio is probably caused by amplitude and phase changes in the circularity control circuits of the transmitting antenna. The change is negligible over the operating range of the Gemini rendezvous radar.

Polarization patterns as a function of position in the receiving aperture were recorded by mounting the polarization probe on the aperture field probe as illustrated in Figure 5.9. Axial ratio as a function of vertical and horizontal position in the aperture is given in Figure 6.7. These patterns were recorded after adjustment of the circularity at the center of the test aperture and without changing the transmitting antenna squint angles.

The variation in axial ratio with horizontal position in the test aperture is largely caused by the off-axis depolarization characteristics inherent in the paraboloidal

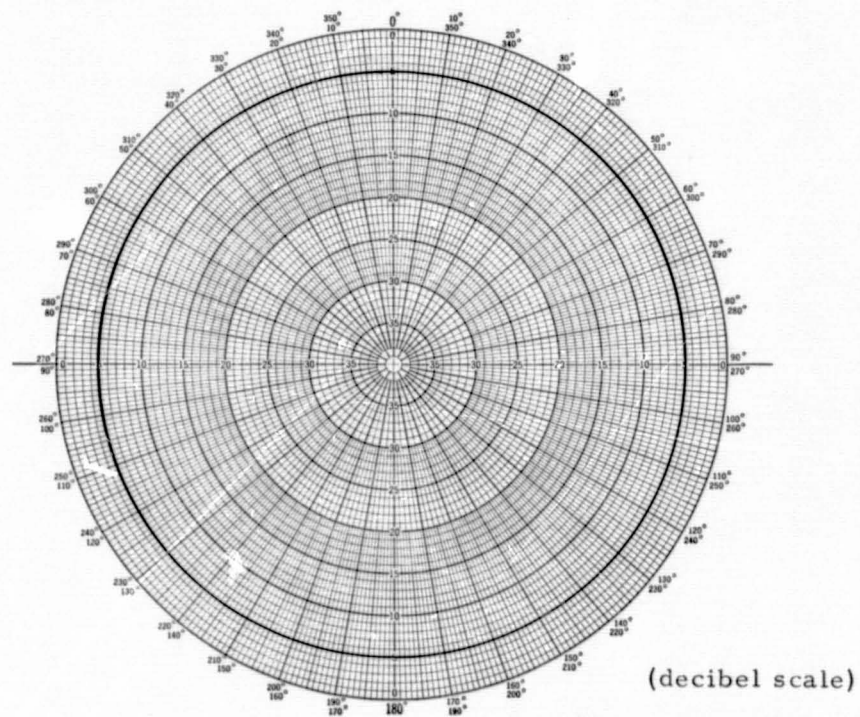


Figure 6.2. Polarization Pattern Measured at Center of Test Aperture

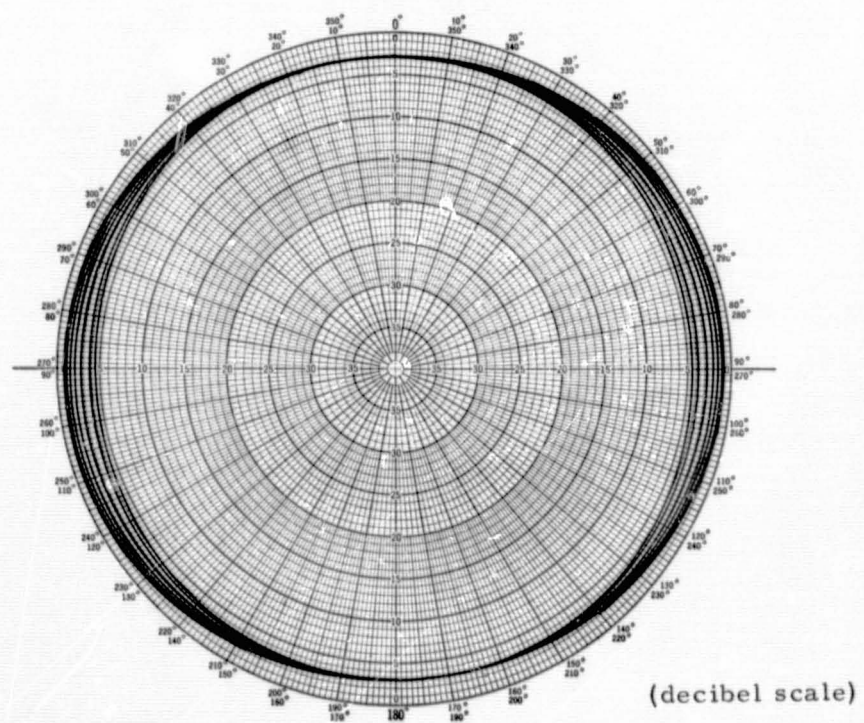
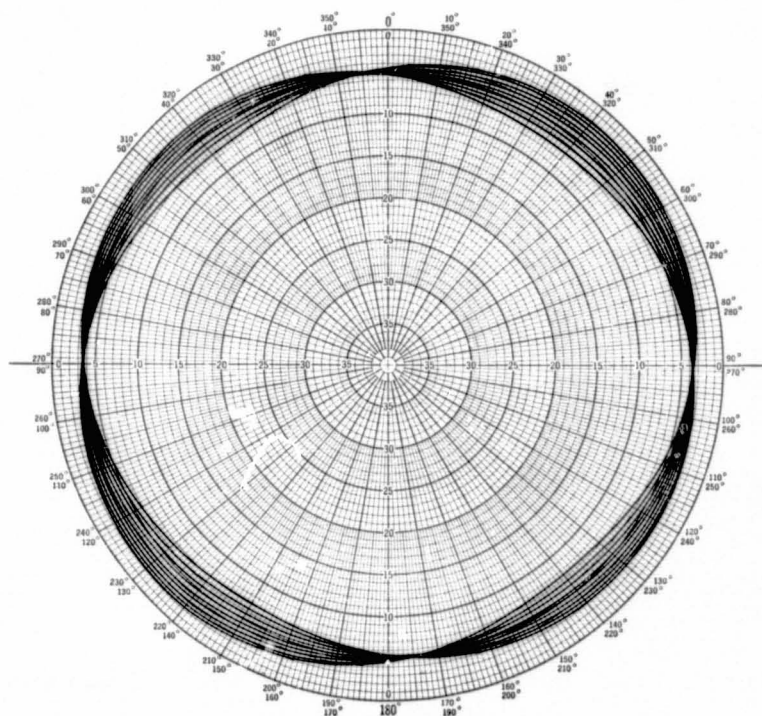
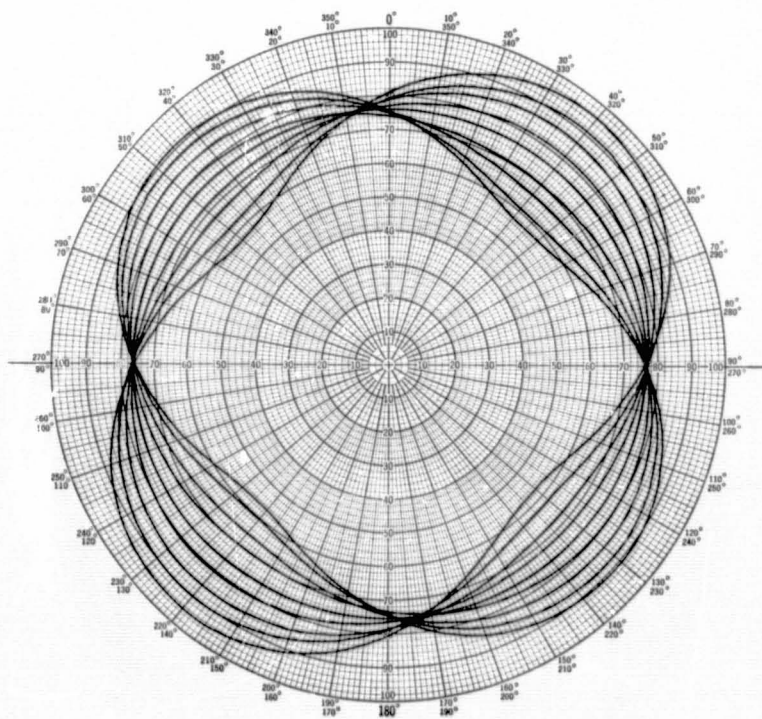


Figure 6.3. Family of Polarization Patterns as a Function of Relative Amplitude of Orthogonal Field Components

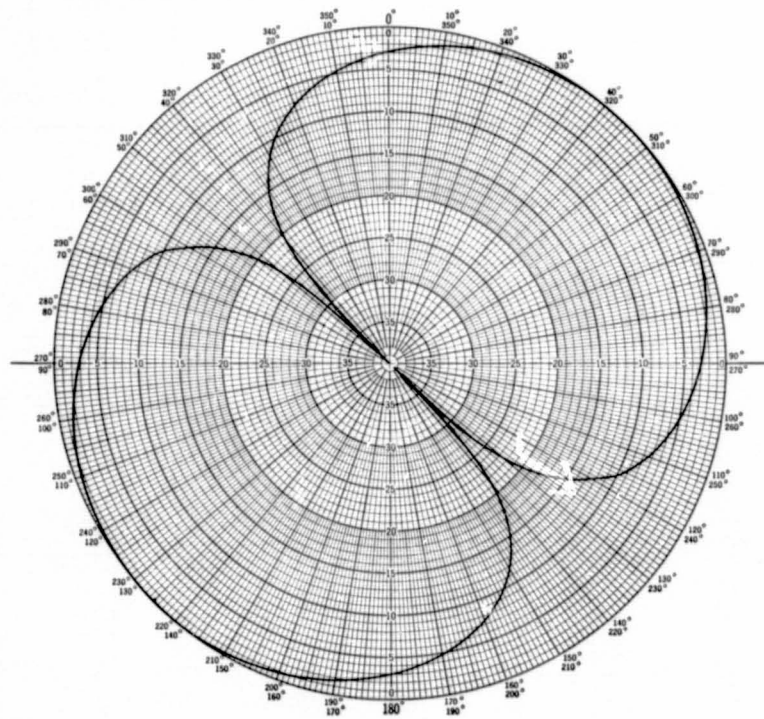


(a) Decibel Scale

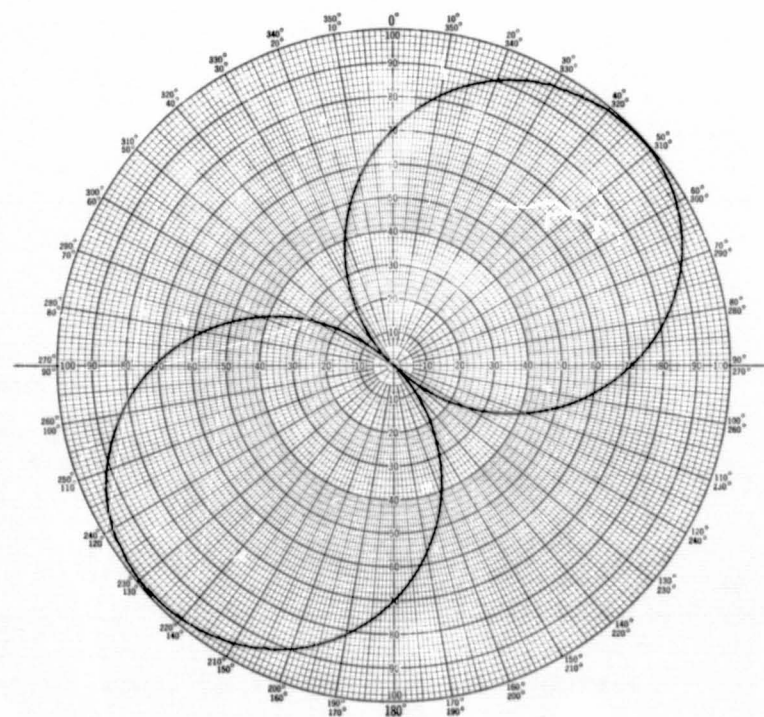


(b) Linear-Voltage Scale

**Figure 6.4. Family of Polarization Patterns as a Function of Relative Phase Between Orthogonal Field Components**



(a) Decibel Scale



(b) Linear-Voltage Scale

Figure 6.5. Polarization Pattern of Linearly Polarized Field

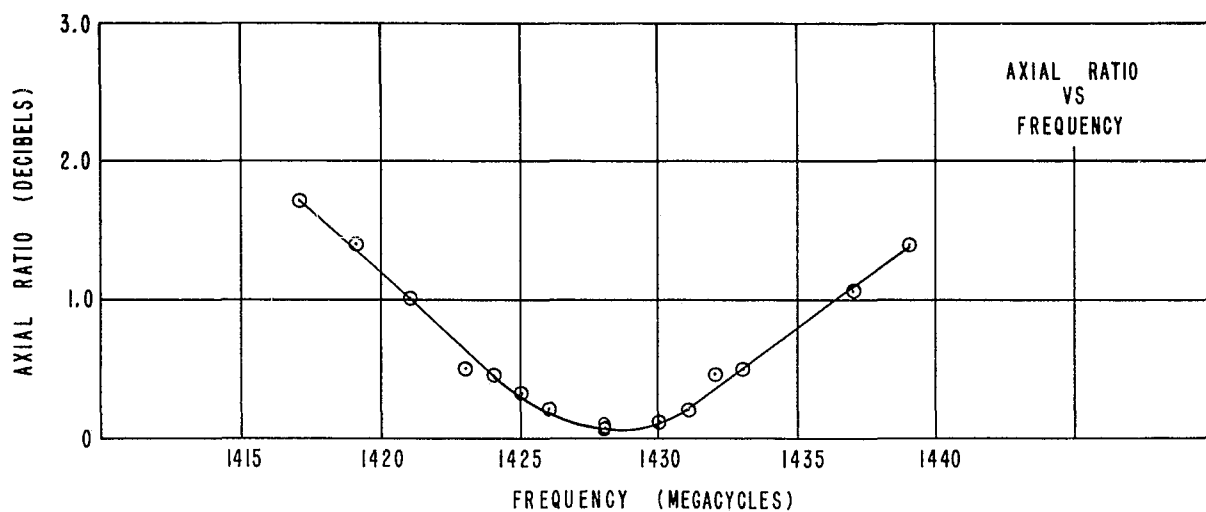


Figure 6.6. Axial Ratio at Center of Test Aperture as a Function of Frequency

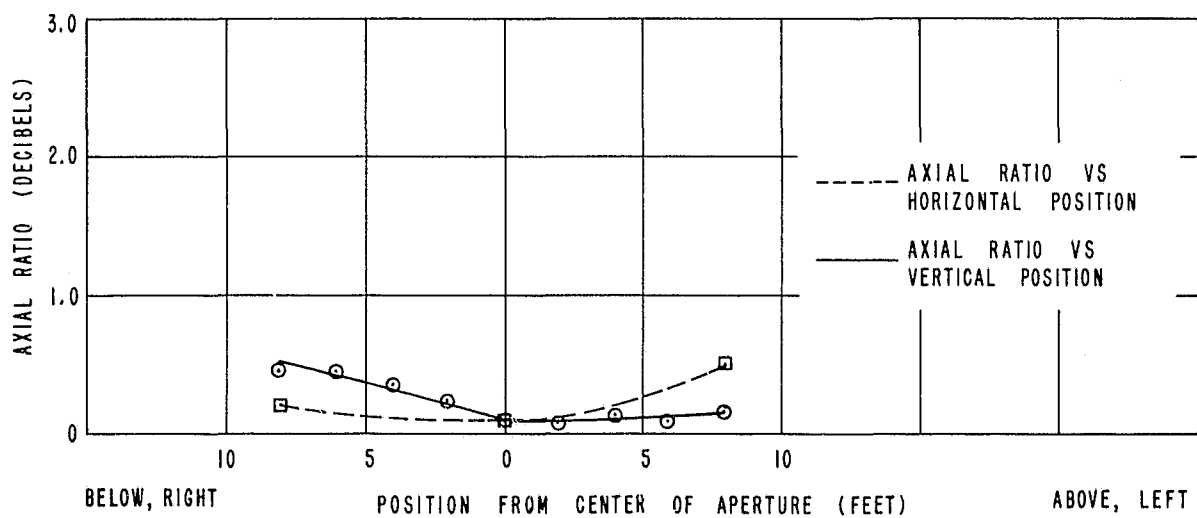


Figure 6.7. Axial Ratio as a Function of Position in the Test Aperture



transmitting antenna. A less directive transmitting antenna would result in both a smaller variation in axial ratio and a smaller taper of the field amplitude with horizontal position, but would increase the susceptibility to extraneous reflections. The directivity employed appears to be a reasonable compromise.

### 6.3 Boresight Measurements

#### 6.3.1 Discussion of the Measurement Problem

To determine the boresight measurement capability of the range, it is necessary to measure the direction of arrival and purity of the phase front of the incident field. The measurements must be made either with a device that does not perturb the incident field or with a measuring technique that is not affected by reflections from the test device. Furthermore, these measurements must be made under conditions that simulate the specific boresight measurement problem. High-directivity antennas cannot be employed in the measuring device because their directivity would discriminate against wide-angle reflections to which the radar is sensitive.

Direct measurement of incident-field phase over the aperture to the required accuracy was considered impractical because of probe-structure reflections and mechanical limitations. It was decided to employ an interferometer with radiation characteristics similar to those of the radar to determine the direction to the apparent source in a manner that cancels errors caused by reflection of energy from the probe-support structure. The spacecraft mockup was employed to support the interferometer so that double-bounce reflections between the support structure and fixed objects would be taken into account, and so that the same degree of shielding of the test positioner which exists during radar boresight measurements would be provided.

#### 6.3.2 Principle of Operation of the Interferometer

The interferometer functions in the manner of the Gemini rendezvous radar to produce nulls in the two interferometer channels which are determined by

- (a) the angles of rotation of the azimuth and elevation spirals relative to the reference spiral,
- (b) the circuit phase delays of the azimuth and elevation channels, and
- (c) the direction to the source of radiation.

A block diagram of the interferometer is given in Figure 6.8. The ground plane and spiral antennas are identical with those of the Gemini rendezvous radar. Rotation of the azimuth and elevation antennas and control of the variable attenuators is



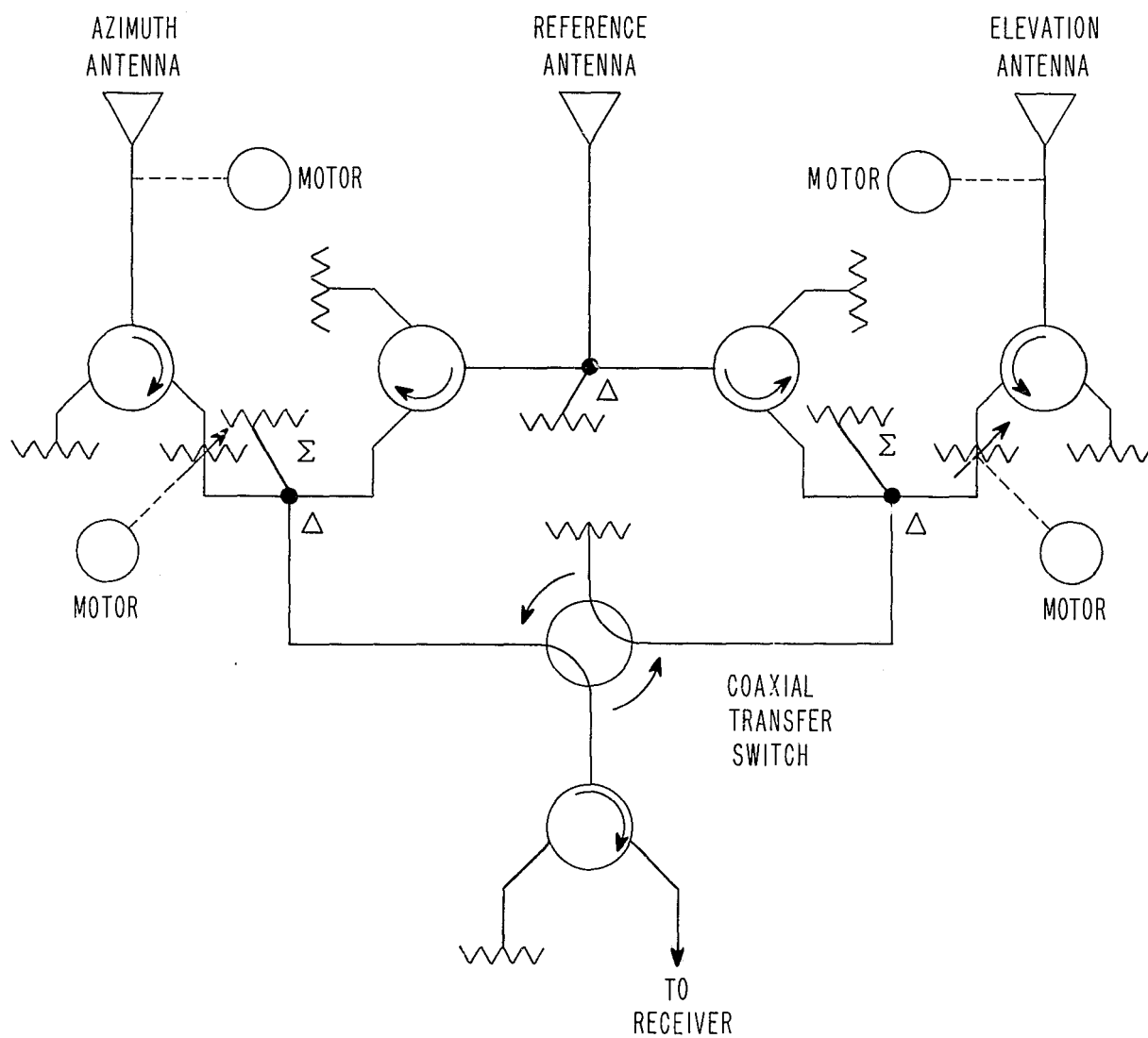


Figure 6.8. Block Diagram of Interferometer

effected from the operating console to obtain a null in each channel. Readout of the rotation of the spiral antennas is not provided; instead, the direction of arrival of the incident field is determined by the following procedure.

- (a) From Figures 5.3 and 6.9 it is seen that the line OT is identically located relative to the spacecraft under two sets of conditions:  
(1) with the spacecraft mockup rotated clockwise about the  $\theta$  axis to a position  $\theta, \phi$ , and (2) with the mockup rotated counterclockwise about the  $\theta$  axis and rolled 180 degrees in  $\phi$  to the same position  $\theta, \phi$ . The position in the latter case is identified by the underscored symbols  $\theta$ ,  $\phi$ .
- (b) The relationship of the line OT to the mockup is unchanged under the two conditions described in (a), but the mockup is inverted and changed in position relative to earth-fixed objects. The source of radiation T' is earth-fixed relative to T and therefore moves in the space-fixed coordinate system to the position T' as illustrated when the positioner is rotated to  $\theta$ ,  $\phi$ .
- (c) If T' is located at T, and if the interferometer is nulled with the mockup positioned to a given  $\theta, \phi$  orientation, a null will also exist when the mockup is rotated counterclockwise about the  $\theta$  axis to the identical  $\theta$ ,  $\phi$  orientation.
- (d) If T' is not coincident with T, the location of T' can be determined by nulling the interferometer at a given  $\theta, \phi$  orientation and, without changing the electrical adjustment, positioning the mockup to a direction  $\theta$ ,  $\phi$  which nulls both channels. This procedure moves T' to its original location T' in the space-fixed coordinate system. The location of T' relative to T can be calculated from the measured  $\theta, \phi$  and  $\theta$ ,  $\phi$  angles.

Reflections from the spacecraft mockup do not introduce measurement errors because the spacecraft illumination is identical for the two null conditions. In addition, the interferometer absolute accuracy is not a factor because the interferometer adjustment is unchanged during the course of a measurement.

The interferometer method described measures the direction of OT' but does not provide information concerning the distance OT'. The direction OT' is defined by the mirror symmetry of the incident field for the clockwise and counterclockwise  $\theta$  orientations. Discussions referring to the location of the apparent source are made on the assumption that the center of phase lies in the plane of the source antenna.

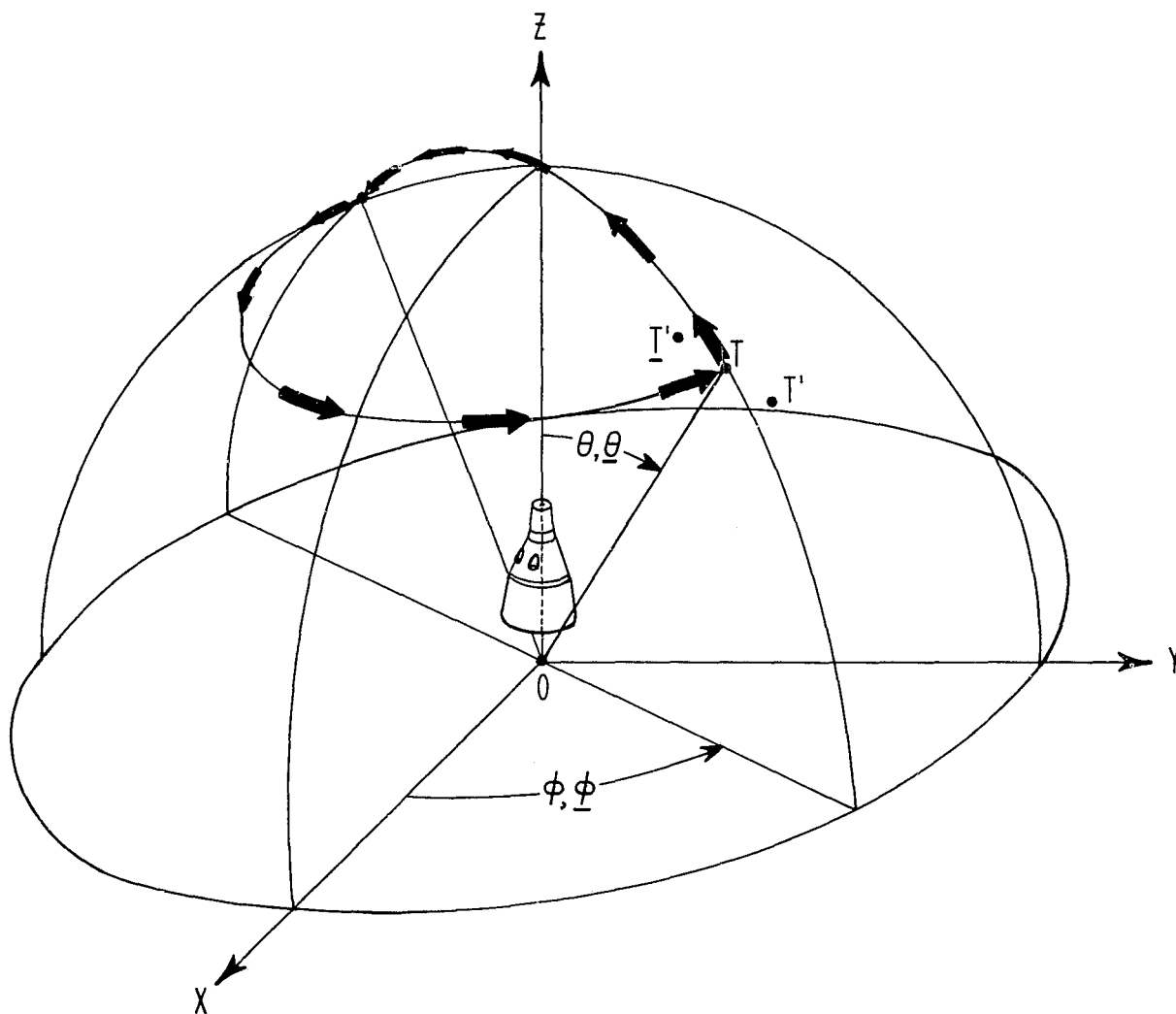


Figure 6. 9. Illustration of the Method Employed for Positioning the Spacecraft to Obtain Two Identical Orientations of the Spacecraft Relative to OT

### 6.3.3 Practical Considerations

The process of positioning the mockup to obtain nulls in both interferometer channels simultaneously as described in paragraph 6.3.2 is time-consuming. Therefore, the procedure illustrated by Figure 6.10 was employed in which the two interferometer channels are nulled independently. The spacecraft mockup is positioned about the roll axis to orient the antennas horizontally and vertically.

One interferometer channel is employed for azimuth measurements and the other for elevation measurements. The interferometer is nulled for the direction  $OT'$  for the clockwise orientation of the  $\theta$  axis as in paragraph 6.3.2. For the counter-clockwise orientation, azimuth nulls are obtained by rotation through  $\Delta\theta$ ; elevation nulls are obtained by rotation in elevation through  $\Delta E$  by means of the elevation axis of the positioner, indicated in Figure 6.10. It is seen that  $OT'$  is located relative to  $OT$  by azimuth and elevation angles  $(\Delta\theta)/2$  and  $(\Delta E \cos \theta)/2$ , respectively.

The effect of extraneous reflections from sources external to the spacecraft mockup is to cause scattering of the measured location of the apparent source as test conditions such as the position of the spacecraft are changed. The magnitude of the effect of extraneous reflections on the measured boresight direction is discussed in paragraph 3.1. It should be noted that the interferometer measurement method is sensitive to at least the following error sources in addition to errors from extraneous reflections:

- (a) spacecraft positioner and angle-readout errors,
- (b) coordinate system misalignment,
- (c) frequency drift,
- (d) amplitude and polarization variations of the incident field,
- (e) RF leakage into the interferometer circuits, and
- (f) interferometer changes caused by gravity.

The measurement procedure requires that the mockup be rolled 180 degrees in moving from  $\theta, \phi$  to  $\underline{\theta}, \underline{\phi}$ , and, therefore, the measurements are sensitive to effects of gravity. For example, loose cables behind the interferometer panel which can change in position as the mockup is rolled can cause large errors by introducing a different field perturbation for the two opposite orientations of the interferometer. Furthermore, the interferometer-measurement procedure provides a means for testing the radar for errors caused by rolling the mockup. It was found during range tests that an error of a few tenths of a milliradian was introduced by the deflection of shock mounts on which the interferometer was mounted.

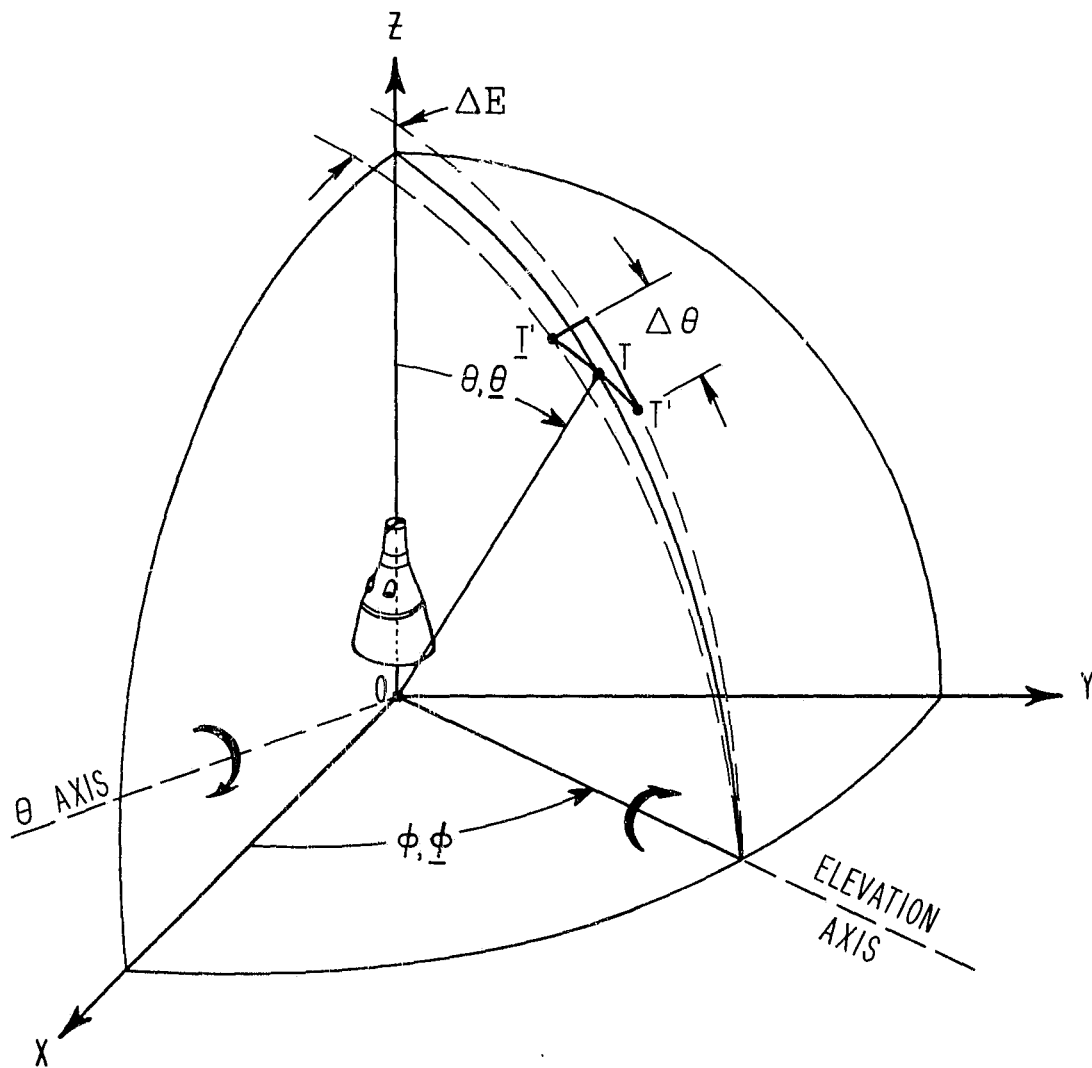


Figure 6.10. Illustration of the Method Employed for Positioning the Spacecraft Mockup to Make  $\underline{T'}$  Coincident with  $T'$

In making the measurements which are presented in the following paragraphs, it was necessary to exercise extreme care in each of the items listed above.

#### 6.3.4 Interferometer Test Results

Figure 6.11 is a scatter plot of the measured azimuth of the apparent source of radiation as a function of  $\theta$  over the range of 0 to 25 degrees. The data were taken over a period of several days and were made in conjunction with apparent-height measurements.

The measured data show a counterclockwise bias of about 0.35 milliradian and a total scatter of about 0.55 milliradian from the mean. The indicated bias is probably a result of an initial optical boresight error which occurred prior to refinement of the optical boresight procedure. The azimuth error appears to be independent of  $\theta$ .

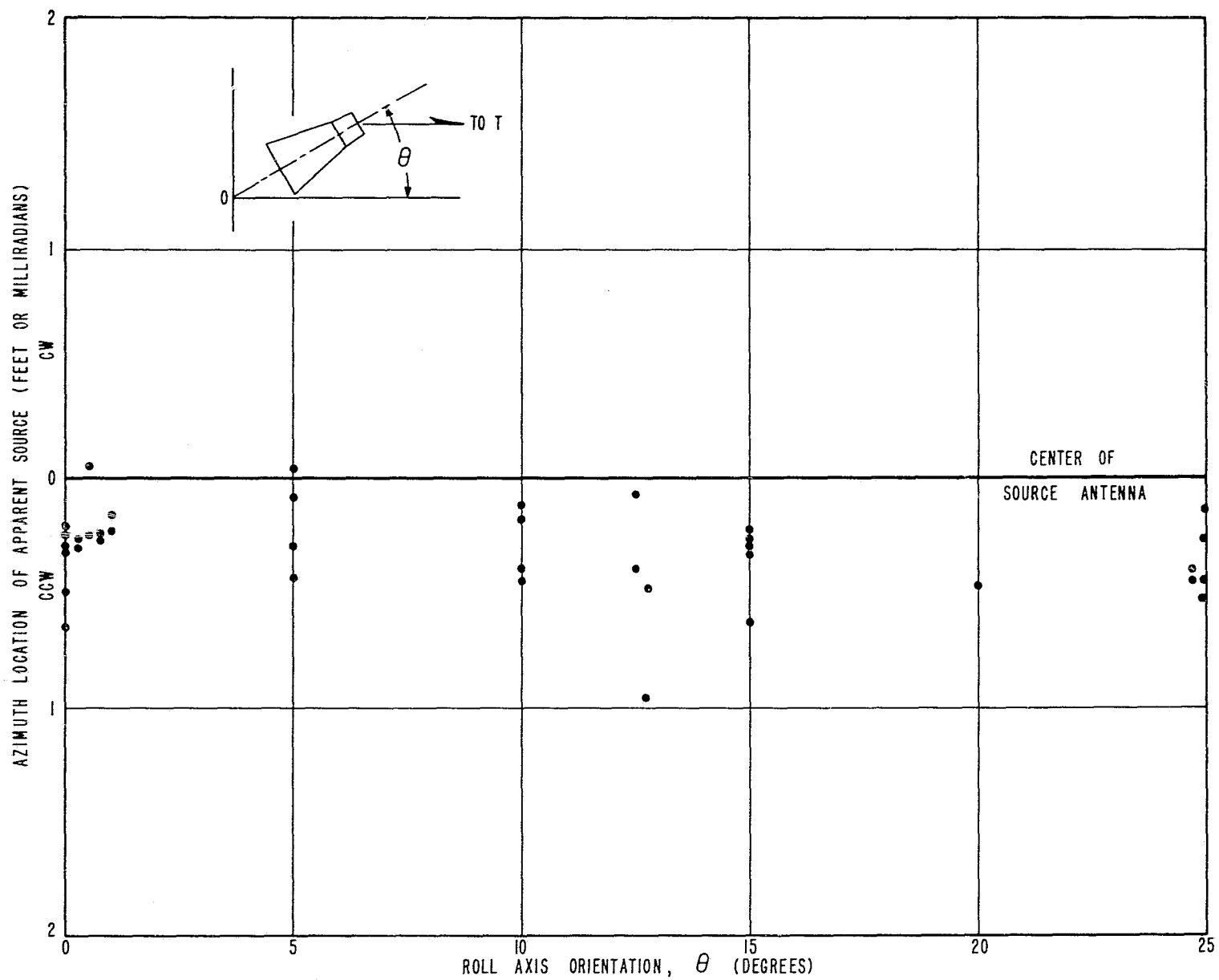
Figure 6.12 shows curves of the measured height of the apparent source as a function of  $\theta$  for an elevation squint angle of  $-0.5$  degree. The measurements were made under a number of different conditions and over a period of several days. After curve (1) was made the coordinate system alignment was checked and the optical boresight tests were repeated before taking the data represented by the remaining curves.

From the data presented, the mean elevation of the apparent source is 0.35 milliradian above the range surface and the maximum error from the mean is 1.17 milliradian. However, it is felt that curve (1) is not representative of the range capabilities because of misalignment errors and, excluding curve (1), the data indicate a mean elevation of 0.25 milliradian above the range surface and a maximum error of 0.55 milliradian from the mean.

The interferometer elevation channel was employed for curves (1) and (2) and the azimuth channel was employed for the remainder of the curves by rolling the spacecraft mockup 90 degrees in  $\phi$ .

For curves (5) and (6) the transmitting antenna was squinted in azimuth to direct the axis of the beam toward the interferometer. From these curves there appears to be a slight improvement from squinting the source antenna, although the effect was not noticed in the azimuth tests.

Figure 6.13 is a graph of the measured height of the apparent source as a function of the elevation squint angle of the source antenna. The dashed curve was calculated from equation (9) on the assumption of a  $(\sin x)/x$  radiation pattern with a 3-decibel elevation beamwidth of 5 degrees and unity reflection coefficient at the range surface. It is seen that the measured data are in general agreement with the calculated data.



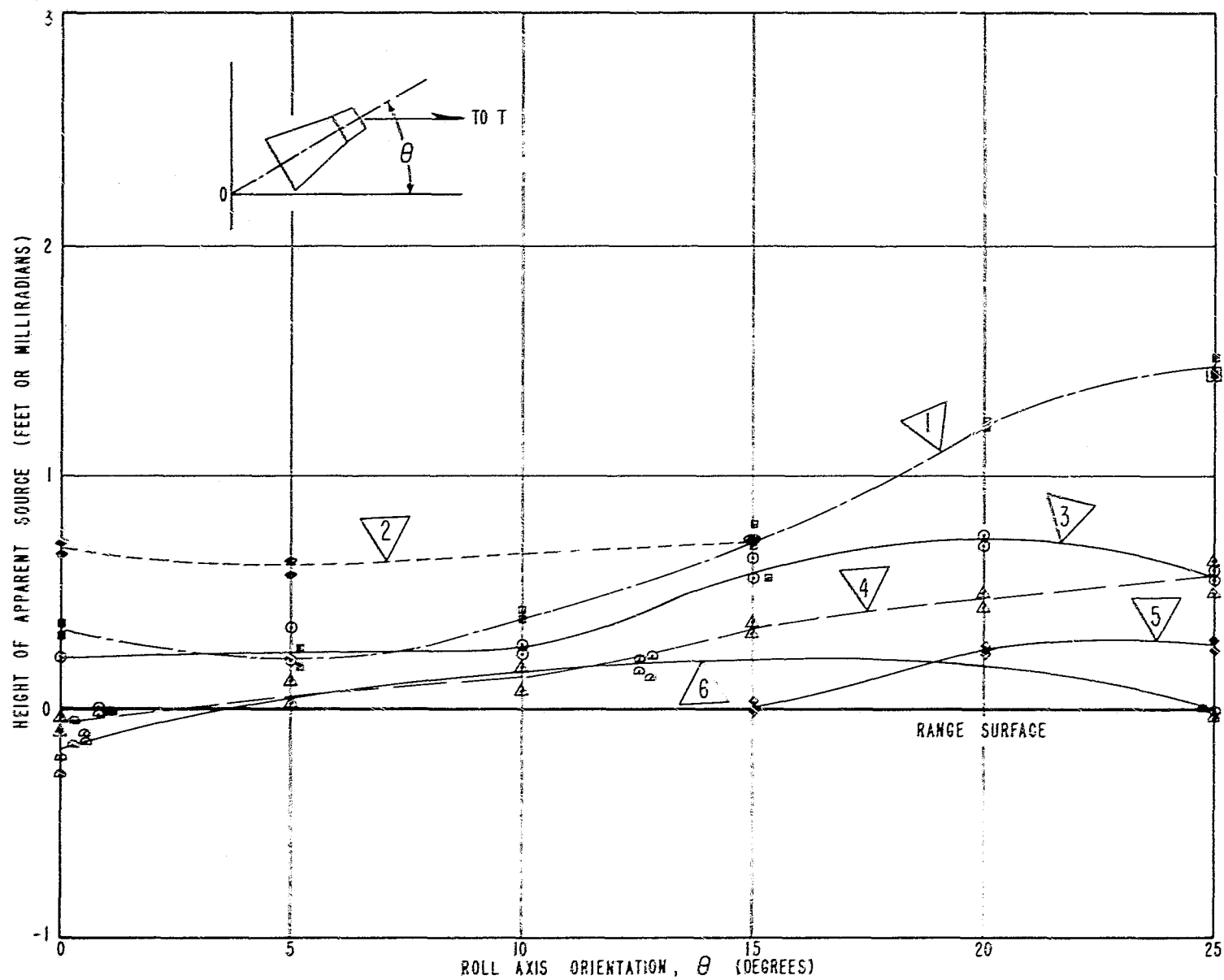


Figure 6.12. Measured Height of the Apparent Source Versus  $\theta$  at L-Band  
The transmitter elevation squint angle is  $-0.5$  degree.



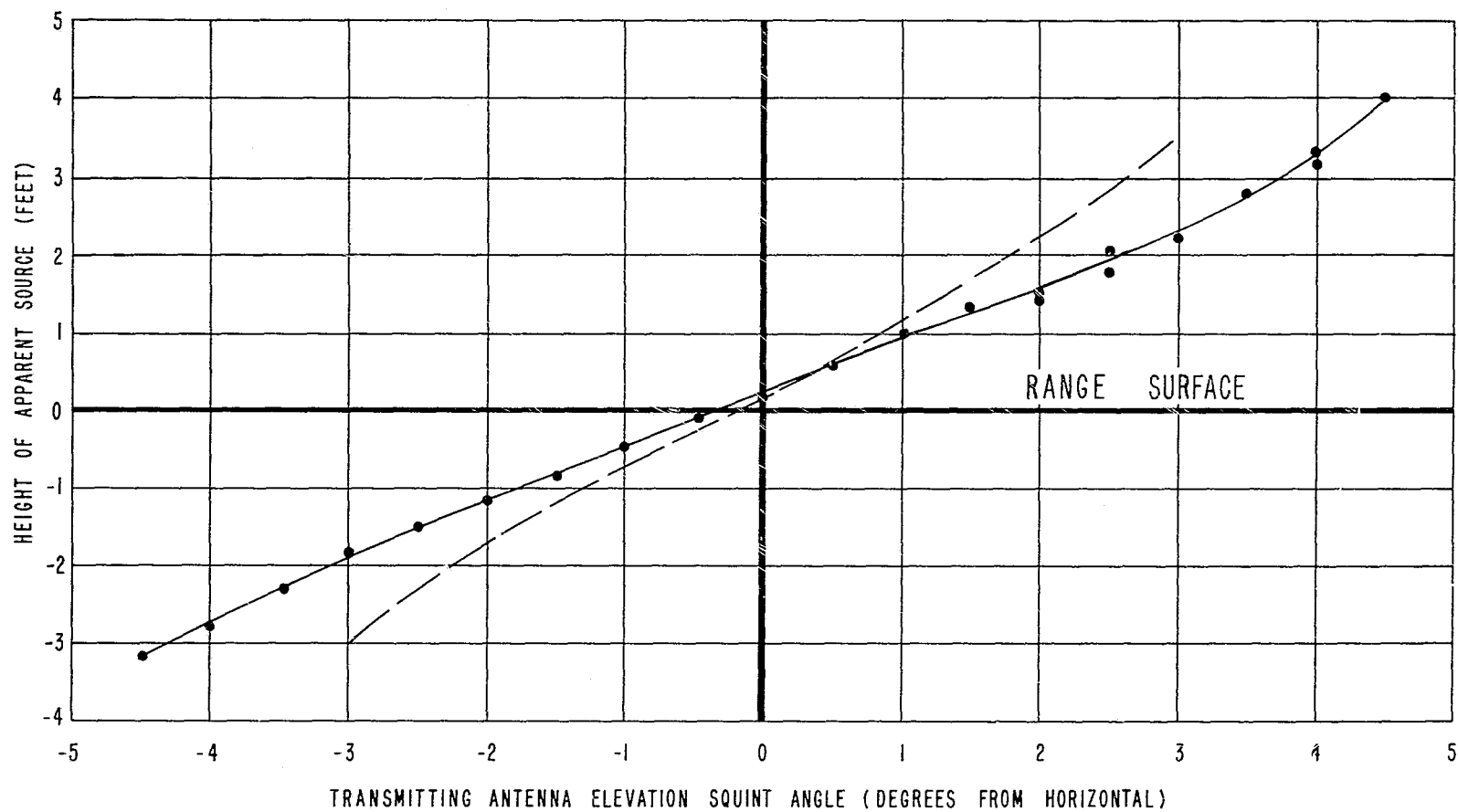


Figure 6.13. Height of Apparent Source as a Function of Transmitting Antenna Squint Angle. The dashed curve was calculated from equation (9).

Furthermore, the smoothness of the experimental curve indicates the high accuracy capability of the interferometer technique.

## 7. SUMMARY

Measurement of the Gemini radar boresight accuracy required development of a test range with suppression of extraneous signals on the order of 60 decibels, establishment of a circularly polarized incident field with low axial ratio and amplitude taper over the active aperture of the spacecraft mockup, and provision for precise positioning of the mockup. Careful design and construction of the ground-reflection range resulted in a low level of extraneous reflections. Aperture amplitude and polarization test probes provide an indication of the proper adjustment of the incident field. A precision multi-axis positioner, controlled by a high-performance servo system, supports and positions the spacecraft mockup with positioning and readout accuracies of 0.01 degree. The accuracy of the optical boresight technique developed for aligning the coordinate system is 0.1 milliradian.

A two-channel interferometer was employed in the L-band range-validation tests to measure the direction to the apparent source and the purity of the phase front by a method which is insensitive to reflections from the probe-support structure. Tests indicate that the measurement accuracy of the interferometer is a few tenths of a milliradian. The measured scatter in the location of the apparent source was within approximately 0.55 milliradian of the mean in azimuth and elevation. The height of the apparent source measured as a function of elevation squint angle of the transmitting antenna is in general agreement with that calculated on the basis of a point source and a plane reflecting surface.

In measurements made to date, the effect of moisture on the range surface has been found to be insignificant at L-band. It is anticipated that the range will be evaluated at higher frequencies, both as an elevated range and as a ground-reflection range, and at lower frequencies as a ground-reflection range.

Experience gained in the operation of the range for preliminary tests of the Gemini rendezvous radar confirms that the range meets the design objectives and has additional merit in the rapidity with which measurements can be made and in the flexibility provided for controlled experiments.

## ACKNOWLEDGEMENTS

The efforts of a number of people are gratefully acknowledged in contributing to the work described. Especially significant were the technical contributions of Dr. Lorimer Clayton and Mr. S. F. Hutchins of Scientific-Atlanta, Inc. throughout the program and the assistance of Mr. Bernard J. Geolat of McDonnell Aircraft Corp. in making the measurements.

## BIBLIOGRAPHY

1. Baker, B. B., and E. T. Copson, The Mathematical Theory of Huygen's Principle, Oxford University Press, London, 1950.
2. Beckmann, Petr, "Shadowing of Random Rough Surfaces," IEEE Transactions on Antennas and Propagation, Volume AP-13, No. 3, May 1965.
3. Beckmann, Petr, and Andre Spizzichino, The Scattering of Electro-Magnetic Waves from Rough Surfaces, The MacMillian Company, 1963.
4. Chastain, J., et.al., Investigation of Precision Antenna Pattern Recording and Display Techniques, Final Report, March 1963, AD415-912.
5. Clarke, R. H., and G. O. Hendry, "Prediction and Measurement of the Coherent and Incoherent Power Reflected from a Rough Surface," IEEE Transactions on Antennas and Propagation, Volume AP-12, No. 3, May 1964.
6. L. Clayton and J. S. Hollis, Antenna Polarization Analysis by Amplitude Measurement of Multiple Components, presented at the Thirteenth Annual Symposium on USAF Antenna Research and Development, University of Illinois, 15-18 October, 1963.
7. L. Clayton and J. S. Hollis, "Calculation of Microwave Antenna Radiation Patterns by the Fourier Integral Method," Microwave Journal, September 1960.
8. "Radar Requirements Report" (confidential) Grumman Aircraft Engineering Corp., LED-540-1, April 1963.
9. "Rendezvous Radar Antenna Location," Grumman Aircraft Engineering Corp., LMO-530-14, May 1963.
10. "Navigation and Guidance Subsystem, Rendezvous Radar/Transponder and Landing Radar Sections, Design Control Specification for" (confidential) Grumman Aircraft Engineering Corp., LSP-370-2A, November 1963.
11. "Summary of Design Review Meeting between Grumman Aircraft Engineering Corporation, Massachusetts Institute of Technology, North American Aviation - S and I. D., and National Aeronautics and Space Administration (Manned Spacecraft Center)" (confidential), LLR-530-4, August 1964.
12. "Analysis of Techniques For Determining Boresight Accuracy in the Fresnel and Fraunhofer Regions," Grumman Aircraft Engineering Corporation, RF-64-6, September 1964.

13. "Test Plan for Radar Antennas at NASA/MSC, Preliminary," Grumman Aircraft Engineering Corporation, LTP-370-203, February 1965.
14. "LEM-Facilities Plan - Apollo Requirements for the MSC RF Systems Test Facility at MILA, Florida -Preliminary," Grumman Aircraft Engineering Corporation, LPL-2-1B, March 1965.
15. "Lunar Excursion Module Familiarization Manual," Grumman Aircraft Engineering Corporation, LMA790-1, October 1965.
16. "Lunar Excursion Module: Proposed Test Plan for Radar Boresight Tests at NASA/MSC," Grumman Aircraft Engineering Corporation, LTP-372-203, January 1966.
17. Hollis, J. S., et. al., Investigation of Precision Antenna Pattern Recording and Display Techniques, Phase II, Final Report, Vol. I, Contract No. AF30(602)-3425, Project No. 4506, Task No. 45064, Report No. RADC-TR-65-534, AD630124.
18. IRIG Standard Coordinate System and Data Format for Antenna Patterns, Inter-Range Instrumentation Group, IRIG Document No. 102-61, AD266697, September 1961.
19. Jenkins, Francis A., and Harvey E. White, Fundamentals of Optics, McGraw-Hill Book Company, 1957.
20. Jordan, E. C., Electromagnetic Waves and Radiating Systems, Prentice-Hall Book Company, 1950.
21. Kerr, D.E., Propagation of Short Radio Waves, Radiation Laboratory Series, Vol. 13, McGraw-Hill Co., 1951.
22. Longhurst, R. S., Geometrical and Physical Optics, John Wiley and Sons, Ltd., 1964.
23. "Primary G and N System Lunar Orbit Operations," (confidential) Massachusetts Institute of Technology Instrumentation Laboratory, 25C 1064-739, April 1963.
24. Determination of Phase Centers and Amplitude Characteristics of Radiating Structures, Tech. Report No. 1, SR 1, Project 898, Stanford Res. Inst., Menlo Park, California, Contract DA04-200-ORD-273, AD68240; March 1965.
25. "LEM Second Quarterly Design Report, Rendezvous Radar/Transponder and Landing Radar," (confidential) Radio Corporation of America, LQR-(P)-3100-2, June 1964.
26. "Apollo Spacecraft Familiarization," North American Aviation, Inc., SM2A-02, December 1965.
27. Rossi, Bruno, Optics, Addison-Wesley Publishing Company, 1965.

28. V.H. Rumsey, G. A. Deschamps, M. L. Kales, and J. I. Bohnert, "Techniques for Handling Elliptically Polarized Waves with Special Reference to Antennas," Proceedings of the IRE 39 pp. 533-552 (1951); also the immediately following paper by M. G. Morgan and W. R. Evans, "Synthesis and Analysis of Elliptic Polarization Loci in Terms of Space-Quadrature Sinusoidal Components."
29. Silver, S., Microwave Antenna Theory and Design, Radiation Laboratory Series, Volume 12, McGraw-Hill Company, 1949.
30. Stratton, J. A., Electromagnetic Theory, McGraw-Hill Book Company, 1941.
31. Twersky, Victor, "On Scattering and Reflection of Electromagnetic Waves by Rough Surfaces," IRE Transactions on Antennas and Propagation, January 1957, pp. 81-90.
32. Twersky, Victor, "Signals, Scatterers, and Statistics," IEEE Transactions on Antennas and Propagation, November 1963, pp. 668-680.